

# Common Focus Point Technology

## **Proefschrift**

ter verkrijging van de graad van doctor  
aan de Technische Universiteit Delft,  
op gezag van de Rector Magnificus,  
Prof. dr. ir. J. Blaauwendraad  
in het openbaar te verdedigen  
ten overstaan van een commissie,  
door het College van Dekanen aangewezen,  
op dinsdag 21 januari 1997 te 10:30 uur

door

Jan Willem THORBECKE

mijnbouwkundig ingenieur  
geboren te Oostzaan

Dit proefschrift is goedgekeurd door de promotor:

Prof. dr. ir. A. J. Berkhou

Samenstelling promotiecommissie:

Rector Magnificus, voorzitter

Prof. dr. ir. A. J. Berkhou, (*TU-Delft, Technische Natuurkunde*), promotor

Prof. dr. ir. J. T. Fokkema, (*TU-Delft, Technische Aardwetenschappen*)

Prof. dr. ir. P. M. van den Berg, (*TU-Delft, Electrotechniek*)

Prof. dr. ir. I. T. Young, (*TU-Delft, Technische Natuurkunde*)

Prof. dr. J. C. Mondt, (*U-Utrecht, Aardwetenschappen*)

Dr. ir. C. P. A. Wapenaar, (*TU-Delft, Technische Natuurkunde*)

Dr. ir. W. E. A. Rietveld, (*Amoco, Exploration and Production Technology Group*)

ISBN 90-9010-123-3

Copyright ©1997, by J. W. Thorbecke, Laboratory of Seismics and Acoustics. Faculty of Applied Physics, Delft University of Technology, Delft, The Netherlands.

All rights reserved. No part of this publication may be reproduced, stored in a retrieval system or transmitted in any form or by any means, electronic, mechanical, photocopying, recording or otherwise, without the prior written permission of the author J. W. Thorbecke, Faculty of Applied Physics, Delft University of Technology, P.O. Box 5046, 2600 GA Delft, The Netherlands.

#### SUPPORT

The research for this thesis has been financially supported by the DELPHI consortium.

Typesetting system: L<sup>A</sup>T<sub>E</sub>X2e

Cover: 'combined snapshots from one point source'

Printed in The Netherlands by: Beeld en Grafisch Centrum Technische Universiteit Delft.

*'Alles komt voort uit de chaos', wordt er in de Griekse Anthologie gezegd. En inderdaad, alles komt voort uit de chaos. Buiten de wiskunde, die enkel met dode getallen en loze formules te maken heeft en derhalve volmaakt logisch kan zijn, is de wetenschap niet meer dan een kinderspel in de schemering, het willen vangen van vogelschaduwen en het willen tegenhouden van de schaduw van gras dat waait in de wind. (290 [479], Pessoa (1990))*



## Preface

---

In January 1991 I finished my MSc project, which was supervised by professor Fokkema and professor Van Den Berg, at the department of applied Earth Sciences. During the MSc project professor Fokkema showed me the good things of seismic research. At the end of the academic year, August 1991, professor Fokkema introduced me to the group of professor Berkhouw where I could begin a PhD study within the DELPHI project. Research in the Geophysical context was something I started to like a lot and working in a team was also an important reason for starting my PhD project in the group of professor Berkhouw. The subject of my PhD project was initially set up to investigate the combination of elastic wavefield decomposition and weathered layer influences. In the first year it became clear that correct estimation of the propagation properties of the weathered layer is very important for the decomposition and all the further processing steps. Therefore the subject of my research changed to weathered layer estimation, using the areal shot record technology. An important side-off project of these first years was an optimization technique I used to construct the decomposition operators. This technique is also very successful for the optimization of extrapolation operators. During my work with areal shot records the areal shot record designed for one point in the subsurface turned out to be a very useful intermediate step for imaging and velocity analysis. So finally the subject changed for the last time to Common Focus Point technology the main subject of this thesis. The last 2 years I have been working intensively on this subject and the results can be found back in this thesis. Note that although it seems that I have been doing a lot of other things besides the main subject of this thesis, all the things I have done before helped me to understand the main geophysical problems and gave me a broad overview.

During the past 5 years I have learned a lot from professor Berkhouw, Kees Wapenaar and Eric Verschuur, who are the driving forces behind the DELPHI research team. The discussions I have had with my fellow PhD students were always stimulating and very useful for understanding the practical implications of the theory. The DELPHI consortium, which is sponsored by the oil and computer industry, reports twice a year the research results at the so called sponsor-meetings. Once a year a book,

with the latest scientific results, is published for the sponsors. At first I found it difficult to give oral presentations at the sponsor meetings, but during the years I have learned how to give a presentation and in the last year I hope the sponsors could follow what I was saying. At this point I wish to thank the participating companies for making the research within DELPHI possible, and for their interest and comments they gave at the sponsor meetings.

There are many people who have helped me in the last 5 years. First of all I would like to thank my promoter, professor Berkhouwt, for supervising this thesis, his enthusiasm about the subject and his stimulating ideas. The comments and suggestions Kees Wapenaar gave me during the years, especially for the theoretical part of this thesis, have been very useful and gave the theoretic parts its clear structure. Eric Verschuur always knew the answers to all my questions, and independent of the subject the answer was always useful.

Beside all the new knowledge about geophysics I've also learned how to work in a team. My colleagues of the first year Greg, Cees and Erwin helped me starting my research. Walter learned me everything, I always wanted to know, about areal shot record technology and showed me how to make up reasons for not running during lunch-time. I also would like to thank Aart-Jan, Frederic and all the incidental 'runners' for running with me during lunch-time. I'm thankful for the patience of Nurul, and all the other students who have worked with my programs, with the build in features/bugs of my programs. During the years Riaz became a very good friend and we have had a lot of good times together. The boys of next door Felix, Frank and Wim are remembered for being very quiet neighbors. I will miss Felix for letting me know the latest news on the wave-equation, and Frank for providing the running group with sun-milk during the run.

Without the system management of JWdB, Leen, Edo and Henry a lot of work couldn't be done at all. JWdB and Felix introduced NEXTSTEP into the group, which resulted in an important improvement in the development of applications and state of the art pictures. Although Alexander is not a part of the system management I will never forget his famous Unix scripts and his willingness to help to get the system up again, after a serious crash. I also would like to thank Bart and Scott of Cray Research in Eagan for offering me a great job at Cray Research / Silicon Graphics. I wish the new PhD students the same good time I have had in the DELPHI team, specially the never ending good weeks during the sponsor meetings and geophysical congresses.

The last months, while I was writing this thesis, my family and Roos kept me on the right track and helped me remembering that there are more things to life than writing a thesis.

# Contents

---

<b>Preface</b>	<b>v</b>
<b>Notation and Terminology</b>	<b>ix</b>
<b>1 Introduction</b>	<b>1</b>
1.1 The importance of imaging . . . . .	1
1.2 The forward model . . . . .	3
1.3 Outline of this thesis . . . . .	4
<b>2 Migration: an overview</b>	<b>5</b>
2.1 Isochrone summation . . . . .	5
2.2 Finite difference . . . . .	7
2.3 Kirchhoff summation . . . . .	9
2.4 Migration in terms of deconvolution . . . . .	13
2.5 Inverse scattering . . . . .	15
2.6 Summary . . . . .	16
<b>3 Two-way and one-way representations</b>	<b>19</b>
3.1 Reciprocity theorems . . . . .	19
3.1.1 Reciprocity theorem for two-way wavefields . . . . .	20
3.1.2 Reciprocity theorem for one-way wavefields . . . . .	21
3.2 Integral representations for two-way wavefields . . . . .	25
3.3 Integral representations for one-way wavefields . . . . .	28
3.4 The <b>WRW</b> model in matrix notation . . . . .	35

<b>4 Imaging by double focusing</b>	<b>39</b>
4.1 Inverse scattering problem . . . . .	39
4.2 Two-way representation of double focusing; full aperture . . . . .	41
4.3 Two-way representation of double focusing; seismic aperture . . . . .	44
4.4 One-way representation of double focusing . . . . .	45
4.4.1 Integral representation . . . . .	46
4.4.2 Matrix representation . . . . .	49
<b>5 CFP technology</b>	<b>53</b>
5.1 Areal shot record technology . . . . .	53
5.2 First focusing step . . . . .	55
5.2.1 Huygens-Fresnel principle . . . . .	57
5.2.2 Construction of CFP trace: dipping layer . . . . .	59
5.2.3 Construction of CFP gathers: synclinal model . . . . .	65
5.2.4 Focusing in emission and focusing in detection . . . . .	70
5.3 Second focusing step . . . . .	71
5.3.1 One-way image ray . . . . .	73
5.3.2 Positioning of the double focusing result . . . . .	74
5.3.3 CFP image-gather . . . . .	78
5.3.4 One-way time image . . . . .	79
5.4 Resolution and amplitude analysis . . . . .	83
5.4.1 Resolution and focusing beams . . . . .	83
5.4.2 Amplitude analysis . . . . .	87
5.5 3-Dimensional CFP gathers . . . . .	91
5.5.1 Common offset contributions in 2-dimensional synthesis . . . . .	91
5.5.2 A simple 3D data example . . . . .	94
5.5.3 Regularization of coarsely sampled data . . . . .	100
5.6 New developments . . . . .	103
<b>6 Operator updating</b>	<b>105</b>
6.1 First focusing step . . . . .	107
6.2 Searching for updating formulas for a flat reflector . . . . .	111
6.2.1 Zero depth and zero velocity error ( $\Delta z = 0$ and $\Delta c = 0$ ) . . . . .	113

---

6.2.2	Depth errors ( $\Delta z \neq 0$ and $\Delta c = 0$ ) . . . . .	114
6.2.3	Velocity errors ( $\Delta z = 0$ and $\Delta c \neq 0$ ) . . . . .	115
6.2.4	CFP corrected shot record . . . . .	115
6.2.5	Move-out corrected CFP gather . . . . .	117
6.3	Operator updating . . . . .	121
6.3.1	Flat reflector . . . . .	122
6.3.2	Dipping reflector . . . . .	127
6.4	Second focusing step . . . . .	132
<b>7</b>	<b>Numerical data examples</b>	<b>137</b>
7.1	Diffraction point . . . . .	137
7.2	One dimensional multi layer model . . . . .	140
7.3	'Void' model . . . . .	145
7.4	Weathered layer model . . . . .	148
7.5	Syncline model . . . . .	152
7.6	Comparison of imaging results for realistic numerical data . . . . .	154
7.6.1	Marmousi model . . . . .	154
7.6.2	SEG/EAGE salt dome model . . . . .	162
<b>8</b>	<b>Field data examples</b>	<b>167</b>
8.1	Mobil . . . . .	167
8.2	ELF . . . . .	177
<b>A</b>	<b>Operator optimization</b>	<b>185</b>
A.1	1-Dimensional operators for 2-dimensional extrapolation . . . . .	185
A.1.1	Analytical space-frequency operators . . . . .	186
A.1.2	From wavenumber domain to spatial convolution operators . .	188
A.1.3	Recursive depth migration . . . . .	198
A.2	2-Dimensional operators for 3-dimensional extrapolation . . . . .	205
A.2.1	Direct method . . . . .	207
A.2.2	McClellan transformation, expansion in $\cos(k_r)$ . . . . .	227
A.2.3	Expansion in $k_z$ . . . . .	242
A.2.4	Expansion in $k_x^2 + k_y^2$ . . . . .	250

A.2.5	Computation times . . . . .	256
A.2.6	Concluding remarks . . . . .	258
<b>B</b>	<b>Matrix notation</b>	<b>263</b>
B.1	2-Dimensional wavefields . . . . .	263
B.2	3-Dimensional wavefields . . . . .	266
<b>C</b>	<b>Algorithms</b>	<b>269</b>
C.1	Processing flow . . . . .	269
C.2	Time- and Frequency-domain processing . . . . .	270
C.3	Numerical implementation (time-domain) . . . . .	272
	<b>Bibliography</b>	<b>277</b>
	<b>Summary</b>	<b>287</b>
	<b>Samenvatting</b>	<b>289</b>
	<b>Curriculum vitae</b>	<b>291</b>

## Notation and terminology

---

The subscript notation for Cartesian vectors and tensors is used. Lower case Latin subscripts  $\{k, l, p, q\}$  are assigned to the values 1, 2 and 3 and lower case Greek subscripts  $\{\alpha, \beta\}$  are assigned to the values 1 and 2. The summation convention applies to repeated subscripts (e.g.  $a_k b_k$  stands for  $\sum_{k=1}^3 a_k b_k$ ). Differentiation of a function with respect to time is denoted as  $\partial_t h_k$ , which stands for  $\{\partial_t h_1, \partial_t h_2, \partial_t h_3\}$ . Differentiation of a vector with respect to the spatial coordinates is denoted as  $\partial_k h_l$  and is the shorthand notation for  $\{\{\partial_1 h_1, \partial_1 h_2, \partial_1 h_3\}, \{\partial_2 h_1, \partial_2 h_2, \partial_2 h_3\}, \{\partial_3 h_1, \partial_3 h_2, \partial_3 h_3\}\}$ . The gradient of a scalar function is written as  $\partial_k \phi$  which stands for  $\{\partial_1 \phi, \partial_2 \phi, \partial_3 \phi\}$ , the divergence of a vector function is notated as  $\partial_k h_k$ . To register a position in space a Cartesian reference frame with an origin  $O$  and three mutually perpendicular base vectors  $\{\mathbf{i}_1, \mathbf{i}_2, \mathbf{i}_3\}$  of unit length is used.

Functions in the space-time domain are denoted by a lower case symbol,  $f(\mathbf{x}, t)$ . The corresponding function in the space-frequency domain are denoted by a upper case symbol  $F(\mathbf{x}, \omega)$ . Functions in the wavenumber-frequency domain have a tilde above their symbol  $\tilde{F}(k_\alpha, \omega)$ . Matrices are denoted in the space-time domain by a bold lower case symbol  $\mathbf{p}$ , in the space-frequency domain by a bold upper case symbol  $\mathbf{P}$  and in the wavenumber frequency domain a tilde above the symbol is used  $\tilde{\mathbf{P}}$ . Vectors are in bold italic fashion  $\mathbf{p}, \mathbf{P}, \tilde{\mathbf{P}}$ . For discrete matrices and discrete vectors sans-serif fonts are used. These notation conventions are summarized in the table given below. Note that there is no difference between an operator in the time-domain and an operator in the frequency domain. However, by looking at the function where the operator is working on, the domain can be derived.

With the above definitions an operator  $\mathcal{L}$  working on the function  $u$  can be represented by the convolution integral

$$\mathcal{L}(x)u(x) = \int_{x_0}^{x_1} L(x, x')u(x')dx'.$$

In discrete notation the integral is replaced by a summation and can be written in

symbol	$x_k - t$	$x_k - \omega$	$k_\alpha, x_3 - \omega$
function	$f(x_k, t)$	$F(x_k, \omega)$	$\tilde{F}(k_\alpha, x_3, \omega)$
vector	$\mathbf{p}$	$\mathbf{P}$	$\tilde{\mathbf{P}}$
matrix	$\mathbf{p}$	$\mathbf{P}$	$\tilde{\mathbf{P}}$
operator	$\mathcal{L}$	$\mathcal{L}$	$\tilde{\mathcal{L}}$
discrete vector	$\mathbf{p}$	$\mathbf{P}$	$\tilde{\mathbf{P}}$
discrete matrix	$\mathbf{p}$	$\mathbf{P}$	$\tilde{\mathbf{P}}$
discrete operator	$\mathbf{L}$	$\mathbf{L}$	$\tilde{\mathbf{L}}$

a matrix vector multiplication given by

$$\mathbf{L}\mathbf{u} = \begin{bmatrix} L_{0,0} & \dots & L_{0,M} \\ \vdots & \ddots & \vdots \\ L_{N,0} & \dots & L_{N,M} \end{bmatrix} \begin{bmatrix} u_0 \\ \vdots \\ u_M \end{bmatrix}.$$

Note that matrices which represent discrete operators or wave fields are written with square [ ] brackets. Matrices with continuous operator kernels are written with normal ( ) brackets

The temporal Fourier transformation from the space-time domain to the space-frequency domain is defined as (Bracewell, 1986)

$$F(\mathbf{x}, \omega) = \int_{-\infty}^{\infty} f(\mathbf{x}, t) \exp(-j\omega t) dt$$

and its inverse as

$$f(\mathbf{x}, t) = \frac{1}{\pi} \Re \left\{ \int_0^{\infty} F(\mathbf{x}, \omega) \exp(j\omega t) d\omega \right\}$$

where  $\Re$  stands for the Real part. The 2-dimensional spatial Fourier transformation from the space-frequency to the wavenumber-frequency domain is defined as

$$\tilde{F}(k_\alpha, \omega) = \iint_{-\infty}^{+\infty} F(x_\alpha, \omega) \exp(jk_\alpha x_\alpha) d^2 x_\alpha$$

and its inverse as

$$F(x_\alpha, \omega) = \left( \frac{1}{2\pi} \right)^2 \iint_{-\infty}^{+\infty} \tilde{F}(k_\alpha, \omega) \exp(-jk_\alpha x_\alpha) d^2 k_\alpha$$

The transpose of a matrix (or vector) is denoted with a superscript  $T$ , the complex conjugate with a superscript  $*$  and the complex conjugate transpose with superscript  $H$  so

$$\mathbf{P} = \begin{pmatrix} P_1 \\ P_2 \\ \vdots \\ P_n \end{pmatrix} \quad \mathbf{P}^* = \begin{pmatrix} P_1^* \\ P_2^* \\ \vdots \\ P_n^* \end{pmatrix}$$

$$\mathbf{P}^T = (P_1 \ P_2 \ \dots \ P_n)$$

$$\mathbf{P}^H = (P_1^* \ P_2^* \ \dots \ P_n)$$

## Terminology

The new concepts used in the CFP approach has led to a number of new terms which are explained below.

- **focusing operator**

Convolution operator working in the time domain on pre-stack seismic data. The operator represents the response of a point in the subsurface measured at the surface and works on the traces in a common detector gather or a common shot gather. Summation over the resulting traces in the gather defines one trace of a CFP gather.

- **focusing in detection**

Result of the focusing operator working on a common shot gather. The result can be interpreted as the measurement of an areal receiver positioned at the focus point in the subsurface, which is related to the focusing operator, and the source position of the used common shot gather.

- **focusing in emission**

Result of the focusing operator working on a common receiver gather. The result can be interpreted as the response of an areal source positioned at the focus point in the subsurface, which is related to the focusing operator, and the receiver position of the used common receiver gather.

- **common focus point (CFP) gather**

The multi-offset response of the subsurface due to a focusing areal source. For focusing in detection the measurements are generated by individual sources with different positions at the surface. For focusing in emission the response is registered by individual receivers with different positions at the surface.

- **focus point response**

The coherent event in a CFP gather, that represents the reflection response from the involved focus point. For a correct macro model the traveltimes defined by the operator and the focus point response are equal ('principle of equal traveltime').

- **one-way offset**

The lateral distance between the position of the focus point and the position of a trace in the CFP gather.

- **one-way image time**

The time defined by the one-way zero-offset trace in the focusing operator.

- **one-way move-out**

Difference in traveltime between the one-way image time and the times given by the focus point response.

- **CFP image condition**

The imaging condition in the CFP method states that a reflection area exists within the earth when the traveltime of the wavefront of the downward continued wavefield is the same as the traveltime of the wavefront of the downward incident wavefield for all offsets.

- **one-way image gather or CFP image gather**

The one-way image gather is constructed of time windows selected from move-out corrected CFP gathers. The CFP gathers used to construct the image gather have their focus points defined at the same lateral position in the model, but at different depth (or time) levels. The lateral position of the image gather is the same as the position of the focus points used to construct the image. Note that the image trace is constructed by a summation over the traces in the image gather and is defined in one-way image time or in depth.

- **CFP corrected shot record**

The CFP corrected shot record is the result of the common shot gather after temporal convolution with the focusing operator but before summation over the traces in the gather. In this corrected shot record the Fresnel zone can be observed.

**Table of notation**

$\{\mathbf{i}_1, \mathbf{i}_2, \mathbf{i}_3\}$	= the basis vectors in 3-dimensional Euclidean space
$\{x_1, x_2, x_3\}$	= $\{x, y, z\}$ = orthogonal Cartesian coordinates
$\mathbf{x} = x_1\mathbf{i}_1 + x_2\mathbf{i}_2 + x_3\mathbf{i}_3$	= vectorial position
$D$	= some bounded domain in 3-dimensional Euclidean space
$d^3\mathbf{x}$	= elementary volume in 3-dimensional Euclidean space
$\partial D$	= the boundary of $D$
$d^2\mathbf{x}$	= elementary area of $\partial D$
$\lambda$	= wavelength [m]
$\delta(\mathbf{x})$	= spatial delta function
$H(x_3)$	= Heaviside step function
$\chi(\mathbf{x}) = \begin{cases} 1, & \text{if } \mathbf{x} \in D \\ \frac{1}{2}, & \text{if } \mathbf{x} \in \partial D \\ 0, & \text{if } \mathbf{x} \in \mathbb{R}^3 \setminus (D \cup \partial D) \end{cases}$	; characteristic function
$a^\circ$	= indicating a dip of 'a' degrees
$\mathbf{P}(z_r, z_s)$	= matrix representation of seismic data (see Appendix C)
$z_r$	= receiver level, in general a function of $x_k$
$z_s$	= source level, in general a function of $x_k$
$\rho$	= the volume density of mass [kg/m <sup>3</sup> ]
$\kappa$	= the compressibility [Pa <sup>-1</sup> = m <sup>2</sup> /N]
$\mathbf{W}^+(z_m, z_0)$	= extrapolation of downgoing wavefields from $z_0$ to $z_m$
$\mathbf{W}^-(z_0, z_m)$	= extrapolation of upgoing wavefields from $z_m$ to $z_0$
$\mathbf{F}^+(z_0, z_m)$	= inverse extrapolation of downgoing wavefields from $z_m$ to $z_0$
	$= [\mathbf{W}^+(z_m, z_0)]^{-1} \approx [\mathbf{W}^-(z_0, z_m)]^*$
$\mathbf{F}^-(z_m, z_0)$	= inverse extrapolation of upgoing wavefields from $z_0$ to $z_m$
	$= [\mathbf{W}^-(z_0, z_m)]^{-1} \approx [\mathbf{W}^+(z_m, z_0)]^*$
$\mathbf{W}^+(z_m, z_0)$	$= [\mathbf{W}^-(z_0, z_m)]^T$
$\mathbf{F}^-(z_m, z_0)$	$= [\mathbf{F}^+(z_0, z_m)]^T$
$\mathbf{R}^+(z_m)$	= matrix representation of reflection operator
$\mathbf{F}_i^-(z_m, z_r)$	= operator for focusing in detection at focal point $\mathbf{x} = \{(x, y)_i, z_m\}$
$\mathbf{F}_j^+(z_s, z_m)$	= operator for focusing in emission at focal point $\mathbf{x} = \{(x, y)_j, z_m\}$
$\mathbf{P}_i^-(z_m, z_s)$	= CFP gather for focusing in detection
$\mathbf{P}_j(z_r, z_m)$	= CFP gather for focusing in emission





# Chapter 1

---

## Introduction

The seismic method is based on measurements from detectors placed at the surface, or in the subsurface, of the earth. The detectors measure the wavefield originating from a source which is positioned at or close to the surface. In figure 1.1 three types of seismic experiments are shown: a marine, land and borehole. In the marine and land configuration a part of the energy emitted by the source travels *along* the surface of the earth directly to the receivers. This wave is called the direct or surface wave. The surface wave contains information about the layers close to the surface of the earth. However, the aim in seismic processing lies in the detection of the structure of the deeper layers (subsurface). Besides the surface wave the source also transmits waves *into* the subsurface, called the body waves. Due to contrasts in the subsurface a downward propagating body wave gets reflected and propagates back towards the surface where it can be measured by the detectors. These reflected wavefields contain the information the geophysicist is interested in. The goal of the geophysicist is to derive from these reflections an accurate image of the subsurface of the earth. The technique to translate the measurements at the surface (called shot records) into a structural representation of the subsurface is called imaging or migration. For a good structural image a large number of shot records is needed, where for every shot record the source and receivers are placed at another position at the surface.

### 1.1 The importance of imaging

In the left-hand side picture of figure 1.2a a raw shot record is shown. This shot record contains the surface related waves and the body waves. For the construction of an image the surface waves are not directly needed and can be removed from the raw shot record. Besides the primary reflections of the layer boundaries, the shot record also contains reflections from the surface of the earth. These waves are called surface related multiples and have travelled more than one time through

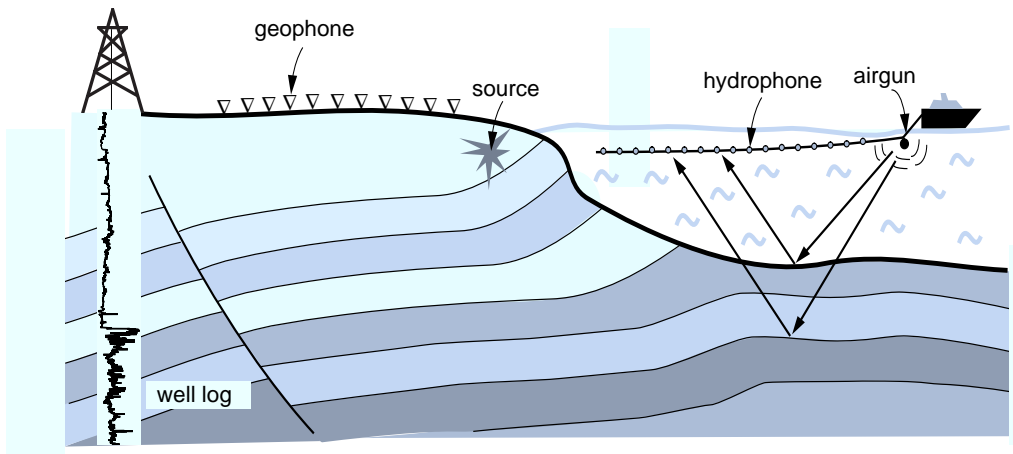


**Figure 1.1** Three types of seismic data acquisition; (1) acquisition at sea where hydrophones are used to measure the response (pressure) from an airgun array near the surface, (2) acquisition on land where geophones are used to measure the response (particle velocity in 3-directions) from a source in the surface, (3) acquisition in a borehole where geophones or hydrophones are mounted on a cable (which is lowered in the borehole) to measure the response from a source at the surface.

the subsurface of the earth. These surface related multiples can distort the image quality significantly and must be removed from the data. After these pre-processing steps the resulting shot record is shown in figure 1.2. From this figure the primary reflections from the subsurface are better visible. However, it is still not clear where in the subsurface these reflections are actually originating from. By making use of an imaging technique the time traces of all pre-processed shot records are transformed into depth traces. For this process a macro model of the earth is needed. This macro model describes the *propagation* properties of the earth, in particular with respect to traveltimes. After the imaging step a geologist can interpret the result and identify the structures and layers in the subsurface of the earth. This interpretation can, for example, be used to make a decision about the position of a future borehole.

If an error has been made in the imaging procedure the structural image, and the interpretation based on it, will be wrong and the borehole may miss its target. Therefore, an error analysis of the quality of the image is very important. Unfortunately, this error analysis can only be carried out successfully if one knows the correct answer, which is equal to the goal of seismic imaging. In this thesis a novel imaging technique is proposed in which the error analysis is carried out in an *intermediate* domain where the operators, used to construct the image, are compared with the 'half image'. Based on this comparison the macro model of the earth or, even better, the operators themselves can be updated. The proposed imaging technique makes use of a double focusing procedure in which the result after one focusing step, the so

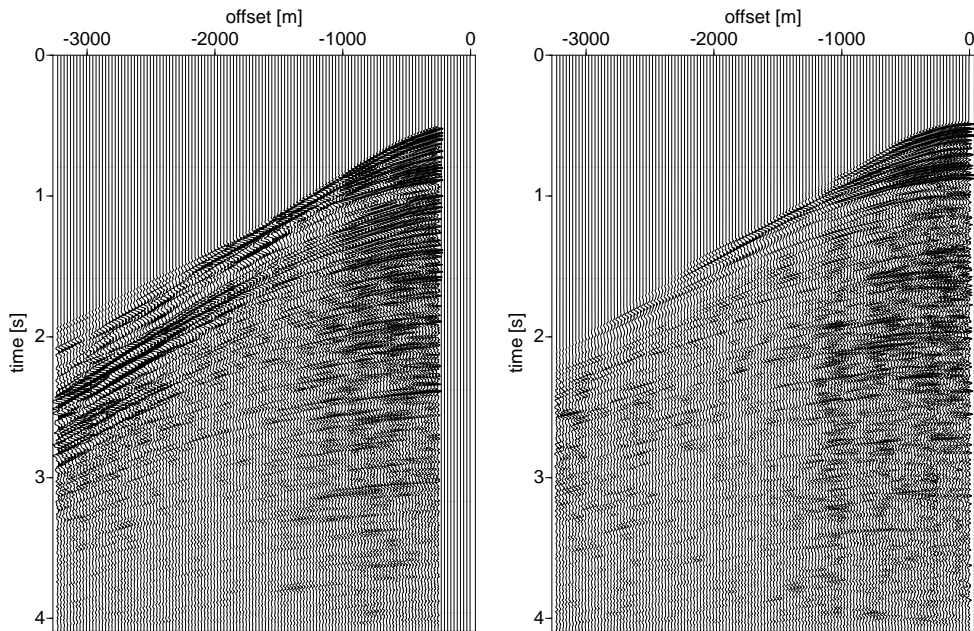


**Figure 1.2** Seismic shot record for a marine acquisition before pre-processing (left) and after pre-processing (right). In the pre-processing step the direct waves and the multiple reflections from the sea surface are removed.

called Common Focus Point (CFP) gather, plays an important role. The theoretical frame work, where the proposed imaging technique is developed in, is the systems oriented **WRW** model (Berkhout, 1982).

## 1.2 The forward model

To describe the seismic experiment in mathematical and physical terms a forward model is needed. The forward model used in this thesis is shown in figure 1.3. The top part of figure 1.3 shows the model used in the imaging, the bottom box of figure 1.3 represents the lithologic inversion. In imaging the aim is to estimate the reflectivity operator  $\mathbf{R}$  by removing the propagation parts  $\mathbf{W}^+, \mathbf{W}^-$  and the surface related effects  $\mathbf{D}^+, \mathbf{D}^-$ . In lithologic inversion the aim is to estimate the rock type e.g. a sand or a shale layer. The connection between the imaging model and the lithological model is the angle dependent reflection property of the layer. In the imaging technique proposed in this thesis the reflection property can be determined in a straightforward way. The different boxes shown in the forward model for the imaging part will become clear in the remainder of this thesis. For the lithologic inversion part the reader is referred the thesis of de Bruin (1992).

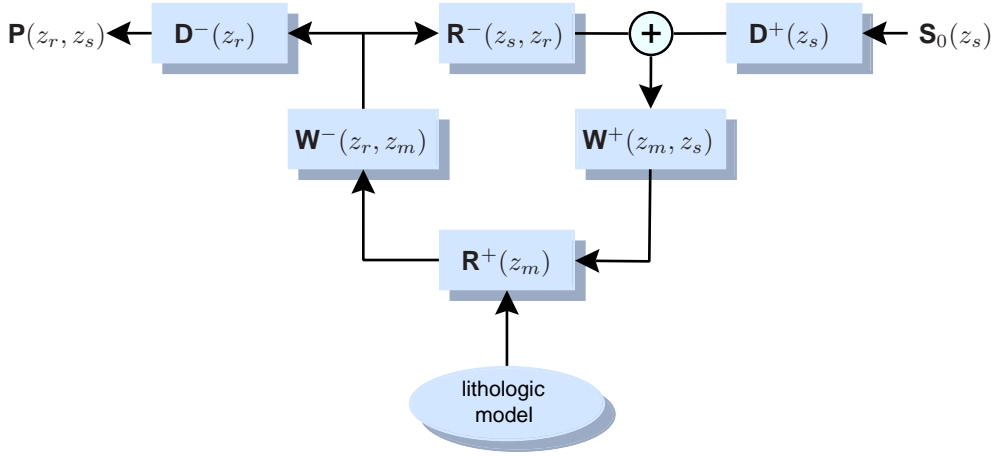


**Figure 1.3** Full WRW forward modeling scheme for seismic data. The connection with the lithologic model is made by the reflection matrix.

### 1.3 Outline of this thesis

Chapter 2 of the thesis starts with a historical overview of seismic imaging to provide a historical context of the seismic imaging technique presented. The forward model used to derive the double focusing procedure is explained in chapter 3. Starting from the one-way and two-way acoustic reciprocity relations integral and matrix representations of seismic data are derived from which the forward model is constructed. Based on the same representations the double focusing procedure is introduced in chapter 4 and explained for one-way and two-way wavefields. At the end of chapter 4 the matrix notation of the double focusing technique is presented. The theory presented in chapter 3 and 4 is illustrated with numerical experiments in chapter 5. For those readers who want to skip the theoretical chapters, chapter 5 is a good starting point to get an understanding of the possibilities of the Common Focus Point technology. The influence of erroneous focusing operators and the updating of the operators is explained with simple numerical examples in chapter 6. Results on numerical modeled data can be found in chapter 7 and results for field data can be found in chapter 8. The numerical data examples are used to show the strength and weakness of the double focusing method. The results obtained with field data are compared with results obtained with other imaging methods.

Appendix A gives an extensive overview of methods to construct extrapolation operators (2D and 3D) for explicit recursive depth extrapolation. The resulting operators are used in an extrapolation algorithm to construct focusing operators in complex subsurfaces. Appendix B explains the matrix notation used in this thesis and appendix C discusses the numerical schemes of the CFP technology. On page ix an overview is given of the notation conventions and definitions used in this thesis. At the end of the thesis a summary is given with the most important conclusions



## Chapter 2

### Migration: an overview

The purpose of this chapter is to provide a historical context of the seismic imaging (migration) technique. It is impossible to give a complete overview of the seismic migration theory in this chapter. Hence, only those parts of the migration history are discussed which will contribute to the understanding of the theory presented. In this chapter the main periods of the migration history are briefly discussed: in a first period the concepts of migration are developed by making use of graphical methods, in the second important period the idea of reflector mapping is introduced and in the last main period computation intensive wave equation based methods for 3-dimensional data are used for imaging<sup>1</sup>. This chapter does not include an overview of the wide range of migration based velocity or macro model estimation techniques. This absence does not mean that the importance of velocity estimation is underestimated; without a good velocity model every depth imaging method will break down.

Migration is the technique used to transform the wavefield of a (stacked) seismic section into a reflectivity image. The migration process influences the position of the reflectors as well as the resolution property along the reflectors. For most migration methods the wave equation is assumed to be the mathematical description of wave propagation in the earth's subsurface.

#### 2.1 Isochrone summation

The earliest migration techniques were graphical and based on geometrical ideas developed systematically by Hagedoorn (1954). Hagedoorn describes migration in terms of propagating wavefronts and tries to avoid the use of non-physical ray paths. Hagedoorn argues that within the seismic frequency band it is impossible to speak of rays in a physical sense of narrow beams. The principle of Huygens-Fresnel,

<sup>1</sup>For a complete overview of migration up to 1985 the collection of reprints of Gardner (1985) is recommended.

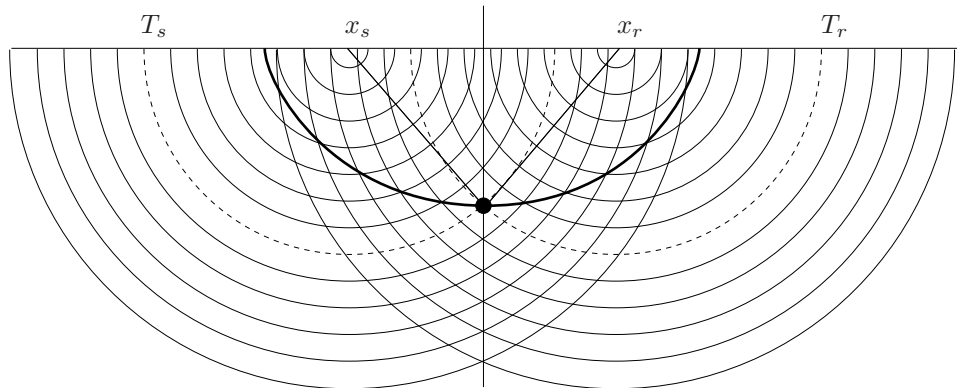


**Figure 2.1** A single source receiver combination defines for every reflection time a surface of equal traveltimes. The vertically plotted point at the surface of equal traveltimes in the middle between source and receiver is used to determine a surface of equal reflection times.

explained in more detail in chapter 5, shows that the beam between source and receiver is at least a half wavelength wide. Therefore it is conceptually better to work with propagating wavefronts than with rays; the ray can be considered as a mathematical abstraction defined as the line perpendicular to the wavefront at each intermediate time. Seismic waves exhibit real diffraction phenomena such as bending around obstacles as well as focusing associated with transmission and reflection from curved interfaces. These phenomena cannot be described correctly by making use of ray-paths. According to Hagedoorn the aim of migration is to position the reflected energy from the wavefront measured at the surface at its correct position in the subsurface. From one reflection arrival time, belonging to a source receiver combination, a so called surface of equal reflection time can be constructed. In figure 2.1 a set of wavefronts, centered at the source position  $x_s$  and the receiver position  $x_r$ , is shown. A reflection time of  $2T$  [s] observed at  $x_r$  can originate from any point on the surface (in a 3-dimensional sense) of equal traveltime consisting of lines of intersection between wavefront surfaces  $T+t$  [s] from  $x_s$  with wavefront surfaces  $T-t$  [s] from  $x_r$ , which is indicated by the thick line in figure 2.1.

So the position of the reflector is not yet known from one single observation, but the surface of equal reflection times is known to be tangential to the actual reflector at some point in space. It is convenient to represent the surface of equal reflection time by one point on it, normally the Common Mid Point (CMP) between source and receiver is chosen as 'reference' point to describe the surface of equal reflection time. This vertically plotted point has no other significance than that of being one point determining a surface of equal reflection times.

Hagedoorn (1954) defined migration as "the procedure of determining the true re-

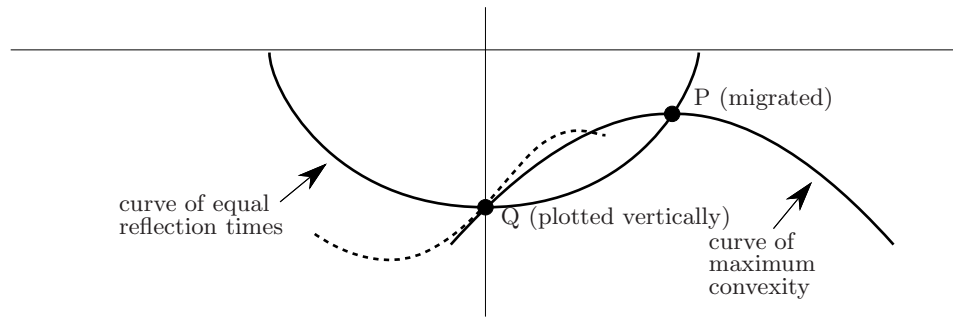


**Figure 2.2** 2-Dimensional graphical procedure to obtain from the curve of equal reflection times and the curve of maximum convexity the migrated position ( $P$ ). The dotted line represents the vertically plotted horizon through  $Q$ .

fecting surface from a surface determined by a number of vertically plotted points". This true surface can be found, in principle, as the envelope to all surfaces of equal reflection time determined by the vertically plotted points of different source receiver combinations. The apparent horizon of several vertically plotted points form a surface of maximum convexity for the reflector. By using these two surfaces, the vertically plotted points and the surface of equal traveltimes, the migration can be carried out in a graphical manner as shown in figure 2.2. In figure 2.2 a chart of curves of equal reflection times is centered on the vertical around  $Q$  and the chart of curves of maximum convexity is moved until the best tangential fit to the vertically plotted horizon at  $Q$  is obtained. Both the traveltimes curves and the maximum convexity curves are based on a (1-dimensional) background model. For any other velocity distribution a new set of charts should be calculated. This method of Hagedoorn (1954) is a graphical procedure where the computer was used to generate the wavefront charts. The surface of maximum convexity (also called Huygens surface) is the 'kinematic image' in the time domain of a point in the depth domain. The surface of equal reflection time (isochrone), on the other hand, is the 'kinematic image' in the depth domain of a point in the time domain (Hubral et al., 1996).

## 2.2 Finite difference

Given waves observed along the earth's surface it is possible, by using some mathematical techniques, to extrapolate these waves into the earth. In this approach the migration process progressively transforms the wavefield measured at the earth's surface into wavefield's that would be observed at progressively increasing depths. This so called inverse extrapolation technique transforms the measured wavefield to virtual receivers on a depth closer to the reflector(s). The basic idea behind it is that the best measurement of any reflector is when the receivers are placed just above the reflector. These extrapolated wavefields are not yet the migrated section, therefore

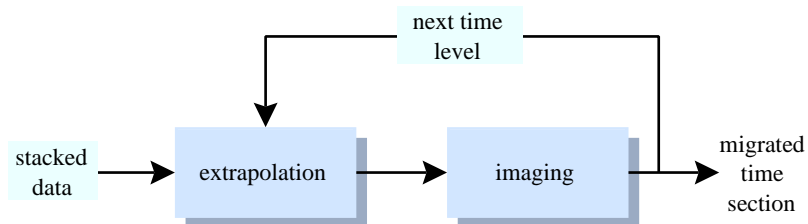


**Figure 2.3** Migration can be considered as the results of two steps; extrapolation and imaging.

an additional imaging step is needed. The imaging principle most seismic imaging methods use are based on the basic principle of reflector mapping introduced by Claerbout (1971). By backpropagating the scattered field from the (combination of) receiver array(s) into the background medium the reflected wavefield is reconstructed in the medium. To image this backpropagated field at every point in the medium the extrapolated field is correlated with the forward extrapolated incident wavefield. This incident wavefield is the solution of the forward problem in the background medium and is obtained by placing a (combination of) source(s) at the surface. If the background model (macro model) is correct then at every reflector the upward reflected field should be equal to the downward source wavefield multiplied with the reflection coefficient. A correlation between the reflected field and the incident field images the reflector at zero-time. So "reflectors exist at points in the earth where the first arrival of the downgoing wave is time coincident with an upgoing wave". In the method of Claerbout implicit use is made of one-way wave propagation through inhomogeneous media. In this one-way wave method only the transmitted field is assumed to be of importance, by assuming that the earth is only weakly inhomogeneous and therefore only a small fraction of the total energy applied at the surface returns to it. The internal multiple reflections are also neglected resulting in an image result with less interference effects from these multiples (see also Berkhou and Wapenaar, 1989).

In this approach seismic migration is considered as an acoustic image reconstruction technique which makes use of two steps as shown in figure 2.3;

- wavefield extrapolation, to simulate registrations at other depth levels
- imaging, to image the extrapolated wavefield

To calculate the incident wavefield and the backpropagated reflected wavefield at all different depth levels of interest several wavefield extrapolation techniques have been introduced. The finite difference method, introduced by Claerbout (1971), uses a discretized version of the wave equation with a floating time reference. The disadvantages of the proposed finite difference implementations are the time domain approach ('time migration') and the small extrapolation angles (typically  $15 - 45^\circ$ ).

In the well-known stacking procedure the traces in the shot records are combined to Common Mid Point (CMP) sections and corrected for the source-receiver geometrical effects (called the Normal Move Out (NMO) correction). Note that the described stacking procedure means that the vertically plotted points of Hagedoorn (1954) are combined into one trace for several source receiver combinations with the same mid point. The process of stacking is also used to provide a good estimate (from a signal to noise point of view) of what a coincident source receiver pair would record (zero-offset). For a 1-dimensional medium, meaning that there are only medium changes in the depth ( $z$ ) direction and not in the lateral directions ( $x$  and  $y$ ), the 'migration' of the move-out corrected and stacked section consists of only a stretch in the time direction to map the time axis to the depth axis. For laterally changing media it is necessary to employ migration techniques to focus the data.

### 2.3 Kirchhoff summation

The Kirchhoff summation method has its basis in ray path and traveltime considerations and the diffraction theory of Huygens and Fresnel. French (1974) describes migration as a process in which each subsurface point is assigned a number which is a measure of the probability that scattered energy has emanated from that possible scattering area. The number is determined by summing the recorded data for all shot points and receiver locations at times where energy from that subsurface point could arrive. This is equivalent to a summation along the hyperbolic Huygens surface (surface of maximum convexity). This operation is repeated for every sample on the seismic output section. The hyperbolic traveltimes, which define the path of the integration, used in this method are calculated by making use of stacking velocities. The advantage of this technique is that it is possible to migrate 3D seismic data within a reasonable computation time. The disadvantage is that the method is based on kinematics only and the wave equation is not used explicitly.

The diffraction summation method implies that the geologic interface acts as a diffuse reflector; that is, each point is assumed to scatter energy all along its corresponding reflection-time surface (French, 1975). So a wavefield at the earth's surface (a seismic section) is interpreted as a superposition of an infinitude of smaller fields from the distribution of scatterers. A reflection events is thus the outcome of constructive and destructive interference of an infinitude of infinitely weak diffraction patterns. In figure 2.4 the principle used in the diffraction summation method is shown for a dipping reflector. The reflector is build by making use of a limited number (in figure 2.4 16 diffraction points are used) of diffraction points positioned on the reflector. The apexes of the diffraction hyperbola define the correct position of the reflecting events, which is indicated with the thick line in figure 2.4. Constructive interference builds up a reflector along the straight-line envelope of the diffraction curves. According to this reasoning the goal in migration is to transform these

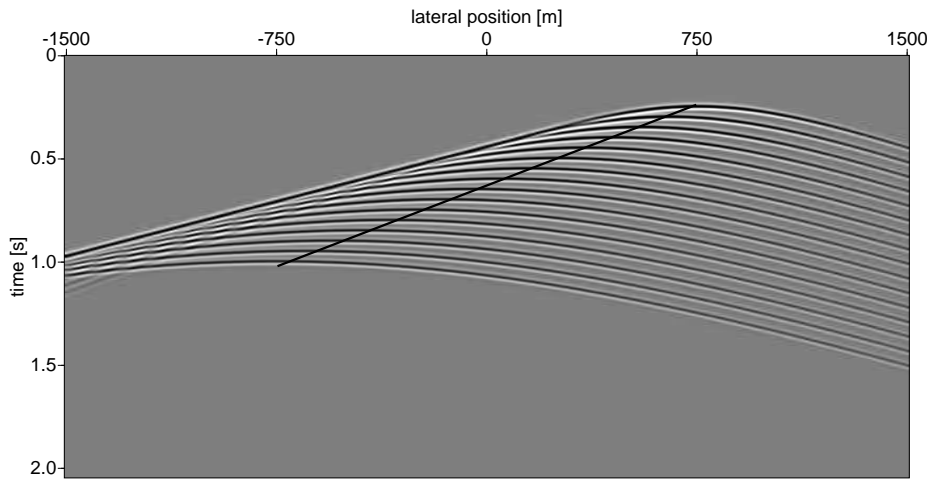


**Figure 2.4** Diffraction stack of a dipping reflector in a homogeneous medium ( $c = 2000$  [m/s]). The thick line, defined through the apexes of the individual diffraction responses, represents the true position of the dipping reflector.

diffractions, and the reflection build up from it, into a reflector segment given by the thick line. The diffraction summation approach exploits this relation between diffraction pattern and scatterer location. A possible subsurface scatterer will have a nearly hyperbolic diffraction curve (assuming a 1-dimensional medium) in the unmigrated time section with an apex at the sample point of the scatterer. Migration then involves summation of the input amplitudes along the diffraction curve and placing the sum at the output apex position. This operation is repeated for every sample point on the seismic output section.

The diffraction summation method approximates the propagation of waves in the earth, it does not describe a physical event. In order to account for frequency-dependent amplitude and phase behavior, wave propagation theory must be introduced in the method. Therefore a new, more physical related, interpretation of the *stacked* seismic section was introduced by Loewenthal et al. (1976). This interpretation became known as the exploding reflector model. At each reflector in the subsurface sources are placed with charges having a local strength proportional to the effective reflectivity. At time  $t = 0$  all sources are fired simultaneously and only the upward traveling waves are propagating to the surface through a medium with a velocity halve of the true velocity. The resulting wavefield at the earth's surface approximates a normal-incidence (with respect to the surface) time section. Loewenthal et al. (1976) used this interpretation to migrate a stacked seismic section with the finite difference method of Claerbout (1971). Within this model it is assumed that the ray paths between a source-receiver location and a point on the reflector is the same for upward and downward propagation (representing the

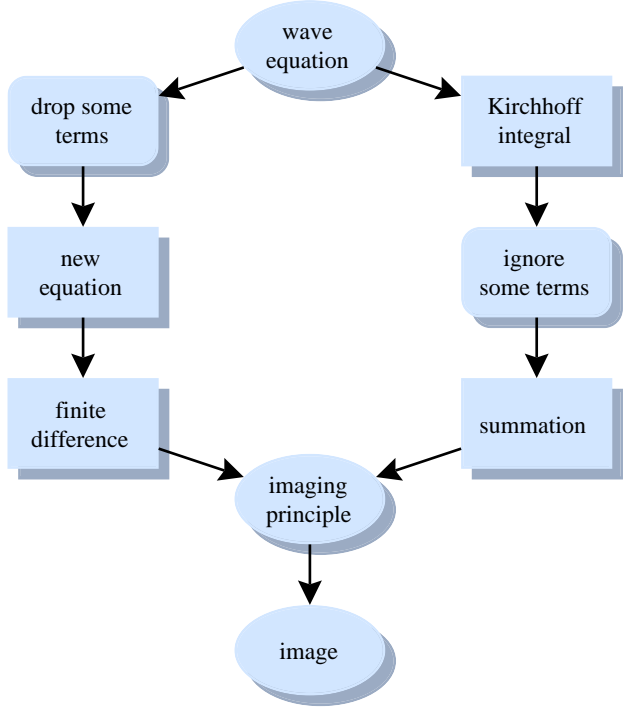


**Figure 2.5** Two wave equation based approaches to migration (after Larner and Hatton, 1990); Kirchhoff migration and finite difference.

normal ray path). In the exploding reflector model the assumption is made that stacked data is equivalent with zero source-receiver offset. Within this interpretation the wavefield observed in the stacked section can be extrapolated downward into the subsurface by using wave equation based methods followed by an imaging principle to image the reflectors (French, 1975). However, using the **WRW** model, Berkhouit (1982) derived the theoretical foundation of the exploding reflector model and showed the conditions for the validity of such a model by transforming **WRW** to a **W<sub>0</sub>R** model for zero-offset data.

Schneider (1978) showed that the Kirchhoff integral formulation has strong ties with the diffraction summation approach, the differences are subtle but significant in terms of amplitude and waveform reconstruction. The Kirchhoff integral method has no limitations on the reflector dip and in principle angles  $> 90^\circ$  can be migrated. Schneider (1978) also showed that the Kirchhoff integral formulation of the diffraction summation approach for stacked seismic data can be used to simulate the angle limitations of finite difference algorithms.

For wave equation based migration the seismic section is posed as a boundary value

problem for the wave equation. Solutions can be derived from either an integral or differential form of the wave equation (see figure 2.5). The method of summation along diffraction hyperbolas is founded on the integral solution. The migration scheme of Claerbout (1971) is based on a solution of differential form (Larner and Hatton, 1990). Both the integral (summation) approach and the differential approach yield approximate solutions of the same wave equation. However, specific approximations inherent in actual computational algorithms differ for the two approaches. Note that both approaches are forms of time migration; so a macro model which described the propagation properties of the subsurface as function of depth is not used explicitly. This means that due to propagation through laterally varying media closer to the surface the shape of the two-way time image of deeper reflectors is altered. Therefore an additional depth migration, which shift time migrated points laterally and vertically to their correct position in depth, is required for proper imaging of the time migrated section when the subsurface overburden exhibits lateral complexity. In Black and Brzostowski (1994) these kind of errors made with time migration are clearly explained.

The Kirchhoff summation method sums signals into the apex of the approximation hyperbolic (Hubral, 1977). The position of the time surface minimum (apex) is the position where a ray from a depth point emerges vertically to the surface. Thus time migration of data has the effect of moving points laterally to their minimum time position (image ray) rather than their true lateral position. This means that a Kirchhoff migration must be followed by an additional time to depth migration for the true depth position to be recovered. This deficiency of Kirchhoff time migration is sometimes called the 'lack of Snell's law', which means that the breaking of the ray along interfaces is not taken into account; the image ray is interpreted as it has vertically traveled through the layers of the earth without breaking. The image ray is defined as the minimum traveltime path from a point on the reflector to the surface and will always emerge vertically at the surface. Note that the image ray is associated with time migration and not with the true diffraction curve. Related to the definition of the image ray is the normal ray which is defined as the ray which travels along the minimum time path from the surface to a reflector and ends, by definition, perpendicular to the target interface (Parkes and Hatton, 1987). Figure 2.6 shows both the image and the normal ray.

The signal positions and two-way times related to the image-rays are not affected by the time migration process, signals for all other rays are migrated. A zero-offset trace (a trace out of a stacked section is assumed to represent a zero-offset trace) is transformed by the migration process into an image ray belonging to a point close to the normal incidence point of the normal ray. Note that image rays can cross each other which means that one depth point may be in fact be imaged in two positions on the time migrated section Hubral (1977). Normal rays cross each other if the curvature of the structure is stronger than the curvature of the wavefront. In that

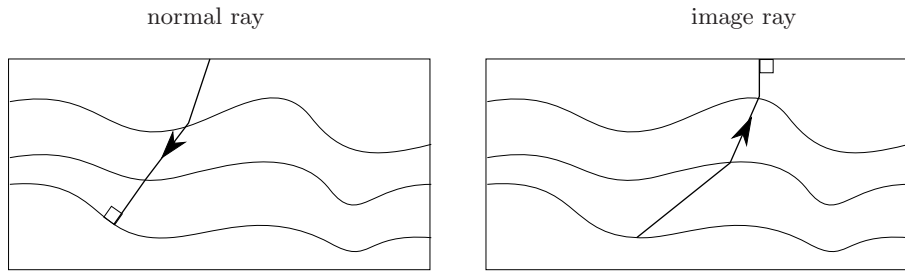


**Figure 2.6** The normal ray represents minimum traveltime from a point on the surface to the reflector and the image ray represents minimum traveltime from a point on the reflector to the surface. Note that a zero-offset recording has traveled two times (down and up) along the normal ray path.

case a bow-tie (indicating multiple arrival times) will be observed at the surface. Due to the smaller curvature of the wavefront at deeper depth levels, a bow-tie is observed for a smaller curvature of the structure. Note that the imaging path of the finite difference method is also along the image ray (see appendix A Hatton et al., 1990). The discussed finite difference migration and the Kirchhoff integration method are both methods which perform a temporal wavefield construction, and in general give a migrated output section in the time domain.

#### 2.4 Migration in terms of deconvolution

A significant improvement in the understanding of the different approaches to migration was introduced by Berkhout and van Wulfften Palthe (1979); Berkhout (1984). Berkhout (1982) showed that the process of wavefield extrapolation involves a convolution process (forward extrapolation) and a deconvolution process (inverse extrapolation) along the spatial axes. This systems view on migration generated in the early eighties a fundamentally different view on migration:

- ① The spatial deconvolution process in migration involves a zero-phasing process, the maximum resolution being given by the bandwidth of the 'spatial wavelet' in the data. If propagation losses are taken into account, the deconvolution operator corrects the spatial amplitude spectrum as well (spatial whitening).
- ② The deconvolution process causes diffractor responses to compress, reflection responses to reposition and reflection amplitudes to adjust. In addition, the deconvolution process decreases Fresnel zones to their minimum (given by the frequency content and aperture angle).
- ③ For laterally homogeneous media the deconvolution operator is not changing along one depth level and the deconvolution process can be efficiently applied by multiplication in the wavenumber domain, yielding the so-called phase shift method (Gazdag, 1978; Stolt, 1978).

- ④ For laterally inhomogeneous media the deconvolution operator is laterally-variant and the deconvolution process can be elegantly represented by a matrix multiplication.
- ⑤ If the Kirchhoff summation approach to migration is applied in a *recursive* way, then the discretized, band-limited, recursive deconvolution operator equals the exact finite-difference operator. In addition, in the wavenumber domain the recursive Kirchhoff operator equals the phase shift operator.
- ⑥ Since the earth is time-invariant during a seismic experiment, the spatial deconvolution process in seismic migration may always be applied in the temporal frequency domain, yielding the so-called F-X and F-X-Y algorithms.
- ⑦ The deconvolution formulation to migration yields directly a *depth* migration algorithm.

If there are large lateral and vertical velocity changes all time migration approaches break down. To overcome these problems depth migration need be applied (Berkhout and van Wulfften Palthe, 1979; Schultz and Sherwood, 1980). The depth migration method proposed by Berkhout (1982), and based on a spatial convolution and deconvolution process in the space-frequency domain, can handle these lateral velocity changes in a simple manner. In his depth migration scheme each frequency component of the wavefield is extrapolated to another depth level by means of a spatial convolution operator. When the velocity changes with lateral position a new convolution (extrapolation) operator is read from a table which is computed in advance (Blacquière et al., 1989). For an overview of the different implicit and explicit extrapolation operators used in the frequency domain the reader is referred to appendix A of this thesis.

Another advantage of recursive depth migration is that it automatically handles energy of multiple paths from upper surface points to depth points, while Kirchhoff depth migration allows a few paths at most to connect a upper surface point with a depth point. However, the success of depth migration is completely dependent on the used velocity model, just like any other migration method. Parkes and Hatton (1987) have shown that positioning errors in the migrated sections are dominated by inaccuracies in the macro model used in the migration algorithm and not by the inadequacies of the algorithms themselves. The highest priority must therefore be assigned to improving methods for estimating the velocity field. The latest developments in depth migration aim at a pre-stack migration technique which can be combined with a detailed velocity analysis.

At the begin of the 80's depth migration methods became more popular and due to the increasing computer power depth migration schemes could also be applied to pre-stack data (Schultz and Sherwood, 1980). By performing migration directly on

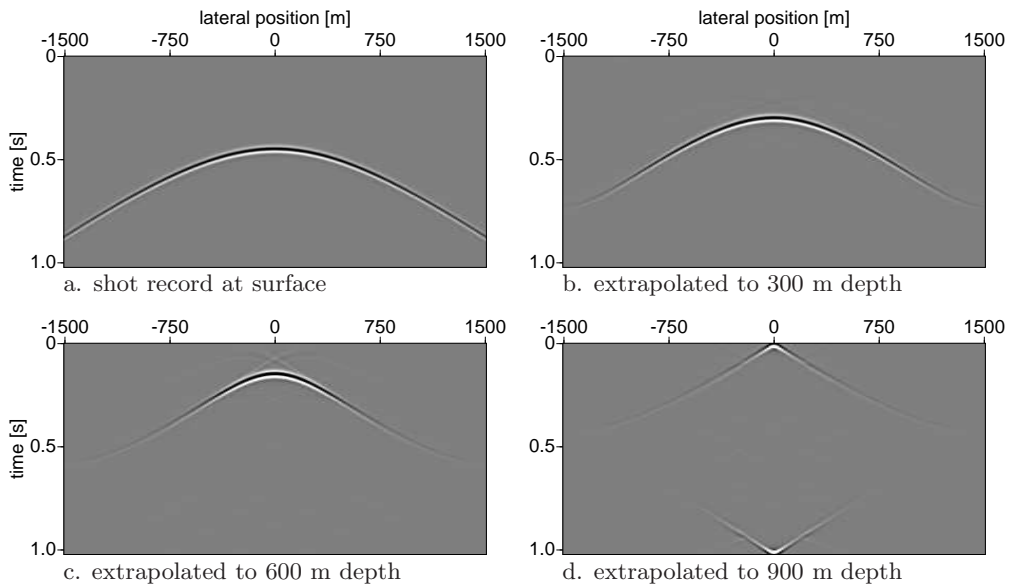


**Figure 2.7** Inverse extrapolation of a diffractor (at 900 [m] depth) response to deeper depth levels involves a spatial deconvolution step. Note that the effective receiver array becomes smaller with increasing depths.

the shot records, and not on stacked data, a much better image can be obtained. The stacking process is based on the assumption of a lateral invariant medium. For most interesting cases this assumption is not valid and the obtained stack can distort the quality of dipping reflectors in the depth image. In pre-stack depth migration the shot records are regarded as the sampling of an upgoing wavefield. Note that this is only true if all the surface related multiples are removed from the data. This wavefield is backward propagated in depth by using recursive extrapolation (spatial deconvolution) schemes. The extrapolation step simulates a downward moving receiver array, as shown in figure 2.7, where a recursive inverse extrapolation algorithm is used to propagate the wavefield to deeper depth levels.

A very computation intensive but accurate extrapolation method is described by McMechan (1983); Mufti et al. (1996), where a time reversed finite difference scheme (Alford et al., 1974) of the two-way wave equation is used to migrate the data. The process of time reversed migration transforms data from the measurement plane to the space depth domain by using the seismic data as boundary conditions for the different time steps. Since the two-way wave equation is used, stable migration of very steep dips is possible. If the velocities for the migration are chosen correctly, the wavefield at  $t = 0$ , obtained by constructive interference of wavefronts, should be considered as the final migrated section.

## 2.5 Inverse scattering

Most of the methods described above make use of some type of extrapolation (de-convolution) algorithm to bring the measured data closer to the reflector (scattering object) and use an additional imaging principle to image the reflector. This extrapolation method is one type of solution of a more general problem of finding the scattering object from measurements surrounding the object; the so called inverse scattering problem. The publications to solve for the inverse scattering problem, outside the seismic literature, are extensive. Here only those methods directly related to the seismic literature are briefly mentioned.

In the inverse scattering theory approach it is explicitly stated that a model is sought, which is the best in a given sense (e.g. the minimization of some functional defined over the model space). Tarantola (1984b) uses a linear inverse scattering theory to solve the seismic problem and has shown that this linearization lead to a solution strongly related to the Kirchhoff migration method. In the forward modeling, which is used in the inversion, only the first order scattering energy is taken into account, multiple reflections are neglected (the so called Born approximation). In another paper Tarantola (1984a) uses a non-linear approach which strongly resembles the migration method based on the imaging principle of Claerbout (1971).

## 2.6 Summary

The desired output of every migration program is a representative image of the earth. In this image all reflectors are positioned at their correct lateral position in depth and the interpreter can immediately pinpoint the interesting areas. In migration however there are several other seismic images involved as shown in figure 2.8 and are given by, the unmigrated shot-record, the stacked section and the time migrated image (after Parkes and Hatton, 1987). The conventional main product of processing is obtained by reordering and summing the shot records in the time domain to a stacked section. Imaging of this stacked section with a time migration method gives the time migrated section and imaging with a depth migration method gives an image of the earth. However, the best imaging results are obtained by a direct map of the (unstacked) shot records to an image of the earth. Unfortunately pre-stack shot record migration is very computational intensive, specially for 3D data, to become a standard processing procedure in the near future. Most methods used today are characterized by a two-stage method; conventional time migration (finite difference or Kirchhoff) followed by a depth migration along the image rays.

The top right box in figure 2.8 represents a new imaging method based on double focusing (Berkhout and Rietveld, 1995). The CFP gather represents a half-way migration result and consists of synthesized shot records. This synthesis process consist of a weighted stack of the traces in a shot record, where the weights are

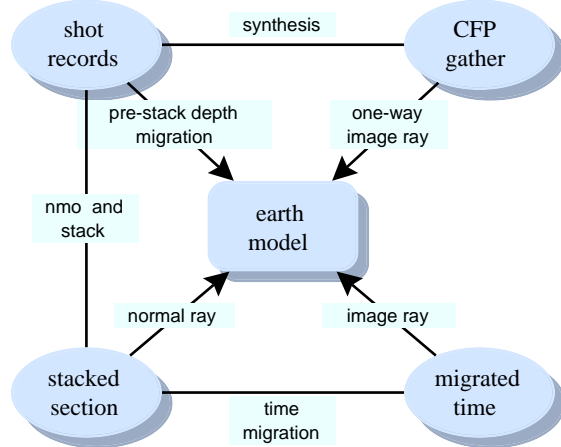


**Figure 2.8** The five seismic domains; the earth is represented by the depth domain, the stacked seismic section to unmigrated time and the time migrated stack to migrated time. Note that the domain at the top right is not yet explained, this domain will be introduced in this thesis.

defined by a solution of the wave equation. The synthesis result defined for one point in the subsurface is the subject of this thesis and is called Common Focus Point (CFP) gather. The new method introduces a new image domain called the *one-way* time image and has a great affinity with Kirchhoff depth migration as shown in figure 2.9. However, there is one fundamental difference between the two methods. In Kirchhoff depth migration the wavefield is focused in one integration step, while in the CFP method two separate focusing steps are carried out. The result after one focusing step transforms the shot records to CFP gathers and, as will become clear in this thesis, this gather is a very suitable domain for velocity (or operator) analysis.

The extension of the discussed migration techniques to 3-dimensional data is not straightforward due to the incomplete acquisition at the surface. The Kirchhoff migration and focusing methods are the most flexible and therefore also the most often used method at the moment. The depth migration scheme's require a regular sampling of the data, which means that a lot of interpolation has to be done (which increases the already large 3D data-volume even more) before the extrapolation can be carried out.

To end the historical overview of migration it must be noted that in the first issue of *Geophysics* Rieber (1936) describes a method which tries to improve the maximum sensitivity of the geophone groups. He argues that if a wave arrives at an angle with respect to the line occupied by the geophone group, it will not reach all of the geophones at the same time instant, and hence their cumulative impulse will not be transmitted into the electrical system in phase. The axis of maximum sensitivity of the geophone group is directed downwards and excludes from the summed record all

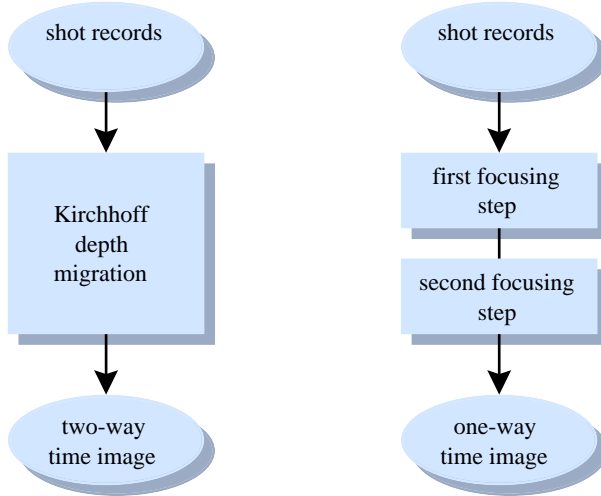


**Figure 2.9** The difference between Kirchhoff depth migration (left) and CFP migration is in the division of the focusing step into two processes. The result after the first focusing step turn out to be a very suitable domain for velocity analysis.

wave components not normal to the geophone group. To improve the sensitivity of the geophone group Rieber introduced controlled directional sensitivity. In the first step the individual geophones are measured and in a second step they are combined not only in their original phase relationship, as is done in ordinary multiple recording, but also in any desired phase relationship. Each trace of the directional analysis strip represents the sum of the outputs of all the detectors, but with a constant phase difference introduced between the outputs from adjacent detectors before cumulation. Current processing methods which use Radon transformations (linear, parabolic, hyperbolic) or inverse ray-tracing are more successful implementations of the same concepts. The idea of combining weighted receivers at the surface is also used in the Common Focus Point technology where the weights are chosen such that the source and receiver sensitivity are focused on *one* point in the subsurface.

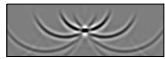
---

Method	high angles	velocity changes	computational speed
Finite Difference	□	□	+
Kirchhoff	++	□	+
Fourier	++	-	++
F-X	+	++	-
CFP	++	++	+

---

**Table 2.1** A simplified overview of the advantages and disadvantages of the different migration methods discussed in this chapter. In the table ++ means preferred, + well suited, □ can be used but not recommended and - means not recommended.





## Chapter 3

### Two-way and one-way representations

The seismic analysis tools which are used within the DELPHI group are all based on the same forward model. This forward model describes the mathematical relationship between the geophysical properties of the earth and the seismic measurements. Once the forward model is defined a related inversion scheme, which estimates the geophysical properties from the seismic measurements, can be derived. In this chapter the forward model is derived and formulated in such a way that it can be used in the inversion scheme described in chapter 4.

The representations for both two-way and one-way wavefields are discussed and compared with each other. Two-way wavefields can be described in terms of the total acoustic pressure and the total particle velocity. These terms are always coupled by the two-way wave equations. One-way wavefields are described in terms of waves traveling in the positive and negative axial direction. If the medium parameters do not vary in the axial direction the up- and downgoing one-way waves are completely decoupled; otherwise the coupling between the up- and downgoing waves is expressed in terms of the axial variations of the medium parameters. Therefore the description in one-way wavefields is useful when there is a clear preferred direction of propagation. In surface seismic exploration the vertical direction is regarded as the preferred direction of propagation, which makes the one-way wave theory very well suited for seismic applications. At the end of this chapter the forward model used in this thesis is formulated by making use of the representations of seismic data which are derived from two- and one-way reciprocity theorems.

#### 3.1 Reciprocity theorems

The aim of seismic wave theory is to solve for the unknown inhomogeneities and the structural layers in the subsurface of the earth given a measurement at the surface of the earth. The measured wavefield represents the inhomogeneities in the subsurface of the earth due to the scattering of the incident source wavefield. Solutions

based on the wave equation try to extract this information, which is limited by the resolution of the method, from the measured data. However, for many wave equation-based solutions it is necessary to know the wavefield propagation properties of the subsurface. Unfortunately these propagation properties are part of the desired information to be extracted from the measured data. Therefore one usually starts with an initial macro model which describes the global propagation properties of the subsurface. To be able to solve for the unknown, a theorem is needed which describes the relationship between the measured wavefield and the wavefield propagation through the macro model. A reciprocity theorem can relate two states that occur in the same domain in space. These two states can be chosen as the measured state and the model state, which makes reciprocity theorems fundamental in seismic wave theory (de Hoop, 1988; Fokkema and van den Berg, 1993). The reciprocity theorems discussed in this chapter interrelate two acoustic states in a time-invariant bounded domain  $D$  and are used to derive representations for seismic wavefields. In this section the mathematical tools are introduced and the two-way and one-way reciprocity theorems are derived. Note that the chapter about symbols and definitions on page ix describes most of the notation conventions used in this thesis.

### 3.1.1 Reciprocity theorem for two-way wavefields

The integral theorem of Gauss interrelates quantities at the surface of a bounded domain  $D$  to quantities inside the domain with the relation

$$\int_{\partial D} E_k n_k d^2 \mathbf{x} = \int_D \partial_k E_k d^3 \mathbf{x}, \quad (3.1)$$

where  $\partial D$  is the boundary of  $D$ , with  $n_k$  the unit vector normal to  $\partial D$  and oriented away from  $D$ ,  $d^3 \mathbf{x}$  the elementary volume in 3-dimensional Euclidean space and  $d^2 \mathbf{x}$  the elementary area of  $\partial D$ . Substituting  $E_k = P_A V_{k,B} - V_{k,A} P_B$  into equation (3.1) gives the following integral relation

$$\int_{\partial D} \{P_A V_{k,B} - V_{k,A} P_B\} n_k d^2 \mathbf{x} = \int_D \partial_k \{P_A V_{k,B} - V_{k,A} P_B\} d^3 \mathbf{x}. \quad (3.2)$$

Equation (3.2) can be used to interrelate two different states, denoted by the subscripts  $A$  and  $B$ . To use this relation for wavefields the quantities  $V_k$  and  $P$  occurring in equation (3.2) must be related to physical parameters which describe the wave phenomena.

The linearized equation of motion and the linearized equation of deformation are the coupled equations which are used to describe the propagation of two-way wavefields. In the frequency domain these equations are given by

$$\partial_k P + j\omega\rho V_k = F_k, \quad (3.3)$$

$$\partial_k V_k + j\omega\kappa P = Q, \quad (3.4)$$

respectively, where  $P$  is the acoustic pressure [ $\text{Pa} = \text{N}/\text{m}^2$ ],  $V_k$  the particle velocity [ $\text{m}/\text{s}$ ],  $\rho$  the volume density of mass [ $\text{kg}/\text{m}^3$ ],  $\kappa$  the compressibility [ $\text{Pa}^{-1} = \text{m}^2/\text{N}$ ],  $F_k$  the volume source density of volume force [ $\text{N}/\text{m}^3$ ] and  $Q$  the volume source density of volume injection rate [ $1/\text{s}$ ]. Using the coupled two-way wave equations (3.3) and (3.4) for two different states  $A$  and  $B$  and the interaction quantity  $\partial_k\{P_A V_{k,B} - V_{k,A} P_B\}$  occurring in equation (3.2) gives

$$\begin{aligned} & \int_{\partial D} \{P_A V_{k,B} - V_{k,A} P_B\} n_k d^2 \mathbf{x} = \\ & j\omega \int_D \{V_{k,A}(\rho_B - \rho_A) V_{k,B} - P_A(\kappa_B - \kappa_A) P_B\} d^3 \mathbf{x} \\ & + \int_D \{F_{k,A} V_{k,B} + Q_B P_A - F_{k,B} V_{k,A} - Q_A P_B\} d^3 \mathbf{x}. \end{aligned} \quad (3.5)$$

Equation (3.5) is called Rayleigh's reciprocity theorem (Rayleigh, 1894; Fokkema and van den Berg, 1993) of the convolution type, since the products in the frequency domain correspond to convolutions in the time domain. Using the interaction quantity  $\partial_k\{P_A^* V_{k,B} + V_{k,A}^* P_B\}$  in equation (3.1) the reciprocity theorem of the correlation type (Bojarski, 1983) is obtained:

$$\begin{aligned} & \int_{\partial D} \{P_A^* V_{k,B} + V_{k,A}^* P_B\} n_k d^2 \mathbf{x} = \\ & -j\omega \int_D \{V_{k,A}^*(\rho_B - \rho_A) V_{k,B} + P_A^*(\kappa_B - \kappa_A) P_B\} d^3 \mathbf{x} \\ & + \int_D \{F_{k,A}^* V_{k,B} + Q_B P_A^* + F_{k,B} V_{k,A}^* + Q_A^* P_B\} d^3 \mathbf{x}. \end{aligned} \quad (3.6)$$

These scalar-wave reciprocity theorems are used to derive wavefield representations of seismic data and the related forward model. Note that by eliminating  $V_k$  from equation (3.3) and equation (3.4) the wave equation in the frequency domain is obtained

$$\rho \partial_k \left( \frac{1}{\rho} \partial_k P \right) + \omega^2 c^{-2} P = -s \quad (3.7)$$

with the acoustic velocity  $c = (\kappa \rho)^{-\frac{1}{2}}$  [ $\text{m}/\text{s}$ ] and the source term  $s = j\omega \rho Q - \rho \partial_k \left( \frac{1}{\rho} F_k \right)$ .

### 3.1.2 Reciprocity theorem for one-way wavefields

In surface seismics the preferred direction of propagation is along the  $x_3$  (vertical) axis; it is therefore useful to reorganize equation (3.3) and equation (3.4) in such a way that the  $\partial_3$  derivatives are separated from the  $\partial_1, \partial_2$  derivatives. Eliminating  $V_1$  and  $V_2$  from equations (3.3) and (3.4) gives the desired result

$$\partial_3 \mathbf{Q} = \mathbf{A} \mathbf{Q} + \mathbf{D}, \quad (3.8)$$

with the two-way wave vector

$$\mathbf{Q} = \begin{pmatrix} P \\ V_3 \end{pmatrix}, \quad (3.9)$$

the source vector

$$\mathbf{D} = \begin{pmatrix} F_3 \\ Q - \frac{1}{j\omega} \partial_\alpha \left( \frac{1}{\rho} F_\alpha \right) \end{pmatrix}, \quad (3.10)$$

and the two-way matrix operator

$$\mathbf{A} = \begin{pmatrix} 0 & -j\omega\rho \\ \frac{1}{j\omega\rho} \mathcal{H}_2 & 0 \end{pmatrix}. \quad (3.11)$$

In the two-way matrix operator of equation (3.11)  $\mathcal{H}_2$  represents the Helmholtz operator which is given by

$$\mathcal{H}_2 = \left( \frac{\omega}{c} \right)^2 + \rho \partial_\alpha \left( \frac{1}{\rho} \partial_\alpha \cdot \right). \quad (3.12)$$

The decomposition of the acoustic two-way wave equation (3.8) into equations for up- and downgoing one-way wavefields is carried out by the inverse of matrix operator  $\mathbf{L}$ . The matrix operator  $\mathbf{L}$  is used in the diagonalization of the matrix operator  $\mathbf{A}$  such that  $\mathbf{A}$  in

$$\mathbf{A} = -j\omega \mathbf{L} \mathbf{A} \mathbf{L}^{-1} \quad (3.13)$$

is a diagonal operator matrix (see Fishman et al. (1987); for references in the seismic context see Wapenaar and Berkhouw (1989); de Hoop (1992)). The composition from the one-way wave vector  $\mathbf{P}$ , which contains downgoing  $P^+$  and upgoing  $P^-$  waves, to the two-way wave vector  $\mathbf{Q}$  is then defined by

$$\mathbf{Q} = \begin{pmatrix} P \\ V_3 \end{pmatrix} = \mathbf{L} \mathbf{P}, \quad (3.14)$$

where  $\mathbf{P} = \begin{pmatrix} P^+ \\ P^- \end{pmatrix}$ . In a similar way the source vector  $\mathbf{D}$  is composed from up-  $S^-$  and downgoing  $S^+$  sources according to

$$\mathbf{D} = \mathbf{L} \mathbf{S}, \quad (3.15)$$

where  $\mathbf{S} = \begin{pmatrix} S^+ \\ S^- \end{pmatrix}$ . Note that the composition matrix  $\mathbf{L}$  can be chosen flux normalized (Ursin, 1983; Wapenaar, 1996c) which is convenient in the derivation of reciprocal relations. Substituting the composition equations (3.14) and (3.15) into equation (3.8) gives the coupled one-way wave equations

$$\partial_3 \mathbf{P} = \mathbf{B} \mathbf{P} + \mathbf{S}, \quad (3.16)$$

where the one-way operator matrix  $\mathbf{B}$  is given by

$$\mathbf{B} = -j\omega\Lambda + \Theta, \quad (3.17)$$

with the diagonal matrix  $\Lambda$  by

$$\Lambda = \begin{pmatrix} *^+ & 0 \\ 0 & *^- \end{pmatrix}, \quad (3.18)$$

where  $*^+ = -\Lambda^-$ . The coupling operator matrix  $\Theta$  is defined as

$$\Theta = -\mathbf{L}^{-1}\partial_3\mathbf{L} = \begin{pmatrix} \mathcal{T}^+ & \mathcal{R}^- \\ -\mathcal{R}^+ & -\mathcal{T}^- \end{pmatrix}, \quad (3.19)$$

where  $\mathcal{R}^\pm$  and  $\mathcal{T}^\pm$  are reflection and transmission operators. From the structure of equations (3.16) to (3.19) it follows that  $-j\omega\Lambda$  accounts mainly for (downward/upward) propagation and  $\Theta$  for scattering mainly due to vertical variations of the medium parameters. This explicit distinction between propagation and scattering is an important advantage of the one-way wave equation over the two-way wave equation.

For a homogeneous medium the coupling operator matrix  $\Theta = \mathbf{O}$  and the diagonal matrix  $\Lambda$  can be written in the wavenumber frequency domain as

$$-j\omega\tilde{\Lambda} = \begin{pmatrix} -jk_z & 0 \\ 0 & jk_z \end{pmatrix}, \quad (3.20)$$

where the vertical wavenumber

$$k_z = \omega\tilde{*}^+ = -\omega\tilde{*}^- = \begin{cases} \sqrt{k^2 - k_\alpha k_\alpha} & k_\alpha k_\alpha \leq k^2 \\ -j\sqrt{k_\alpha k_\alpha - k^2} & k_\alpha k_\alpha > k^2 \end{cases}. \quad (3.21)$$

A solution of the one-way wave equation (3.16) in a homogeneous medium is given by the well known phase shift operator (Gazdag, 1978). For a more detailed discussion about the properties of the one-way wave equation the reader is referred to Fishman et al. (1987); Wapenaar and Berkhout (1989); Wapenaar and Grimbergen (1996).

Starting from the one-way wave equation (3.16) and the interaction quantity

$$\partial_3\{P_A^+P_B^- - P_A^-P_B^+\} \quad (3.22)$$

the reciprocity theorem of the convolution type for one-way wavefields is derived. Note that the interaction quantity (3.22) contains waves that propagate in opposite directions. To simplify the notation this interaction quantity is rewritten to

$$\partial_3\left\{(P_A^+P_A^-)\begin{pmatrix} 0 & 1 \\ -1 & 0 \end{pmatrix}\begin{pmatrix} P_B^+ \\ P_B^- \end{pmatrix}\right\} = \partial_3\{\mathbf{P}_A^T\mathbf{N}\mathbf{P}_B\}. \quad (3.23)$$

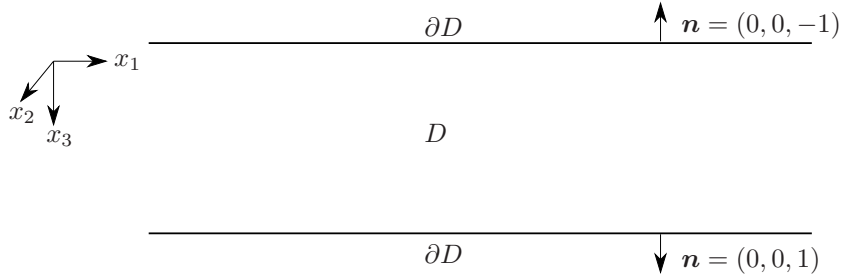


**Figure 3.1** Configuration for one-way reciprocity theorems.  $D$  is a volume enclosed by two infinite parallel surfaces normal to the  $x_3$  axis with the outward pointing vector  $\mathbf{n}$  defined on  $\partial D$ . The combination of these two surfaces is denoted by  $\partial D$ .

In figure 3.1 the domain used in the one-way reciprocity theorem is shown. The domain  $D$  is a volume 'enclosed' by two infinite parallel surfaces normal to the  $x_3$  axis. The combination of these two surfaces is denoted by  $\partial D$ . Substituting equation (3.23) into equation (3.2) with the domain configuration of figure 3.1 and by making use of a specific symmetry property of the one-way operator matrix  $\mathbf{B}$  (Wapenaar, 1996b; Wapenaar and Grimbergen, 1996) yields the following one-way reciprocity theorem of the convolution type

$$\begin{aligned} & \int_{\partial D} \mathbf{P}_A^T \mathbf{N} \mathbf{P}_B n_3 d^2 \mathbf{x} = \\ & \int_D \mathbf{P}_A^T \mathbf{N} (\mathbf{B}_B - \mathbf{B}_A) \mathbf{P}_B d^3 \mathbf{x} \\ & + \int_D \{ \mathbf{P}_A^T \mathbf{N} \mathbf{S}_B + \mathbf{S}_A^T \mathbf{N} \mathbf{P}_B \} d^3 \mathbf{x}. \end{aligned} \quad (3.24)$$

The clear distinction between propagation and scattering in the one-way wave equation can be observed by substituting equation (3.17) into equation (3.24) yielding

$$\begin{aligned} & \int_{\partial D} \mathbf{P}_A^T \mathbf{N} \mathbf{P}_B n_3 d^2 \mathbf{x} = \\ & -j\omega \int_D \{ \mathbf{P}_A^T \mathbf{N} (\Lambda_B - \Lambda_A) \mathbf{P}_B - \frac{1}{j\omega} \mathbf{P}_A^T \mathbf{N} (\Theta_B - \Theta_A) \mathbf{P}_B \} d^3 \mathbf{x} \\ & + \int_D \{ \mathbf{P}_A^T \mathbf{N} \mathbf{S}_B + \mathbf{S}_A^T \mathbf{N} \mathbf{P}_B \} d^3 \mathbf{x}. \end{aligned} \quad (3.25)$$

Note that the one-way reciprocity theorem of the convolution type has the same form as the two-way reciprocity relation given in equation (3.5); a surface integral over the interaction quantity on one side and volume integrals containing a contrast function and sources on the other side. The contrast term  $(\mathbf{B}_B - \mathbf{B}_A)$  has the

property that it vanishes when the medium parameters in state  $A$  and state  $B$  are identical. In equation (3.25) it can be seen that the contrast functions allow an independent choice of  $\mathbf{\Lambda}$  (propagation) and  $\mathbf{\Theta}$  (scattering).

The one-way reciprocity theorem of the correlation type is obtained by using the interaction quantity

$$\partial_3 \left\{ (P_A^+ \quad P_A^-)^* \begin{pmatrix} 1 & 0 \\ 0 & -1 \end{pmatrix} \begin{pmatrix} P_B^+ \\ P_B^- \end{pmatrix} \right\} = \partial_3 \{ \mathbf{P}_A^H \mathbf{J} \mathbf{P}_B \} \quad (3.26)$$

in Gauss's theorem which results in

$$\begin{aligned} \int_{\partial D} \mathbf{P}_A^H \mathbf{J} \mathbf{P}_B n_3 d^2 \mathbf{x} &\approx \\ \int_D \mathbf{P}_A^H \mathbf{J} (\mathbf{B}_B - \mathbf{B}_A) \mathbf{P}_B d^3 \mathbf{x} \\ + \int_D \{ \mathbf{P}_A^H \mathbf{J} \mathbf{S}_B + \mathbf{S}_A^H \mathbf{J} \mathbf{P}_B \} d^3 \mathbf{x}. \end{aligned} \quad (3.27)$$

The approximation sign in equation (3.27) refers to the use of an approximation in the derivation of a modified symmetry property of the one-way operator matrix  $\mathbf{B}$ . In this approximation evanescent wave modes are erroneously handled. For a detailed comparison between the one-way and two-way reciprocity theorem and the symmetry properties of the one-way operator matrix  $\mathbf{B}$  the reader is referred to Wapenaar (1996b). The one-way reciprocity theorems of the convolution and correlation type are used to derive one-way representations of seismic data.

### 3.2 Integral representations for two-way wavefields

An integral representation expresses a wavefield quantity at some point in a medium in terms of boundary and volume integrals over the wavefield, the source distribution and the contrast function. Integral representations for two-way wavefields are derived by using the reciprocity theorems derived in section 3.1.1 and taking some special choices for the two states  $A$  and  $B$  in the reciprocity relation. Acoustic representations have been introduced by Lord Rayleigh (Rayleigh, 1894). For the derivation of a general representation of an acoustic wavefield the domain  $D$  consist of a reference medium  $\{\bar{\kappa}(\mathbf{x}), \bar{\rho}(\mathbf{x})\}$  where a contrasting medium  $\Omega \{\kappa(\mathbf{x}), \rho(\mathbf{x})\}$  is embedded. The wavefield of state  $A$  in the reciprocity theorem is the Green's wavefield propagating in the reference medium with a point source at  $\mathbf{x}'$  inside  $D$ . Note that the wavefield described by the Green's function is chosen to be causally related to the source function. For state  $B$  the wavefield in the actual medium is chosen, with a source position which lies outside the scattering part  $\Omega$  of domain  $D$  and the observation point at  $\mathbf{x}$  is a point inside  $D$ .

Substituting these states, which are summarized in table (3.1), into the reciprocity

State A	State B
$\partial_k G(\mathbf{x}, \mathbf{x}') + j\omega \bar{\rho}(\mathbf{x}) \Gamma_k(\mathbf{x}, \mathbf{x}') = 0$	$\partial_k P(\mathbf{x}) + j\omega \rho(\mathbf{x}) V_k(\mathbf{x}) = 0$
$\partial_k \Gamma_k(\mathbf{x}, \mathbf{x}') + j\omega \bar{\kappa}(\mathbf{x}) G(\mathbf{x}, \mathbf{x}') = \delta(\mathbf{x} - \mathbf{x}')$	$\partial_k V_k(\mathbf{x}) + j\omega \kappa(\mathbf{x}) P(\mathbf{x}) = S(\mathbf{x})$

**Table 3.1** States for a general representation of two-way wavefields.

theorem of the convolution type (equation (3.5)) gives the following general representation

$$\begin{aligned} & \oint_{\partial D} \{G(\mathbf{x}, \mathbf{x}') V_k(\mathbf{x}) - \Gamma_k(\mathbf{x}, \mathbf{x}') P(\mathbf{x})\} n_k d^2 \mathbf{x} = \\ & j\omega \int_D \{\Gamma_k(\mathbf{x}, \mathbf{x}') (\rho(\mathbf{x}) - \bar{\rho}(\mathbf{x})) V_k(\mathbf{x}) - G(\mathbf{x}, \mathbf{x}') (\kappa(\mathbf{x}) - \bar{\kappa}(\mathbf{x})) P(\mathbf{x})\} d^3 \mathbf{x} \\ & + \int_D S(\mathbf{x}) G(\mathbf{x}, \mathbf{x}') d^3 \mathbf{x} - P(\mathbf{x}'). \end{aligned} \quad (3.28)$$

By using  $G(\mathbf{x}, \mathbf{x}') = G(\mathbf{x}', \mathbf{x})$ ,  $\Delta \rho(\mathbf{x}) = \rho(\mathbf{x}) - \bar{\rho}(\mathbf{x})$ ,  $\Delta \kappa(\mathbf{x}) = \kappa(\mathbf{x}) - \bar{\kappa}(\mathbf{x})$ ,  $\partial_k n_k = \partial_n$ ,  $\Gamma_k(\mathbf{x}, \mathbf{x}') = \frac{-1}{j\omega \bar{\rho}(\mathbf{x})} \partial_k G(\mathbf{x}, \mathbf{x}')$ ,  $V_k(\mathbf{x}) = \frac{-1}{j\omega \rho(\mathbf{x})} \partial_k P(\mathbf{x})$  and interchanging  $\mathbf{x}$  with  $\mathbf{x}'$  gives

$$\begin{aligned} P(\mathbf{x}) = & \int_D G(\mathbf{x}, \mathbf{x}') S(\mathbf{x}') d^3 \mathbf{x}' + \\ & \frac{1}{j\omega} \oint_{\partial D} \left\{ \frac{1}{\rho(\mathbf{x}')} G(\mathbf{x}, \mathbf{x}') \partial'_n P(\mathbf{x}') - \frac{1}{\bar{\rho}(\mathbf{x}')} (\partial'_n G(\mathbf{x}, \mathbf{x}')) P(\mathbf{x}') \right\} d^2 \mathbf{x}' + \\ & \frac{1}{j\omega} \int_D \left\{ \frac{\Delta \rho(\mathbf{x}')}{\bar{\rho}(\mathbf{x}') \rho(\mathbf{x}')} (\partial'_k G(\mathbf{x}, \mathbf{x}')) \partial'_k P(\mathbf{x}') + \omega^2 \Delta \kappa(\mathbf{x}') G(\mathbf{x}, \mathbf{x}') P(\mathbf{x}') \right\} d^3 \mathbf{x}'. \end{aligned} \quad (3.29)$$

This integral representation is known in the acoustic literature as the Kirchhoff-Helmholtz integral (see, for instance Schneider, 1978; Clayton and Stolt, 1981; Berkhout, 1987). The three terms on the right hand side of equation (3.29) can be interpreted as follows (see also Figure 3.2): The first term ①, a volume integral over the source domain, represents the direct field traveling from the source distribution to the observation point at  $\mathbf{x}$ . The second term ②, a surface integral over  $\partial D$ , represents the contributions from sources and scatterers outside the domain  $D$ . The third term ③, a volume integral over the domain  $D$ , can be interpreted as the contribution from scattering objects inside  $D$ . If the actual medium  $\rho(\mathbf{x}), \kappa(\mathbf{x})$  differs from the reference medium  $\bar{\rho}(\mathbf{x}), \bar{\kappa}(\mathbf{x})$  this volume integral has a contribution to the field  $P(\mathbf{x})$ . The strength of this contribution is dependent on the contrast between the actual medium and the reference medium.

Define the incident field  $P^i$  as the wavefield in the reference medium and the scattered wavefield  $P^s$  as the difference of the total wavefield  $P$  and the incident

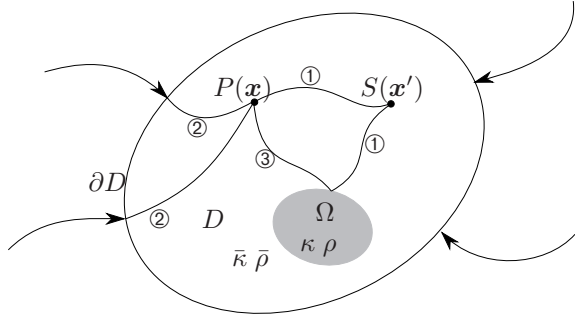


**Figure 3.2** General representation of the wavefield in domain  $D$  with a scattering area  $\Omega$ , where  $\mathbf{x}$  represents the point of observation and  $\mathbf{x}'$  represents the source position inside  $D$ . Note that it is possible to distinguish three different contributions at the point of observation.

field according to

$$\begin{aligned} P^s(\mathbf{x}) &= P(\mathbf{x}) - P^i(\mathbf{x}), \text{ with} \\ P^i(\mathbf{x}) &= \int_D G(\mathbf{x}, \mathbf{x}') S(\mathbf{x}') d^3 \mathbf{x}'. \end{aligned} \quad (3.30)$$

An integral representation of the scattered wavefield can be obtained by assuming that the surface  $\partial D$  in equation (3.29) is a sphere with infinite radius, so that the surface integral ② vanishes on account of Sommerfeld's radiation condition, (Bleistein, 1984)). The integral representation for the scattered wavefield is then given by

$$P^s(\mathbf{x}) = \frac{1}{j\omega} \int_{\Omega} \left\{ \frac{\Delta\rho(\mathbf{x}')}{\bar{\rho}(\mathbf{x}')\rho(\mathbf{x}')} (\partial'_k G(\mathbf{x}, \mathbf{x}')) \partial'_k P(\mathbf{x}') + \omega^2 \Delta\kappa(\mathbf{x}') G(\mathbf{x}, \mathbf{x}') P(\mathbf{x}') \right\} d^3 \mathbf{x}'. \quad (3.31)$$

According to this representation the scattering object can be replaced by a set of distributed sources, which are the product of the contrasting terms and the total field inside the scatterer. This representation of the scattered field will be used in the derivation of the double focusing procedure described in chapter 4.

Another useful representation for the wavefield inside  $D$  can be obtained by assuming that the domain  $D$  has a finite extent and does not contain any contrasts, so the volume integral with the contrast terms  $\Delta\kappa$  and  $\Delta\rho$  in equation (3.29) vanish completely. The resulting representation of the scattered field is then given by

$$P^s(\mathbf{x}) = \frac{1}{j\omega} \oint_{\partial D} \frac{1}{\rho(\mathbf{x}')} \{ G(\mathbf{x}, \mathbf{x}') \partial'_n P^s(\mathbf{x}') - (\partial'_n G(\mathbf{x}, \mathbf{x}')) P^s(\mathbf{x}') \} d^2 \mathbf{x}'. \quad (3.32)$$

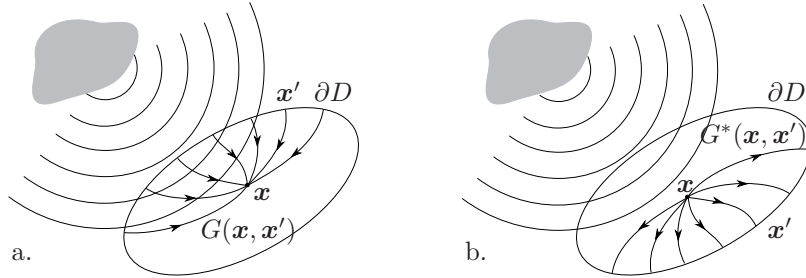


**Figure 3.3** a) Forward propagating version of the Kirchhoff integral; the Green's function propagates inward starting from the surface  $\partial D$ . b) Backward propagating version of the Kirchhoff integral; the Green's function propagates outward starting from the surface  $\partial D$ .

In equation (3.32)  $\mathbf{x}'$  can be interpreted as the position of a secondary source located on the surface  $\partial D$ . This secondary source has a strength equal to the wavefield at  $\mathbf{x}'$  and is determined by the wavefields originating from sources and scattering objects located outside  $D$ . The integral representation describes forward propagation of the measured wavefield at the surface towards a position  $\mathbf{x}$  inside the medium  $D$ . If parts of the surface  $\partial D$  are extended to infinity the contribution of these surfaces vanishes on account of Sommerfeld's radiation condition.

By replacing  $G$  with the complex conjugate of  $G^*$  in equation (3.32) the backward propagating version of the Kirchhoff integral is obtained (Bojarski, 1983; Wapenaar et al., 1989). Note that  $G^*$  is also a solution of the two-way wave equation and represents the anti-causal Green's wavefield. Replacing  $G$  with  $G^*$  in equation (3.32) gives

$$P^s(\mathbf{x}) = \frac{1}{j\omega} \oint_{\partial D} \frac{1}{\rho(\mathbf{x}')} \{ G^*(\mathbf{x}, \mathbf{x}') \partial'_n P^s(\mathbf{x}') - (\partial'_n G^*(\mathbf{x}, \mathbf{x}')) P^s(\mathbf{x}') \} d^2\mathbf{x}'. \quad (3.33)$$

The integral representation describes backward propagation of the measured field at the surface towards a position  $\mathbf{x}$  inside the medium  $D$ . If parts of the surface  $\partial D$  are extended to infinity the contribution of these surfaces will not vanish. The Sommerfeld's radiation condition requires that the Green's function propagates outward through  $\partial D$ , in the same direction as the total wavefield and this condition is not satisfied for the backward propagation Green's function.

Equations (3.32) and (3.33) are the basis for forward and inverse wavefield extrapolation techniques and are graphically illustrated in figure 3.3. By choosing appropriate (fully reflecting) boundary conditions for the Green's function in equation (3.32) and (3.33) the Rayleigh I (rigid boundary) and Rayleigh II (compliant boundary) integrals for forward and inverse extrapolation can be derived (see Berkhout, 1987; Berkhout and Wapenaar, 1989).

### 3.3 Integral representations for one-way wavefields

Integral representations for one-way wavefields are derived by using the reciprocity theorem derived in section (3.1.2) and taking some special choices for the two states  $A$  and  $B$  in the reciprocity relation. The domain  $D$  is a volume 'enclosed' by two infinite parallel surfaces normal to the  $x_3$  axis, see figure 3.1.

State A	State B
$\partial_3 \mathbf{G}(\mathbf{x}, \mathbf{x}') - \bar{\mathbf{B}}(\mathbf{x}) \mathbf{G}(\mathbf{x}, \mathbf{x}') = \mathbf{I} \delta(\mathbf{x} - \mathbf{x}')$	$\partial_3 \mathbf{P}(\mathbf{x}) - \mathbf{B}(\mathbf{x}) \mathbf{P}(\mathbf{x}) = \mathbf{S}(\mathbf{x})$

**Table 3.2** States for general representation of one-way wavefields.

For the derivation of a general one-way representations state  $A$  in the reciprocity theorem is replaced by a one-way Green's function and state  $B$  by the actual one-way wavefield. The Green's function is defined with reference operator  $\bar{\mathbf{B}}$  and a point source at  $\mathbf{x}'$  inside  $D$ . In the acoustic one-way wave equation the Green's operator matrix defined by these choices is given by

$$\mathbf{G}(\mathbf{x}, \mathbf{x}') = \begin{pmatrix} G^{+,+} & G^{+,-} \\ G^{-,+} & G^{-,-} \end{pmatrix}(\mathbf{x}, \mathbf{x}'), \quad (3.34)$$

where the superscripts refer to the propagation direction at  $\mathbf{x}$  and  $\mathbf{x}'$  respectively, see also figure 3.4. For state B, with the actual operator  $\mathbf{B}$ , the source is positioned inside  $D$  at  $\mathbf{S}(\mathbf{x})$ . These two states, which are used to derive the general representation, are summarized in table (3.2).

Substituting these two states into the reciprocity theorem of the convolution type,

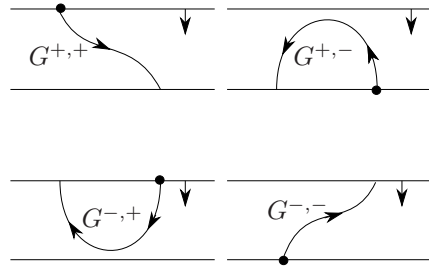


**Figure 3.4** The elements in the one-way Green's function. Note that the Green's functions for the direction converted waves  $G^{+,-}$  and  $G^{-,+}$  are only non-zero if  $\Theta(\mathbf{x}) \neq 0$ .

given by equation (3.25), gives the following expression;

$$\begin{aligned}
& \int_{\partial D} \mathbf{G}^T(\mathbf{x}, \mathbf{x}') \mathbf{N} \mathbf{P}(\mathbf{x}) n_3 d^2 \mathbf{x} = \\
& -j\omega \int_D \mathbf{G}^T(\mathbf{x}, \mathbf{x}') \mathbf{N}(\Lambda(\mathbf{x}) - \bar{\Lambda}(\mathbf{x})) \mathbf{P}(\mathbf{x}) d^3 \mathbf{x} \\
& + \int_D \mathbf{G}^T(\mathbf{x}, \mathbf{x}') \mathbf{N}(\Theta(\mathbf{x}) - \bar{\Theta}(\mathbf{x})) \mathbf{P}(\mathbf{x}) d^3 \mathbf{x} \\
& + \int_D \mathbf{G}^T(\mathbf{x}, \mathbf{x}') \mathbf{N} \mathbf{S}(\mathbf{x}) d^3 \mathbf{x} + \mathbf{N} \mathbf{P}(\mathbf{x}'). \tag{3.35}
\end{aligned}$$

This equation can be simplified by making use of a reciprocity relation between two one-way Green's functions (Wapenaar, 1996a). This relation is given by

$$\mathbf{G}^T(\mathbf{x}, \mathbf{x}') = -\mathbf{N} \mathbf{G}(\mathbf{x}', \mathbf{x}) \mathbf{N}^{-1} \tag{3.36}$$

and is obtained by applying the reciprocity relation of the convolution type (3.27) to two Green's states defined in the same medium, where the wavefield in state *A* is given by  $\mathbf{G}(\mathbf{x}, \mathbf{x}')$  and the wavefield of state *B* by  $\mathbf{G}(\mathbf{x}, \mathbf{x}'')$ . The medium outside *D* is chosen homogeneous and isotropic. Note that this reciprocity relation for the Green's function holds due to the flux normalization of the composition operator matrices  $\mathbf{L}$ .

Multiplying equation (3.35) with  $\mathbf{N}^{-1}$ , using the reciprocity relation of equation (3.36) and interchanging  $\mathbf{x}$  and  $\mathbf{x}'$  gives the following representation for the one wavefield at  $\mathbf{x}$

$$\begin{aligned}
\mathbf{P}(\mathbf{x}) = & \int_D \mathbf{G}(\mathbf{x}, \mathbf{x}') \mathbf{S}(\mathbf{x}') d^3 \mathbf{x}' \\
& - \int_{\partial D} \mathbf{G}(\mathbf{x}, \mathbf{x}') \mathbf{P}(\mathbf{x}') n_3 d^2 \mathbf{x}' \\
& - j\omega \int_D \mathbf{G}(\mathbf{x}, \mathbf{x}') (\Lambda(\mathbf{x}') - \bar{\Lambda}(\mathbf{x}')) \mathbf{P}(\mathbf{x}') d^3 \mathbf{x}' \\
& + \int_D \mathbf{G}(\mathbf{x}, \mathbf{x}') (\Theta(\mathbf{x}') - \bar{\Theta}(\mathbf{x}')) \mathbf{P}(\mathbf{x}') d^3 \mathbf{x}'. \tag{3.37}
\end{aligned}$$

Note the analogy with the two-way representation of equation (3.29). The right hand-side of equation (3.37) contains respectively, a direct wave contribution, a boundary integral over the interaction quantity, a volume integral over the contrast term for propagation and a volume integral over the contrast term for scattering.

This general one-way representation is used to derive volume and surface integral representations of the scattered one-way wavefield. A volume integral representation is obtained by letting the boundary integral over  $\partial D$  vanish by choosing domain *D* equal to  $\mathbb{R}^3$ . Further subtracting the incident wavefield

$$\mathbf{P}^i(\mathbf{x}) = \int_D \mathbf{G}(\mathbf{x}, \mathbf{x}') \mathbf{S}(\mathbf{x}') d^3 \mathbf{x}' \tag{3.38}$$

from the result of equation (3.37) gives

$$\begin{aligned}\mathbf{P}^s(\mathbf{x}) &= -j\omega \int_D \mathbf{G}(\mathbf{x}, \mathbf{x}') (\mathbf{\Lambda}(\mathbf{x}') - \bar{\mathbf{\Lambda}}(\mathbf{x}')) \mathbf{P}(\mathbf{x}') d^3x' \\ &\quad + \int_D \mathbf{G}(\mathbf{x}, \mathbf{x}') (\mathbf{\Theta}(\mathbf{x}') - \bar{\mathbf{\Theta}}(\mathbf{x}')) \mathbf{P}(\mathbf{x}') d^3x', \\ &= \int_D \mathbf{G}(\mathbf{x}, \mathbf{x}') (\mathbf{B}(\mathbf{x}') - \bar{\mathbf{B}}(\mathbf{x}')) \mathbf{P}(\mathbf{x}') d^3x',\end{aligned}\quad (3.39)$$

which represents the scattered one-way wavefield due to a contrasting medium in domain  $D$ . The operators  $\bar{\mathbf{\Theta}}$  and  $\bar{\mathbf{\Lambda}}$  for the Green's state can be chosen independently from each other, for example by choosing  $\bar{\mathbf{\Theta}} = \mathbf{O}$  and  $\bar{\mathbf{\Lambda}} = \mathbf{\Lambda}$  only one integral remains in equation (3.39).

Another useful representation is obtained when the domain  $D$  is source free and does not contain any contrasts. Then all the volume integrals in equation (3.37) vanish which leaves

$$\mathbf{P}^s(\mathbf{x}) = - \int_{\partial D} \mathbf{G}(\mathbf{x}, \mathbf{x}') \mathbf{P}^s(\mathbf{x}') n_3 d^2\mathbf{x}'.\quad (3.40)$$

Note that the most important contribution at  $\mathbf{x}$  is the integral over that part of the surface  $\partial D$  which is positioned between  $\mathbf{x}$  and the source position  $\mathbf{x}_s$  (see figure 3.5). If the upper half-space, shown in figure 3.5, is chosen source free (outside  $D$ ) and homogeneous and  $\mathbf{x}_s$  is chosen below  $\partial D_0$  then the contribution of the surface integral over  $\partial D_1$  vanishes and only the surface integral over  $\partial D_0$  remains. This resulting equation (3.40) describes 'one-way wavefield extrapolation', as it is commonly named in the literature on seismic exploration (see for example Claerbout, 1976; Berkhout, 1982). Another way to derive equation (3.40) is to substitute  $P = P^+ + P^-$  into the two-way representation of equation (3.32) and rewriting the resulting expression (see for example Berkhout and Wapenaar, 1989).

The backward propagating version of equation (3.40) can be obtained by using the reciprocity relation of the correlation type (equation (3.27)) and following the same steps as before which results in

$$\begin{aligned}\mathbf{P}^s(\mathbf{x}) &\approx -j\omega \int_D \mathbf{KG}^*(\mathbf{x}, \mathbf{x}') \mathbf{K}(\mathbf{\Lambda}(\mathbf{x}') - \bar{\mathbf{\Lambda}}(\mathbf{x}')) \mathbf{P}(\mathbf{x}') d^3x' \\ &\quad + \int_D \mathbf{KG}^*(\mathbf{x}, \mathbf{x}') \mathbf{K}(\mathbf{\Theta}(\mathbf{x}') - \bar{\mathbf{\Theta}}(\mathbf{x}')) \mathbf{P}(\mathbf{x}') d^3x', \\ &= \int_D \mathbf{KG}^*(\mathbf{x}, \mathbf{x}') \mathbf{K}(\mathbf{B}(\mathbf{x}') - \bar{\mathbf{B}}(\mathbf{x}')) \mathbf{P}(\mathbf{x}') d^3x',\end{aligned}\quad (3.41)$$

representing the backpropagating counterpart of equation (3.39) with

$$\mathbf{K} = \mathbf{J}^{-1} \mathbf{N} = \mathbf{N}^{-1} \mathbf{J} = \begin{pmatrix} 0 & 1 \\ 1 & 0 \end{pmatrix}.\quad (3.42)$$

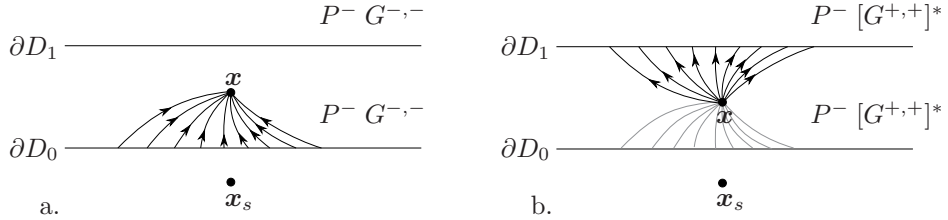


**Figure 3.5** Forward (a) and inverse (b) extrapolation with the forward and backward propagating Green's function. Note that for forward propagation the surface integral over  $\partial D_1$  vanishes and the only contributions comes from the surface integral over  $\partial D_0$ . For inverse extrapolation the surface integral over  $\partial D_0$  does not vanish and represents the evanescent waves. The propagating waves are represented by the surface integral over  $\partial D_1$ .

Using now the same domain as used in the derivation of equation (3.40) yields

$$\mathbf{P}^s(\mathbf{x}) \approx - \int_{\partial D} \mathbf{K} \mathbf{G}^*(\mathbf{x}, \mathbf{x}') \mathbf{K} \mathbf{P}^s(\mathbf{x}') n_3 d^2 x', \quad (3.43)$$

In equation (3.43) the operators on the diagonal of  $\mathbf{G}^*$  can be interpreted as an approximation of the inverse operators of the diagonal elements in the Green's function  $\mathbf{G}$ , since forward and backward propagation of the one-way wavefield over the same distance should yield the original input wavefield. The exact inverse of the Green's operator cannot be used in numerical implementations because it blows up the evanescent fields. In the 'matched filter' approximation (equation (3.43)) the evanescent modes are erroneously handled. Although this limits the maximum obtainable spatial resolution, it also assures stability since the evanescent wave modes are suppressed instead of amplified, Wapenaar and Berkhouw (1989). In the remainder of this thesis the approximation sign  $\approx$  is replaced with an equal  $=$  sign if only the evanescent waves are neglected.

The most important contribution in the backward propagating solution at  $\mathbf{x}$  is the surface integral over  $\partial D_1$  if the source is positioned below  $\partial D_0$ . If it would be possible to use the exact inverse of the Green's operator then the contribution of the surface  $\partial D_1$  would be sufficient to represent the field inside  $D$ . However by using the matched filter approach the surface integral over  $\partial D_0$  must be included to get a correct representation of the evanescent wavefield. Usually one is only interested in the propagating wavefield and the surface integral over  $\partial D_0$  can be neglected. In figure 3.5 the lines starting at the boundaries indicate the propagation direction of the Green's wavefields  $G^{-,-}$  and  $[G^{+,+}]^*$ . The gray lines refer to the contribution of the evanescent waves and the solid lines refer to the propagating wavefield. The actual wavefield  $P^-(\mathbf{x})$  originates from a source below the surface  $\partial D_0$ . Note that if one is only interested in the propagating wavefield the contribution from the surface  $\partial D_0$  can be neglected in the backward propagating integral representation. A

more detailed discussion of the approximations involved in the backward propagating version of the two-way and one-way representation can be found in Wapenaar and Berkhouwt (1989).

Finally all the tools are ready to derive the forward model used in this thesis. The forward model for (primary) scattered data is derived by using the states indicated in table (3.3) in the representation of equation (3.37).

State A	State B
$\partial_3 \mathbf{G}(\mathbf{x}, \mathbf{x}') + j\omega \mathbf{\Lambda}(\mathbf{x}) \mathbf{G}(\mathbf{x}, \mathbf{x}') = \mathbf{I}\delta(\mathbf{x} - \mathbf{x}')$	$\partial_3 \mathbf{P}(\mathbf{x}) - \mathbf{B}(\mathbf{x}) \mathbf{P}(\mathbf{x}) = \mathbf{S}(\mathbf{x})\delta(\mathbf{x} - \mathbf{x}_s)$

**Table 3.3** Reciprocity states for scattered one-way wavefields.

The propagation operator  $\bar{\mathbf{\Lambda}} = \mathbf{\Lambda}$  for the Green's state is chosen the same as in the actual medium and the scattering operator for the Green's state is chosen equal to zero,  $\mathbf{\Theta} = \mathbf{O}$ . The Green's function used in the representation is causally related to the source function. With these choices the Green's matrix  $\mathbf{G}(\mathbf{x}, \mathbf{x}')$  contains only diagonal elements which are given by

$$\mathbf{G}(\mathbf{x}, \mathbf{x}') = \begin{pmatrix} H(x_3 - x'_3)W_p^+(\mathbf{x}, \mathbf{x}') & 0 \\ 0 & -H(x'_3 - x_3)W_p^-(\mathbf{x}, \mathbf{x}') \end{pmatrix}, \quad (3.44)$$

where  $H(x_3)$  is the Heaviside step function.  $W_p^+(\mathbf{x}, \mathbf{x}')$  and  $W_p^-(\mathbf{x}, \mathbf{x}')$  are referred to as the primary propagators in the actual medium for downgoing and upgoing waves. Note that for a homogeneous medium the primary propagators can be written in a closed form. These closed form expressions are useful in the numerical implementation of the forward model which is sketched in the next section. For non-homogeneous media the primary propagator can be built up recursively (Berkhouwt, 1982; Wapenaar, 1996a).

The actual wavefield  $\mathbf{P}$  in the representation originates from the downgoing source

$$\mathbf{S}(\mathbf{x}) = \begin{pmatrix} S_0^+ \\ 0 \end{pmatrix}(\mathbf{x}). \quad (3.45)$$

The domain  $D$  in equation (3.37) spans the entire space  $\mathbb{R}^3$  in which the upper half-space  $x_3 \leq x_{3,m}$  is homogeneous and the lower half-space  $x_3 > x_{3,m}$  is inhomogeneous. The source and receiver are positioned in the homogeneous upper half-space. In this configuration the surface integral in equation (3.37) vanishes which leaves the following expression for a detector position at  $\mathbf{x}_r$  in the homogeneous halfspace

$$\mathbf{P}(\mathbf{x}_r) = \mathbf{P}^i(\mathbf{x}_r) + \int_{\Omega} \mathbf{G}(\mathbf{x}_r, \mathbf{x}) \mathbf{\Theta}(\mathbf{x}) \mathbf{P}(\mathbf{x}) d^3x, \quad (3.46)$$

where  $\mathbf{P}^i(\mathbf{x}_r)$  represents the incident field defined by equation (3.38). Writing equation (3.46) into up- and downgoing components by using the Green's matrix of

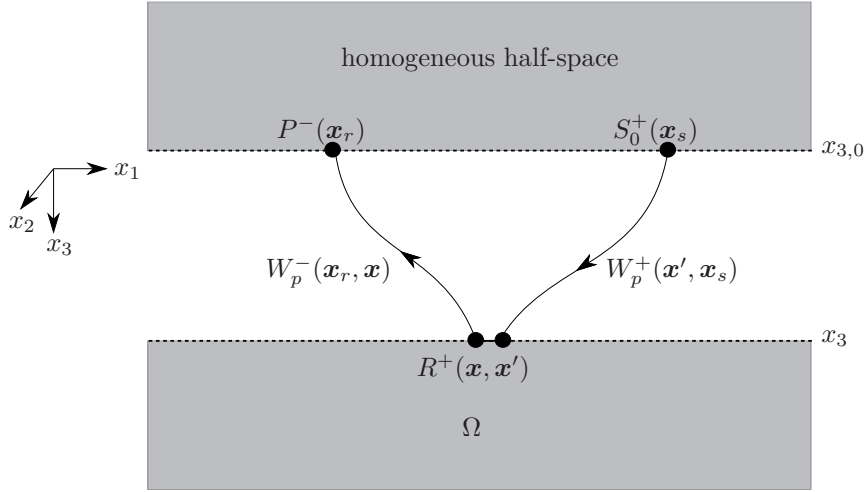


**Figure 3.6** Configuration for scattered one-way wavefields using primary propagators  $W_p^+(\mathbf{x}', \mathbf{x}_s)$  and  $W_p^-(\mathbf{x}_r, \mathbf{x})$  in the medium between the source and receiver positions and the contrast medium.

equation (3.44) gives for the upgoing wave at  $\mathbf{x}_r$

$$P^-(\mathbf{x}_r) - P^{-,i}(\mathbf{x}_r) = \int_{\Omega} W_p^-(\mathbf{x}_r, \mathbf{x}) \mathcal{R}^+(\mathbf{x}) P^+(\mathbf{x}) d^3x + \int_{\Omega} W_p^-(\mathbf{x}_r, \mathbf{x}) \mathcal{T}^-(\mathbf{x}) P^-(\mathbf{x}) d^3x, \quad (3.47)$$

where  $\Omega$  denotes the lower half-space  $x_3 > x_{3,0}$ , see figure 3.6. The upgoing scattered wavefield  $P^{-,s} = P^- - P^{-,i}$  at  $\mathbf{x}_r$  consists of two elements; the transmitted upgoing wavefield  $\mathcal{T}^- P^-$  and the reflected downgoing wavefield  $\mathcal{R}^+ P^+$  originating from the inhomogeneities in the domain  $\Omega$ . Note that the reflection operator  $\mathcal{R}^+(\mathbf{x})$  in equation (3.47) can be represented by the integral

$$\mathcal{R}^+(\mathbf{x}) P^+(\mathbf{x}) = \int_{\mathbb{R}^2} [R^+(\mathbf{x}, \mathbf{x}') P^+(\mathbf{x}')]_{x'_3=x_3} d^2\mathbf{x}', \quad (3.48)$$

where  $R^+(\mathbf{x}, \mathbf{x}')$  is the kernel of operator  $\mathcal{R}^+(\mathbf{x})$ , with  $\mathbf{x}' = (x'_1, x'_2, x'_3 = x_3)$  a point defined on the horizontal reflector, see figure 3.6. An expression for primary scattered data is obtained by replacing  $\mathbf{P}(\mathbf{x})$  in the right-hand side of equation (3.46) with  $P^{+,i}(\mathbf{x}) = W_p^+(\mathbf{x}, \mathbf{x}_s) S_0^+(\mathbf{x}_s)$  and  $P^-(\mathbf{x}) = 0$ . In this replacement the field  $\mathbf{P}(\mathbf{x})$  which is represented completely by equation (3.37) is approximated by the incident wavefield (the first right hand-side term in equation (3.37)). Using this

approximation in equation (3.47) gives for the upgoing scattered wavefield

$$P^{-,s}(\mathbf{x}_r, \mathbf{x}_s) = \int_{\Omega} \int_{\mathbb{R}^2} W_p^-(\mathbf{x}_r, \mathbf{x}) [R^+(\mathbf{x}, \mathbf{x}') W_p^+(\mathbf{x}', \mathbf{x}_s)]_{x'_3=x_3} S_0^+(\mathbf{x}_s) d^2\mathbf{x}' d^3\mathbf{x}. \quad (3.49)$$

Equation (3.49) can be read from right to left as follows;  $S_0^+$  represents the down-going source function at  $\mathbf{x}_s$ , the propagation operator  $W_p^+$  propagates the source wavefield from the source position downwards to the scattering medium at  $\mathbf{x}'$ , here the wavefield gets reflected by  $R^+(\mathbf{x}, \mathbf{x}')$  which is represented by the surface integral over  $\partial\Omega$ , finally the reflected wavefield is propagated upwards by the propagation operator  $W_p^-$  to a receiver position at  $\mathbf{x}_r$ . This useful representation of seismic data was first introduced in a discrete formulation by Berkhou (1982) for acoustic one-way wavefields.

An alternative more mathematical interpretation of equation (3.49) is that it represents the first order term of a Bremmer series (Corones, 1975; Wapenaar, 1996a). The Bremmer series is a straightforward one-way representation of primary and multiple reflection data. In the Bremmer series every term represents an independent part of the wavefield, while in a Neumann series (which is used in two-way methods) the wavefield represented by the first term is also adjusted by the higher order terms. Note that the one-way reflection operator  $\mathcal{R}^+$  is proportional to the vertical variations of the medium parameters which makes it very suitable for seismic applications because in seismic applications the vertical variations are much more pronounced than the horizontal variations. Compared with the two-way representation, where a contrast term is defined between the actual and the background medium, the one-way representation is more convenient for layered media. Note also that it is possible to replace in representation (3.49) the primary propagators  $W_p^\pm(\mathbf{x}, \mathbf{x}')$  by generalized primary propagators in which internal multiple scattering is taken into account in a consistent manner (see Wapenaar, 1996a). So the representation of equation (3.49) is not limited to simple configurations, complicated propagation effects (for example due to fine layering) can be taken into account by the  $\mathcal{W}$  operators and reflection is included by the  $\mathcal{R}$  operator.

### 3.4 The WRW model in matrix notation

Although integral representations of seismic data are sometimes more appealing, in real life seismic measurements are always sampled on discrete 'points' in space and time and therefore a matrix notation is more convenient. Another advantage of the matrix notation is that it makes the numerical implementation of the derived scheme straightforward. The matrix notation used in this thesis is based on the notation of Berkhou, (Berkhou, 1982, chapter VI). For a detailed discussion of the matrix representation of seismic data and the matrix notation the reader is referred to Appendix B.

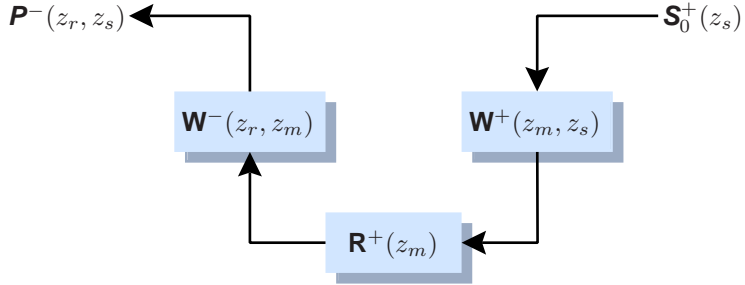


**Figure 3.7** WRW scheme for one seismic experiment and one reflector.

The representation of scattered one-way wavefields given by equation (3.49) is written in matrix notation as

$$\mathbf{P}^-(z_r, z_s) = \sum_m \mathbf{W}^-(z_r, z_m) \mathbf{R}^+(z_m) \mathbf{W}^+(z_m, z_s) \mathbf{S}_0^+(z_s), \quad (3.50)$$

where the elements in the vector  $\mathbf{P}^-(z_r, z_s)$  represent the discrete detector positions of one seismic experiment for one frequency. The propagation matrices  $\mathbf{W}^\pm$  and the reflection matrix  $\mathbf{R}^+$  are discrete version of the kernels in equation (3.49). Figure 3.7 shows a block diagram of equation (3.50). The extension of the single experiment expression of equation (3.50) to a multiple experiment expression is easily done by combining the individual experiments  $\mathbf{P}^-(z_r, z_s)$  into one matrix  $\mathbf{P}^-(z_r, z_s)$  in which every column represents one experiment (see also Appendix B).

The propagation matrices represented by  $\mathbf{W}^\pm$  can be implemented in several ways. One of the implementations makes use of a recursive extrapolation scheme in the space-frequency domain. In this recursive extrapolation scheme a spatial convolution operator is used which extrapolates the data from one depth level to another depth level (where the depth step is in general small compared with the wavelength). This recursive extrapolation scheme can be represented in matrix notation by

$$\mathbf{W}^+(z_m, z_s) = \mathbf{W}^+(z_m, z_{m-1}) \dots \mathbf{W}^+(z_1, z_0) \mathbf{W}^+(z_0, z_s), \quad (3.51)$$

where every matrix  $\mathbf{W}^+$  represents an extrapolation step from one depth level to another. The columns of the  $\mathbf{W}^+$  matrices contain the spatial convolution operators. These operators are calculated only once for the velocity and frequency range of interest and stored in a table. During the extrapolation the operator needed for the position of interest is read from the table (Blacquière, 1989).

Note that within the spatial operator length the medium is assumed to be homogeneous, with the velocity given by the central point of the operator. If the medium varies strongly in the lateral direction this assumption is pushed to its limits (Grimbergen et al., 1996). Therefore in the design of the spatial convolution operators the

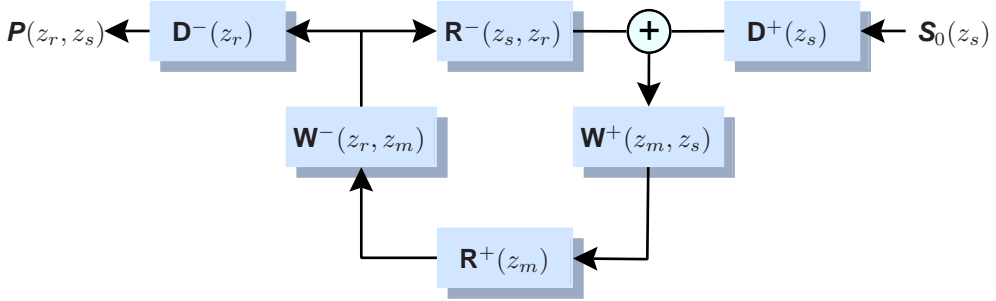


**Figure 3.8** WRW forward modeling scheme for seismic data including the surface related multiples.

aim is to make the length of the operators as short as possible for a certain maximum angle of propagation. For a detailed discussion about the calculation of these short optimized extrapolation operators for 2- and 3-dimensional extrapolation the reader is referred to appendix A.

Starting from the scheme given in figure 3.7 it is very easy to add the influence of surface-related multiples. The multiple free response  $\mathbf{X}_0(z_r, z_s)$  is defined as the total spatial impulse response of the lower half space  $z > z_0$  without the multiples related to depth level  $z_0$ . So with this definition equation (3.50) can be rewritten as

$$\mathbf{P}^-(z_r, z_s) = \mathbf{X}_0(z_r, z_s) \mathbf{S}_0^+(z_s), \quad (3.52)$$

The surface-related multiples are represented by a feed back loop from the left branch of the scheme to the right branch (Verschuur, 1991) scaled by the reflection operator  $\mathbf{R}^-(z_0)$  at the surface of the earth. The total spatial impulse response of the lower half space  $z > z_0$  that includes all the multiples related to depth level  $z_0$  is written as

$$\begin{aligned} \mathbf{X}(z_r, z_s) &= [\mathbf{I} - \mathbf{X}_0(z_r, z_s) \mathbf{W}^+(z_s, z_0) \mathbf{R}^-(z_0) \mathbf{W}^-(z_0, z_r)]^{-1} \mathbf{X}_0(z_r, z_s), \\ \text{or} \\ \mathbf{X}(z_r, z_s) &= [\mathbf{I} - \mathbf{X}_0(z_r, z_s) \mathbf{R}^-(z_s, z_r)]^{-1} \mathbf{X}_0(z_r, z_s), \end{aligned} \quad (3.53)$$

Equation (3.53) forms the basis of the surface-related multiple removal scheme developed by Berkhout (1982) and Verschuur (1991). Note that in this equation the generation of surface-related multiples is explicitly described. The relation between the reflection matrix  $\mathbf{R}^-(z_0)$  and  $\mathbf{R}^-(z_r, z_s)$  is that the latter includes the propagation from the surface  $z_0$  to the source and receiver positions.

The decomposition of the source and the received wavefield into up- and downgoing waves and the directivity of the source and receiver arrays can be included by adding the operators  $\mathbf{D}^\pm$  in the scheme. These surface-related operators and the feed back loop for the surface-related multiples are included in the block diagram of figure 3.8.

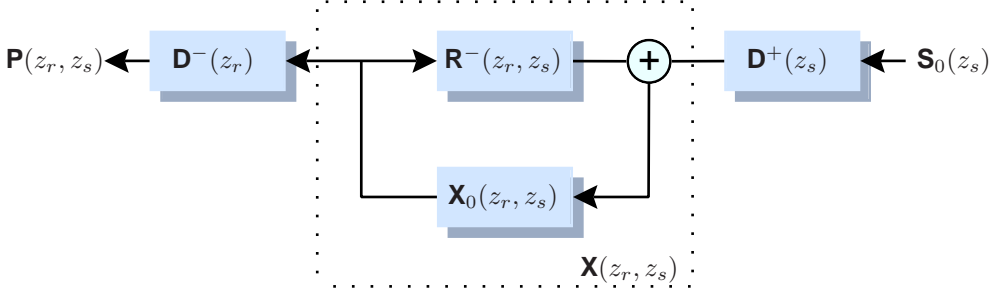


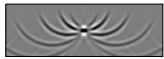
**Figure 3.9** Full WRW forward modeling scheme for seismic data, which includes all surface-related and internal multiples.

The relation between the multiple free data and the data which includes all the surface-related multiples is shown in its most simple form in figure 3.9 and is represented by

$$\mathbf{P}(z_r, z_s) = \mathbf{D}^-(z_r) \mathbf{X}(z_r, z_s) \mathbf{D}^+(z_s) \mathbf{S}_0(z_s), \quad (3.54)$$

where the vector  $\mathbf{P}$  is replaced with matrix  $\mathbf{P}$  to represent the multiple shot experiment. .

Figure 3.9 shows the complete forward modeling scheme of seismic data. The same scheme can also be used for the representation of elastic wave propagation (Wapenaar and Berkhout, 1989). For elastic wave propagation the  $\mathbf{D}$  operators are (de) composition operators which decompose the elastic wavefield into up- and downgoing potentials for compressional and shear wavefields.



## Chapter 4

# Imaging by double focusing

The main goal in seismic data processing is to image the geological structures in the subsurface of the earth. In this chapter it will be shown that the procedure of imaging seismic data can be split into two focusing steps. The intermediate result which is obtained after one focusing step is in a very suitable domain for velocity and AVO analysis. The second focusing step yields a representation of the seismic image, which can be interpreted by a geologist to identify the geological structures of the subsurface. In this chapter the double focusing procedure is explained for two-way and one-way wave fields. However, the one-way solution is preferred because it is more convenient for seismic wave fields.

The two- and one-way representations derived in the previous chapter are used in this chapter to explain the double focusing procedure. In the first section the representations are used to describe the two-way inverse scattering problem. It will be shown that the inverse scattering problem is represented by a non-linear equation. In the last sections a solution of this non-linear equation is expressed in a double focusing procedure for two-way and one-way wave fields. In the double focusing procedure the backward propagating version of the Kirchhoff integral of equation (3.33) plays an important role.

### 4.1 Inverse scattering problem

The integral equation formulation of the scattering problem can be written into two related equations which are based on equations (3.31) and (3.30). In order to keep the notation simple the density is taken to be constant everywhere in space ( $\rho = \bar{\rho}$ ), so the density contrast in equation (3.31) vanishes. The medium configuration which is used to describe the scattering problem is shown in figure 4.1, where the scattering domain is denoted by  $\Omega$ . The source positioned at  $\mathbf{x}_s$  is located inside  $D$ , but outside  $\Omega$ . The Green's function  $G(\mathbf{x}, \mathbf{x}')$  satisfies the Helmholtz equation defined in a background medium with appropriate boundary conditions. The resulting equation

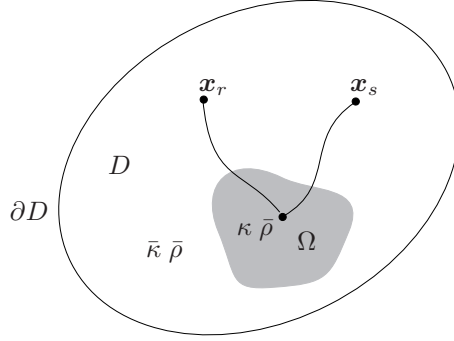


**Figure 4.1** General representation of the wave field in domain  $D$  with scattering domain  $\Omega$ .

represents the measured data at a point  $\mathbf{x}_r$  outside the scattering domain  $\Omega$  and is given by

$$\chi(\mathbf{x}_r)P(\mathbf{x}_r, \mathbf{x}_s) = P^i(\mathbf{x}_r, \mathbf{x}_s) + P^s(\mathbf{x}_r, \mathbf{x}_s), \quad (4.1)$$

where  $P(\mathbf{x}_r, \mathbf{x}_s)$  represents the measured data at the receiver positions  $\mathbf{x}_r$  due to a source at  $\mathbf{x}_s$ . In equation (4.1)  $P^i(\mathbf{x}_r, \mathbf{x}_s)$  represents the incident field and  $P^s(\mathbf{x}_r, \mathbf{x}_s)$  the scattered field which is given by

$$P^s(\mathbf{x}_r, \mathbf{x}_s) = -j\omega \int_{\Omega} G(\mathbf{x}_r, \mathbf{x}') \Delta\kappa(\mathbf{x}') P(\mathbf{x}', \mathbf{x}_s) d^3x', \quad (4.2)$$

where

$$\chi(\mathbf{x}_r) = \begin{cases} 0 & \mathbf{x}_r \in \Omega \\ \frac{1}{2} & \mathbf{x}_r \in \partial\Omega \\ 1 & \mathbf{x}_r \in \mathbb{R}^3 \setminus (\Omega \cup \partial\Omega). \end{cases} \quad (4.3)$$

In equation (4.1) the field inside the scattering domain  $P(\mathbf{x}', \mathbf{x}_s)$  can be represented by a second equation (again based on equation (3.31)) which is given by

$$P(\mathbf{x}', \mathbf{x}_s) = P^i(\mathbf{x}', \mathbf{x}_s) - j\omega \int_{\Omega} G(\mathbf{x}', \mathbf{x}'') \Delta\kappa(\mathbf{x}'') P(\mathbf{x}'', \mathbf{x}_s) d^3x'', \quad (4.4)$$

with  $\mathbf{x}' \in \Omega$  and  $P(\mathbf{x}'', \mathbf{x}_s)$  being the total field inside the scattering domain  $\Omega$  originating from a source positioned at  $\mathbf{x}_s$  and where  $\Delta\kappa(\mathbf{x}'')$  represents the medium properties inside the scattering domain. The integral sign  $\int_{\Omega}$  means integration over the domain  $\Omega$  with a symmetric exclusion for the singular point  $\mathbf{x}' = \mathbf{x}''$ .

In the set of equations (4.1) and (4.4) there are two unknowns. 1) the field inside the scatterer  $P(\mathbf{x}', \mathbf{x}_s)$  and 2) the contrast function  $\Delta\kappa(\mathbf{x}')$ . By substituting equation

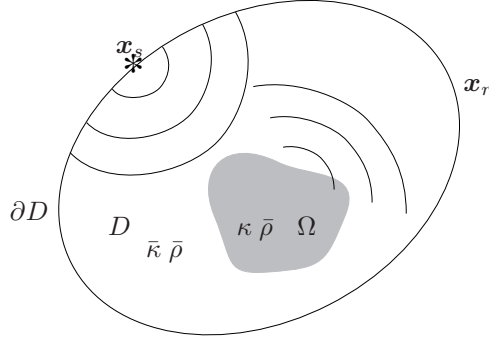


**Figure 4.2** An impulsive point source successively occupies all positions on the surface  $\partial D$  surrounding the object. For each source position the scattered field is recorded by receivers at all positions on the surface.

(4.1) into equation (4.4) the non-linear relation between the measured data and the contrast function becomes evident.

There are many possible routes to obtain approximate solutions of this non-linear set of equations. The most well known solution is probably the Born approximation which linearizes the problem by neglecting the contrast term in equation (4.4). In this thesis only the solution based on a double focusing technique will be discussed.

#### 4.2 Two-way representation of double focusing; full aperture

To explain the double focusing procedure for two-way wave fields the following experimental set up is chosen; a 3-dimensional scattering domain is illuminated by an impulsive point source which successively occupies all positions on a surface surrounding the object, see figure 4.2. For each source position the scattered field is recorded by receivers at all positions on the surface. Note that with this data set all other possible experiments can be synthesized. The aim is to express the contrasting medium  $\Delta\kappa(\mathbf{x}')$  inside the surface in terms of the measured data at the surface and the Green's functions.

An expression of the scattered field inside the domain  $D$ , in terms of the measurements at the surface  $\partial D$ , is obtained by using the focusing integral

$$\Phi^s(\mathbf{x}, \mathbf{x}_s) = \frac{1}{j\omega\bar{\rho}} \oint_{\partial D} \{ G^*(\mathbf{x}, \mathbf{x}_r) \partial_n^r P^s(\mathbf{x}_r, \mathbf{x}_s) - (\partial_n^r G^*(\mathbf{x}, \mathbf{x}_r)) P^s(\mathbf{x}_r, \mathbf{x}_s) \} d^2\mathbf{x}_r. \quad (4.5)$$

Note that equation (4.5) has a similar structure as the backward propagating Kirchhoff-Helmholtz integral of equation (3.33). Physically  $\Phi^s(\mathbf{x}, \mathbf{x}_s)$  can be interpreted as a wave field obtained by backpropagating the scattered field  $P^s(\mathbf{x}_r, \mathbf{x}_s)$

from the receiver locations  $\mathbf{x}_r$  into the scattering region using the Greens function  $G^*(\mathbf{x}, \mathbf{x}_r)$ . An alternative interpretation is that it corresponds to focusing the receiver array (common shot gather) at an arbitrary image point inside the surface  $\partial D$  using the Kirchhoff integral, Oristaglio (1989). Backpropagating the data from a receiver array as an intermediate step to imaging or inversion is well known in seismic migration (Claerbout, 1971; Schneider, 1978; Berkhouit, 1982) and diffraction tomography (Devaney, 1982). Note that  $P^s(\mathbf{x}_r, \mathbf{x}_s)$  represents the scattered field measured at  $\mathbf{x}_r$  due to a source at  $\mathbf{x}_s$ .

With multiple sources there is a scattered field  $P^s(\mathbf{x}_r, \mathbf{x}_s)$  at the receiver position  $\mathbf{x}_r$  for each source position  $\mathbf{x}_s$ . This additional degree of freedom can be used to derive another expression of the scattered field related to the source dependence of the scattered field.

$$\Phi^s(\mathbf{x}, \mathbf{x}_r) = \frac{1}{j\omega\bar{\rho}} \oint_{\partial D} \{G^*(\mathbf{x}, \mathbf{x}_s) \partial_n^s P^s(\mathbf{x}_r, \mathbf{x}_s) - (\partial_n^s G^*(\mathbf{x}, \mathbf{x}_s)) P^s(\mathbf{x}_r, \mathbf{x}_s)\} d^2\mathbf{x}_s. \quad (4.6)$$

Physically  $\Phi^s(\mathbf{x}, \mathbf{x}_r)$  can be interpreted as an image wave field obtained by back-propagating the scattered field  $P^s(\mathbf{x}_r, \mathbf{x}_s)$  caused by sources at locations  $\mathbf{x}_s$  into the scattering region using the Greens function  $G^*(\mathbf{x}, \mathbf{x}_s)$ . An alternative interpretation is that it corresponds to focusing the source array (common receiver gather) at an arbitrary image point inside the surface  $\partial D$  using the Kirchhoff integral.

Substituting the result of equation (4.5) into equation (4.6), by replacing  $P^s(\mathbf{x}_r, \mathbf{x}_s)$  with  $\Phi^s(\mathbf{x}, \mathbf{x}_s)$ , combines the focusing steps for both the source and receiver arrays and gives

$$\Phi^s(\mathbf{x}, \mathbf{x}) = \frac{1}{j\omega\bar{\rho}} \oint_{\partial D} \{G^*(\mathbf{x}, \mathbf{x}_s) \partial_n^s \Phi^s(\mathbf{x}, \mathbf{x}_s) - (\partial_n^s G^*(\mathbf{x}, \mathbf{x}_s)) \Phi^s(\mathbf{x}, \mathbf{x}_s)\} d^2\mathbf{x}_s, \quad (4.7)$$

with  $\Phi^s(\mathbf{x}, \mathbf{x}_s)$  given by equation (4.5). This last equation can be interpreted as follows; first the image field  $\Phi^s(\mathbf{x}, \mathbf{x}_s)$  is formed by focusing the receiver array at a point  $\mathbf{x}$  in the interior of  $\partial D$  by integrating over  $\mathbf{x}_r$ ; second, the source array is focused on the same point by an integral over the source positions  $\mathbf{x}_s$  on  $\partial D$ .

Substituting the representation for the scattered field of equation (4.1) in the backward propagating Kirchhoff integral of equation (4.5) gives an expression for the single focused scattered field in terms of the Greens function, the contrast function and the scattered field measured at the surface.

$$\begin{aligned} \Phi^s(\mathbf{x}, \mathbf{x}_s) &= \frac{1}{\bar{\rho}} \oint_{\partial D} (\partial_n^r G^*(\mathbf{x}, \mathbf{x}_r)) \left\{ \int_{\Omega} G(\mathbf{x}_r, \mathbf{x}') \Delta\kappa(\mathbf{x}') P(\mathbf{x}', \mathbf{x}_s) d^3\mathbf{x}' \right\} d^2\mathbf{x}_r - \\ &\quad \frac{1}{\bar{\rho}} \oint_{\partial D} G^*(\mathbf{x}, \mathbf{x}_r) \partial_n^r \left\{ \int_{\Omega} G(\mathbf{x}_r, \mathbf{x}') \Delta\kappa(\mathbf{x}') P(\mathbf{x}', \mathbf{x}_s) d^3\mathbf{x}' \right\} d^2\mathbf{x}_r. \end{aligned} \quad (4.8)$$

Interchanging volume and surface integrals and making use of the fact that  $\partial_n^r$  works

only on  $\mathbf{x}_r$  gives (after Esmersoy and Oristaglio, 1988),

$$\Phi^s(\mathbf{x}, \mathbf{x}_s) = \int_{\Omega} E_r(\mathbf{x}, \mathbf{x}') \Delta\kappa(\mathbf{x}') P(\mathbf{x}', \mathbf{x}_s) d^3x', \quad (4.9)$$

with

$$E_r(\mathbf{x}, \mathbf{x}') = \frac{1}{\bar{\rho}} \oint_{\partial D} \{(\partial_n^r G^*(\mathbf{x}, \mathbf{x}_r)) G(\mathbf{x}_r, \mathbf{x}') - G^*(\mathbf{x}, \mathbf{x}_r) \partial_n^r G(\mathbf{x}_r, \mathbf{x}')\} d^2\mathbf{x}_r. \quad (4.10)$$

From equations (4.9) and (4.2) it is observed that the scattered field and the extrapolated field have a similar integral representation. The difference is that the kernel  $E_r$  in equation (4.9) replaces the Green's function in equation (4.1). The kernel  $E_r$  can be interpreted as a Green's function for the extrapolated field. It relates the contribution of the secondary sources  $\Delta\kappa(\mathbf{x}') P(\mathbf{x}', \mathbf{x}_s)$  at  $\mathbf{x}'$  to the field extrapolated back to  $\mathbf{x}$ . The field at  $\mathbf{x}$  is the superposition of backpropagated waves measured at the surface  $\partial D$ . For a full acquisition geometry  $E_r$  reduces to a so called 'homogeneous' Green's function (Oristaglio, 1989) which is characterized by both incoming and outcoming (causal and non-causal) waves at infinity and is given by

$$\begin{aligned} E_r(\mathbf{x}, \mathbf{x}') &= -j\omega \{G(\mathbf{x}, \mathbf{x}') - G^*(\mathbf{x}, \mathbf{x}')\} \\ &= -j\omega G_h(\mathbf{x}, \mathbf{x}') \end{aligned}$$

and is obtained by using Green's theorem and the two-way wave equations for the Green's functions  $G^*(\mathbf{x}, \mathbf{x}_r)$  and  $G(\mathbf{x}_r, \mathbf{x}')$ . An important property of the homogeneous Green's function  $G_h(\mathbf{x}, \mathbf{x}')$  is that  $-j\omega G_h(\mathbf{x}, \mathbf{x}')$  evaluated at  $t = 0$ , thus after integration over all frequencies, yields a spatial delta function (see appendix in Oristaglio, 1989).

Substituting equation (4.9) into the double focusing result of equation (4.7) gives

$$\begin{aligned} \Phi^s(\mathbf{x}, \mathbf{x}) &= \frac{1}{j\omega\bar{\rho}} \oint_{\partial D} G^*(\mathbf{x}, \mathbf{x}_s) \partial_n^s \left\{ \int_{\Omega} E_r(\mathbf{x}, \mathbf{x}') \Delta\kappa(\mathbf{x}') P(\mathbf{x}', \mathbf{x}_s) d^3x' \right\} d^2\mathbf{x}_s - \\ &\quad \frac{1}{j\omega\bar{\rho}} \oint_{\partial D} (\partial_n^s G^*(\mathbf{x}, \mathbf{x}_s)) \left\{ \int_{\Omega} E_r(\mathbf{x}, \mathbf{x}') \Delta\kappa(\mathbf{x}') P(\mathbf{x}', \mathbf{x}_s) d^3x' \right\} d^2\mathbf{x}_s. \end{aligned} \quad (4.11)$$

Interchanging volume and surface integrals and making use of the fact that  $\partial_n^s$  works only on  $\mathbf{x}_s$  gives

$$\Phi^s(\mathbf{x}, \mathbf{x}) = \int_{\Omega} E_r(\mathbf{x}, \mathbf{x}') \Delta\kappa(\mathbf{x}') E_s(\mathbf{x}', \mathbf{x}) d^3x', \quad (4.12)$$

with

$$E_s(\mathbf{x}', \mathbf{x}) = \frac{1}{j\omega\bar{\rho}} \oint_{\partial D} \{G^*(\mathbf{x}, \mathbf{x}_s) \partial_n^s P(\mathbf{x}', \mathbf{x}_s) - (\partial_n^s G^*(\mathbf{x}, \mathbf{x}_s)) P(\mathbf{x}', \mathbf{x}_s)\} d^2\mathbf{x}_s. \quad (4.13)$$

Equation (4.12) is the double focusing result and represents an integral over the scattering domain. This expression can be used to derive an inversion formula for the scattering object  $\Delta\kappa(\mathbf{x}')$  at all positions within the domain enclosed by the surface occupied by the sources and receivers.

The Born approximation for the scattered wave field in equation (4.12) is obtained by replacing  $P(\mathbf{x}', \mathbf{x}_s)$  in equation (4.13) by  $P^i(\mathbf{x}', \mathbf{x}_s) = G(\mathbf{x}', \mathbf{x}_s)S(\mathbf{x}_s)$ . Note that for the Born approximation equation (4.13) becomes equal to equation (4.10) (apart from a scaling factor  $S$ ), if the sources and receivers occupy the same positions at the boundary  $\partial D$

$$\begin{aligned} E_s(\mathbf{x}', \mathbf{x}) &= \frac{1}{j\omega\bar{\rho}} \oint_{\partial D} S(\mathbf{x}_s) \{G^*(\mathbf{x}, \mathbf{x}_s) \partial_n^s G(\mathbf{x}', \mathbf{x}_s) - (\partial_n^s G^*(\mathbf{x}, \mathbf{x}_s)) G(\mathbf{x}', \mathbf{x}_s)\} d^2\mathbf{x}_s \\ E_s(\mathbf{x}', \mathbf{x}) &= G_h(\mathbf{x}', \mathbf{x})S(\mathbf{x}_s). \end{aligned} \quad (4.14)$$

Within the Born approximation it is possible to arrive at an explicit expression for the contrast  $\Delta\kappa(\mathbf{x}')$  function by using the property of the Kernels  $E_r$  and  $E_s$  that in the time domain their time derivative evaluated at  $t = 0$  equals a spatial delta function. A detailed inspection of the kernels  $E_s$  and  $E_r$  is beyond the scope of this thesis but can be found in Esmersoy and Oristaglio (1988); Oristaglio (1989).

### 4.3 Two-way representation of double focusing; seismic aperture

Using the backward propagating Kirchhoff-Helmholtz integral of equation (3.29) an expression of the scattered field inside the domain  $D$ , in terms of the measurements at the surface  $\partial D$  and a volume integral over the contrasting domain, is obtained

$$\begin{aligned} P^s(\mathbf{x}, \mathbf{x}_s) &= \frac{1}{j\omega\bar{\rho}} \oint_{\partial D} \{G^*(\mathbf{x}, \mathbf{x}_r) \partial_n^r P^s(\mathbf{x}_r, \mathbf{x}_s) - (\partial_n^r G^*(\mathbf{x}, \mathbf{x}_r)) P^s(\mathbf{x}_r, \mathbf{x}_s)\} d^2\mathbf{x}_r \\ &\quad - j\omega \int_{\Omega} G^*(\mathbf{x}, \mathbf{x}') \Delta\kappa(\mathbf{x}') P(\mathbf{x}') d^3\mathbf{x}'. \end{aligned} \quad (4.15)$$

Note that in comparison with equation (4.5) there is an additional volume integral which represents the scattering due to the contrasting domain  $\Omega$  inside  $D$ . The backpropagated field represented by equation (4.15) is now expressed in the true pressure of the scattered wave field and therefore the symbol  $P^s$  can be used again.

The contribution from the volume integral over  $\Omega$  can be neglected if the seismic acquisition geometry shown in figure 4.3 is taken into account. There are three contributions to the backpropagated wave field at  $\mathbf{x}$ ; ① represents a causal contribution from the surface  $\partial D_1$ ; ② is a contribution from the surface  $\partial D_0$  which is non-causal; ③ is the contribution from the scattering domain  $\Omega$  which is also non-causal. For the configuration in figure 4.3 it can be argued that these non-causal contributions will cancel each other (except for the evanescent wavefield) and thus can be left out in the back propagated result.

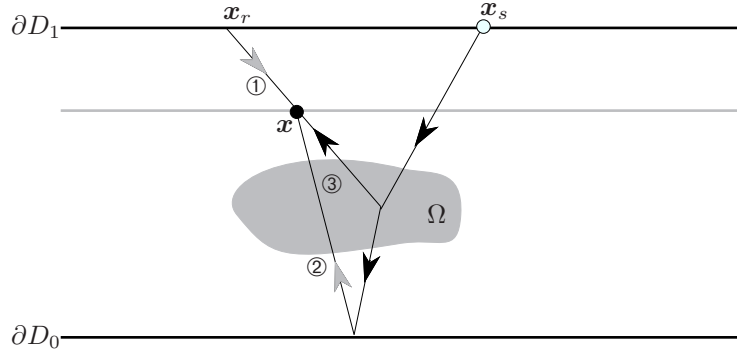


**Figure 4.3** Focusing of the receiver array for a seismic acquisition aperture; the sources and receivers are positioned on the surface  $\partial D_1$ . The backpropagating contributions from the surface  $\partial D_0$  and the scattering volume  $\Omega$  are non-causal which leaves only causal contribution of the surface integral over  $\partial D_1$ .

By using this approximation in equation (4.15) it reduces to

$$P^s(\mathbf{x}, \mathbf{x}_s) = \frac{1}{j\omega\bar{\rho}} \int_{\partial D_1} \{G^*(\mathbf{x}, \mathbf{x}_r) \partial_n^r P^s(\mathbf{x}_r, \mathbf{x}_s) - (\partial_n^r G^*(\mathbf{x}, \mathbf{x}_r)) P^s(\mathbf{x}_r, \mathbf{x}_s)\} d^2\mathbf{x}_r, \quad (4.16)$$

which is similar to equation (4.5). Analogous to the previous section (but now with  $\Phi^s$  replaced by  $P^s$ ) the following expression of the scattered field is obtained

$$P^s(\mathbf{x}, \mathbf{x}) = \int_{\Omega} E_r(\mathbf{x}, \mathbf{x}') \Delta\kappa(\mathbf{x}') E_s(\mathbf{x}', \mathbf{x}) d^3\mathbf{x}'. \quad (4.17)$$

which is similar to equation (4.12). Note that  $E_r$  in equation (4.17) is represented by equation (4.10) and  $E_s$  by equation (4.13), but now with the surface of integration replaced by  $\partial D_1$ . Note also that due to the limited seismic aperture it is not possible to replace the kernels  $E_r$  and  $E_s$  with the homogeneous Green's function.

Due to a limited aperture of the receiver array at  $\partial D_1$  the focused field  $P^s(\mathbf{x}, \mathbf{x}_s)$  in equation (4.16) and the scattered field of equation (4.2) can differ significantly. In this sense the focused field represents a good estimate of the full scattered field that can be obtained from the observed scattered field at the surface by a linear operation (backpropagation) that uses no prior knowledge about the nature of the scattering object.

#### 4.4 One-way representation of double focusing

The double focusing process can also be expressed in the one-way representation formulation of Berkhol't (1996a, 1996b). The advantage of the one-way formulation

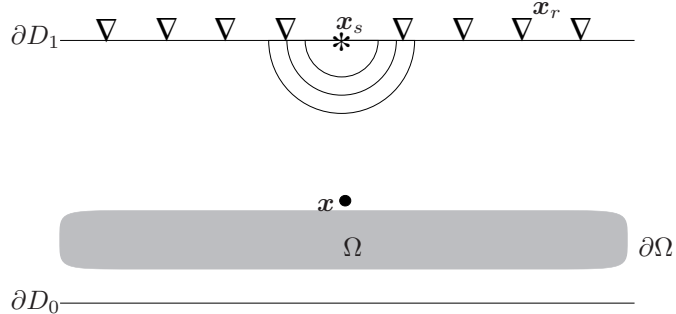


**Figure 4.4** Focusing of the source and receiver arrays to a point in the subsurface. Note that if the halfspace above (and including)  $\partial D_1$  is taken homogeneous and isotropic then the field measured at  $\partial D_1$  consists of only upgoing waves.

is that it clearly shows the relation between the result after the first focusing step and the used macro model to construct the backpropagating Green's function. At the end of this section the double focusing procedure is also shown in the more convenient matrix notation.

To explain the double focusing procedure for one-way wave fields the following experimental set up is chosen; a 3-dimensional scattering object is illuminated by an impulsive point source which successively occupies all positions on two planar surfaces above and below the object ( $\partial D_1$  and  $\partial D_0$ , see figure 4.4). For each source position the scattered field is recorded by receivers at all positions on the surface. The aim is to express the scattering operator  $\Theta$  inside the surface in terms of the measured data at the surface  $\partial D_1$  alone.

#### 4.4.1 Integral representation

To derive the integral representation of the double focusing procedure for one-way wave fields the following Green's state is chosen: the propagation operator  $\bar{\Lambda} = \Lambda$  is chosen the same as in the actual medium and the scattering operator for the Green's state is equal to zero,  $\Theta = \mathbf{O}$ . With these choices the Green's matrix  $\mathbf{G}(\mathbf{x}, \mathbf{x}')$  contains only diagonal elements which are given by equation (3.44). Note that the source is positioned outside domain  $D$  and the scattering domain is chosen inside domain  $D$ .

Backward propagation of the measurements at the detector position to a point  $\mathbf{x}$  inside domain  $D$  can be done by using the backpropagating surface integral representation of equation (3.41). The backward propagated result with the detector

positions at the surface  $\partial D$  is then given by

$$\begin{aligned} \mathbf{P}^s(\mathbf{x}, \mathbf{x}_s) = & - \int_{\partial D} \mathbf{K} \mathbf{G}^*(\mathbf{x}, \mathbf{x}_r) \mathbf{K} \mathbf{P}^s(\mathbf{x}_r, \mathbf{x}_s) n_3 d^2 \mathbf{x}_r + \\ & \int_{\Omega} \mathbf{K} \mathbf{G}^*(\mathbf{x}, \mathbf{x}') \mathbf{K} (\Theta(\mathbf{x}') - \bar{\Theta}(\mathbf{x}')) \mathbf{P}(\mathbf{x}') d^3 \mathbf{x}' \end{aligned} \quad (4.18)$$

Note that there is an extra volume integral in comparison with equation (3.43). This volume integral is due to the presence of the scattering domain  $\Omega$  inside domain  $D$ . Taking the configuration shown in figure 4.4 into account there is only an upgoing scattered wave field at the surface  $\partial D_1$ . Suppose that, unlike in figure 4.4, the surface  $\partial D_0$  is positioned above the scattering domain then the volume integral vanishes and the surface integral over  $\partial D_0$  can be neglected, again ignoring evanescent waves (see also the discussion after equation (3.43)) which leaves only the surface integral over  $\partial D_1$ . If the surface  $\partial D_0$  is positioned below the scattering domain (as in figure 4.4) it is evident that the contribution from the surface  $\partial D_1$  is not changed which means that the contributions from the volume integral and the surface integral over  $\partial D_0$  cancel each other. Taking these arguments into account gives for the backpropagated upgoing scattered field

$$P^{-,s}(\mathbf{x}, \mathbf{x}_s) = \int_{\partial D_1} W_p^{+,*}(\mathbf{x}, \mathbf{x}_r) P^{-,s}(\mathbf{x}_r, \mathbf{x}_s) d^2 \mathbf{x}_r, \quad (4.19)$$

where, according to equation (3.44)  $W_p^+(\mathbf{x}, \mathbf{x}_r) = G^{+,+}(\mathbf{x}, \mathbf{x}_r)$  and where  $P^{-,s}(\mathbf{x}, \mathbf{x}_s)$  represents the scattered wave field at  $\mathbf{x}$  after focusing of the receiver array.

Making use of the redundancy present in the data the same focusing procedure used in equation (3.43) can also be used for the surface  $\partial D_1$  at the positions where the sources are placed. This focusing step along the source surface is represented by

$$P^{-,s}(\mathbf{x}, \mathbf{x}_r) = \int_{\partial D_1} W_p^{+,*}(\mathbf{x}, \mathbf{x}_s) P^{-,s}(\mathbf{x}_r, \mathbf{x}_s) d^2 \mathbf{x}_s, \quad (4.20)$$

where  $P^{-,s}(\mathbf{x}, \mathbf{x}_r)$  represents the scattered wave field at  $\mathbf{x}$  after focusing of the shot array (common receiver gather).

The double focusing result for one-way wave fields is obtained by substituting the result of the focused receiver array of equation (4.19) into the focused source array of equation (4.20) by replacing  $\mathbf{x}_r$  by  $\mathbf{x}$  in  $P^{-,s}(\mathbf{x}_r, \mathbf{x}_s)$  using  $W_p^{+,*}(\mathbf{x}, \mathbf{x}_s) = W_p^{-,*}(\mathbf{x}_s, \mathbf{x})$ , gives

$$\begin{aligned} P^{-,s}(\mathbf{x}, \mathbf{x}) = & \int_{\partial D_1} P^{-,s}(\mathbf{x}, \mathbf{x}_s) W_p^{-,*}(\mathbf{x}_s, \mathbf{x}) d^2 \mathbf{x}_s \\ = & \int_{\partial D_1} \int_{\partial D_1} W_p^{+,*}(\mathbf{x}, \mathbf{x}_r) P^{-,s}(\mathbf{x}_r, \mathbf{x}_s) W_p^{-,*}(\mathbf{x}_s, \mathbf{x}) d^2 \mathbf{x}_r d^2 \mathbf{x}_s. \end{aligned} \quad (4.21)$$

Note that both the source and receiver array are focused on the same point  $\mathbf{x}$  in space. Equation (4.21) shows that the double focusing procedure is carried out by integrating the measured data over the source and receiver surface towards a point in the subsurface.

The scattered field  $P^{-,s}(\mathbf{x}_r, \mathbf{x}_s)$  occurring in equation (4.21) can be represented by the volume integral of equation (3.49)

$$P^{-,s}(\mathbf{x}_r, \mathbf{x}_s) = \int_{\Omega} W_p^-(\mathbf{x}_r, \mathbf{x}') \mathcal{R}^+(\mathbf{x}') W_p^+(\mathbf{x}', \mathbf{x}_s) S_0^+(\mathbf{x}_s) d^3 \mathbf{x}'. \quad (4.22)$$

Note that in this equation  $\mathcal{R}$  is a reflection operator defined by equation (3.48). Substituting this  $WRW$  representation of the scattered wave field into equation (4.21) gives after some manipulations

$$P^{-,s}(\mathbf{x}, \mathbf{x}) = \int_{\Omega} E_r^-(\mathbf{x}, \mathbf{x}') \mathcal{R}^+(\mathbf{x}') E_s^+(\mathbf{x}', \mathbf{x}) d^3 \mathbf{x}', \quad (4.23)$$

where it is assumed that the scattering domain  $\Omega$  and the focus point  $\mathbf{x}$  are both positioned below the surface  $\partial D_1$ .  $E_r^-$  and  $E_s^+$  are then given by

$$E_r^-(\mathbf{x}, \mathbf{x}') = \int_{\partial D_1} W_p^{+,*}(\mathbf{x}, \mathbf{x}_r) W_p^-(\mathbf{x}_r, \mathbf{x}') d^2 \mathbf{x}_r \quad (4.24)$$

$$E_s^+(\mathbf{x}', \mathbf{x}) = \int_{\partial D_1} W_p^+(\mathbf{x}', \mathbf{x}_s) S_0^+(\mathbf{x}_s) W_p^{-,*}(\mathbf{x}_s, \mathbf{x}) d^2 \mathbf{x}_s \quad (4.25)$$

Making use of the integral expression for the reflection operator and writing the surface integral explicitly for the horizontal plane gives

$$P^{-,s}(\mathbf{x}, \mathbf{x}) = \int_{\Omega} \int_{\mathbb{R}^2} [E_r^-(\mathbf{x}, \mathbf{x}') R^+(\mathbf{x}', \mathbf{x}'') E_s^+(\mathbf{x}'', \mathbf{x})]_{x_3''=x_3'} d^2 \mathbf{x}'' d^3 \mathbf{x}' \quad (4.26)$$

An interpretation of equations (4.24), (4.25) and (4.26) is shown in figure 4.5.  $E_r^-$  in equation (4.26) can be interpreted as forward propagation from a reflection point at  $\mathbf{x}'$  to the receiver array at the surface followed by backward propagation from the receiver array to a point  $\mathbf{x}$  in the subsurface. Note that by choosing  $\mathbf{x} = \mathbf{x}'$  the receiver array is focused on a point on the reflector. This means that the scattered data measured by the receivers at  $\partial D_1$  is used to construct the scattered field at  $\mathbf{x}$  originating from a source positioned at  $\mathbf{x}_s$ .  $E_s^+$  represents backward propagation of the contributions of the different sources at the reflection point  $\mathbf{x}'$  to a point  $\mathbf{x}$  in the subsurface.

Equation (4.26) can be simplified further by making use of the fact that the complex conjugate of the propagation operators  $W_p$  are an approximation of the inverse propagation operators (see the discussion after equation (3.43)). Using this property

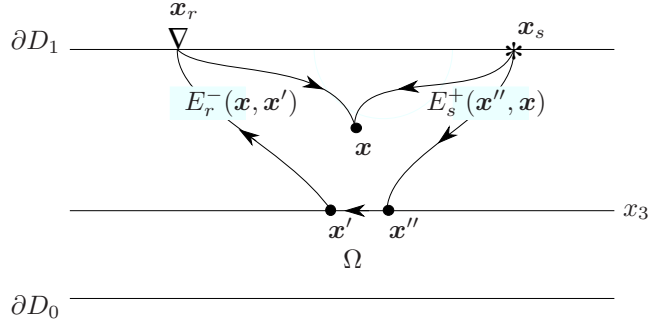


**Figure 4.5** Focusing of the source and receiver arrays to a point in the subsurface. Note that the interior of both the source and receiver domains must have an intersection in which the double focusing can be carried out.

equations (4.24) and (4.25) can be interpreted as follows;

$$\begin{aligned} E_r^-(\mathbf{x}, \mathbf{x}') &= \int_{\partial D_1} W_p^{+,*}(\mathbf{x}, \mathbf{x}_r) W_p^-(\mathbf{x}_r, \mathbf{x}') d^2 \mathbf{x}_r \\ &= \delta(\mathbf{x}_\alpha - \mathbf{x}'_\alpha) \quad \text{if } x'_3 = x_3 \end{aligned} \quad (4.27)$$

$$\begin{aligned} E_s^+(\mathbf{x}'', \mathbf{x}) &= \int_{\partial D_1} W_p^+(\mathbf{x}'', \mathbf{x}_s) S_0^+(\mathbf{x}_s) W_p^-(\mathbf{x}_s, \mathbf{x}) d^2 \mathbf{x}_s \\ &= \delta(\mathbf{x}''_\alpha - \mathbf{x}_\alpha) S_0^+ \quad \text{if } x'_3 = x_3 \end{aligned} \quad (4.28)$$

where the assumption is made that the downgoing source function is independent of the source position;  $S_0^+(\mathbf{x}_s) = S_0^+$ . So, the surface integral can be represented by the delta function if the depth of the focus point is chosen equal to the depth of the reflector. Which is equivalent with the statement that the back transformation of  $E_r$  and  $E_s$  to the time domain gives a spatial delta function at  $t = 0$  (if  $x'_3 = x_3$ ) (note the resemblance with the two-way expressions). The non-causal times ( $t < 0$ ) can be interpreted as the influence of the scattering domain above the focus point (if  $x'_3 < x_3$ ) and the causal times ( $t > 0$ ) are the contributions from the scattering domain below the focus point (if  $x'_3 > x_3$ ). Substituting these results into equation (4.26) gives the following representation of the reflection operator

$$P^{-,s}(\mathbf{x}, \mathbf{x}) = R^+(\mathbf{x}, \mathbf{x}) S_0^+ + \varepsilon_1 + \varepsilon_2, \quad (4.29)$$

where  $\varepsilon_1$  represents the non-causal contribution and  $\varepsilon_2$  the causal contribution with respect to the focus point. Equation (4.29) shows that the double focusing procedure gives a recovery of the reflection operator at  $t = 0$ . The obtained reflectivity information is constrained by the strength of the reflection, the aperture of the receiver, the coverage of the sources and the bandwidth of the data. The double focusing procedure can be interpreted as a consistent way of integrating the redundancy present in the ensemble of all the data.

#### 4.4.2 Matrix representation

The focusing process for one-way wave propagation can be expressed in the **WRW** matrix formulation which was introduced in section (3.4). The derived forward model of seismic reflection data, backscattered from one depth level at  $z_m$ , is given by

$$\mathbf{P}(z_r, z_s) = \mathbf{D}^-(z_r) \mathbf{W}^-(z_r, z_m) \mathbf{R}^+(z_m) \mathbf{W}^+(z_m, z_s) \mathbf{D}^+(z_s) \mathbf{S}(z_s), \quad (4.30)$$

where  $z_r$  represents the receiver level,  $z_m$  the reflection level and  $z_s$  the source level. Focusing in emission can be regarded as a weighted summation (in phase and amplitude) along the common receiver arrays in such a way that the constructed wave front originates from a notional source at a point in the subsurface. The weighting operator used in this process is also called the focusing or synthesis operator, because the operator synthesizes the response of a focusing areal source from the seismic data. The principle of combining shot gathers at the surface for the synthesis of areal source responses, also referred to as areal shot record technology, was already introduced by Berkhou (1992) for controlled illumination in prestack depth migration. Rietveld (1995) has shown many examples for different illuminating areal sources. Note that one row of the matrix  $\mathbf{P}(z_r, z_s)$  represents one common receiver array and one column represents one common shot gather (see also Appendix B). Thus the synthesis operator for focusing in emission works on the rows of the matrix  $\mathbf{P}(z_r, z_s)$  and a synthesis operator for focusing in detection works on the columns of the matrix  $\mathbf{P}(z_r, z_s)$ .

The focusing operator is defined with respect to the coordinates of a common receiver or common source array. The focusing operator for the receiver array, applied to the left side of the right-hand side of equation (4.30), is defined as

$$\begin{aligned} \mathbf{F}_i^-(z_m, z_r) \mathbf{D}^-(z_r) \mathbf{W}^-(z_r, z_m) &= \mathbf{I}_i^-(z_m) \\ \mathbf{F}_i^-(z_m, z_r) &\approx \mathbf{I}_i^-(z_m) [\mathbf{W}^+(z_m, z_r)]^* [\mathbf{D}^-(z_r)]^{-1} \end{aligned} \quad (4.31)$$

with  $\mathbf{I}_i^-(z_m)$  a unit row vector with a 1 at the  $i^{th}$  position at depth  $z_m$  and  $\mathbf{F}_i^-(z_m, z_r)$  the focusing operator acting at the receiver positions at the surface. Note that the approximation in equation (4.31) refers to the approximation of the inverse of the propagation operator  $\mathbf{W}^-(z_r, z_m)$  by its matched filter  $[\mathbf{W}^-(z_r, z_m)]^{-1} \approx [\mathbf{W}^+(z_m, z_r)]^*$ .

The focusing operator for the source array, applied to the right side of the right-hand side of equation (4.30), is defined as

$$\begin{aligned} \mathbf{I}_j^+(z_m) &= \mathbf{W}^+(z_m, z_s) \mathbf{D}^+(z_s) \mathbf{S}(z_s) \mathbf{F}_j^+(z_s, z_m) \\ [\mathbf{D}^+(z_s) \mathbf{S}^+(z_s)]^{-1} [\mathbf{W}^-(z_s, z_m)]^* \mathbf{I}_j^+(z_m) &\approx \mathbf{F}_j^+(z_s, z_m) \end{aligned} \quad (4.32)$$

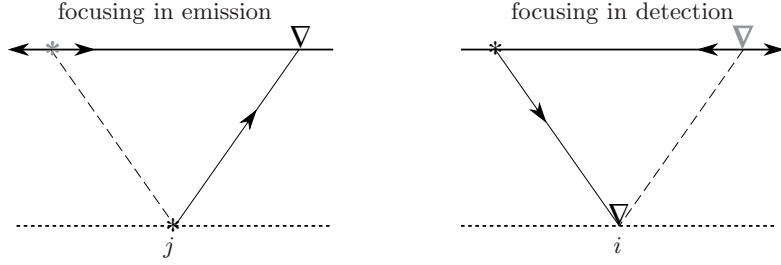


**Figure 4.6** Focusing in detection positions a virtual receiver on a reflecting boundary and focusing in emission positions a virtual source on a reflecting boundary.

with  $\mathbf{I}_j^+(z_m)$  a unit column vector with a 1 at the  $j^{th}$  position at depth  $z_m$  and  $\mathbf{F}_j^+(z_s, z_m)$  the focusing operator acting at the source positions. The focusing operators  $\mathbf{F}^\pm$  perform a summation along the receiver positions ( $\mathbf{F}^-$ ) in a common shot gather or a summation along the source positions ( $\mathbf{F}^+$ ) in a common receiver gather. This summation (or synthesis) is carried out for all source and receiver positions available. The focusing operator for detection is given by the  $i^{th}$  row of  $[\mathbf{W}^+]^*[\mathbf{D}^-]^{-1}$  and the focusing operator for emission is given by the  $j^{th}$  column of  $[\mathbf{D}^+ \mathbf{S}^+]^{-1}[\mathbf{W}^-]^*$ .

Substituting equation (4.31) into equation (4.30) gives an expression of the data after focusing of the detector array

$$\mathbf{F}_i^-(z_m, z_r) \mathbf{P}(z_r, z_s) = \mathbf{P}_i^-(z_m, z_s) = \mathbf{I}_i^-(z_m) \mathbf{R}^+(z_m) \mathbf{W}^+(z_m, z_s) \mathbf{D}^+(z_s) \mathbf{S}(z_s) \quad (4.33)$$

where equation (4.33) is an expression for the so called Common Focus Point (CFP) gather for focusing in *detection* and is shown in figure 4.6.

Note that if the backpropagating Green's function, which is expressed by  $\mathbf{F}_i^-(z_m, z_r)$ , represents correct propagation then the result of the first focusing step  $\mathbf{P}_i^-(z_m, z_s)$ , represented by equation (4.33), is in traveltime equal to the time reversed focusing operator  $\mathbf{F}_j^+(z_s, z_m)$ , represented by equation (4.32). This is a very important property of the first focusing step and is called the principle of equal traveltime. This principle plays a fundamental role in the updating procedure described in chapter 5 where a seismic image can be built up without knowing the background model. The principle can also be used to update the initial background model of the Green's function. Note that for a CFP gather designed for focusing in detection one should compare the traveltimes for an operator defined at the source position, which is the operator for focusing in emission.

Substituting equation (4.32) into equation (4.30) gives an expression for the focusing of the source array

$$\mathbf{P}(z_r, z_s) \mathbf{F}_j^+(z_s, z_m) = \mathbf{P}_j^-(z_r, z_m) = \mathbf{D}^-(z_r) \mathbf{W}^-(z_r, z_m) \mathbf{R}^+(z_m) \mathbf{I}_j^+(z_m) \quad (4.34)$$

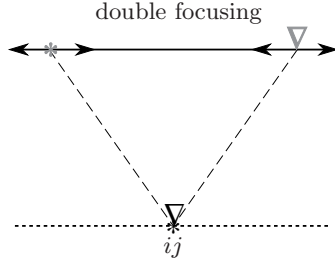


**Figure 4.7** Focusing in detection and emission positions a virtual source and a virtual receiver on a reflecting boundary. In confocal imaging  $i=j$ .

where equation (4.34) is an expression for the Common Focus Point (CFP) gather for focusing in *emission* and is shown in figure 4.6.

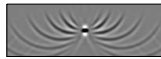
Focusing of both the detector and the source array by combining equation (4.31) and equation (4.32) into equation (4.30) gives

$$\begin{aligned} P_{ij}^-(z_m) &= \mathbf{F}_i^-(z_m, z_r) \mathbf{P}(z_r, z_s) \mathbf{F}_j^+(z_s, z_m) \\ &= \mathbf{I}_i^-(z_m) \mathbf{R}^+(z_m) \mathbf{I}_j^+(z_m) \\ &= R_{ij}^+(z_m) \end{aligned} \quad (4.35)$$

which is the *double focusing* result shown in figure 4.7 for one reflecting depth level. Taking into account the presence of the out-of-focus responses from the other depth levels as well, equation (4.35) need be replaced by

$$P_{ij}^-(z_m) = R_{ij}^+(z_m) + \varepsilon_{ij}^1 + \varepsilon_{ij}^2 \quad (4.36)$$

where  $\varepsilon_{ij}^1$  represents the contribution from above and  $\varepsilon_{ij}^2$  from below the focusing level. Note that this result is the same as equation (4.29) when  $i = j$ .



## Chapter 5

# CFP technology

For those readers who have skipped the theoretical chapters, this chapter is a good starting point to get an understanding of the possibilities of the Common Focus Point (CFP) technology. The schemes and expressions, which were derived in the previous chapters, are in this chapter explained by using simple numerical experiments which show clearly the fundamental principles of the double focusing procedure. At the end of this chapter it will be made clear that the double focusing procedure is a good starting point for the analysis and imaging of seismic data.

The interpretation and understanding of CFP gathers has led to significantly new insights and new processing schemes. In section 5.2 the construction of a CFP gather and the applications of the CFP technology is explained and illustrated with simple numerical examples. In section 5.3 the second focusing step is explained and the CFP imaging technique is discussed. In the last sections, resolution and amplitude analysis (5.4), the construction of 3-dimensional CFP gathers (5.5) and the latest developments (5.6) are discussed and illustrated.

### 5.1 Areal shot record technology

The common focus point technology has its origin in the areal shot record technology which was proposed by Berkhout (1992) and developed within the DELPHI project by Walter Rietveld (1995). An areal shot record represents the response of the subsurface due to a source wave field with lateral extent. Such an areal shot record can be constructed by integration of weighted common receiver gathers followed by combining the integration results into one gather. The weighting of the individual sources in the common receiver gathers is determined by a so-called synthesis operator which is calculated by a forward modeling step in the macro model. The synthesis operator is designed in such a way that the illumination of the desired target takes place. For example an illuminating wave field perpendicular to a reflector at the target (normal incidence) is very useful to determine the macro boundaries

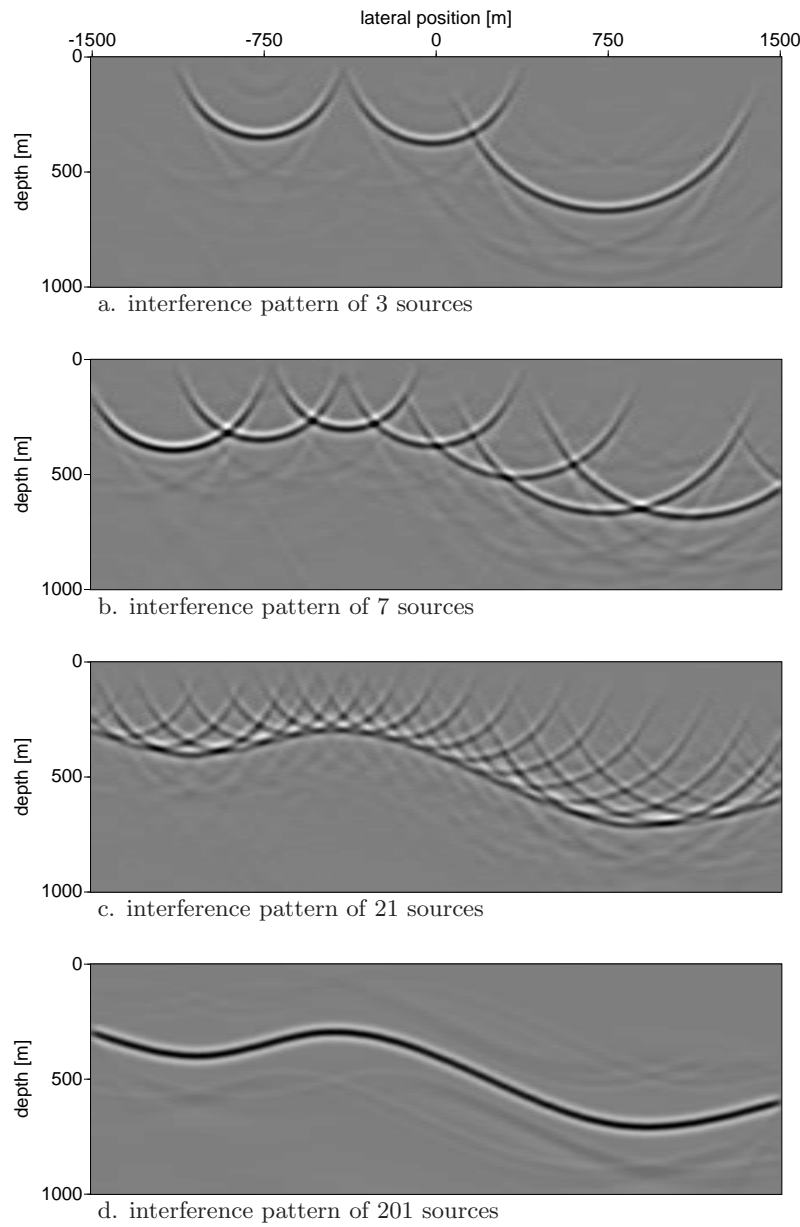


**Figure 5.1** Huygens-Fresnel construction for a wavefront in the subsurface by using a different number of sources at the surface. Note that in figure d), where 201 sources are used to construct the wavefront, only a small part of the individual wavefronts, visible in a,b and c, (the Fresnel zone) give a constructive contribution to the total wavefront.

in the area of interest. In general every desired wave field in the subsurface can be built up by using weighted sources at the surface. This so called Huygens principle is shown in figure 5.1 for 2-dimensional point sources (which are equivalent to 3-dimensional line sources) at the surface and an areal wavefront in the subsurface. From figure 5.1 it can also be seen that due to the interference of the different circular wavefronts, originating from the individual sources at the surface, only a small part of the wavefronts have a contribution to the actual wavefront. This combination of Huygens construction with the principle of interference is called the Huygens-Fresnel principle (Born and Wolf, 1970). The basic idea of the Huygens-Fresnel theory is that the wave field at an observation point can be constructed from the superposition of secondary sources positioned at a surface between the observation point and the source. In the previous chapter this idea was mathematically expressed in the Kirchhoff integral of equation (3.40). In this chapter it will be made clear that the Fresnel zone plays an important role in the construction of CFP gathers.

One of the advantages of controlled illumination is that it is an efficient and accurate way of performing a pre-stack depth migration. By using only a limited number of illumination angles at target level a good pre-stack depth image can be obtained. Examples of the imaging results obtained with controlled illumination on numerical and real data can be found in Rietveld (1995). A special case of controlled illumination is a point illumination. This point illumination was initially used for macro model verification, but by recognizing and using the special properties of the point illumination it became clear that it is an excellent intermediate domain for velocity and AVO analysis as well. The areal source wave field defined for a grid-point in the subsurface is called the Common Focus Point gather.

## 5.2 First focusing step

The Common Focus Point (CFP) gather is constructed from seismic data acquired within a pre-specified source and detector aperture. To construct the CFP-gather from the data an initial synthesis (also called focusing) operator is needed. This initial synthesis operator can be based on stacking velocities or an initial macro model. The initial synthesis operator is calculated by positioning a point source at the desired grid-point in the subsurface followed by a forward modeling algorithm to calculate the source response at the surface. Measuring its response at the detector positions defines an operator for focusing in detection and measuring its response at the source positions defines an operator for focusing in emission. As shown by equations (4.31) and (4.32), the time reverse (complex conjugate in frequency domain) of the forward modeled response defines the synthesis operator. In figure 5.2, a synthesis operator is shown for a grid-point defined in the middle of a synclinal model, at the synclinal reflector. The forward modeling scheme used to model the response is a 2-dimensional recursive depth extrapolation based on weighted

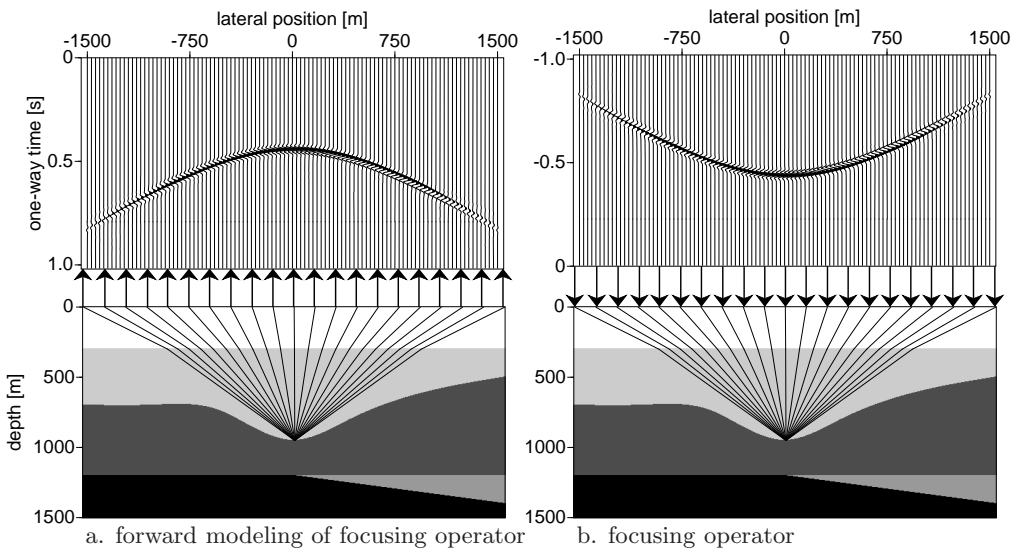


**Figure 5.2** Modeling of the focusing operator in the synclinal model. Note that the time-reversed focusing operator is equal to the forward modeling result.

least-square operators as described in appendix A. Figure 5.2a shows the forward modeling result and figure 5.2b shows the focusing operator. If the forward operator is calculated in the correct model the focusing operator will have its focus on the defined grid-point. Note that the vertical axis along the operator is the one-way time axis.

To calculate one trace out of a CFP gather for focusing in detection the synthesis operator measured at the detector positions must be convolved in time with a shot record followed by a summation along all traces in the record. This procedure is also shown by the integral of equation (4.19) and the matrix multiplication of equation (4.31). Performing this procedure, with the same operator for all shot records available defines the CFP gather for focusing in detection. As mentioned before not all traces in the shot record have an equal contribution to the CFP trace, only that part of the CFP corrected shot record (the result after convolution with the operator but before summation of the traces) which lies in the Fresnel zone contributes to the CFP trace. Note that the assumption is made that the high frequency approximation is valid such that it is allowed to speak of a Fresnel zone. The Fresnel zone represents that part of the shot record which is related to the chosen focus point and is therefore dependent on the focusing operator. The acquisition geometry of the shot record also plays a role because the measured data should at least contain reflection information from the defined focus point. It is therefore important to discuss first the Huygens-Fresnel principle before the *first* focusing step is explained in more detail.

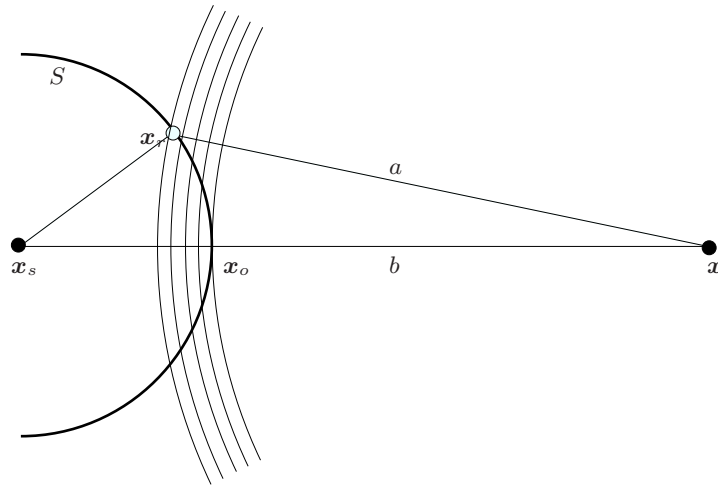


**Figure 5.3** Pictorial representation of the Fresnel zone. Due to the interference of the secondary sources on the wavefront  $S$  only a small part of  $S$ , the Fresnel zone, contributes to the wave field at  $\mathbf{x}$ . The contribution depends on the path difference between  $\mathbf{x}$  and a point on the wavefront  $S$ ,  $\mathbf{x}_r$ .

### 5.2.1 Huygens-Fresnel principle

There are many ways to introduce the Fresnel zone. In this thesis a definition close to the original definition of Fresnel is used. In figure 5.3 a circular wavefront  $S$  is shown which originates from a source at  $\mathbf{x}_s$  and with  $\mathbf{x}$  the point where the wave field is to be determined. In accordance with the Huygens-Fresnel principle each element on the wavefront  $S$  is regarded as the center of a secondary point source. Now let  $b = |\mathbf{x} - \mathbf{x}_o|$  the shortest distance between the point of observation and the wavefront  $S$ . Then by assuming a homogeneous medium in-between  $\mathbf{x}_s$  and  $\mathbf{x}$  the most important contribution from the wavefront at  $\mathbf{x}$  comes from the point at  $\mathbf{x}_o$ . The contribution of the point  $\mathbf{x}_r$  on the wavefront to  $\mathbf{x}$  is determined by the distance  $a = |\mathbf{x} - \mathbf{x}_r|$ . This contribution is *constructive* if the path difference  $a - b = k * \lambda$  with  $k$  a positive integer, and  $\lambda$  the wavelength. *Destructive* interference occurs when the path difference  $a - b = (2k + 1) * \frac{\lambda}{2}$ .

Using stationary phase analysis (Bleistein, 1984) this interference behavior can be made more clear in a mathematical sense. The contribution from all secondary sources to  $\mathbf{x}$  is represented by a summation along the wavefront given by the integral

$$P(\mathbf{x}, \mathbf{x}_s) = \int_S P(\mathbf{x}_r, \mathbf{x}_s) A_g(\mathbf{x}, \mathbf{x}_r) \exp(j\Phi_g(\mathbf{x}, \mathbf{x}_r)) d^2 \mathbf{x}_r, \quad (5.1)$$

where  $A_g$  and  $\Phi_g$  represent respectively the amplitude and phase of the Green's function traveling from a point on the wavefront  $S$  to the point of observation  $\mathbf{x}$ . As the point  $\mathbf{x}_r$  runs along the surface of integration, the function  $\Phi_f =$

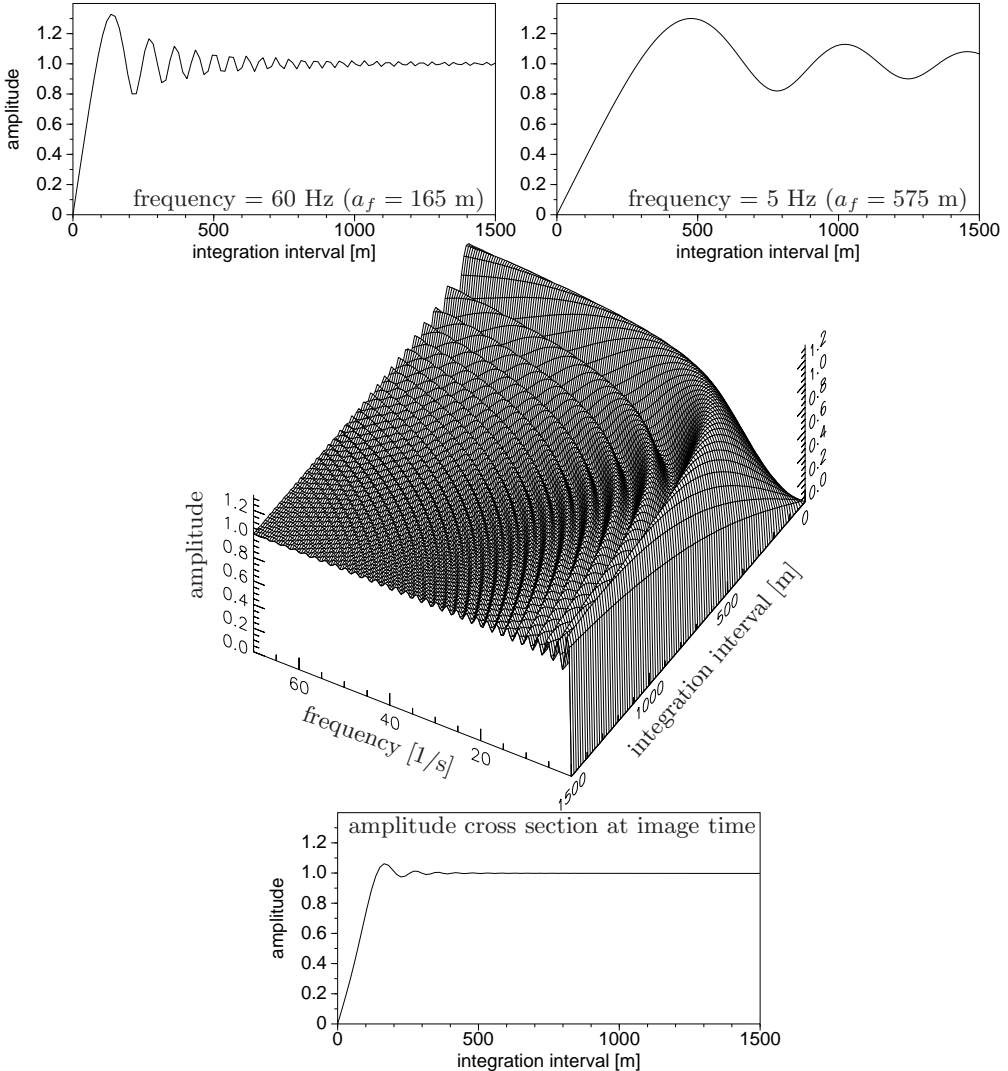


**Figure 5.4** The two top pictures show the amplitude of the integral in equation (5.1) as function of the integration interval for two different frequencies. The kernel consists of the 2-dimensional Green's function for a dipole source in a homogeneous medium with  $c = 2000$  m/s and a depth of 800 m. The 3-dimensional picture in the middle shows the same amplitude for a range of frequencies and integration intervals.

$\Phi_p(\mathbf{x}_r, \mathbf{x}_s) + \Phi_g(\mathbf{x}, \mathbf{x}_r)$ , where  $\Phi_p(\mathbf{x}_r, \mathbf{x}_s)$  is the phase of the wavefront  $P(\mathbf{x}_r, \mathbf{x}_s)$  at  $S$ , will change very many cycles, so that both the real and imaginary parts of the integrand will change sign many times. As a consequence the contributions from the various elements will in general virtually cancel each other out (destructive in-

terference). The situation is, however, different for an element which surrounds a point (called critical point or pole, in figure 5.3 the point  $\mathbf{x}_o$ ) where  $\Phi_f$  is stationary. Here the integrand varies much more slowly and may be expected to give a significant contribution. Hence, when the wavelength is sufficient small, the value of the integral is determined substantially by the behavior of  $\Phi_f$  in the neighborhood of points where  $\Phi_f$  is stationary.

The area of constructive interference surrounding the stationary phase point is called the Fresnel zone. The limit of constructive interference is defined differently by various authors in terms of fractions of the wavelength  $\lambda$ . Note, however that the Fresnel zone is a weighting function with no sharp cut off point (Lindsey, 1989). In this thesis the definition of Berkhou (1984),  $a_f = 2\sqrt{(z + \frac{\lambda}{8})^2 - z^2}$  is used for convenience. By choosing in equation (5.1)  $P(\mathbf{x}_r, \mathbf{x}_s) = 1$ ; a plane wave with zero phase on the flat surface  $S$ , the interference behavior around the Fresnel zone can be analyzed by calculating the amplitude of the integral. This amplitude should be equal to 1 to get a correct amplitude in the integration result. In figure 5.4 the amplitude of the integral in equation (5.1) is shown for different integration intervals and frequencies. The kernel consists of the 2-dimensional Green's function for a dipole source in a homogeneous medium with  $c = 2000$  m/s and a distance of 800 m.

The two top pictures of figure 5.4 show the amplitude as function of the integration interval for two different frequencies. Note that even for the high frequency (small  $\lambda$ ) a large integration interval must be taken to obtain a correct amplitude in the integration result. For someone who is interested in true amplitudes this seems a disappointing result, because it means that very large apertures should be taken into account to obtain correct amplitudes in the integration result. However, by looking at the 3-dimensional picture in the middle of figure 5.4 it can be argued that due to the interference off all frequencies, the integration result in the time domain will give a better result. In the bottom picture the cross-section at the imaged time ( $\frac{z}{c}$ ) is shown for different integration lengths. In this picture it is observed that an integration length of 200 m, corresponding to the Fresnel zone of the central frequency of 35 Hz, is sufficient to obtain the correct amplitude in the integration result (for more details see Rietveld, 1995, appendix B).

### 5.2.2 Construction of CFP trace: dipping layer

To illustrate the importance of the Fresnel zone in the first focusing step a simple numerical example is used. In this example a CFP gather is constructed from data modeled with a fixed receiver spread above a dipping reflector. The focus point is chosen on the dipping reflector in the middle of the acquisition geometry (see figure 5.5c). The center of the reflector is positioned at 800 m depth and the velocity above the reflector is 2000 m/s.

Figure 5.5 shows how a CFP trace for focusing in detection is constructed by using

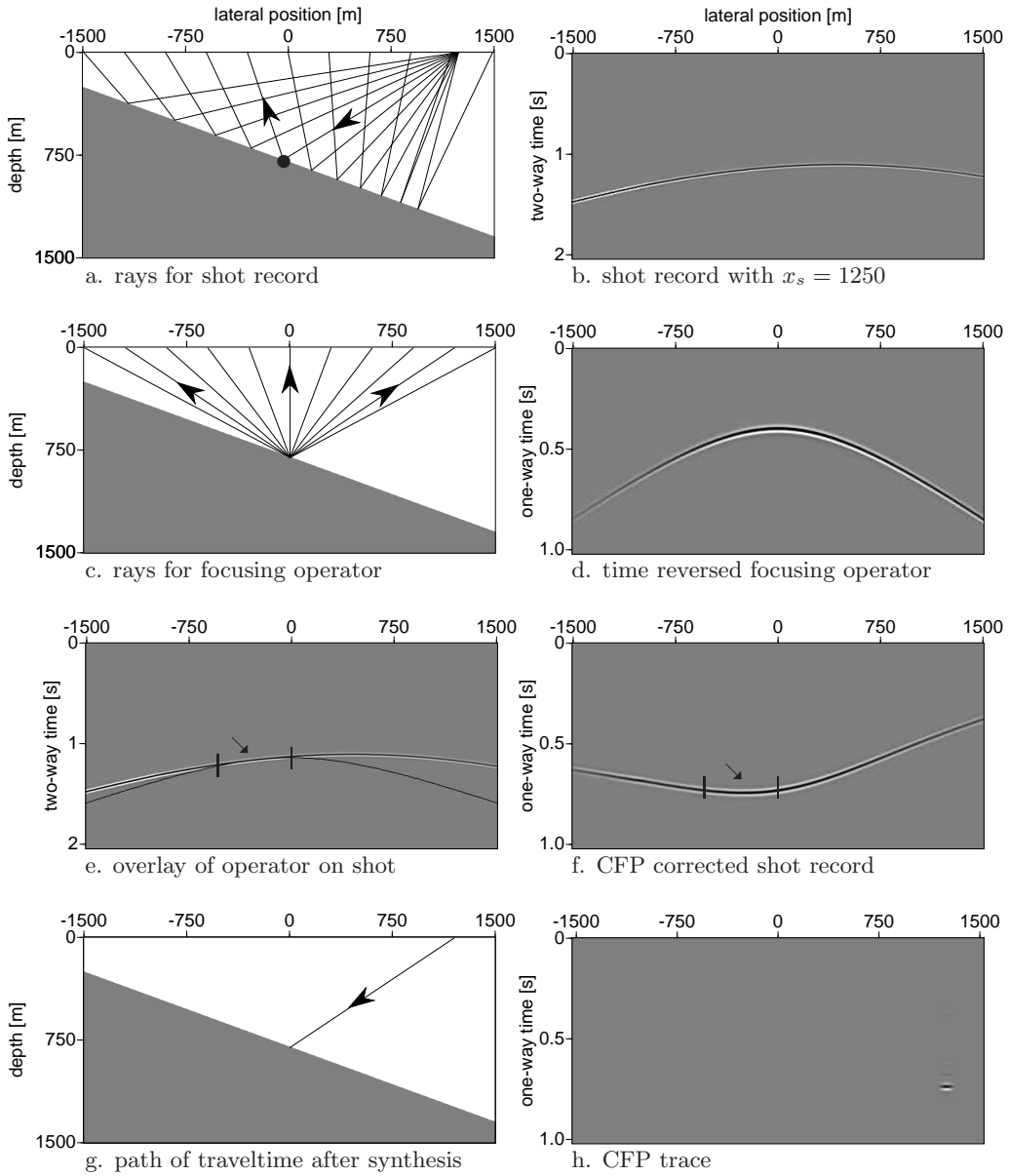


**Figure 5.5** Construction of one CFP trace for focusing in detection given a shot record (b) and a focusing operator (d). The only contribution in the CFP trace (h) comes from the Fresnel zone (approximately 350 m) indicated with an arrow in (e) and (f).

a shot record (b) and a focusing operator (d). Time convolution of the synthesis operator with the shot record gives the CFP corrected shot record shown in (f). The arrow in the pictures (e) and (f) indicates the Fresnel zone. The lateral position of the center of the Fresnel zone (the stationary phase point) can be determined by following the ray-path from the source, via the focus position, to the receiver position (indicated with an arrow in figure 5.5a). Another way to determine the stationary phase point can be done by superimposing the times of the operator over the shot record and shifting the operator times along the vertical axis until a part of the operator is tangent to the event in the shot record (e).

After summation over all the traces in the CFP corrected shot record (f) the CFP trace is obtained. The only constructive 'interference' of the event in (f) occurs at the Fresnel zone, which is indicated with an arrow. The constructed CFP trace is positioned in the CFP gather at the lateral position of the source in the shot record (h). The CFP trace is positioned at the source position because the time of the event in the CFP trace is equal to the time the wavefield needs to propagate from the source at the surface to the focus point at the reflector (g). This result is in agreement with equation (4.33) where it has been shown that one 'leg' of the two-way traveltime is compensated by the focusing operator in the first focusing step. By using more shot records more CFP traces can be constructed with the same operator and finally when all available shot records are used the CFP gather is completed.

Another way to show how a CFP gather is built up from different shot records is shown in figure 5.6. The same operator and model configuration of figure 5.5 is used, but now all shots are used to construct the CFP gather (201 shots with a sampling distance equal to the (minimum) receiver spacing = 15 m) and the number of receivers is different for the different results shown in figure 5.6. In figure 5.6a only 7 receiver per shot record are used in the construction of the CFP gather for focusing in detection. This means that the Fresnel zone as shown in figure 5.5f is sparsely sampled and constructive interference does not occur after summation of only 7 traces. By looking carefully in figure 5.6a the 7 contributions of the individual receivers can still be recognized. Using more receivers in the shot record shows, from picture (a) to (d), how the Fresnel zone is built up in the CFP domain.

In figure (e) the complete CFP gather is shown with the times of the synthesis operator superimposed on the result. Remembering the principle of equal travelttime, introduced in the previous chapter; which states that if the focusing operator represents correct propagation in the model then in the time domain the result of the first focusing step  $\mathbf{P}_i^-(z_m, z_s)$ , represented by equation (4.33), is in travelttime equal to the time reversed focusing operator  $\mathbf{F}_i^-(z_m, z_r)$ , represented by equation (4.32).

However, by looking at the overlay (e) it is observed that in the left part in the CFP gather, the times of the operator don't match with the times of the CFP response. This seems confusing at first sight, but considering the lateral position

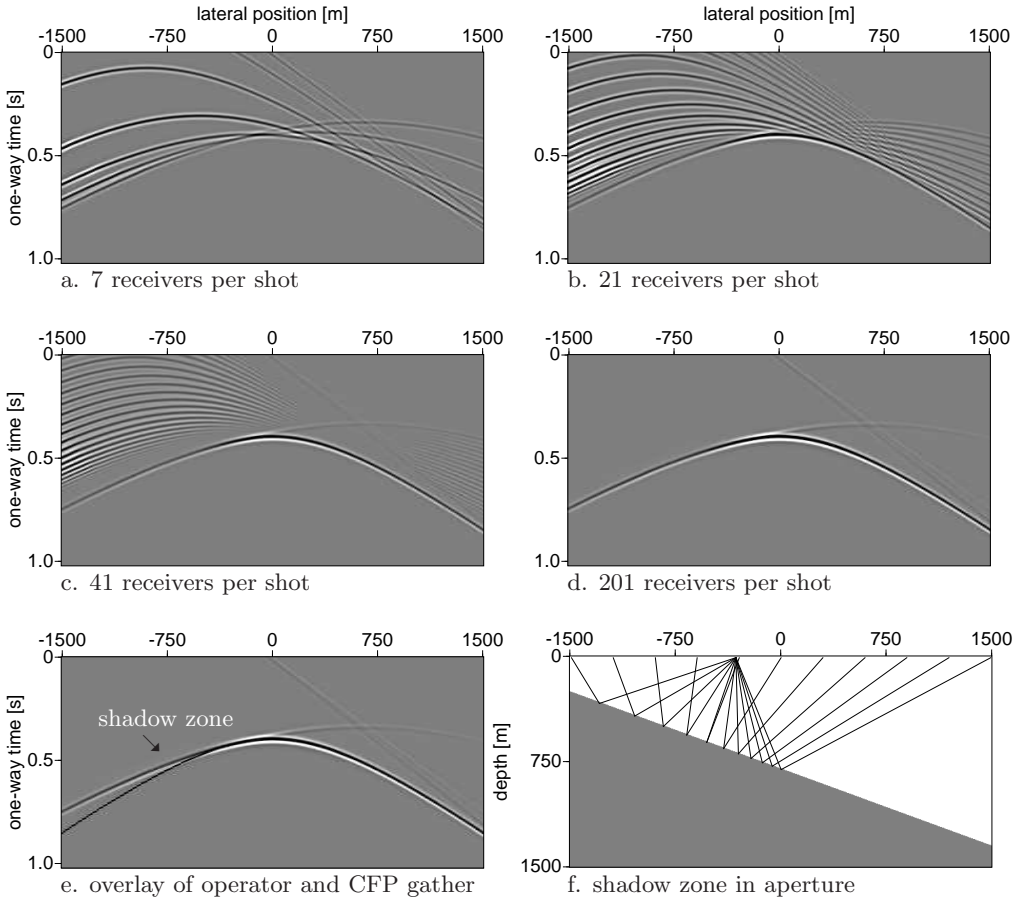


**Figure 5.6** Construction of one CFP gather by using all shots, but with a different number of receivers per shot record. Note that due to the limited aperture there is a shadow zone in the CFP gather (f).

of the Fresnel zone for the shots positioned at the left side it is observed that the Fresnel zone falls outside the receiver aperture. So, the mismatch in time between the focusing operator and the CFP response is due to limited aperture. The zone where the Fresnel zone is 'shifted' outside the aperture is called the shadow zone. The ray paths of the shot record with its stationary phase ray just inside the receiver aperture is shown in (f). The CFP gather shows clearly that the shot records in the shadow zone don't contain the full reflection information of the defined focus on the reflector.

Another thing which can be observed in the CFP gather (d) is that there are two artifacts present above the CFP response. These artifacts are due to the finite aperture of the receiver array and originates from the truncation of the synthesized

reflection response in figure 5.5f. The destructive interference of the traces at the boundaries of the CFP corrected shot record is not complete due to the 'missing' contribution of the traces outside the aperture. There are several ways to reduce these artifacts; one method is tapering around the Fresnel zone in the CFP corrected shot record, another method makes use of an analytical method to remove finite aperture artifacts. In the next subsection the analytical method is discussed in more detail because of its elegant solution to the finite aperture problem.

### Removal of finite aperture artifacts

In the frequency domain implementation of the synthesis process, the shot record and the focusing operator are transformed to the frequency domain and multiplied together. The result of this multiplication is summed over all receivers in the shot record to produce one trace of the CFP gather. Wapenaar (1991) has shown that due to the finite aperture of the data, artifacts are introduced in this final result. These artifacts can be suppressed by using a taper at the edges of the data set. However, tapering only suppresses the artifacts (and a part of the data as well) but does not remove the artifacts completely. Therefore Wapenaar (1991) proposed a new technique (worked out in detail by Timmerman (1993)) which calculates in an analytical way (using diffraction theory), the artifacts originating from the finite aperture and subtract these calculated artifacts from the integration result. This analytical method gives more insight in the influence of the acquisition geometry in constructing a CFP gather and shows the importance of the Fresnel zone. The summation over all receivers in a shot gather, to obtain one trace in the CFP gather, is represented by the following integral (which is the same as equation (5.1))

$$I = \int_{-\infty}^{\infty} f(x)e^{j\phi(x)} dx, \quad (5.2)$$

where  $f(x)$  and  $\phi(x)$  represent the amplitude and phase, respectively. Due to the finite acquisition aperture, equation (5.2.2) is approximated by

$$\langle I \rangle = \int_{x_a}^{x_b} f(x)e^{j\phi(x)} dx, \quad (5.3)$$

where  $x_a$  and  $x_b$  are the begin- and end-points of the acquisition aperture. These finite integration limits cause artifacts. Wapenaar expresses the correct result  $I$  in terms of the approximated result  $\langle I \rangle$  plus two correction terms, as follows:

$$I = \langle I \rangle + I_a + I_b \quad (5.4)$$

where

$$I_a = \int_{-\infty}^{x_a} f(x)e^{j\phi(x)} dx \quad (5.5)$$

and

$$I_b = \int_{x_b}^{\infty} f(x)e^{j\phi(x)} dx. \quad (5.6)$$

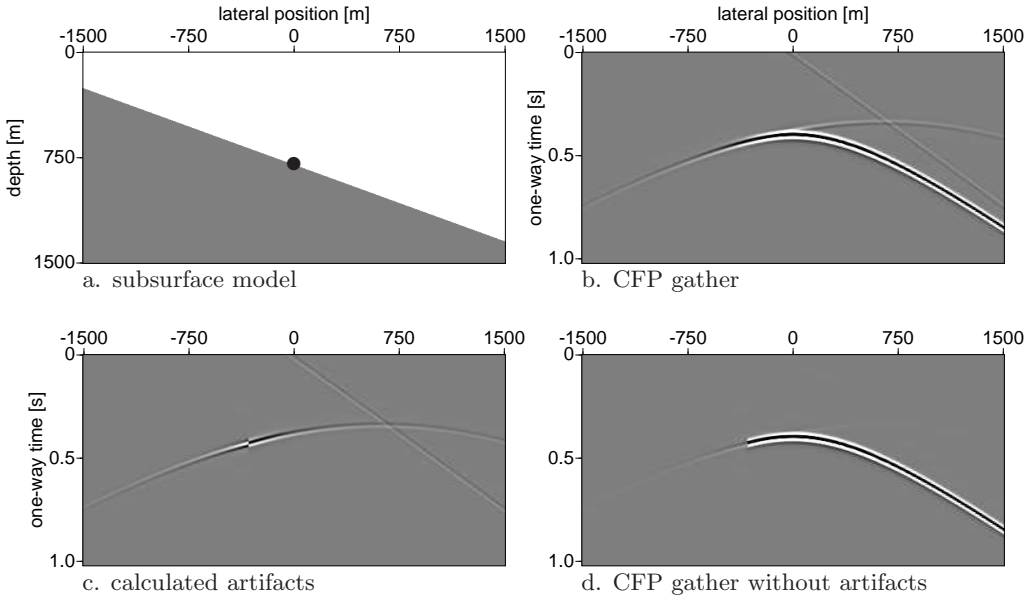


**Figure 5.7** Finite aperture artifacts removal in the CFP gather. The sharp cutoff in the artifacts free CFP response at  $x = -330$  m represents the start of the shadow zone and is given by the shot record indicated in figure 5.6f. Note that all figures are plotted on the same scale.

By adding  $I_a$  and  $I_b$  to the finite integration result the finite aperture artifacts are fully compensated. The method of Wapenaar makes a first and second order approximation to the finite aperture artifacts described in equations (5.5) and (5.6). The CFP gather in figure 5.7b is shown for the same dipping reflector example which was discussed earlier. Note that the artifact which starts on the upper left side of figure 5.7b disturbs the CFP response at the right side. The calculated artifacts, based on the second order approximation, are shown in figure 5.7c. Subtraction of these artifacts from figure 5.7b gives the artifacts free result of figure 5.7d. Note the almost perfect removal of the 'shadow zone' present in figure 5.7b. The remaining part of the artifact is approximately 5% of the amplitude of the main event. The sharp cutoff in the artifacts-free CFP response at  $x = -330$  m represents the start of the shadow zone and is given by the shot record indicated in figure 5.6f.

The proposed method breaks down if more than one event is present in the integration Kernel, in that case the phase cannot be determined uniquely for a single event. This limitation of the method can be taken into account by selecting one event in a time window around the times given by the CFP operator. However, removal of the finite aperture artifacts is not essential in further processing steps because they don't disturb image quality or the amplitude response in the CFP gather.

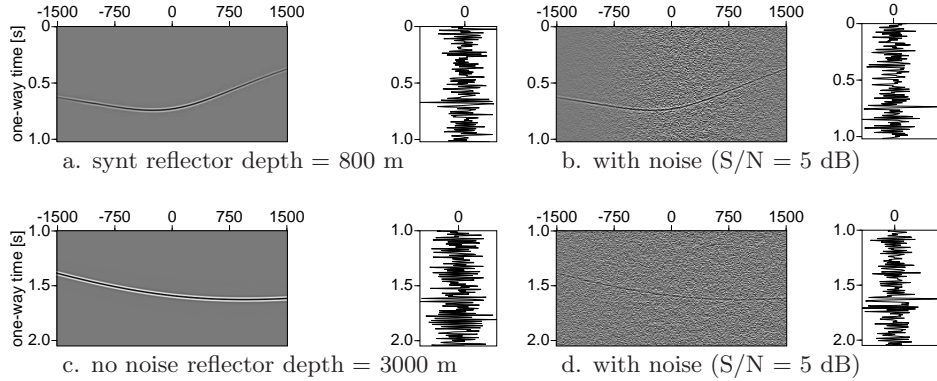


**Figure 5.8** Signal enhancement due to the constructive summation in the CFP corrected shot record. For a deeper reflector (b) the Fresnel zone is larger and hence the signal to noise ratio in the CFP gather will be better (right trace) than the ratio in one single trace (left trace).

### The influence of noise

Noise in the data will in general distort the quality of the CFP gather, however, due to the summation of the events in the Fresnel zone the signal to noise ratio in the CFP gather is improved in comparison with the signal to noise ratio in the shot records the CFP gather is built from. This is illustrated in the CFP corrected shot record of figure 5.8a where 'random' noise is added to the shot record, shown in figure 5.5b. Also for a deeper reflector, which has an even worse S/N ratio and shown in figure 5.8d, the Fresnel zone is larger and the signal to noise ratio of the CFP trace shown in figure 5.8d is better than the signal to noise ratio of a single trace in the shot record (left trace).

#### 5.2.3 Construction of CFP gathers: synclinal model

The construction of a CFP gather in a more complicated model is explained by using numerical data based on the model shown in figure 5.9a. The numerical data is modeled with a fixed acquisition spread where the source positions are defined at every receiver position (201 shot positions with  $\Delta x = 15$  m). The source has a dipole character and its signature is given by a Ricker wavelet with a frequency peak at 26.4 Hz. For the forward modeling of the data an acoustic finite difference algorithm is used. The subsurface model includes a diffraction point at  $z = 1000$ ,  $x = -750$  m and a negative reflection coefficient for the wedge located in the right corner of the model. In the remainder of this chapter this syncline model will be used to explain the different processes in the double focusing procedure.

The synthesis process for a focusing receiver with a focus point defined at the synclinal interface at  $x = 0$  and  $z = 950$  m (the focus point is indicated with a black bullet in figure 5.9a) is shown in detail in figure 5.9. The time reversed focusing

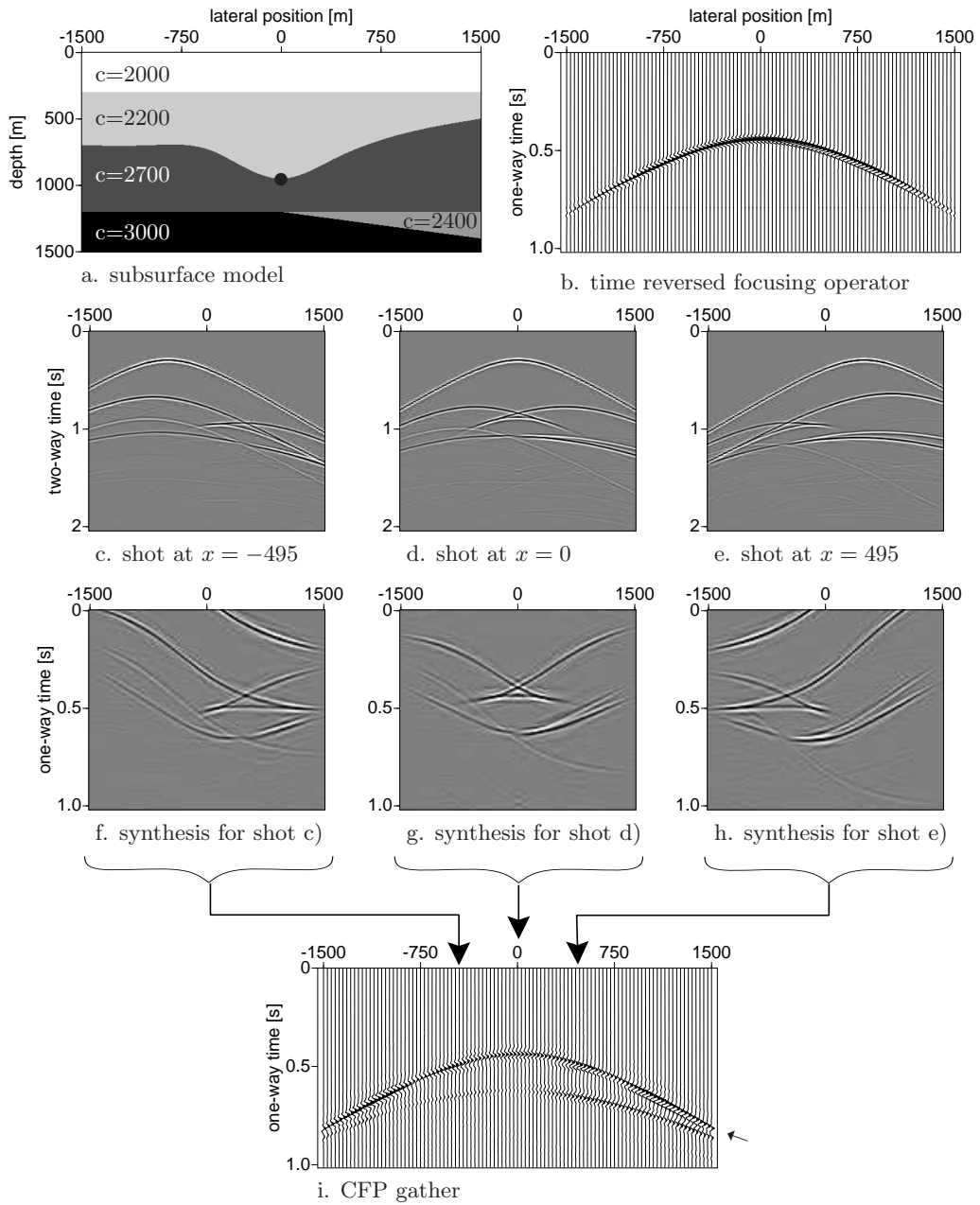


**Figure 5.9** Construction of a CFP gather for focusing in detection. Every common shot gather contributes to one trace, positioned at the source position, in the CFP gather. Note the contribution of the Fresnel zones in figure 5.9f, g and h to figure 5.9i. The focus point response has been indicated with an arrow. Note also the relative simplicity of the CFP gather.

operator for the defined focus is shown in figure 5.9b. This operator is applied to all common shot gathers available. Three different common shot gathers with source positions at  $x = -495, x = 0$  and  $x = 495$  m are shown in figure 5.9c, d and e respectively. Convolution along the time axis of the traces in the shot gathers with the traces in the synthesis operator gives the intermediate synthesis results shown in figure 5.9f, g and h. Note that in these intermediate synthesis results the bow-tie of the syncline interface is still present. Summation over all the traces in the intermediate synthesis result defines one trace of the CFP gather. The most important contribution in the integrated result is determined by the Fresnel zone related to the focus point. If the focusing operator is correct then the operator time at the source position is identical with the time of the event present in the CFP trace (for a detailed discussion about erroneous operators see chapter 6). The summed trace is placed in the CFP gather at the position of the source. By carrying out the convolution and integration along the traces in the gather for all shot gathers available the CFP gather for focusing in detection is constructed.

The events which are present in the shot record are also present in the intermediate synthesis result in figure 5.9f, g and h. In figure 5.9f four events are observed. The top event originates from the first reflector and can be regarded as a 'non-causal' event with respect to the focus. This event is 'non-causal' because the focus is placed below the first reflector, or said differently, the 'non-causal' event appears before the times of the used synthesis operator. The event with the triplication in it originates from the syncline boundary, the weak S-shaped event originates from the diffraction point and the last event originates from the deepest boundary. In the CFP gather shown in figure 5.9i the reflection from the syncline (indicated by an arrow) and the deeper boundary are clearly visible. The response of the first reflector is moved outside the time window. Note that the bow-tie event in the shot gather (figure 5.9d) is focused in the CFP gather (figure 5.9i) to a single event which is much simpler to interpret. So due to the construction of the CFP gather the shot records are transformed to a domain which is focused on only one grid-point in the subsurface which can be less complicated.

In figure 5.10 another focus point is chosen in the syncline model. Now the contributions of the same shot records (c,d,e) in the CFP gather are different from figure 5.9. Only the deep reflector gives a contribution to the CFP response. Note that before the CFP response a 'non-causal' event is observed, which originates from the syncline interface.

The event, indicated with an arrow, in the CFP gathers of figure 5.9i and figure 5.10i corresponding to the synthesis operator, called the focus point response, is exactly equal in traveltime with the synthesis operator. This means that the used synthesis operator contains no errors. If the source and receivers are defined at the same positions in space then the same focusing operator can be used for the second focusing step which operates on the CFP gather. In section (5.3) this second focusing

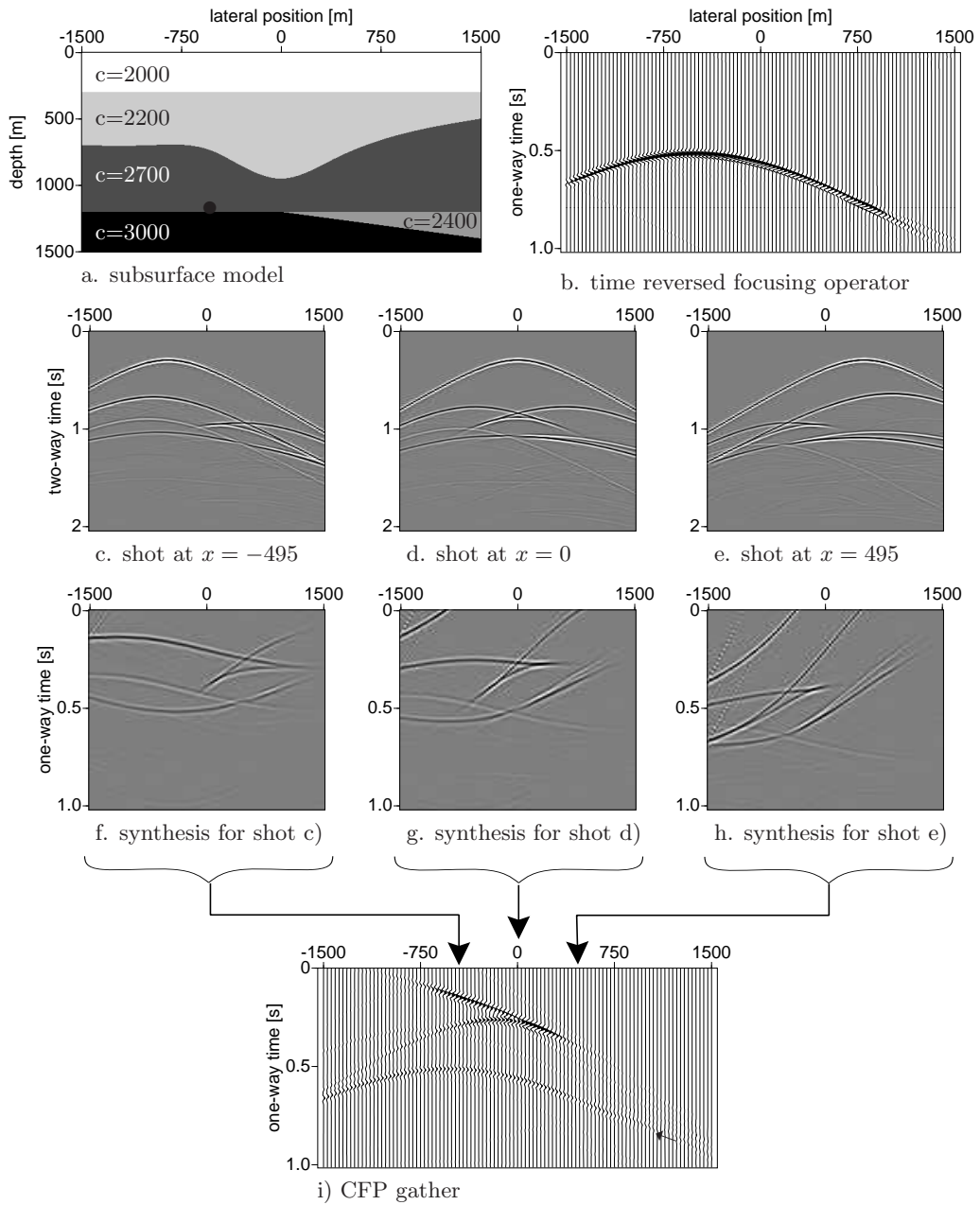


**Figure 5.10** Construction of a CFP gather for focusing in detection. Every common shot gather contributes to one trace, positioned at the source position, in the CFP gather. Note the contribution of the Fresnel zones in figure 5.10f, g and h to figure 5.10i. The focus point response has been indicated with an arrow.

step is discussed in more detail. If the synthesis operator is in traveltime not equal with the event of interest in the CFP gather the synthesis operator needs to be updated, a process which is discussed in chapter 6. Note that by updating synthesis operators (and not the initial macro model) a correct one-way time image of the subsurface can be obtained without updating the initial macro model. To convert this one-way time image to a structural model (a depth image) a macro model is needed. This macro model can be estimated by using the collection of synthesis operators and the obtained one-way time image. This tomographic inversion is subject of another PhD project carried out in the Center for Technical Geoscience by Rob Hegge (Hegge and Fokkema, 1996).

#### 5.2.4 Focusing in emission and focusing in detection

In all previous shown CFP gathers, focusing in detection was carried out in the first focusing step. The focusing operator was defined at the receiver positions and the traces in the CFP gather were defined at the source positions. However, it is also possible to do focusing in emission in the first focusing step. The focusing operator must then be defined at the source positions and the resulting CFP gather will have its traces positioned at the receiver positions.

To show clearly the differences between focusing in emission and focusing in detection a flat reflector at 800 m depth with a velocity above the reflector of 2000 m/s is chosen. The shot and receivers are moving above the reflector from left to right, the first receiver is positioned at the source position and the last receiver is positioned 3000 m to the right of the first receiver, the distance between the receivers is 30 m. The shots are positioned at 30 m from each other in figure 5.11a,b and at 60 m in figure 5.11c,d. Comparing figure 5.11a with 5.11b it is observed that due to the marine type of acquisition geometry the focus is illuminated differently for focusing in detection and focusing in emission.

In figure 5.11c the source spacing is 60 m and the receiver spacing is 30 m. Focusing in detection gives a CFP gather sampled with traces 60 m (the shot distance) from each other. Every trace is built from a shot record with the sampling distance of the receivers. In the result for focusing in emission as shown in figure 5.11d the CFP trace spacing is 30 m (the receiver distance). Every trace in this CFP gather is built from a common receiver gather which is sampled with the source distance. Due to the 'coarse' source sampling the Fresnel zone is not properly sampled, which gives the alias artifacts present in the top right hand-side of figure 5.11d. Note that these artifacts are the same as the interference effects shown in figure 5.6.

The results of focusing in detection and focusing in emission can be combined into one gather as shown in figure 5.11e and f. These combined CFP gathers are very useful in the updating of erroneous focusing operators and the estimation of a macro model (see chapter 6).

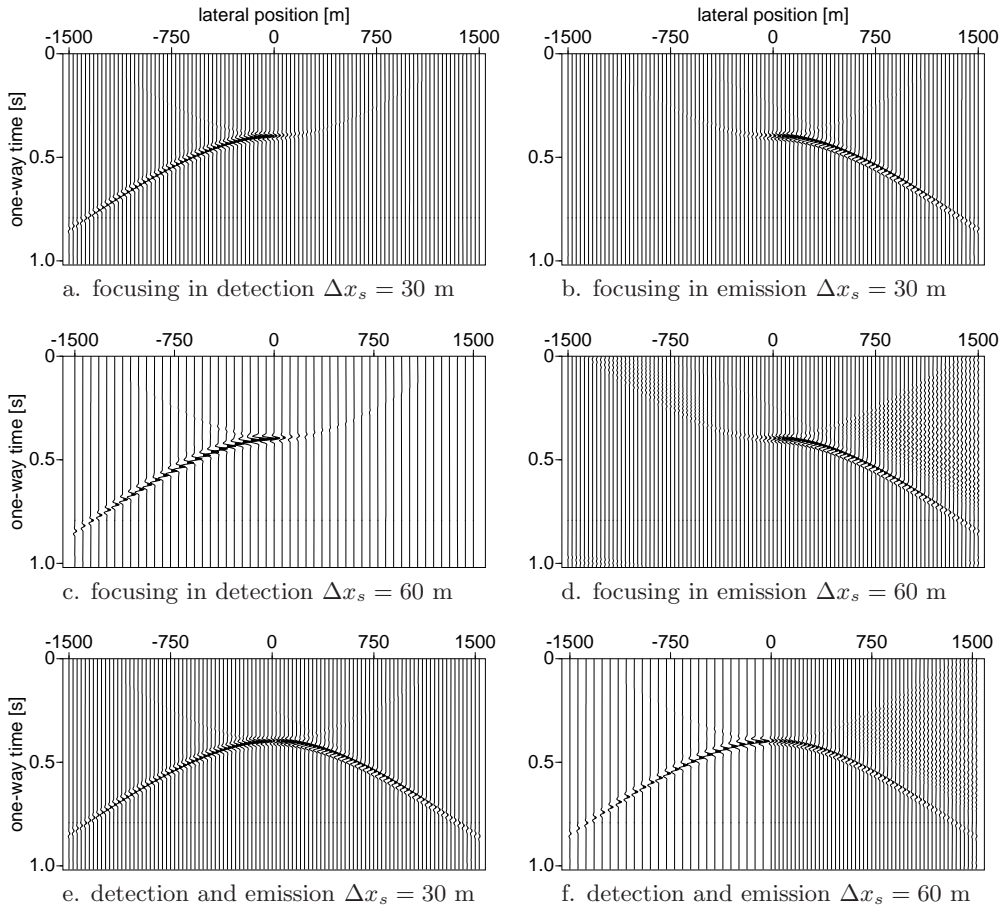


**Figure 5.11** Focusing in detection and focusing in emission for different source sampling intervals. Note the difference in illumination and the distance between the traces in the CFP gather.

A simplified computation scheme for the first focusing step is shown in figure 5.12 where the difference between focusing in emission and focusing in detection is made explicitly. The focusing operator defines the traveltimes from the focus to the source and receiver positions which belongs to the input trace. The focusing blocks use this traveltime to weight the input trace. The weighting of the input trace consist in general of a time shift, a 45 degrees phase rotation and an amplitude scaling. The weighted input trace is positioned into the CFP gather at the source and/or receiver position. Other input traces which have their source or receiver position in common with the previous input trace(s) will be added to the result.

**In conclusion;** focusing in emission synthesizes areal sources that aim at remote illumination of single subsurface grid-points; the involved synthesis process trans-

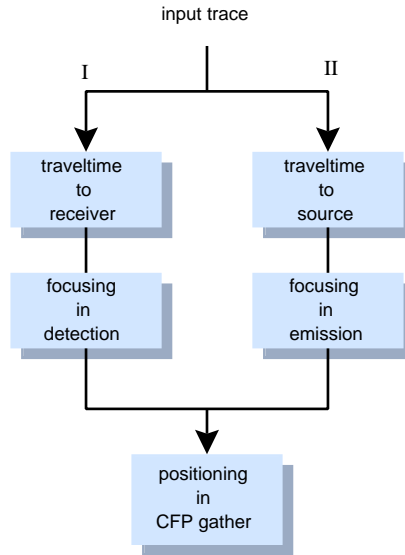


**Figure 5.12** Block diagram for the traveltimes in the first focusing step. Every input trace can be used for both focusing in detection (I) and emission (II). The weighted input trace is positioned in the CFP gather.

forms field records into CFP gathers. Hence, each CFP gather defines an areal shot record that represents the response of a focusing source. A single event in the CFP gather may be interpreted as the response of a source at the defined grid-point measured at the surface. Focusing the CFP gather gives a double focusing result. A single event in the double focusing result may be interpreted as the output of a simulated physical experiment; the response of a focusing source being measured by a focusing detector with the same focus point (confocal) or with a different focus point (bifocal). How the second focusing step is calculated will be explained in the next section.

### 5.3 Second focusing step

The response of the focusing operator in the CFP gather contains information which belongs to the same focus point. In the second focusing step this information is added together and positioned in the one-way image gather. For this operation the focusing operator which was already used in the first focusing step can be used again. Two phases can be distinguished in this second focusing step; 1) move-out correction with the focusing operator and 2) addition and positioning in the one-way image gather. The first phase is obtained by a 1-dimensional convolution (in time) between the CFP gather and its operator, the second phase is obtained by summation over the traces in the CFP gather. Note that the combination of phase 1 and phase 2

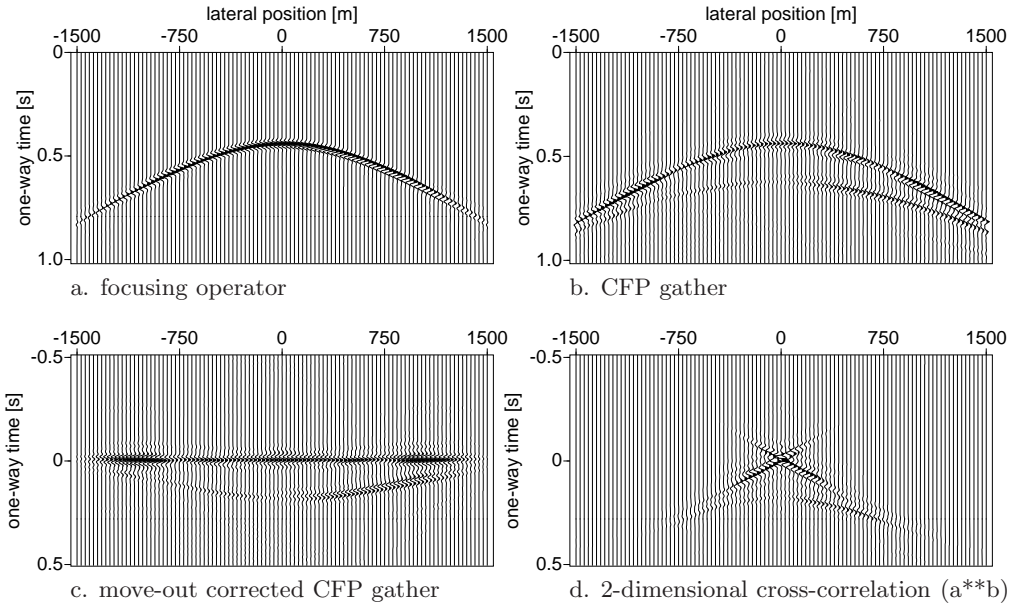


**Figure 5.13** The two phases in the second focusing step consists of a move-out correction (c) on the CFP gather (b) using the focusing operator (a), followed by a summation over all traces. In (d) the 2-dimensional cross-correlation between the CFP gather and its time reversed operator is shown, the trace at  $x = 0$  represents the image trace.

can be considered as the spatial zero-lag trace of a 2-dimensional cross-correlation (in time and space) between the CFP gather and its time reversed operator. In chapter 6 it will be shown that the 1-dimensional convolution result is important for velocity analysis and operator updating, in section (5.4) it will be shown that the 2-dimensional cross-correlation is important in AVO analysis. In this section the imaging aspects of the second focusing step will be explained.

Figure 5.13 shows the second focusing procedure for the same focus point as defined in figure 5.9. The time reversed focusing operator (a) time convolved with the CFP gather (b) gives the move-out corrected CFP gather shown in figure 5.13c. For a correct focusing operator all events of the focus point response in the move-out corrected CFP gather occur at zero time. For the reflector at which the focus point is positioned, this is indeed observed in figure 5.13c. The event occurring after zero time is from a reflector which is positioned deeper than the focus point. From the analysis of the time difference between the zero-time line and the response of the deeper reflector a new operator can be estimated which should be correct for the deeper reflector. An alternative approach, to focus the deeper reflector, is that given the time shifts between the event and the zero-time line the initial macro model can be updated (differential time shift (DTS) analysis) and a new operator can be calculated based on this updated model.

The time reversed focusing operator (a) 2-dimensional cross-correlated with the CFP gather (b) gives the so called reflectivity function (see section (5.4)) shown in figure 5.13d. The trace at  $x = 0$  is the addition of all the traces in figure 5.13c and represents, around zero time, the information of the focus point used in the imaging. This information is positioned in the one-way image gather at a position defined by the one-way image ray. Therefore the one-way image ray involved in the double focusing technique must be defined first.

### 5.3.1 One-way image ray

In migration techniques there are several rays defined which play an important role in time and depth migration (Hubral, 1977; Parkes and Hatton, 1987). Parkes and Hatton (1987) define the image ray as "the ray associated with the minimum traveltime from a subsurface point to the surface". The normal ray is associated with the minimum traveltime from a coincident source/receiver pair to any particular interface. By definition the normal ray is perpendicular to the target interface and the image ray is perpendicular to the surface. Depth migration of data has the effect of moving points along their image ray to their correct position. Time migration of data has the effect of moving points laterally to their minimum time positions (the normal ray), rather than their 'true' time positions.

By the CFP technology a new ray is introduced: the one-way image ray. The one-way image ray is associated with the traveltime of a focus point in the subsurface to a receiver at the same lateral position as the focus point at the surface. In figure (5.14) the one-way image ray is displayed together with the image ray and the normal ray (in order to observe a better difference between the different ray paths the velocities of the syncline model are modified). Note that if the image ray is used for imaging

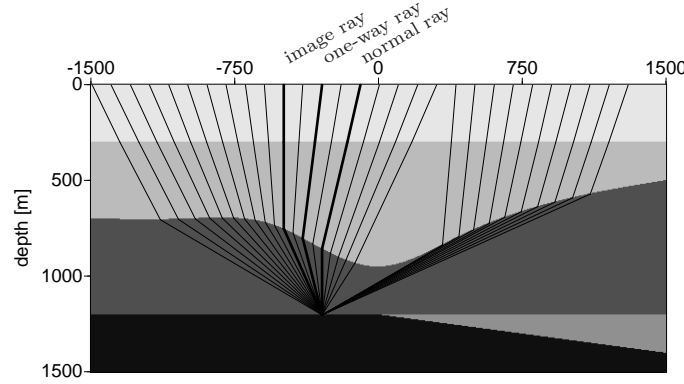


**Figure 5.14** Normal, image and one-way image ray for a focus point in the subsurface in the syncline model. The one-way image time is given by the time of the zero CFP offset trace in the synthesis operator. Note that in general the one-way image ray is bended.

a lateral shift of the data points is needed to position the reflector at its correct position. With the definition of the one-way image ray the result of the double focusing procedure for one focus point is positioned in the one-way image gather at the lateral position of the focus point at the one-way image time. Therefore in the CFP imaging procedure the one-way image ray is, by definition, positioned at the correct lateral position and there is no need to shift the data points in the conversion to a depth image.

The one-way image ray defines where the result of the double focusing procedure must be positioned in the one-way image gather. The positioning of the double focusing result is explained in detail in the next subsection.

### 5.3.2 Positioning of the double focusing result

The focusing operator is defined in one-way traveltimes. The synthesis process converts the two-way time of the data to a mixed version of one-way and two-way traveltimes. The one-way part of the CFP gather is located at the operator times. The events in the CFP gather above and below the operator times are associated with a two-way travelttime with respect to the defined focus point. In figure 5.15 this is explained with a 1 dimensional model with 3-reflectors (a). The velocity in the 1-dimensional medium is chosen constant at  $c = 2000$  m/s and at 400, 800 and 1200 m (= 0.4 seconds difference in two-way travelttime), the reflectors in the model are defined by a density contrast. The CFP gather for the first ① and third ③ reflector are shown in figure 5.15d and f and the focusing operators are shown in c and e respectively. Note that the focusing operators are time coincident with the related response in the CFP gather, indicating that the correct focusing operators are used. In the CFP gather for the third reflector (f) the response of the first reflector ① is shifted to negative times and is located at the bottom of the picture. Looking at the traveltimes for the trace at  $x = 0$  in the zoomed pictures (g) and (h) it is observed that the time between the position where the focus point is defined and the other layers is the two-way interval travelttime between the layer and the point (0.4 seconds for  $x = 0$ ). The time of the focus point response is the one-way travelttime of the focus point to the surface. This mixture of one-way and two-way traveltimes must be taken into account for a proper positioning of the events in-between two focus points defined at the same lateral position but at different one-way image time levels.

Suppose that there are only two focus points defined; one at the first and one at the third reflector as shown in figure 5.15a and that the aim is to image the middle reflector ②. Using the one-way image ray and the second focusing step the imaging procedure can be carried out for the two focus points. Figure 5.16 shows the move-out corrected CFP gather for the first reflector (a) and for the third reflector (b). According to the one-way image ray the first reflector must be imaged at the one-

way time of 0.2 seconds, the second reflector at 0.4 seconds and the third reflector

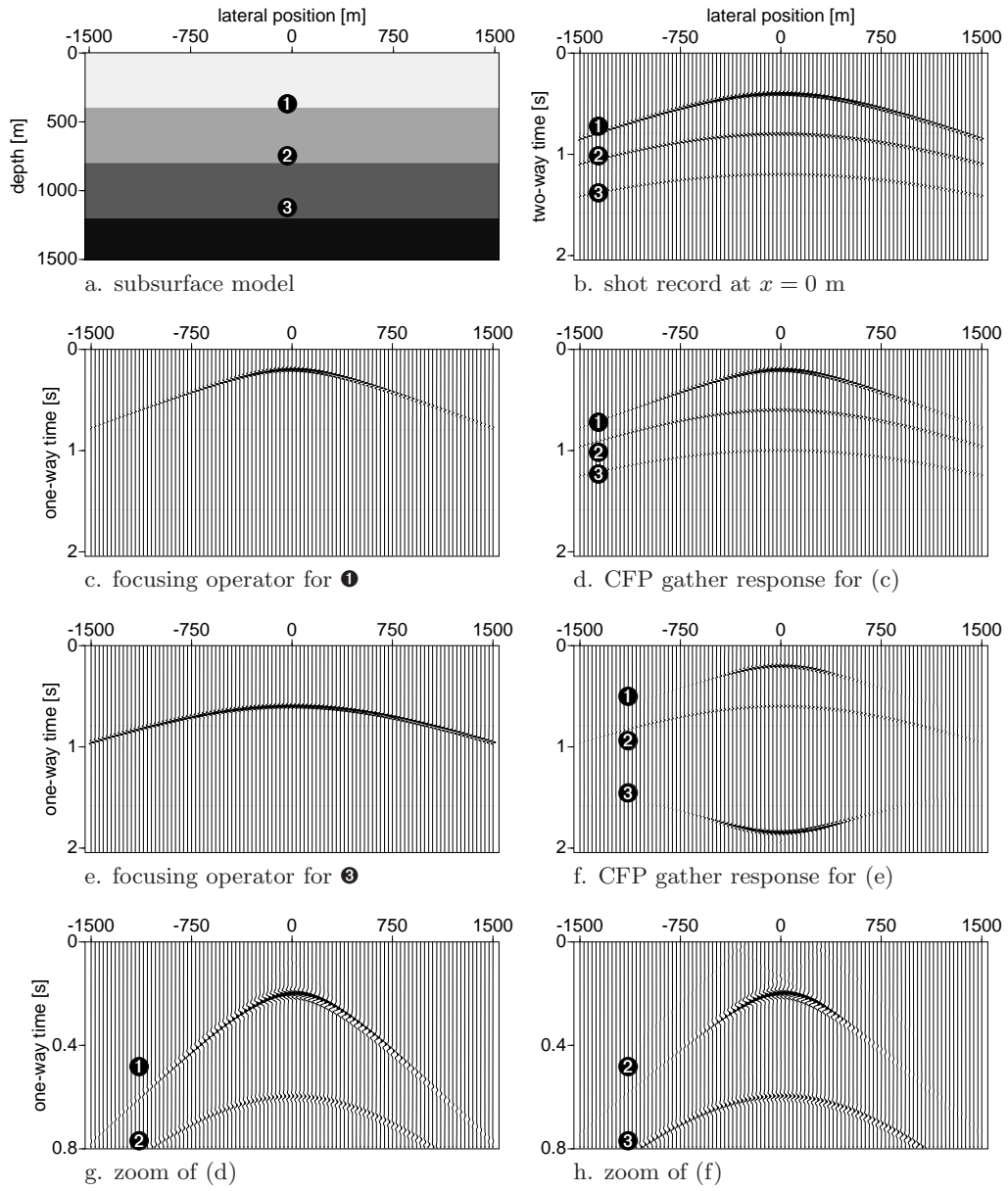


**Figure 5.15** Traveltimes in the CFP gather. The time between the focus point response and the other reflectors is the two-way interval traveltimes. This is observed in (g) where the time between ① and ② at  $x = 0$  is a two-way traveltimes ( $= \frac{2d}{c} = \frac{800}{2000} = 0.4s$ ).

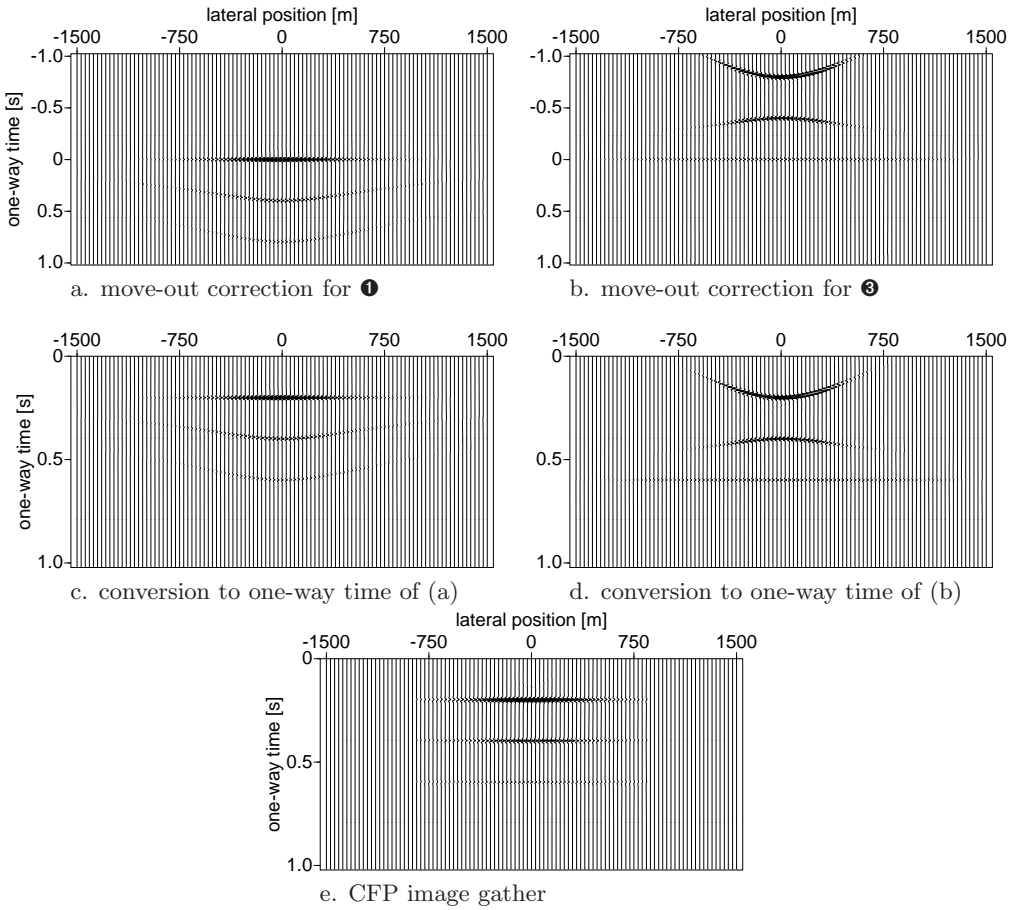


**Figure 5.16** Second focusing step and positioning at the one-way image time. The CFP image gather is obtained by combining the results of (c) and (d) and using interpolated operators to correct for the move-out in between the defined focus points.

at 0.6 seconds. Note that in figure 5.16a the time between the response of the first and the second reflector is 0.4 seconds. To image the second reflector at the correct one-way time (0.4 s), by using the CFP gather with a focus point defined at the first reflector, the two-way time between the second reflector and the focus point should be converted to one-way time. The result of this conversion is positioned at the one-way image time of the focus point and is shown in 5.16c for the first reflector and in 5.16d for the third reflector.

Note that at the one-way image time of the focusing operator (0.2 s) in figure 5.16c the move-out corrected response for the first reflector is flat and the response of the second reflector (around 0.4 s) is not flat. The non-flatness of the second reflector is due to the fact that the wrong operator (defined only for the first reflector) is

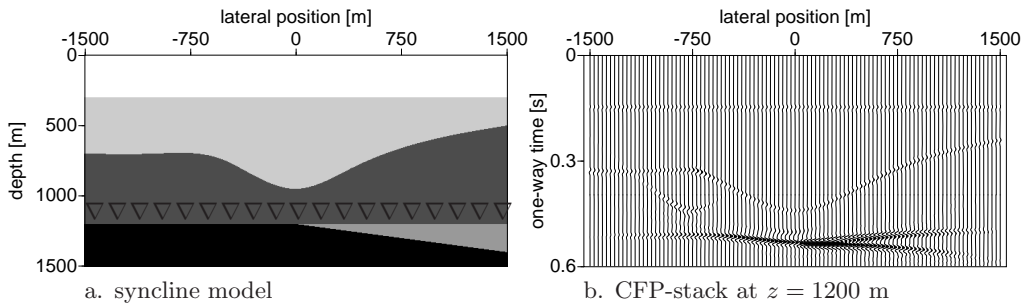


**Figure 5.17** The CFP-stack gives a local image around the defined focus points. Note that all the other events present in the syncline model, like the syncline interface and the wedge, are imaged at the correct one-way image time as well.

used for the move-out correction in the second focusing step. Therefore one should use in the second focusing step, for every different image-time a different operator. These intermediate operators can be obtained by interpolating the operators used in the first focusing step. How sparse the operators can be chosen in the first focusing step is investigated in section (5.4) where the resolution and focusing beam of the operator is analyzed.

The results of the second focusing step combined into one gather is shown in figure 5.16e and is called the CFP image gather. Interpolated operators are used to correct for the move-out in between the defined focus points. There is a time window used to select the contribution from the CFP gather with a focus point on the first reflector which is determined by the difference in one-way image time between the focusing operator at the third reflector. This time window around the focus point response is chosen such that the contribution of the CFP gathers below and above just overlap. Figure 5.16e is obtained by combining the response of the first and third reflector. The constructed CFP image gather is of special interest and will be discussed in the next section.

Another useful gather is the CFP stack. The CFP-stack is defined as a move-out corrected CFP-gather converted to one-way time followed by a summation over all the traces in the gather. In the CFP-stack the event at the image time of the defined focus point is equal to the double focusing result. Around the one-way image time the CFP-stack will give a good representation of the area surrounding the focusing point. The CFP-stack can be used to get quick an idea of the main reflectors in the data, but it can also be used to investigate a particular reflector or depth level.

For example by calculating CFP gathers with focus points following, in the lateral direction, a horizon or a reflector, followed by the CFP stacking procedure builds up an image for the horizon or boundary of interest. Figure 5.17b shows a CFP-stack for focus points defined at the deep flat reflector in the syncline model. Note that

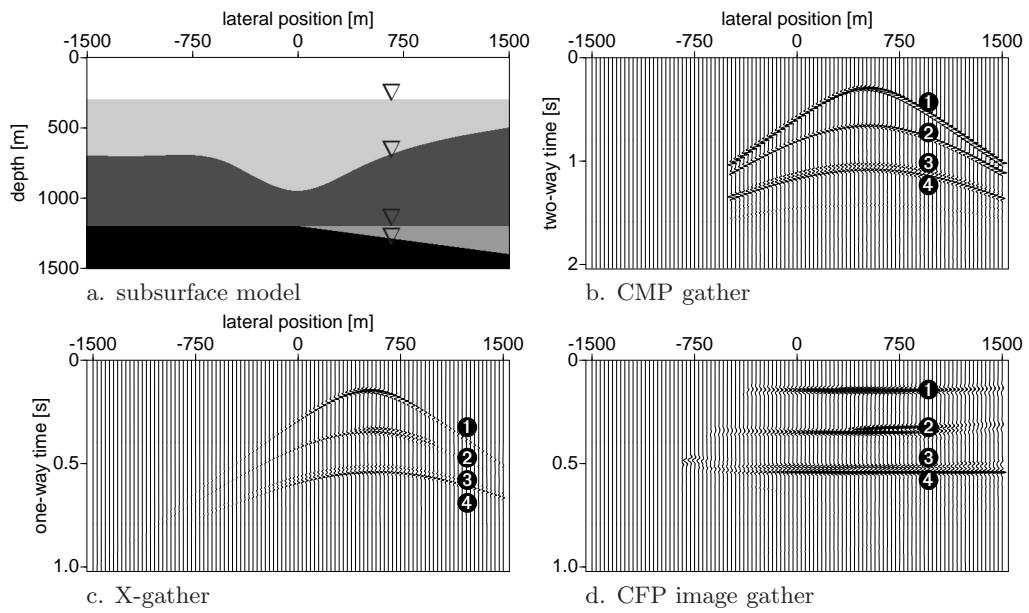


**Figure 5.18** For the calculation of a CFP image gather at one lateral position the response of several focus points (in depth) are combined in one gather. Note that if the correct operators are used the events in the CFP image gather all line up horizontally.

all the other events present in the syncline model, like the syncline interface and the wedge, are imaged at the correct one-way image time as well. This remarkable property of the CFP method is discussed in section (6.4), but first the CFP image gather and the CFP image must be discussed in more detail to be able to fully appreciate this property of the CFP method.

### 5.3.3 CFP image-gather

The CFP gather gives the response from one focus point in the subsurface. The most important information in the CFP gather is therefore concentrated around the focus point response. The CFP image gather is constructed by selecting samples from the CFP gather around a time window, defined by the focusing operator, and placing these selected time samples into one gather. This procedure is repeated for different CFP gathers constructed with focusing operators defined at the same lateral position, but at different depths (or one-way times). In the CFP image gather the samples from the CFP gather are converted to one-way time with respect to the one-way image time of the focusing operator. For the move-out correction in the CFP image gather at every one-way time sample an operator is needed. These operators are obtained by a linear interpolation (in offset or in ray-parameter  $p$ ) of the operators used in the first focusing step. With these operators the CFP image gather can be move-out corrected and stacked to get the image trace. This move-

out corrected multi focus gather represents the CFP image gather in one-way image time. If the move-out correction is not applied the gather is called an X-gather (X from exploding).

In figure 5.18d a CFP image gather, positioned at  $x = 500$  m, is shown for the syncline model. The image gather is constructed from 4 CFP gathers with their focus points defined at the boundaries of the model (a). Event ❶ originates from the flat top reflector, ❷ from the right flank of the syncline (note the finite aperture artifact due to the dip at the flank), ❸ originates from the deep flat reflector (note the negative reflection coefficient) and ❹ from the wedge in the right part of the model. The X-gather (c) can also be used as an alternative for the CMP gather which is shown for comparison in 5.18b.

Building the CFP image gather, by making use of traveltime operators, introduces a stretch of the wavelet due to the convergence of the operator times at the higher offsets. This stretched part at the higher offsets can be removed from the CFP image gather by setting a stretch parameter. In figure 5.18d the stretched wavelet at the higher offsets is clearly visible.

#### coherency measurement

In the CFP image gather all events should align at the same one-way image time, if an event is not aligned this indicates that an erroneous focusing operator was used or that the response of the focus point was not measured. Any misalignment with respect to a reference trace can be calculated and used as a quality measurement of the image. Therefore the following coherency measurement is introduced (after Neidell and Taner, 1971)

$$C_j = \frac{\sum_{k=j-N/2}^{j+N/2} A_k B_k}{\sqrt{\sum_{k=j-N/2}^{j+N/2} A_k^2 \sum_{k=j-N/2}^{j+N/2} B_k^2}}, \quad (5.7)$$

where  $C_j$  is the coherency measurement at time sample  $j$ ,  $A$  a trace of the CFP image gather and  $B$  the reference trace. The ideal choice for  $B$  is the image trace itself, an alternative would be the image trace which is built up during the imaging.

#### 5.3.4 One-way time image

The CFP-stack, which was explained in the previous subsection, represents a local image around the defined focus points. By defining focus points not only at one boundary but in the whole subsurface a complete one-way time image can be built up. As mentioned before it is not necessary to define in the first focusing step a focus point at every time position for all lateral positions. Using the resolution in the focusing beam an optimum focus point distribution can be determined (see

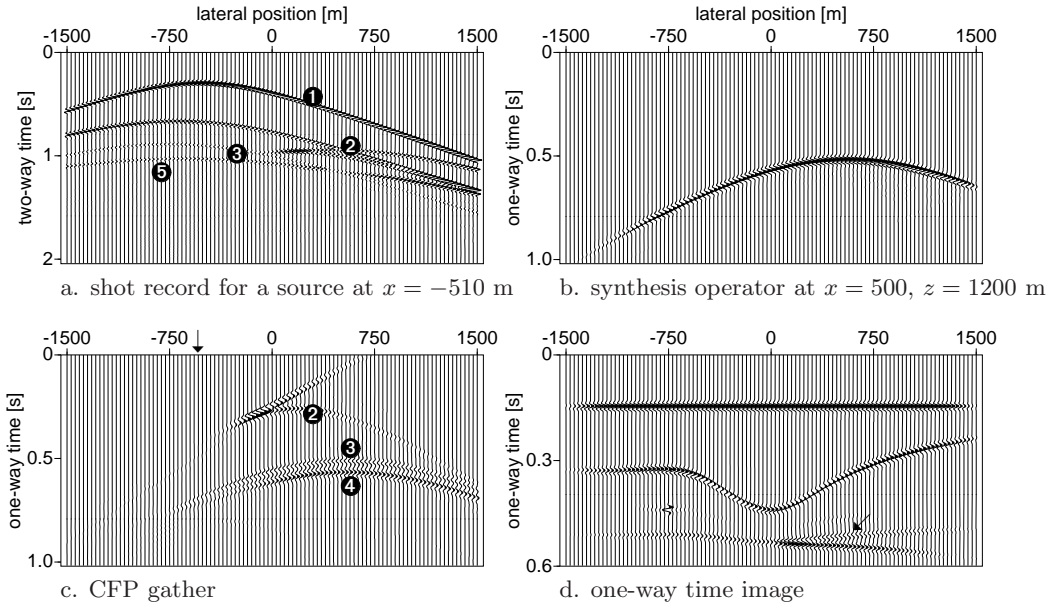


**Figure 5.19** The contribution from a shot record (a) in the CFP image (d) depends on the used focusing operator (b). Note that in this example only a small part of the shot record contributes to the image position (indicated with an arrow).

section (5.4)). For example a good choice would be a focusing operator positioned at every macro boundary in the model.

The imaging procedure is explained in figure 5.19 by using the data of the syncline model. For the imaging procedure a focus point is chosen at every 15 m at the three main boundaries in the model and at the diffraction point. The shot record shown in figure 5.19a has a contribution in the CFP gather (constructed with the focusing operator shown in figure 5.19b) at its source position  $x = -510$ , which is indicated by the arrow in 5.19c. Note that event ⑤ in the shot record originates from the diffraction point. The focusing operator (b) has its focus point defined at  $x = 500, z = 1200$ . Performing a second focusing step on the CFP gather with the same operator of figure 5.19b and selecting the samples around the operator times gives the contribution indicated by the arrow in the one-way time image of figure 5.19d. The lateral position in the image is by definition equal to the lateral position of the focusing operator. The imaging for the samples in between two focusing operators at the same lateral position is done with interpolated focusing operators (the second focusing step). Along the times given by these second focusing operators the samples are stacked and positioned at the one-way image time. The time window, which determines which samples are included from the CFP gather in the image, is determined by the time difference between the two operators. Note that due to the fixed spread acquisition geometry the edges of the model are sparsely

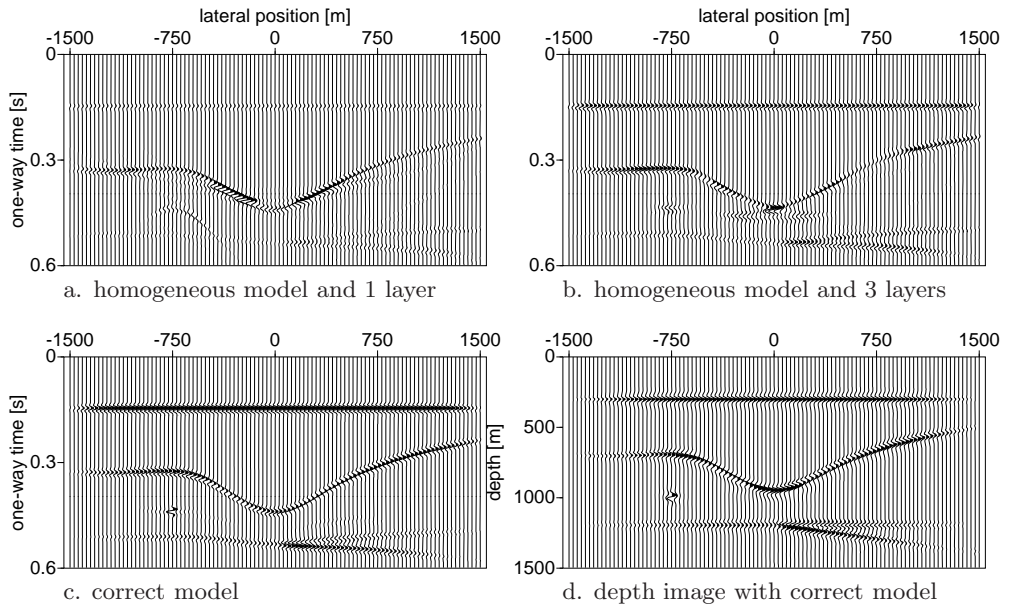


**Figure 5.20** Imaging results for the double focus procedure using synthesis operators based on a homogeneous model; with only one level of focus points (a), with three levels of focus points (b) and the correct model (c). Result (d) shows the pre-stack depth migration result using the correct macro model. Note that result (a) means stacking of CFP gathers.

illuminated in the image (d). Note also that the imaging condition used in the CFP method states that a reflector exists within the earth when the wavefront curvature of the downward continued wavefield is the same as the curvature of the downward incident wavefield for all offsets.

To show the robustness and sensitivity of the imaging procedure the same imaging procedure is carried out with synthesis operators which are based on an erroneous initial macro model. For the erroneous macro model a homogeneous model is chosen with the velocity  $c = 2200$  m/s. Figure 5.20a shows the imaging result by using the homogeneous model with only one layer defined at  $z = 800$ . The focusing operators are not updated during the imaging procedure. Figure 5.20b shows the imaging result with three depth levels at  $z = 400$ ,  $z = 800$  and  $z = 1200$  m in the homogeneous model where the focusing operators are defined. For a good comparison the imaging result using the correct model is shown in figure 5.20c and the result obtained with conventional prestack depth migration using the correct model is shown in figure 5.20d. Note that the one-way time image obtained with the homogeneous model gives already a good indication of the reflectors present in the model. The images obtained with the homogeneous macro model show also that the reflectors are all imaged at the same one-way image time, there is only a difference in amplitude.

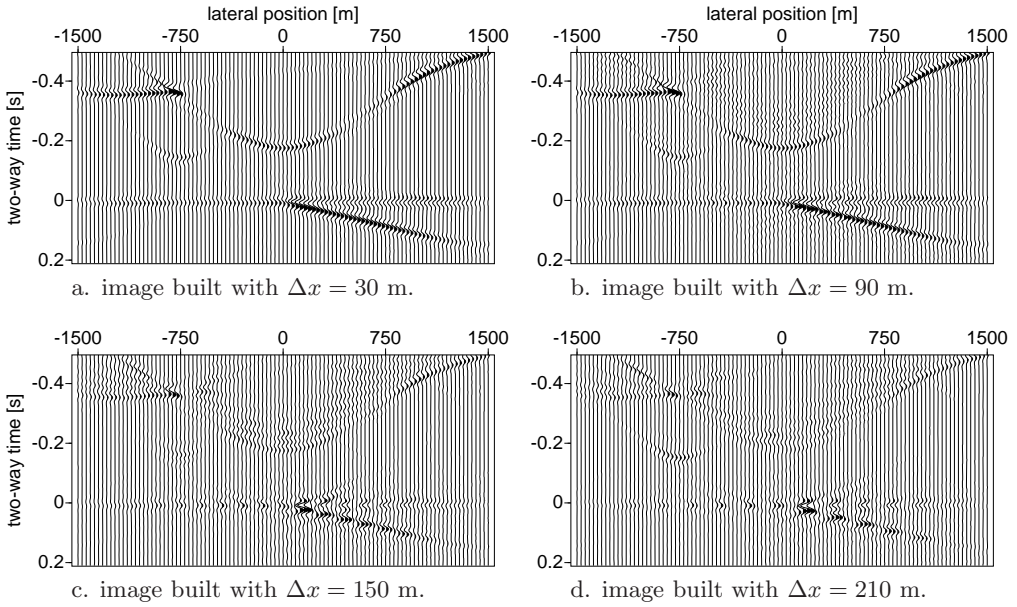


**Figure 5.21** CFP imaging by a summation of bifocal images for different lateral spacings; the image of the third boundary ( $t = 0$ ) is aimed for only.

This same effect was already observed in the discussion about the CFP-stack and will be explained in section (6.4). Comparing the depth migration with the one-way time image shows that the conversion from the one-way time image to the depth image consists only of a (non-linear) stretching of the time axis, a lateral shift is not needed. The one-way time image can be calculated with any set of focusing operators, which makes it a suitable method for analysis in a special regions of interest. The CFP imaging method can also be implemented in an efficient way by making use of a processing method which is done entirely in the time domain (see appendix C).

The one-way time image can also be built up in another more efficient, but less accurate, way. After the construction of the CFP-gather, it can be cross-correlated (2-dimensional) with its time reversed synthesis operator. The cross-correlation can be interpreted as a double focusing result where it is assumed that the reflector is locally flat. The result of this cross-correlation is placed in the image gather at the lateral position of the focusing operator. In the imaging procedure discussed above only the spatial zero-lag trace (confocal result) of the 2D cross-correlation was placed in the imaging result, now every trace (bifocal result) is placed in the image. In this way the spatial width of the bifocal image can be used in an optimal way and it is not necessary to use a laterally dense sampled set of focus points. The result of this imaging procedure is shown in figure 5.21 for different spatial sampling rates between the focusing positions on the deep flat reflector. Note that the one-way time

re-sampling is not carried out in the examples shown in figure 5.21, so the data is still in two-way time. Note also that in figure 5.21 the samples around  $t = 0$  represent the result which can be used in the one-way time image, the synclinal event which occurs at negative times can not be used directly in the one-way time image. For a complete construction of the one-way time image with the cross-correlation method, at every macro boundary focus points must be chosen and combined to construct the image.

The images shown in figure 5.21 can be interpreted as a plane wave (normal incidence on the reflector) response measured at the deep flat reflector in the syncline model. In this interpretation both the sources and receivers are positioned at the deep reflector. Using this interpretation one can migrate the constructed image with an areal shot record migration algorithm (Rietveld, 1995). The obtained migration result will not be as good as a 'conventional' areal shot record migration because the assumption is made that the operators can be shifted laterally, which means that the medium is 1-dimensional.

## 5.4 Resolution and amplitude analysis

Thus far no attention has been paid on the resolution of the focusing method. In the discussed imaging procedure it was implicitly assumed that the focusing area around the focus point has an extent in the vertical (time) direction. By using this assumption it was argued that it is not necessary to place at every time sample a focusing operator in the first focusing step. The resolution analysis in this section will show that this assumption is indeed valid. Further it will be shown that besides the imaging properties, the focusing method also provides a method of determining the reflection coefficient.

### 5.4.1 Resolution and focusing beams

Modeling the energy for a propagating wavefront of the synthesis operator through the subsurface model gives an indication how the areas in the subsurface are illuminated by this synthesis operator. From this so called focusing beam it is also possible to determine which aperture at the surface is most important for the illumination. With these illumination areas in the subsurface the distribution of the focus points in the subsurface can be determined in order to obtain an efficient and optimum illumination procedure of the subsurface. In figure 5.22 three focusing beams are shown for the syncline model introduced earlier. The beams are constructed by performing an inverse recursive depth extrapolation of the focusing operators through the model and calculating at every depth level the energy of the wavefield as function of the lateral position. Note that for the construction of the beams only the synthesis operators and a macro model are needed.

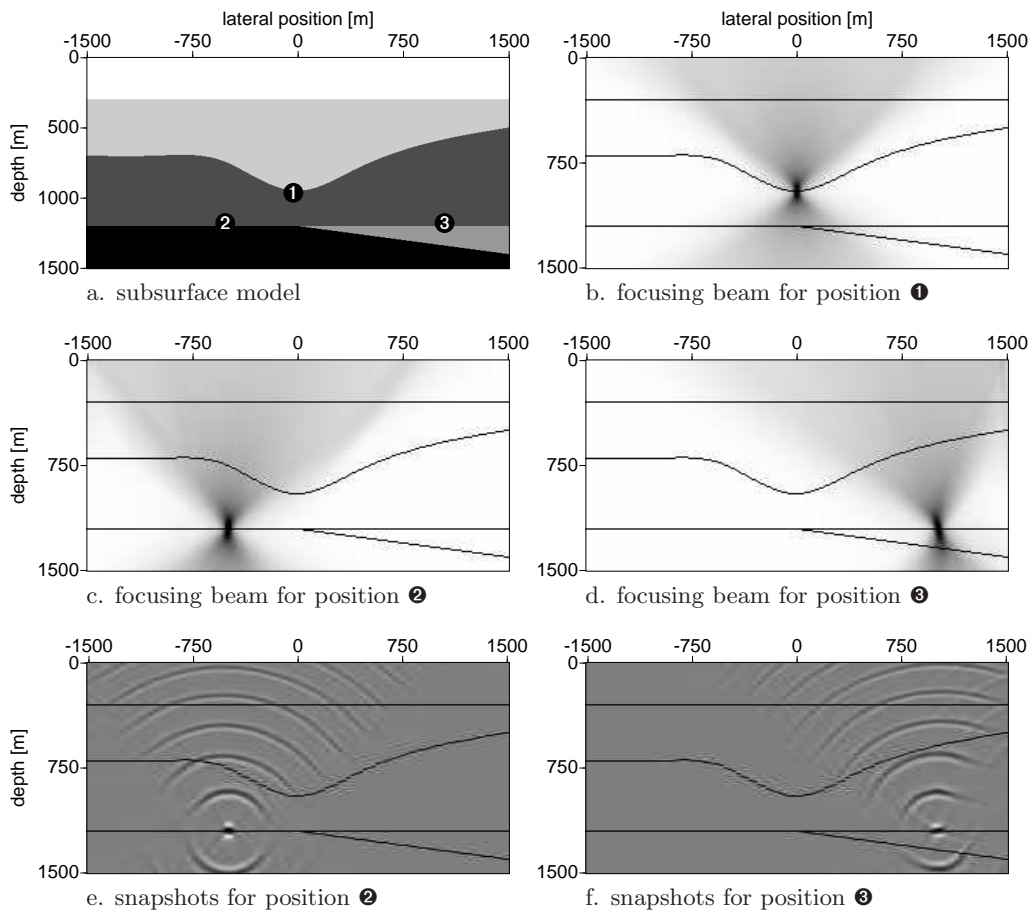


**Figure 5.22** Focusing beams through the subsurface model given in a). Note the tube like shape of the different focusing areas.

From the focusing beams in figure 5.22 it is observed that around the actual focus point most of the energy is focused in a tube like shaped area. The black center of the tube has a lateral extent which is smaller than the vertical extent. The shape of the focusing area is directly related to the resolution at the focusing point. The lateral and vertical resolution of a focus point are determined by the acquisition geometry and the subsurface model. By using this information combined with the information from the focusing beams it is possible to define at which vertical sampling density the focus points have to be chosen to illuminate the subsurface properly.

In figure 5.23 a zoomed version of the focusing area in figure 5.22c is shown. Figure 5.23a shows that the focusing area is not limited to the defined focus point but has an extension in the horizontal and vertical direction. In the contour plot, plotted with equidistant contour values, it is observed that the inner contour lines are close

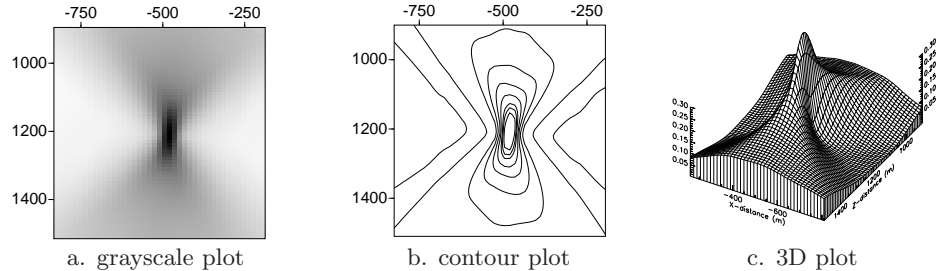


**Figure 5.23** Details of the focusing beam for focusing position ❷ in figure 5.22c. Note that the focusing area is not limited to the defined focus point at  $x = -500$ ,  $z = 1200$  m.

together. In the 3D plot this is observed as a broad peak at the focus point position. For this example a good illumination in the horizontal direction can be obtained by placing at every 50 m a focus point and a good illumination in the vertical direction can be obtained by placing a focus point at every 100 m.

In figure 5.24 different combinations of focusing operators are used to illuminate the subsurface. The illumination shown in figure 5.24a is obtained by placing three focus points at the same lateral position in the model (one at every boundary). This illumination is not sufficient to illuminate the events in-between the boundaries. Reducing the distance between the focus point gives the results shown in figure 5.24b

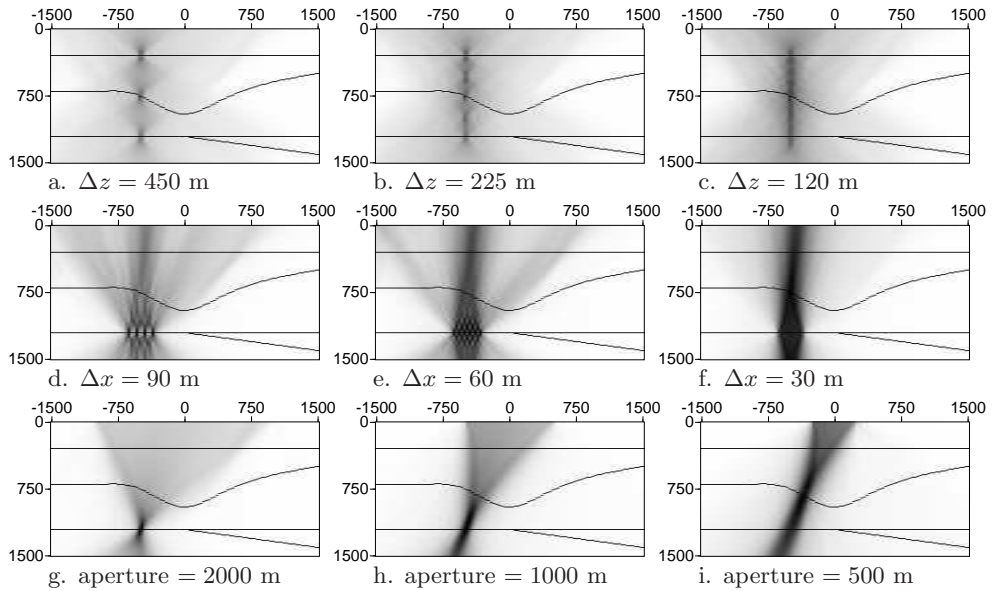


**Figure 5.24** Different focus point distributions in lateral and vertical direction. Note that for a complete illumination a sparse distribution of the focus points is sufficient.

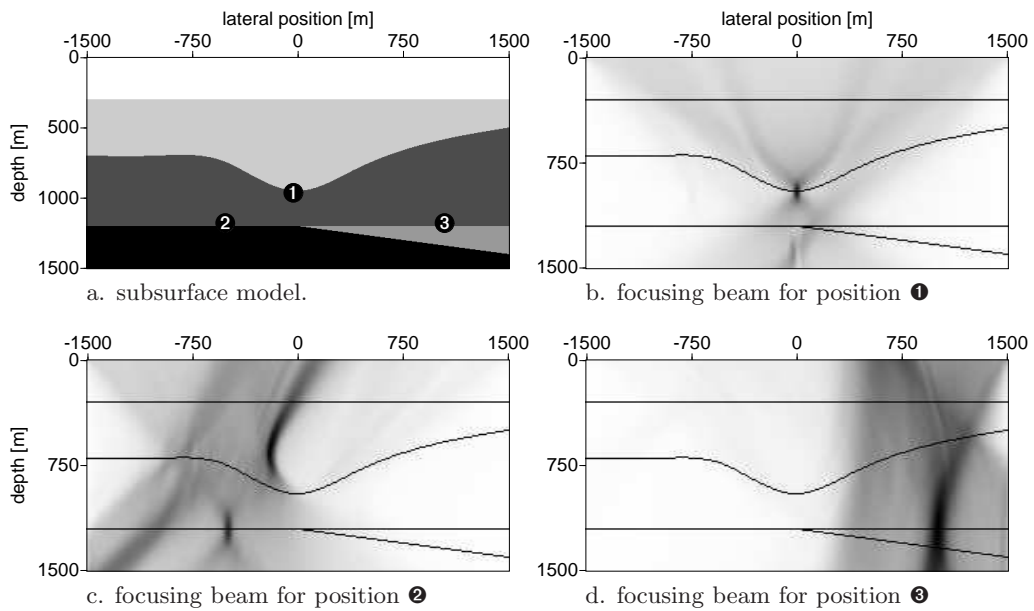


**Figure 5.25** Focusing beams of CFP gathers extrapolated through the subsurface model given in a). Note that there are more focusing areas than in figure 5.22.

and 5.24c. From these experiments it can be concluded that in the first focusing process focus points distributed with a vertical distance of  $\pm 100$  m are sufficient to illuminate the events in-between the focus points correctly. This is of significant importance for efficiency, particularly in 3D.

The horizontal distance between the two focus points must be chosen smaller than the vertical distance to obtain a sufficient illumination. In figure 5.24d,e and f three different horizontal focus point distributions are shown. The distance of  $\Delta x = 60$  m, shown in figure 5.24e, is still not sufficient for a proper illumination. Another way to influence the horizontal illumination is by limiting the operator aperture such the focusing beams become broader in the lateral direction as shown in figure 5.24g,h and i. By limiting the operator aperture (which means reducing the maximum angle which can be focused) a broader focusing beam is obtained which gives a less accurate image, but this image can be obtained by using less operators.

The introduced analysis with focusing beams are a helpful tool in determining the focus point distribution in the subsurface. The focusing beams give more information than ray-traces, because the resolution of the focusing energy is shown as well. The same beam-focusing algorithm can also be used for monitoring the focusing of all the events present in the constructed CFP gather. In figure 5.25 the focusing beams are shown for the CFP gathers constructed with the operators used to construct the beams of figure 5.22. At the defined focus point the focusing beam should be the same as the focusing beam of the operators. Due to the presence of the

angle dependent reflection coefficient in the CFP gather, figure 5.25b gives a slightly different focusing pattern as in figure 5.22b. Beside a beam at the defined focus point the other out of focus reflections are also visible. Below the main focus point in figure 5.25b there are two focus areas visible which originate from the deeper reflections. Note that these focus areas are not positioned on a boundary. In figure 5.25c (Figure 5.10i shows the construction of the CFP gather used in the calculation of the beam in figure 5.25c) a strong focusing area is present above the defined focus point. The strong 'non-causal' event in the CFP gather above the traveltime of the operator gives rise to the observed strong focusing area. This area cannot be interpreted physically because it originates from a 'non-causal' event present in the CFP gather. If one wants to do analysis on beams calculated from CFP gathers, the 'non-causal' events in the CFP gather should be muted out. In figure 5.25d it is observed that another focusing area is present at a deeper depth level due to the presence of the deeper reflector.

#### 5.4.2 Amplitude analysis

If the correct focusing operator is used the time-reversed focusing operator and the focus point response have equal traveltimes. The only difference between the focus point response and its time-reversed focusing operator is in amplitude. According to equations (4.33) and (4.31), which are repeated below,

$$\mathbf{F}_i^-(z_m, z_0) = \mathbf{I}_i^-(z_m) [\mathbf{W}^+(z_m, z_0)]^* [\mathbf{D}^-(z_0)]^{-1} \quad (5.8)$$

$$\mathbf{P}_i^-(z_m, z_0) = \mathbf{I}_i^-(z_m) \mathbf{R}^+(z_m) \mathbf{W}^+(z_m, z_0) \mathbf{D}^+(z_0) \mathbf{S}(z_0) \quad (5.9)$$

the difference in amplitude along the traveltime curve is given by the angle dependent reflection property at the focus point  $\mathbf{I}_i^-(z_m) \mathbf{R}^+$ , the surface operators  $\mathbf{D}^\pm$  and the source signature  $\mathbf{S}(z_0)$ . Assuming that the source signature is the same for all experiments  $\mathbf{S}(z_0) = \mathbf{I}S$  and that there are omni-directional receivers at the surface  $\mathbf{D}^-(z_0) = \mathbf{I}$  it is possible to derive a simple procedure which can extract the reflection information from the CFP gathers and its focusing operator. Note that in equation (5.9) the limited spatial bandwidth is represented by the (limited) size of the  $\mathbf{D}$  matrices. Before the amplitude analysis in a CFP gather is discussed in detail first the amplitudes for an individual trace of a shot record, a focusing operator and a CFP gather are considered.

The amplitudes present in the CFP gather can be interpreted by looking at the construction of the CFP gather for the top flat layer in the syncline model shown in figure 5.9a. The synthesis operator is defined for a focus point at the reflector at  $x = 0$  and  $z = 300$  m. The stationary phase contribution in the CFP gather of the shot record with a source position at  $x = -300$  is given by the trace at  $x = 300$ . This stationary phase trace is shown at the left hand side of figure 5.26. The amplitude in this trace consists of  $\frac{RS}{\sqrt{2r}}$ , where  $S$  represents the amplitude of the wavelet,  $R$

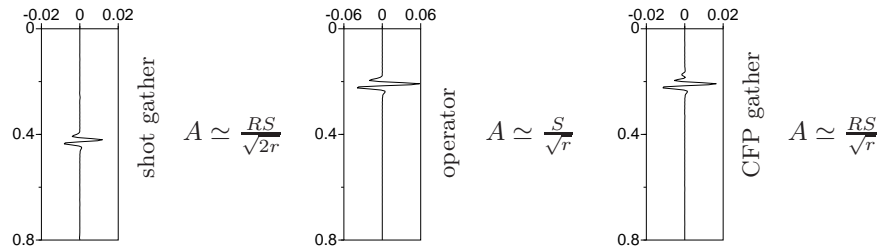


**Figure 5.26** Amplitudes of a trace from a shot gather, synthesis operator and CFP gather, where  $S$  represents the amplitude of the wavelet,  $R (= 0.29)$  the reflection coefficient at  $45^\circ$  and  $r$  the distance between the focus point and the receiver at the surface.

the reflection coefficient at  $45^\circ$  and  $r$  the distance between the focus point and the receiver at the surface (in the given example  $r = \sqrt{2 * 300^2}$ ). The operator trace at  $x = 300$ , the middle trace in figure 5.26, has an amplitude proportional to  $\frac{1}{\sqrt{r}}$ . The trace on the right hand side of figure 5.26 represents the contribution of the shot gather in the CFP gather. The amplitude in the CFP gather is proportional to  $\frac{RS}{\sqrt{r}}$ . Compared with the trace in the shot record there is a strong amplitude effect due to the summation in the Fresnel zone. Dividing (in a least-squares sense) the CFP gather by its synthesis operator, weighted with the wavelet (the second trace in figure 5.26) gives the reflection coefficient for an angle of incidence of  $45^\circ$ . This relationship between the CFP gather and the synthesis operator can be used to determine the AVO behavior at the focus point. Before this procedure is explained in detail first another aspect of the amplitudes is discussed.

From the foregoing discussion it can be concluded that it is possible to quantify the angle-dependent reflection property of the focus point by computing for each offset the amplitude ratio between the focus point response and the time-reversed focusing operator. This is illustrated for a flat reflector in figure 5.27; the reflector is positioned at 800 m depth and an acoustic contrast is used. The amplitude ratio shown in figure figure 5.27d has been computed in the time domain in a least-squares manner: for each offset the zero-lag temporal cross-correlation between the response and the focusing operator is divided by the zero-lag temporal autocorrelation of the operator. The critical reflection angle occurs at an offset of 1060 m, which is the starting point for the estimated AVO curve to deviate from the theoretical curve.

AVP (amplitude versus ray-parameter) analysis is more suitable for angle-dependent reflection purposes than AVO analysis. For AVP analysis the bifocal version of CFP migration is required (Berkhout, 1996b). In CFP imaging the confocal result (2-dimensional cross-correlation between the time-reversed operator and the CFP gather with only a zero-shift in the spatial direction) of the second focusing step is used only, for AVP analysis the bifocal result (2-dimensional cross-correlation with

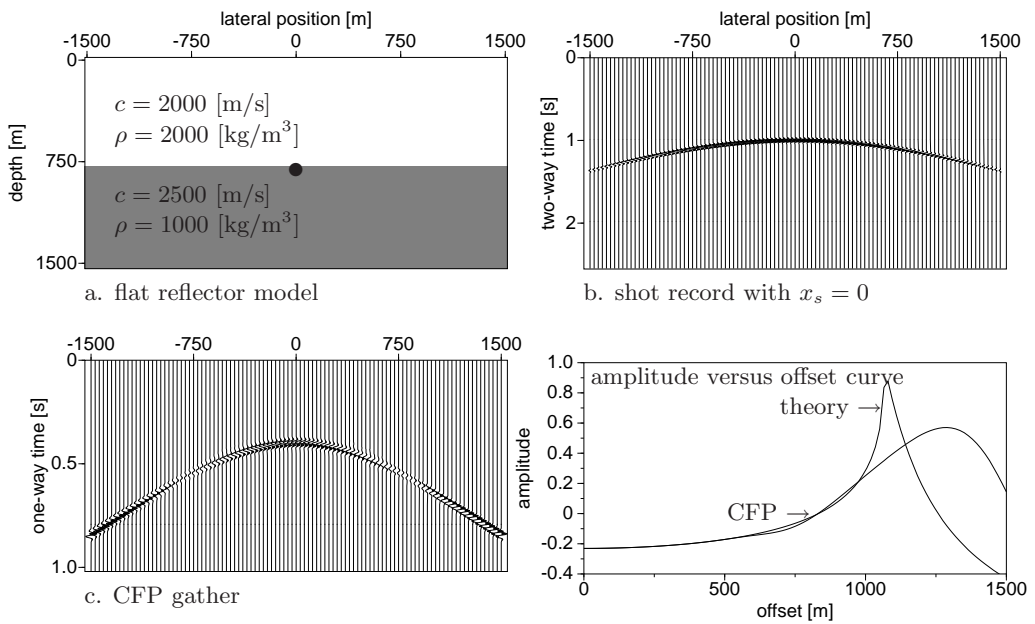


**Figure 5.27** Amplitude versus offset curves obtained by a least-squares estimation in the time domain. Note that the critical reflection angle occurs at an offset of 1060 [m].

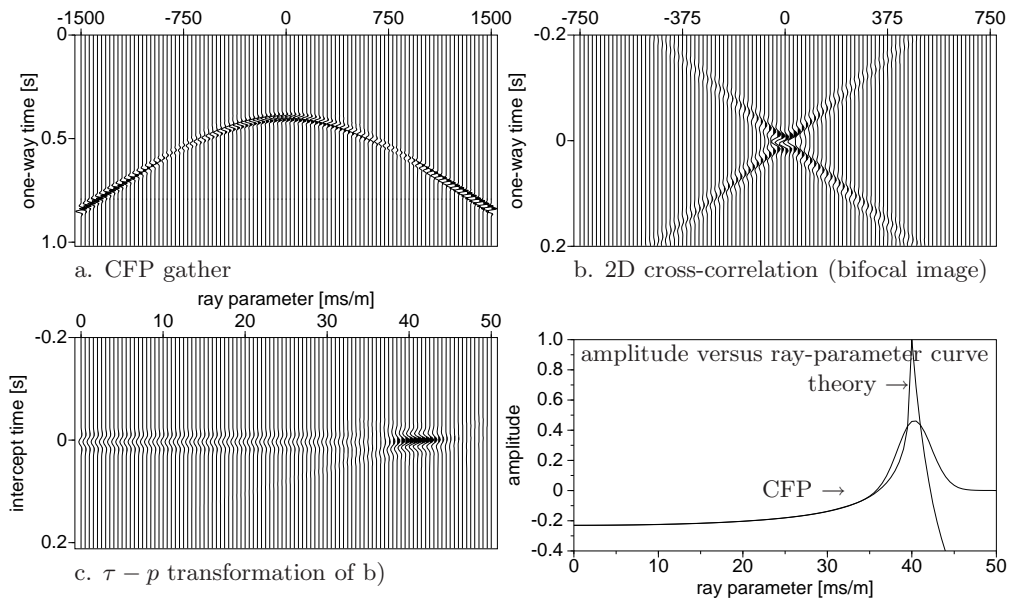


**Figure 5.28** Amplitude versus ray-parameter curve obtained by a  $\tau - p$  transformation of the bifocal image. Note that the critical reflection angle occurs at an ray-parameter of  $40 \times 10^{-3}$  [s/m].

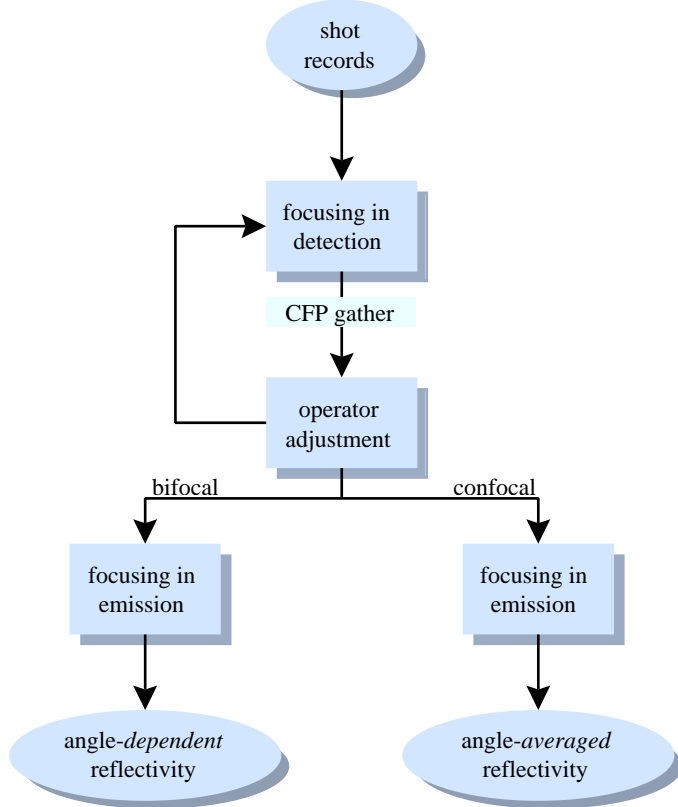


**Figure 5.29** Diagram for bifocal imaging and AVO analysis. After the first focusing step bifocal and confocal imaging can be carried out resulting in different reflectivity

'all' shifts in the spatial direction) is used. The bifocal result of the CFP gather is shown in figure 5.28b, the trace at  $x = 0$  is used in the confocal imaging procedure. By performing a linear Radon ( $\tau - p$ ) transformation on the bifocal image, the bifocal image is decomposed in local plane waves (ray-parameters) (c). The amplitude at  $\tau = 0$  (d) of every ray-parameter represents the amplitude of the (band limited) reflection operator at the focus point. The critical reflection angle occurs at the ray-parameter value of  $40 \times 10^{-3}$  s/m, which is the starting point for the estimated AVP curve to deviate from the theoretical curve.

The flow scheme of the bifocal imaging procedure is shown in figure 5.29. After focusing in detection and optionally updating of the focusing operator the second focusing step can be carried out. The integration of velocity analysis, imaging and AVO analysis can all be combined within the same double focusing process. The analysis and processing modules are included between the two focusing steps. This

does not only allow a better control on the structural solution and the reservoir characterization problem, it also offers new solutions to the well known surface-related problems (Berkhout and Verschuur, 1996b).

In the foregoing examples the amplitude analysis has only been shown for a single flat reflector. AVO analysis of more complicated examples is beyond the scope of this thesis and subject of another PhD project carried out by Aart-Jan van Wijngaarden.

## 5.5 3-Dimensional CFP gathers

As might be expected the CFP technology can also be used to process three dimensional seismic data. However, due to the irregular sampling in the cross-line direction special care should be taken in the first focusing step to obtain an appropriate summation in the Fresnel zone. If the Fresnel zone is positioned outside the seismic aperture or if the sampling is inaccurate the contribution in the CFP trace originating from the Fresnel zone will get distorted. To investigate the influence of irregular and sparse sampling first some 2-dimensional common offset contributions of the CFP gather are discussed. After this discussion the construction of a 3-dimensional CFP gather is much easier to understand. At the end of this section a method is proposed which can regularize CFP gathers in the coarse sampled (cross-line) direction.

### 5.5.1 Common offset contributions in 2-dimensional synthesis

Suppose that a CFP gather is constructed from shot records which contain only one trace. Then the CFP gather will consist of this single trace convolved with the appropriate trace of the focusing operator. In figure 5.30 this is shown for two offsets for the model used before; a single flat reflector at 800 m depth and sources moving from -1500 m to 1500 m with an interval of 15 m. The focusing operator is defined for a focus point positioned at the reflector at  $x = 0$ . In figure 5.30b the contribution of the zero offset trace is shown and in (d) the contribution of a trace with an offset of 1005 m is shown. Note that the common-offset section of a flat reflector gives a flat response. Convolution with the focusing operator and positioning at the source position gives the results shown in figure 5.30. The focusing operator can be recognized easily in the result of the zero-offset contribution. The traveltimes of the time-reversed focusing operator are represented by the spiky event. The contribution from the receiver with an offset of 1005 m is tangent with the time reversed focusing operator at the lateral position  $x = \frac{-1005}{2}$  m, which originates from a source position at  $\frac{1005}{2}$  m.

By taking more offsets into account the CFP gather will be built up completely. It is interesting to investigate how many offsets must be taken into account to build up the CFP gather completely. The best way to compare the different results, obtained

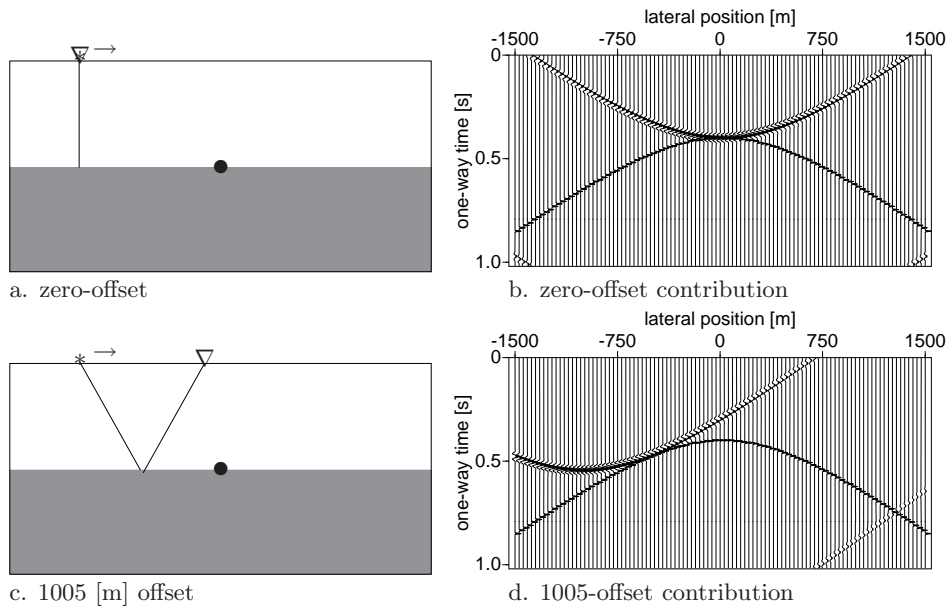


**Figure 5.30** Common offset contribution to the CFP gather. The traveltimes of the time-reversed focusing operator are represented by the spiky event. Note that the focusing operator can be recognized in the contribution of the single offset.

with different number of offsets, is with the aid of the one-way image trace. The number of offsets which are taken into account are varied by changing the detector spacing. In figure 5.31 several source and receiver sampling rates are used to build up the image trace. Beside the detector spacing the source spacing can also be varied. The acquisition spread is moving together with the source distance, like in a marine acquisition geometry. The sources are ranging from -1500 (receiver range from -1500, 1500) to 1500 (receivers range from 1500, 4500). The middle figures represent the move-out corrected CFP gather (= image gather) with a source sampling of 30 m. The trace on the left-hand side is the one-way image trace obtained with a source sampling of 15 m. The one-way image trace at the right-hand side is obtained with a source sampling of 150 m.

Due to the acquisition geometry the shot records with a position  $x > 0$  do not have a stationary phase ray which is measured by the receivers. The missing Fresnel zone is observed in the vanishing amplitude of the focus point response shown in figure 5.31d for positions where  $x > 0$ . In 5.31a the receiver spacing is 600 m and the individual contributions of the different offsets are clearly visible. In (d) the different offsets are destructively interfering at  $t > 0.4$  s which leaves only the undisturbed focus point response at  $t = 0.4$ . The image trace is constructed from the move-out corrected CFP gathers by an addition of all the traces. Using a dense source sampling (15 m) gives for all the different receiver spacings a correct image trace shown in the

traces on the left-hand side. A sparse source sampling (150 m) gives a distorted

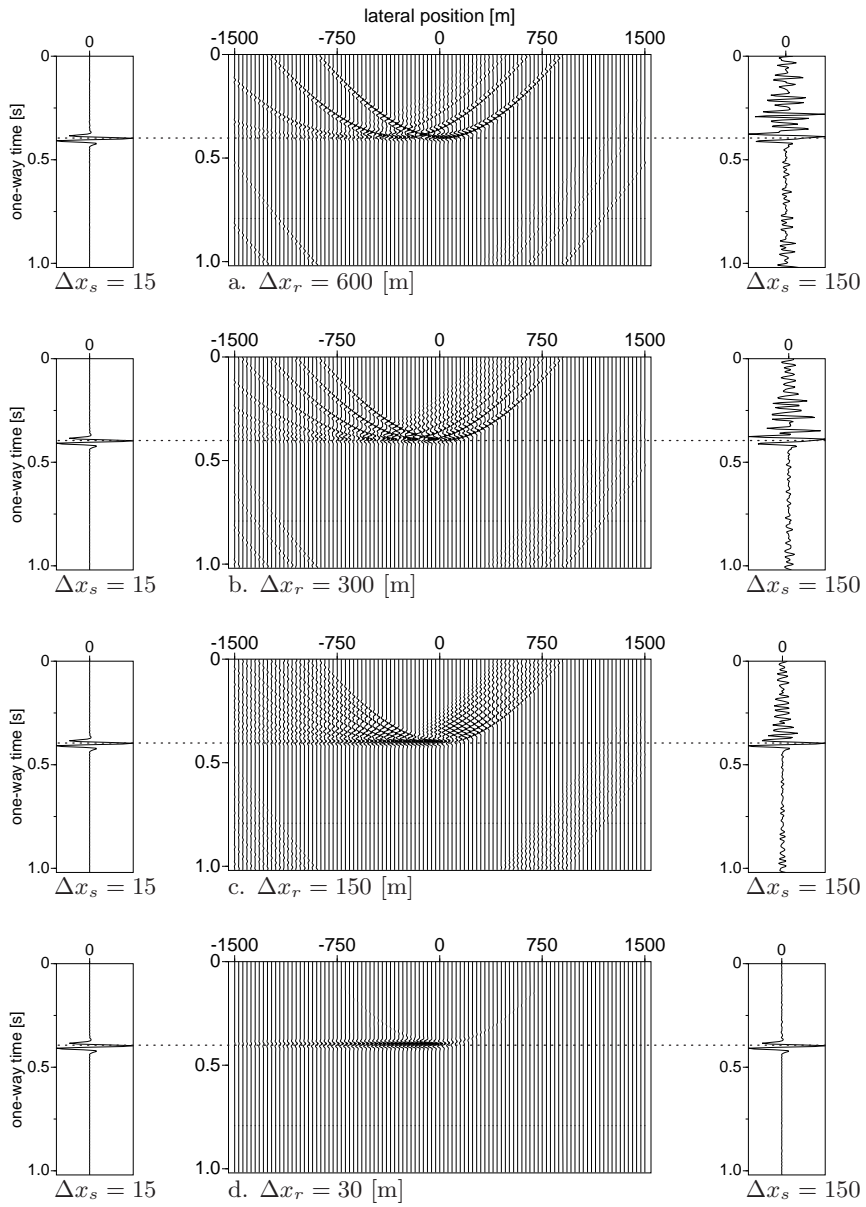


**Figure 5.31** Common offset contributions for different source ( $\Delta x_s$ ) and receiver ( $\Delta x_r$ ) sampling rates. The traces on the left and right-hand side are image traces. Note that for the image trace it is sufficient that either the source or the receiver sampling is dense.

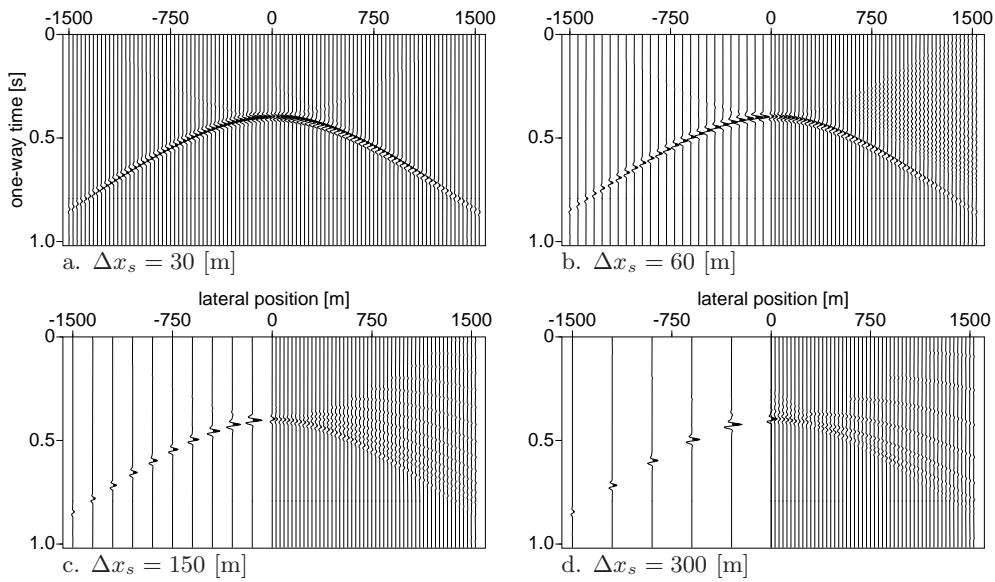


**Figure 5.32** Combining focusing in detection and focusing in emission for the first focusing step. The receiver sampling is fixed at 30 m and the source sampling is varying. Note that the focusing in detection results (positioned on the source positions) are undistorted. The result for focusing in emission (positioned on the receiver positions) gets distorted due to the sparse source sampling.

image traces if the receivers are also sparsely sampled. However, a dense receiver sampling and a coarse source sampling gives again a undistorted image trace. These observations are of importance if one considers the 3D marine acquisition geometry where the sampling in the cross-line direction is often coarse but the source sampling is dense.

In the examples shown above the first focusing step was carried out for focusing in detection. It is also possible to carry out the first focusing step for focusing in emission and combine these results with the results for focusing in detection. The results of these combined first focusing processes for different source sampling rates were already shown in figure 5.11. In figure 5.32 the same result are shown but now with a different source sampling rate. In this figure it is interesting to observe that due to the dense receiver spacing, which is kept constant at 30 m for all figures, the traces for focusing in detection (left-hand side) are always undistorted. Due to the sparse sampling for the source positions the traces for focusing in emission are distorted. This distortion is observed in the right-hand side of the pictures in figure 5.11.

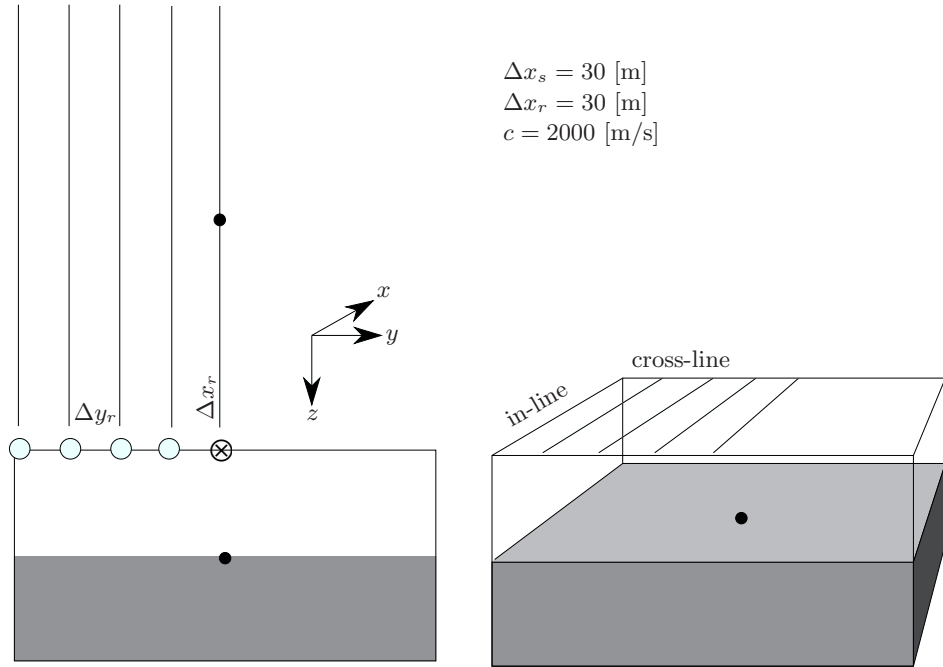


**Figure 5.33** 3-dimensional acquisition geometry which is used to explain some aspects of the construction of 3D CFP gathers. The streamer arrays are fixed and the source is only moving along the  $x = 0$  streamer line.

### 5.5.2 A simple 3D data example

Now that the results of sparse sampling in the 2-dimensional case have been investigated in the previous subsection, the principles of construction a CFP gather for 3-dimensional data can be discussed. In this section only the principles and some guidelines and pitfalls are given for the construction of a CFP gather in 3 dimensions. The construction of 3D CFP gathers for more complicated examples is subject of another research project carried out by John Bolte.

In figure 5.33 the subsurface model is shown which is used to explain the construction of a 3D CFP gather. The model consists of one flat reflector at a depth of 800 m and a velocity of 2000 m/s above the layer. The focus point is chosen at  $x = 0, y = 0, z = 800$ . The marine like acquisition geometry is also shown in figure 5.33; the sources are moving in the  $x$ -direction from  $x = -1500, y = 0$  to  $x = 1500, y = 0$  with  $\Delta x_s = 30$  m, the streamer lines are positioned in between  $y = 0$  and  $y = -1500$  m. The in-line receiver sampling  $\Delta x_r$  is 30 m and the cross-line receiver distance  $\Delta y_r$  is variable for the different experiments.

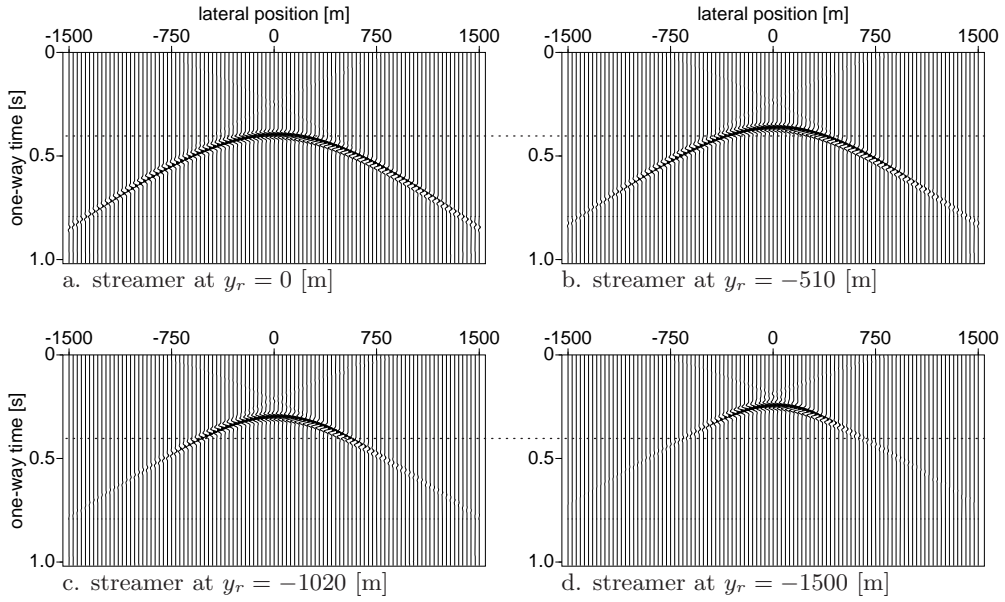


**Figure 5.34** Focusing in detection of four different streamer arrays. The dotted line in the plot indicates  $t = 0.4$  [s]. Note that the streamer at  $y_r = 0$  contains the stationary phase contribution at  $x_s = 0$ .

The first experiment carried out is a focusing in detection for every streamer array separately. For a complete first focusing result the focused streamers should be added together to obtain one trace out of the 3D CFP gather. However, by looking at the individual contributions of the streamers the construction of the 3D CFP trace can be studied in more detail. In figure 5.34 four focused streamer arrays are shown, along the horizontal axis the source position is shown. Note that the correct time of the focus point response should occur at  $t = 0.4$  s. This time is only observed for the focused streamer at  $y_r = 0$  with the source positioned at  $x_s = 0$ . In the other focused streamer arrays the focus point response is not observed at this time, meaning that the stationary phase ray is not measured by these streamers. In figure 5.35 the synthesized streamer traces are shown for a section in the cross-line direction. In these cross-sections the addition of the different streamer contributions can be observed. For the densely sampled sections shown in figure 5.35 the addition of the different streamers will give an undistorted CFP trace. However, by taking a sparse sampling in the  $y$ -direction the individual contributions of the streamers will become visible in the CFP trace. This effect is similar to the 2D CFP trace which was built with sparsely sampled receivers as discussed in the previous section.

The effect of sparsely sampled streamer arrays in the cross-line direction is shown in figure 5.36. The pictures presented in figure 5.36 are in fact 3D CFP gathers for one source line; the synthesis is carried out for all receivers belonging to one shot

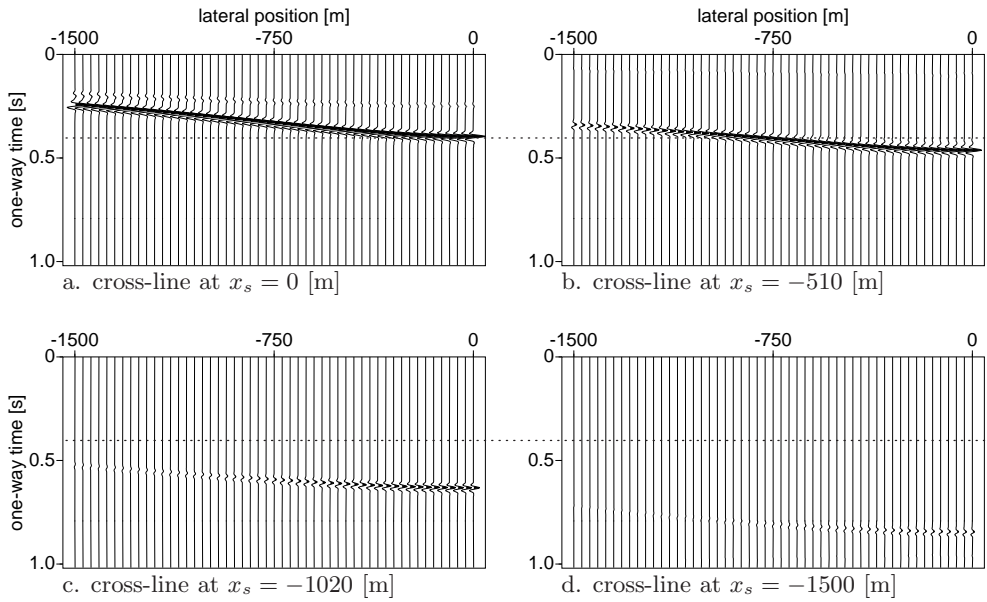


**Figure 5.35** Focusing in detection of four different streamer arrays. The dotted line in the plot indicates  $t = 0.4$  [s]. Note that the cross-section for  $x_s = 0$  contains the stationary phase trace. All traces are plotted on the same scale.

position. The situation shown in figure 5.36c is representative for the acquisition geometry for marine data. Note that due to the sparse sampling in the  $y$ -direction the individual contributions of the streamers become visible in the CFP gather. Building an CFP image trace with only the source contributions from one  $y$ -level (as shown in figure 5.36) will give a poor image. However, according to the discussion from the previous section the quality of the image trace can be saved if the source sampling in the  $y$ -direction is dense. The image trace for two different sampling rates in the  $y$ -direction and several streamer distributions in the  $y$ -direction are shown, together with the move-out corrected CFP gathers in figure 5.37. Note the similarity with figure 5.31.

From figure 5.37 and the foregoing examples it is concluded that:

- For focusing in detection the shot sampling can be coarse but the receiver sampling must be fine.
- For focusing in emission the receiver sampling can be coarse but the shot sampling must be fine.
- The Fresnel stack in 3D CFP gathers is distorted in the coarse sampled direction.
- To combine the contributions into an alias free image either the shot or receiver sampling must be fine for both the in-line and cross-line direction.

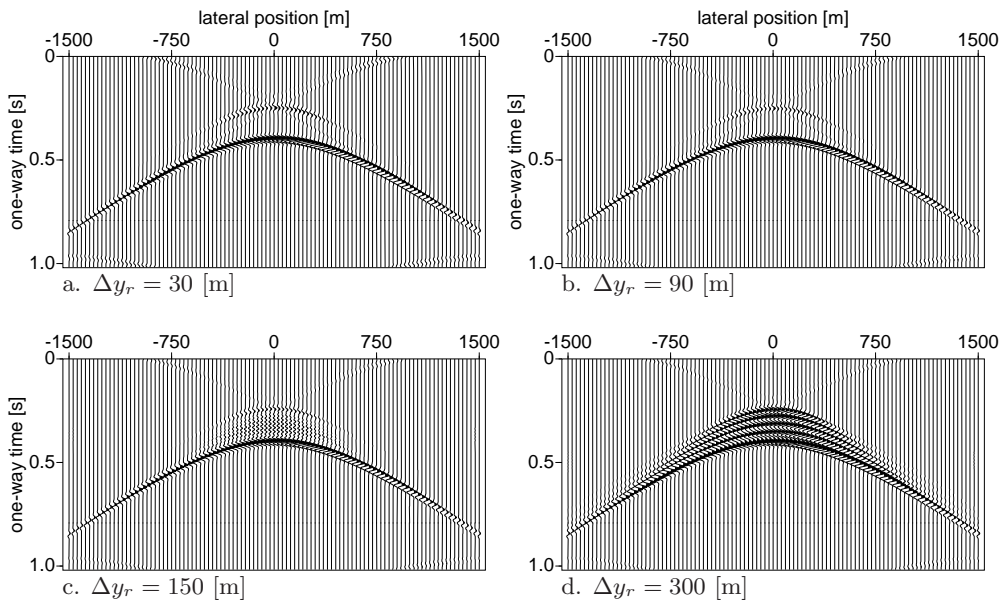


**Figure 5.36** Addition of the individual streamers for different distances between the streamer lines. Note that for a streamer spacing of 150 [m] the contribution of the individual streamers can still be recognized.

For the construction of a correct image gather it is important that the Fresnel zone is sampled properly. If the sampling in the  $x$  or  $y$  direction is coarse it means that a regularization algorithm must be used to interpolate the data in the coarsely sampled direction in such a way that the image trace can be built up without the aliasing effects. How the CFP technology can be used to regularize the data is explained in the next subsection.

In the foregoing example the response of a flat reflector was considered, which means that for a focus point positioned within the acquisition geometry the Fresnel zone will always be measured by one of the streamers. For a dipping reflector it is argued, from the examples shown for the 2-dimensional situation, that the Fresnel zone is easily shifted outside the acquisition aperture. For the 3-dimensional situation this means that if a layer is dipping in the cross-line direction the streamers arrays (with a typical maximum width of 500 m) in the  $y$ -direction will easily 'miss' the Fresnel zone for a focus point positioned within the acquisition geometry. In that case the different contributions of the streamers will not give a constructive contribution to the image trace and interpolation will not help either. The desired acquisition width as function of the dip and depth of the reflector is given by  $width = z \tan(2\alpha) + a_f$ , where  $z$  is the depth of the focus on the reflector positioned below the source position,  $\alpha$  the dip of the layer and  $a_f$  the width of the Fresnel zone. Note that a solution to this problem can be found by shifting the focus point until one of the streamers

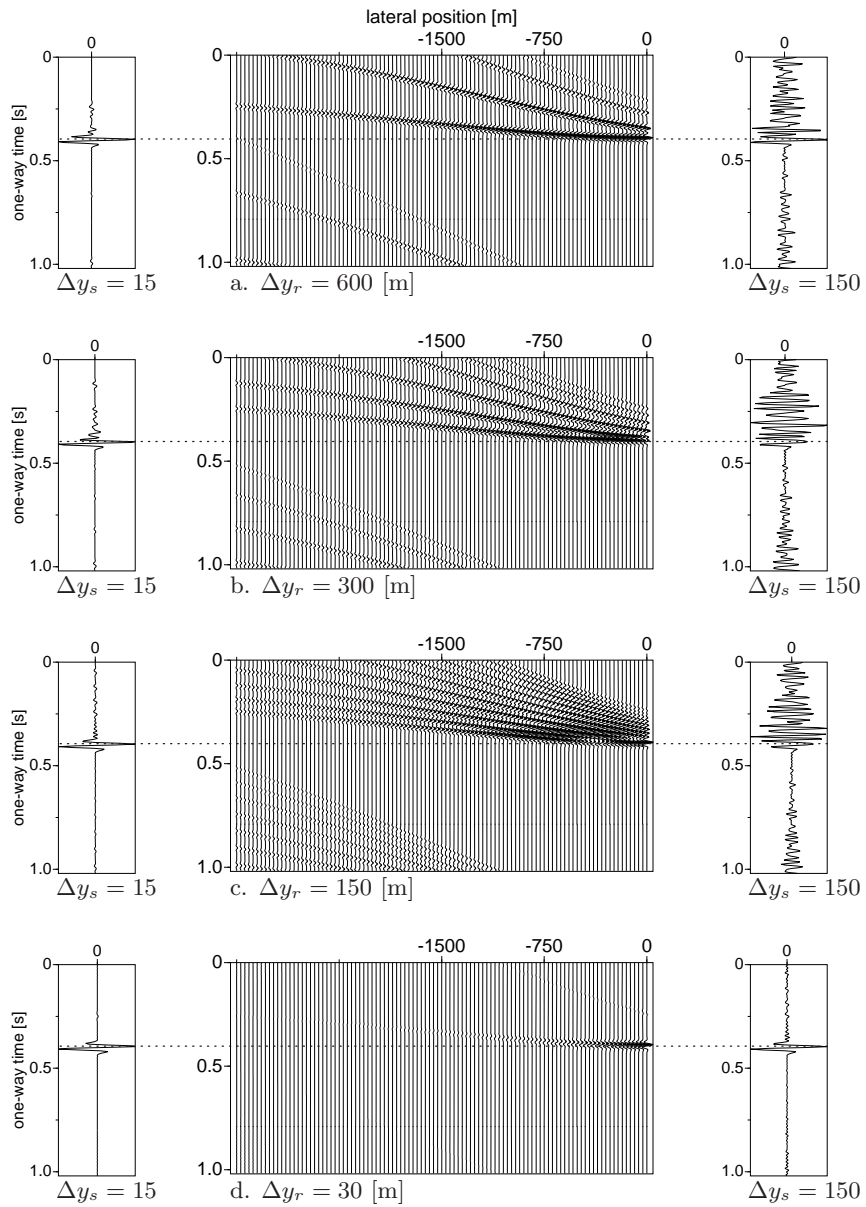


**Figure 5.37** Common offset contributions for different source ( $\Delta y_s$ ) and receiver ( $\Delta y_r$ ) sampling rates where  $x_s (= 0)$  is kept constant. The traces on the left and right-hand side are image traces. Note that for the image trace it is sufficient that either the source or the receiver sampling is dense.

detects the Fresnel zone of the defined focus point. The Fresnel zone is characterized by a (local) minimum arrival time of the focus point response.

The influence of feathering, irregular shooting patterns and land acquisition geometries are not treated in this thesis. For a detailed discussion about irregular sampling and different acquisition geometries in 3D data the reader is referred to the work of Koek et al. (1996); Koek (1997). Choosing an optimum acquisition geometry given a certain focus point illumination can be investigated by using the focusing beams as explained in section 5.4. The resolution at the focus point is defined by the source and receiver patterns at the surface. The focusing beam for the imaging result is defined by the *multiplication* of the beam for focusing in detection with the beam for focusing in detection. The resolution beam for two streamers is determined by *addition* of the beams for focusing in detection for both streamer arrays (for more about resolution aspects see Berkhout, 1984; Wapenaar, 1997).

### 5.5.3 Regularization of coarsely sampled data

Due to the coarse sampling in the cross-line direction the Fresnel zone is inadequately sampled which gives rise to a bad image quality. Therefore a regularization algorithm based on the CFP technology can be helpful to avoid a bad construction of the image trace. The CFP gather is an excellent domain for interpolation, because all events in the CFP gather belong to the same point in the subsurface. The input of the CFP based regularization algorithm is a coarsely sampled CFP gather and a finely sampled focusing operator. The first step in the regularization scheme is a 2-dimensional cross-correlation between the (coarsely sampled) CFP gather with the (finely sampled) focusing operator. The resulting bifocal image is tapered around zero-time and zero-spatial lag to remove the aliased energy which is positioned around its center. The next step, a 2-dimensional convolution of the filtered bifocal image with the finely sampled focusing operator, will restore the CFP gather on the finely sampled grid of the focusing operator. The obtained interpolated traces are inserted in the original coarsely sampled CFP gather to avoid distortion of the original traces. Note that a second iteration can improve the result of the interpolated traces even more.

An illustration of the proposed regularization scheme is given in figure 5.38. The input CFP gather represents the focus point response for focusing in detection of a point at 800 m depth on a dipping reflector (20°). The resulting CFP gather (a) is sampled with the source sampling rate of 120 m. The focusing operator (b) is sampled at 30 m. The 2-dimensional cross-correlation is shown in figure 5.38c, the aliased energy is positioned around the bifocal result. Removing the aliased energy from the bifocal result and convolution with the fine sampled focusing operator gives a reconstruction of the CFP gather on the sampling rate of the focusing operator. The traces missing in the coarse sampled CFP gather are now filled in by the traces

obtained with the result after convolution (f). The result after a second iteration of

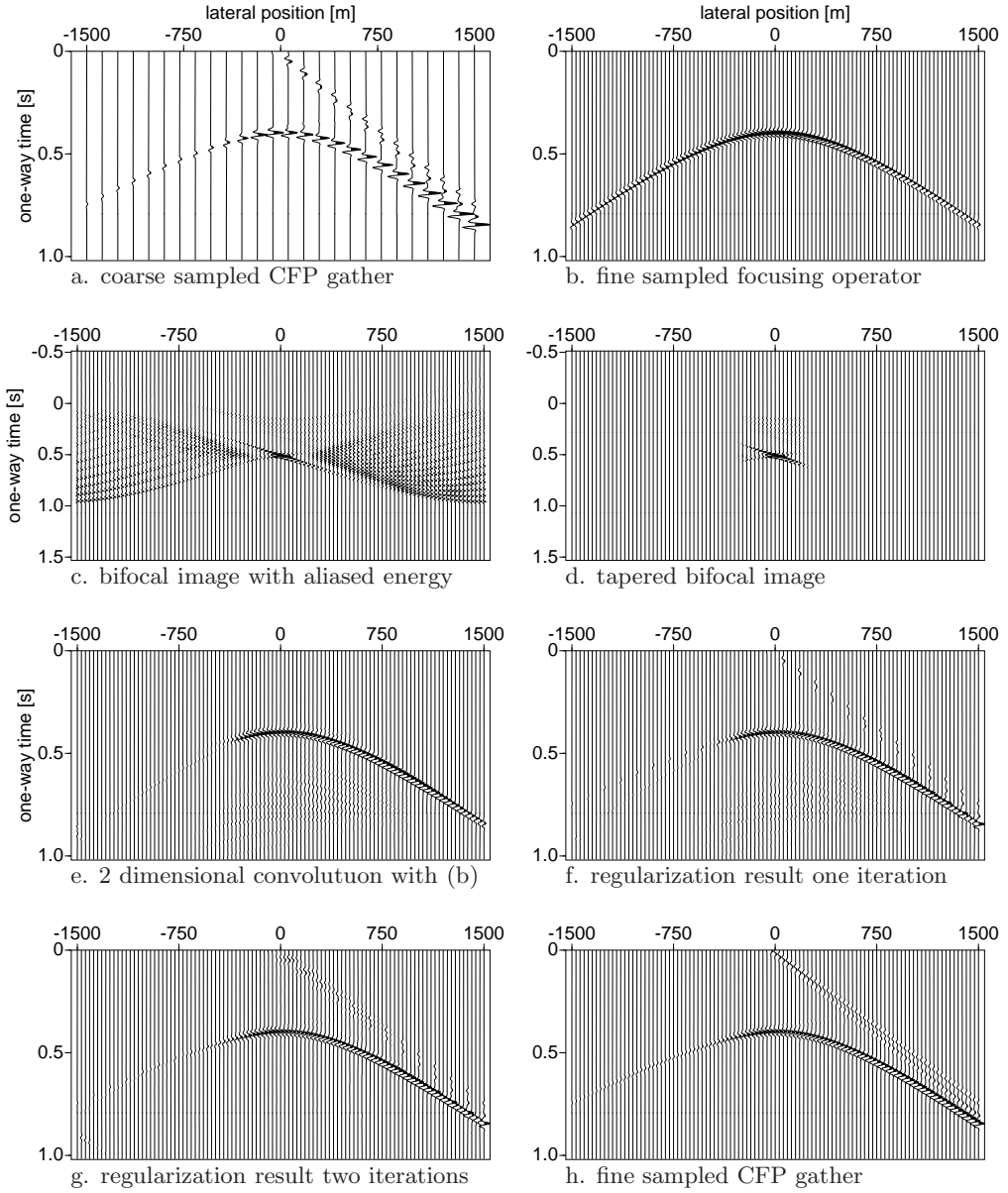


**Figure 5.38** Regularization of a CFP gather with the scheme as discussed in the text. Due to the tapering (d) of the bifocal result (c) the aliased energy is removed and convolving with the focusing operator gives the interpolated traces (e). In (h) a fine sampled CFP gather is shown for comparison.

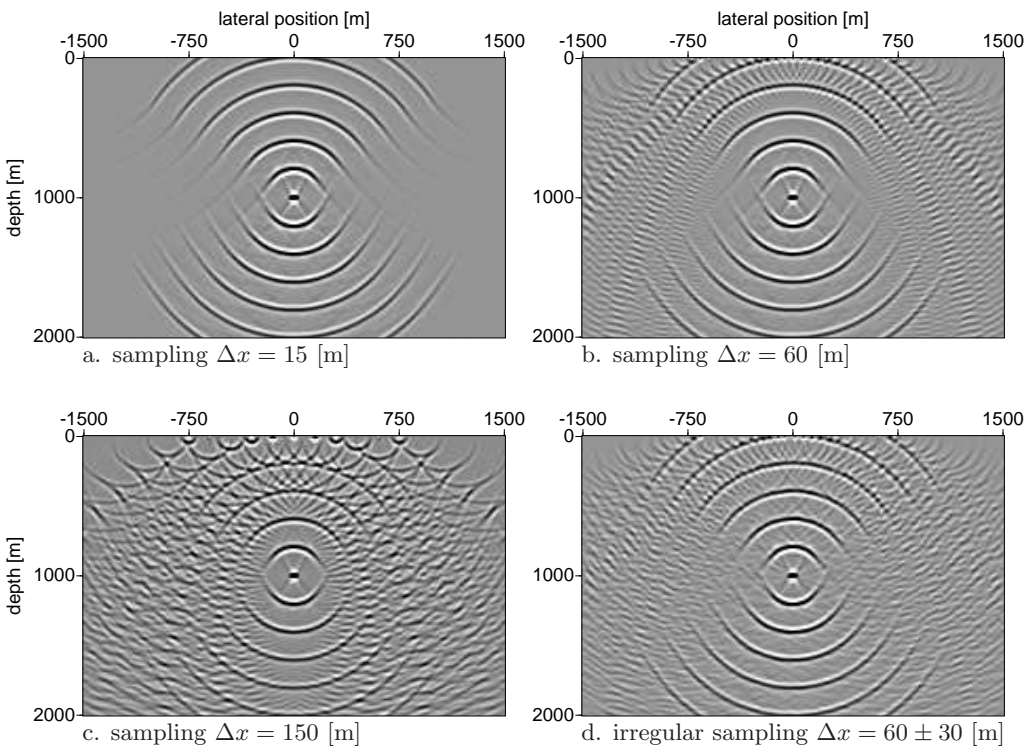


**Figure 5.39** Focusing wavefronts for different acquisition patterns at the surface. Note the difference between the wavefronts above and below the focus point at  $z = 1000$  m.

the same procedure is shown in figure 5.38g. The CFP gather calculated with a fine source sampling rate is shown in (h). Comparing figure 5.38h with the result shown in figure 5.38g it is observed that for the offset close to the edge the interpolated traces have a slightly lower amplitude than the traces from the CFP gather, more iteration will probably solve this problem. The traces at the small CFP offsets fit perfectly within the original traces. Note that the finite aperture artifact in the right upper side of the CFP gathers is not reconstructed very well.

The regularization algorithm is based on the principle shown in figure 5.39. Figure 5.39 shows how wavefronts, traveling in a homogeneous medium, are focused for different acquisition patterns at the surface. For a coarse sampling interval of  $\Delta x = 60$  m as shown in (b), or  $\Delta x = 150$  m as shown in (c), between the traces at the surface it is observed that the wavefront below its focus point is less disturbed by the coarse sampling. During the propagation the wavefront gets reconstructed. For the irregular data set, shown in (d), the same kind of reconstruction is observed. This reconstruction property can also be used in the estimation of weathered layer properties and will be discussed briefly in chapter 7. Note that the focus at depth

level  $z = 1000$  m has the same sharp resolution for all the used examples. The output of the regularization algorithm is in fact the measurement of the wavefront at  $z = 2000$  m after an lateral selection around the focused wavefront at  $z = 1000$  m. The topic of regularization in the CFP domain is an important subject in the data acquisition programme of the DOLPHIN consortium (Berkhout and Thorbecke, 1996).

## 5.6 New developments

The applications of CFP gathers are still growing, new techniques which are based on CFP gathers are developed and tested. In chapter 7 and 8 some of these new techniques are shown on field and synthetic data, in this section the applications of CFP gathers which might become important in the near future are briefly discussed to make the overview of the possibilities of CFP gathers complete.

### Target focusing; focusing of CFP gathers

By choosing several focus points close to each other, for example on the same lateral position but at different depth levels, and making use of the interpretation that a CFP gather for focusing in emission is the response of a source at the focus point and receivers at the surface, a second focusing step can be applied on the CFP gathers. In this way it is possible to collect the data from a specific point in the subsurface which is difficult to detect in the surface data. In figure 5.40 an application of this idea is sketched; close to a flank of a salt dome focus points are chosen at several depth levels (the gray dots). After the calculation of the CFP gathers for focusing in emission a second focusing step is used to focus the focus point responses on a point positioned on the flank of the salt dome (the black dot). Application of this idea can be useful if the macro model is already accurate and one want to image the flank of the reflector better. Note that in this method only the direct reflections of the flank are used and not the second order reflections.

Krebs et al. (1996) have shown that the use of accurate migration operator can improve the quality of the image of the flank of a salt dome. In the paper accurate migration operators are obtained by *measuring* the focus point responses, from a well close to the flank of the salt dome, at the surface. In the CFP method accurate operators can be obtained by using the operator updating mechanism which will be discussed in the next chapter.

### CFP imaging of elastic data

CFP imaging of elastic data can be done in two ways. One can first apply a decomposition into  $P$ - and  $S$ -wave potentials and then carry out CFP imaging per data type using the acoustic algorithm, or one can integrate the decomposition and CFP construction into one process (Berkhout et al., 1996). The integration of the synthesis operator with the decomposition process was part of a MSc. project car-

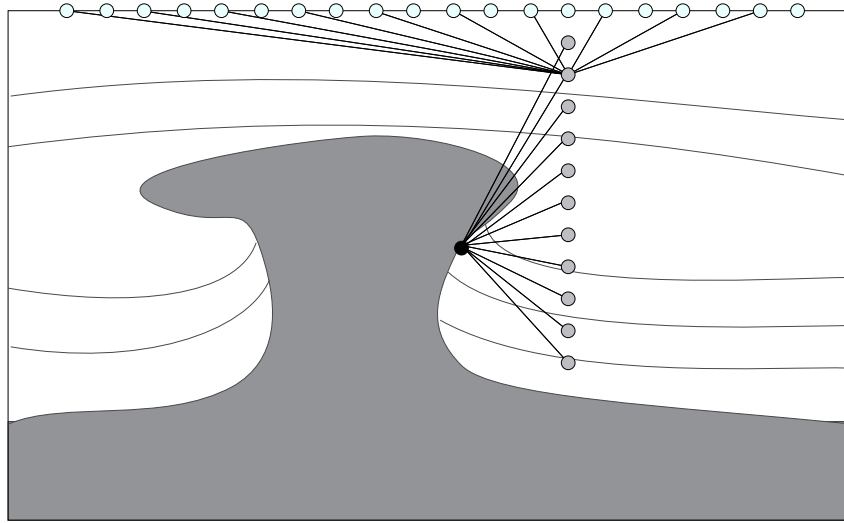
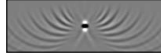


**Figure 5.40** Focusing of CFP gathers to illuminate the flank of a salt dome. If direct reflection information of the flank of the salt dome is measured at the surface then it is possible to unveil this information by a secondary focusing step.

ried out by Hondius (1993) and Hulshoff (1993) and its currently under investigation again. Note that by using the automatic operator updating process on elastic data one does not know if the event the operator is converging to belongs to a  $P$ - or  $S$ -wave. If it is possible to determine to what kind of converted wave the operator belongs to one can build  $P$ - and  $S$ -wave one-way image gathers and by using the operator inversion scheme it is also possible to estimate a  $P$ - and  $S$ -wave macro model.

#### Integration of CFP technology and multiple removal

The successful multiple removal scheme of Verschuur (1991) was originally developed for shot records. However, it has recently been shown (Berkhout and Verschuur, 1996b) that the same multiple removal scheme also works on CFP gathers without the need for any changes to the multiple removal algorithm. An advantage of the CFP approach is that it is easier to apply the multiple removal scheme on 3D data. Another advantage is that the multiple removal of interbed multiples can be combined with the imaging. By making use of bifocal images it is also possible to image the energy of the multiples as shown in Berkhout and Verschuur (1996a).



## Chapter 6

### Operator updating

The influence of erroneous focusing operators on the constructed CFP gather is of great importance, because by analyzing the synthesis process an important link with the correct focusing operator can be found. To describe how the CFP gather is built with an erroneous focusing operator some additional theory is needed. To describe this theory the matrix notation introduced in chapter 4 is used.

The focusing operator for focusing in detection is defined as (after equation (4.31))

$$\mathbf{F}_i^-(z_m, z_r) = \mathbf{I}_i^-(z_m) [\mathbf{W}^+(z_m, z_r)]^* [\mathbf{D}^-(z_r)]^{-1} \quad (6.1)$$

with  $\mathbf{I}_i^-(z_m)$  a unit row vector with a 1 at the  $i^{th}$  position at depth  $z_m$  and  $\mathbf{F}_i^-(z_m, z_r)$  the focusing operator acting at the receiver positions at the surface.

Using equation (6.1) into the **WRW** representation of equation (4.30) gives an expression of the data after focusing of the detector array

$$\mathbf{P}_i^-(z_m, z_s) = \mathbf{I}_i^-(z_m) \mathbf{R}^+(z_m) \mathbf{W}^+(z_m, z_s) \mathbf{D}^+(z_s) \mathbf{S}(z_s), \quad (6.2)$$

where equation (6.2) is an expression for the CFP gather for focusing in detection.

Note that if  $[\mathbf{W}^+(z_m, z_r)]^*$  represents correct propagation in the background model then the result of the first focusing step  $\mathbf{P}_i^-(z_m, z_s)$ , represented by equation (6.2), is in traveltime equal to the time reversed focusing operator  $\mathbf{F}_j^+(z_s, z_m)$ , represented by equation (4.32). To investigate the influence of erroneous operators on the CFP gather our only interest is in traveltimes. Therefore the following assumptions are made; the source and receiver directivity operators  $\mathbf{D}^\pm$  are represented by unit matrices, the source function is assumed to be independent of the source position,  $\mathbf{S}(z_s) = \mathbf{I}S_0$ . Note that if the sources and receiver occupy the same positions in space (indicated with  $z_0$ ) the focusing operators are related by  $\mathbf{F}_i^+(z_0, z_m) = [\mathbf{F}_i^-(z_m, z_0)]^T$ . With these assumptions equation (6.1) and (6.2) re-

due to

$$\mathbf{F}_i^-(z_m, z_0) = \mathbf{I}_i^-(z_m) [\bar{\mathbf{W}}^+(z_m, z_0)]^*, \quad (6.3)$$

$$\mathbf{P}_i^-(z_m, z_0) = \mathbf{I}_i^-(z_m) \mathbf{R}^+(z_m) \mathbf{W}^+(z_m, z_0) S_0, \quad (6.4)$$

where a distinction is made between propagation in the macro model  $\bar{\mathbf{W}}^+(z_m, z_0)$  and propagation in the true model  $\mathbf{W}^+(z_m, z_s)$ . Equation (6.3), the focusing operator, and equation (6.4), the CFP gather, show the 'principle of equal traveltime' in its most simple form, if the propagation matrices are equal,  $\bar{\mathbf{W}}^+(z_m, z_r) = \mathbf{W}^+(z_m, z_s)$ , then the time-reversed focusing operator is in traveltime equal with the CFP response. Suppose that the macro model is not correct and that the true propagation matrix can be represented by

$$\mathbf{W}^-(z_0, z_m) = \bar{\mathbf{W}}^-(z_0, z_m) \Delta \mathbf{W}(z_m), \quad (6.5)$$

where  $\Delta \mathbf{W}(z_m)$  is the propagation effect of the macro model error. Then the time reversed focusing operator is defined as

$$[\mathbf{F}_i^-(z_m, z_0)]^* = \mathbf{I}_i^-(z_m) [\Delta \mathbf{W}(z_m)]^* \mathbf{W}^+(z_m, z_0), \quad (6.6)$$

where  $[\bar{\mathbf{W}}^+(z_m, z_0)]^*$  in equation is replaced by  $\Delta \mathbf{W}(z_m) [\mathbf{W}^+(z_m, z_0)]^*$ , and the CFP response as

$$\mathbf{P}_i^-(z_m, z_0) = \mathbf{I}_i^-(z_m) \Delta \mathbf{W}(z_m) \mathbf{R}^+(z_m) \mathbf{W}^+(z_m, z_0) S_0. \quad (6.7)$$

Assuming that  $\Delta \mathbf{W}(z_m)$  and  $\mathbf{R}^+(z_m)$  are Toeplitz matrices, which means that the reflection and propagation properties don't change with respect to the lateral position in the area of interest, they can be interchanged, which results in

$$\mathbf{P}_i^-(z_m, z_0) = \mathbf{R}_i^+(z_m) \Delta \mathbf{W}(z_m) \mathbf{W}^+(z_m, z_0) S_0, \quad (6.8)$$

where  $\mathbf{R}_i^+(z_m)$  is a row vector representing the  $i^{th}$  row of the reflection matrix  $\mathbf{R}^+(z_m)$ .

From equations (6.6) and (6.8) it follows that the propagation errors  $\Delta \mathbf{W}(z_m)$  in the time reversed focusing operator and the related focus point response are equal in magnitude and opposite in phase. This is not a surprise because the propagation time which is subtracted too much in the first focusing step should be too little in the CFP response since the total propagation time of the data is fixed (Berkhout, 1996b). After the construction of the CFP gather the arrival times of the erroneous focusing operator can be compared with the response in the CFP gather. As indicated by equation (6.6) and (6.8) the principle of equal traveltime is no longer valid for the erroneous operator and the related focus point response. The macro model and/or the operator must be updated to obtain a correct operator which obeys the principle of equal traveltime.

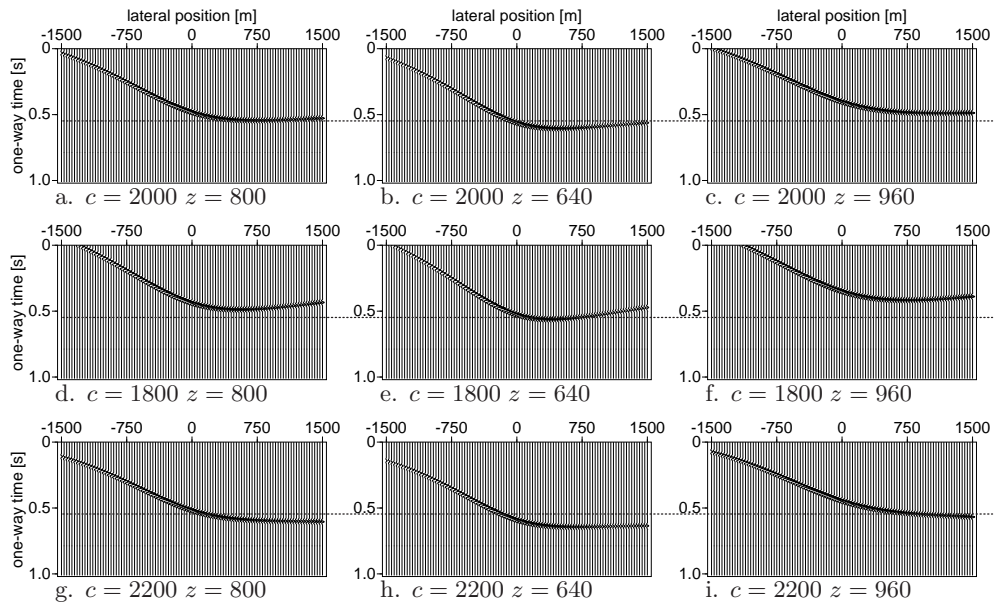


**Figure 6.1** CFP corrected shot record with different erroneous focusing operators. The shot record used is the 50<sup>th</sup> shot ( $x = -750$ ) in a fixed acquisition geometry and one flat reflector at 800 m depth. The upper left picture (a) gives the correct CFP corrected shot record. Note that the integration along the receiver position gives one trace in the CFP gather.

In the following sections the influence of an erroneous focusing operator in the first and the second focusing step will be discussed. An attempt is made to detect from the erroneous CFP gather an update formula for the macro model where the initial focusing operator is modeled in. Finally a proposal is made where the erroneous focusing operators are updated to a correct focusing operator.

### 6.1 First focusing step

Using an erroneous focusing operator will give a different construction of the CFP gather. This is shown in figure 6.1 for several errors in the focusing operator applied on one shot record with a source position at  $x = -750$  (the 50<sup>th</sup> out of a range of 201 shot records) from a 1-dimensional medium with a fixed acquisition spread ranging from -1500 to 1500 m. The reflector in the 1-dimensional medium is positioned at 800 m depth and the velocity of the first layer is 2000 m/s. The CFP gathers constructed with the erroneous synthesis operators are shown in figure 6.3. Note that the trace at the lateral position  $x = -750$  of the CFP gather in figure 6.3 is the summation along the traces of figure 6.1. The introduced errors in the focusing operators give CFP gathers which are not time coincident with the times defined by the operator (indicated by the spiky event in the CFP gathers of figure 6.3). In

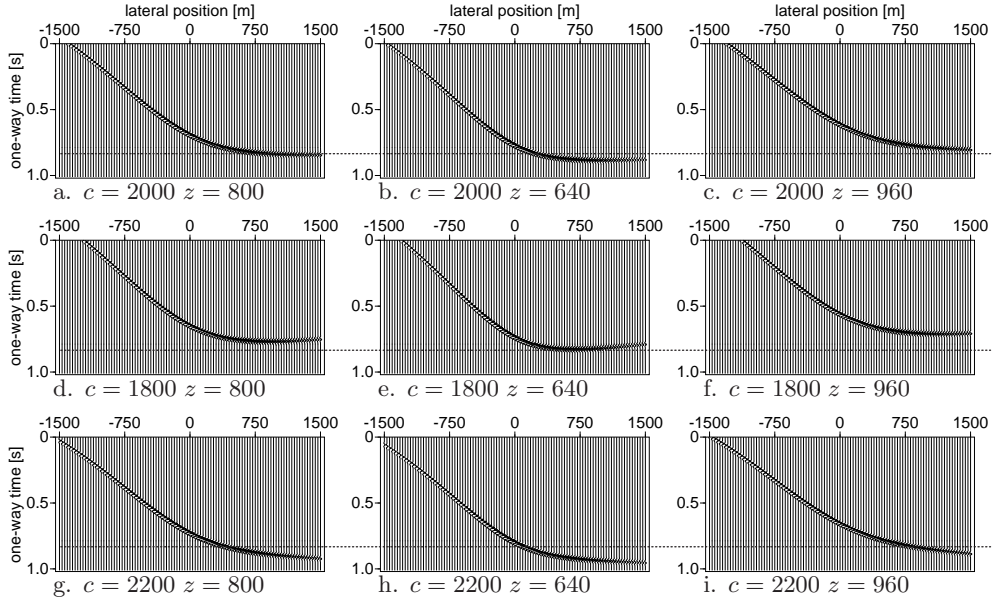


**Figure 6.2** CFP corrected shot record with different erroneous focusing operators. The shot record used is the 1<sup>rst</sup> shot ( $x = -1500$ ) in a fixed acquisition geometry ranging from  $-1500$  to  $1500$  m with one flat reflector at  $800$  m depth.

figure 6.1, where the correct time of the stationary phase contribution is indicated by the dotted line, it is observed that the Fresnel zone is shifted in time and space, with respect to the correct position (a), due to the error in the operator. This shift in the Fresnel zone disturbs the integration result rigorously when the Fresnel zone is shifted outside the aperture range. In figure 6.2 the same erroneous operators are used but now for a shot with a source position at  $x = -1500$ , which gives the trace at  $x = -1500$  in the CFP gathers shown in figure 6.3. This shot record is positioned at the edge of the model and the Fresnel zone can be easily shifted outside the aperture range due to an erroneous operator. For example in figure 6.2i the Fresnel zone is shifted outside the aperture and the contribution in the CFP gather at  $x = -1500$  of figure 6.3i cannot be used for a macro model or operator update. Note that the focusing operators with a positive velocity error can be interpreted as a high angle filter which cuts out the higher angles in the CFP gather response as shown in figures 6.3g, h and i.

If the Fresnel zone for an erroneous operator stays within the aperture range then the CFP gather can be corrected for the erroneous operator and the calculation of a new CFP gather with an updated operator is not necessary. It can be advantageous to look at methods which keep the Fresnel zone within the aperture range. In figure 6.2g, h and i it is observed that the Fresnel zone is shifted outside the aperture range due to the error in the operator. The first synthesis process may be improved

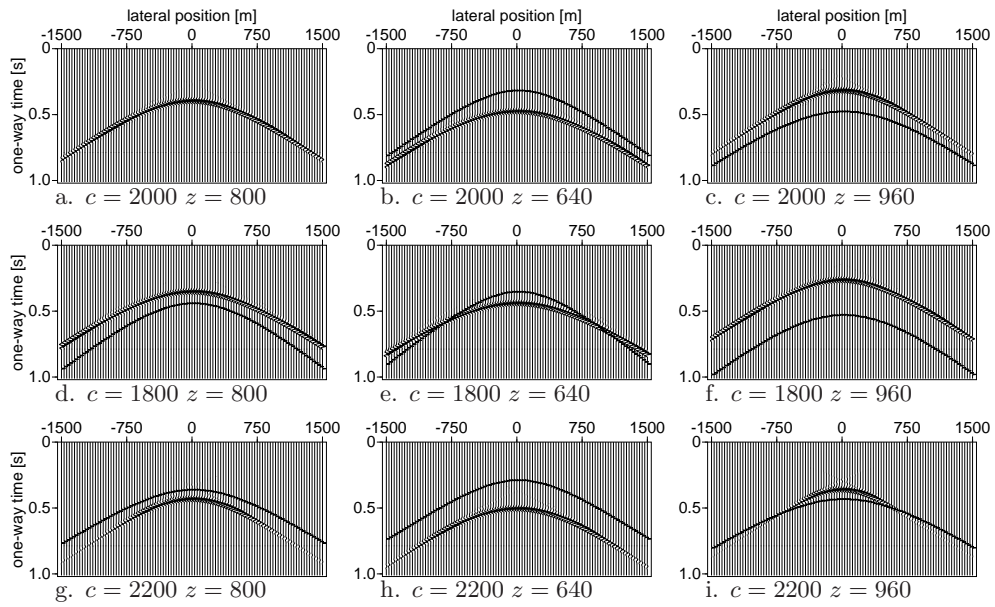


**Figure 6.3** CFP gathers for a flat reflector with different erroneous operators. The shot records are simulated in a fixed acquisition geometry. The spiky event in the gather indicate the traveltimes of the used focusing operator.

if not only one trace for the CFP gather is calculated, but also neighboring traces of different CFP gathers, constructed with a lateral shifted operator, are used. In figure 6.4 the shot record with a source at  $x = -1500$ , corrected with the erroneous synthesis operator which was also used in 6.2i, is shown for different lateral shifts in the synthesis operators. In these results it is observed that the Fresnel zone, which was initially shifted outside the aperture range due to an erroneous operator, can be included in the CFP gather by shifting the focusing operator laterally and using these results in the construction of the CFP gather. Note that the laterally shifted synthesis operators, which defines another focus point, are able to bring the Fresnel zone back in the aperture range at a different time with a different amplitude after integration. Note also that in considering all possible laterally shifted operators within the aperture range means that a 2-dimensional cross-correlation is carried out between the shot record and the synthesis operator. This 2-dimensional cross-correlation can also be used to built up a CFP gather more efficiently.

In figure 6.5a, b and c the 2-dimensional cross-correlation between the *correct* operator used in figure 6.2a and three shot records at positions  $x = -1500$ ,  $x = -750$  and  $x = 0$  is shown. The trace which is also present in the CFP gather of figure 6.3a is positioned at respectively  $x = -1500$ ,  $x = -750$  and  $x = 0$ . Note that for a 1-dimensional medium a 2-dimensional cross-correlation between the operator and a shot record can be interpreted as building a CFP gather with different shot

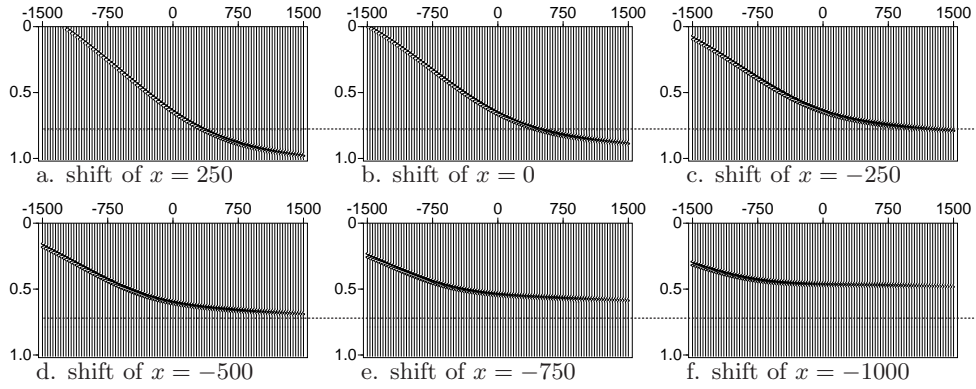


**Figure 6.4** 1-dimensional cross-correlation between laterally shifted erroneous focusing operators ( $c = 2200$   $z = 960$ ) and one shot record with a source at  $x = -1500$ .

records where the spatial sampling rate of the shot positions is given by the spatial sampling rate of the focusing operator. The 2-dimensional cross-correlation gives for a 1-dimensional medium exactly the same result (beside the finite aperture artifacts) as the full synthesis process in the spatial domain using all shot records. In combining these 2-dimensional cross-correlation results in the construction of the CFP gather, the lateral position of the traces in the cross-correlation result must be mirrored around the source position. Or in other words; the synthesis result of a shifted operator and a shot record is in a 1-dimensional medium equivalent with the synthesis of the non-shifted operator and a shifted shot record, where the shift of the shot record is in the other direction than the shift of the synthesis operator. In figure 6.5d, e and f three CFP gathers are shown which are constructed by using only a few shot records and the 2-dimensional cross-correlation between the correct

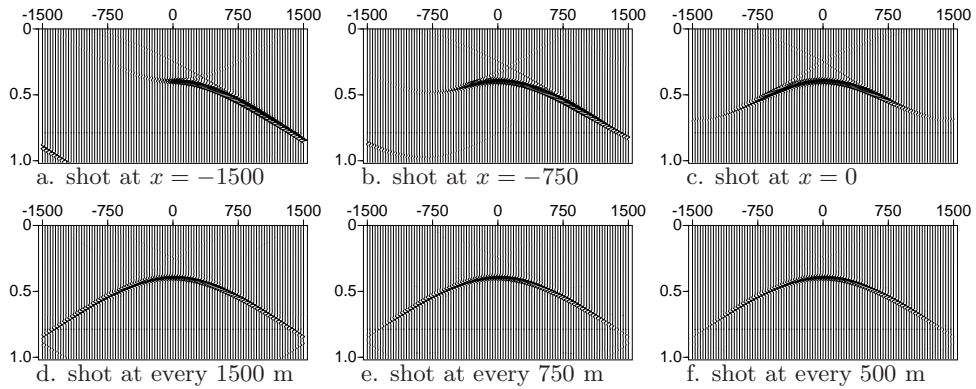


**Figure 6.5** 2-Dimensional cross-correlation between the correct focusing operator and three shot records (a, b and c). Addition of a limited number of cross-correlated shot records is shown in d, e and f.

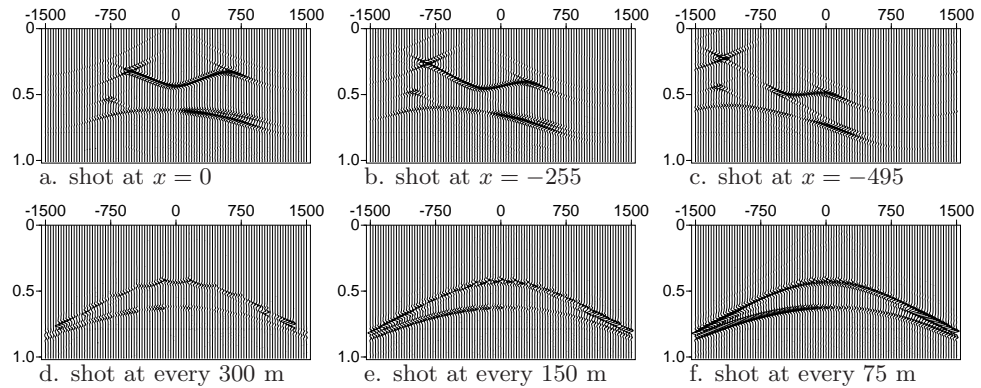


**Figure 6.6** 2-Dimensional cross-correlation between the correct operator and three shot records (a, b and c) from the syncline model. Making use of a limited number of shot records and the 2-dimensional cross-correlation an image can be built up as shown in d,e and f.

operator and these selected shot records.

Using the 2-dimensional cross-correlation to build up the CFP gather is only possible for the 1-dimensional medium as presented in figure 6.5, because in a 1-dimensional medium a laterally shifted shot record represents a correct shot record. In the syncline model with a focus point defined at the deepest point of the syncline this is not the case. In figure 6.6 the 2-dimensional cross-correlation is shown for three shot records with source positions at  $x = 0$ ,  $x = -255$  and  $x = -495$  m. In this experiment it is known that due to the lateral variation in the medium the 2-dimensional cross-correlation gives only a correct contribution in the CFP gather for the zero-lag trace, the laterally shifted operators are not correct anymore. However, in figure 6.6 it can be observed that the traces close to the zero lag trace are still useful, further away from the zero-lag trace the focusing breaks down and is not useful anymore. In figure 6.6d, e and f CFP gathers are shown which are constructed with the 2-dimensional cross-correlation by using a selection of all available shot records. The 'missing' shot positions are obtained from the 2-dimensional cross-correlation.

**In conclusion;** the 2-dimensional cross-correlation result can be used to built up the CFP gather if the assumption that the medium is laterally invariant is valid. If the medium is strongly laterally variant only the zero-lag trace can be used (which in fact is done in the full synthesis process by using all shot records). If there is a big gap between two shots records the 2-dimensional cross-correlation between the focusing operator and the shot record can be used as an interpolation operator for the gap between the shots. The 'missing' shot in the gap is created by copying the neighboring shot and changing the source coordinate, which is obviously wrong for a non 1-dimensional medium.

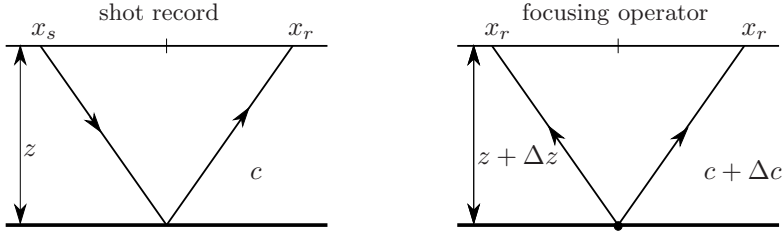


Figure 6.7 Ray paths for a shot record of a flat reflector and an (erroneous) focusing operator.

## 6.2 Searching for updating formulas for a flat reflector

In this section an attempt is made to derive analytical expressions for the curves observed in the CFP corrected shot record for a flat reflector in the subsurface. In the analysis only the arrival times of the reflections are taken into account. The well known traveltime curve for a flat reflector at depth  $z$  with a source at position  $x_s$  and a receiver at  $x_r$  is described by

$$T_d(x_s, x_r) = \frac{\sqrt{4z^2 + (x_r - x_s)^2}}{c}, \quad (6.9)$$

where the subscript  $d$  in  $T_d$  refers to the data measured at the receiver positions  $x_r$  at the surface and  $c$  is the velocity of the medium above the reflector. The travelttime curve for a time-reversed focusing operator with a focusing point in the subsurface is given by

$$\bar{T}_s(x, x_r) = \frac{\sqrt{(z + \Delta z)^2 + (x_r - x)^2}}{c + \Delta c}, \quad (6.10)$$

where the subscript  $s$  in  $\bar{T}_s$  refers to the synthesis operator (see also figure 6.7) and  $\Delta z$  and  $\Delta c$  represent the depth and velocity error with respect to the true model. Application of the focusing operator to a common shot gather (fixed  $x_s$ ) can be interpreted as a time convolution between the traces of the data and the traces of the focusing operator. In terms of traveltimes this time convolution is represented by

$$T_d(x_s, x_r) - \bar{T}_s(x, x_r) = \frac{\sqrt{4z^2 + (x_r - x_s)^2}}{c} - \frac{\sqrt{(z + \Delta z)^2 + (x_r - x)^2}}{c + \Delta c}. \quad (6.11)$$

From the two-way traveltime from source to reflector and back to receiver, the one-way travelttime, from reflector to receiver, is peeled off by the synthesis operator. The synthesis process itself is an integration over all the convolved traces of the CFP corrected common shot gather (see also equation (5.1) so,

$$P(x, x_s) = \int_{\partial D} A(x_r, x_s, x) \exp(j\omega\Phi(x_r, x_s, x)) dx_r, \quad (6.12)$$

where  $A$  is an amplitude factor and  $\Phi$  represents the traveltime function defined by equation (6.11). Equation (6.12) gives the synthesized trace, in the frequency domain, for one common shot gather. Repeating the process for all common shot gathers will give the CFP gather for focusing in detection. The stationary phase approximation simplifies the integration in equation (6.12) to the evaluation of the stationary points with respect to  $x_r$ . The stationary points of equation (6.11) are given by

$$\frac{\partial}{x_r} \Phi(x_r, x_s, x) = 0$$

$$\frac{(x_r - x_s)}{c\sqrt{4z^2 + (x_r - x_s)^2}} - \frac{(x_r - x)}{(c + \Delta c)\sqrt{(z + \Delta z)^2 + (x_r - x)^2}} = 0 \quad (6.13)$$

which solution is equivalent to

$$(x_r - x_s)(c + \Delta c)\sqrt{(z + \Delta z)^2 + (x_r - x)^2} - (x_r - x)c\sqrt{4z^2 + (x_r - x_s)^2} = 0 \quad (6.14)$$

Solving equation (6.14) for  $x_r$  in a closed form is not trivial, but by considering only a depth or velocity error for a focus point at  $x = 0$  it is possible to derive, by inspection and numerical evaluation, some properties of the stationary point and the CFP corrected shot record. Having found the stationary point it is possible to replace the integration in equation (6.12) by the stationary phase solution (Bleistein, 1984). The stationary phase solution for the traveltimes can be calculated by substituting the stationary point in equation (6.11). By doing this calculation for all common shot gathers (variable  $x_s$ ) the traveltime curve for the CFP gather is found.

### 6.2.1 Zero depth and zero velocity error ( $\Delta z = 0$ and $\Delta c = 0$ )

Using the correct macro model will give for the CFP gather exactly the same hyperbola as the focusing operator. For the focus point at  $x = 0$  equation (6.14) reduces then to

$$(x_r - x_s)c\sqrt{z^2 + x_r^2} - x_r c\sqrt{4z^2 + (x_r - x_s)^2} = 0 \quad (6.15)$$

which has the simple solution  $x_r = -x_s$ . Substituting this solution (stationary point) in equation (6.11) for all shot positions gives for the CFP gather

$$T_{cfp}(x = 0, x_s) = T_d(x_s, x_r = -x_s) - \bar{T}_s(x = 0, x_r = -x_s)$$

$$= \frac{\sqrt{z^2 + x_s^2}}{c}, \quad (6.16)$$

with the synthesis operator

$$\bar{T}_s(x = 0, x_s) = \frac{\sqrt{z^2 + x_s^2}}{c}. \quad (6.17)$$

Note that equation (6.17) is indeed the same as equation (6.16).

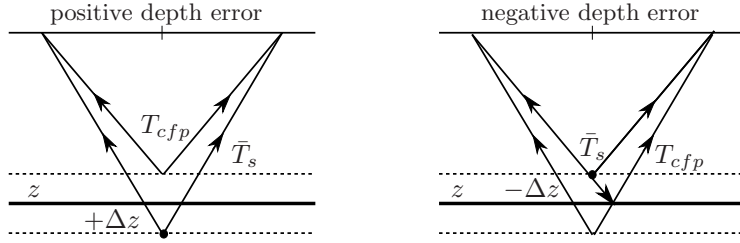


**Figure 6.8** Depth errors in the focusing operator: depth too deep (a) and depth too shallow (b) gives different CFP gathers, which can be interpreted as the response of a virtual source above (a) or below (b) the reflector.

### 6.2.2 Depth errors ( $\Delta z \neq 0$ and $\Delta c = 0$ )

In the case of a depth error and a zero velocity error equation (6.14) reduces to

$$(x_r - x_s)c\sqrt{(z + \Delta z)^2 + x_r^2} - x_r c\sqrt{4z^2 + (x_r - x_s)^2} = 0. \quad (6.18)$$

The solution for the stationary points in this equation can still be expressed in a closed form and is given by

$$x_r = x_s \frac{\Delta z + z}{\Delta z - z}. \quad (6.19)$$

Substitution of this solution in equation (6.11) gives for the CFP gather

$$T_{cfp}(x = 0, x_s) = \frac{\sqrt{(z - \Delta z)^2 + x_s^2}}{c}, \quad (6.20)$$

where the synthesis operator is given by

$$\bar{T}_s(x = 0, x_s) = \frac{\sqrt{(z + \Delta z)^2 + x_s^2}}{c}. \quad (6.21)$$

From equation (6.21) it is observed that the time correction, to the downgoing source wave field at the surface, with the synthesis operator is for a positive  $\Delta z$  too large.

The resulting CFP gather represented by equation (6.20) can be interpreted as the response of a virtual source positioned  $\Delta z$  m above the reflector (see left picture in figure 6.8). For a negative depth error the time correction with the synthesis operator is too small and the CFP gather can be interpreted as the response of a virtual source below the reflector position (or alternatively as the reflected response from a source above the reflector, see right picture in figure 6.8).

With the derived solution of equation (6.19) it is possible to arrive at an analytical updating formula for the macro model, by using equations (6.20) and (6.21) and solving for the two unknowns  $z$  and  $\Delta z$ .

### 6.2.3 Velocity errors ( $\Delta z = 0$ and $\Delta c \neq 0$ )

If there is only a velocity error in the synthesis operator equation (6.14) reduces to

$$(x_r - x_s)(c + \Delta c)\sqrt{z^2 + x_r^2} - x_r c \sqrt{4z^2 + (x_r - x_s)^2} = 0 \quad (6.22)$$

Unfortunately it is difficult to find a closed form solution for this equation. Therefore equation (6.22) is solved numerically for a set of different parameters. Based on these numerical results the following observations are made:

- If the velocity error  $\Delta c$  is negative, thus using a velocity in the calculation of the synthesis operator which is too low there is always one real numerical solution of equation (6.22). This means that there is at least one stationary point which gives a single contribution to the CFP gather.
- If the velocity error  $\Delta c$  is positive, thus using a velocity in the calculation of the synthesis operator which is too large, there are always at least two real numerical solutions found. This means that there are two stationary points which both give both a contribution to the CFP gather. The numerical experiments also showed that one of the two stationary points found lays far away from  $x_r = 0$ .

### 6.2.4 CFP corrected shot record

The traveltime of the CFP corrected shot record prior to integration, thus before summation over all the traces, will give more insight in the influence of erroneous operators in the CFP gather. These traveltimes can be calculated for different parameters by using equation (6.11). For the travelttime calculation a simple model is chosen with only one reflector at 300 m below the surface and a velocity of 2000 m/s above the reflector. The receivers in this model are positioned from -1500 m to 1500 m with a spatial interval of 15 m. The 201 shots are positioned at all detectors positions from the first detector position at -1500 m to the last detector position at 1500 m with a spatial interval of 15 m.

In figure 6.9 four different time sections, calculated by using equation (6.11), show the influence of for depth and velocity errors as function of the receiver position in the model for three different shot records. The shot gathers with their shot position at  $x_s = 0$  show for the depth errors only one stationary point at  $x_r = 0$ . The other shot positions ( $x_s = 450$  and  $x_s = 900$ ) have a shifted stationary point position which position on the  $x_r$ -axis is given by equation (6.19). The time sections with a velocity used in the focusing operator which is smaller than the true velocity show that there exists indeed only one stationary point, although it was not (yet) possible to derive it analytically. For a velocity higher than the true velocity it is not possible to observe a stationary point for the shot positions at  $x_s = 450$  and  $x_s = 900$  which makes it difficult to forecast, with the aid of the time section, what

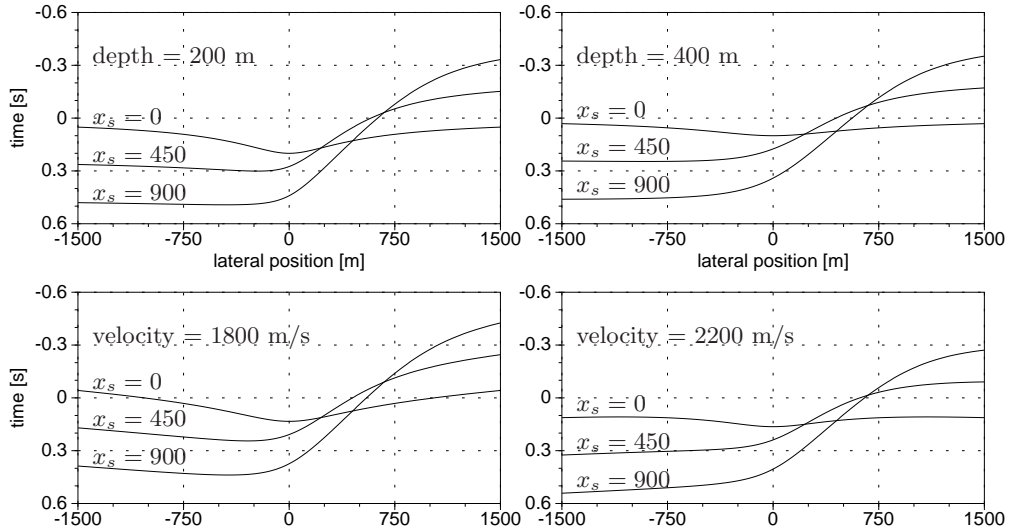


**Figure 6.9** Time sections of three shot gathers ( $x_s = 0, 450, 900$  m) prior to integration for different depth and velocity errors in the focusing operator (equation (6.11)). Note that for a positive velocity error the stationary point is shifted outside the aperture.

the CFP corrected shot record will look like. It is therefore not possible to derive a closed form expression for the updating formula's to update a macro model. The curves in figure 6.9 show clearly that the stationary phase point is shifted due to erroneous operators, for large errors the point can shift outside the aperture and the CFP trace will consist of artifacts only. This was already observed in section (6.1).

An alternative of equation (6.11), to calculate the time sections for the shot gathers prior to synthesis, the same result can be obtained by convolving the shot gather under consideration with the time-reversed focusing operator. The resulting record

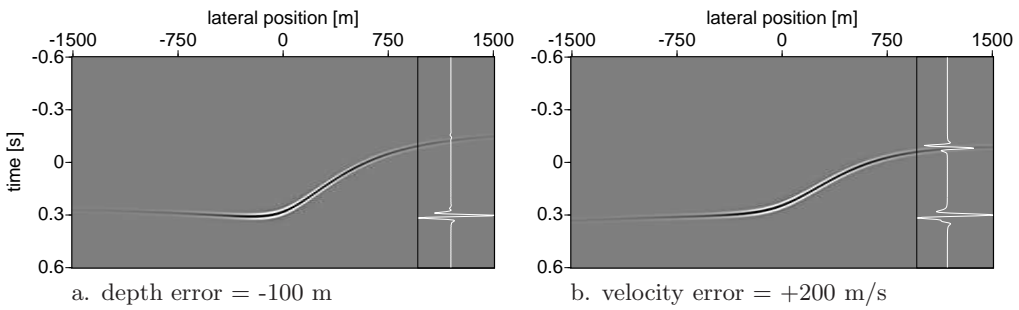


**Figure 6.10** Erroneous synthesis result for a shot record with  $x_s = 450$ . Note the double contribution in the integrated trace with the positive velocity error (b).

is shown in figure 6.10a for a shot gather at position  $x_s = 450$  and a depth error in the synthesis operator of -100 m (depth = 200 m). In figure 6.10b the same shot gather is shown but now with a synthesis operator with a velocity error of +200 m/s (velocity = 2200 m/s) and the correct depth. In both pictures the same shape of the time section as in figure 6.9 can be observed. The result of the summation over all traces is also given in figure 6.10. The summation shows that the position of the stationary point in figure 6.10a is indeed the only contribution in the summation. However, in figure 6.10b two contributions are observed in the synthesized trace.

### 6.2.5 Move-out corrected CFP gather

The integration over all the receivers in a common shot gather must be done for all available shot gathers to construct the CFP gather. It was already shown that if the correct macro model is used to generate the focusing operator the principle of equal traveltime is valid. For an erroneous macro model this principle is no longer valid. An expression of the derivation in traveltime of the CFP gather with the erroneous focusing operator is given by

$$T_{mv}(x, x_s) = T_{cfp}(x, x_s) - \bar{T}_s(x, x_s). \quad (6.23)$$

This time difference can be used to find an update for the initial macro model which was used to model the focusing operator. If the exact travelttime curve for  $T_{mv}$  is known for a certain error in the model then it is possible to compare these analytical curves (in a least squares way) with the observed curve and determine the velocity and depth errors made in the macro model. It has been shown that for a depth error in the macro model it is possible to derive a closed form expression for  $T_{mv}$ . In this ideal case only one update is sufficient to arrive at the correct macro model. For a velocity, or a depth and velocity error it is not possible to derive such a closed form. In that case numerical methods are used to calculate the stationary points in equation (6.11) in order to determine  $T_{mv}$ . The scheme given in figure 6.11 calculates  $T_{mv}$  in a numerical way such that it can be used in the updating scheme discussed later. The calculation of the roots of equation (6.14) is done with

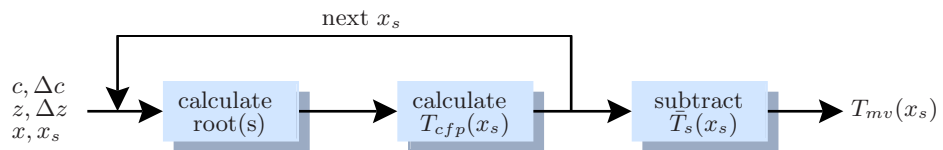


**Figure 6.11** Numerical calculation of  $T_{mv}$  for a CFP gather with a velocity and a depth error in the focusing operator  $\bar{T}_s$ .

the method of Newton-Raphson (Press et al., 1992). For negative velocity errors and negative and positive depth errors there is only one root and the method can be used without any problems. For positive velocity errors a-priori knowledge of the position of one of the roots has to be built in the algorithm.

In figure 6.12 the move-out corrected CFP gathers are shown for different velocity and depth errors in the macro model which is used to calculate the focusing operator. If the correct model is used the move-out panel shows an event which aligns at zero time. For a negative velocity error the move-out panels contain one simple event (originating from the single stationary point), positive velocity errors give more complicated move-out panels (originating from the multiple stationary points). The positive and negative depth errors are symmetric with respect to the zero time lag in the move-out panels and contain only one single event. The same panels can also be found in the work of Cox (1991) who calls them Common Depth Point gathers. These CDP gathers are obtained after shot record redatuming followed by correction with the incident source wave field (the move-out in the focusing operator) and stacking (which is similar to the synthesis process in the first focusing step). Cox (1991) showed already that the CDP gather (called in this thesis move-out corrected CFP gather) contains information which can be used to estimate the macro model.

In figure 6.13 numerically calculated curves, according to the scheme given in figure 6.11, are shown for the different velocity and depth errors used in figure 6.12. The curves for the depth errors are calculated correctly for both positive and negative depth errors. The curves for the velocity errors are only correct for the negative velocity errors, the positive velocity errors show the contribution for one stationary point only.

In figure 6.14 the move-out corrected CFP gather is shown for different combinations of depth and velocity errors. For a positive velocity error a more complicated panel is observed again. The results for the negative velocity errors combined with a positive or negative depth error are used in a macro model estimation scheme which makes use of the numerical scheme of figure 6.11.

After numerical calculation of the move-out curve  $T_{mv}$  this curve is compared in a least squares manner with the tracked time section of the event in figure 6.14. The domain, in which the search for a match with the tracked time curve is carried out, is in depth varying from 100 to 500 m with steps of 5m and in velocity from 1600 to 2400 m/s with steps of 10 m/s. The results are shown in table 6.1 for the five best matches. Note, that the estimated depth and velocity update gives directly the correct answer. From table 6.1 it can be seen that the best match, based on the least squares criterion, can be distinguished clearly from the other four nearest matches. The best match together with the tracked time section are shown in figure 6.15. Note the good match between the tracked time section and the calculated curve.

The foregoing examples have shown that it is possible to calculate analytical curves

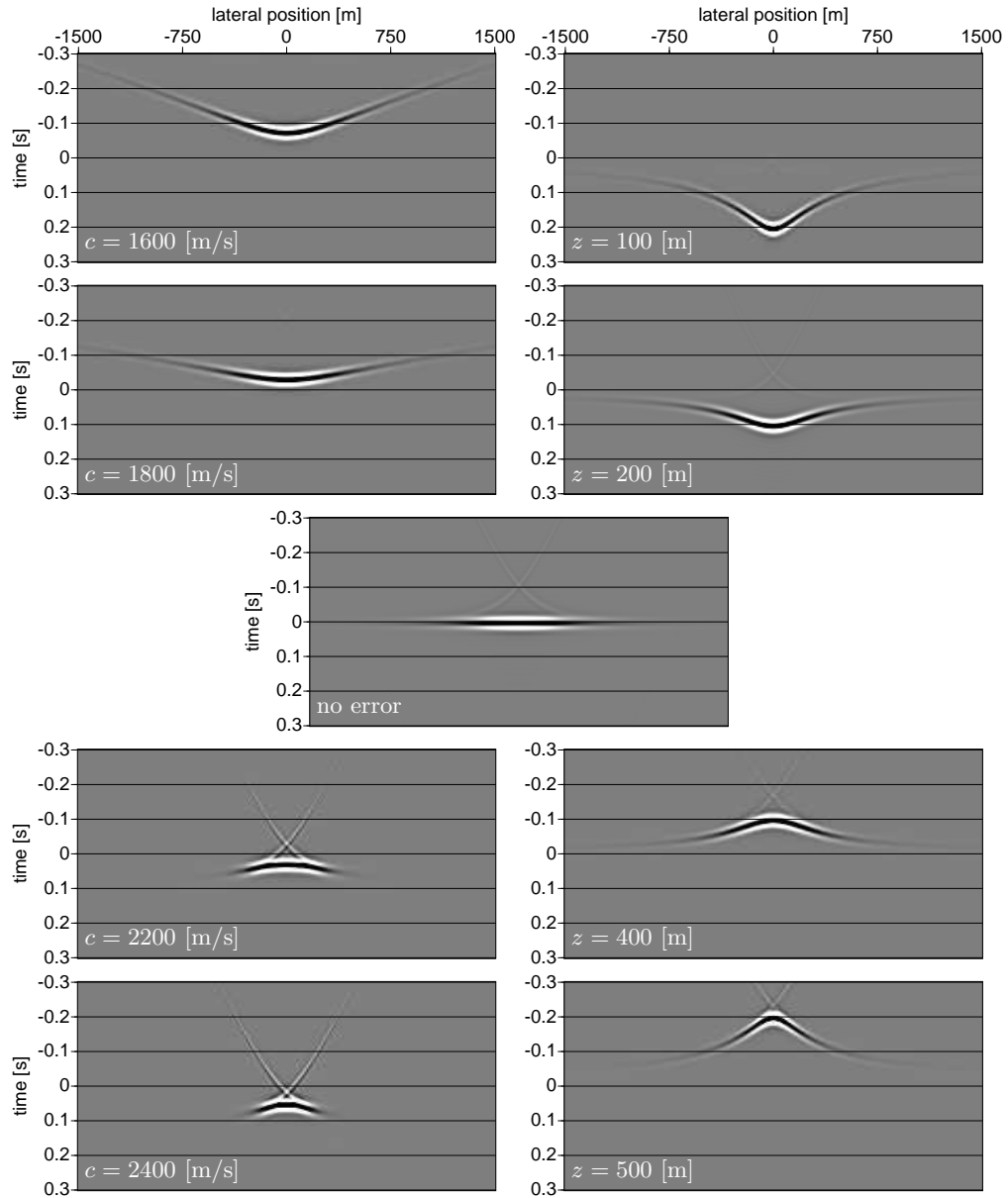


**Figure 6.12** Move-out corrected CFP gathers for different types of erroneous focusing operators. Note that if the correct model is used the move-out panel shows an event which aligns at zero time. On the left side the influence of velocity errors is shown and on the right side the influence of depth errors is shown.

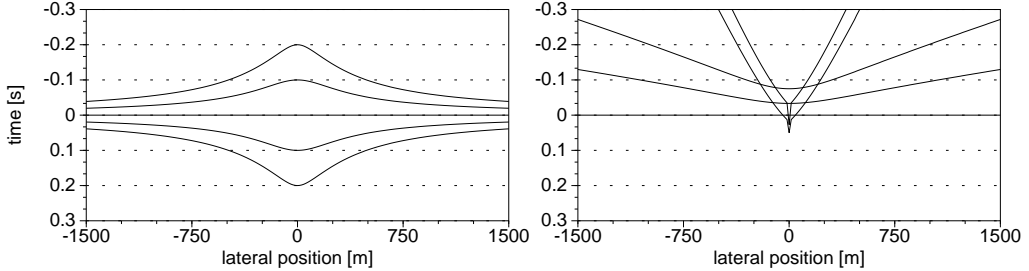


**Figure 6.13** Move-out curves for different depth (left) and velocity (right) errors in the focusing operator.

for the different depth and velocity errors in a single reflector model. By comparing the tracked time section of the move-out corrected CFP gather with the calculated curves it is possible to estimate a macro model. With this new macro model a new focusing operator and a CFP gather can be calculated. This procedure can be applied recursively and will terminate when the move-out corrected CFP gather has a straight event at zero time. In that case the synthesis operator and the event under consideration in the CFP gather are exactly the same, obeying the principle of equal traveltime. Note that for a correct migration output horizontal alignment is a necessary condition but not a sufficient one. In addition to horizontal alignment the differential time with the focusing operator should be zero (Berkhout, 1996b).

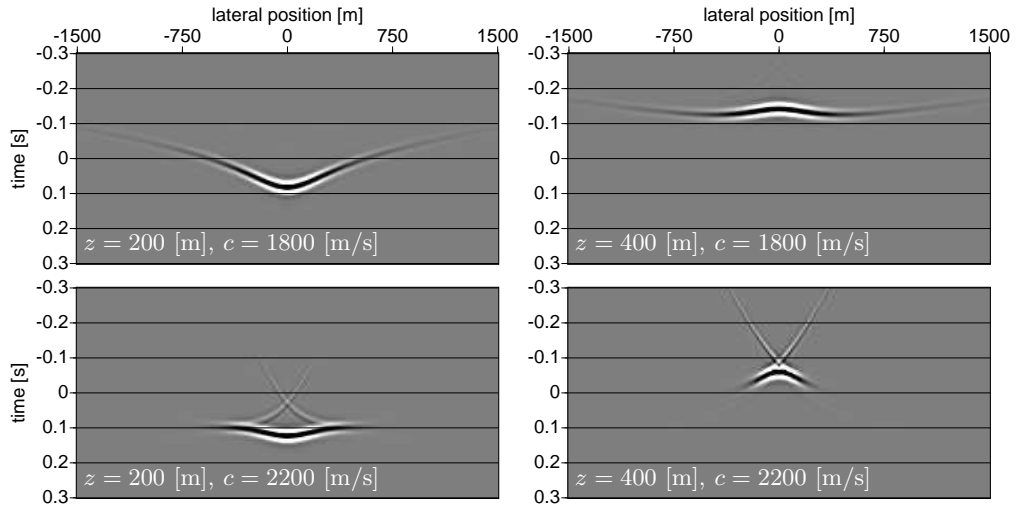


**Figure 6.14** Move-out corrected CFP gathers for combined depth and velocity errors in the focusing operators. Note that for negative velocity errors simple curves are observed.

initial $c=1800$ $z=200$			initial $c=1800$ $z=400$		
velocity [m/s]	depth [m]	$L_2$ fit	velocity [m/s]	depth [m]	$L_2$ fit
2000	300	2.62e-04	2000	300	2.76e-04
2000	305	1.52e-03	2010	305	1.33e-03
2010	305	1.79e-03	2010	300	2.27e-03
2010	310	2.94e-03	2020	310	4.08e-03
2020	310	5.77e-03	2030	310	7.67e-03

**Table 6.1** The five best matches for the time section of figure 6.14 with the negative velocity errors. The correct model can be distinguished clearly from the other matches.

**In conclusion;** the move-out corrected CFP gather contains information about the depth and velocity errors in the macro model. Using a focusing operator derived from an initial macro model there are in general two unknowns: the velocity of the medium, and the depth of the reflector. To find an update for an initial guess, analytically (or numerically) calculated traveltime curves can be used to find the best fit with the tracked curve. In the ideal case only one iteration is needed to arrive at the correct model. But due to tracking errors and multiple arrival times in complicated media there are in general more iterations needed.

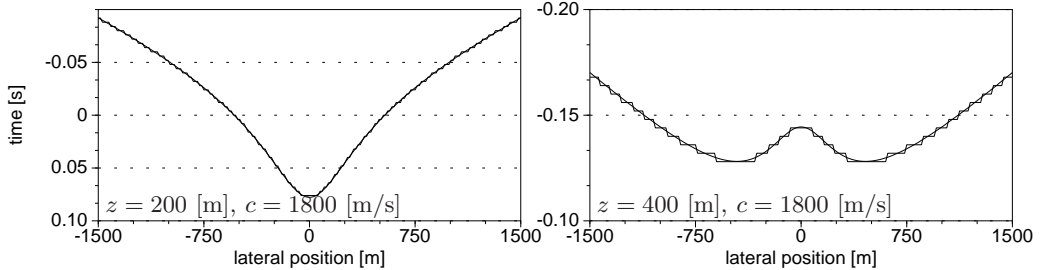


**Figure 6.15** Fitted move-out curves for the combined depth and velocity errors as shown in the top two pictures in figure 6.14.

### 6.3 Operator updating

In the previous section an attempt was made to derive update formula's for depth and velocity errors in a 1-dimensional macro model. It was shown that it is possible to derive a closed form solution of the update formula in case of a depth error in a one layer model. For other errors and more complicated models a numerical method can be used to find a better macro model (Kabir, 1997). However, there is a different approach possible which can be used to derive the correct focusing operator. Given an erroneous focusing operator it is possible to update the focusing operator and not

the macro model. The operator is updated to any suitable event close to the initial operator. How the correct operator can be found, from the focus point response and the initial operator, is explained in this section for a flat and a dipping layer.

### 6.3.1 Flat reflector

Let us assume that the correct focusing operator for the chosen event is positioned 'in between' the initial operator and the event of interest (principle of equal complexity). To illustrate the concept of 'in between', assume a hyperbolic time behavior for the initial synthesis operator ( $T_s^0$ ) and the focus point response ( $T_{cfp}$ )

$$\bar{T}_s^0(x_r) = \frac{\sqrt{\bar{z}^2 + x_r^2}}{\bar{c}} \quad (6.24)$$

$$T_{cfp}(x_r) = \frac{\sqrt{z^2 + x_r^2}}{c} \quad (6.25)$$

with  $\bar{z}$  the depth of the focus point,  $\bar{c}$  an average (or rms) velocity and  $x_r$  a receiver position.  $\bar{T}_s^0(x_r)$  describes the time behavior of the initial synthesis operator and  $T_{cfp}(x_r)$  describes the time behavior of the focus point response. The update of the synthesis operator is given by

$$\bar{T}_s^1(x_r) = \bar{T}_s^0(x_r) + T_c(x_r) \quad (6.26)$$

where  $T_c(x_r)$  is the update. An intuitive operator update is chosen as

$$T_c(x_r) = \frac{T_{cfp}(x_r) - \bar{T}_s^0(x_r)}{2}, \quad (6.27)$$

which is the traveltime in between the operator and the focus point response at every offset. This operator update approach gives the correct operator (using hyperbolic operators) for  $x_r = 0$ , but for larger CFP offsets the linear update is less accurate. The accuracy at the larger offsets can be improved by making use of a second updating step. In figure 6.16 two examples from the previous section, shown in figure 6.3e and f, are used to demonstrate the convergence of the proposed updating scheme. The examples contain a combined depth/velocity error in the focusing operator for a model with one flat layer. From the results shown in figure 6.16 it is observed that although the initial macro model and the CFP gather are different in both examples they converge to the same answer within one iteration. The updating of the CFP gather can be carried out in an automatic way by a time-convolution of the traces in the CFP gather with the traces in the time-reversed focusing operator (hence each trace is delayed with its erroneous response), followed by a renumbering to one-way time.

In the results after the first update in figure 6.16 the correct focusing operator is indicated by the spiky event. Careful inspection of the updated result after one iteration shows that for the higher CFP offsets the convergence to the correct operator

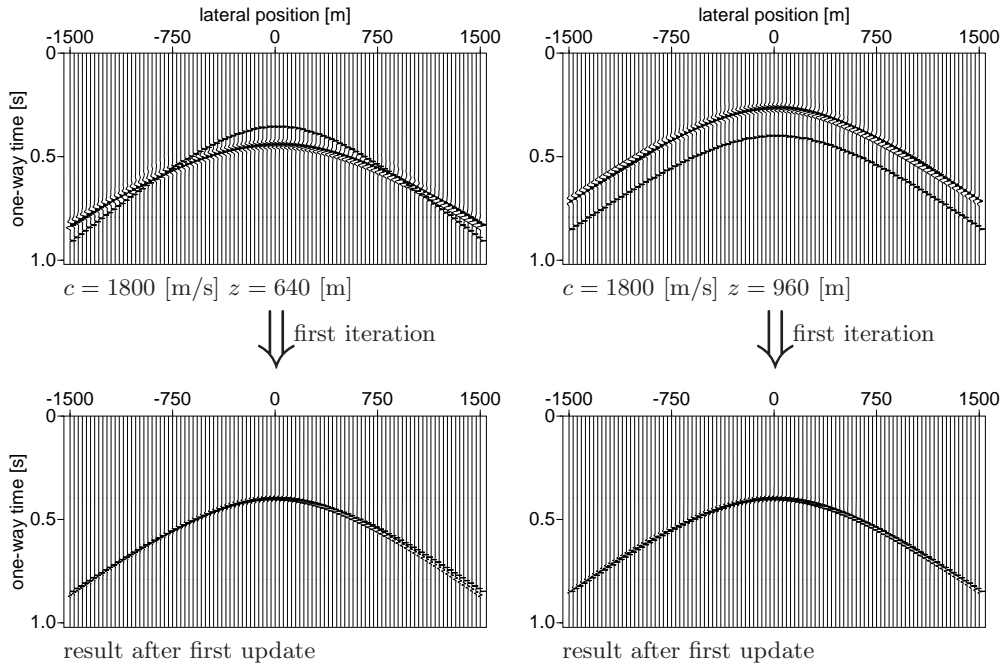


**Figure 6.16** Synthesis operator updating by taking the traveltime in between the operator and the CFP response. Note that both CFP gathers converge very fast to the same CFP gather with a focus point on the reflector. One iteration seems to be sufficient.

is not perfect. A second iteration will give a better convergence for the higher offsets. However, there is also an alternative updating scheme possible which converges, for the examples in figure 6.16, within one iteration to the correct operator.

Two-dimensional convolution (in space and time) of the erroneous time-reversed focusing operator with its erroneous focus point response can be written in a matrix-vector multiplication. For example the 2-dimensional convolution of equation (6.6), the erroneous focusing operator, with equation (6.8) the focus point response, can be represented by

$$\begin{aligned}
 \mathbf{Q}_i^-(z_m, z_0) &= \mathbf{P}_i^-(z_m, z_0) [\mathbf{F}_i^-(z_m, z_0)]^* & (6.28) \\
 &= \mathbf{R}_i^+(z_m) \Delta \mathbf{W}(z_m) \mathbf{W}_i^+(z_m, z_0) [\Delta \mathbf{W}(z_m)]^* \mathbf{W}_i^+(z_m, z_0) S_0 \\
 &= \mathbf{R}_i^+(z_m) [\mathbf{W}_i^+(z_m, z_0)]^2 \mathbf{S}_0,
 \end{aligned}$$

where  $[\mathbf{F}_i^-(z_m, z_0)]^*$  is a Toeplitz matrix, constructed from equation (6.6), given by

$$\mathbf{F}_i^-(z_m, z_0) = \Delta \mathbf{W}(z_m) \mathbf{W}_i^+(z_m, z_0). \quad (6.29)$$

Note that convolution result (6.28) represents the focus point response with the correct propagation properties doubled (the error matrix  $\Delta \mathbf{W}(z_m)$  has been removed by

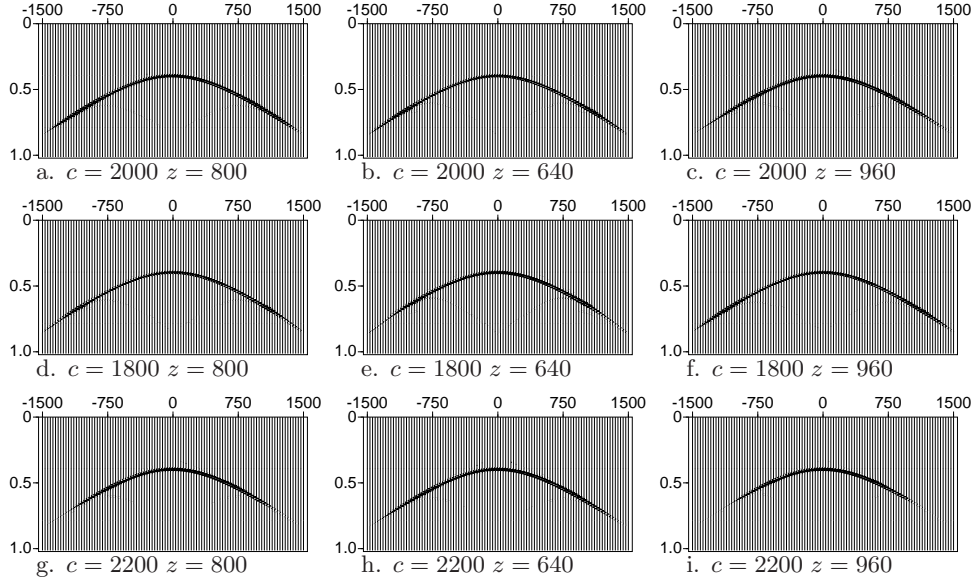


**Figure 6.17** 2-Dimensional convolution between the CFP gather and its operator for different erroneous operators. Note that all convolutions give the same result, meaning that erroneous CFP gathers can be automatically updated.

the convolution). Hence, if the first focusing step is followed by the convolution process then the **WRW** response has been modified to a **RW<sup>2</sup>** response, despite the use of an erroneous synthesis operator. The traveltimes for the correct focusing operator are obtained from the convolution result by halving the time scale. By making use of the 2-dimensional convolution the assumption is made that the medium above the focus point is laterally invariant, which means that  $\mathbf{W}^+(z_m, z_0)$  and  $\Delta\mathbf{W}(z_m)$  are both Toeplitz matrices (see also the discussion after the derivation of equation (6.8)).

The 2-dimensional convolution between the CFP gather and its synthesis operator is shown in figure 6.17 for the same erroneous synthesis operators as in figure 6.3. The time and offset of the convolution results are displayed by halving the original spatial and time sampling rate. Note that all convolution results are in traveltime identical with the correct focusing operator. Note also that the amplitudes in the different convolution results are weaker for the positive velocity errors. This means that the Fresnel zone is shifted outside the aperture in the first focusing step.

The operator updating by the 2-dimensional convolution can be interpreted as a time interpolation in plane wave components. By making use of the linear Radon transform the erroneous focusing operator and its CFP response can be expressed in terms of intercept time  $\Delta\tau$  for each ray-parameter component  $p$ . The correct focusing operator can then be found by averaging for each  $p$ -value the intercept

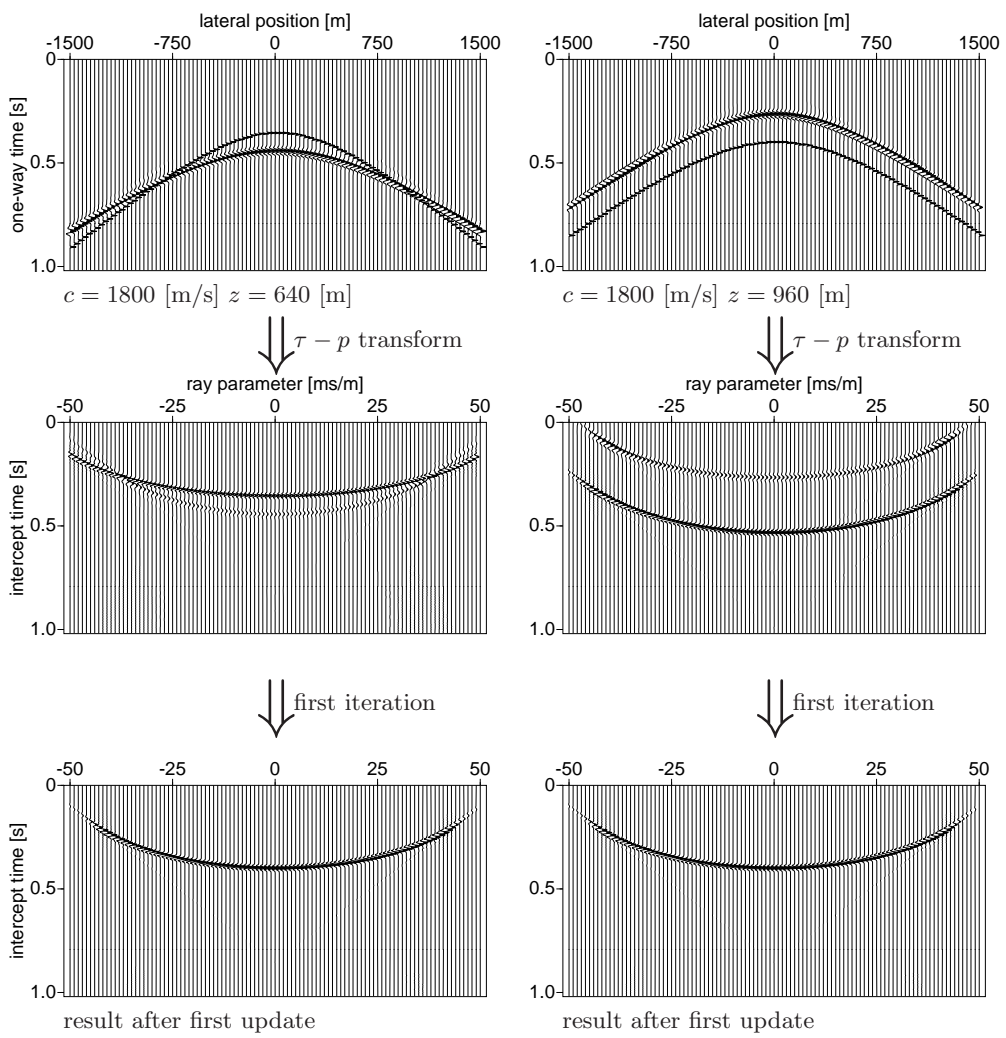


**Figure 6.18** The correct focusing operator can be found by choosing for each  $p$  value the intercept time exactly in the middle of the erroneous operator and erroneous response intercept times. Note that only one iteration is needed to obtain the correct focusing operator.

times of the time-reversed focusing operator and the related focus point response. Averaging in the  $\tau - p$  domain means that the focusing operator and its focus point response are compared in points with equal slopes. An example for the updating scheme in  $\tau - p$  is shown in figure 6.18. For a 1-dimensional medium the correct operator is obtained in one step.

So there are two methods to update an erroneous focusing operator to a correct focusing operator: interpolation in offset or interpolation in ray-parameter. The difference of the two methods is explained in figure 6.19. If the assumption of a

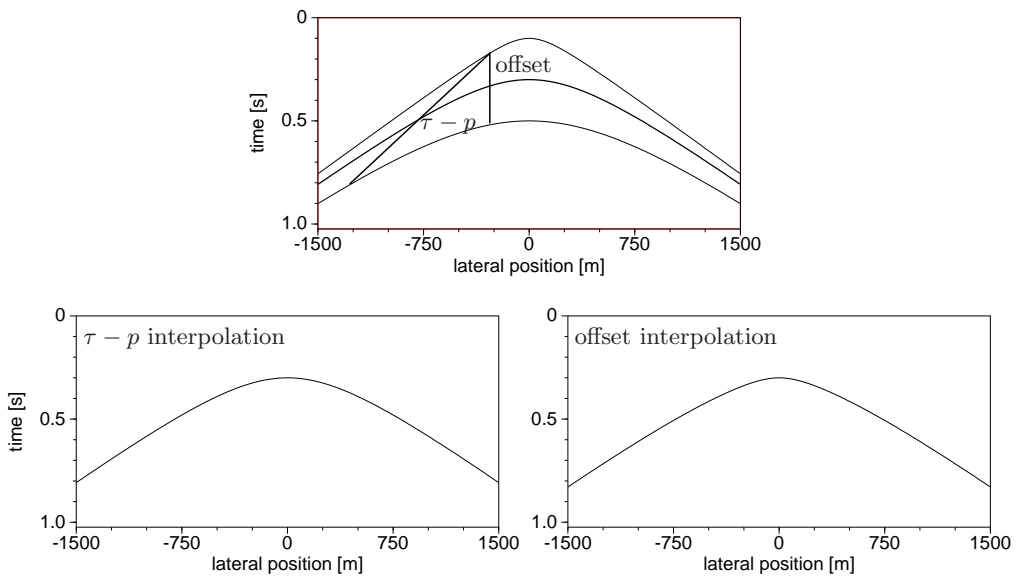


**Figure 6.19** Operator updating by averaging the times for common ray-parameter (left) or for common offset traces (right). The ray-parameter method converges for a 1D medium within one step to the correct operator. Note the small difference with the offset interpolation method.

laterally invariant medium is valid then the ray-parameter scheme will converge in one iteration to the correct operator. The method to obtain the correct operator is the same for both methods: time convolution of the erroneous operator with the CFP gather and halving the time scale of the result. This method works in the frequency domain by multiplication of the CFP gather with its operator. A disadvantage of the frequency domain implementation is that it takes a lot of computation time to transform the data and the operator to the frequency domain and the convolution result back to the time domain. An advantage of the frequency domain method is that it can handle complex operators.

An alternative and more faster method is based on (automatic) tracking of the erroneous response in the CFP gather. In this way all the computation can be done in the time domain (see appendix C). However, depending on the complexity of the medium the time domain method can give problems with complicated operators. Morton and Thorbecke (1996) have shown that it is possible to do automatic operator updating for 3-dimensional numerical seismic data. A flow scheme of this operator driven migration process is shown in figure 6.20. This operator driven migration process takes properly into account any unknown traveltime effects due to ray bending, anisotropy or anything else that may occur in the subsurface. This can be easily understood if one bears in mind that the focusing operators are directly determined from the data. Hence, in the CFP method the focusing operators in the

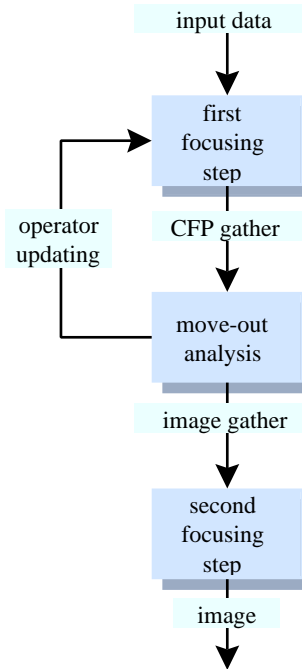


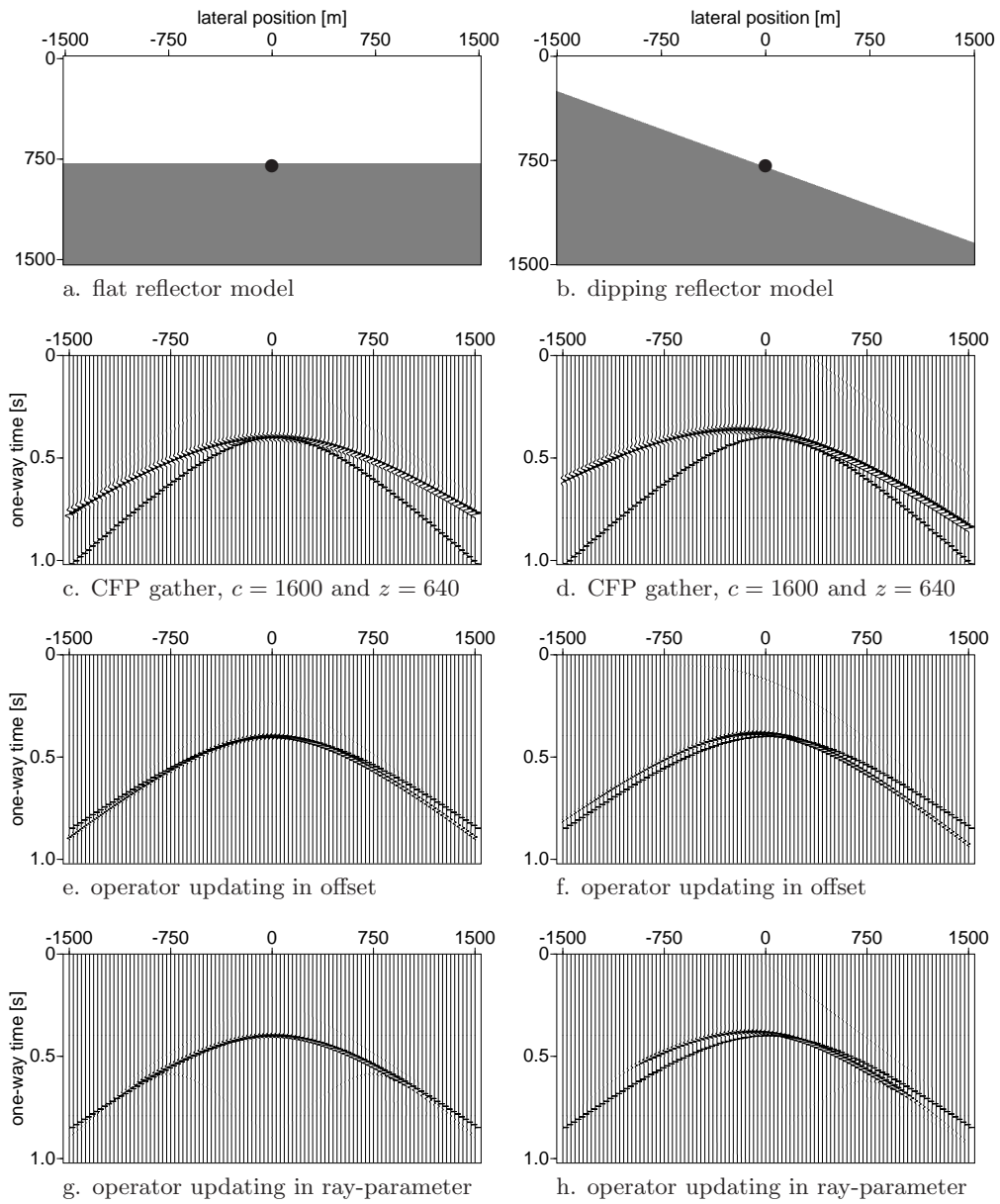
**Figure 6.20** Operator driven migration process. The output of the CFP migration is not in depth but in one-way image time.

migration process are not limited by the restrictions inherent to any user-specified parametric subsurface model. A subsurface model need only be specified in the post processing step for time to depth conversion of the one-way time image. This subsurface model can be obtained by a global inversion of the estimated focusing operators. The calculation of the global inversion is beyond the scope of this thesis.

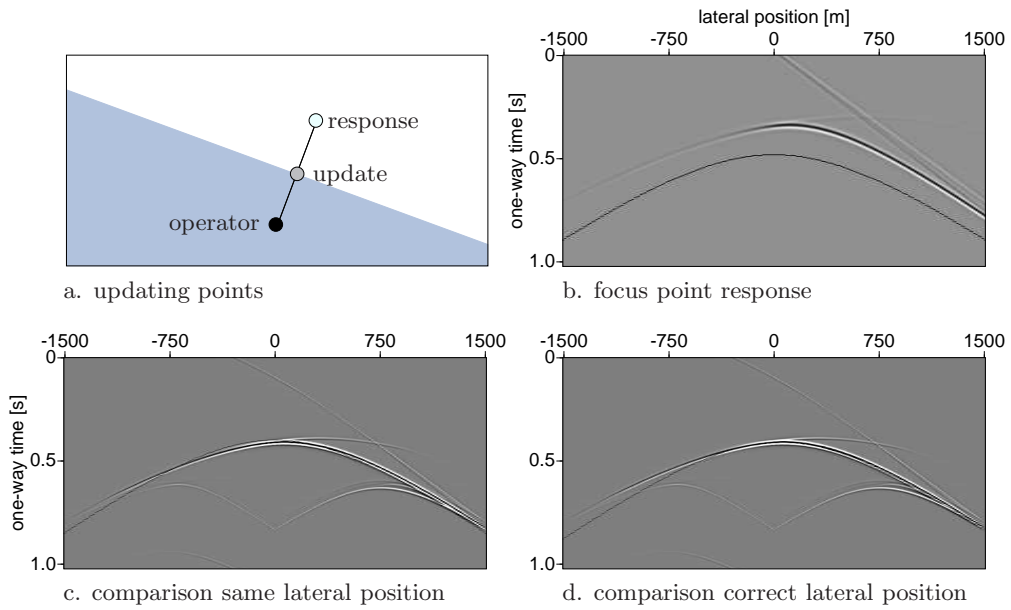
### 6.3.2 Dipping reflector

In the previous section the operator updating was explained with a flat reflector, in this section the updating for a dipping reflector is discussed. In figure 6.21 the response of a flat reflector and a dipping reflector are shown. The same model is used as before; velocity above the reflector 2000 m/s and the reflector depth is 800 m, the dip is chosen at  $20^\circ$ . In both examples an erroneous focusing operator is used with a velocity of 1600 m/s and a depth of 640 m. In figure 6.21c,d the response in the CFP gather is shown together with its erroneous operator (the spiky event). Note that due to the shadow zone the left hand side in the dipping reflector response does not contain useful information. The focusing operator is updated from the erroneous CFP gather with the two methods discussed in the previous section. The offset

interpolation shows after one iteration still a deviation from the correct operator



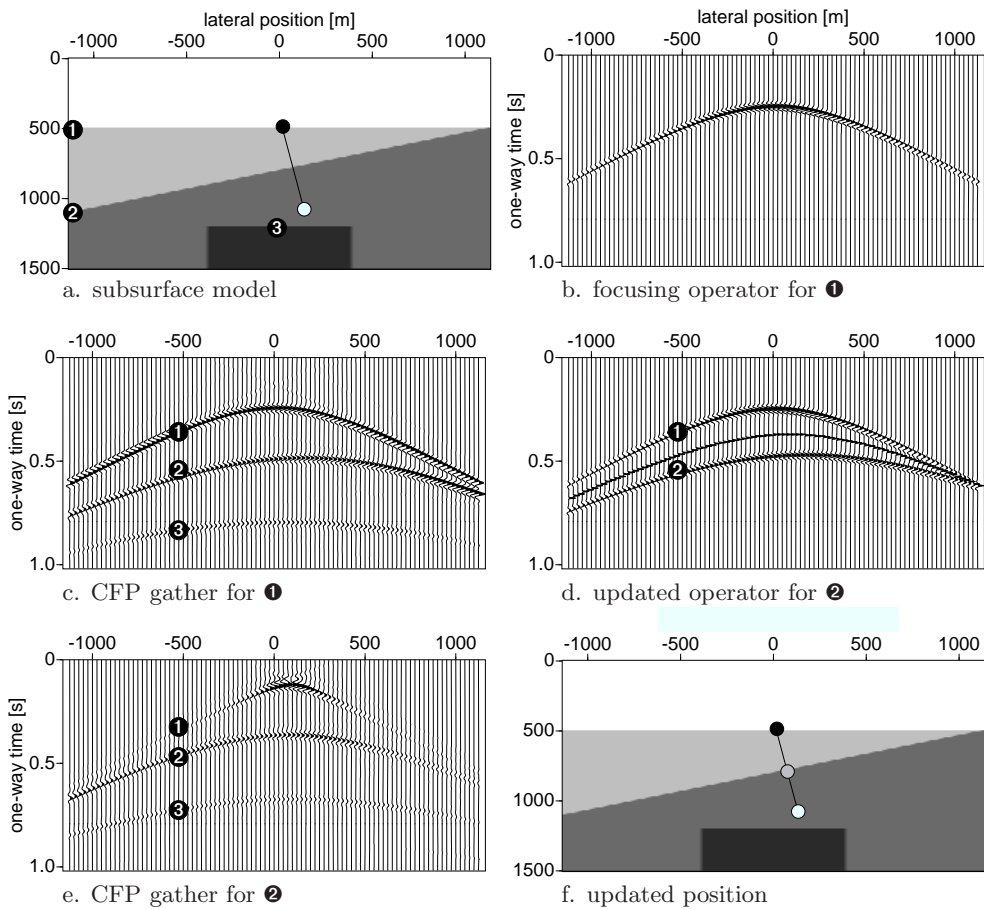
**Figure 6.21** Operator updating for a flat (left) and dipping (right) reflector. Ray-parameter interpolation gives in one iteration the correct operator for the flat reflector. The updated operator for the dipping reflector seems to deviate from the correct operator.



**Figure 6.22** Updating of a dipping reflector response. Note that the updated operator (in  $\tau - p$  domain) has a lateral shift with respect to the original focus point position.

(the spiky event). The ray-parameter interpolation method gives in one iteration the correct focusing operator for the flat reflector (g). However, the ray-parameter interpolation method for the dipping reflector still gives a deviation from the correct operator (h). Careful inspection of the apex of the hyperbola in figure 6.21h shows that the apex of the updated operator is not positioned at the same lateral position as the apex of the correct operator.

To show what happened for the updated focusing operator in the dipping reflector example the same dipping model is used as before but now with only a depth error in the focusing operator (depth error of  $+20\% = 960\text{ m}$ ). In figure 6.22a three dots are drawn in the correct subsurface model, the black dot represents the position of the erroneous focusing operator, the white dot represents the focus point response and the gray dot is the position of the updated operator obtained after ray-parameter interpolation. The position of the erroneous focus point response is, analogous to the flat layer, on the opposite side of the reflector. Due to the updating in the ray-parameter domain, thus interpolation of the intercept-time for waves with the same ray-parameter value, the updated operator is positioned exactly in the middle of the two points. This updated operator has, for a layer with a constant dip around the focus point, its focus point exactly on the reflector. However, the lateral position of the focus point of the updated focusing operator is shifted down-dip (for a negative depth error the shift is up-dip) in comparison with the initial focusing operator. In



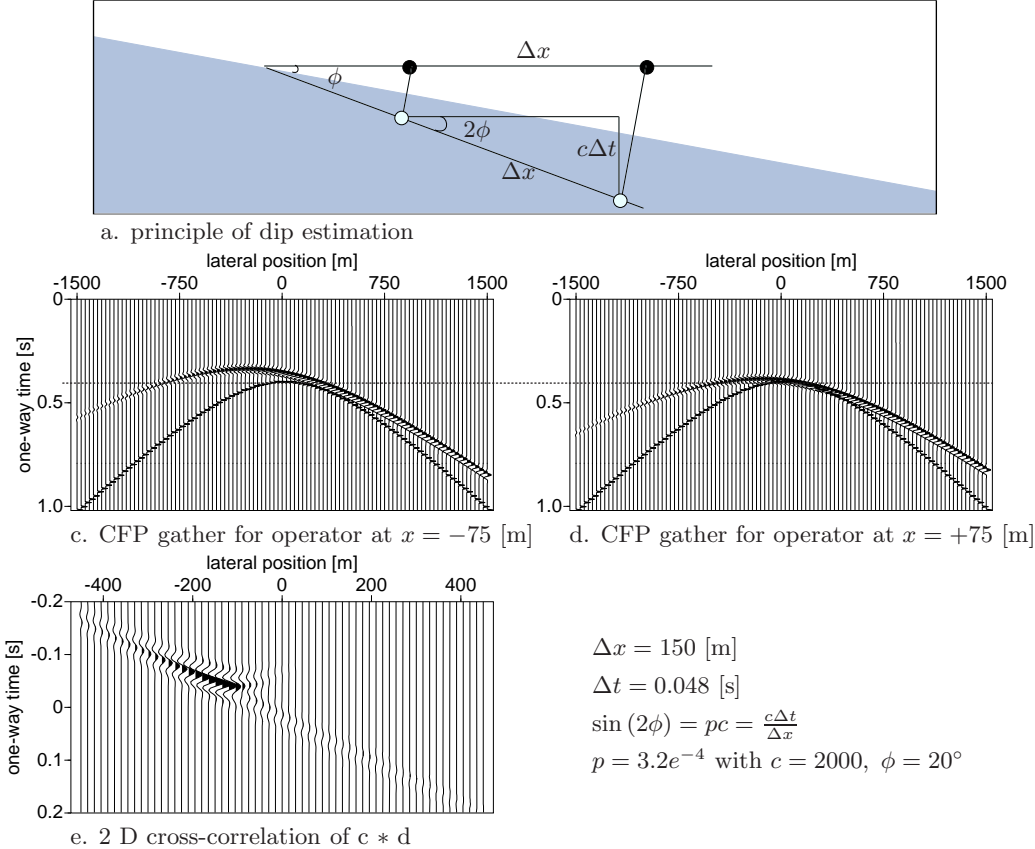
**Figure 6.23** Illustration of the update procedure for a simple model. The focusing operator for the first boundary has been chosen as an initial estimate for the second boundary.

figure 6.22b the focus point response is shown together with the focusing operator. The updated operator after the ray-parameter interpolation step is shown in figure 6.22c, the spiky event represents the operator at the same lateral position as the initial operator. Note that the updated operator has a lateral shift with respect to the original focus point position. The lateral shift can be calculated by using the interpretation shown in figure 6.22a. Taking this shift into account the shifted focusing operator on the reflector is identical with the updated operator which is shown in figure 6.22d.

A nice example of the operator updating scheme is shown in figure 6.23. In this example the updated focusing operator for the first depth level is used as an estimate for the next one. The example shows that in CFP migration a CFP gather should not be computed only *along* its time-reversed synthesis operator but it should be

computed *around* its time-reversed focusing operator in order to avoid loosing the focus point response (Berkhout, 1996b) and to be able to jump to the next interface. Once the updated focusing operator is computed the second focusing step can be carried out. In the imaging step, which was discussed in section 5.3, the result of the second focusing step is positioned at the lateral position of the focus point. However, due to the updating in the first focusing step the lateral position of the focus point can be shifted in the case of a dipping reflector. The lateral shift of the focus point is dependent on the dip of the reflector. There are two ways to compensate for this lateral error in the final image; in the global inversion of all the focusing operators to a (depth) macro model the local dip of the reflector can be computed from the one-way time image and be taken into account in the global inversion. Another way is to provide an estimate of the local dip during the imaging, and taking the correct position of the updated focus point into account in the positioning in the one-way time image.

By making use of the lateral shift in the focus point response of an erroneous focusing operator it is possible to estimate the local dip of the reflector. In figure 6.24 the dip estimation procedure is explained. Two focus points are chosen above (or below) the reflector of interest at the same depth level but with a different lateral position. The focus point response is calculated for both focus points. Assuming that the medium around the area of the two focus points is laterally invariant in the direction of the dip then the local dip of the reflector can be estimated by using the 2-dimensional cross-correlation between the two CFP gathers. The CFP gather can be interpreted as the response of a point below the reflector, where the focus point (the black dot) and the focus point response (the white dot) are positioned on a line perpendicular on the dip of the reflector. By using the lateral distance between the two focus points and the difference in arrival time of the focus point responses the local ray-parameter [s/m] value of the reflector can be determined. The lateral distance between the two focus points is chosen by the user, the difference in arrival time between the two focus point responses is measured from the 2-dimensional cross-correlation. If an estimation of the velocity is available the reflector angle in degrees can be computed. In figure 6.24 the CFP gathers are computed with erroneous focusing operators (defined with a velocity  $-20\% = 1600$  m/s and at depth level 640 m) which are 150 m separated from each other. From the 2-dimensional cross-correlation shown in figure 6.24d the time delay  $\Delta t = 0.048$  is determined. With this time delay the angle can be computed by using the correct velocity of the medium above the reflector resulting in the correct angle of  $20^\circ$ . The sensitivity of the method dependents on the accuracy of the arrival time measurement from the cross-correlation, an error of one time sample (4 ms) gives a deviation of  $2^\circ = 10\%$  in the example of figure 6.24. Note that the erroneous macro model used to generate the focusing operators does not distort the dip estimation in the example.



**Figure 6.24** Local reflector dip estimation with two focus points at the same depth level. Note that the principle works with any pair of (erroneous) focusing operators defined at the same depth level.

#### 6.4 Second focusing step

The influence of erroneous focusing operators in the second focusing step is of importance if the updating step is not used and one is interested in the quality of the resulting one-way time image. In the previous chapter the property was observed that all events in a one-way time image are imaged at the correct one-way image time independent of the used operators. To examine this property one trace out of a CFP gather is calculated for one shot record for different depth and velocity errors in the focusing operator. The same single reflector model is used as before. In figure 6.25b the used shot record, with the source  $x_s = 0$  and the receivers positioned in  $[-1500, 1500]$  with a receiver distance of 15 m, is shown. The one-way image time for the reflector is at 0.4 s, this time is found in figure 6.25b at the trace belonging

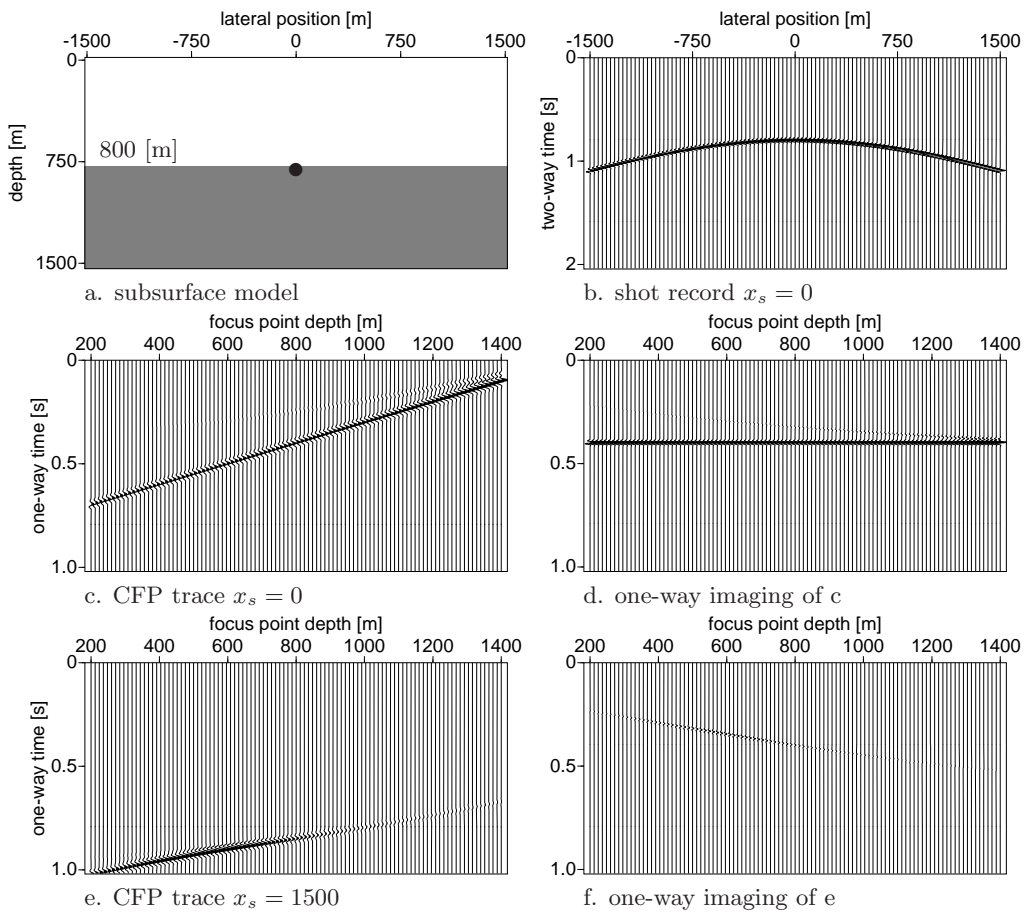


**Figure 6.25** The influence of depth errors in the imaging step. Note that for  $x_s = 0$  (d) all move-out corrected traces are positioned at the correct one-way image time independent of the depth of the focus point.

to the correct depth of 800 m. Every trace in figure 6.25c represents a CFP trace calculated with a focusing operator for a certain depth level. The CFP traces calculated for the shot with  $x_s = 0$  represent the top of the apex of the erroneous focus point response. Figure 6.25d represents the traces in (c) after move-out correction with the erroneous focusing operator followed by positioning at one-way image time (again defined by the erroneous focusing operators). Note that all traces are now positioned at the correct one-way image time independent of the depth of the focus point. The CFP trace calculated for an other source position ( $x_s = 1500$ ) shown in figure 6.25f does not align up at the correct one-way image time.

The observed property can be explained by considering only the stationary phase contribution in the first focusing step. For the focus point in the middle of the flat

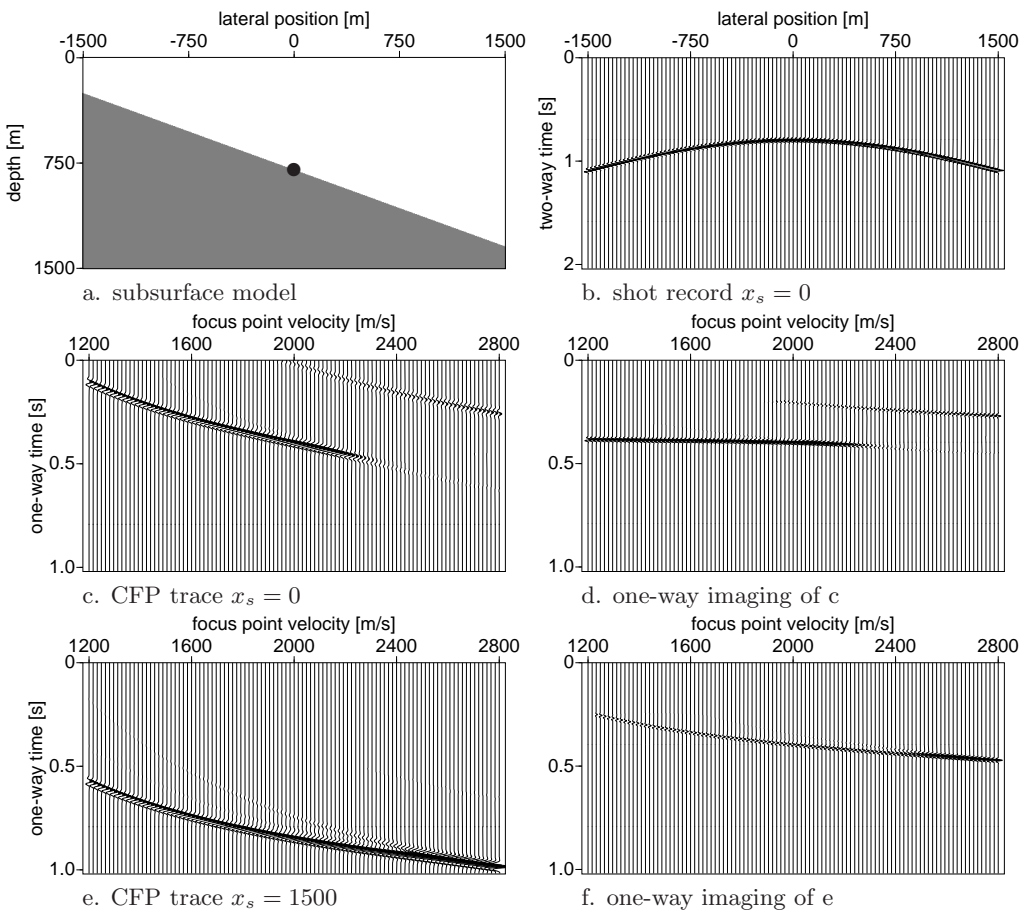


**Figure 6.26** The influence of velocity errors in the imaging step. Note that for  $x_s = 0$  (d) all move-out corrected traces are positioned at the correct one-way image time independent of the velocity above the focus point.

reflector the stationary phase trace for the shot record at  $x_s = 0$  is  $x_r = x_s = 0$ . This trace ( $T_d$ ) is corrected with the time defined by the focusing operator ( $T_d - T_s$ ). For the imaging step the trace after the first focusing step is corrected again with the time defined by the focusing operator ( $= T_d - 2*T_s$ ), positioned at the one-way image time ( $T_s$ ) and renumbered to one-way times ( $T_i = 0.5*(T_d - 2*T_s) + T_s = 0.5*T_d$ ). So imaging with an erroneous focusing operator places the stationary phase contribution of the shot record (for the focus point of interest) at the correct one-way image time. Note, that this procedure can also be carried out by a summation over all the (uncorrected) traces in the shot gather followed by halving the time scale. This procedure selects the stationary trace for a focus point defined at the source position. By using more accurate focus points the contributions of the different shot gathers

in the CFP image gather will be better aligned and the image quality will be better. Note also that due to an erroneous focusing operator the Fresnel zone can be shifted outside the aperture which will give artifacts in the one-way time image.

The same experiment as shown in figure 6.25 is repeated for a dipping layer and velocity errors in the focusing operator. Again the stationary phase trace originates from the shot record with  $x_s = 0$ . The imaged traces for this shot record are shown in figure 6.26. Note that for positive velocity errors ( $c > 2000$  m/s) the Fresnel zone around the stationary phase position is quickly shifted outside the aperture and the strongest contribution in the CFP trace is an artifact. The contribution from the shot record with its source position at  $x_s = 1500$  shows only the correct trace for the correct velocity. If the Fresnel zone remains within the aperture the velocity error in the focusing operator has no influence on the one-way image time of the stationary phase trace.

The foregoing analysis has shown that the time position in the one-way time image is not very sensitive for errors in the focusing operator. However, the image quality is very sensitive for erroneous operators. This sensitivity of the CFP image gather is used in the coherency measurement discussed before.





## Chapter 7

### Numerical data examples

To give more insight in the CFP processing techniques several numerical data examples are used. Section 7.1 shows the focus point response for a single diffraction point in the subsurface for several erroneous focusing operators. A 1-dimensional medium based on a well log measurement is shown in section 7.2. With this model the construction of a CFP image gather is illustrated. In section 7.3 a model is chosen which defines a multi-valued focusing operator for a deep reflector. This example is used to show the limitations of a simple implementation of the operator updating procedure. The influence of groundroll and a weathered layer on the CFP gather is shown in section 7.4. In section 7.5 the syncline model is used to show the integration of CFP gathers and pseudo VSP data. The integration is shown to give more insight in the illumination aspects of the CFP gather. In the last section the Marmousi and the SEG/EAGE salt dome model are used to compare the CFP image gather with imaging results obtained with other imaging methods.

#### 7.1 Diffraction point

The diffraction point is a suitable experiment for testing the construction and imaging of a CFP gather. In a homogeneous medium a diffraction point is chosen in the middle of the model at a depth of 500 m and a fixed acquisition spread at the surface is used. In figure 7.1 several CFP gathers are shown which are constructed with different synthesis operators. Note that only the focusing operator with its focus point defined at the diffraction point gives the correct focus point response. For a positive (negative) depth error in the synthesis operator the constructed event in the CFP gather is positioned above (below) the correct position. This is shown in figure 7.1g and e, where the black line represents the operator and the event with the wavelet represents the focus point response. In the updating procedure, where the updated operator is chosen in between the operator and the CFP gather, the correct operator will be obtained in one step.

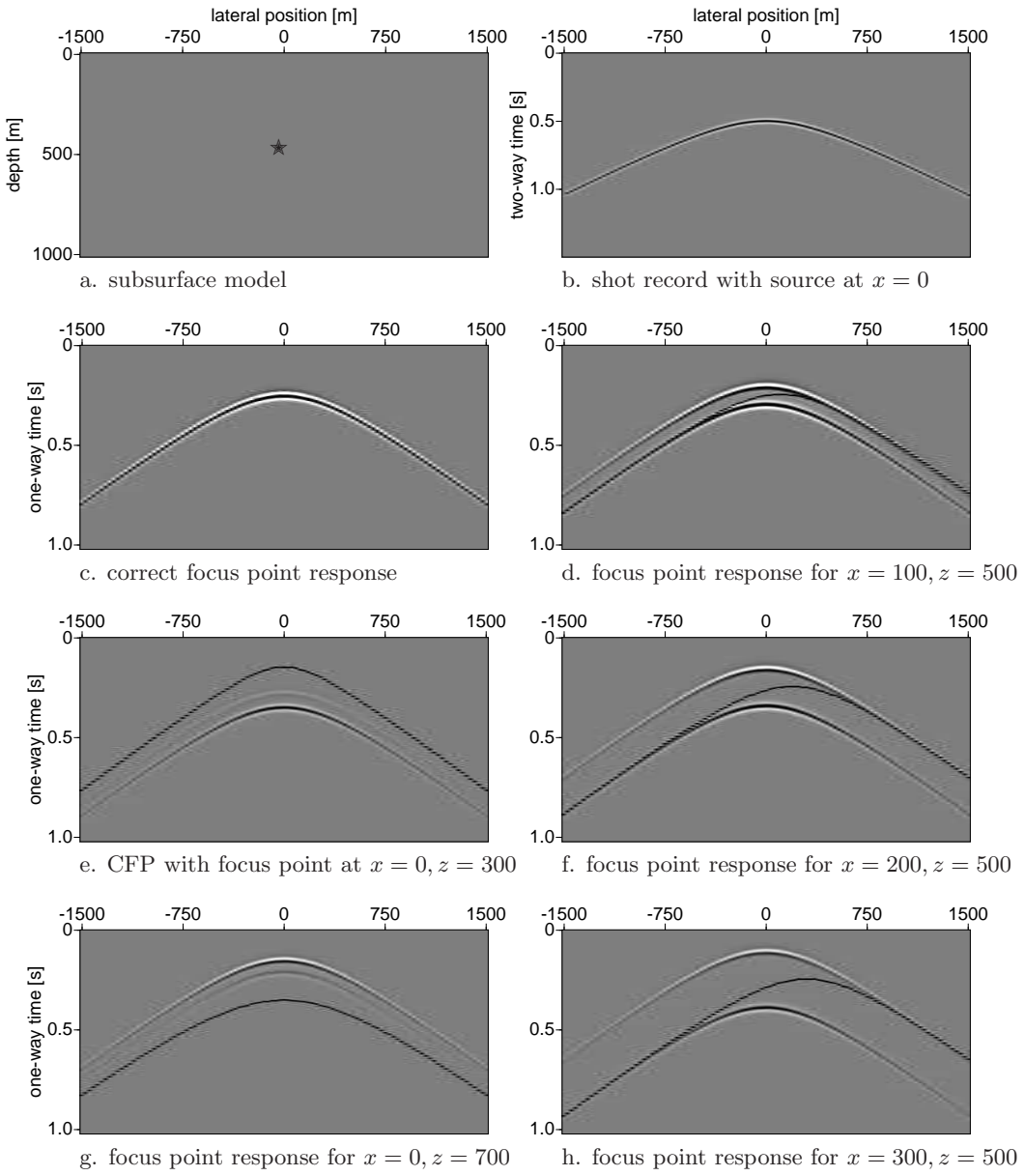


**Figure 7.1** CFP gather for a single diffraction point in the subsurface constructed with different synthesis operators. The scaling in the pictures in the CFP gathers for the depth errors (0.1) and the lateral errors (0.02) is not the same. The black line indicates the focusing operator. Note the two events in the CFP gather for a focusing operator with a lateral error.

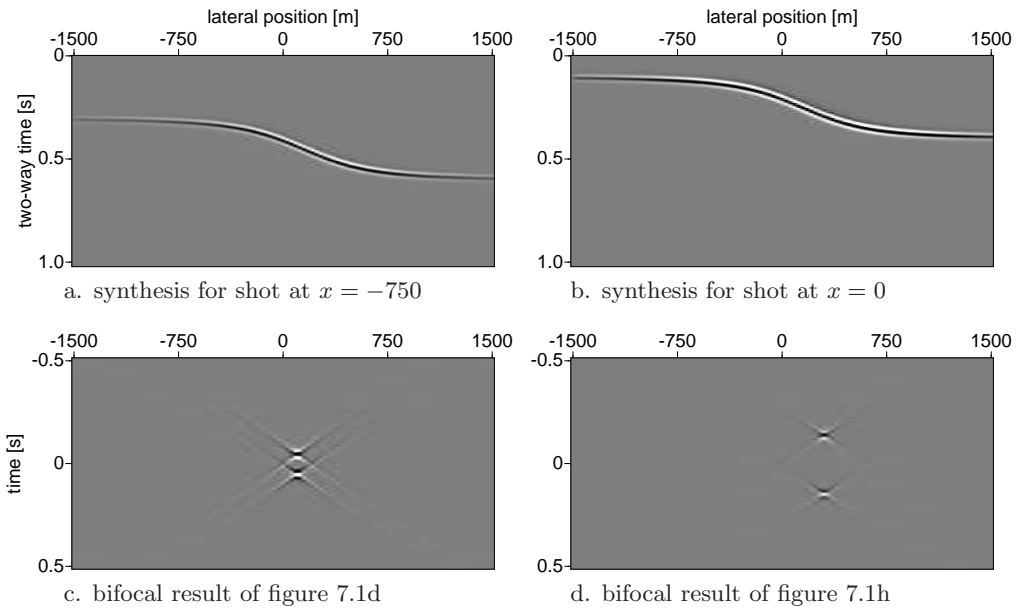


**Figure 7.2** The CFP corrected result between the operator with a lateral shift of 300 [m] and a shot record with its shot position at  $x = -750$  (a) and at  $x = 0$  (b). In the bifocal results (c) and (d) part of the imaging finite aperture artifacts can be recognized.

For a synthesis operator with a lateral error the CFP gather is shown in figure 7.1d, f and h for a lateral error of respectively 100, 200 and 300 m. In the updating procedure the operator can converge, after a few iterations and selecting consequently the same event, to the correct synthesis operator, but in the second focusing step step the focus point response will be positioned at the wrong lateral position, namely the position of the initial operator. This position error can be taken care of if one determines the shift of the apex of the updated focusing operator with respect to the initial focusing operator. Note, that the amplitudes of the focus point responses with a lateral error have a maximum amplitude 5 times lower than the responses with a depth error. This lower amplitude is an indication that the energy of the focus point response is low for an operator not positioned at the diffraction point position. To investigate the origin of the two events visible in the focus point responses for a focusing operator with a lateral error the CFP corrected shot records are investigated.

In figure 7.2a the synthesis result between the operator with a lateral shift of 300 m and a shot record with its shot position at  $x = -750$  and a shot position at  $x = 0$  is shown in figure 7.2. In these figures we see two zones on the edges of the acquisition aperture which give the double contribution in the CFP gather. For the ideal situation the integration of the results shown in figure 7.2a and b should give no contribution in the CFP gather. If the aperture would be extended to infinity

the result at the edges will asymptotically go to a Fresnel zone, but never reach it. The bifocal result (2D cross-correlation between operator and CFP gather) for the CFP gather are shown in figure 7.2c and d. From these bifocal results it is more clearly observed that the results obtained with a shifted focusing operator represent the artifact for the correct image of the diffraction point. From this last observation it is concluded that the double events present in the CFP gathers shown in figure 7.2 originate from the finite acquisition aperture.

## 7.2 One dimensional multi layer model

The shot record shown in figure 7.3a is modeled in a 1-dimensional medium based on a well log shown in figure 7.3b and is used as input data for the CFP processing scheme. Due to the presence of the many layers in the model this synthetic data set is used to clarify the concept of CFP image-gathers. Choosing a synthesis operator at the top (❶), middle (❷) and bottom (❸) of the model and scaling the constructed CFP gather to one-way times gives the results shown in figure 7.3d, e and f. The scaling is carried out with respect to one-way image time; the traveltimes between the focus point and the source position at the surface.

In figure 7.3d, e and f it is observed that in the focusing area of the synthesis operator the CFP-gather gives a good representation of the subsurface. Further away from the focusing area the construction is less accurate and finite aperture artifacts distort the events in the CFP gather. Constructing the CFP image-gather from these CFP gathers is carried out by a time selection and time correction, given by interpolated focusing operators, for all time samples. This construction is shown in steps in figure 7.3g, h and i. In figure 7.3g the three single focus gathers d, e and f are combined to one multiple focus gather. This is done by combining the samples around a window of the focusing operator times and placing these selections into one file. The overlap between the contributions of different CFP gathers is chosen at a few time samples. The following step, from figure 7.3g to h, is a move out correction defined by the focusing operators used in the first focusing step. In figure 7.3h it is observed that only the events at the operator times are perfectly flat and will give a good representation of the reflector present at the defined focus point. The events in between the focus points of the first focusing step are not very well aligned. Thus for the second focusing step a focusing operator is needed at every time sample. These focusing operators are obtained by linear interpolation, for every offset, of the operators from the first focusing step. The result of this second focusing step is shown in figure 7.3i. In this gather the events around the focus point are all aligned, the events in between focus points are only good aligned for the deeper events. The operators which have a focus point at deeper layers give a better alignment due to the smaller move out correction for the higher offsets. The shallow part shows a significant wavelet stretching for the higher offsets due to the convergence of the

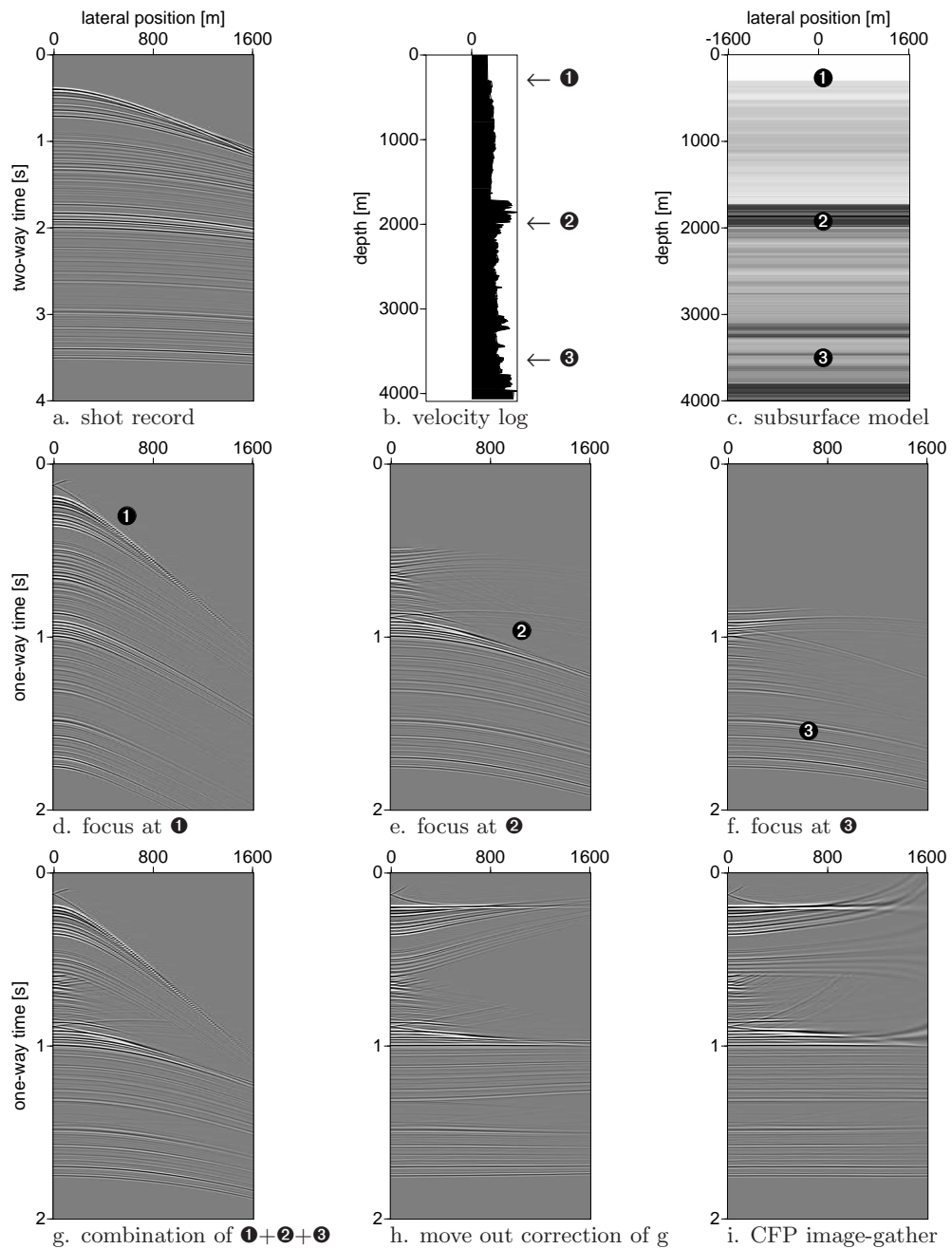


**Figure 7.3** Construction of CFP image-gathers in a 1-dimensional medium. The arrow indicates where the focus points are chosen. It is interesting to see that only 3 focus points yield already a reasonable CFP image-gather. Note the stretching of the wavelet due to the convergence of the traveltimes at the higher offsets.

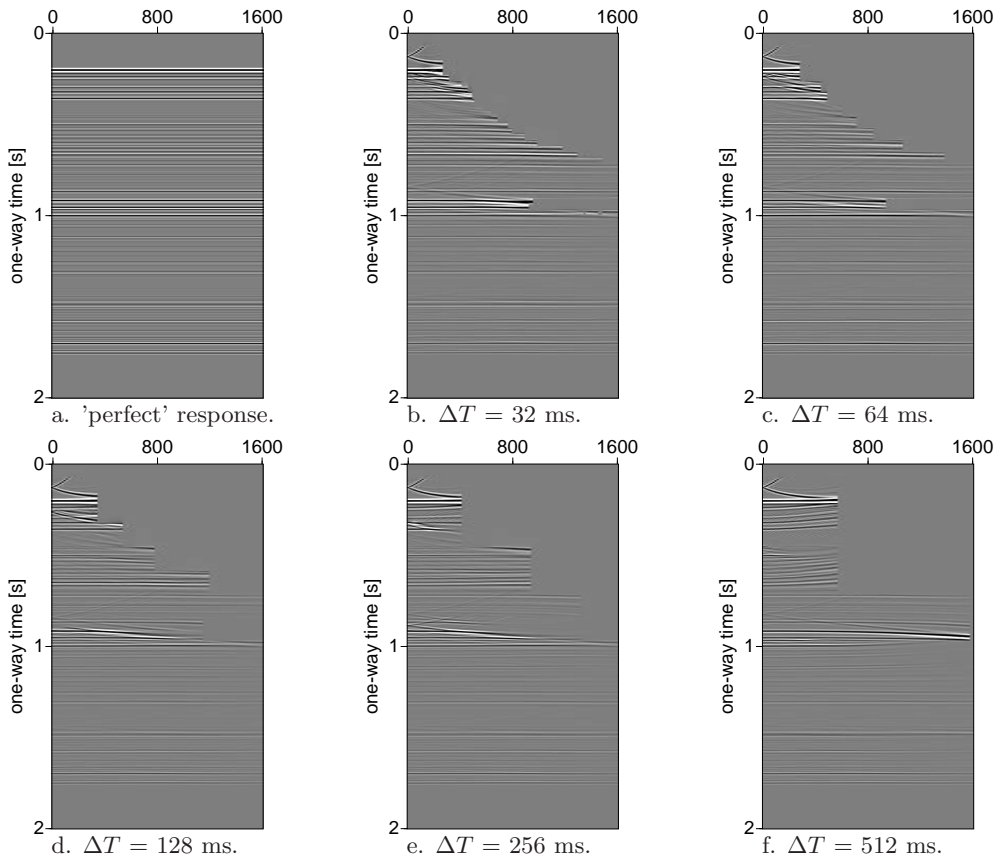


**Figure 7.4** CFP image gathers in a 1-dimensional medium for different sampling rates, in one-way image time, of the focus points. Note that the CFP image-gathers clearly identify that the focusing operators around 1 second are not correct.

time curves of the synthesis operators at higher offsets. These stretched events are normally not included in the construction of the image and are muted out for stretch values greater than a certain threshold. To have a better alignment for the shallow part more focus point must be used to construct the CFP image-gather.

The influence of the number of operators, used in the first focusing step, on the quality of the CFP image-gather is shown in figure 7.4 for several numbers of operators. In figure 7.4a the time response of the ideal CFP image-gather is shown (which is for a 1-dimensional medium equal to the zero offset trace displayed in one-way time). By constructing CFP image-gathers with different sampling rates, in one-way image time, for the focusing operators in the first focusing step and comparing these results with the ideal gather (a) gives an indication of the focusing area of the synthesis operators. Comparing the result of figure 7.3i with the double focus gather in figure

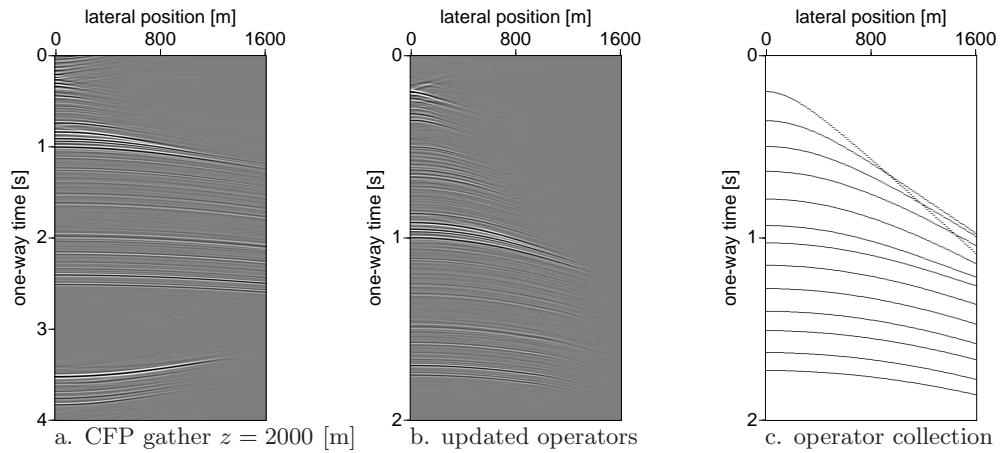


**Figure 7.5** Operator updating in a 1-dimensional medium is very easy; within one step all events can be updated to the correct focusing operator.

7.4a shows already that three synthesis operators are not sufficient to illuminate the whole depth range. However, for the focus points defined in the deeper parts of the model the focusing area is bigger than for a focus point close to the surface. By selecting a focus at every 32 ms (one-way time) in the subsurface a better CFP image-gather is built up which is shown in figure 7.4b. Note that in this gather the stretched events are muted out of the result. To connect the contributions from the different CFP gathers an overlapping window with a cosine taper is used. Comparing the results in figure 7.4 indicates that a focus point sampling of 64 or 128 ms is sufficient to illuminate all events in between the defined operators. Note also that the CFP image-gathers clearly identify that the focusing operators just before 1 second are not correct.

Operator updating in a 1-dimensional medium is very easy; from one (erroneous) CFP gather all other focusing operators could be determined. This is due to the fact that for a 1-dimensional medium the operator updating procedure in the  $\tau - p$  domain always converges in one step to the correct operator for all events in the CFP gather (see the discussion after equation (6.28)). Figure 7.5a shows a CFP gather constructed with a focusing operator defined at  $z = 2000$  m. After 2-dimensional convolution between operator and CFP gather and a renumbering to one-way time and CFP offset gives the collection of updated operators shown in (b). Note that due to the erroneous operator for the levels above the correct operator the Fresnel zone is shifted outside the acquisition aperture. For comparison a collection of correct traveltimes is shown in (c). Note that this updating method can be used for an initial guess of the focusing operators in a more complicated medium.

A reflection coefficient gather of the 1-dimensional model can be constructed according to the scheme given in figure 7.6. To show the principle of the construction of

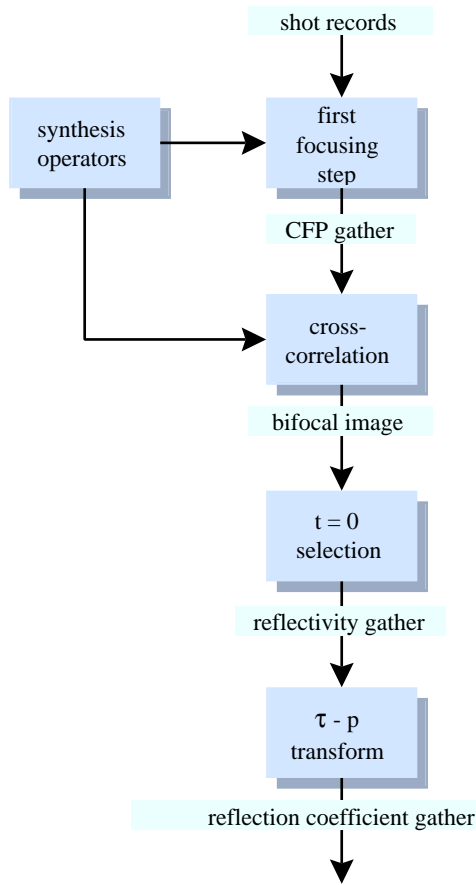


**Figure 7.6** Scheme for the construction of a reflection coefficient gather. The selection around  $t = 0$  consists of a small time window defined by the one-way time distance between the operators.

the reflection coefficient gather only the density well log measurement is used while the velocity is chosen constant at  $c = 2000$  m/s. At every 8 m ( $= 4$  ms) in depth of the subsurface a focus point is chosen and a focusing operator is calculated. The operator is used to construct the CFP gather for the defined focus point. The construction of the CFP gather is followed by a 2-dimensional cross-correlation between the operator and the CFP gather. From the cross-correlation result the  $t = 0$  level is selected and placed in the reflectivity gather. This process is repeated until all focus points have been handled. The resulting collection of  $t = 0$  selections is shown in figure 7.7a and is called the reflectivity gather. This reflectivity gather contains all the reflection information for the same lateral position in the model. A transformation of the reflectivity gather to the  $\tau - p$  domain gives the reflection coefficient gather

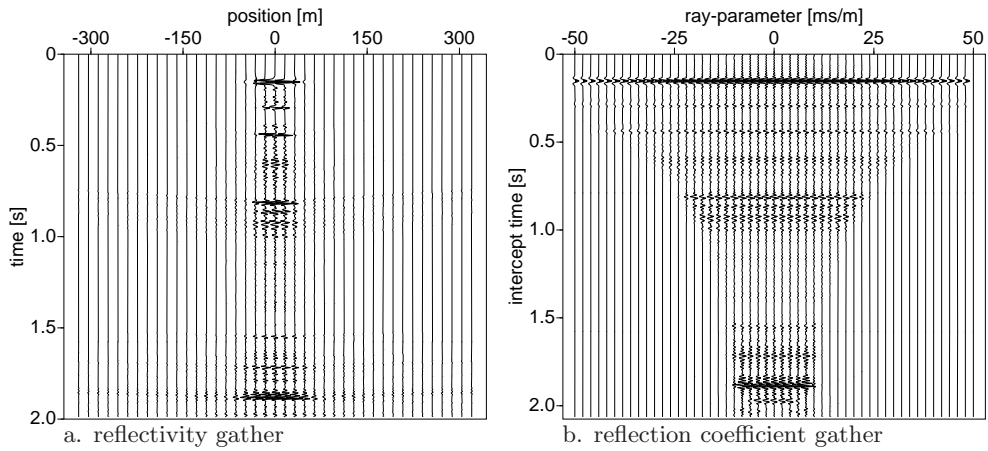


**Figure 7.7** The reflectivity gather, for a 1D model based on density contrasts only, constructed according to the scheme of figure 7.6. The reflection coefficient gather (b) is obtained by a  $\tau - p$  transformation of (a).

which is shown in figure 7.7b. This procedure is similar to the one discussed in section 5.4.2. Note that the procedure to obtain the reflection coefficient gather can be made more efficient by selecting more samples from the cross-correlation result. The reflection coefficient gather is the input for the lithologic inversion scheme as shown in the introduction.

### 7.3 'Void' model

The model shown in figure 7.8a is developed to test the operator updating procedure which was introduced in the previous chapter. A dipping reflector is positioned below a velocity 'void' which distort the reflection in a such a way that the reflected event at the surface contains multiple arrivals. The dipping reflector is a line defined through the points  $(x = -1500, z = 600)$  and  $(x = 1500, z = 975)$ , where the velocity above the reflector is 2000 m/s, below the reflector 2200 m/s and in the middle of the 'void' the velocity is 1000 m/s. The shot record with a source position at  $x = 0$  is shown in figure 7.8b. Note the breaking of the reflection event originating from the middle part of the dipping reflector. The two events above the main reflection event are due to the breaking in three parts of the downgoing source wave field. The middle part of the downgoing wave field gives rise to the reflection observed in the middle of the shot record. The two other downgoing wave fields give rise to the events above and aside of this main reflection event.

A focus point is chosen on the reflector at  $x = 0$  and two methods to calculate a CFP gather are used; one in the frequency-domain and one in the time-domain, where the last method only takes the first arrival times into account (see Appendix C about

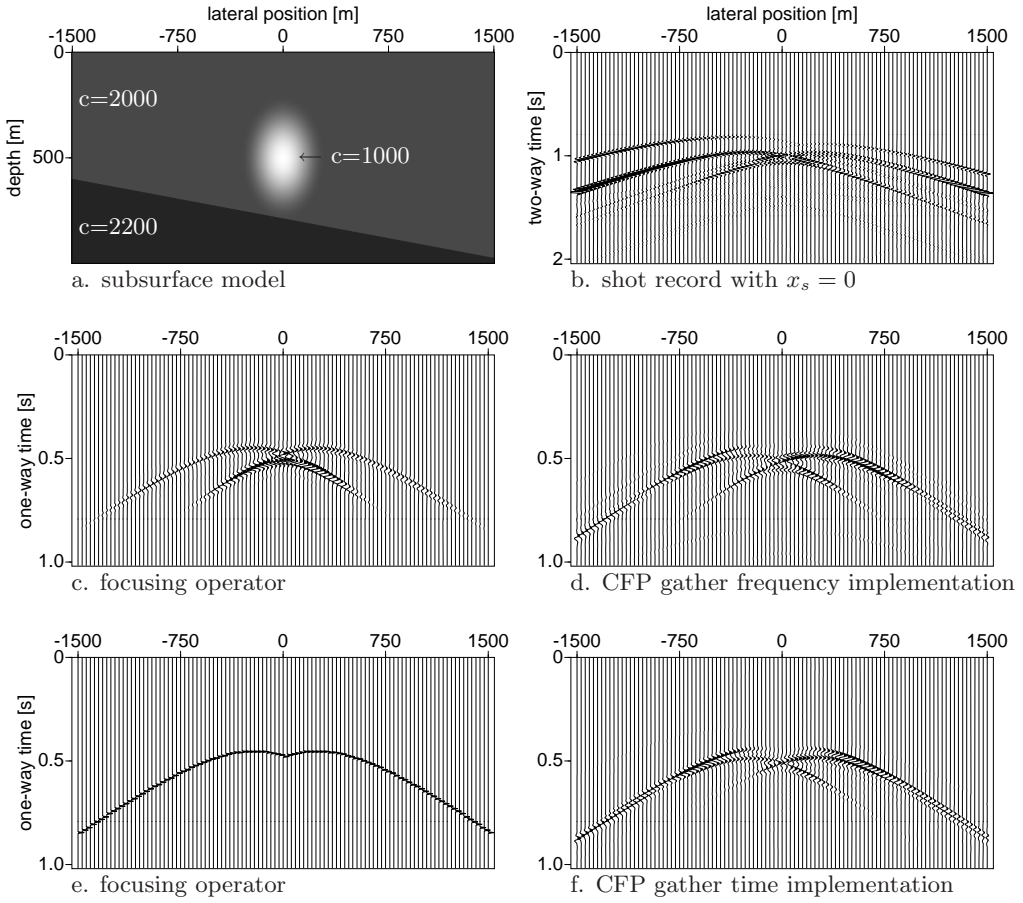


**Figure 7.8** A subsurface model with a velocity 'void' distorts all reflection events below the 'void'.

Note that if the correct model is used there is no big difference in the CFP gather between the frequency and time method.

the different implementations of the CFP method). The focusing operator which is used in the frequency method is shown in figure 7.8c and the operator used in the time-domain scheme is shown in figure 7.8e. Note that the traveltime operator is only defined at the first arrival times. The CFP gather obtained with the frequency method (d) and the time method (f) are, with respect to the first arrival times, not very different. This is an important observation because it means that, at least for this model, first arrival times are sufficient to calculate the focus point response. For the later arrival times the frequency method gives a focus point response which resembles the events in the focusing operator.

In the next example an erroneous initial focusing operator is used to investigate whether the operator updating method from the previous chapter can be used to

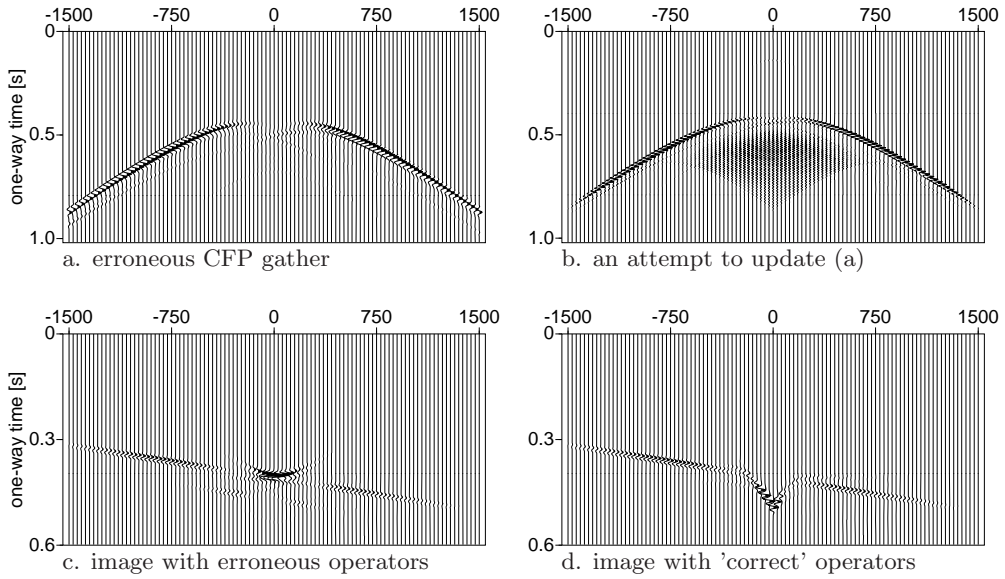


**Figure 7.9** CFP gather constructed with an erroneous focusing operator. Note that updating of the operators will not lead to the correct operators and therefore an incorrect image will be obtained (c).

update the (first) arrival times of the operator. The erroneous operator is calculated for a homogeneous medium with a velocity of 2000 m/s. In the resulting CFP gather, shown in figure 7.9a, it is observed that updating of the operator in the middle part of the model is complicated. In an attempt of tracking the focus point response an error is easily made, therefore the automatic operator updating, by means of a 2-dimensional convolution as explained in section 6.3, is preferred. The updated CFP gather is shown in figure 7.9b and shows only the correct operator times at the sides of the model, the middle of the operator is still not well defined. In the foregoing example it has been shown that for a complicated subsurface model and a complicated focusing operator it is difficult to obtain a correct operator from an erroneous CFP gather. In these difficult situations the user must be able to define, from the erroneous CFP gather, the updated operator times from an interactive display environment. The influence of an erroneous operator on the CFP image quality is shown in figure 7.9c, where a homogeneous model is used for the calculation of the operators defined on the dipping reflector. The image obtained with the 'correct' (only first arrival times) operators is shown in figure 7.9d. From these two CFP images it is concluded that for the defined example the use of erroneous focusing operators is disturbing the quality of the CFP image significantly.

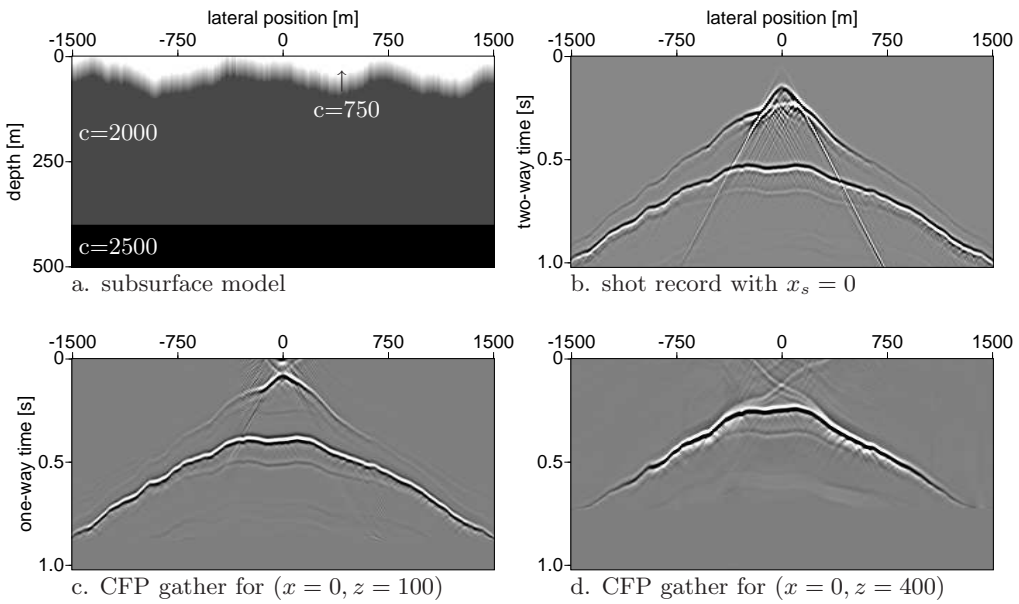


**Figure 7.10** 'Removal' of surface waves (direct wave and dispersive groundroll) by the synthesis process for focus points below the weathered layer. Note the irregular shaped 'hyperbola' of the deeper flat reflector.

#### 7.4 Weathered layer model

The linear events in a seismic shot record, the direct wave and the (dispersive) groundroll, are the low velocity events which are not desired in the CFP gather. To remove these events in a proper way a macro model of the weathered layer should be estimated. It has been shown that by using the areal shot record technology it is possible to estimate an effective weathered layer model which accounts for the propagation properties in the weathered layer (see Thorbecke et al., 1992; Thorbecke, 1994). However, after the synthesis process the linear events have only a small contribution in the relevant part of the CFP-gather due to their low apparent velocities. This is illustrated in figure 7.10. In this example two different focusing operators are used which have their focus points at respectively 100 and 400 meter below the surface. Note that close to the surface of the model a layer with a vertical velocity gradient is used to make the surface waves more dispersive and simulate a weathered layer. A fixed acquisition spread is used with a source and receiver sampling of 10 m and positions at the surface. In figure 7.10c the linear events only have a contribution in the CFP gather close to zero time. If the focus point is chosen deeper, as shown in (d), the effects of the direct wave and the groundroll are shifted to 'negative' times. In this way the linear near surface effects are not disturbing the focus point response.

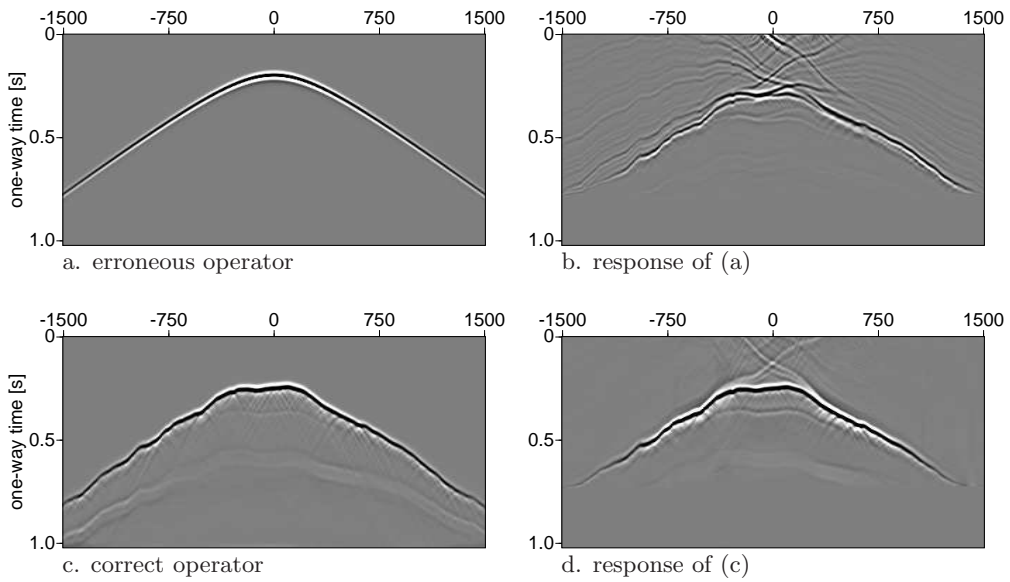


**Figure 7.11** By using the information in the erroneous CFP gather information of the weathered layer disturbances can be obtained. Note that the correct focusing operator contains all the weathered layer disturbances at the receiver side.

The response of an erroneous focusing operator, defined in a model without the effects of the weathered layer, can be helpful in determining the influence of the weathered layer. Comparing the (erroneous) operator and the CFP gather gives information about the propagation disturbances due to the weathered layer (Thorbecke, 1992). An iterative updating procedure of the focusing operator can take all the geometrical propagation effects into account. If the matching of the focusing operator with the selected event (the flat reflector at 400 m depth) is correct then the operator of the deeper layer should come out correctly including the disturbing effects of the weathered layer. The same model as shown in figure 7.10a is used to illustrate the proposed method.

The initial synthesis operator is a pulse response of a source at 400 m depth in a homogeneous medium with a velocity of 2000 m/s as given in figure 7.11a. The CFP gather constructed with this synthesis operator is shown in figure 7.11b. Note the mismatch between the synthesis operator and the CFP gather. This mismatch can be used to iterate to the correct operator. After several iterations the correct synthesis operator shown in figure 7.11c should be obtained, the focus point response is in travel-time identical with the synthesis operator so the second focusing step can be carried out.

In the seismic industry sometimes buried sources are used to avoid the disturbances of the weathered layer at the source side. In this technique the sources are

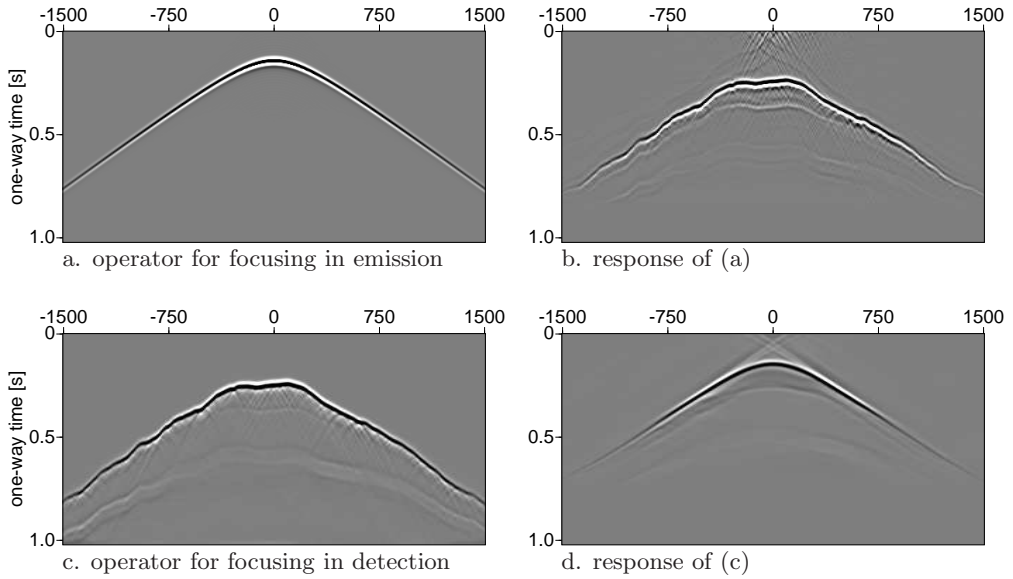


**Figure 7.12** By making use of buried sources the weathered layer influence at the source side is avoided. Note that the difference in depth level between source and detector is clearly visible between the CFP gathers for focusing in emission (b) and focusing in detection (d).

positioned below the weathered layer and only the measured wave field at the surface contains the disturbing influence of the weathered layer. This technique is simulated for the weathered layer model from figure 7.10, where the sources are positioned below the weathered layer (at  $z = 110$  m, which is useful for the defined model but is an unrealistic depth position). The results for focusing in detection are shown in figure 7.12b and for focusing in emission in figure 7.12d. From these results it can clearly be seen that the operator for focusing in emission is in traveltime equal with the focus point response for focusing in detection (and visa versa).

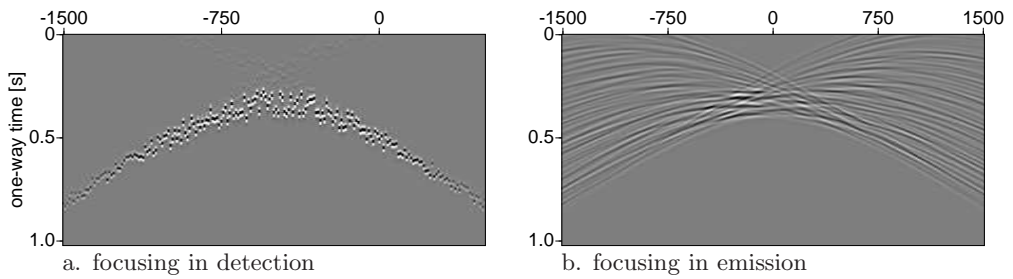


**Figure 7.13** By using a random source depth a very rough weathered layer is simulated. Note the great difference between focusing in emission and focusing in detection.

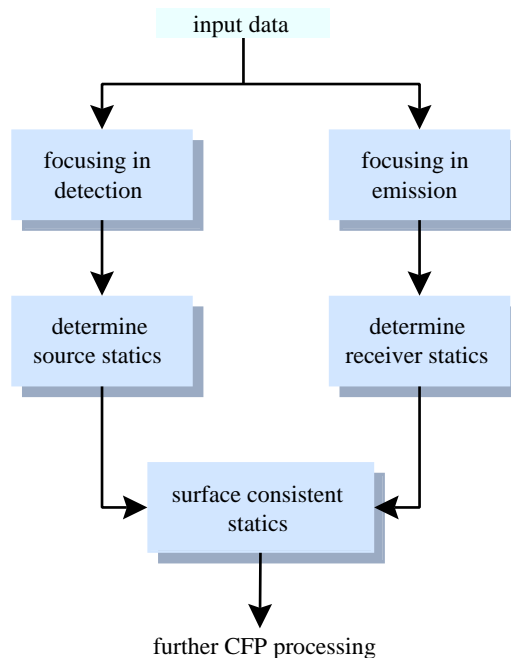


**Figure 7.14** Weathered layer correction by making use of the difference in information content between focusing in emission and focusing in detection.

Note that if the weathered layer disturbances are even stronger as used in the foregoing example then the construction of the CFP gather will fail due to the destruction of the Fresnel zone. This is shown in figure 7.13 where a 'random' depth shift, a maximum depth of 250 m is used to show the effects more pronounced, is applied to the source positions for shot records containing the response of one single reflector. Note that for focusing in emission the Fresnel zone is totally destroyed and the individual contributions of the different common receiver gather is visible in the CFP gather. The CFP gather for focusing in detection show the different static shifts caused by the changing the depth level of the sources. Note that with the aid of this gather is is very easy to obtain the (relative) static shift at the source side. The (relative) static shift for the detectors can be obtained from the CFP gather for focusing in emission result after the source shifts have been determined from the CFP gather for focusing in detection. This idea is shown schematically in figure 7.14.

A wave emitted by a source at the surface propagates down, gets reflected from deeper interfaces and propagates back to the receiver at the surface. It thus travels at least two times through the weathered layer; the first time when it is emitted by the source and the second time just before it is recorded at the surface. These

propagation effects through the weathered layer are of a different kind, after emission at the source position the wave travels to a reflector in the *far* field (related to the weathered layer) in which the wave field has partly recovered from the disturbed influence of the weathered layer. After reflection, the reflected wave field travels upward and close to the surface it has to propagate through the weathered layer again before it can be measured by the receivers. After propagation through the weathered layer the wave field is measured immediately by the receivers, so the receivers measure the *near* field of the weathered layer influence. These assumptions about the propagation behavior of the wave field through the weathered layer explains why the scheme of figure 7.14 can work (Thorbecke and Berkhouwt, 1993).

## 7.5 Syncline model

The syncline model was used in the previous chapter to illustrate the applications of CFP technology. In this chapter the syncline model is used to illustrate the connection with other kinds of illumination techniques. The Vertical Seismic Profile (VSP) is often used to get a more detailed view of the subsurface around the borehole. By using CFP gathers for focusing in detection, for focus points chosen at different depth levels in the subsurface and selecting only one lateral position out of these CFP gathers, a gather can be built up which can be interpreted as a VSP gather. The

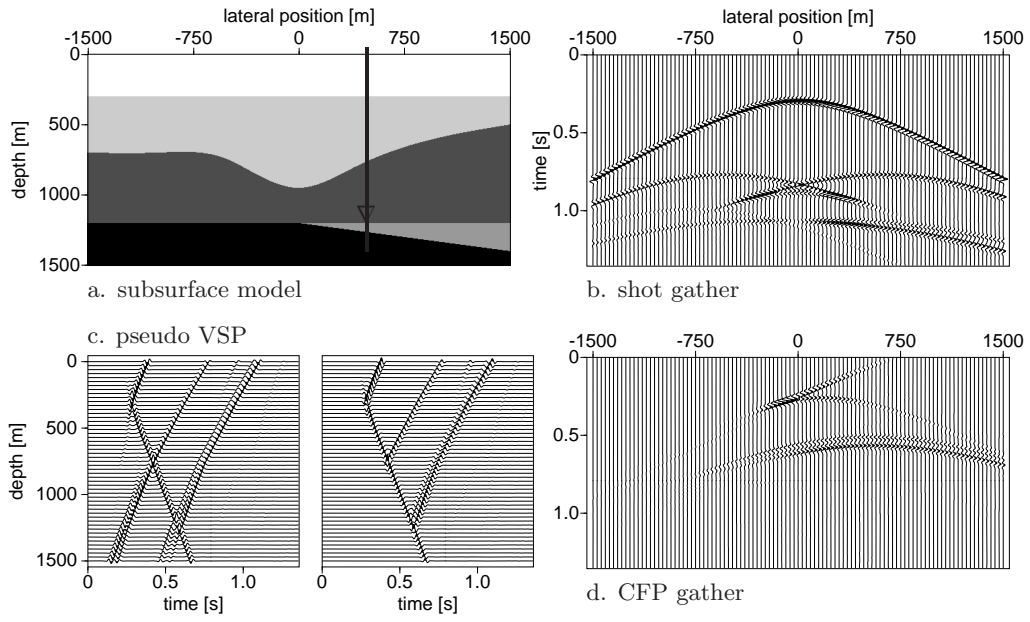


**Figure 7.15** One shot record out of the syncline model is used to generate the pseudo VSP (c). The CFP in (d) has its focus point defined at the indicated position in the model (a).

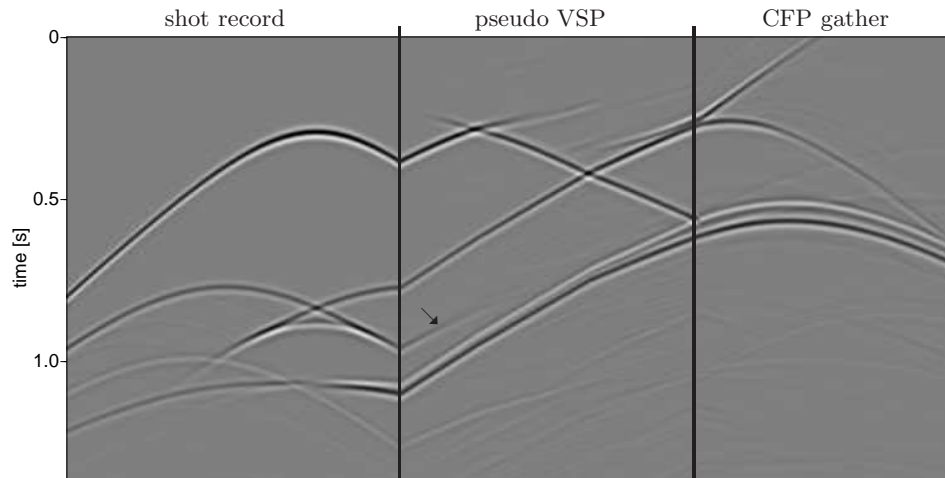


**Figure 7.16** The integration between a shot record at the surface (left part) and a CFP gather (right part) via the pseudo VSP (middle part), for a focus point in the subsurface.

interpretation and use of pseudo VSP data, which is generated from surface data, in the imaging process can be found in the work of Alá'i (1997). Here, the integration with the pseudo VSP gather is shown to give more insight in the illumination aspects of the CFP gather. Figure 7.15 shows the model (a), the shot record (b) used to generate the pseudo VSP (c) and the CFP with its focus point at the indicated position in the model. The right picture in figure 7.15c shows the pseudo VSP after removal of the non-causal events.

Figure 7.16 show the integration between a shot record in the middle of the model and a CFP gather with a focus point at the position  $x = 495$  m,  $z = 1200$  m in the model. The left part of figure 7.16 shows the shot record. At the position of the last receiver,  $x_r = 495$  m, of the shot record a pseudo VSP measurement is simulated by selecting the wavefield at the same lateral position at successively deeper depth levels obtained with an inverse extrapolation algorithm in the space-frequency domain. The last part of the figure shows the CFP gather which starts with the trace at the lateral position of the shot record ( $x_s = 0$  m). The pseudo VSP generation shows that only one branch of the triplication in the shot record, originating from the syncline, is propagated to the depth position of the focus point. The other branch, indicated with an arrow, is slowly loosing its energy for deeper depth levels. The event in the pseudo VSP, which travels from top-left to middle-right represents the propagation of the direct source wavefield to the focus point. The downgoing source wavefield corresponds to the selection of one offset from the focusing operator per depth level. All events above this line represent non-causal wavefields, note that these wavefields are also observed in the CFP gather.

## 7.6 Comparison of imaging results for realistic numerical data

There are several numerical data sets available which are modeled for the purpose of testing the performance of migration algorithms in a controlled way. The Marmousi data set is probably the most well-known data set for that purpose. Recently new modeling results, based on a realistic 3-dimensional velocity model, became available which can be used to test the imaging result beneath a salt dome. Both numerical data sets are used in this thesis to show the strength and limitations of the CFP migration method.

### 7.6.1 Marmousi model

The Marmousi data set of the Institut Français du Pétrole (IFP, Versteeg and Grau (1991)) is generated by using a very complicated geologic model, shown in figure 7.17, and provides a challenge for any migration method, even when the correct velocities are used. The Marmousi dataset was initially set up as a blind test experiment to evaluate the quality of the industries inversion and pre-stack depth migration methods. The data was modeled with a second order (time and space) acoustic finite difference scheme. The acquisition geometry is a marine type of acquisition (end of spread) containing 96 geophone groups, with a minimum offset of 200 m and a receiver spacing of 25 m. The modeled data contained 240 shots which are 25 m separated from each other. The first shot was positioned at position 3000 m in the model (see figure 7.17); the last shot was positioned at 8975 m. A single trace has a

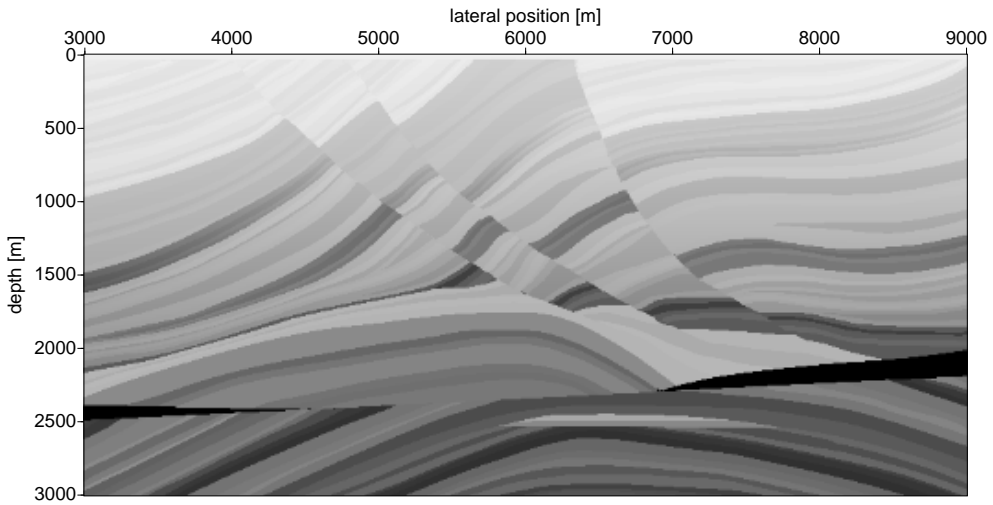


**Figure 7.17** Gray scale representation of a part of the Marmousi model. The potential hydrocarbon reservoir is positioned around  $x = 7000$ ,  $z = 2500$ . Note the complicated structure above the reservoir.

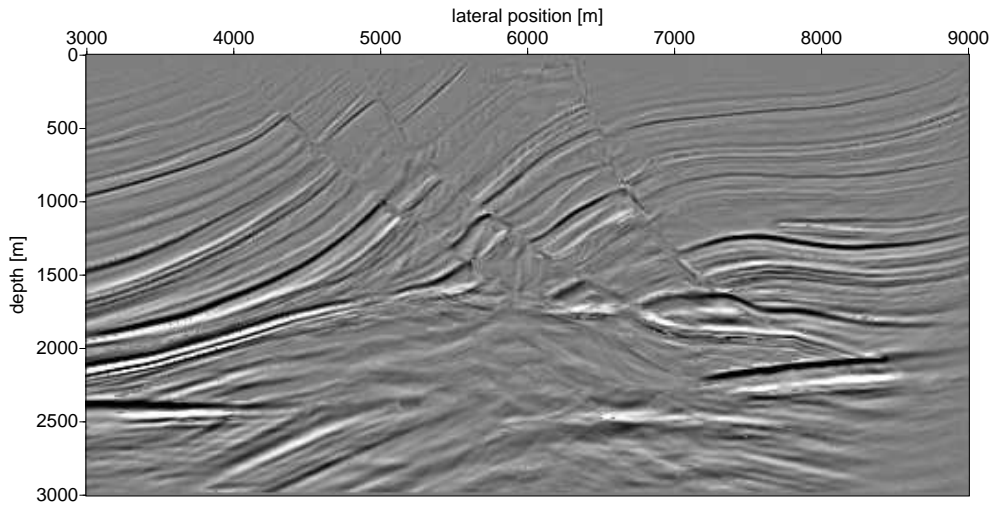


**Figure 7.18** Kirchhoff depth migration of the Marmousi model. Note the poor image quality at the turtle back ( $x = 600, z = 2500$ ) due to the complex overburden.

length of 4 s and a sampling interval of 4 ms. The potential hydrocarbon reservoir is positioned around  $x = 7000, z = 2500$  and can be recognized by the horizontal levels in the turtle-back structure. This objective was modeled as a structural high representing a hydrocarbon-bearing sand with a large acoustic impedance contrast. On top of the reservoir, above the unconformity, a complicated over thrust structure is present. This over thrust structure will distort the wavefields, which are emitted at the surface, at the target zone significantly and are the most important reason why it is difficult to get a good image of the target zone.

The pre-processing for the Marmousi data set was carried out in a two step approach (described in Rietveld, 1995, p. 56) in which the surface related multiples and the thin layer reverberations were removed. The near offsets were interpolated using a CMP interpolation technique. This pre-processed data set, including the interpolated offsets, is used as the input for the different migration algorithms. The migration results shown in this chapter are carried out with three different methods; Kirchhoff depth migration, recursive depth migration and CFP imaging.

### Kirchhoff migration

The Kirchhoff depth migration result shown in figure 7.18 is obtained from the internet and is shown here to be able to make a comparison possible with the other migration methods. The imaged result is obtained with a computational efficient implementation of a 2-D Kirchhoff pre-stack depth imaging algorithm written by Joe Matarese (MIT). The imaging result is obtained by using first-arrival traveltimes for the true velocity model. Note that due to the complex overburden the image quality in the middle of the image, below  $z = 2500$  m, is poor.

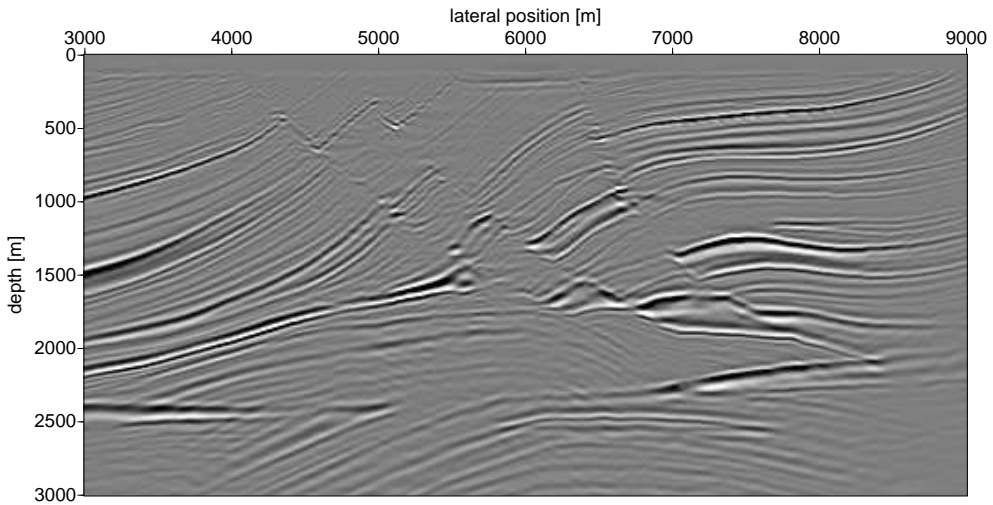


**Figure 7.19** Recursive depth migration of the Marmousi model. The turtle back structure is well imaged, however, due to the presence of shadow zones (e.g. at  $x = 5500, z = 2500$ ) some parts of the model cannot be imaged very well.

#### Recursive depth (F-X) migration

The recursive depth migration is carried out with the WLSQ extrapolation operators as described in appendix A. For the inverse extrapolation of the surface data a depth step of 12.5 m, an extrapolation operator length of 25 points, a maximum design angle of  $65^\circ$  and a maximum frequency of 55 Hz was used. The recursive depth migration result is shown in figure 7.19. In this imaging result the deeper part is imaged very well and the turtle back structure is clearly visible. The great accuracy of the F-X migration makes it a useful standard for comparison with the results obtained from other imaging methods. The F-X migration result clearly shows the faults in the upper part of the model and the image objective; the flat event centered at a depth of about 2440 m at  $x = 6000$ . The better image quality of the F-X migration compared with the Kirchhoff depth migration is due to the fact that recursive depth extrapolation automatically handles energy multi pathing from upper surface points to depth points, while Kirchhoff migration allows a few paths at most (in the result shown in figure 7.18 only one) to connect an upper surface point with a depth point.

#### CFP imaging

For the CFP imaging the time-domain implementation of the CFP method was used (see appendix C) and only the first arrival times of the focusing operators were used. The traveltime operators were calculated by making use of a scheme based on the work of Vidale (1988) and a smoothed version of the original velocity model. For the first focusing step the focus points were chosen at every 50 m starting at depth

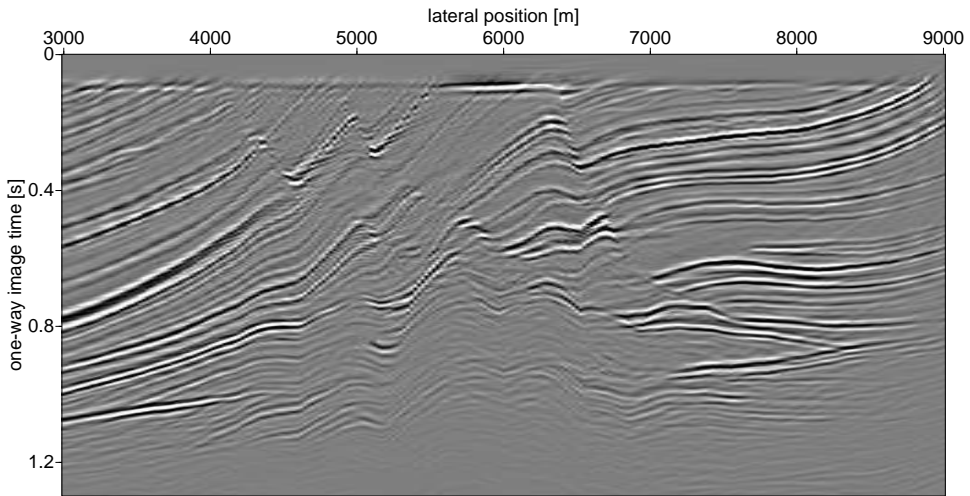


**Figure 7.20** CFP one-way time image of the Marmousi model. Due to the complex overburden the focusing operator for the deeper part of the model are calculated erroneously which results in a distorted image of the layers below  $z = 2500$ .

level  $z = 50$  m, which means that 60 operators are used for every lateral position. A coarser operator grid in the first focusing step gives an inferior result due to the many details in the model. The CFP image in one-way image time is shown in figure 7.20 and the depth image is shown in figure 7.21. Due to the complex overburden the focusing operator for the deeper part of the model are calculated erroneously in the used ray-tracing scheme which results in a distorted image of the layers below  $z = 2500$ . There are several reasons why the focusing operators are calculated erroneously:

- taking only the first arrival times into account can give an operator time which belongs to a ray which travels along a high velocity layer of the model (head wave), this ray contains less energy than the ray traveling through the layers.
- the complex overburden gives rise to timing errors in the travelttime calculation program. Vidale (1988) showed that for certain areas an error of 5-10% is possible.

Geoltrain and Brac (1993) have also argued that it is difficult to image Marmousi with only first arrival times obtained with an Eikonal solver. They have used Kirchhoff depth migration in conjunction with traveltimes computed by finite-differencing the Eikonal equation. Their disappointing results did not originate because of the intrinsic limitations of Kirchhoff migration, but rather from the failure of finite-differencing to compute traveltimes representative of the energetic part of the wave field. The consequence is that energetic seismic events are imaged with an incorrect operator and turn out mis-positioned. The solution for this problem is using a better

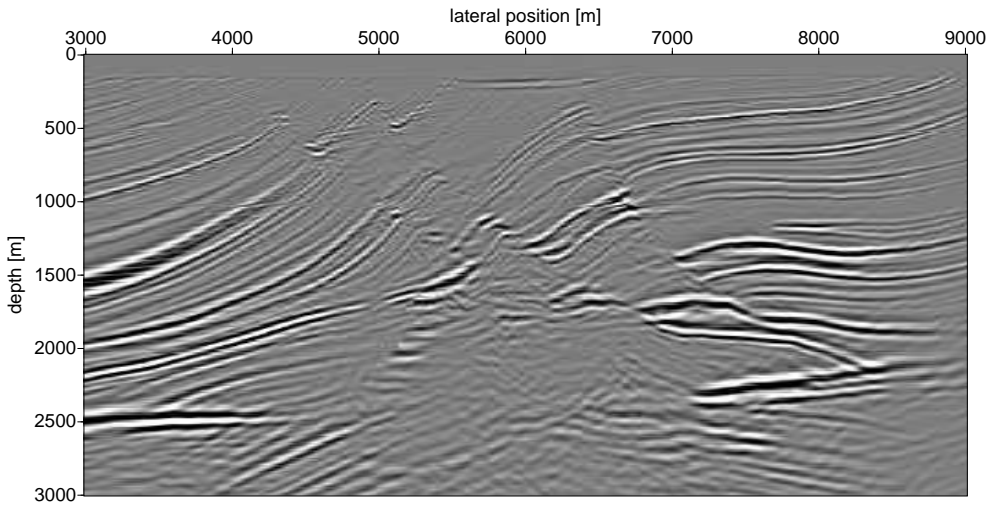


**Figure 7.21** CFP depth image result of the Marmousi model. Note that below  $z = 2500$  the layers in the middle are visible, but imaged at the wrong position due to errors in the used focusing operators.

ray-tracer which calculates traveltimes that correlate very well with the energetic events in the correct focusing operators (Gray and May, 1994).

To investigate the image quality of the result obtained with the CFP method the coherency measurement, as introduced in the chapter 5 page 79, is used; the result of this measurement is shown in figure 7.22. This normalized coherency measurement gives an indication how the different events in the CFP image gathers are aligned before summation to the final image trace. If correct operators are used all events should align and give a high (black in figure 7.22) coherency measurement. The coherency measurement shows clearly where erroneous focusing operators have been used; the middle lower part of the model.

The coherency measurement gives an indication of the alignment in a CFP image gather. In figure 7.23 two image gathers are shown; one for a position at  $x = 4000$  and one for a position at  $x = 6000$  in the model. The gather taken at  $x = 4000$  represent a part of the model which is not very complicated, this is observed in the good alignment of the events in the image gather, meaning that the used traveltime operators described the energetic part of the wavefront correctly. The other image gather at  $x = 6000$ , shows that the alignment of the deeper events is poor, meaning that the first arrival times of the used traveltime operators were not able to describe the energetic part of the wavefront correctly. Note that observed differences in the alignment of the traces in the CFP image gather are well represented by the coherency measurement of figure 7.22

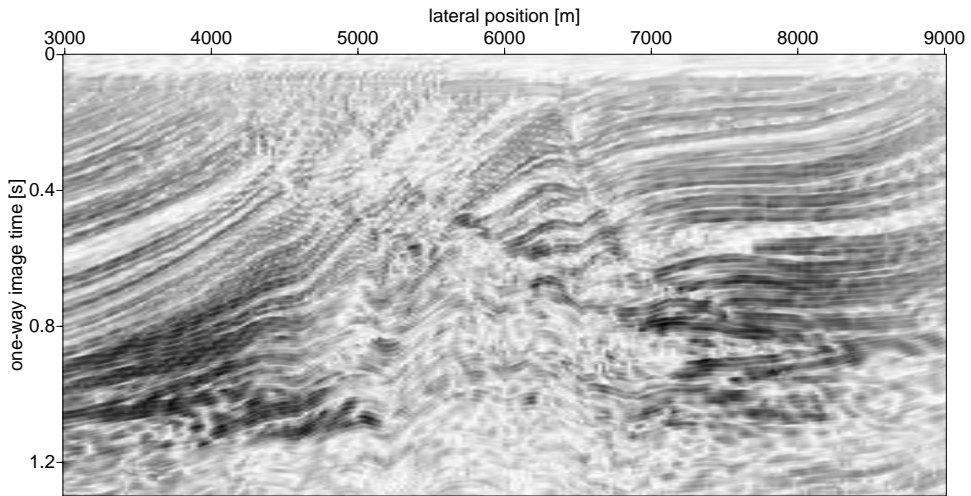


**Figure 7.22** Coherency measurement of the CFP image gathers used in the construction of the one-way time image. In the figure the color black (coherency value of 0.7) means a good coherency and white (0.0) means no coherency. The measurement should be compared with the one-way time image of figure 7.20.

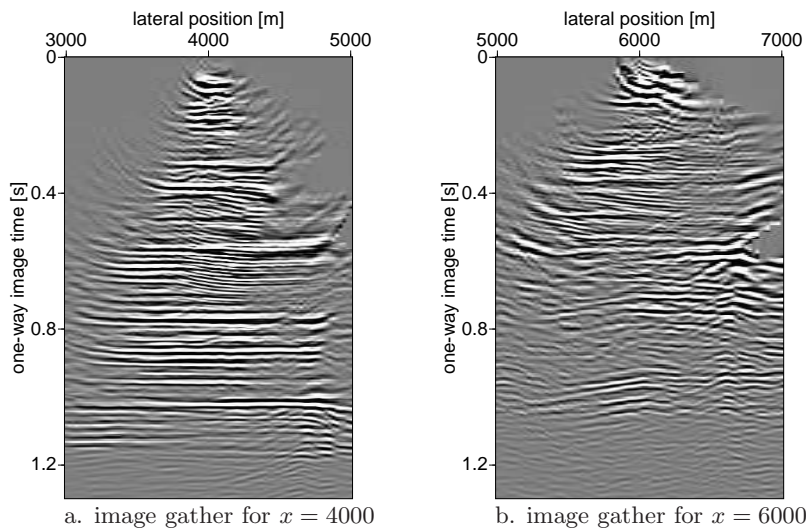


**Figure 7.23** Image gathers for two different lateral positions in the model. The image gather for the less complicated part of the model (a), shows a good alignment of the events. The image gather taken in the more complicated part of the model (b) is not as well aligned.

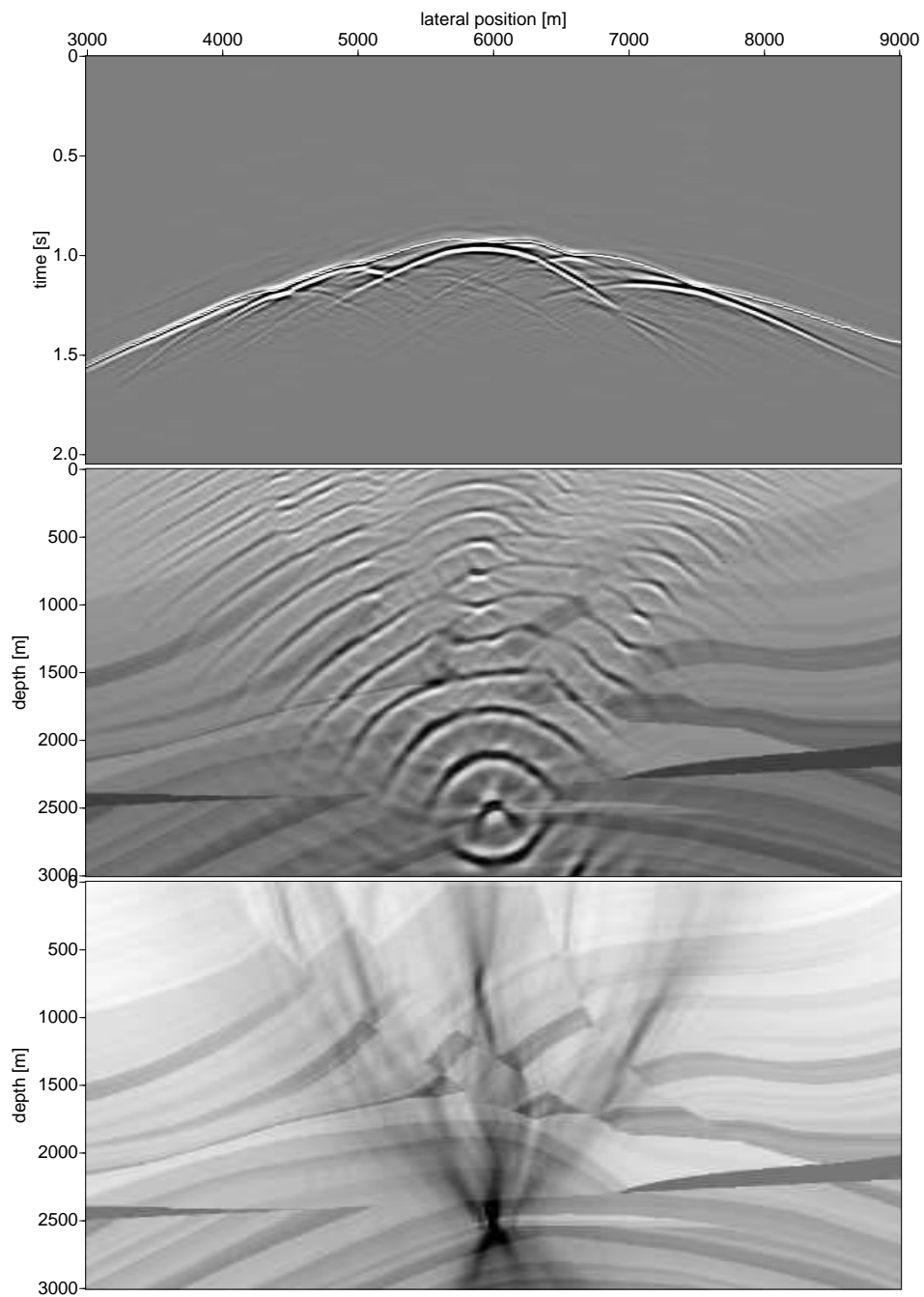


**Figure 7.24** Focusing beam and snapshot for a focusing operator at  $x = 6000, z = 2500$  in the Marmousi model. The used traveltime operators are superimposed as a white line on the top picture.

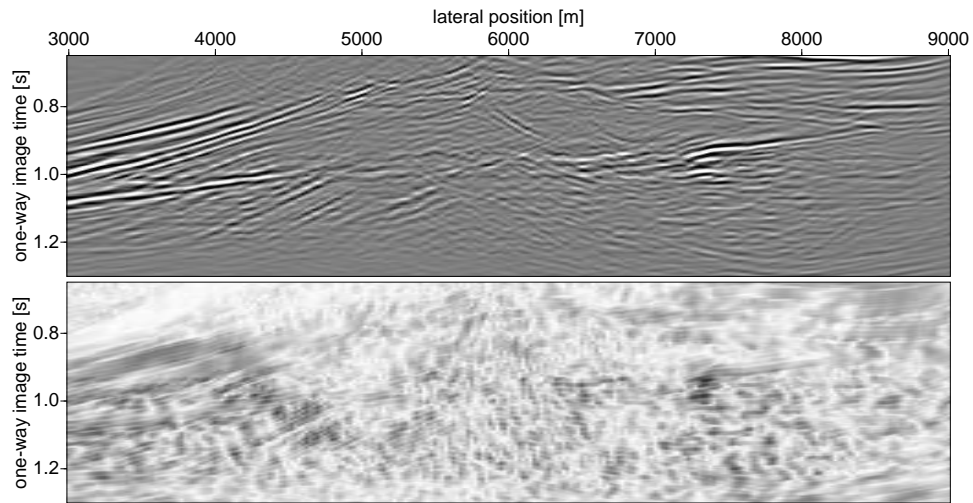


**Figure 7.25** Coherency measurement (bottom) of the CFP imaging result (top) based on operators calculated in a 1-dimensional macro model. Note the low coherency compared with figure 7.22, both coherency measurements are displayed with the same scale factor.

In figure 7.24 a focusing operator together with its snapshot and focusing beam is shown to illustrate how complicated the propagation through the overburden can get. The wavefront at the surface, observed in the top picture, is completely broken due to the propagation through the complex overburden in the model. The beam shows clearly the illumination area for the defined focus point, during the propagation several other areas are focused and de-focused due to the complex structure in the model. To generate the results in figure 7.24 use was made of the extrapolation operators as defined in appendix A. To be able to use time-domain methods the most energetic part of the wavefront shown in figure 7.24 must be approximated in an efficient way by a traveltimes operator. The used Eikonal solver is not designed for this task, which is observed in the white line in the top picture representing the calculated traveltimes used in the imaging.

By using a 1-dimensional model for the generation of the operators the sensitivity of the coherency measurement to a wrong macro model can be tested. In the 1-dimensional velocity model a linear velocity gradient is defined with  $c = 1500$  m/s at  $z = 0$  m and  $c = 3660$  m/s at  $z = 3000$  m. The focus points are only defined for the deeper part of the model from  $z = 2000$  m to  $z = 3000$  m with a depth step of 50 m. The imaged result is shown in figure 7.25. Note that the events are positioned at the same one-way image time as in the result obtained with the correct model (see section 6.4 on page 132), a map in depth will give an erroneous position. The left part of the model is less complicated and gives a reasonable image quality and coherency measurement, however, the middle and right part of the coherency measurement show that the image quality is poor.

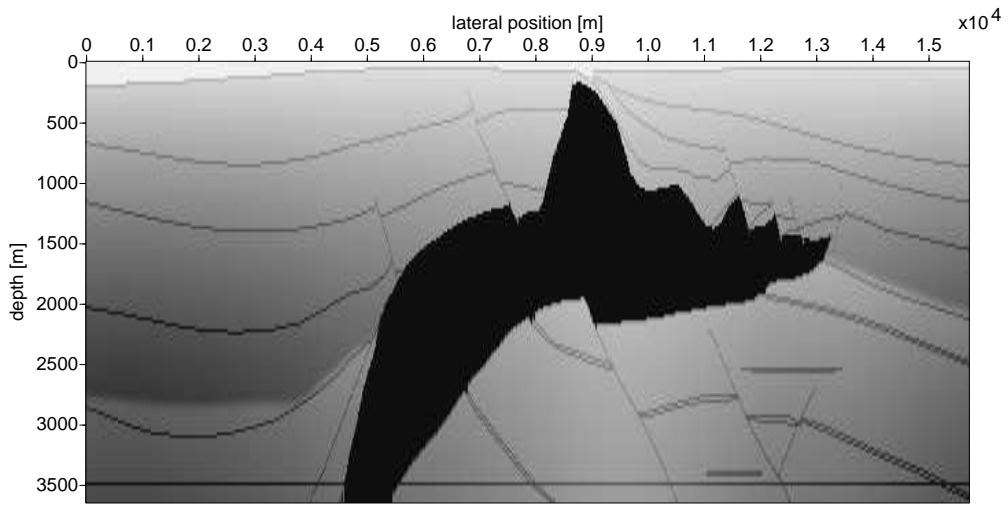


**Figure 7.26** Profile A-A' from the SEG-EAGE salt model crosses many of the more difficult structural elements in the model. For a complete overview of the 3D model the reader is referred to <http://sepwww.stanford.edu/seg/research/3Dmodel/SALTHOME/segsalt.html>.

#### 7.6.2 SEG/EAGE salt dome model

The recently developed SEG-EAGE salt model was built to address data quality issues encountered around the types of salt features found on the US Gulf Coast (Aminzadeh et al., 1995). A part of the modeled data, generated for a 2D slice along profile A-A' of this model (see figure 7.26), has been used by O'Brien and Gray (1996) to compare migration results of Kirchhoff and F-X migration. At this point I would like to thank Mike O'Brien and Walter Rietveld, of Amoco Exploration and Production Technology Group in Tulsa, for providing me with the modeling results along the 2D profile. The modeled data consists of 325 shot records moving from left to right through the model. The first shot has its shots position at  $x = 0$ , and the receiver line belonging to this first shot starts at  $x = -4267.2$  m ( $= -14000$  ft) and ends at  $x = 0$ . The next shot, and its receiver line belonging to it, is positioned 48.768 m ( $= 160$  ft) at the right of the first shot. The receiver sampling interval is 24.384 m ( $= 80$  ft), the time sampling is 8 ms and the maximum frequency present in the data is about 25 Hz. The reflectors in the model are modeled by spikes (with a velocity 120 % of the background velocity) positioned in a smoothly varying background, the salt structure is presented by a high velocity ( $c = 4480$  m/s) area as shown in figure 7.26.

Figure 7.27 shows the zero-offset section extracted from the shot records. The reflections and diffractions related to the salt body are very complicated and are a real challenge for the migration algorithms. In the zero-offset section the base of the salt, and the structures below it, are not clearly visible. A lot of diffraction curves,

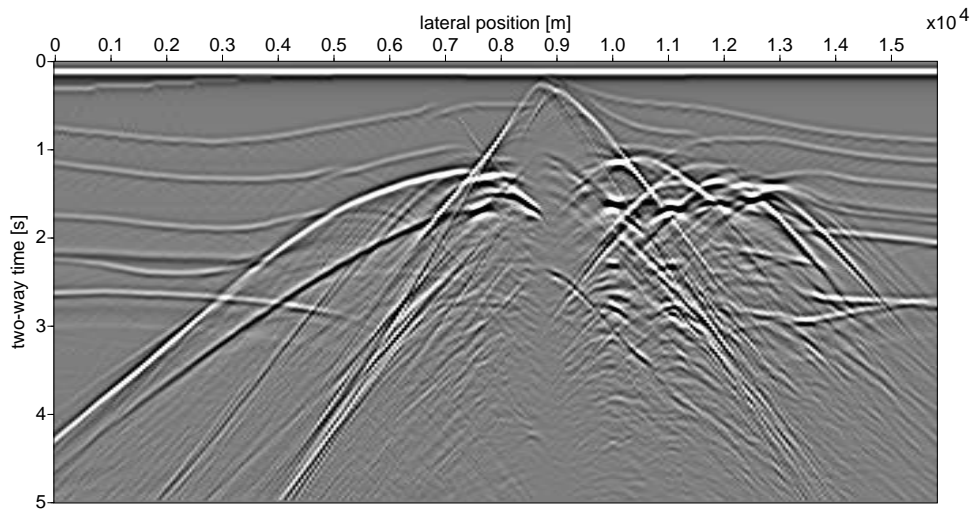


**Figure 7.27** Zero-offset section extracted from the modeled shot records. Note the complicated area right from the salt dome at  $x = 12000$  and  $t = 2.0$ . An exponential taper is used to display the deeper events better.

originating from the high velocity contrast of the salt body, are observed instead.

The CFP imaging result in one-way time is shown in the top picture of figure 7.28 the CFP depth result is shown in the bottom picture of figure 7.29. The CFP images are obtained by placing a focus point at every 100 m in depth, starting at 25 m, for all receiver positions, meaning that in total 38 operators are used for every lateral position. The quality of this image is not as good as F-X migration result due to the problems with the used traveltimes modeling program, which provided the traveltimes for the focusing operators. For a comparison with a Kirchhoff depth migration result the reader is referred to O'Brien and Gray (1996). The coherency plot belonging to the one-way image is shown in the bottom picture of figure 7.28, where it is observed that below the salt body the coherency value is very low, indicating that the used Eikonal operators are not accurate enough.

The top picture in figure 7.29 shows the F-X migrated section. This image is considered as a reference image for the other migration results. The depth step used in the extrapolation algorithm was 12 m. For the extrapolation carried out in the migration the WLSQ operators (see appendix A) were used with a convolution length of 25 points and a maximum propagation angle of 65°. To be able to image energy for the large angles the shot records are positioned into the velocity model with some additional zero-traces (150 traces) added on both sides of the shot record. In this way the data in the shot record is allowed to migrate outside its own acquisition aperture. Below the salt body several structures, like the steep fault planes, are not reconstructed because the energy of these reflectors did not reach the receiver at the surface (due to a limited acquisition aperture or the energy from the steep fault

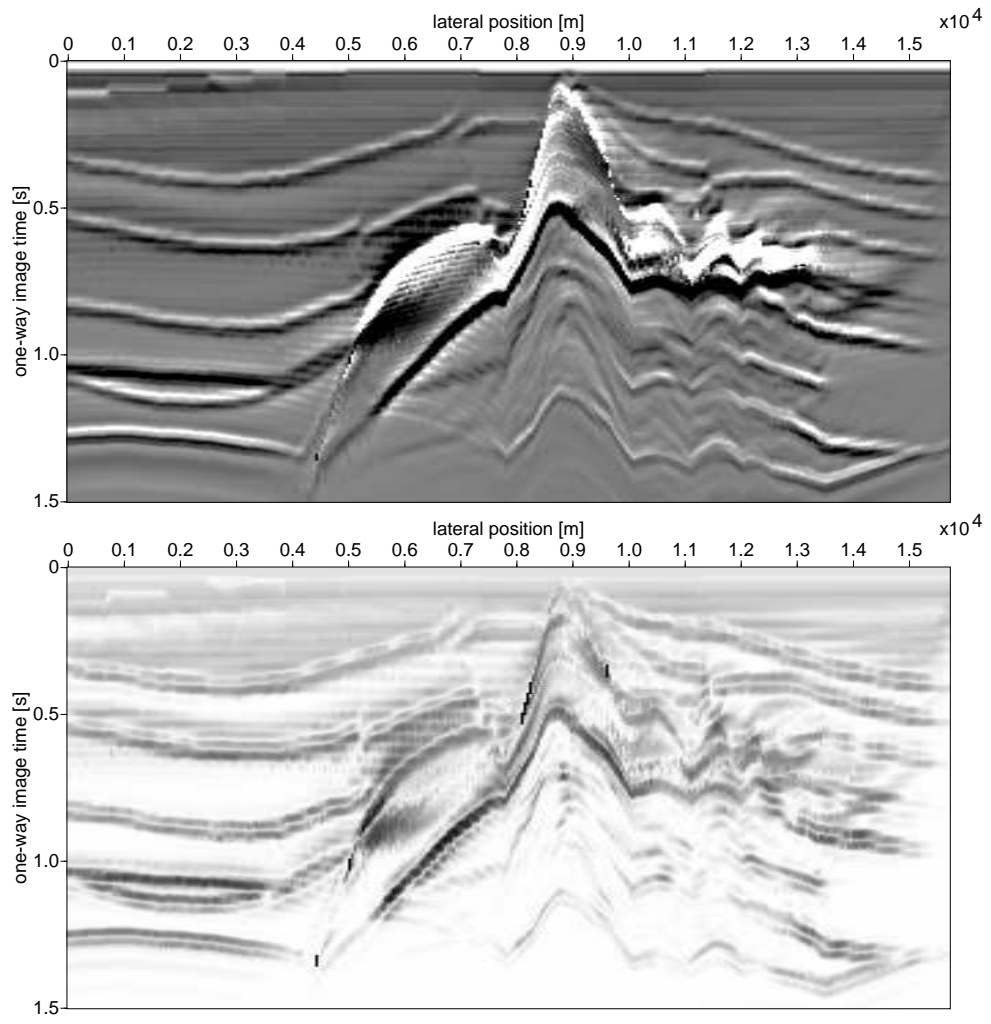


**Figure 7.28** CFP migration result in one-way time (top), the coherency measurement (bottom). In the migration results all the reflectors are visible. The coherency plot shows that the coherency is large at the boundaries in the model, indicating a good alignment of the image gathers. Note that below the salt dome the illumination is poor.

planes was trapped in the model and did not reach the surface at all). Note that the computation time of the CFP image (including the time of the calculation of the operators) is about 10 times faster than the F-X migration.

In figure 7.30 a focusing operator is shown together with its snapshot and focusing beam. The wavefront measured at the surface is not as broken as the operator for the Marmousi model shown in figure 7.24. In the operator picture (top) it is observed that the first arrival times for this operator position (white line) are in most cases

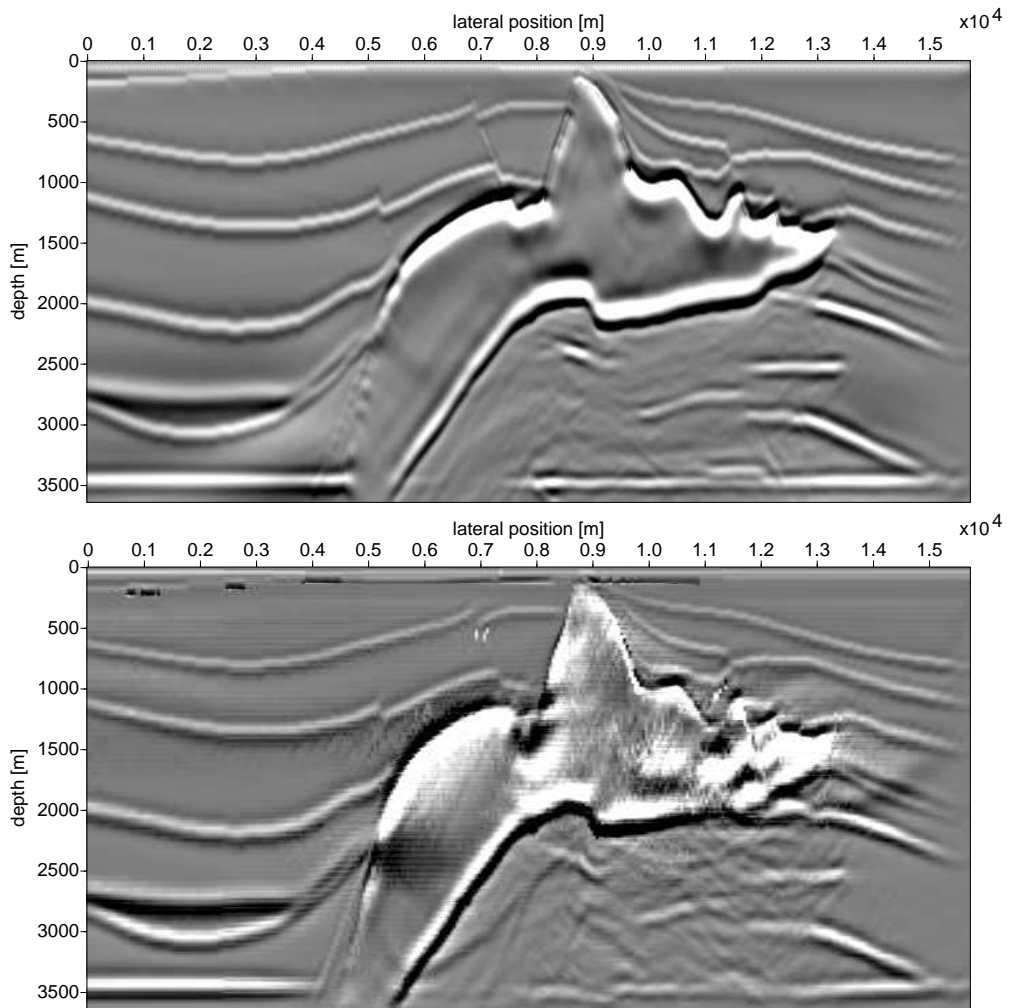


**Figure 7.29** F-X migration (top) and the CFP depth migration (bottom) result of the SEG salt dome model. The flat layers below the salt structure are very well imaged. At the bottom of the image not all the steep faults present in the model are imaged.

time coincident with the wavefront which contains most of the energy. Note that only for the higher offsets on the left-hand side the calculated traveltime deviates from the first arrival times defined by the wavefront. This means that by taking into account only the first arrivals in the CFP imaging algorithm, it should be possible to obtain a good image of the subsurface. The snapshot in figure 7.30 (middle picture) shows how the wavelet is stretched due to the high velocity in the salt dome.

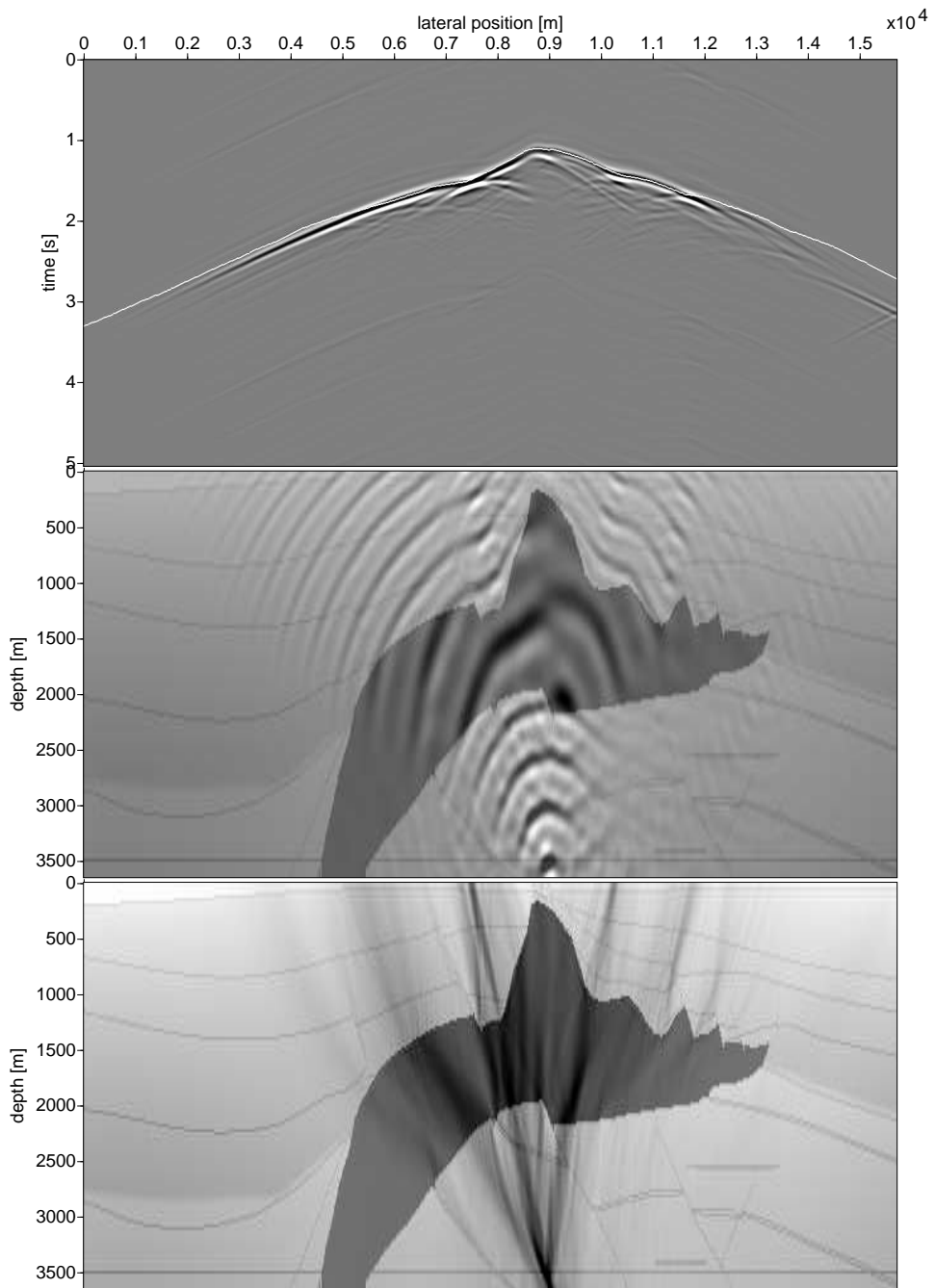


**Figure 7.30** Focusing beam and snapshot for a focusing operator at  $x = 9000, z = 3500$ , below the salt body in the SEG salt model. The wavefront which contains most of the energy coincide for a great part with the first arrivals used in the CFP imaging method.



## Chapter 8

### Field data examples

In this chapter two field data sets, which are shown with the permission of the sponsors of the DELPHI consortium who provided the data, are used to show how the CFP method performs on field data. All field data examples presented in this chapter represent 1-dimensional marine acquisition lines. The first data set discussed is from the Northern part of the North sea and does not contain many complicated structures. The second data set includes the reflection of a salt body, which makes it an interesting data set from an imaging point of view.

#### 8.1 Mobil

The field data set used in this section has been provided by Mobil Research and Development Corporation and has been made available for the purpose of testing seismic inversion methods and comparing them in a workshop. The data set contains marine seismic data and two well log measurements within the seismic line. The data has been acquired above the North Viking Graben in the North Sea and contains an area with hydrocarbon reservoirs. The primary reservoir objectives in the North Viking Graben are Jurassic clastic sediments. The reservoirs in these sediments are sometimes vertically stacked and separated by shales. Hydrocarbon traps are usually fault-bounded structures, but some traps are associated with the unconformity at the base Cretaceous. This unconformity will become visible in the one-way time image at approximately 1.0 seconds.

The seismic line consists of 1001 shot records, oriented in a structural dip direction, each shot record contains 120 channels. The shot point interval and receiver group interval are 25 m. The seismic data were acquired in approximately 350 meters of water, meaning that there are strong surface related multiples present in the data. To remove these surface related multiple the method of Verschuur et al. (1992) was used.

For the imaging, the shot numbers 354 to 1053 have been selected, with 1024 samples

per trace. The pre-processing steps carried out on these shots consists of

- direct wave mute.

The direct wave is muted out of the data because it does not contain any information of the subsurface of the earth.

- 3D to 2D spherical correction.

A simple gain has been applied to simulate line source instead of point source responses. After this correction 2-dimensional processing schemes can be used.

- replacing bad traces.

The bad traces were removed from the shot record and re-interpolated from the good traces using rough NMO correction and spline interpolation. The tradeoff being made here is that the influence of a bad trace on the image quality is considered to be much worse than the influence of an interpolated trace.

- wavelet deconvolution

A predictive deconvolution has been applied with a gap of 20 ms and a filter length of 240 ms. This deconvolution is applied to get a better multiple removal in the next processing step.

- receiver sensitivity correction.

The receivers showed a consistent sensitivity behavior through the different shot records. Least-squares inversion techniques were used to correct these amplitude fluctuations. The fluctuations present in the sources have been left in the data. Unbalanced traces give rise to a lower quality of the image.

- interpolation of missing shots and near offsets.

Application of the surface-related multiple elimination method requires a full coverage of the shot and receivers up to zero-offset. In the selected shot range 6 shot records were missing, and have been inserted and interpolated in the common offset plane. Approximately 10 near offset traces were missing in each shot. They have been created by using the parabolic Radon transform to extrapolate the data to zero-offset in the CMP domain (Kabir and Verschuur, 1993). These interpolated traces are not used in the imaging.

After these basic pre-processing steps the multiple elimination step has been carried out. The surface related multiple elimination method is based on wave theory. Verschuur et al. (1992) have proven that by taking temporal and lateral auto-convolutions of seismic data, an accurate prediction of the surface related multiples can be obtained. Subsurface information is not needed, but information on the free surface reflectivity (assumed to be -1 for marine data) and the source wavefield is required. As the latter is not known in practice, the method is applied adaptively: by eliminating the multiples the source signature is estimated as well.

An initial macro model was estimated with the areal shot record technology as

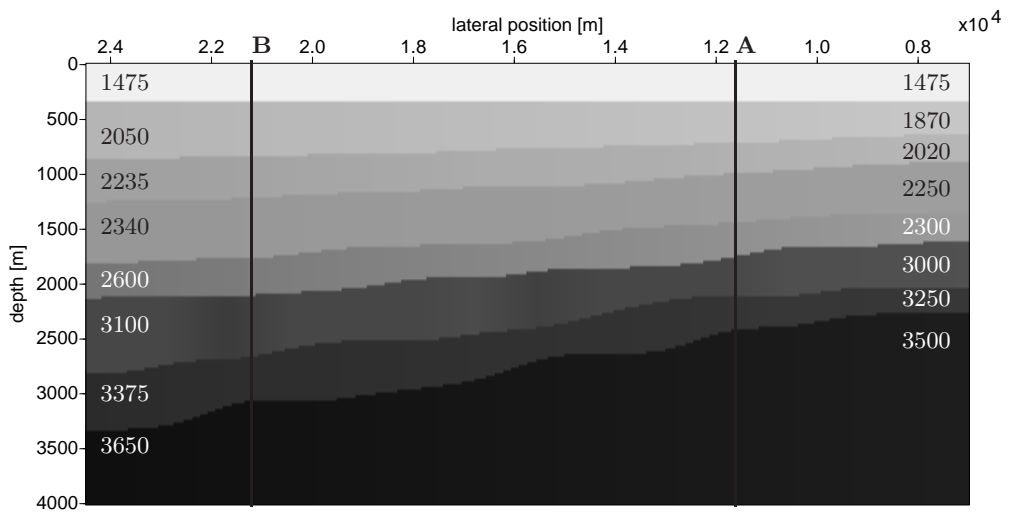


**Figure 8.1** The estimated macro model for the Mobil data set. The line indicate the positions of the wells, indicated with A and B, where the CFP analysis is done.

proposed in Rietveld and Thorbecke (1994). Last year (1996) this macro model was updated by using the CFP move-out analysis (Kabir and Verschuur, 1996). The updated estimated macro model consists of seven macro layers as shown in figure 8.1. By using the same technology for the estimation of the macro model and the imaging, the macro model estimation and the imaging are closely connected to each other and model errors observed in the construction of the image can be directly used to update the macro model.

The data set contains two well positions, indicated in figure 8.1, within the seismic line. The CFP analysis presented in this chapter is concentrated on these two well positions. For a first analysis focusing beams are calculated for focus points at every macro boundary below the two well positions A (at position  $x = 11700$  m) and B (at position  $x = 21250$  m). In figure 8.2 the focusing beams and the focusing operators are shown. The beams show the focusing of energy, for the different synthesis operators, at the defined macro boundaries. Note that in between the boundaries the illumination energy will not be sufficient to image the events in between the boundaries correctly. So for a good second focusing step more operators are needed as used in figure 8.2. The combination of beams also show that close to the surface the energy in the beam is reduced due to the used extrapolation operator and the energy for the deeper part of the model is reduced due to the limited aperture range of the acquisition. For a better analysis of the illumination energy different beams were calculated where the distance between the focus points was changed. From these experiments it is concluded that for  $\Delta z = 150$  m a sufficient illumination of the subsurface is obtained.

An X-gather is defined at the position of well A and is constructed with synthesis

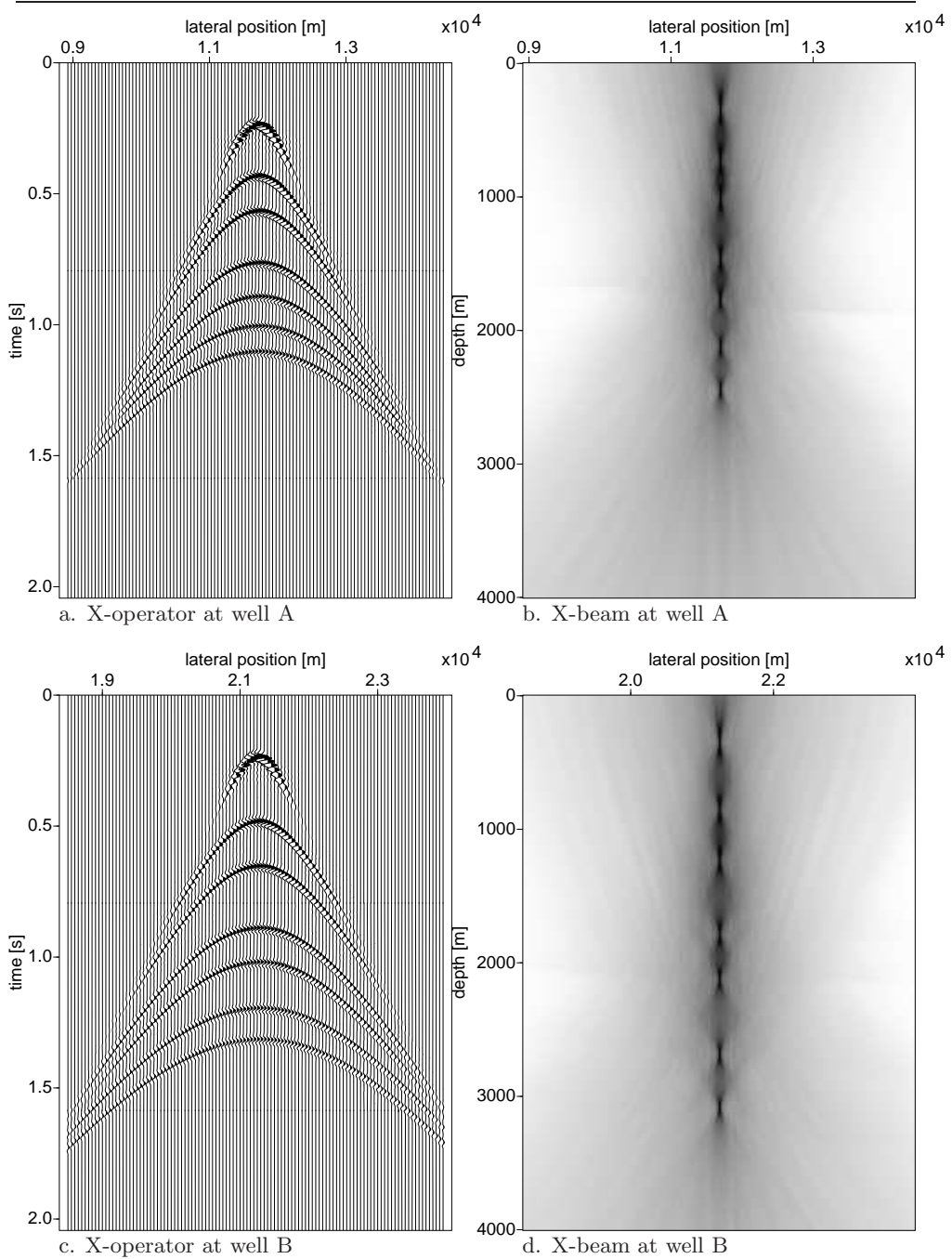


**Figure 8.2** Focusing operators and focusing beams for focus points defined at every macro boundary at the lateral position of the wells. The information in the beams is used to determine the focus point density in the first focusing step.

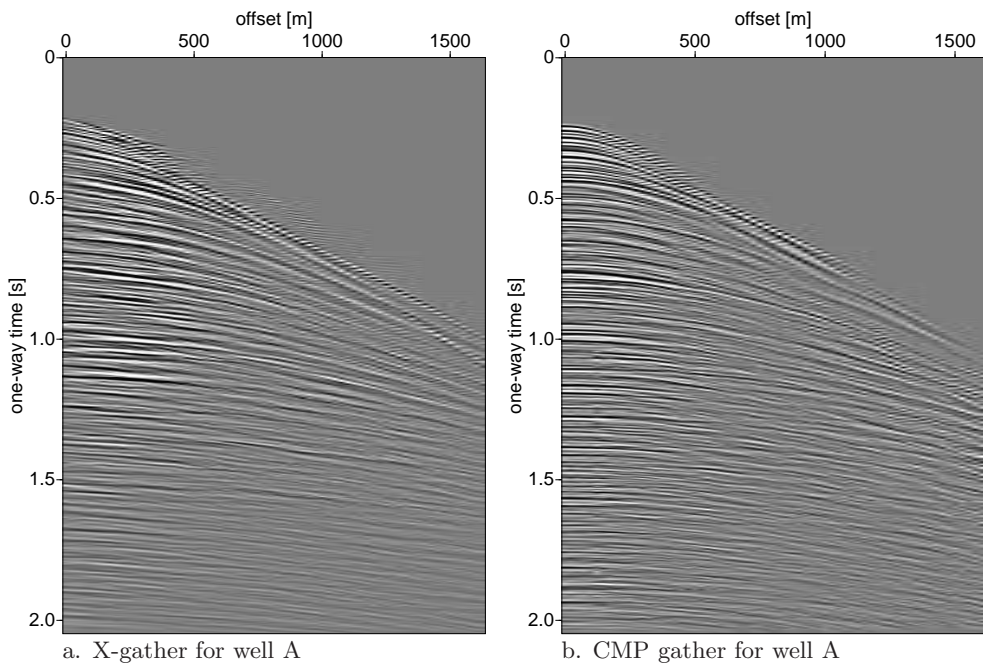


**Figure 8.3** *X-gather and CMP gather at the position of well A. Note that the first 10 traces in the CMP gather are interpolated traces.*

operators defined for focus points with a sampling rate of  $\Delta z = 150$  m ( $\Delta T \approx 150$  ms). Figure 8.3 shows the X-gather and the CMP gather defined for the same lateral position. The CMP gather is displayed with the same time sampling and offset range as the X-gather. Note that the first 10 traces (until offset 250 m) in the CMP gather are interpolated traces, the X-gathers are constructed without the interpolated traces. In figure 8.3 it is observed that for the higher offsets the X-gather shows more continuous events than the CMP gather. The two main differences between the CMP gather and the X-gather are: ① the CMP gather has its mid-point defined at the *surface*, while for the X-gather the focus points are defined at different depth levels in the *subsurface* at the same lateral position. ② the traces in the X-gather are constructed by means of a *synthesis* step and are the result of a Fresnel summation, the traces in the CMP gather are *selections* from the traces of the shot records.

The constructed X-gathers are the input for the second focusing step. In figure 8.4 for both well positions A and B the move out corrected X-gathers (CFP image gathers) are shown with focusing operators defined at every 50 ms of the one-way image time. The interpolated traces are not used in the calculation and an overlapping area of 10 sample points is used between two adjoined CFP gathers. In the CFP image gathers the good alignment of the events is observed. Note that for the shallow part more

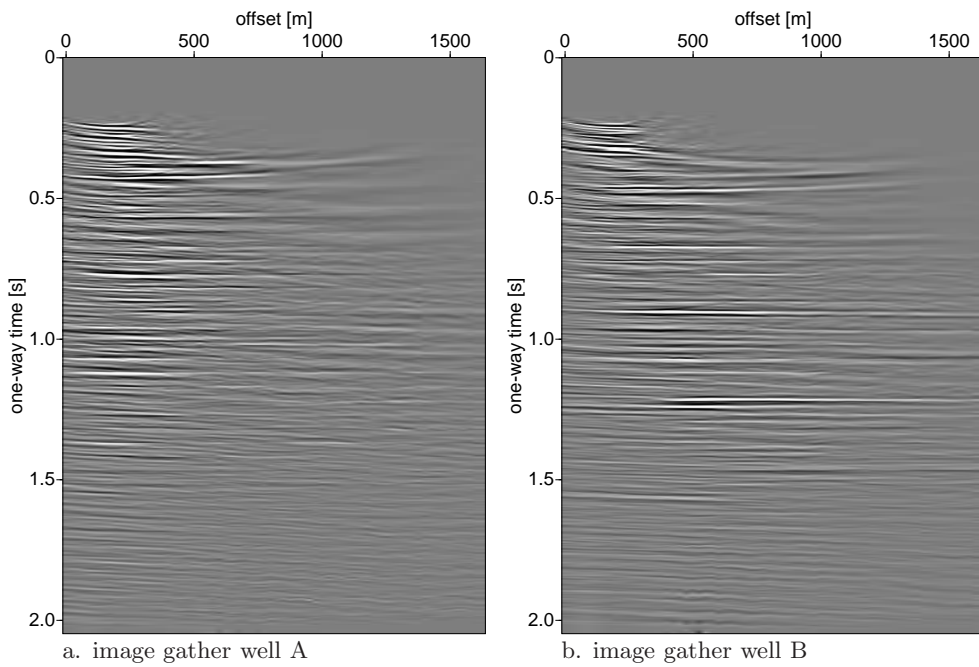


**Figure 8.4** CFP image gather at the positions of well A and well B where at every  $\Delta T = 50$  ms a focusing operators is defined for the first focusing step.

operators are needed than for the deeper part. It is therefore more efficient to use operators which are differently sampled in one-way image time; dense sampled close to the surface and more sparsely sampled for the deeper parts. However if one is only interested in the deeper parts of the image the focusing operators at the surface need not to be calculated at all.

The CFP migration result is shown in figure 8.5. The migration result is obtained with synthesis operator sampled with approximately 80 ms in single vertical time, which is equivalent with a depth step of  $\Delta z = 150$  m. Due to the tube like shape of the focusing beams this focus point sampling in the first focusing step is sufficient to obtain a good image of the subsurface. To build the one-way time image a total of 19896 operators were used in the first focusing step (24 per lateral position for 829 lateral positions). The interpolated near offset traces are not used in the imaging step, because these artificial traces give a strong disturbing contribution to the final imaging result.

The image shown in figure 8.5 shows an unconformity at 1.1 seconds. Above the unconformity the layers are well imaged and there are some overlapping structures visible below  $x = 22000$  m at 0.6 seconds. Below the unconformity several block structures, for example at  $x = 13000$ ,  $t = 1.2$ , are present. These block structures could contain hydrocarbon reservoirs.

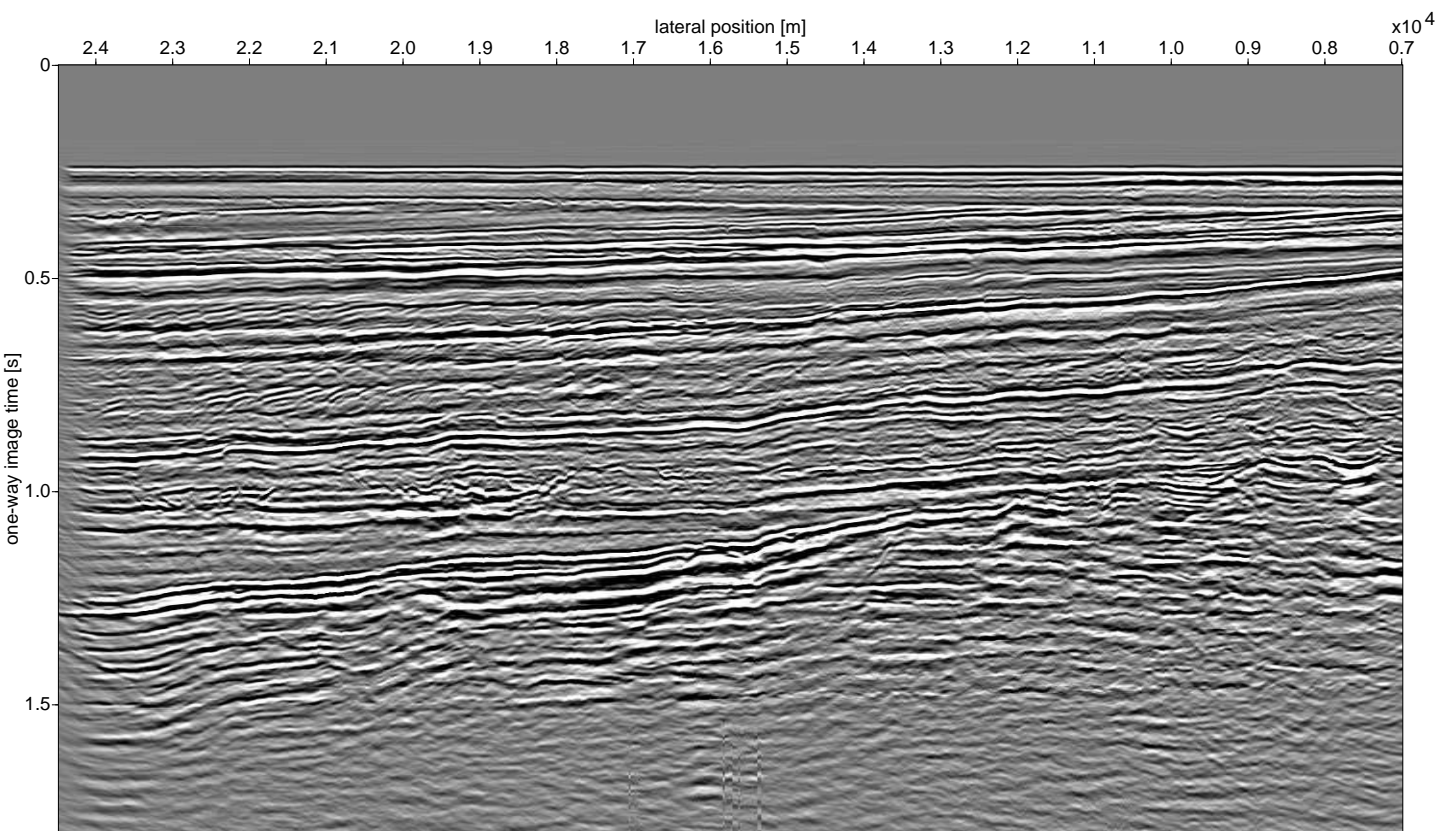


**Figure 8.5** Prestack migration result obtained with CFP migration method. Note that only a limited number of operators is used in the first focusing step to construct the complete image:  $\Delta T = 80$  ms. An exponential gain in the time-direction was used to amplify the weaker events in the image.

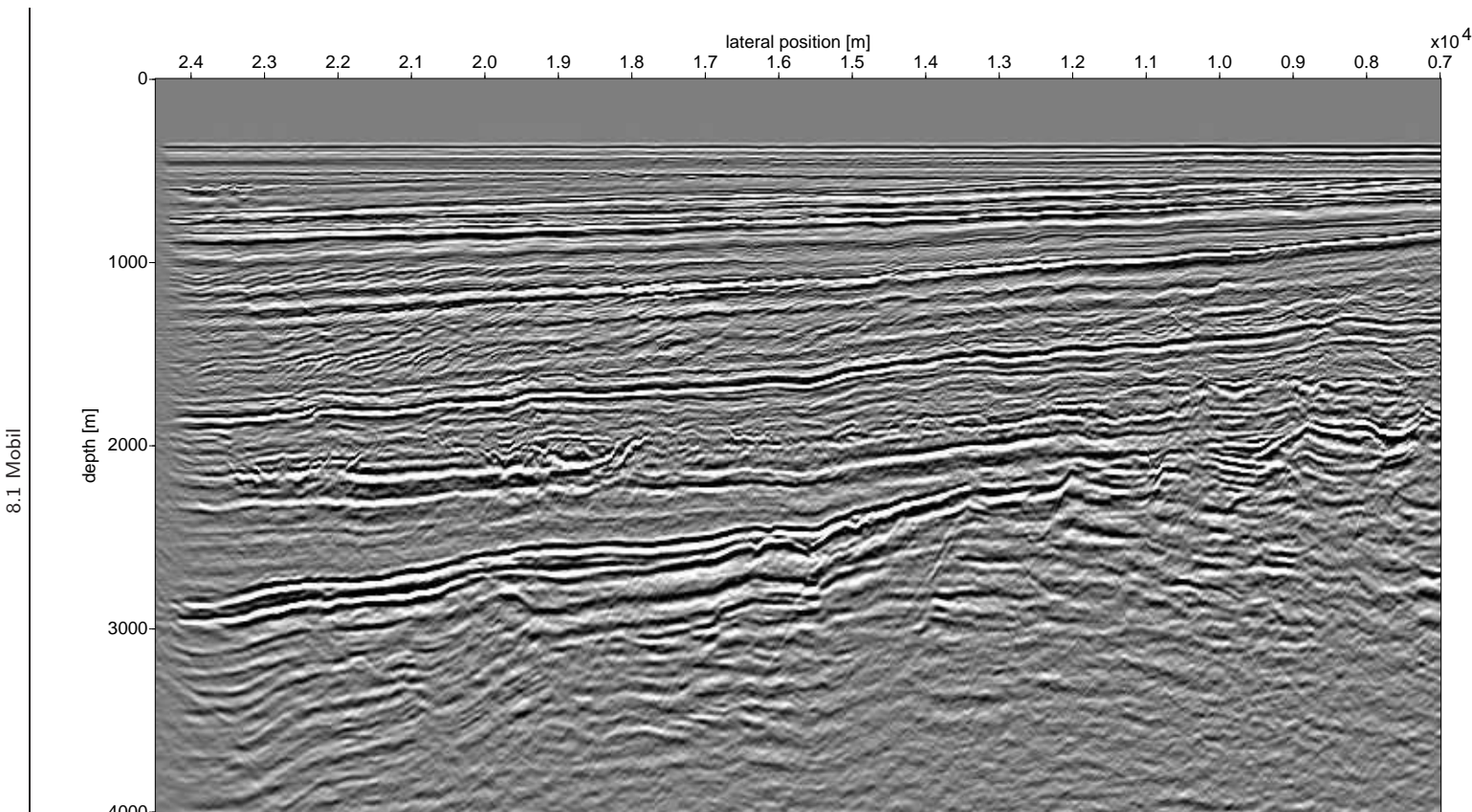


**Figure 8.6** Prestack depth migration result obtained with recursive F-X migration. The depth step in the recursive extrapolation was chosen 10 m and the WLSQ extrapolation operators, as discussed in appendix A, were used.

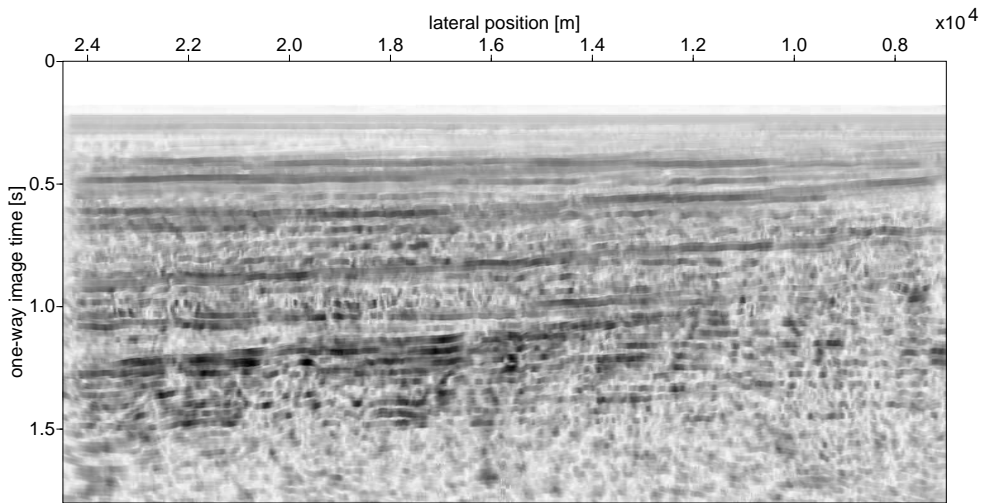


**Figure 8.7** Coherency measurement of the one-way time image. Black indicates a high coherency, meaning that the event in the CFP image gather is well aligned.

The F-X migration result is shown in figure 8.6, here the same kind of structures, as in the one-way time image, are observed. However there are also some differences; just above the unconformity, from  $x = 16000$  to  $x = 23000$ , the one-way time image seems to have resolved the structures better. Below the unconformity the F-X migration shows the blocks better, but with field data it remains difficult to tell which image is the best.

Figure 8.7 shows the coherency measurement of the image shown in figure 8.5. In the coherency measurement it is observed that the layers close to the surface can be imaged better by making use of a denser sampling in depth for the focus points in the first focusing step. Below 1.5 seconds the alignment in the image gathers is poor, indicating wrong focusing operators, a low signal to noise ratio or the absence of a reflector. Figure 8.8 shows the steps to be taken to extract reflectivity information for one focus point. First a CFP gather is calculated for the focus position of interest. The quality of this CFP gather is checked by means of a move-out panel, if the event aligns at  $t = 0$  then the used operator gives a good description of the propagation properties. If the panel does not indicate a good alignment the operator needs to be updated until a good alignment in the move-out panel is the result. In the panel shown in figure 8.8b it is observed that there is a reflection event below  $t = 0$  s which is flat, indicating that the used focusing operator is not perfect. Next a 2-dimensional cross-correlation between the CFP gather and the focusing operator can be carried out to obtain the reflectivity gather as shown in figure 8.8c. Around  $t = 0$  and  $x = 0$  this reflectivity gather contains the reflection information of the defined focus point measured at the surface. Using a  $\tau - p$  transformation on this part of the reflectivity gather gives the reflectivity function of the focus point in terms of the ray-parameter shown in figure 8.8d.

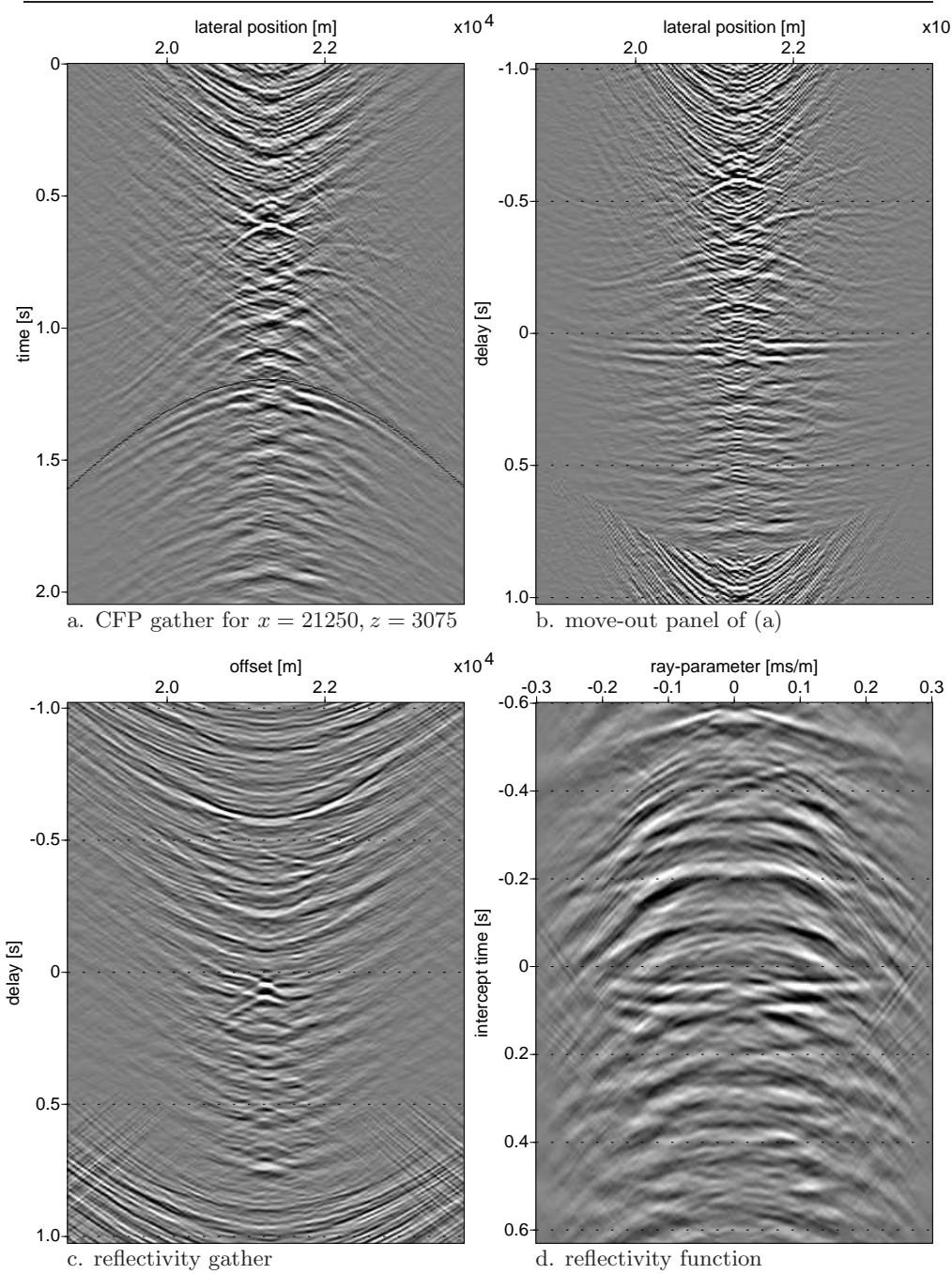


**Figure 8.8** The gathers involved in the calculation of a reflectivity function for one point in the subsurface. The analysis is carried out for a focus point at the position of well B at a depth  $z = 3075$  m.

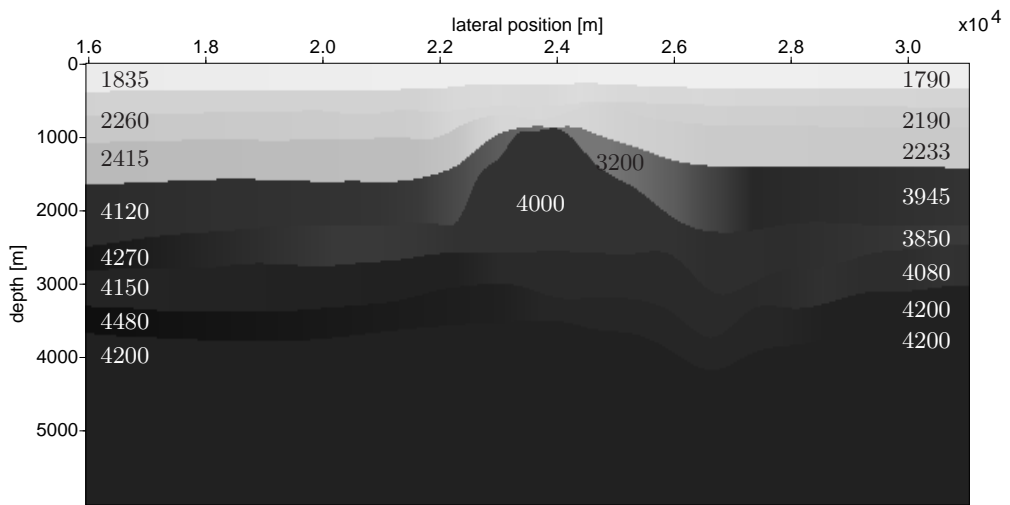


**Figure 8.9** The estimated macro model for the ELF data set. The model consists of 7 layers which are estimated by making use of CFP move-out panels.

## 8.2 ELF

The data used in this section was originally owned by ELF and has been made available by Institut Français du Pétrole (IFP) for the use in the Integrated Structural Imaging project (ISI project) of the Joule II program of the European Committee. Below the acquisition surface a complicated salt structure is present which is probably triggered by faulting of the basement. The left flank of the salt structure can be an overhang and is an interesting area for imaging. The marine line used in this thesis is one out of two streamer lines of the same shot acquisition. The used line contains 378 shot records with an offset range from -187.5 m (trace 1) to -3362 m (trace 120). The receiver spacing is 26.66 m, the shot spacing 40 m and every trace contains 1250 samples sampled with 4 ms. The first shot position starts in the model at position 16020 m and the last shot position end at 31100 m. The macro model shown in figure 8.9 is used in the recursive depth migration and for the modeling of the focusing operators used in the CFP migration. The model consists of 7 layers which are estimated by making use of CFP move-out panels (Kabir, 1997).

As a first experiment on this data set CFP gathers are constructed for positions left and right from the estimated position of the salt structure. In figure 8.10 move-out corrected CFP gathers are shown with a focus point defined at a depth of 2500 m in the macro model (approximately 1 second one-way image time) for  $x = 22000$  m. The difference between the two CFP gathers shown in figure 8.10 is that the left CFP gather is constructed for focusing in detection and the right one for focusing in emission, but both gathers are defined for the same focus point. For focusing in detection the move-out corrected CFP gather is constructed at the source positions

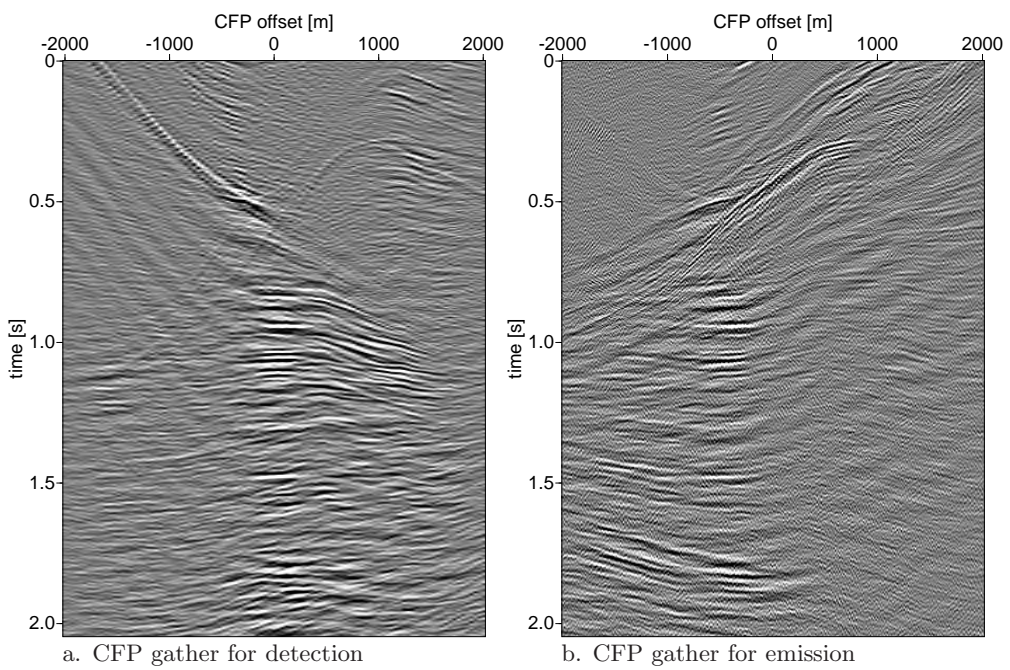


**Figure 8.10** CFP gathers for a position left of the flank of the salt dome ( $x = 22000$  m). Figure a shows the CFP gather for focusing in detection and b shows the CFP gather for focusing in emission.

with a sampling interval of 40 m. Note that due to the used acquisition geometry flat events should occur at positive CFP offsets. Any events occurring at the negative offsets indicate the occurrence of non flat reflectors. The CFP gather for focusing in emission, sampled at the half of the receiver sampling, 13.33 m, shows the alignment of the events at the negative CFP offsets. At this side of the flank of the salt structure it is not expected that with the used acquisition geometry much information is measured from the flank of the salt structure. Note that the difference between the two gathers is that for focusing in emission the remaining traveltime is defined from the focus point to the receiver position at the surface, while for focusing in detection the remaining traveltime is from the focus point to the source position. Note also that for the construction of one trace out of the CFP gather for focusing in detection 120 traces (receivers per shot position) are used while for focusing in emission only 40 traces (sources per receiver position) are used.

Choosing a focus point on the other side of the flank of the salt structure, at  $x = 26000$  m and  $z = 2500$  m, it is observed in figure 8.11 that the CFP gathers contain more information about the right side of the salt structure. This information is clearly visible in the CFP gather for focusing in emission at the positive offsets. By choosing more focus points on this side of the flank and combining the information in the calculated CFP gathers a good image can be obtained from the flank of the salt

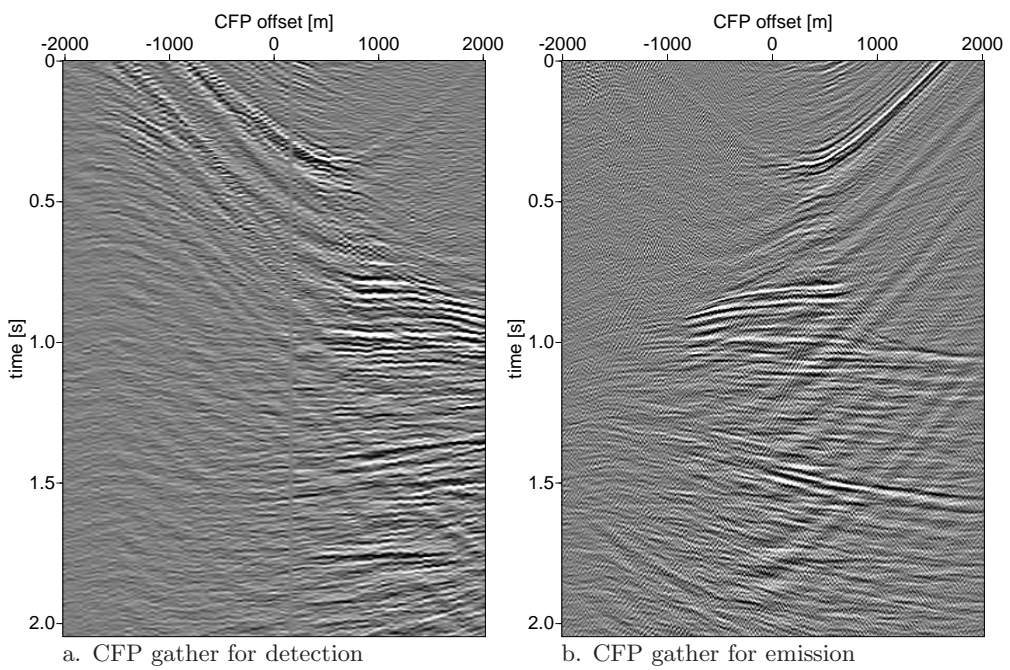


**Figure 8.11** CFP gathers for a position right of the flank of the salt dome ( $x = 26000$  m). Figure a shows the CFP gather for focusing in detection and b shows the CFP gather for focusing in emission.

structure as shown by Alá'i (1997). Note that due to the sampling of the sources at 40 m, the construction for focusing in emission is done with a relative large sampling interval, giving rise to aliased results.

The image result of the recursive pre-stack depth migration, with a depth step of 10 m, is shown in figure 8.12. In this image the right flank of the salt structure is visible, the left flank is not as clear due to the, already discussed influence, acquisition geometry. A deep synclinal structure is observed around the position  $x = 27000$  m and  $z = 3000$  m. The overhang which could be present in the structure for geological reasons is not observed in the obtained depth image. Note that the possible information of the overhang cannot be imaged with the used pre-stack depth migration method scheme because of the use of one-way propagation operators, which are not able to take multiple reflections from one layer into account (Wapenaar and Berkhouwt, 1989).

Figure 8.13 shows the CFP migration result where a reflection, which could originate from the bottom of the salt body, can be observed at  $x = 24000$  and  $t = 1.2$  s. Note that this reflection is not as clear present in the recursive depth migration result. At the bottom of the image, after 1.5 seconds, some linear artifacts are visible related to the interpolation of the focusing operators in the second focusing step. The coherency measurement of figure 8.14 indicates good alignment of the events

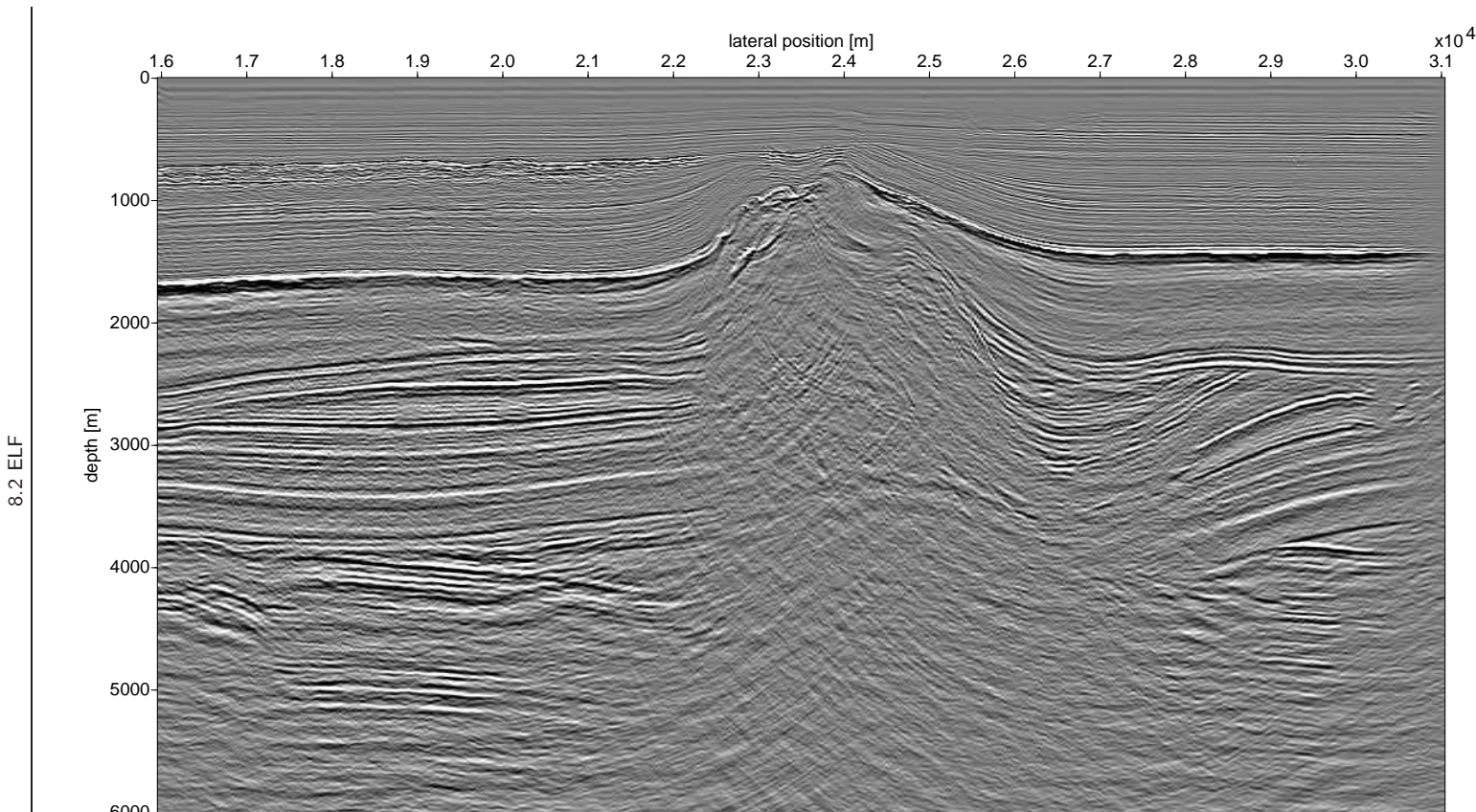


**Figure 8.12** Prestack depth migration result obtained with F-X migration. The depth step in the recursive extrapolation was chosen 10 m and the WLSQ extrapolation operators as discussed in appendix A were used.

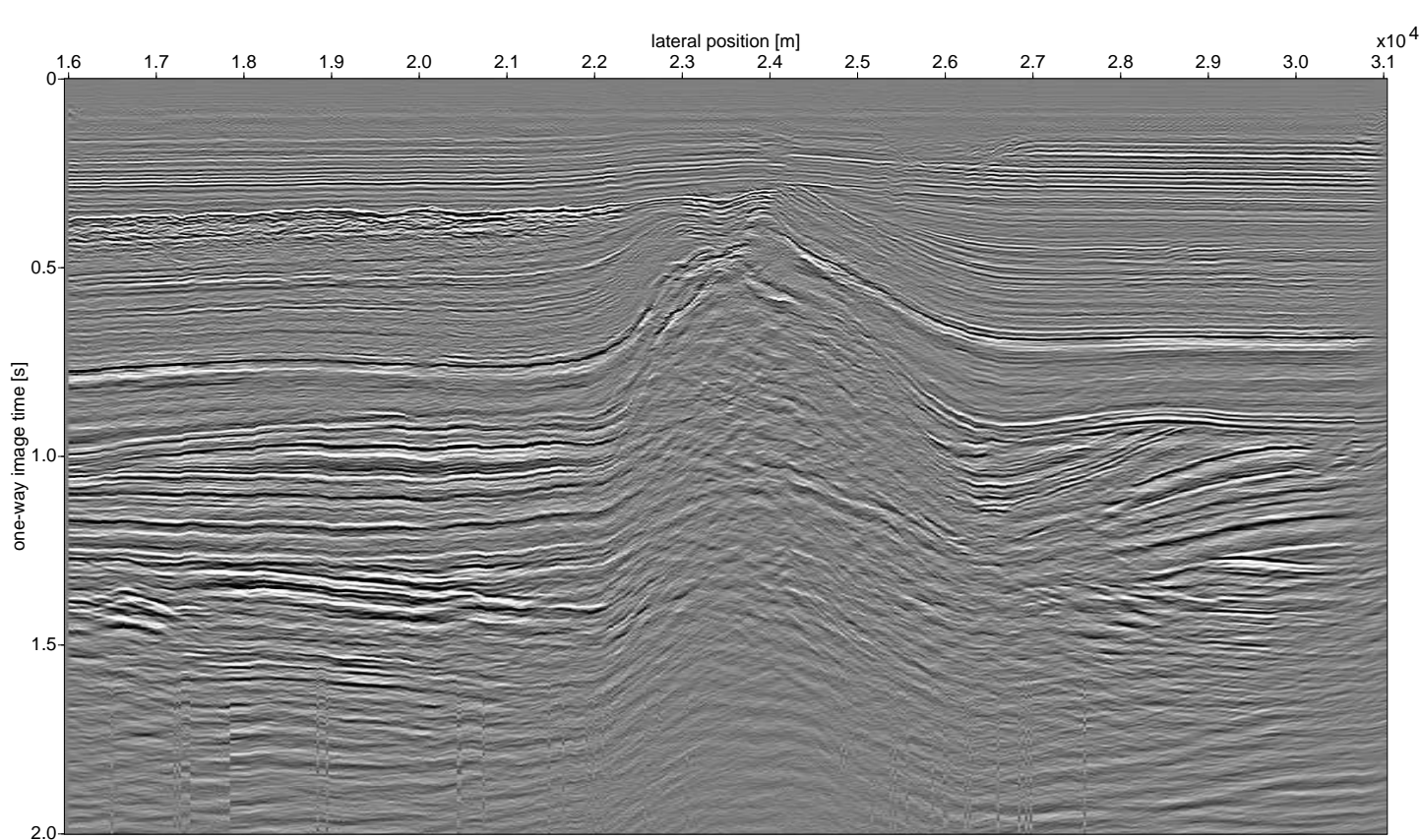


**Figure 8.13** Prestack migration result obtained with the CFP migration method. Note that only a limited number of operators is used in the first focusing step to construct the complete image:  $\Delta T = 80$  ms.

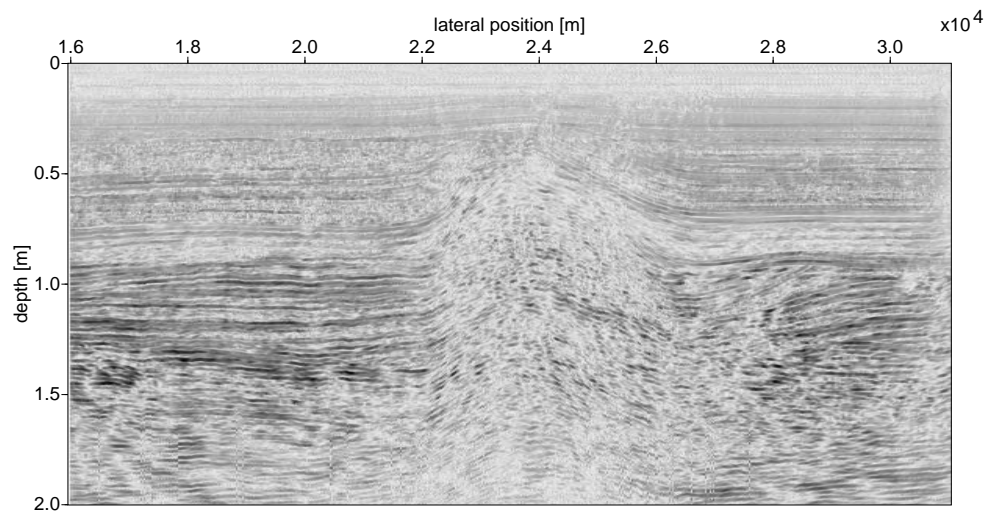


**Figure 8.14** Coherency measurement of the one-way time image. Black indicates a high coherency, meaning that the event in the CFP image gather is well aligned.

between 1 and 1.5 seconds. Inside the salt structure the image quality is poor except for the event starting at  $x = 24000$  m and  $t = 1.2$  s. The top part of the image shows a low coherency value caused by the chosen focus point distribution.

Finally a CFP stack is shown for focus points defined at depth level  $z = 3500$  m and a lateral distance between the focus points of 26.66 m. The CFP stack gives a good indication of the events around the defined depth level.

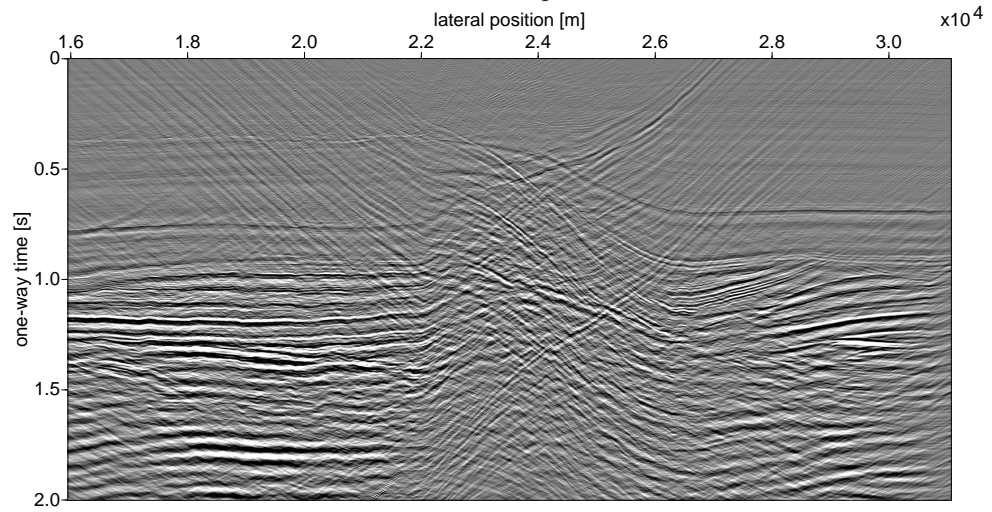


**Figure 8.15** CFP stack for focus point defined at depth level  $z = 3500$  m. Note that at approximately 1.3 s the result is well focused.

# Appendix A

## Operator optimization

In homogeneous media the one-way extrapolation operator in the  $k_x, k_y - \omega$  (wavenumber-frequency) domain is a simple analytical function, called the phase shift operator and given by (Gazdag, 1978):

$$\tilde{Y}(k_x, k_y, \omega, \Delta z) = \exp(-j\sqrt{\frac{\omega^2}{c^2} - (k_x^2 + k_y^2)}\Delta z) \quad (\text{A.1})$$

with  $\Delta z$  being a small extrapolation step,  $c$  the propagation velocity of the medium and  $\omega$  the angular frequency. The advantage of using the phase shift operator in the  $k_x, k_y - \omega$  domain is that the desired extrapolation result is obtained by multiplication of the data with the phase shift operator. But simple multiplication in the  $k_x, k_y - \omega$  domain rules out the possibility of applying a laterally varying operator. Another disadvantage is the numerical artifact in  $x$  due to under sampling in wavenumber domain. To allow laterally varying medium functions and less numerical artifacts a convolution operator in the  $x, y - \omega$  (space-frequency) domain should be used. When the spatial extrapolation operator is used in an explicit recursive depth migration algorithm it must be calculated in such a way that it gives reliable and stable results within a reasonable computation time. To arrive at this goal two steps must be taken; the first step is an optimum design of the spatial operator and the second step deals with a fast implementation of the spatial convolution. It turns out that the most efficient algorithms combine these two steps and design a spatial operator in such a way that it can be implemented in a fast way. In this appendix extrapolation operators are derived for 2-dimensional and 3-dimensional media.

### A.1 1-Dimensional operators for 2-dimensional extrapolation

There are several ways to obtain a 1-dimensional spatial convolution operator. For homogeneous media one usually starts with the exact analytical expression in the wavenumber-frequency domain and transforms this operator back to the spatial domain. In recent years many methods have been developed to do this transformation

in an efficient and optimum way. For the one-way wavefield extrapolation operator Holberg (1988), Blacquière et al. (1989), Hale (1991b) and Nautiyal et al. (1993) have proposed methods to arrive at spatial operators which are unconditionally stable in a recursive extrapolation scheme. In subsection A.1.2 of this appendix an alternative method is presented for an efficient and controlled transformation from the wavenumber domain back to the spatial domain. This method can be used to calculate extrapolation operators which are stable and accurate in a recursive depth migration algorithm. Before this new method is discussed first some examples of extrapolation operators for homogeneous media are given to illustrate the problems in operator optimization. At the end of this section the proposed method is compared with other numerical optimization methods by calculating the impulse response of a recursive depth migration algorithm.

### A.1.1 Analytical space-frequency operators

In the  $k_x - \omega$  domain the extrapolation operator is, for a 2-dimensional medium, given by the familiar phase-shift operator of equation (A.1) with  $k_y = 0$

$$\tilde{Y}(k_x, \omega, \Delta z) = \exp(-j\sqrt{k^2 - k_x^2}\Delta z), \quad (\text{A.2})$$

$$\tilde{Y}(k_x, \omega, \Delta z) = \exp(-jk_z\Delta z), \quad (\text{A.3})$$

with

$$k_z = \begin{cases} \sqrt{k^2 - k_x^2} & k_x^2 \leq k^2 \\ -j\sqrt{k_x^2 - k^2} & k_x^2 > k^2 \end{cases}. \quad (\text{A.4})$$

in which  $k$  is defined as  $\frac{\omega}{c}$ . Note that for wavenumber values larger than  $k$ , the wavefield becomes evanescent (exponentially decaying). The analytical inverse Fourier transform of equation (A.2) is a scaled Hankel function (see Berkhout, 1984):

$$Y(x, \omega, \Delta z) = \frac{-jk\Delta z}{2r}, H_1^{(2)}(kr) \quad (\text{A.5})$$

with  $r = \sqrt{(x^2 + \Delta z^2)}$  and  $H_1^{(2)}(kr)$  ( $= J_1(kr) - jY_1(kr)$ ) the zero order Hankel function of the second kind.

To illustrate the behavior of the phase shift operator the same parameters as Hale (1991b) and Nautiyal et al. (1993) are used;  $\Delta z = \Delta x = 12.5$  m,  $\omega = 40\pi$  [radians/s], 512 wavenumber samples and  $c = 1000$  m/s. In figure A.1 the amplitude of equation (A.5) is given as function of  $x$ , with the chosen parameters. In the same figure the amplitude of the wavenumber spectrum of a truncated Hankel function (dashed line) is displayed together with the phase shift operator  $\tilde{Y}(k_x, \omega, \Delta z)$  (solid line). The horizontal axis in figure A.1 represents normalized wavenumber cycles ( $\frac{n\pi}{N}$ , radians per sample in the  $x$  direction; e.g. 0.25 is equivalent to the wavenumber  $k_x = k$  and represents propagation at  $90^\circ$  and 0.1 is equivalent to an angle of  $36^\circ$ ). The number

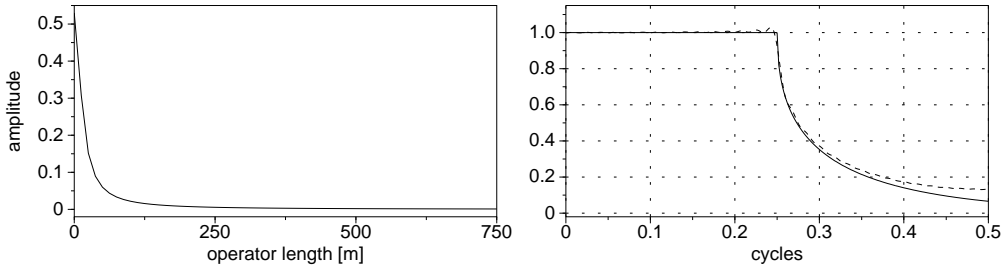


**Figure A.1** Analytical spatial extrapolation operator (left) and its wavenumber spectrum (right). The dashed line is related to the truncated analytical operator (121 points) and the solid line to the phase shift operator. Note the excellent agreement; for 121 points the truncation error is negligible.

of samples points in the spatial domain is chosen at 121. In all figures shown in this section only the positive values for  $k_x$  and  $x$  are displayed because of the symmetry of the operators, meaning that in figure A.1 only 61  $x$ -positions are shown. From figure A.1 it can be seen that the Hankel function is a long operator and is therefore not very well suited for recursive depth extrapolation. From a computational point of view long spatial operators are not desired because multiplication in the wavenumber-frequency domain is replaced by a convolution in the space-frequency domain. Further, the locally homogeneous assumption in inhomogeneous media is for a long operator pushed to its limits. If we truncate the Hankel function to a more suitable number of points (for example 39 points) then it is observed in figure A.2 that the wavenumber spectrum is not stable for a wavenumber close to  $k$ . Recursive application of this operator in a homogeneous medium causes the waves, traveling with the wavenumber related with the deviation above the amplitude = 1 line, to be amplified at every extrapolation step which can in the end 'blow up' the extrapolation result.

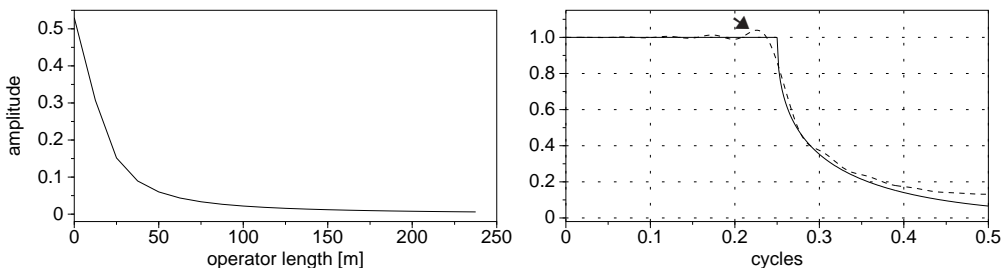


**Figure A.2** Same illustration as in figure A.1, but now with the number of points reduced to 39 points. Note the unacceptable truncation effect, indicated by the arrow in the right picture.

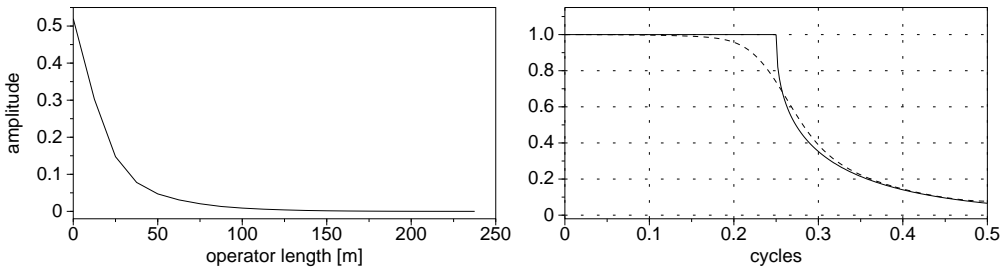


**Figure A.3** Same illustration as in figure A.2, but now with a spatial Gaussian taper applied on the spatial operator. Note the strong amplitude decay at the higher propagation angles ( $> 0.2$ ).

A solution for the unstable behavior of the truncated operator is given by Nautiyal et al. (1993). They argued that accuracy is important for any numerical method but stability is crucial because an unstable, accurate method is even less useful than a stable but inaccurate one. They propose to taper the spatial wavelet with a Gaussian taper (which guarantees a stable extrapolation operator). To illustrate the method a Gaussian taper is applied to the operator shown in figure A.2. The chosen Gaussian taper decays from a value of 1 at  $x = 0$  to a value of  $\cos^2(\frac{\pi N}{2(N+1)})$  at  $x = dx * (N - 1) * 0.5$ , with  $N = 39$ . The results are shown in figure A.3. Note that the Hankel function is designed as the inverse Fourier transform of the phase shift operator and not as the Hankel function directly in the spatial domain. In this way aliasing of the higher wavenumbers is avoided. It is observed that the wavenumber spectrum is now unconditionally stable for all wavenumbers, but the accuracy is reduced for higher wavenumbers. Another disadvantage is that the effective wavenumber band, in which the filtered analytical operators work, is not under control. It will be shown that control over the bandwidth of the spatial operator is essential for a desired operator functionality. Another and better way to obtain stable extrapolation operators is to start in the wavenumber domain and transform the wavenumber expression back to the space domain. There are many ways to do this transformation in a desired way. In the next subsection four different transformation methods, including the new method, will be discussed.

### A.1.2 From wavenumber domain to spatial convolution operators

The most straightforward way to obtain a spatial convolution operator from the expression in the  $k_x - \omega$  domain is to calculate the inverse Fourier transform of this expression in the space-frequency domain and truncate this operator to a desired convolution length. Unfortunately this simple method is not stable for all wavenumbers and can therefore not be used in a recursive migration scheme.

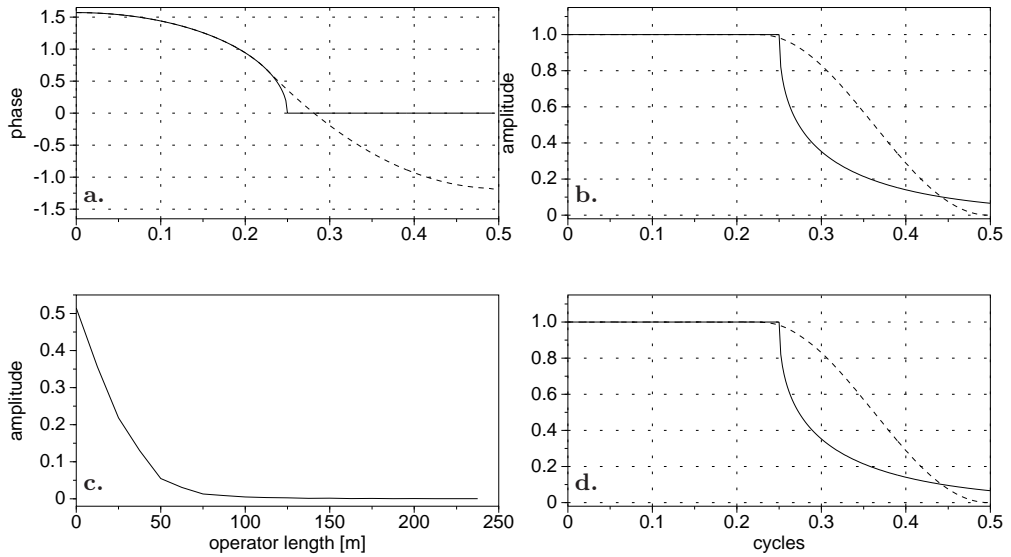


**Figure A.4** Due to small derivatives of the operator in the wavenumber domain the artifacts for the truncated operators remains small. The top pictures show the operator design in the wavenumber domain and the lower pictures show the 39 point operator and its related amplitude spectrum. Note the short spatial length of the spatial operator.

#### Smoothed wavenumber operator

Another way to obtain a useful operator is to design a  $k_x - \omega$  operator in such a way that the inverse Fourier transform is short, so that truncation does not significantly effect the spectrum of interest. The trick in this method is that the phase of the phase shift operator, given by  $k_z \Delta z$  which has a singular point for  $k_x = k$ , is altered such that it is smoothly deviating from the correct phase for angles larger than the maximum design angle. The extrapolation operator is then obtained by taking the exponent of this smoothed phase,  $\exp(-j\phi(k_x))$ . This function is then filtered with respect to the maximum design angle to control the amplitude behavior of the operator. In this way the amplitude spectrum of the operator is not decaying with the exponentially slope known from the phase shift operator but is determined by the slope of the used wavenumber filter. It is known from Fourier analysis that large amplitude derivatives in the wavenumber domain as well as large phase derivatives give rise to large operator lengths (Blacquière, 1989). So the wavenumber filter should keep the operator as smooth as possible to arrive at a short spatial operator, for example by using a filter with a cosine taper to  $\frac{\pi}{\Delta x} = k_{Nyquist}$ . The amplitude spectrum of the operator is shown in figure A.4b for a maximum design angle of 70°. The phase of this operator is smoothly deviating from the exact operator (the solid line in figure A.4a) for angles greater than the design angle. In figure A.4c the truncated operator (39 points) and in figure A.4d the wavenumber spectrum is

shown. In comparison with figure A.2 it is observed this truncated operator is stable for all wavenumbers of interest.

For the methods discussed above the performance of the method was determined from the wavenumber spectrum of the operator. The final aim in the design of a spatial convolution operator is an optimal solution. The optimized result must be designed accurate within the band of interest and stable outside this band. In order to solve this problem the notion accuracy must be defined in a mathematical way. Therefore a weighted error function, which measures the deviation from the true function, is defined as

$$\|\varepsilon(x)\| = \|W(x)|Y(x) - P(x)|\|. \quad (\text{A.6})$$

where  $Y(x)$  is the true function and  $P(x)$  the approximation. There are several possible choices available for the norm function ( $\|\cdot\|$ ) in equation (A.6). The most widely used are the  $L_\infty$  (also called the minimax, or Chebychev) norm and the  $L_2$  (least-squares) norm. The  $L_2$  and  $L_\infty$  norm are respectively defined as

$$\|Y(x)\|_2 \equiv \left[ \int_b^a |Y(x)|^2 dx \right]^{\frac{1}{2}} \quad (\text{A.7})$$

$$\|Y(x)\|_\infty \equiv \max_{a \leq x \leq b} |Y(x)| \quad (\text{A.8})$$

Peaks and overshoots in the frequency domain are typical of frequency sampling and least-squares designs. Windowing techniques, as discussed above, are attempts to reduce the peaks in the error function (Parks and Burrus, 1987). The theory of Chebychev approximation provides algorithms to find the coefficients of a convolution operator with the minimum value for the maximum error in the peaks. Operators that have this minimum value of the maximum error exhibit an equiripple behavior in their frequency response. A practical reason for using the  $L_\infty$  norm is that when in computer calculations a complicated mathematical function is estimated by one that is easy to calculate then it is usually necessary to ensure that the greatest value of the error function  $\varepsilon$  is less than a fixed amount. This is just the required accuracy of the approximation which is a condition on the norm  $\|Y - P\|_\infty$ .

After defining the accuracy in a desired way a computation method must be found to calculate the solution of the approximation problem. By using the  $L_\infty$  norm the minimization problem is usually not solvable explicit in terms of formulas. However, by formulating the  $L_\infty$  optimization problem as a Chebychev approximation problem a set of conditions is provided which completely characterize the optimal filter (Powell, 1981; Thorbecke, 1995). The Remez exchange algorithm, which is discussed briefly below, calculates the unique solution in the  $L_\infty$  norm. The weighted least-squares method which satisfies the  $L_2$  norm is discussed first.

### Weighted least-squares

The goal in the optimization procedure is to obtain a short spatial convolution operator which has a wavenumber spectrum which is, over a desired wavenumber band, equal or close to the exact formulation in the frequency-wavenumber domain. This problem can be written as an integral equation given by

$$\tilde{Y}(k_x) = \int_{x_1}^{x_2} \exp(jk_x x) Y(x) dx \text{ for } k_1 \leq k_x \leq k_2. \quad (\text{A.9})$$

In this integral equation the integration is carried out over a limited spatial domain, representing the short operator, and the frequency-wavenumber domain of the operator is bandlimited. The discrete counterpart of this integral equation is

$$\tilde{Y}(n\Delta k_x) = \Delta x \sum_{m=M_1}^{M_2} \exp(jn\Delta k_x m\Delta x) Y(m\Delta x) \text{ for } N_1 \leq n \leq N_2. \quad (\text{A.10})$$

Written more explicitly in matrix notation

$$\begin{bmatrix} \tilde{Y}(N_1\Delta k_x) \\ \vdots \\ \tilde{Y}(0) \\ \vdots \\ \tilde{Y}(N_2\Delta k_x) \end{bmatrix} = \Delta x \begin{bmatrix} \exp(jN_1\Delta k_x M_1\Delta x) & \dots & 1 & \dots & \exp(jN_1\Delta k_x M_2\Delta x) \\ \vdots & \ddots & \vdots & \dots & \vdots \\ 1 & \dots & 1 & \dots & 1 \\ \vdots & \ddots & \vdots & \ddots & \vdots \\ \exp(jN_2\Delta k_x M_1\Delta x) & \dots & 1 & \dots & \exp(jN_2\Delta k_x M_2\Delta x) \end{bmatrix} \begin{bmatrix} Y(M_1\Delta x) \\ \vdots \\ Y(0) \\ \vdots \\ Y(M_2\Delta x) \end{bmatrix}$$

or

$$\tilde{\mathbf{Y}} = \mathbf{B} \mathbf{Y} \quad (\text{A.11})$$

with  $\mathbf{Y}$  the desired short operator and  $\tilde{\mathbf{Y}}$  being its spatial Fourier transform, yielding an approximation of the exact phase shift operator. Further  $m = M_1 \dots M_2$  represents the length of the desired short operator and  $n = N_1 \dots N_2$  the length of the Fourier transformation and where the wavenumber sampling is given by

$$\Delta k_x = \frac{2\pi}{(N_1 + N_2 + 1)\Delta x}. \quad (\text{A.12})$$

The number of samples in the frequency-wavenumber domain ( $N_1 + N_2 + 1$ ) must be chosen in such a way that the short spatial operator is zero outside its working length. This means for the extrapolation operators that the number of samples must be greater or equal to the number of traces to be extrapolated.

Matrix equation (A.11) has, with respect to the unknown spatial operator, more equations than unknowns, meaning that it is usually impossible to find an unique solution which satisfies all the equations. To solve this problem a solution is sought which approximately satisfies all the equations in a least-squares manner. Therefore the following error function is defined

$$\tilde{\varepsilon} = \tilde{\mathbf{E}}^H \tilde{\mathbf{\Lambda}} \tilde{\mathbf{E}}, \quad (\text{A.13})$$

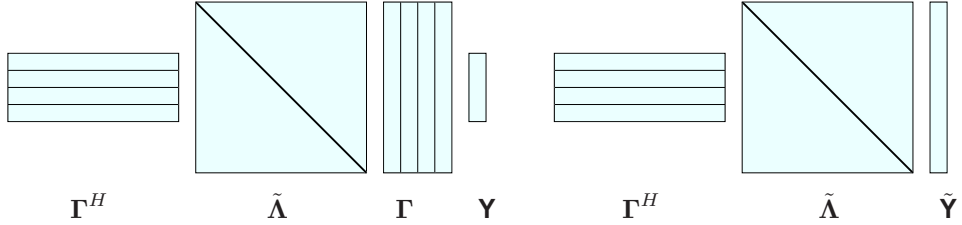


**Figure A.5** The matrices used in a weighted least-squares implementation of a Fourier inversion. Note that if  $\tilde{\Lambda} = \mathbf{I}$  the matrix equation is equivalent to the DFT.

where superscript H denotes complex-conjugate transpose, with

$$\tilde{\mathbf{E}} = \mathbf{\Gamma} \mathbf{Y} - \tilde{\mathbf{Y}} \quad (\text{A.14})$$

and  $\tilde{\Lambda}$  a diagonal matrix containing a weighting function on its diagonal. In this so called weighted least-square procedure (abbreviated as WLSQ) the weighting function is defined in such a way that the wavenumbers of interest are given a high weight. The wavenumbers which are not of interest are ‘abused’ to make the operator as good as possible (given a low weight factor). The method described by Hale (1991b) also uses some part of the wavenumber spectrum (called the degrees of freedom) to force the amplitude spectrum to zero in the evanescent region. So by introducing the weighting function a good control is obtained for the desired function of the space-frequency operators. The least-squares solution of equation (A.13) is given by

$$\frac{\partial \varepsilon}{\partial (\mathbf{Y}^H)_i} = 0 \quad \forall (\mathbf{Y}^H)_i \quad (\text{A.15})$$

with

$$\tilde{\varepsilon} = (\mathbf{Y}^H \mathbf{\Gamma}^H - \tilde{\mathbf{Y}}^H) \mathbf{\Lambda} (\mathbf{\Gamma} \mathbf{Y} - \tilde{\mathbf{Y}}) \quad (\text{A.16})$$

The solution of equation (A.16) is given by the normal equations (slightly modified after Claerbout (1976))

$$\mathbf{\Gamma}^H \mathbf{\Lambda} (\mathbf{\Gamma} \mathbf{Y} - \tilde{\mathbf{Y}}) = 0 \quad (\text{A.17})$$

or

$$\mathbf{Y} = [\mathbf{\Gamma}^H \tilde{\mathbf{\Lambda}} \mathbf{\Gamma}]^{-1} \mathbf{\Gamma}^H \tilde{\mathbf{\Lambda}} \tilde{\mathbf{Y}} \quad (\text{A.18})$$

In figure A.5 the weighted least-squares solution of equation (A.18) is given in a matrix representation. The components of the Fourier transform and in the inverse Fourier transform matrices are given by

$$\begin{aligned} \Gamma_{nm} &= \exp(jn\Delta k_x m\Delta x) \\ \Gamma_{mn}^H &= \exp(-jn\Delta k_x m\Delta x) \end{aligned}$$

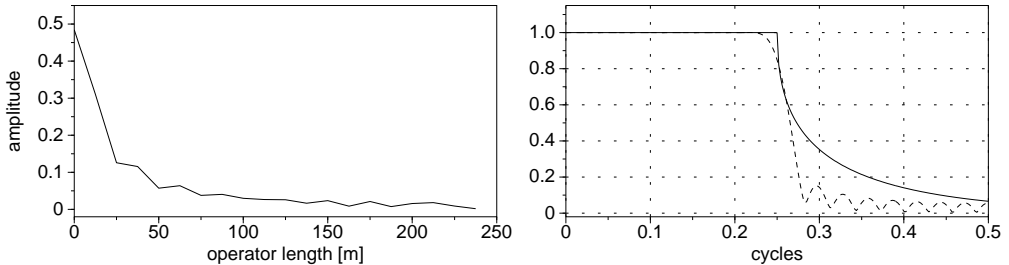


**Figure A.6** Weighted least-square operator (left) of 39 points and its wavenumber spectrum (right). The solid line is related to the spectrum of the exact phase shift operator and the dashed line to the optimized operator. Note the perfect match in the propagating part of the wavenumber domain.

The weight function, which is a diagonal matrix, is given by

$$\Lambda_{nm} = w(n\Delta k_x)\delta_{nm}$$

The total matrix,  $\mathbf{\Gamma}^H \tilde{\mathbf{\Lambda}} \mathbf{\Gamma}$  which stands before the unknown, is a square  $M \times M$  matrix which has to be inverted. For the 1-dimensional optimization problem this matrix has a Toeplitz structure and can be inverted very fast by using the Levinson scheme. If in equation (A.18) the weight matrix is chosen identical to the unit matrix  $\mathbf{I}$  then the right hand side of equation (A.18) is an inverse Fourier transform (N-points) which is truncated to M-points in the spatial domain. In this specific case no optimization is carried out.

For the extrapolation operator it is possible to neglect the operator behavior on the evanescent waves because they are not present in the data above the noise level. The recursive extrapolation scheme only demands a stable (amplitude < 1) behavior of the wavenumbers in the evanescent region. The used weighting function can therefore be a simple block with a weight of one inside the range of angles of interest (the propagating waves) and a small value (1e-5) outside this band. How these optimized operators, with the same parameters as before, behave is shown in figure A.6. The spatial operator has a less ‘smooth’ character, but the wavenumber spectrum is stable for all wavenumbers and is accurate within the band of interest. Note the special character of the evanescent part of the wavenumber spectrum. It is not smoothing down but varying. This is observed better in figure A.7 where a collection of operators is shown, again with the same parameters as before but within a frequency range from 0 to 60 Hz. Holberg (1988) used a same illustration and argued that when the phase and amplitude errors are oscillating functions of the wavenumber these errors will not accumulate at the maximum possible rate when waves are propagated through inhomogeneous media. So the obtained operators could be used in a stable manner in a recursive migration scheme. In the calculation done to obtain figure A.7 a search for a suitable weighting function was carried

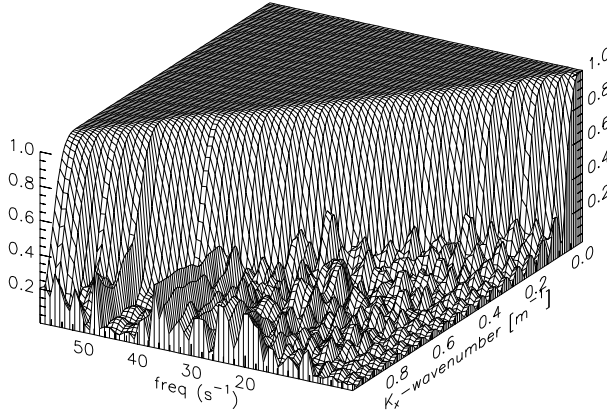


**Figure A.7** Collection of wavenumber-frequency spectra of the weighted least-squares operators with the same parameters as before but with varying  $k = \frac{\omega}{c}$ . The evanescent region is stable and the propagating region is accurate and stable for the whole  $k$  range.

out in such a way that the amplitude of the wavenumber operator is ensured to be  $< 1.0001$ .

Note that the WLSQ method can also be used to obtain other spatial convolution operators, for example elastic decomposition operators as described in Herrmann (1992). The method can be further improved by using more optimization steps; for example the Lawson algorithm (Rice and Usow, 1968), which will adjust the weight function in such a way that after several steps the solution will converge to a Chebychev-norm ( $L_\infty$ ) solution see for example Algazi et al. (1986). In the next subsection a spatial convolution operator with a Chebychev norm is obtained directly, by using the Remez exchange algorithm.

#### Remez exchange algorithm

The Remez exchange algorithm is based on the  $L_\infty$  norm and the related Chebychev polynomial. The Chebychev polynomial is a powerful function in approximation theory, because of the special properties of the Chebychev polynomials (Parks and Burrus, 1987). The Chebychev approximation  $P(x)$  of a real function  $Y(x)$  is defined as

$$Y(x) \approx P(x) = \frac{a_0}{2} + \sum_{m=1}^M a_m T_m(x) \quad (\text{A.19})$$

for  $-1 \leq x \leq 1$ , with  $T_m(x)$  the Chebychev polynomial of order  $m$  and  $a_m$  the expansion coefficients (see for example Johnson and Riess, 1977; Ralston, 1967; Kogbetliantz, 1960). The Chebychev polynomials  $T_m(x)$  are usually defined in terms

of trigonometric functions by:

$$\begin{aligned} T_m(x) &= \cos(m \arccos(x)) & \text{for } |x| \leq 1 \\ T_m(x) &= \cosh(m \cosh^{-1}(x)) & \text{for } |x| > 1. \end{aligned}$$

Using the variable substitution  $x = \cos(\phi)$  the Chebychev polynomials can be re-written as

$$T_m(x) = \cos(m\phi).$$

With this variable substitution some properties of the Chebychev polynomials can easily be derived

$$2T_m(x)T_n(x) = T_{n+m}(x) + T_{n-m}(x) \quad (\text{A.20})$$

$$\begin{aligned} T_{m+1}(x) &= \cos((m+1)\phi) = 2\cos(\phi)\cos(m\phi) - \cos((m-1)\phi) \\ &= 2xT_m(x) - T_{m-1}(x) \end{aligned} \quad (\text{A.21})$$

$$T_2(x) = 2x^2 - 1 \quad (\text{A.22})$$

$$T_3(x) = 4x^3 - 3x \text{ etc.} \quad (\text{A.23})$$

with  $T_0(x) = 1$  and  $T_1(x) = x$ . The most important property is the recurrence relation given in equation (A.21) and will be used in the derivation of 2-dimensional convolution operators (used for 3-dimensional extrapolation) discussed in the next section. Equations (A.22) and (A.23) show that  $T_m(x)$  can be written as  $\sum b_m x^m$ , a polynomial in  $x$ . The Chebychev polynomial have some special properties, for example  $T_m(x)$  has  $m$  zeros which all fall in the interval  $[-1, 1]$  and are located at the points

$$x_i = \cos\left(\frac{\pi(2i+1)}{2m}\right) \quad (\text{A.24})$$

The polynomials oscillate between +1 and -1 for  $-1 \leq x \leq 1$  and go monotonically to  $\pm\infty$  outside that domain. In figure A.8 the Chebychev polynomials for the 0,1,2,3 and 4<sup>th</sup> order are plotted.

By using the orthogonal property of the Chebychev polynomials it can be proven (Powell, 1981, p.144) that the Chebychev approximation  $P(x)$  in equation (A.19) is very nearly the minimax polynomial, which (among all polynomials of the same degree) has the smallest maximum deviation for the true function  $Y(x)$ . A property of this particular approximating polynomial of equation (A.19) is that it can be truncated to a polynomial of lower degree  $n \leq M$  that does again yield the "most accurate" approximation of degree  $n$ . So the accuracy of the approximation improves when the number of terms is increased. Since the  $T_m(x)$  are all bounded between  $\pm 1$ , the difference between the truncated( $n$ ) and the larger polynomial( $M$ ) can be no larger than the sum of the neglected terms. In fact if the terms are rapidly decreasing, then the error is dominated by  $c_n T_n(x)$  an oscillatory function with

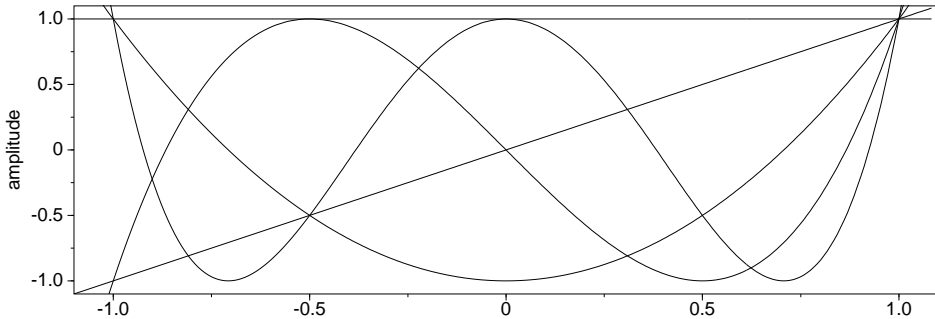


**Figure A.8** Chebyshev polynomials for the 0,1,2,3 and 4th order within the interval  $[-1, 1]$ . Note that outside this interval the polynomials of orders  $\geq 2$  approach  $\pm\infty$ .

$(n+1)$  equal extreme distributed smoothly over the interval  $[-1, 1]$ . This smooth spreading out of the error is a very important property Press et al. (1992).

The Remez Exchange algorithm is to the Chebyshev approximation as the normal equations are to the minimum least-squares solution. In both cases a set of expansion coefficients  $a_i$  is calculated that "best fit" a set of basis functions to the data. If the definition of "best fit" is to minimize the sum of squares then get the normal equations are used to calculate the  $a_i$ 's. If the "best fit" is defined to minimize the maximum error (min-max or Chebyshev fit) then the Remez Exchange algorithm gives the answer. The Remez exchange algorithm for Chebyshev approximation converges from any initial reference to his unique answer.

The McClellan and Parks (1972); McClellan et al. (1973) algorithm, which is used in the extrapolation operator calculation, is based on the Remez exchange algorithm and Chebyshev approximation theory. The operators are optimal in the sense that the maximum error between the desired frequency response and the actual frequency response is minimized for a given weighting function. Operators designed this way exhibit an equiripple behavior in their frequency response, and hence are sometimes called equiripple filters. In figure A.9 the wavenumber spectrum of the spatial extrapolation operator, with the same parameters as before, is shown.

#### Non-linear optimization

The most advanced and complicated method to compute a spatial convolution operator is by non-linear optimization. Holberg (1988) and Blacquière (1989) have both used a non-linear optimization method to compute stable and accurate extrapolation operators. In non-linear optimization methods an objective function and a constraint function have to be defined. The objective function is defined in that part of the wavenumber domain in which the operator must be accurate and the constraint function is defined in the remaining part of the wavenumber domain where the operator must be stable. The objective function used in the non-linear

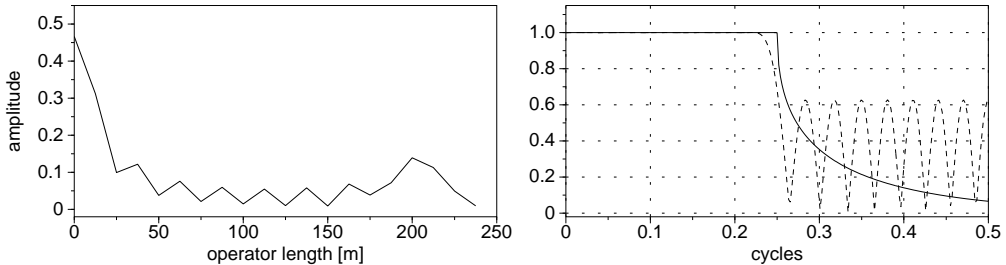


**Figure A.9** Extrapolation operators obtained with the Remez exchange algorithm. Note the equiripple behavior in the evanescent part of the spectrum.

schemes is defined as the summation of the squared amplitude and phase errors over all wavenumbers in the domain of interest. The constraint function is designed to suppress the larger wavenumber to a value smaller than 1.0 in order to obtain stable operators.

Two different non-linear optimization routines were used; the CFSQP routine written by Tits and Zhou (1996) and a (old) NAG lib routine. The initial guess, which must be provided, is for both methods the truncated spatial operator. If the methods fails to find a solution with the provided initial guess the smoothed phase or the weighted least-squares solution is taken as a new initial guess. The results for the CFSQP algorithm are shown in figure A.10. Both non-linear methods give stable and accurate results. A disadvantage of the NAG method is that the computation time is very long and it does not always find a solution. However, a slight change in the input parameters (for example by changing the maximum angle of interest) can give a correct solution. Due to these practical disadvantages the CFSQP method is preferred.

In the foregoing subsections six types of optimization methods (Truncation, Gaussian filtering, smoothed phase, weighted least-squares, Remez exchange and non-linear

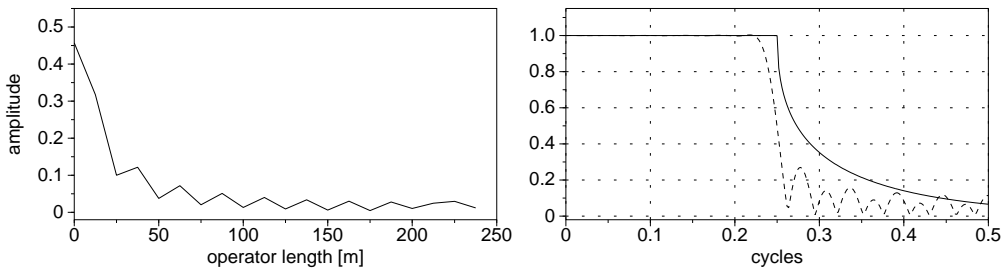


**Figure A.10** Extrapolation operators obtained with non-linear optimization using the CFSQP algorithm.

optimization) have been introduced for obtaining extrapolation operators. To make a good comparison between the different methods their resulting phase and amplitude spectra are plotted together into one figure. The same parameters are used as before only this time with an operator length of 19 points to show the differences more pronounced. The results are shown in figure A.11.

From the spatial wavelet in figure A.11 it is observed that the weighted least-squares and the non-linear optimization procedure have relative high amplitude variations for the greater offsets. So the contribution from the off-center points is greater in the non-linear and the weighted least-squares methods than in the other methods. Application of these operators (with a long operator length) in strongly inhomogeneous media can therefore give rise to artifacts in the extrapolation result. The other spatial wavelets decays more ‘smoothly’ from the off-center points. In the wavenumber spectrum the differences between the operators can be interpreted more meaningful. The phase and amplitude errors of the operators are displayed in the middle pictures of figure A.11. From the wavenumber spectrum it is observed that the Gaussian operator is rapidly loosing amplitudes for higher angles. The truncated operator is not stable for all wavenumbers especially for the wavenumbers just before the point where the evanescent part starts (0.25 on the horizontal axis) the amplitude exceeds amplitude 1 significantly. The smoothed phase operator is in this area more stable and accurate than the truncated operator. The weighted least-square operator is stable and accurate for all wavenumbers. In the evanescent region the amplitude is larger than the other operators (but still smaller than 1). The phase errors are very small and the amplitude errors are smaller than 0.001. The Remez exchange operator shows its nice equiripple behavior and is very accurate for both amplitude and phase. The non-linear optimized operator is as good as the weighted least-squares and Remez operator but has a little different behavior as shown in the bottom pictures of figure A.11. The non-linear solution has a relatively large error peak close to the edge of the maximum design angle and may become unstable for waves traveling with these wavenumbers.

In this subsection is has been shown that there are several ways to obtain a spatial convolution operator. From the examples given above it can be concluded that the spatial bandwidth of a desired spatial convolution operator must, in the optimization procedure, be constrained to a desired bandwidth. To overcome exponentially amplifying of certain propagating wavenumbers in a recursive depth migration it must also have a stable behavior. In the next subsection the discussed operators are used in an explicit recursive migration scheme to observe the effects of the different operators in a depth section. From the foregoing results it is not possible to say something about the performance in a migration algorithm. It is interesting to see how the differences observed in figure A.11 above can be found back in a migrated depth section.

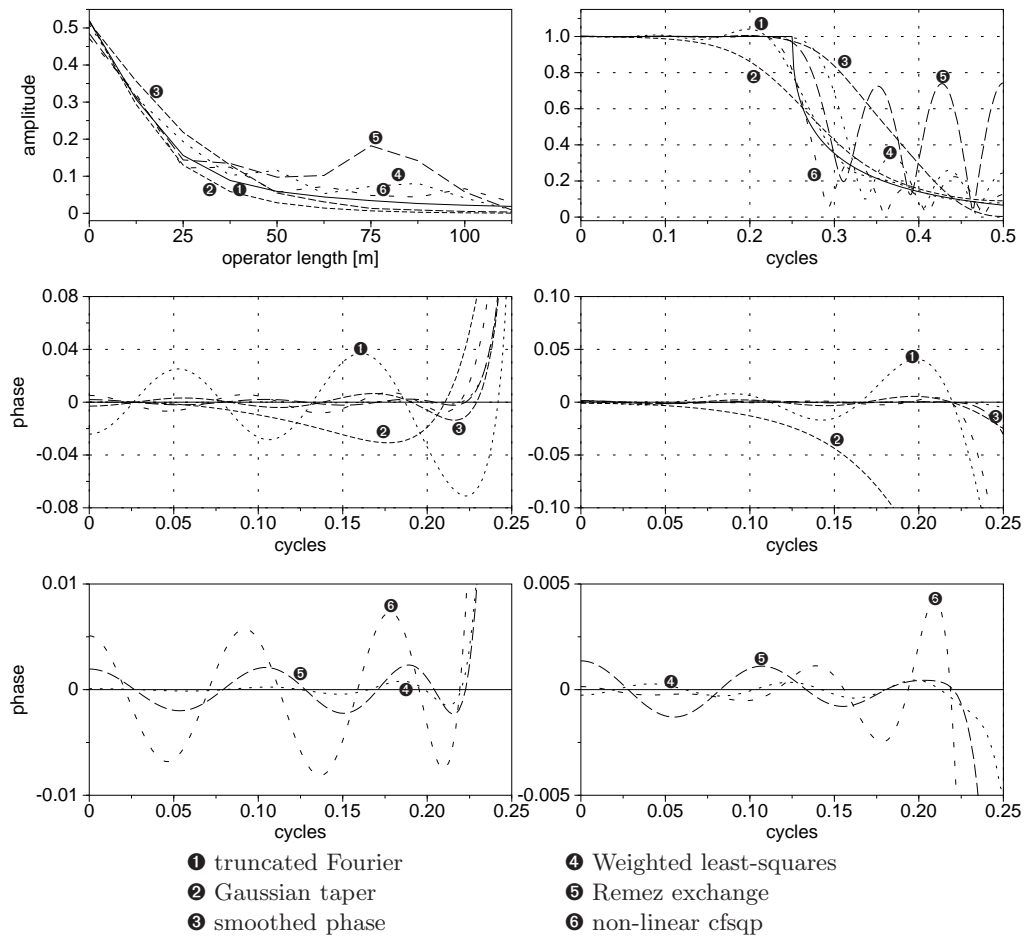


**Figure A.11** The two top pictures show the amplitude of six different 19 point extrapolation operators in space (left) and the related wavenumber spectrum (right). The middle pictures show the phase (left) and amplitude (right) errors for the operators shown on the top. The two bottom pictures show a detailed view in the propagating region for the phase (left) and amplitude (right) errors.

### A.1.3 Recursive depth migration

In recursive depth migration lateral varying convolution operators are used to extrapolate seismic data through inhomogeneous media. The extrapolation operators in the  $x - \omega$  domain are locally homogeneous operators for each grid point  $(x, z)$  as shown in figure A.12. Based on the frequency  $\omega$  and the local velocity  $c$  in gridpoint  $(x, z)$  the extrapolation operator is computed, or in general read from an operator table which is computed in advance based on the frequency range of interest and the minimum and maximum velocity found in the macro model. Note that the

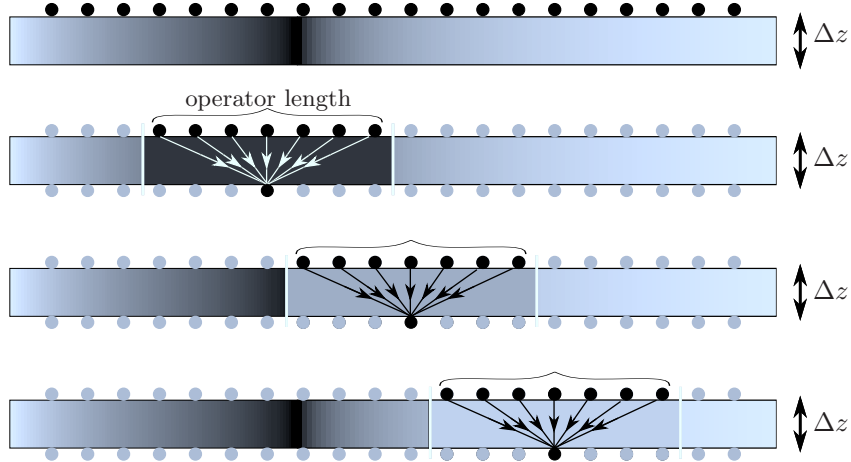


**Figure A.12** The principle of recursive extrapolation with spatial convolution operators. In principle at every lateral position a new operator is used to extrapolate the data from one depth level to another depth level. Within the operator length the medium is assumed to be homogeneous.

homogeneous extrapolation operator is symmetric around its center and can be implemented in an efficient way. Because of the assumption of locally homogeneous media, the extrapolation depth step should be small and the operator length short. To obtain reliable extrapolation results the operators must be accurate and remain stable in the recursion scheme. In the previous section it was shown that with these constraints it is possible to use different methods to design the operators. In this section six different extrapolation operators are considered: the truncated, smoothed phase, Gaussian tapered, non-linear (CFSQP), Remez exchange, and the weighted least-squares operator.

Homogeneous shot record migration experiments are carried out in a medium with a velocity of 2000 m/s, a length of 2000 m and a depth of 1000 m with the spatial and depth intervals,  $\Delta x = \Delta z = 10$  m. The zero offset trace in the shot record contains three Ricker wavelets at 0.3, 0.6 and at 0.9 s (all the other traces are filled with zeros). The source wavelet is sampled with 4 ms and has an amplitude spectrum up to 60 Hz. In figure A.13 twelve depth sections are shown for six different extrapolation operators and two different operator lengths. The left-hand side pictures give depth sections made with an operator length of 19 points and designed to be accurate for angles up to 65 degrees. The right-hand side pictures represent depth sections obtained with an operator length of 39 points and a maximum design angle of 85 degrees. Note that the events observed in the depth images lie on concentric semi circles with centers at the origin.

The truncated operator results in figure A.13 is not stable for the 19 point operator. In the deepest event in the depth section of the 19 point result the cumulative error can be observed in the distorted semi circle. The 39 point operator is stable but the edge effects of the operator disturb the image strongly. The migration results with the Gaussian tapered operator has the smallest artifacts in it but the price is that the higher angles are strongly attenuated and for the 19 point operator the deepest event is almost vanished. The results obtained with the smoothed phase operators is stable but contains noise for the 85 degrees experiment and the higher angles in the 65 degrees experiment are less accurate than the weighted least-square optimized result. The weight function used in the WLSQ method to obtain these results is the simple box function described earlier. Only the higher angles ( $> 65^\circ$ ) in the 19 point operator are not perfect and the steeper dips are attenuated, which is due to the short length of the operator, the 39 point operator gives almost perfect results. The Remez exchange operators give also good results which are comparable with the results obtained with the weighted least-square method. The result obtained by using non-linear optimization operators shows for the 19 point operator a good section up to the higher angles, at the higher angles there are some artifacts visible. The non-linear 39 point operator gives a better result but it takes a very long time, compared with the other methods, to compute the operator table.

In table A.1 the computation times of the operator table used for the different methods of the migration experiments in figure A.13 are given. The operator table which is calculated in advance consists of 101 operators. The truncated, Gaussian and smoothed phase operator calculation use the same amount of computation time, the weighted least-squares and the Remez exchange method consume more time (respectively 3 and 10 times more). The non-linear optimization method takes a very long time to compute all operators. It is therefore not very efficient to compute the operator table with a non-linear optimization routines.

Method	19 points	39 points
Truncated	0.13	0.13
Gaussian	0.13	0.13
Smoothed phase	0.13	0.13
WLSQ	0.23	0.30
Remez	1.0	3.37
Non-linear	125.0	565.0

**Table A.1** Computation time in seconds, on a DEC Alpha (3000-500), for the operator table used to calculate the results in figure A.13.

The possibilities and limitations of the weighted least-squares procedure are illustrated with some simple examples. From a computational point of view the desired

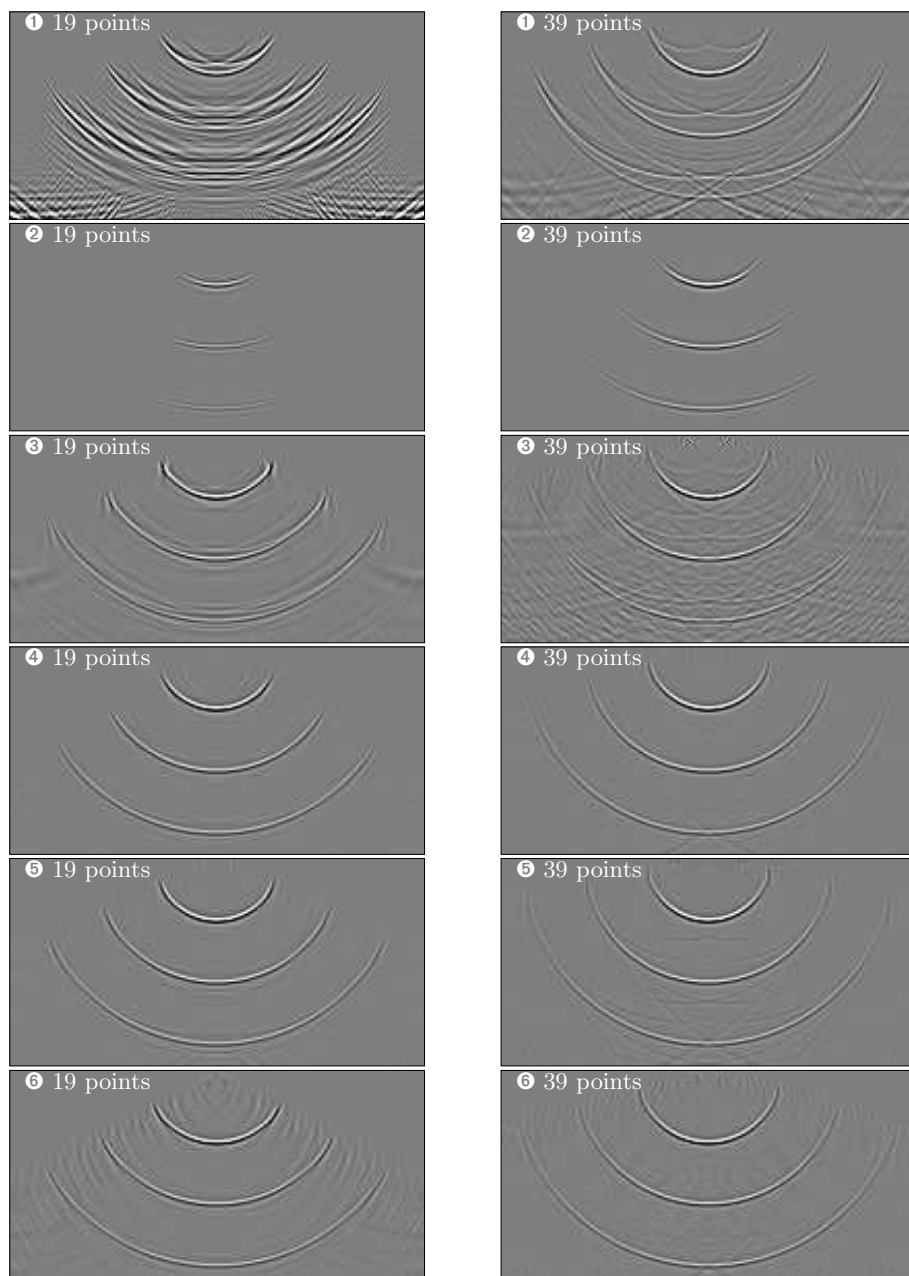


**Figure A.13** Impulse responses for six different extrapolation operators. The left-hand side pictures gives a depth section calculated with an extrapolation operator length of 19 points which is designed to be accurate for angles up to  $65^\circ$ , the right-hand side pictures represent a depth section obtained with an operator length of 39 points and a maximum design angle of  $85^\circ$ .

operator length must be made as short as possible. To illustrate the influence of reducing the number of operator points the experiment of figure A.13 is repeated for different operator lengths. The results are shown in figure A.14. The results obtained with the 11 point operator is inaccurate and unstable for the steeper dips, the 13 point operator is stable but for steeper dips it is still inaccurate. This inaccuracy can be observed most clearly in the smallest semi circle. It is remarkable that the 13 point operator is so much better than the 11 point operator. The 15 point operator is both accurate and stable, the 19 point operator is stable and even more accurate but this is hardly visible. From these migration results it is difficult to predict how an operator with a certain length behaves. The only practical rule is that a longer operator in a homogeneous medium will always be more accurate and stable than a shorter operator. The wavenumber spectra, for a representing frequency, of the different operators gives more information about the accuracy and stability of the operator. It is remarkable that the unstable 11 points operator has a stable behavior in the propagating region and is unstable for the evanescent region. This is also observed in the migrated section which contains high frequency artifacts. This behavior can be influenced by choosing a higher weight value for the wavenumber in the evanescent region. However, this will also give rise to higher peaks, meaning less accurate, in the propagating region. In the wavenumber spectra it is also observed that by using more operator points in the spatial domain will give smaller amplitude errors in the propagating region.

When the maximum angle of interest is reduced the operator length can also be reduced to obtain the same result with a shorter computation time. In the limit a 1 point operator is sufficient to extrapolate a plane wave. In figure A.15 the wavenumber and phase spectrum is shown for a 7 point operator for different maximum design angles. The parameters are the same as before, the frequency shown in the bottom pictures of figure A.15 is 20 Hz. In the amplitude spectrum an interesting property is observed; for higher design angles the operator has a bigger amplitude at the evanescent region, for the 50° operator even bigger than 1. This property is also observed in the right-hand side depth section of figure A.15, this depth section, with operators designed for 45°, is inaccurate for the higher angles. For the operator designed with a maximum angle of 30° the depth section is more accurate and the higher angles of propagation are attenuated. With these simple experiments it is shown that an operator cannot be both short and accurate for steep dips. In designing a short operator the higher angles must be attenuated to overcome steep dip distortion and unstable properties.

**In conclusion;** the weighted least-squares method is a good candidate to compute the operator table used in recursive depth migration schemes, because of its stable and accurate behavior for a broad range of operators, and the relatively small computation time needed to compute the operators. Reducing the operator length will decrease the computation time, but for very short operators the steeper dips

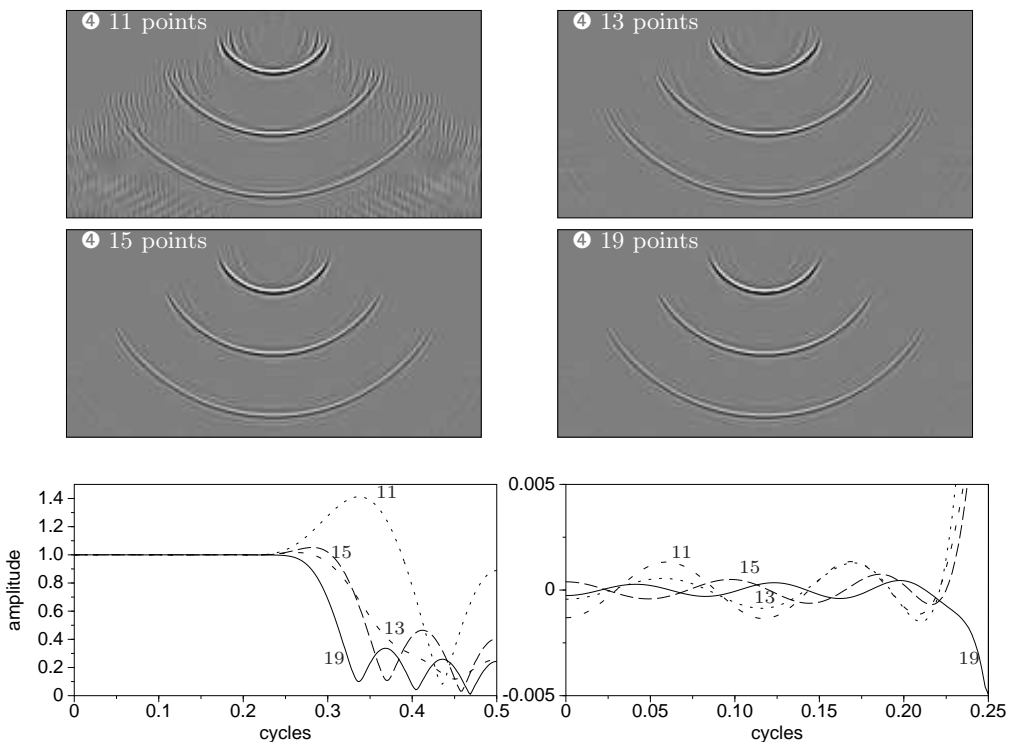


**Figure A.14** Depth sections obtained with different operator lengths in the WLSQ method, but with a fixed maximum design angle of  $65^\circ$ . The two bottom pictures show a detailed view of the operator errors at 20 Hz. The artifacts which are observed in the depth section can be found back in the behavior of the operator.

will become inaccurate and unstable. The weight function used in the optimization procedure can also be optimized in order to give the spatial operator an even more controlled behavior. This optimization of the weight function has been carried out by Rice and Usow (1968) and is called the Lawson algorithm. Note that the length of the optimized operator is for a certain error a function of the wavenumber. In calculating the table of operators this length dependency could be taken into account to arrive at an even more efficient extrapolation.

## A.2 2-Dimensional operators for 3-dimensional extrapolation

To visualize the 3-D subsurface of the earth 3-D migration algorithms are needed which give accurate results within a reasonable computation time. In this section several *recursive depth migration* algorithms are discussed and compared with each other. The backbone of every recursive depth migration method is a 3-dimensional extrapolation algorithm. In lateral homogeneous media the extrapolation algorithm

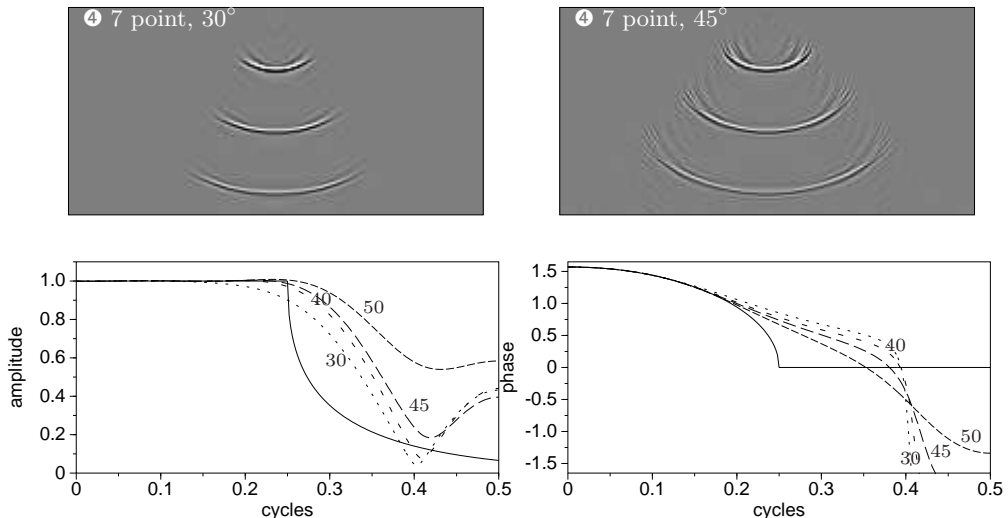


**Figure A.15** Using the WLSQ method with a fixed length of 7 points, the influence of different maximum design angle is investigated. Due to the behavior of the operator in the evanescent region (bottom pictures) high frequency artifacts are observed in the depth section.

can be a simple multiplication in the wavenumber domain, but extrapolation through 3-dimensional inhomogeneous media is a more computation intensive operation and requires a space-variant 2-dimensional spatial convolution. Recently various authors (Hale (1991b); Sollid and Arntsen (1994); Gaiser (1994); Biondi and Palacharla (1994); Kao et al. (1994); Thorbecke and Berkhou (1994, 1995); Soubaras (1996)) have published articles which pay attention to an optimized calculation and efficient implementation of 3-dimensional extrapolation operators in a recursive depth migration. This section will give an overview of the existing methods and introduces several efficient optimization and implementation methods that have not yet been discussed in the Geophysical literature. The computation times of the different algorithms are compared with each other and the performance of the extrapolation algorithm is checked with the aid of a simple synthetic experiment.

A **first** subdivision between the different optimization methods can be made with respect to the type of expansion of the analytical phase shift operator (equation (A.1)) in the wavenumber domain. This expansion can be a (Taylor) series expansion of the analytical phase shift operator with respect to  $k_z = \sqrt{k^2 - (k_x^2 + k_y^2)}$  (as presented in this section), an expansion with respect to  $k_r^2 = k_x^2 + k_y^2$  (Berkhou (1982), Soubaras (1996), Sollid and Arntsen (1994), Hoff (1995) and this section) or an expansion with respect to the cosine terms of the 1-D Fourier transformation Hale (1991a). In equations (A.27) to (A.29) these different approximation to the

expansion	optimization	implementation
$\cos(k_x) \cos(k_y)$	Least Squares	2-D convolution
$\cos(\sqrt{k_x^2 + k_y^2})$	Weighted Least Squares	1-D convolution
$\sqrt{k^2 - (k_x^2 + k_y^2)}$	Non-Linear	Chebychev
$k_x^2 + k_y^2$	Remez Exchange	Series

**Table A.2** Three criteria which are used to discriminate between different 3-dimensional extrapolation algorithms. Note that in principle many combinations between the elements in the three blocks are possible.

phase shift operator are shown

$$\tilde{Y}_0(k_x, k_y) = \exp(-jk_z\Delta z), \quad (\text{A.25})$$

$$\approx \sum_{m=0}^M \sum_{n=0}^N Y_{mn} \cos(k_x m \Delta x) \cos(k_y n \Delta y), \quad (\text{A.26})$$

$$\approx \sum_{m=0}^M Y_m \cos(k_r m \Delta x), \quad (\text{A.27})$$

$$\approx \sum_{m=0}^M a_m [k_x^2 + k_y^2]^m, \quad (\text{A.28})$$

$$\approx \sum_{m=0}^M b_m [k_z]^m. \quad (\text{A.29})$$

Equation (A.26) is the so called direct method which calculates the 2-D extrapolation operator  $Y_{mn}$  by a direct optimization method and can be regarded as a weighted expansion in 2-dimensional cosine terms. The operators obtained with the direct method require the implementation of a full 2-dimensional spatial convolution. Equation (A.27) is a reduction of the 2-dimensional filter problem to a 1-dimensional filter problem by using the circular symmetry of the 2-D phase shift operator and is represented by an expansion in 1-dimensional cosine terms. The 1-dimensional filter problem, to obtain  $Y_m$ , can be solved with any preferred 1-D optimization method. The cosine terms in equation (A.27) are approximated by small 2-dimensional convolution filters.

Equation (A.28) and (A.29) are expansions of the operator in non-spectral polynomials. The terms  $a_m$  and  $b_m$  in the series expansions can be obtained by calculating the coefficients from a Taylor series expansion Berkhou (1982), or optimizing the coefficients with an error definition in a preferred norm, for example the  $L_2$  or  $L_\infty$  norm. The basic polynomials  $k_x^2 + k_y^2$  and  $k_z$  which occur in equations (A.28) and (A.29) are approximated by short and accurate convolution operators.

A **second** subdivision between the different extrapolation algorithms can be made

with respect to the kind of optimization method used to obtain the spatial convolution operator. The type of implementation of the spatial convolution is a **third** criterion to discriminate between the different methods. table A.2 gives an overview of the different techniques which can be used in the expansion, optimization and implementation. Note that in principle many combinations between the elements in the three blocks are possible. For example Holberg (1988) and Blacquière et al. (1989) use a non-linear optimization technique for the operator optimization in a 2-dimensional cosine series (equivalent to a weighted inverse Fourier transformation according to equation (A.26)) and have implemented this operator as a full 2-D convolution. Hale (1991a) makes use of the McClellan transformation in equation (A.27) and uses the coefficients of a 1-D convolution operators in a Chebychev recursion scheme. Soubaras (1996) uses the Remez exchange algorithm in the optimization of the 1-D convolution operators and in the optimization of the expansion factors (with respect to powers of  $k_x^2 + k_y^2$ ) of the phase shift operator in equation (A.28). In this section the weighted least squares optimization method is introduced as a fast alternative method for the optimization of the 2-D convolution operators and in the optimization of the factors in the series expansions. The McClellan method is discussed in detail and several schemes which optimize the original McClellan method are discussed briefly. The series expansions with respect to  $k_z$  and  $k_x^2 + k_y^2$  given in equation (A.28) and (A.29) are worked out in more detail and compared with the other extrapolation methods.

### A.2.1 Direct method

The most straightforward method which does not make use of any series expansion is called, after Berkhout (1982), the direct method. In the direct method the optimization for the convolution operator is defined by the Fourier transformation from wavenumber to spatial domain and implemented by means of an optimization scheme (see Holberg (1988); Blacquière et al. (1989) for the results with a non-linear optimization scheme). The advantage of the direct method is the uncomplicated optimization of the operator and the simple implementation. A disadvantage of this direct method is that in the space-frequency domain the full 2-D convolution has to be carried out for every spatial position. For an operator with a typical operator size of  $25 \times 25$  points this means 625 complex multiplications and summations for every grid point! By using the even symmetry in the operator the number of multiplications can be reduced by a factor of 4 by folding the data into a quarter and application of the convolution to this folded part. However the number of flops remains high, especially if one takes into account that this convolution has to be carried out for every gridpoint, for every frequency of interest and for all the depth steps. In this section the results obtained with the direct method are used as a reference result for comparison with the other, non-direct, methods. In this section three different methods, to calculate the 2-D direct convolution operators, are dis-

cussed with respect to accuracy and efficiency. To compare the results a synthetic migration experiment is introduced which calculates the impulse response of the used operators.

### Weighted Least Squares optimization

The most simple way to obtain space-frequency operators is an inverse Fourier transformation of the exact operators from the wavenumber-frequency domain back to the space-frequency domain. Despite of its simple form this solution is not very efficient because the spatial convolution operator obtained in this way must be very long to give stable and accurate results. Tapering the spatial operator gives some improvements (Nautiyal et al., 1993) but for accurate extrapolation results tapering cannot be used as pointed out by in the previous section. The aim in the design of the operator is a short convolution operator with a wavenumber-frequency spectrum which is, over a desired wavenumber band, equal or close to the phase shift operator in the  $k_x, k_y$ - $\omega$  domain. The starting point in the analysis of this optimization problem is the inverse Fourier transformation which is defined as

$$\tilde{Y}(k_x, k_y) = \int_{-\infty}^{\infty} \int_{-\infty}^{\infty} Y(x, y) \exp(jk_x x) \exp(jk_y y) dx dy. \quad (\text{A.30})$$

Using the discrete version of the Fourier integral and the even symmetry in the phase shift operator equation (A.30) is rewritten in a discrete equation (Blacquière, 1989, after)

$$\tilde{Y}(k_x, k_y) \approx \Delta x \Delta y \sum_{m=0}^M \sum_{n=0}^N S_{mn} Y(m \Delta x, n \Delta y) \cos(k_x m \Delta x) \cos(k_y n \Delta y), \quad (\text{A.31})$$

with  $S_{mn}$  defined as

$$S_{mn} = \begin{cases} 1 & \text{for } m = n = 0, \\ 2 & \text{for } m = 0 \vee n = 0, \\ 4 & \text{for } n \neq 0 \wedge m \neq 0 \end{cases} \quad (\text{A.32})$$

Using the Circular symmetry in the operator by interchanging  $n$  and  $m$  and the fact that  $\sum_{m=0}^M \sum_{n=0}^m = \sum_{n=0}^N \sum_{m=n}^M$  the number of equations can be further reduced to 1/8 of the original number of equations (this reduction is only possible if  $\Delta x = \Delta y$ )

$$\begin{aligned} \tilde{Y}(k_x, k_y) \approx & \Delta x^2 \sum_{m=0}^M \sum_{n=0}^m Y(m \Delta x, n \Delta y) \left[ S_{mn} \cos(k_x m \Delta x) \cos(k_y n \Delta y) \right. \\ & \left. + S'_{nm} \cos(k_x n \Delta x) \cos(k_y m \Delta y) \right], \end{aligned} \quad (\text{A.33})$$

with  $S'_{nm}$  defined as

$$\begin{cases} 0 & \text{for } n = m, \\ 2 & \text{for } n = 0 \vee m = 0, \\ 4 & \text{for } m \neq 0 \wedge n \neq 0 \end{cases} \quad (\text{A.34})$$

and  $M \times N$  being the user specified size of the desired short operator. Using the shorter matrix notation equation (A.33) can be rewritten as

$$\tilde{\mathbf{Y}}' = \mathbf{■Y}, \quad (\text{A.35})$$

with  $\tilde{\mathbf{Y}}$  the desired short operator and  $\tilde{\mathbf{Y}}'$  being its spatial Fourier transform, yielding an approximation of the exact phase shift operator. Equation (A.31) with the quarter, or equation (A.33) with the octal part has to be solved for the unknown operator coefficients  $Y_{mn} = Y(m\Delta x, n\Delta y)$  for all wavenumbers  $(k_x, k_y)$  of interest. Therefore the same weighted error function  $\tilde{\varepsilon}$  as introduced in the previous section is used and the same solution is obtained

$$\mathbf{Y} = \left[ \mathbf{\Gamma}^H \tilde{\mathbf{A}} \mathbf{\Gamma} \right]^{-1} \mathbf{\Gamma}^H \tilde{\mathbf{A}} \tilde{\mathbf{Y}}, \quad (\text{A.36})$$

where  $\mathbf{\Gamma}^H \tilde{\mathbf{A}} \mathbf{\Gamma}$  is a square matrix. The weighted least-squares method can be used in the calculation of short (2-D) spatial convolution operators but also in the calculation of series expansion factors discussed later. For the 1-dimensional optimization problem the WLSQ method can be inverted fast by using the Levinson scheme. For the 2-dimensional problem, the Toeplitz structure is not present anymore and standard LINPACK routines are used to calculate a QR decomposition of the matrix  $\mathbf{\Gamma}^H \tilde{\mathbf{A}} \mathbf{\Gamma}$  and with this decomposition the solution of matrix equation (A.36) can be found. In figure A.16 the wavenumber spectrum of a WLSQ optimized,  $19 \times 19$  points spatial convolution operator is given for  $128 \times 128 k_x, k_y$  points with  $c = 1000 \text{ m/s}$ ,  $f = 25 \text{ Hz}$ ,  $\Delta x = \Delta y = \Delta z = 10 \text{ m}$  and a maximum angle of interest ( $\alpha_{max}$ ) of  $65^\circ$ . In the remainder of this section, about 2-dimensional operators, these parameters will be used in all further examples which represent a phase shift operator in the wavenumber domain. The WLSQ method gives an accurate operator which has a wavenumber spectrum close to the exact phase shift operator as shown in figure A.16. Note that due to the optimization on a rectangular grid the operator has a somewhat square symmetrical shape. If  $\Delta x = \Delta y$  the matrix definition which uses the octal symmetry, given in equation (A.33), can be used in the implementation of the WLSQ solution. This scheme reduces the operator calculation time with a factor of 2 in comparison with equation (A.31), where a quarter of the operator is taken into account, and the matrix equation contains less degrees of freedom so the unknown parameters are better defined.

#### Impulse response of an extrapolation operator

An impulse response experiment is used to test the behavior of the extrapolation operator in an explicit recursive depth migration algorithm. In the middle of a spatial

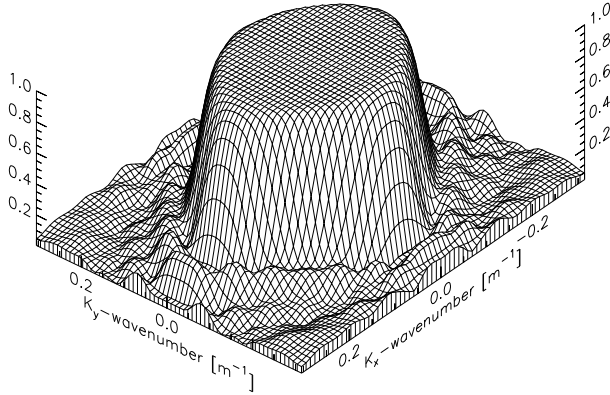


**Figure A.16** The wavenumber spectrum of a WLSQ optimized operator with  $19 \times 19$  spatial points,  $128 \times 128 k_x, k_y$  points with  $c = 1000$  m/s,  $f = 25$  Hz,  $\Delta x = \Delta y = \Delta z = 10$  m and a maximum angle of interest of  $65^\circ$ .

limited homogeneous medium a point source is defined with the source signature shown in figure A.17. This zero-phase Ricker wavelet is centered at 0.512 seconds and has its frequency peak at 13 Hz. The constructed input data set, which contains the wavelet, is transformed to the frequency domain and extrapolated to deeper depth levels for every frequency of interest. At every depth level an imaging step is carried out and the depth image is stored in memory. At the end of the calculation for all frequencies the final depth image is written to disk. The block-diagram of this algorithm is shown in figure A.18. For the other extrapolation algorithms discussed in this subsection the operator optimization block in figure A.18 is replaced with the optimization method of interest, everything else in the scheme remains the same. For this synthetic experiment the following parameters are used:  $c = 1000$  m/s,  $f_{min} = 1$  Hz and  $f_{max} = 45$  Hz,  $\Delta x = \Delta y = \Delta z = 10$  m,  $\Delta t = 0.004$  s and 55 depth steps are taken on a x,y grid of  $111 \times 111$  samples wide. Note that the maximum frequency is positioned in the wavenumber domain at  $0.9 * \frac{\pi}{\Delta x} (= k_N)$ .

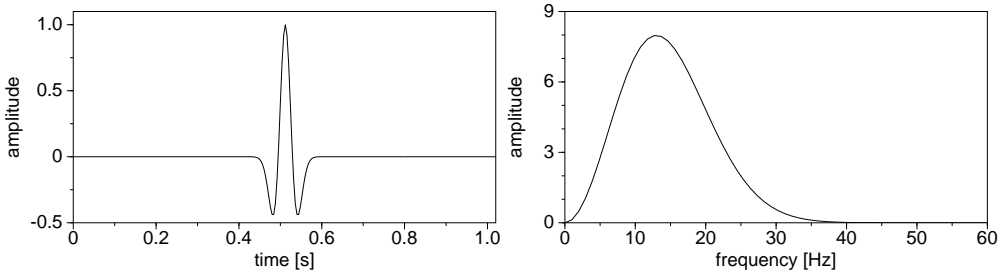


**Figure A.17** Time signature (left) and Amplitude spectrum (right) of the wavelet used in the migration experiments.

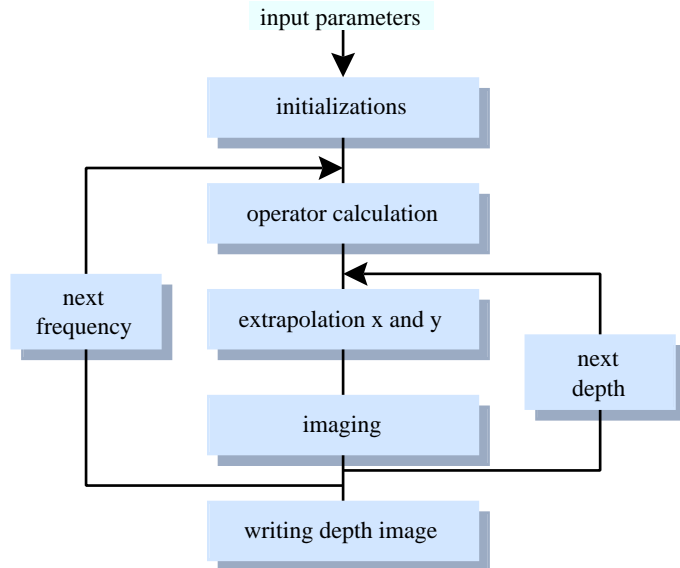


**Figure A.18** Processing scheme for the impulse response experiment. Note that the extrapolation and the operator calculation block in the scheme is different for every different extrapolation method discussed in this section.

The exact response for the described experiment can be calculated by making use of the dipole pulse response which is given by

$$G_0(r, k, \phi) = \frac{1 + jkr}{r^2} \cos \phi \exp(-jkr), \quad (\text{A.37})$$

with  $k = \frac{\omega}{c}$ ,  $\cos \phi = \frac{z}{r}$  and  $r = \sqrt{z^2 + x^2 + y^2}$ . Using the complex conjugate  $G_0^*$  of the dipole response in a non-recursive version of the scheme given in figure A.18 a reference impulse response can be calculated for the synthetic experiment described above. This reference response is discussed first to indicate what the interesting points in the impulse response are.

In figure A.19 the time responses for several depth steps are shown together in one picture. The imaging step at a certain depth level is equivalent with selecting the zero time value for all x- and y-positions. The lowest event in figure A.19 is the time response of the pulse after an inverse extrapolation step of 100 m, every higher event represents a depth level 100 m deeper. It is observed that for the deeper event the crossing with  $t = 0$  is converging to the  $x = 0$  position and will finally disappear if the depth exceeds 512 m, it is also observed that every depth slice corresponds to a certain dip angle. For example for a depth slice at 200 m the dip angle is given by  $\cos \phi = z(ct_0)^{-1} \Rightarrow \phi \approx 67^\circ$ . In figure A.20 three cross-sections out of the 3-D depth image of the reference experiment are shown; the right-hand side pictures

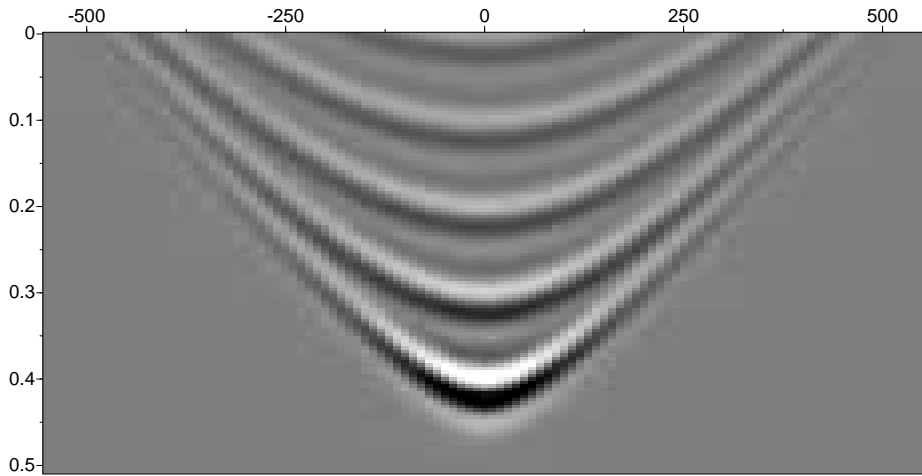


**Figure A.19** Time responses for several depth steps. The lowest event is the time response of the pulse after an inverse extrapolation of 100 m every higher event represents a depth level 100 m deeper.

in figure A.20 show a vertical cross-section for  $x = 0$  (top picture) and a diagonal section for  $x = y$  (bottom picture) and the left hand side picture in figure A.20 shows a horizontal cross-section at a depth of 220 m which corresponds to a reflector dip of 65 degrees. Note that everywhere in this section the presentation of impulse responses will be the same as presented in figure A.20, meaning that the clipping level of the gray scales is the same for all the shown impulse response. Note also that in the diagonal cross-section the distance between two traces is  $\sqrt{2}\Delta x$ , where  $\Delta x$  is the distance between the traces in the vertical  $x = 0$  section.

Using the 2-dimensional  $19 \times 19$  convolution operators obtained with the introduced WLSQ method gives the depth image shown in figure A.21a. In the spatial convolution scheme the even symmetry in the operator is used explicitly by folding the data into common operator point parts, which reduces the number of multiplications significantly. In the calculation of the convolution operator only 1/8 th of the total spectrum is used by making use of the circular symmetry in the operator and the fact that  $\Delta x = \Delta y$ . In figure A.21a it is observed that the artifacts in the depth image consists of inner 'circular' events at the higher angles which have a square structure. This square structure is due to the fact that the solution of the optimization problem is calculated on a rectangular grid. In the presentation of the paper of Kao et al. (1994) similar features were observed. Using a longer 2-D convolution operator as shown in figure A.21b for a  $25 \times 25$  points operator these rectangular artifacts have almost vanished. A more detailed discussion of the errors in the extrapolation operators will be given below.

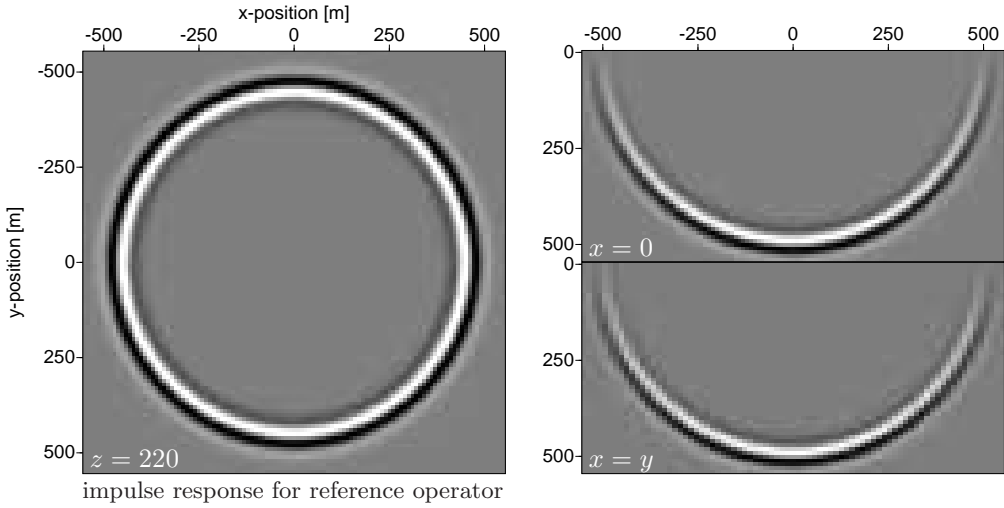


**Figure A.20** Reference output for the migration experiment with left the depth slice at  $z = 220$  m. Top right shows a vertical slice for  $x=0$  and bottom right a diagonal slice for  $x=y$ . Note the perfect circular shape and the accuracy at the higher angles.

### Hankel Transformation

A disadvantage of the direct optimization method discussed in the previous section is that the use of a rectangular grid is visible in the results and the circular symmetry of the operator is not used to its limits. By using the circular symmetry in the phase shift operator the operator optimization problem is better defined because less equations are used to solve for the unknowns. This may reduce the artifacts caused by the use of a rectangular grid and will consume less computation time. The circular optimization problem can be derived by rewriting the continuous Fourier transform pair

$$\begin{aligned}\hat{Y}(k_x, k_y) &= \int \int_{-\infty}^{\infty} Y(x, y) \exp(jk_x x) \exp(jk_y y) dx dy, \\ Y(x, y) &= \frac{1}{4\pi^2} \int \int_{-\infty}^{\infty} \hat{Y}(k_x, k_y) \exp(-jk_x x) \exp(-jk_y y) dk_x dk_y,\end{aligned}$$

with the aid of polar coordinates. For a circular symmetric function in the wavenumber domain with  $k_r = \sqrt{k_x^2 + k_y^2}$ ,  $k_x = k_r \cos \theta$ ,  $k_y = k_r \sin \theta$  and the Jacobian  $dk_x dk_y = k_r dk_r d\theta$  the continuous inverse Fourier transform can be rewritten to

$$\begin{aligned}Y(x, y) &= \frac{1}{4\pi^2} \int_0^{2\pi} \int_0^{\infty} \hat{Y}(k_r) \exp(-jk_r x \cos \theta) \exp(-jk_r y \sin \theta) k_r dk_r d\theta, \\ Y(x, y) &= \frac{1}{4\pi^2} \int_0^{\infty} \hat{Y}(k_r) k_r dk_r \int_0^{2\pi} \exp(-jk_r(x \cos \theta + y \sin \theta)) d\theta.\end{aligned}$$

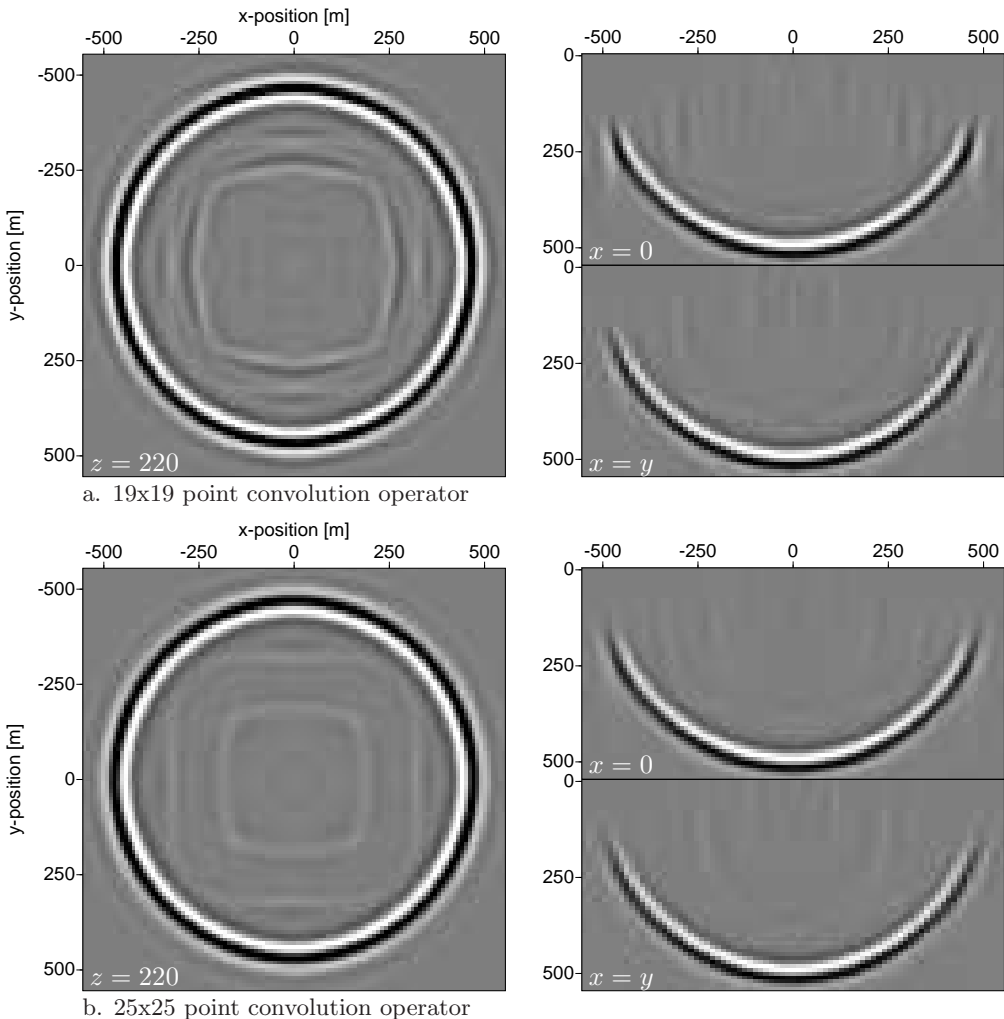


**Figure A.21** Results of the WLSQ optimized operators for different operator sizes. Note that the artifacts which are present in the result for the 19x19 operator disappear for the larger operator size.

Introducing  $r = x \cos \varphi + y \sin \varphi = \sqrt{x^2 + y^2}$  ( $x = r \cos \varphi$ ,  $y = r \sin \varphi$ ) gives

$$Y(r, \varphi) = \frac{1}{2\pi} \int_0^\infty \hat{Y}(k_r) k_r dk_r \frac{1}{2\pi} \int_0^{2\pi} \exp(-jk_r r \cos(\theta - \varphi)) d\theta, \quad (\text{A.38})$$

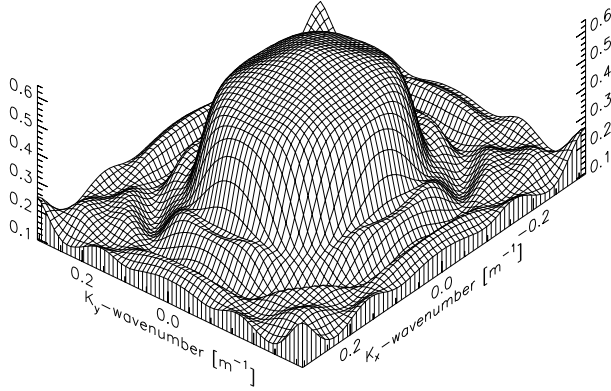


**Figure A.22** The wavenumber spectrum of a circular WLSQ optimized operator with  $19 \times 19$  spatial points and  $128 \times 128$   $k_x, k_y$  points with  $c = 1000$  m/s,  $f = 25$  Hz,  $\Delta x = \Delta y = \Delta z = 10$  m and a maximum angle of interest of  $65^\circ$ . This operator is not useful in a recursive extrapolation scheme.

with the definition of the zero order Bessel function as (equation 9.1.18 in Abramowitz and Stegun (1968) )

$$\begin{aligned} J_0(\tau) &= \frac{1}{\pi} \int_0^\pi \cos(\tau \cos(\theta)) d\theta, \\ J_0(\tau) &= \frac{1}{2\pi} \int_0^\pi \exp(-j\tau \cos(\theta)) + \exp(j\tau \cos(\theta)) d\theta, \\ J_0(\tau) &= \frac{1}{2\pi} \int_0^{2\pi} \exp(-j\tau \cos(\theta)) d\theta \end{aligned}$$

substituted into equation (A.38) gives

$$Y(r) = \frac{1}{2\pi} \int_0^\infty \hat{Y}(k_r) J_0(k_r r) k_r dk_r. \quad (\text{A.39})$$

This equation expresses that the spatial convolution operator and its Fourier transformation are both circular symmetric and are related by the Hankel transform. This is illustrated by the following formulations in polar coordinates

$$\begin{aligned} Y(r) &= \frac{1}{2\pi} \int_0^\infty \hat{Y}(k_r) J_0(k_r r) k_r dk_r, \\ \hat{Y}(k_r) &= 2\pi \int_0^\infty Y(r) J_0(k_r r) r dr. \end{aligned}$$

The spectral limited and discrete version of the Hankel transform is given by

$$Y(p\Delta r) = \frac{1}{N\Delta r} \sum_{n=0}^N \hat{Y}(n\Delta k_r) J_0(n\Delta k_r p\Delta r) n\Delta k_r,$$

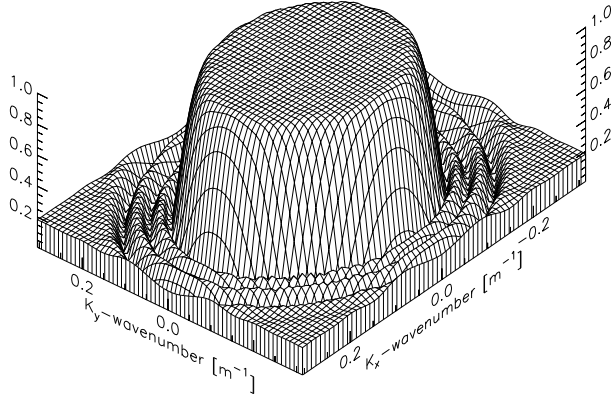


**Figure A.23** The wavenumber spectrum of a rotated Fourier reconstructed operator with  $19 \times 19$  spatial point,  $128 \times 128 k_x, k_y$  points with  $c = 1000 \text{ m/s}$ ,  $f = 25 \text{ Hz}$ ,  $\Delta x = \Delta y = \Delta z = 10 \text{ m}$  and a maximum angle of interest of  $65^\circ$ .

with  $\Delta k_r = \frac{2\pi}{N\Delta r}$ . This last equation is implemented in the WLSQ optimization scheme of equation (A.36) in which the matrix  $\mathbf{\Gamma}$  is defined by the zero order Bessel function  $J_0(k_r r)$  in place of the cosine terms of the Fourier transform. The solution of this problem is an optimized short operator as function of  $r$ . In the optimization problem we can choose the points  $r$  in such a way that they coincide with the rectangular spatial grid the extrapolation is carried out. The wavenumber spectrum of the calculated solution is shown in figure A.22, with the same parameters as used in figure A.16. The spectrum shown is far from good and cannot be used in an extrapolation algorithm. The problem with the Hankel transformation is that for the spatial position  $r = 0$  it is not possible to define a suitable value. If we make it zero we get a singular matrix and making it non-zero is a random choice. So the Hankel transformation cannot be used directly to design circular symmetric convolution operators.

#### Rotated Fourier reconstruction

The idea of rotating a 1-dimensional operator is very useful in the wavenumber domain. In the previous section it was shown that the desired 2-dimensional convolution operator must have a circular symmetric frequency response. The projection onto a line oriented with an angle  $\phi$  from one of the spatial axes is identical with an optimal 1-D convolution operator (Kato and Matsumoto, 1982). A slice along the same orientation in the Fourier domain corresponds to the Fourier transform of the 1-D convolution operator. This is known as the projection slice theorem. Thus the circularly symmetric frequency response is exactly described by one single projection. The problem of obtaining the circular 2-D convolution operator from the spectrum of the optimized 1-D convolution operator can be solved in several ways.

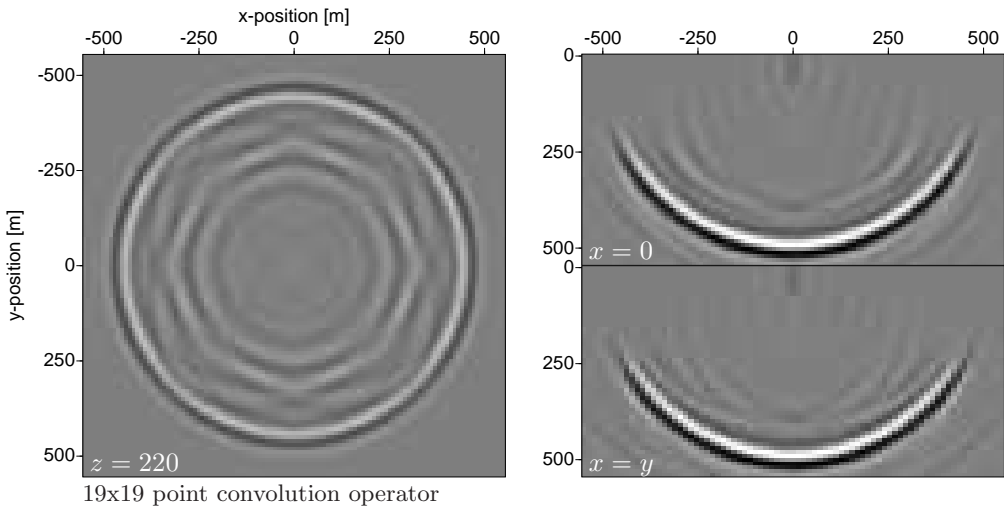


**Figure A.24** Results of the rotated Fourier reconstructed operators for a 19x19 point convolution operator. Note that the artifacts in the result for the 19x19 operator will become weaker by using a larger operator.

The McClellan transformation is one of them and described in subsection A.2.2. Another method is the Fourier reconstruction method which is described below.

Basically the rotated Fourier reconstruction method consists of designing a 1-D optimized spatial operator, computing and rotating its frequency response in the 2-D wavenumber plane, filling the undetermined region with the Nyquist value of the 1-D wavenumber response, performing the 2-D inverse Fourier transformation and then windowing the result. The outer region of the circle is filled with the Nyquist value of the 1-D spectrum to eliminate the Gibbs phenomenon. Note that the rotated wavenumber spectrum has the circular symmetry only in the circular centum, therefore the projection of the 2-D spectrum is only identical with the 1-D spectrum along the vertical and horizontal directions. The projection along any other direction is not exactly identical with the 1-D spectrum but gives a good approximation. After the inverse Fourier transform the result is truncated to the original length of the 1-D convolution operator ( $N \times N$ ). Since the projection is of finite length  $N$ , the obtained 2-dimensional convolution operator has a nearly finite support. Therefore the rectangular windowing distorts the circular frequency response only slightly.

The wavenumber spectrum of an operator obtained in this way is shown in figure A.23. The impulse responses for the operator size  $19 \times 19$  is shown in figure A.24. Note that the depth image has a perfect circular symmetry but in the middle of the circle there are some irregular artifacts visible. In the vertical cross-section a ghost event is observed after and before the main event. An improvement of this method should aim at an reduction of these artifacts to use this very simple and attractive

method to calculate 2-D operators in a more sophisticated way. For example it is possible to use another (non-linear) interpolation method, or a smooth window to truncate the operator in the spatial domain.

### Error analysis

From an engineering point of view it is interesting to investigate how the different parameters in the optimization procedure must be chosen to obtain efficient operators which are accurate up to a desired maximum angle. For this analysis it is necessary to define accuracy in a useful way. In Powell (1981) the most common used definitions of accuracy are given. In this section we will use the  $L_2$  and the  $L_\infty$  norms in a certain domain of interest. The domain of interest is defined by  $k_r < k \sin(\alpha_{max}) (= k_r^{max})$  with  $k = \frac{\omega}{c}$ .

The following  $L_2$  and  $L_\infty$  error norms are defined over the domain of interest

$$\varepsilon_2 = \left[ \frac{\int_{\phi=0}^{\frac{\pi}{4}} \int_{k_r=0}^{k_r^{max}} \|Y(k_r) - \hat{Y}(k_r, \phi)\|^2 k_r dk_r d\phi}{\int_{\phi=0}^{\frac{\pi}{4}} \int_{k_r=0}^{k_r^{max}} \|Y(k_r)\|^2 k_r dk_r d\phi} \right]^{\frac{1}{2}} \quad (\text{A.40})$$

$$\begin{aligned} \varepsilon_\infty^a &= \max_{0 \leq k_r \leq k_r^{max}} |\|Y(k_r)\| - \|\hat{Y}(k_r)\|| \quad (\text{A.41}) \\ &+ \max_{k_r^{max} < k_r \leq k_N} |1 - \|\hat{Y}(k_r)\|| \quad \{\text{if } \|\hat{Y}(k_r)\| > 1.0\} \end{aligned}$$

$$\varepsilon^p = \left[ \int_{\phi=0}^{\frac{\pi}{4}} \int_{k_r=0}^{k_r^{max}} \left\| \frac{\partial E_p}{\partial k_r} k_r \right\|^2 dk_r d\phi \right]^{\frac{1}{2}}, \quad (\text{A.42})$$

with

$$E_p = \arg Y(k_r) - \arg \hat{Y}(k_r, \phi),$$

where  $\hat{Y}(k_r)$  is an approximation to the true function  $Y(k_r)$ ,  $\varepsilon_2$  is the normalized least-squares error,  $\varepsilon_\infty^a$  the maximum amplitude error and  $\varepsilon^p$  a measurement for the derivative of the phase error with respect to the polar distance  $k_r$ . The normalized  $\varepsilon_2$  error is a global error and is related to the accuracy of the operator. The amplitude  $\varepsilon_\infty^a$  error gives an indication of the stability of the operators in a recursive extrapolation scheme. Note that  $\|Y(k_r)\|^2 = 1$  in the domain of interest. Included in the  $\varepsilon_\infty^a$  error is a stability measurement for  $k \sin(\alpha_{max}) < k_r \leq k_N$ . If the amplitude of the operator in this domain is higher than 1.0 then it contributes to the  $\varepsilon_\infty^a$  error. The  $\varepsilon^p$  error is defined in such a way that it is sensitive to errors in the circular symmetry of the operator. In the ideal case the  $\varepsilon^p$  error should be zero because of the circular symmetry of the operator. To compute the derivative with respect to  $k_r$

a three point finite difference operator is used to compute the derivative with respect to  $k_x$  and  $k_y$ . With these derivatives the  $\frac{\partial}{\partial k_r} = \frac{\partial}{\partial k_x} \frac{\partial k_x}{\partial k_r} + \frac{\partial}{\partial k_y} \frac{\partial k_y}{\partial k_r}$  is calculated. If the phase error is large and the derivative with respect to  $k_r$  is also large then the operator will have a detectable non-circular character.

To determine the errors due to the recursive use of the operator in a homogeneous medium (which is a worst case situation) the difference with respect to the reference impulse response is calculated for every depth slice according to

$$\varepsilon_s(z) = \left[ \frac{\int_{x=0}^{x_{max}} \int_{y=0}^{y_{max}} \|Y(x, y, z) - \hat{Y}(x, y, z)\|^2 dx dy}{\int_{x=0}^{x_{max}} \int_{y=0}^{y_{max}} \|Y(x, y, z)\|^2 dx dy} \right]^{\frac{1}{2}}. \quad (\text{A.43})$$

This spatial error will be presented in an error curve as function of the angle. The calculation of the wavenumber errors given by equations (A.40), (A.41) and (A.42) gives three values for one operator defined for one frequency. For a more useful definition three frequencies, within the frequency range of interest, are analyzed: one at a low frequency (in our example 5 Hz), a central frequency (20 Hz) and at a high frequency (40 Hz). To have a better idea how the different errors in the operators are exposed in the depth image a number of experiments is carried out where the most important parameters in the operator design are changing. From these experiments it is possible to derive an error criterion for the calculated operator errors which can be used as a measure of accuracy for the extrapolation result. These experiments are done with different WLSQ optimized operators with a varying weight function, a change in operator size and a varying maximum angle of interest. All other parameters remain the same.

The error for three characterizing frequencies is given in table A.3 for different weighting factors, which are given in the first column. The weighting factor is defined as the value of the box-shaped weight function outside the domain of interest. Inside this domain the weight function is given the value 1.0. A practical

Operator	5 Hz			20 Hz			40 Hz			
	weight	$\varepsilon_2$	$\varepsilon_\infty^a$	$\varepsilon^p$	$\varepsilon_2$	$\varepsilon_\infty^a$	$\varepsilon^p$	$\varepsilon_2$	$\varepsilon_\infty^a$	$\varepsilon^p$
1e-5		1.5e-3	1.9e-2	4.4e-4	5.6e-4	2.8e-2	8.4e-4	3.9e-4	1.3e-2	1.1e-3
5e-5		2.9e-3	2.6e-3	8.4e-4	1.4e-3	2.3e-3	1.6e-3	8.3e-4	4.2e-3	1.4e-3
1e-4		4.1e-3	3.8e-3	1.2e-3	1.7e-3	3.6e-3	2.1e-3	1.3e-3	5.3e-3	1.5e-3
5e-4		6.9e-3	7.4e-3	1.9e-3	2.8e-3	7.3e-3	2.6e-3	1.9e-3	8.1e-3	2.5e-3
1e-3		7.9e-3	9.1e-3	2.0e-3	3.4e-3	9.4e-3	2.7e-3	2.4e-3	9.2e-3	3.2e-3
5e-3		1.0e-2	1.6e-2	2.1e-3	6.0e-3	1.7e-2	2.8e-3	4.0e-3	1.1e-2	7.6e-3
1e-2		1.2e-2	2.0e-2	2.1e-3	8.0e-3	2.4e-2	3.6e-3	5.4e-3	1.3e-2	1.1e-2
5e-2		2.1e-2	3.6e-2	1.6e-3	1.5e-2	3.5e-2	9.4e-4	1.1e-2	2.3e-2	2.2e-2

**Table A.3** Error analysis for different weighting factors with a constant operator size (19 × 19) and maximum angle of interest (60°).

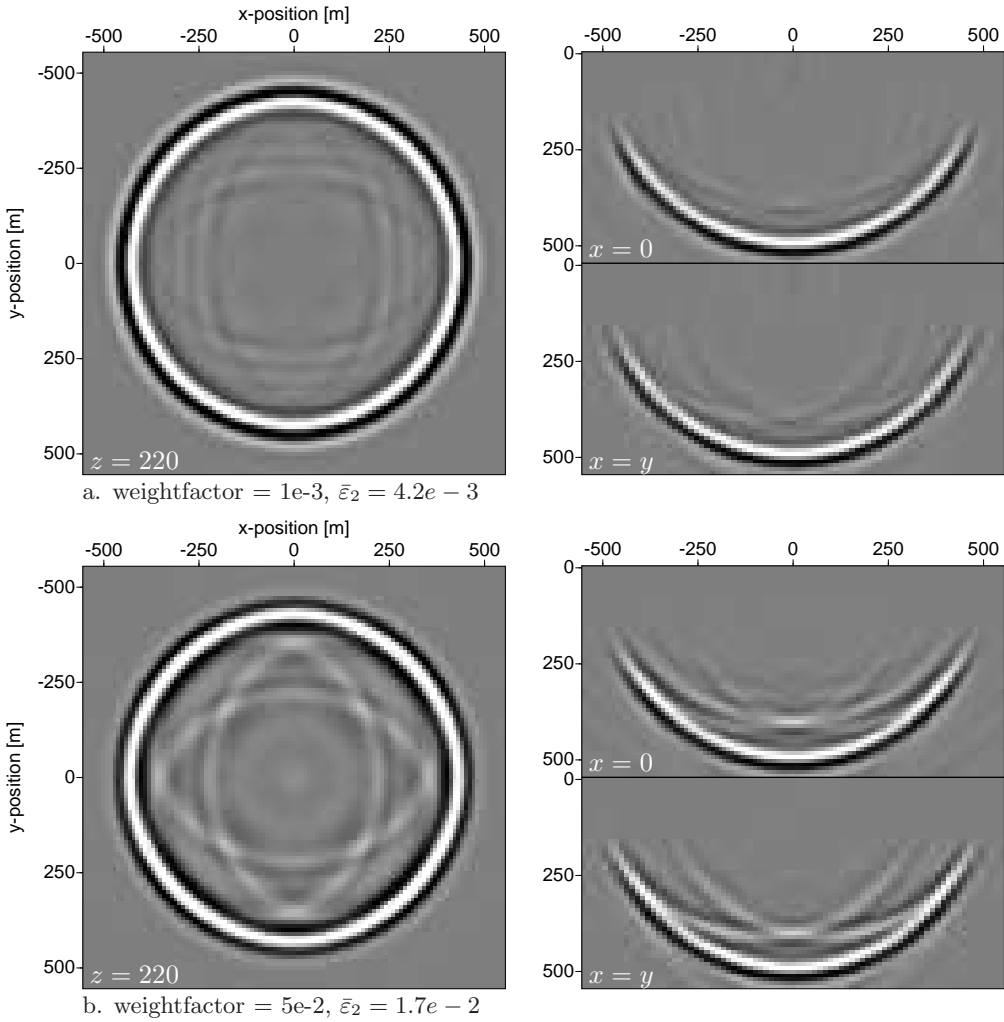


**Figure A.25** The impulse response as function of the weighting factor. The depth cross section is equivalent with an angle of  $65^\circ$ . Note that for larger weighting factors the error grows and the result contains more artifacts.

limit of the weighting factor is  $5e-5$ , because smaller factors gives unstable operators (reflected in the  $\varepsilon_\infty^a$  error).

- *changing weight factor*

In figure A.25 two impulse responses are displayed which differ with respect to the used weighting factor in the operator calculation. The  $\bar{\varepsilon}_2$  error given in the figures is the average error over the three characterizing frequencies. From this figure and

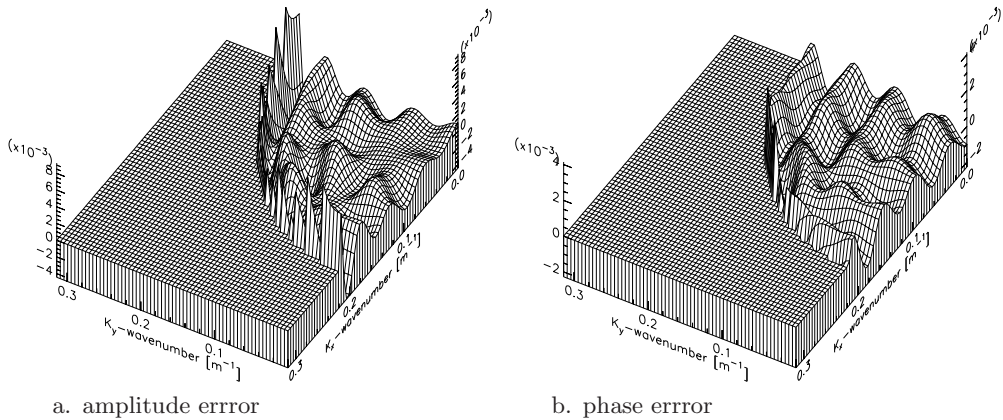


**Figure A.26** Amplitude and phase errors for an operator at 40 Hz with a weight factor of 1e-3 and an operator size of  $19 \times 19$  points. Note the high error values at the edges of the domain of interest.

table A.3 the following conclusions can be drawn;

- (1) For the stable weight factors the  $\varepsilon_2$  and the  $\varepsilon_\infty^a$  errors are increasing if the weighting factor increases. The unstable weight factor (1e-5) is only reflected in the stability part (second equation on the right hand side of equation (A.41)) of the  $\varepsilon_\infty^a$  error. The  $\varepsilon^p$  and the  $\varepsilon_2$  error are not sensitive for instabilities outside the domain of interest. The best weighting factor is therefore that factor which gives an operator which remains just stable. This factor is easily to determine because it turned out that this factor remains almost constant for all frequencies of interest with a fixed operator size.
- (2) An average  $\varepsilon_2$  error smaller than 2e-3 gives an accurate depth image up to the desired maximum angle. A larger  $\bar{\varepsilon}_2$  error gives unacceptable artifacts 'inside' the main event as observed in figure A.25.
- (3) If the  $\varepsilon_2$  error is small than the other errors are not by definition small too. This fact can be explained by looking at the amplitude and phase errors which are shown in figure A.26 for an operator at 40 Hz with a weight factor of 1e-3. The amplitude error function (a) shows a large peaks at the higher angles, the phase error function (b) has its largest error at the maximum design angle. In the calculation of the global  $\varepsilon_2$  error these peaks are averaged out. In the depth images of figure A.25 these peaks in the error function are also not visible, but one can imagine that if these peaks become too big the recursion scheme can become unstable and inaccurate.

- *changing operator size*

In figure A.27 two different operators are displayed which differ with respect to the operator size. From this figure, figure A.21 and table A.4 the following conclusions can be drawn;

Operator	5 Hz			20 Hz			40 Hz		
	$\varepsilon_2$	$\varepsilon_\infty^a$	$\varepsilon^p$	$\varepsilon_2$	$\varepsilon_\infty^a$	$\varepsilon^p$	$\varepsilon_2$	$\varepsilon_\infty^a$	$\varepsilon^p$
13x13	6.1e-3	3.7e-3	1.9e-3	3.1e-3	3.1e-3	4.2e-3	2.7e-3	4.4e-3	6.6e-3
19x19	2.9e-3	2.6e-3	8.4e-4	1.3e-3	2.3e-3	1.6e-3	8.3e-4	4.2e-3	1.4e-3
25x25	1.7e-3	1.8e-3	4.4e-4	6.1e-4	1.6e-3	6.3e-4	4.1e-4	2.0e-3	6.8e-4
31x31	1.3e-3	1.0e-3	2.7e-4	3.5e-4	1.0e-3	3.1e-4	2.5e-4	7.6e-4	5.8e-4
37x37	8.5e-4	1.1e-3	1.6e-4	2.4e-4	6.8e-4	2.7e-4	1.8e-4	2.3e-2	4.7e-4

**Table A.4** Error analysis for different operator sizes with a constant weighting factor (5e-5) and maximum angle of interest ( $60^\circ$ ).

(1) A larger operator size will give more accurate results, but for a certain accuracy (which is reached for this problem at an operator size of  $25 \times 25$  points with an average  $\varepsilon_2$  error in the order of 1e-3) the improvement, by using a larger operator size, on the result is little. So there exists an optimum efficient operator size.

(2) The large  $\varepsilon_\infty^a$  error for 40 Hz operator with size  $37 \times 37$  is due to the fact that the operator has a little amplitude jump after  $60^\circ$  on the diagonal  $k_x = k_y$  which is taken into account by the stability part in the  $\varepsilon_\infty^a$  error. This effect can be detected by the small  $\varepsilon_2$  and  $\varepsilon^p$  error. Choosing a slightly bigger maximum angle ( $65^\circ$ ) will give a stable operator. The jumps at the edges of the domain of interest are typically for least squares design methods. These peaks can be suppressed by changing the weighting function at the edges of the domain or by using an additional optimization step which uses the results of the first step.

(3) Using a small operator and defining a relative large maximum angle gives errors which are typically of the form as shown in the vertical cross section of figure A.27a). These artifacts are due to errors at the higher angles and are most clearly represented by the  $\varepsilon_2$  error in table A.4. These artifacts are due to the error peaks at the edges of the domain of interest. At these critical edges the phase error is for angles larger than the maximum design angle already large while the amplitude of the operator is still close to 1. So the large phase error is not suppressed by a small amplitude error and gives artifacts as observed in the figures. Hoff (1995) has investigated some methods to suppress these artifacts.

- *changing maximum angle*

In figure A.28 two different depth images are displayed which differ with respect to the maximum angle of interest in the operator. The operator size is chosen fixed at  $13 \times 13$ . The result with a maximum angle of  $75^\circ$  is unstable and not displayed. From this figure, figure A.27a and table A.5. The following conclusions can be drawn;

(1) A smaller maximum angle does not automatically gives a better performance for an operator with the same size. From the  $\varepsilon_\infty^a$  error in table A.5 it is observed that there exists an optimum angle which is, for the  $13 \times 13$  operator with the chosen weight factor (5e-5), an angle between 30 and 45 degrees.

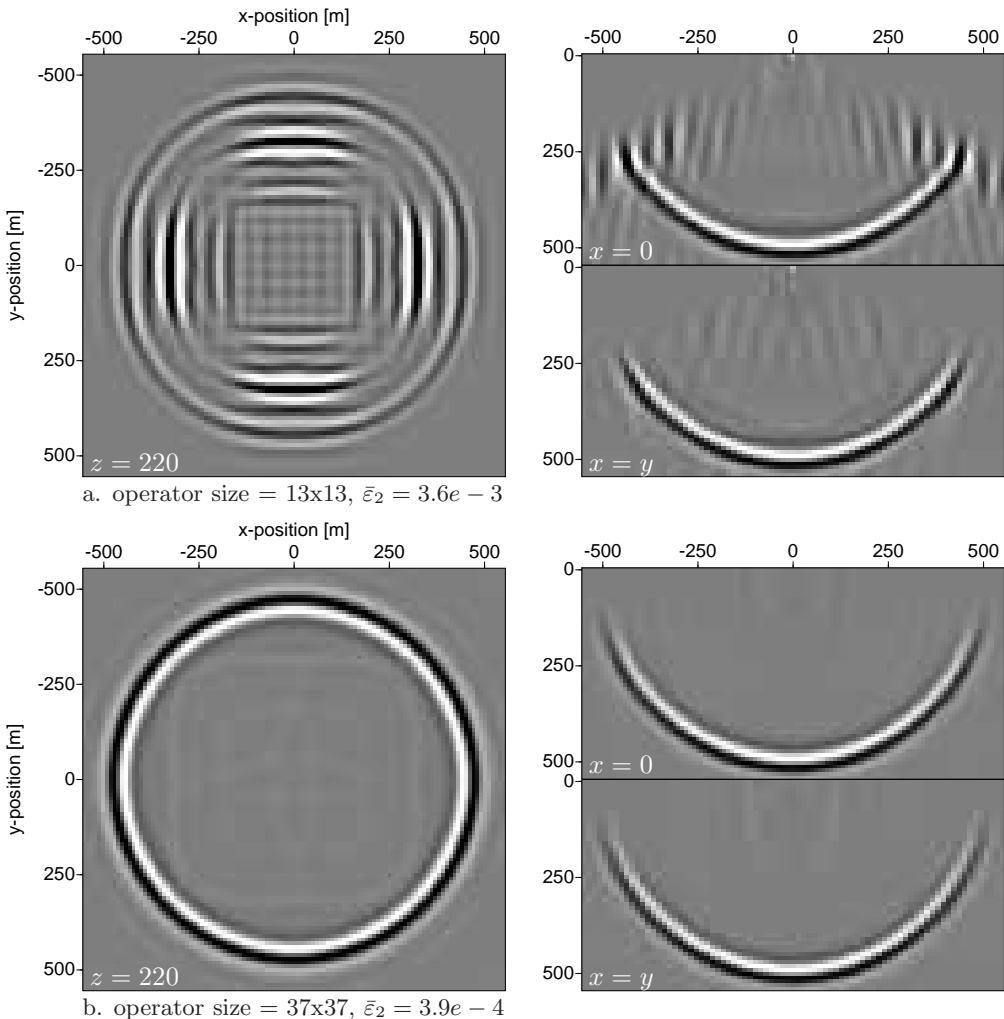


**Figure A.27** The impulse response as function of the operator size. The depth cross section is equivalent with an angle of  $60^\circ$ . Note that a small operator size gives problems at higher angles.

- (2) The  $\varepsilon_2$  and  $\varepsilon^p$  are of little use because these are not defined for angles outside the domain of interest.
- (3) Note that we kept the weighting factor constant throughout the different experiments, by changing the weight factor it is possible to make a very short operator which is also stable outside the domain of interest.

From the experiments described above we can develop a criterion which can be used to determine if a certain operator calculation method gives stable and accurate

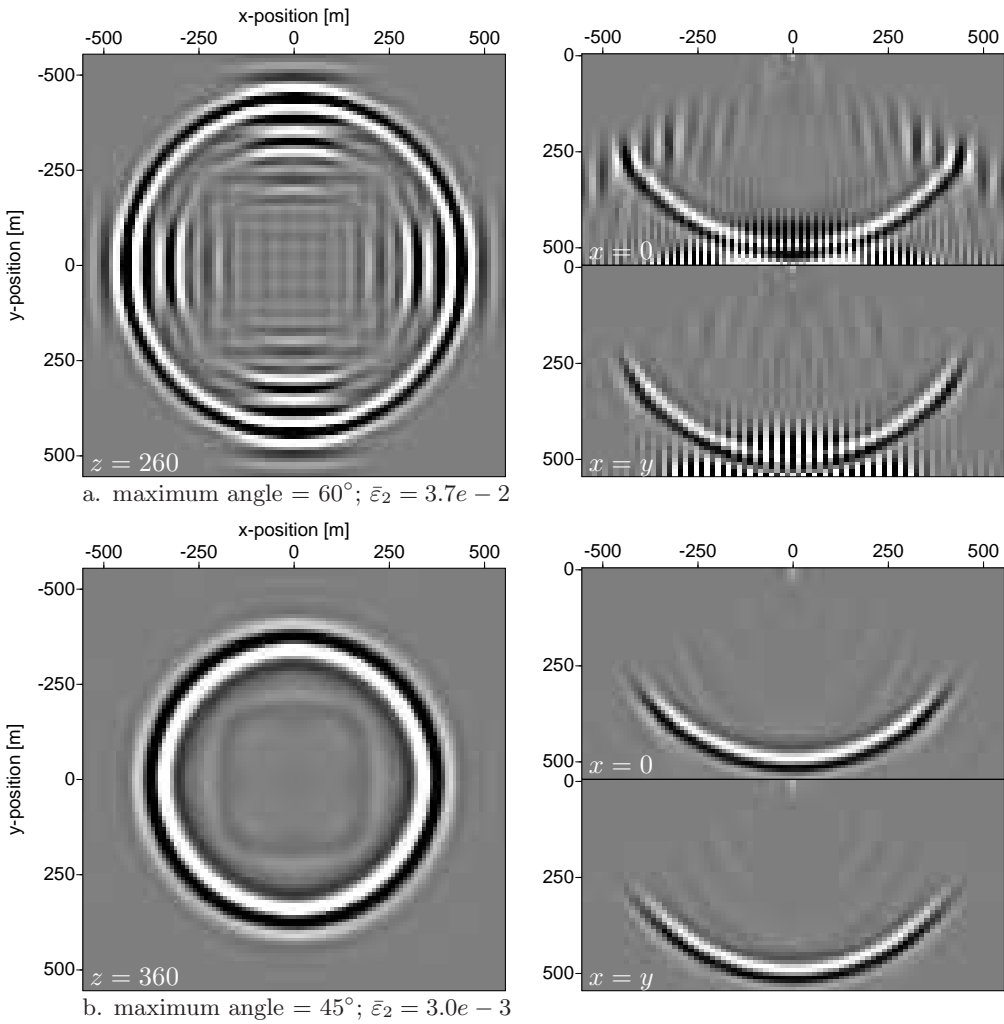


**Figure A.28** The impulse response as function of the maximum angle of interest with an operator size of  $13 \times 13$ . The depth cross section is taken at the maximum angle of interest. Note that the very small angles give problems.

results in a recursive extrapolation algorithm. To use this criterion the wavenumber spectrum of the operator must be calculated for three characterizing frequencies and the  $\varepsilon_2$ ,  $\varepsilon_\infty^a$  and  $\varepsilon^p$  errors have to be calculated for every frequency. These errors must obey the following relations;

- $\bar{\varepsilon}_2 \leq 2e^{-3}$  accuracy measurement
- $\varepsilon_\infty^a \leq 3e^{-3}$  stability measurement
- $\varepsilon^p \leq 1e^{-2}$  circularity measurement

Operator	5 Hz			20 Hz			40 Hz		
	angle	$\varepsilon_2$	$\varepsilon_{\infty}^a$	$\varepsilon^p$	$\varepsilon_2$	$\varepsilon_{\infty}^a$	$\varepsilon^p$	$\varepsilon_2$	$\varepsilon_{\infty}^a$
15	2.1e-3	3.3e-3	-	7.6e-4	5.4e-2	2.0e-5	6.2e-4	9.6e-2	4.9e-5
30	1.2e-3	1.5e-3	4.1e-5	7.2e-4	1.1e-3	1.2e-4	5.3e-4	6.6e-2	1.5e-4
45	2.9e-3	3.0e-3	4.7e-4	1.0e-3	3.2e-3	3.1e-4	8.0e-4	3.0e-3	4.8e-4
60	6.1e-3	3.7e-3	1.9e-3	3.1e-3	3.1e-3	4.2e-3	2.7e-3	4.4e-3	6.6e-3
75	1.2e-2	3.1e-3	6.5e-3	7.8e-3	3.9e-1	2.4e-2	6.14e-3	1.3e-0	3.8e-2

**Table A.5** Error analysis for different maximum angles with a constant weighting factor (5e-5) and a fixed operator size of  $13 \times 13$ .

The  $\varepsilon^p$  error is not tested very well in this section, but in the section about the McClellan method the  $\varepsilon^p$  error turns out to be very useful and the  $\varepsilon^p$  criterion can be defined better.

The performance of the rotated Fourier reconstruction method can be analyzed with the defined error criteria. In table A.6 the errors are given for different operator sizes. The 1-D operators are obtained by using the Remez exchange algorithm (similar results were obtained by using a WLSQ operator). The large  $\varepsilon_2$  errors indicate that the overall spectrum of the operator is inaccurate. A better interpolation method (better than linear) or a smoother window in the spatial domain may improve the result. With the used linear interpolation method a larger operator size does not improve the result significantly.

Operator	5 Hz			20 Hz			40 Hz		
	size	$\varepsilon_2$	$\varepsilon_{\infty}^a$	$\varepsilon^p$	$\varepsilon_2$	$\varepsilon_{\infty}^a$	$\varepsilon^p$	$\varepsilon_2$	$\varepsilon_{\infty}^a$
19x19	2.4e-2	3.9e-2	4.0e-3	5.7e-3	1.3e-2	6.2e-3	4.6e-3	1.0e-2	6.7e-3
25x25	1.8e-2	3.2e-2	2.4e-3	4.8e-3	1.3e-2	3.8e-3	2.3e-3	1.0e-2	1.6e-3
31x31	1.9e-2	3.6e-2	2.5e-3	3.7e-3	1.3e-2	2.2e-3	1.6e-3	5.1e-3	2.8e-3

**Table A.6** Fourier reconstructed operators which are accurate up to a maximum angle of  $60^\circ$ . The 1-D operators are obtained by using the 1D WLSQ method.

Up to now the errors were calculated in the wavenumber domain and interpreted in the spatial domain, but with the aid of the reference result and equation (A.43) it is possible to calculate an error directly in the spatial domain. In figure A.29 this error is shown for the  $19 \times 19$  and  $25 \times 25$  WLSQ operators which impulse response is displayed in figure A.21. The vertical cross section is displayed for the diagonal  $x = y$  and the horizontal cross section for an angle of  $65^\circ$ . The top picture on the right hand side shows the error as function of the angle (=depth). From these errors the following observations are made:

(1) The increasing error line for higher angles as displayed in figure A.29 is due to

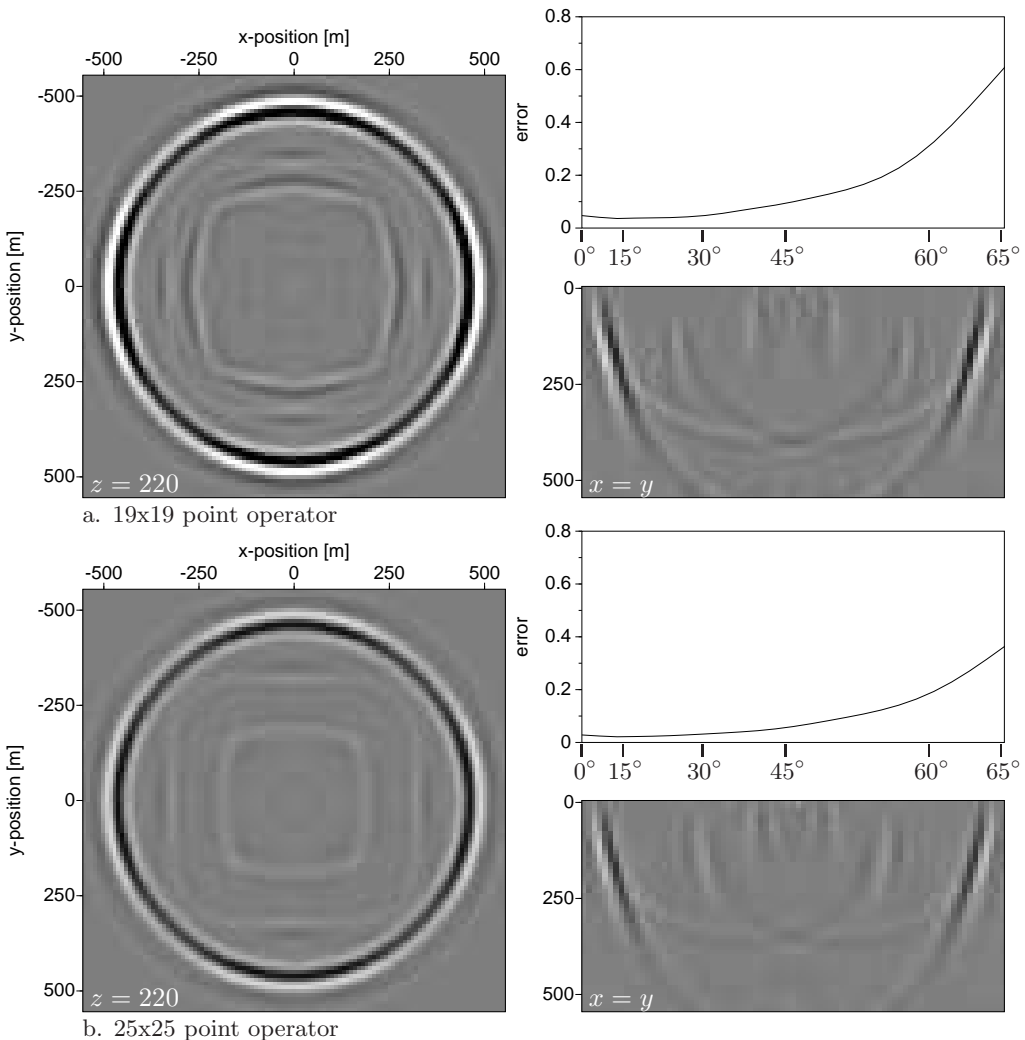


**Figure A.29** The spatial error as function of angle (=depth) together with a horizontal (for  $65^\circ$ ) and vertical (for  $x = y$ ) cross section of the error. Note that the all cross sections are displayed with the same scaling factor.

amplitude errors and artifacts at the higher angles.

- (2) Increasing the operator size increases the accuracy; less artifacts and a better amplitude.
- (3) From the impulse response alone it is difficult to interpret the accuracy of the operator, comparing it with the reference operator gives a good indication of the errors in the operator and the influence of the recursive application of the operators.

Given the error criteria we can also determine how the weight factor and the operator

size must be chosen for a maximum angle of interest. The results of these experiments are summarized in table A.7. The small angles  $15^\circ$  and  $30^\circ$  are difficult to optimize for the given maximum angle, but by choosing a slightly bigger angle the operator can become stable and accurate for the smallest operator size possible. For example to get the operator for  $30^\circ$  a maximum design angle of  $40^\circ$  degrees has to be chosen. For the higher angles this problem does not occur. If one wants to design operators with small maximum angles of interest and suppression of all the higher angles a larger operator size must be chosen than the one given in table A.7. The larger  $\bar{\varepsilon}^p$  error in the  $75^\circ$  operators is not as bad as it looks, the largest error peaks are positioned at the edges of the domain of interest.

Note that for small operator sizes the higher frequencies are most sensitive to errors, for the larger operators the lower frequencies are more sensitive to errors. This behavior is related to the WLSQ optimization method. A very small operator has a limited number of 'error' peaks in the frequency domain due to the limited number of contributing wavenumber components. The WLSQ optimization method with a limited number of wavenumber components cannot have very large peaks (Berkhout, 1984). If there are more wavenumber components the WLSQ method can build up large peaks in the error function (Gibbs phenomenon).

Operator			20 Hz			Average		
angle	size	weight	$\varepsilon_2$	$\varepsilon_\infty^a$	$\varepsilon^p$	$\bar{\varepsilon}_2$	$\bar{\varepsilon}_\infty^a$	$\bar{\varepsilon}^p$
15	5x5	1e-5	1.6e-3	3.2e-3	1.6e-5	2.4e-3	2.2e-3	7.1e-5
30	9x9	2e-5	1.4e-3	3.0e-3	5.6e-4	1.9e-3	2.9e-3	2.7e-4
45	13x13	4e-5	1.0e-3	3.3e-3	3.5e-4	1.5e-3	3.1e-3	3.9e-4
60	19x19	4e-5	1.2e-3	2.4e-3	1.6e-3	1.5e-3	2.9e-3	1.2e-3
75	31x31	6e-5	1.7e-3	1.2e-3	4.8e-3	1.9e-3	1.4e-3	4.3e-3

**Table A.7** Optimum operators which are accurate up to a maximum angle of interest. Note that for small angles these operators are stable but don't suppress all higher angles.

### A.2.2 McClellan transformation, expansion in $\cos(k_r)$

The McClellan transformation transforms a 1-D convolution operator to a 2-D convolution operator with a certain symmetry. This transformation is of interest because the implementation is simple and the computation of the transformation coefficients can be done efficiently. Hale (1991a) introduced the McClellan transformation into the Geophysical world and described two related techniques which replace the 2-dimensional direct spatial convolution: (1) transformation of the *non-recursive* 1-dimensional symmetrical filter in a 1-dimensional *recursive* filter by using the Chebychev recursion formula, (2) the McClellan transformation of a 1-dimensional filter to a circular symmetric 2-dimensional filter. In this subsection first the transformation from a 1-dimensional filter to a 2-dimensional filter will be discussed. Next the Chebychev recursion formula is explained and at the end of this section several methods are discussed which optimize the steps and coefficients used in the McClellan transformation.

#### McClellan Transformation form 1-D to 2-D

If the operator has a circular symmetry it is possible to reduce the computation time of the 2-dimensional filter by means of a McClellan transform. The McClellan transform (McClellan, 1973) defines a mapping from a 1-D wavenumber axis to the 2-D wavenumber domain. The change of variables to be described depends on the fact that both the operator approximations in 1- and 2-dimensions can be written as sums of cosine functions. The 1-dimensional filter problem of an even symmetrical operator can be rewritten as (note the similarity with equation (A.31))

$$\tilde{Y}(k_r) \approx Y(0) + 2 \sum_{m=1}^M Y(m\Delta x) \cos(k_r m\Delta x), \quad (\text{A.44})$$

$$\tilde{Y}(k_r) \approx \sum_{m=0}^M Y'_m(m\Delta x) \cos(k_r m\Delta x), \quad (\text{A.45})$$

$$\tilde{Y}(k_r) \approx \sum_{m=0}^M \hat{Y}(m\Delta x) \cos(k_r \Delta x)^m, \quad (\text{A.46})$$

with the choice of a suitable set of coefficients  $\hat{Y}(m\Delta x)$  that approximate the 1-D extrapolation operator  $\tilde{Y}(k_r)$ . In equation (A.45)  $Y'_m = 2Y_m$  for  $m = 1, \dots, M$  and  $Y'_0 = Y_0$  for  $m = 0$ . The step from equation (A.45) to equation (A.46) can be seen by letting  $\phi = \cos(k_r \Delta x)$ , then  $\cos(k_r m\Delta x) = \cos(m \arccos(\phi)) = T_m(\phi)$ , where  $T_m(\phi)$  is the Chebychev polynomial of order  $m$  as introduced in equation (A.21). Each cosine term in equation (A.45) may then be expressed in the form

$$\cos(k_r m\Delta x) = \sum_{n=0}^N \alpha_{m,n} \cos(k_r \Delta x)^m, \quad (\text{A.47})$$

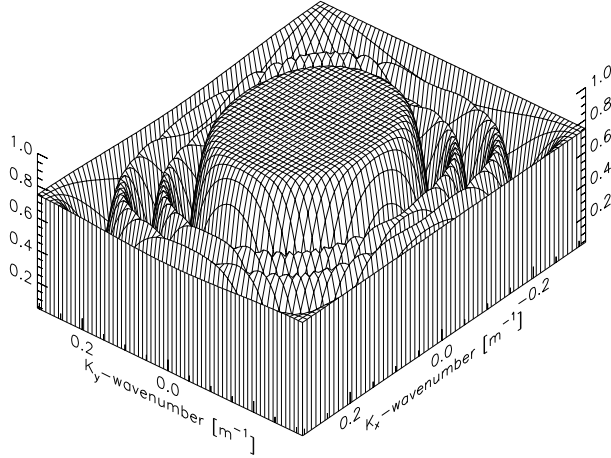


**Figure A.30** The wavenumber spectrum of a first order McClellan operator with a 1-D operator of 19 spatial point,  $128 \times 128 k_x, k_y$  points with  $c = 1000 \text{ m/s}$ ,  $f = 25 \text{ Hz}$ ,  $\Delta x = \Delta y = \Delta z = 10 \text{ m}$  and a maximum angle of interest of  $65^\circ$ .

where the  $\alpha_{m,n}$  are real coefficients and easily obtained with the Chebychev recursion formula. Equation (A.45) reduces then further to

$$\tilde{Y}(k_r) \approx \sum_{m=0}^M Y'(m\Delta x) T_m(\phi) = \sum_{m=0}^M \hat{Y}(m\Delta x) \phi^m, \quad (\text{A.48})$$

where both right-sides of the equation are now polynomials in  $\phi$ .

The cosine terms in equation (A.46) can be approximated by a 2-dimensional filter (assuming  $\Delta x = \Delta y$ )

$$\cos(k_r \Delta x) \approx \sum_{p=0}^P \sum_{q=0}^Q c_{pq} \cos(k_x p\Delta x) \cos(k_y q\Delta y), \quad (\text{A.49})$$

where  $c_{pq}$  are called the McClellan factors after McClellan (1973). By making the substitution of equation (A.49) into equation (A.46) it reduces to

$$\tilde{Y}(k_r) \approx \sum_{m=0}^M \sum_{n=0}^N \ddot{Y}(m\Delta x, n\Delta y) \cos(k_x m\Delta x)^m \cos(k_y n\Delta y)^n, \quad (\text{A.50})$$

which can be put in the form (using Chebychev's recursion formula again)

$$\tilde{Y}(k_r) \approx \sum_{m=0}^M \sum_{n=0}^N \check{Y}(m\Delta x, n\Delta y) \cos(k_x m\Delta x) \cos(k_y n\Delta y), \quad (\text{A.51})$$

which is the desired form for a 2-dimensional filter which was already shown in equation (A.31) (Note that  $\check{Y}$  and  $\tilde{Y}$  are scaled versions of  $Y$ ). For example for

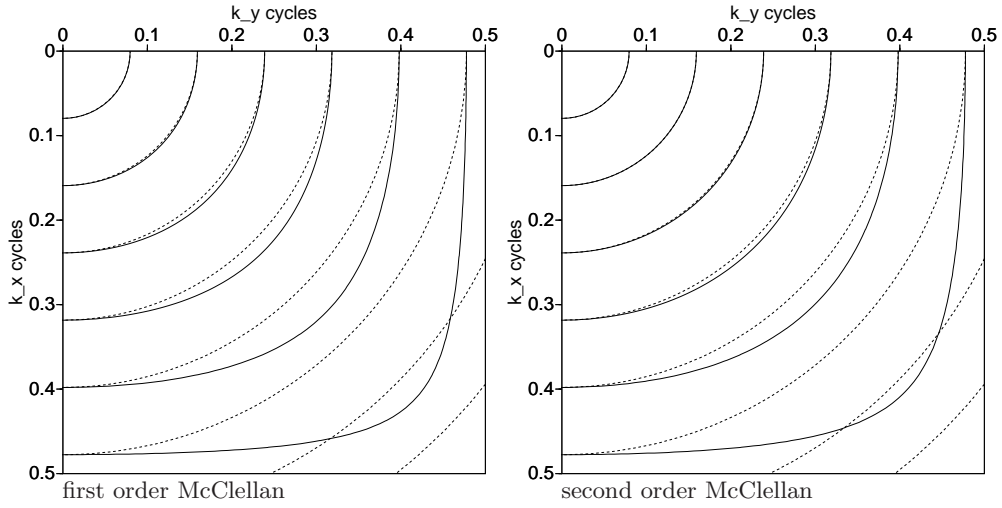


**Figure A.31** Contour plots for the first and second order McClellan transformation. Note that for higher wavenumbers both approximations deviate from the ideal circular (dashed) line.

If  $P = Q = 1$  the transformation for circular symmetry reduces to a 9-term McClellan convolution operator (also called a first order approximation) which is given by Hale (1991a) where  $-c_{00} = c_{10} = c_{01} = c_{11} = 0.5$  and

$$\cos(k_r \Delta x) \approx -1 + 0.5(1 + \cos(k_x \Delta x))(1 + \cos(k_y \Delta y)). \quad (\text{A.52})$$

In figure A.30 an extrapolation operator is shown which is designed with the first order McClellan transformation of equation (A.52) and a 1-D operator  $Y(m\Delta x)$  of 10 points (19 point full operator length). Note the square shape of the operator for the wavenumbers near the Nyquist wavenumber (the edges of the figure). Choosing  $P = Q = 2$  gives a 17-term McClellan transform (second order approximation), which is also given by Hale (1991a)

$$\begin{aligned} \cos(k_r \Delta x) \approx & -1 + 0.5(1 + \cos(k_x \Delta x))(1 + \cos(k_y \Delta y)) \\ & - 0.5c(1 - \cos(2k_x \Delta x))(1 - \cos(2k_y \Delta y)), \end{aligned} \quad (\text{A.53})$$

with  $c = 0.0255$ . The McClellan factors  $c_{pq}$  can be derived by defining points in the  $k_x, k_y$  plane which map to a point on the  $k$ -axes of the 1-D operator such that all coefficients are uniquely defined (for the first order McClellan transform only 4 mapping points are needed). The problem with the McClellan transform, given the original McClellan factors in equations (A.52) and (A.53), is that for higher angles the transformation deviates from the ideal circular shape. The contour plots shown in figure A.31 represent the contours of the first order McClellan ( $P = Q = 1$ ) and the second order McClellan ( $P = Q = 2$ ) transformation. In the contour plots

the deviation from the ideal circular shape for the higher wavenumbers is observed clearly. The second order transformation reduces the deviation a little but remains still significant.

#### Chebychev recursion formula

The second improvement in the computation scheme is the transformation of the non-recursive 1-dimensional filter to a 1-dimensional recursive filter derived from the recursive formula of the Chebychev polynomials

$$\cos(m\phi) = 2\cos(\phi)\cos((m-1)\phi) - \cos((m-2)\phi). \quad (\text{A.54})$$

This Chebychev filter structure is not useful for 1-dimensional filters. Direct convolution is both simpler and more efficient. The Chebychev structure is more advantageous for 2-dimensional operators with an even symmetry, such as the circular symmetric extrapolation operators. Writing equation (A.54) for the first four terms in the 1-dimensional case gives

$$\begin{aligned} \tilde{Y}(k_x) &= Y_0 + 2 \sum_{m=1}^M Y_m \cos(k_x m) \\ &= Y_0 \\ &\quad + 2Y_1[\cos(k_x)] \\ &\quad + 2Y_2[2\cos(k_x)\cos(k_x) - 1] \\ &\quad + 2Y_3[2\cos(k_x)\left(2\cos(k_x)\cos(k_x) - 1\right) - \cos(k_x)] \\ &\quad + 2Y_4[2\cos(k_x)\left(2\cos(k_x)\left(2\cos(k_x)\cos(k_x) - 1\right) - \cos(k_x)\right) - (2\cos(k_x)\cos(k_x) - 1)] \end{aligned} \quad (\text{A.55})$$

and is shown in figure A.32. This recursive scheme can be implemented in the computer without much effort. McClellan and Chan (1977) have analyzed this so called Chebychev structure in detail and observed that the scheme requires the minimum number of multiplications in comparison with the direct scheme and it is the most stable scheme with respect to the round-off noise. Note that only the coefficients of the 1-D operator are involved. Hence, the number of computations

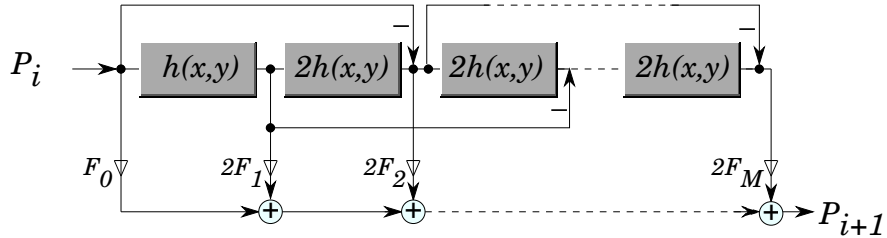


**Figure A.32** Chebychev recursion scheme. The  $h(x, y)$  boxes represent the 2-D McClellan transformation of  $\cos(k_r)$ ,  $Y_m$  represents the coefficients of the 1-D convolution operator.

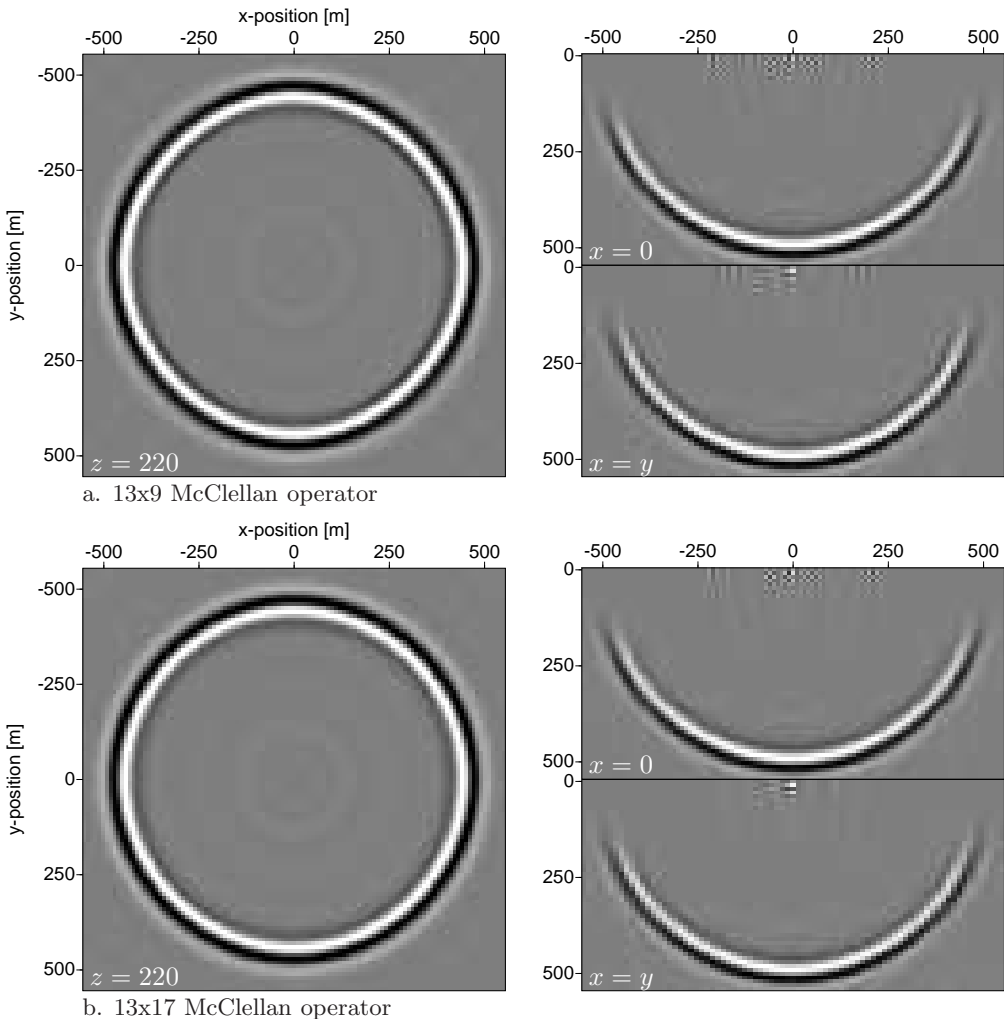


**Figure A.33** Depth images obtained with the original McClellan transformation. For the higher angles both operators deviate from the ideal circular shape. Note the deviation at the higher angles in the diagonal slice.

depends linearly on the length  $N$  of the 1-D operator and not on  $N^2$  as in the implementation of a direct 2-D convolution. The computation times for several 1-D operator lengths and different McClellan operators are given at the end of this section.

In figure A.33 the migration results of the McClellan transformation combined with the Chebychev recursion scheme are shown for both the first (a) and second (b) order McClellan transformation. The used optimized 1-D convolution operators

have a full length of 25 points and are obtained with the Remez exchange algorithm. The Chebychev recursion scheme makes use of the even symmetry in the operator so only 13 points of the 1-D operator are needed as expansion terms in the recursive scheme. The notation of the operator size used in figure A.33 gives first the number of terms in the expansion and second the size of one single term. For example the notation  $13 \times 9$  means that the expansion is done in 13 terms where every term consists of an operator with 9 points.

The cross-sections in figure A.33 give a good illustration how the McClellan transformation handles the higher angles. Note that the deviation of the ideal circle for the second order (17 term) is only a little less than for the first order (9 term) McClellan transformation. The noise around the source position in the vertical slices are an artifact of the used 1-D operator. Despite the deviation at the higher angles the McClellan transformation combined with the Chebychev recursion scheme is a very powerful and useful approach. The performance at higher angles can be improved in several ways. In the the following paragraphs four improvements are discussed.

### Hazra and Reddy Coefficients

Optimizing the design of the McClellan factors  $c_{pq}$  in equation (A.49) is a good way to improve the performance of the McClellan transformation. The first order filter is of special interest because it is a small and therefore fast operator. The aim of the technique proposed by Hazra and Reddy (1986) is to make the maximum contour of interest of the 2-D operator approximate a circle with a high degree of accuracy. This better approximation is achieved by mapping an additional point, defined by the maximum wavenumber of interest  $k_r^{max}$ , of the 2-D operator onto the maximum wavenumber of interest ( $k_x^{max}$ ) of the 1-D filter. This mapping of the additional point is obtained by making the wavenumber  $k_x^{max}$  of the 1-D filter as one of the design parameters. A consequence of this is that the maximum wavenumber of interest of the 2-D operator on the  $k_x$ -axis and  $k_y$ -axis may be different from the maximum wavenumber of interest of the 1-D filter.

The first order original McClellan transformation maps the origin  $(0,0)$  in the  $(k_x, k_y)$  plane onto the point  $k_x = 0$  of the  $k_x$ -axis in the wavenumber response of the 1-D operator. The points  $(k_{x,N}, 0)$ ,  $(0, k_{y,N})$  and  $(k_{x,N}, k_{y,N})$  from the  $(k_x, k_y)$  plane all map onto  $k_x = k_{x,N}$ . With the definition of these four points the coefficients in the first order McClellan transform are uniquely determined. This mapping has the following properties: (1) the contours of the McClellan transformation are approximately circular for low values of  $k_r$  and deviates considerably from circular contours as  $k_r$  increases and is square at  $k_r = k_{Nyquist}$ , (2) the original McClellan transformation makes the frequency response of the 2-D operator along the  $k_x$ -axis and along the  $k_y$ -axis identical to the frequency response of the original 1-D operator. The contour plots in figure A.31 show that the deviation from the circular contour is maximum near the neighborhood of the diagonal joining the points  $(0,0)$

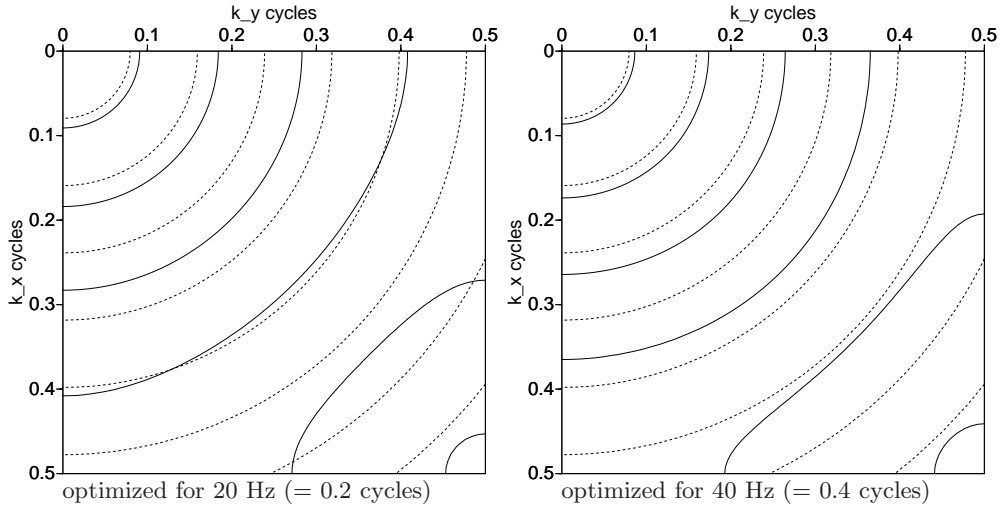


**Figure A.34** Contour plots of the optimized Hazra and Reddy transformation for two different frequencies. Note the improvement in the circular shape in comparison with the original McClellan transformation.

and  $(k_{x,N}, k_{y,N})$  in the  $(k_x, k_y)$  plane. It is possible, for a given maximum  $k_r^{\max}$ , to improve the contour by forcing an appropriate point on this diagonal to be on the circular contour. With this mapping of an extra point on the circular contour, it is not possible, to make the frequency response of the 1-D operator identical to the frequency response of the original 1-D operator along the  $k_x$ -axis and along the  $k_y$ -axis. Thus the mapping of the extra point on the diagonal is only possible when the maximum wavenumber of interest along the  $k_x$  axes is one of the design parameters. The McClellan factors according to Hazra and Reddy are dependent on the maximum wavenumber of interest and are given by

$$c_{11} = \frac{ab - 2ac}{2bc^2}, \quad c_{01} = c_{10} = \frac{1}{g} - c_{11}, \quad c_{00} = 1 - c_{01} - c_{10} - c_{11},$$

where

$$b = \sin^2\left(\frac{k_r^{\max}}{2}\right), \quad c = \sin^2\left(\frac{k_r^{\max}}{2\sqrt{2}}\right), \quad g = 2 + \frac{b - 2c}{c^2}, \quad a = \frac{b}{g} \quad (\text{A.56})$$

$$k_x^{\max} = 2 \sin^{-1}(\sqrt{a})$$

where  $k_r^{\max}$  is the maximum wavenumber of interest of the circular symmetric 2-D filter and  $k_x^{\max}$  the maximum wavenumber of interest of the 1-D operator. For a more detailed discussion on the derivation of the parameters in equation (A.56) the reader is referred to Hazra and Reddy (1986). In figure A.34 two contour plots are shown for two different frequencies. Up to the desired maximum value these contours are circular, outside the desired value the contours are not circular shaped.

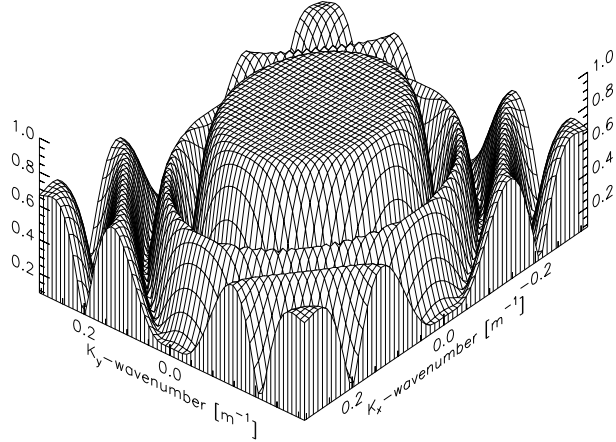


**Figure A.35** The wavenumber spectrum of a first order McClellan operator with the optimized Hazra and Reddy coefficients and a 1-D operator of 19 spatial points with  $128 \times 128 k_x, k_y$  points with  $c = 1000 \text{ m/s}$ ,  $f = 25 \text{ Hz}$ ,  $\Delta x = \Delta y = \Delta z = 10 \text{ m}$  and a maximum angle of interest of  $65^\circ$ .

The operator calculated with these optimized contours is shown in figure A.35. Note the difference with figure A.30.

In the extrapolation algorithm first the McClellan factors are calculated according to A.56 for a given  $k_r^{max}$  which gives besides the optimized McClellan factors also a  $k_x^{max}$  for the 1-D operator. With this calculated  $k_x^{max}$  value the 1-D operator is designed. Note that  $k_x^{max}$  is always smaller than  $k_r^{max}$ . Due to the choice of the coefficients this 1-D operator is stretched to the desired 2-D operator. To compensate for this stretch the 1-D convolution operator must be calculated with a scaled  $\Delta z$ . This can be explained by regarding the effect of the optimized Hazra and Reddy factors as a scaling to the  $k_x$ -axis. The 1-D phase shift operator is then given by

$$\begin{aligned} \tilde{Y}(k_x) &= \exp(-j [k^2 - (\alpha k_x)^2]^{\frac{1}{2}} \Delta z) \\ &= \exp(-j [(\frac{k}{\alpha})^2 - k_x^2]^{\frac{1}{2}} \alpha \Delta z) \end{aligned} \quad (\text{A.57})$$

where  $\frac{k}{\alpha} = k_x^{max}$  and  $\alpha \Delta z$  is the scaled depth step.

The migration results for the Hazra and Reddy optimized coefficients are shown in figure A.36. The circular shape of the depth slice is good and the artifacts at the diagonals, which were present in the original McClellan transformation, are absent. Note that the computation time of the optimized coefficients is very small, only a few multiplications and additions per frequency, so the same computation effort is required as for the original McClellan transformation which makes the method very attractive. It will be interesting to investigate if it is possible to adjust the 17-points McClellan transformation with the same method.

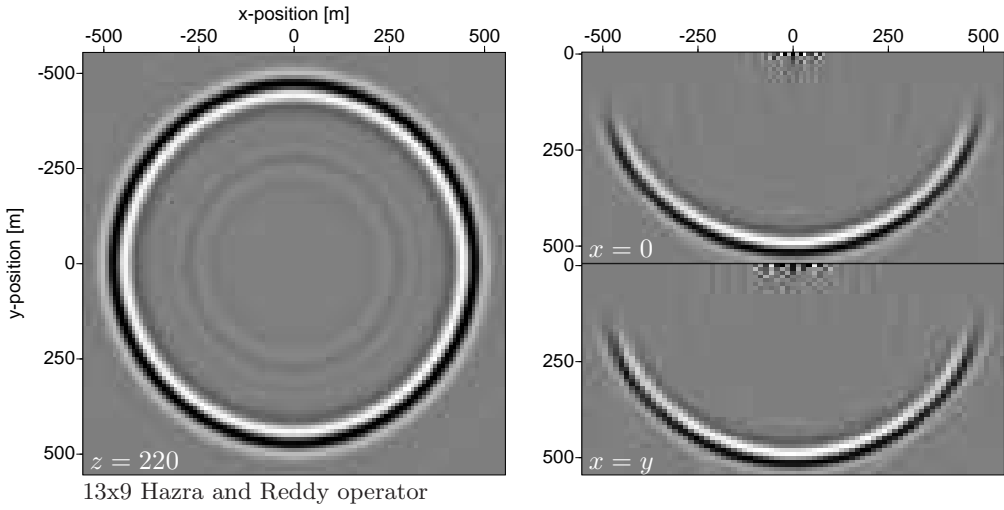


**Figure A.36** Depth images obtained with the optimized Hazra and Reddy transformation. Note the improvement in the circular shape in the depth slice in comparison with the original McClellan transformation.

#### Optimized McClellan factors

The aim in optimizing the McClellan transformation is to choose the McClellan factors  $c_{pq}$  in equation (A.49) such that the contours produced by the transformation have some desired shape. For some examples it is sufficient to control the shape of one single contour. In other problems it is necessary to design the shape of the contours in a specific part of the wavenumber domain (Mersereau et al., 1976). The error function which has to be optimized for a circular contour design is given by

$$E = M(c_{pq}, k_x, k_y) - \cos \sqrt{k_x^2 + k_y^2} \quad \text{with} \\ M(c_{pq}, k_x, k_y) = \sum_{p=0}^P \sum_{q=0}^Q c_{pq} \cos(k_x) \cos(k_y) \quad (\text{A.58})$$

Equation (A.58) is a non-linear function of the unknown parameters, so a computation intensive non-linear optimization scheme must be used for the minimization. However, it is possible to reformulate the problem as a linear approximation problem to arrive at a sub optimum solution, Mersereau et al. (1976). In the example shown in this section a non-linear optimization scheme (CFSQP, Tits and Zhou (1996)) is used. With this scheme several contours are optimized within the band of interest

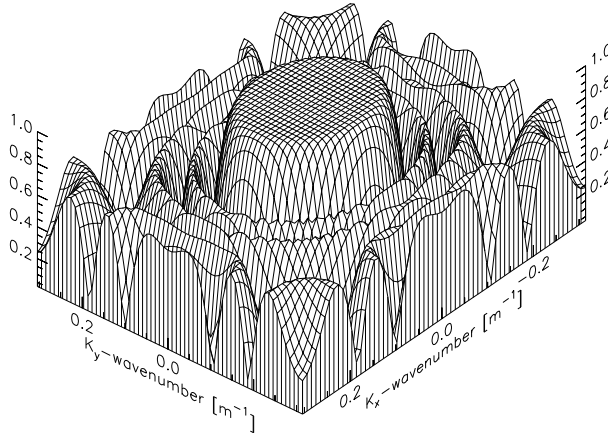


**Figure A.37** The wavenumber spectrum of a second order McClellan operator with optimized coefficients and a 1-D operator of 19 spatial points with  $128 \times 128 k_x, k_y$  points with  $c = 1000 \text{ m/s}$ ,  $f = 20 \text{ Hz}$ ,  $\Delta x = \Delta y = \Delta z = 10 \text{ m}$  and a maximum angle of interest of  $65^\circ$ .

and the constraint

$$\begin{aligned} \left| \sum_{p=0}^P \sum_{q=0}^Q c_{pq} \cos(k_x p \Delta x) \cos(k_y q \Delta y) \right| &\leq 1 \quad (\text{A.59}) \\ 0 \leq k_x \leq k_{x,N} \left(= \frac{\pi}{\Delta x}\right), 0 \leq k_y \leq k_{y,N} \left(= \frac{\pi}{\Delta y}\right) \end{aligned}$$

is put for all points of the mapping in the  $(k_x, k_y)$  plane. The contours to be optimized in the objective function of equation (A.58) are defined by the maximum wavenumber value of interest. With this definition of the optimization problem the first order McClellan transformation cannot be optimized any further, but the second order transformation (with an expansion to 25 points, which means that all cross terms within the second order are used) can be improved. In the implementation for the optimization of the McClellan operators explicitly use is made of the circular symmetry in the McClellan operator if  $\Delta x = \Delta y$ . In figure A.38 the migration pulse response is shown for the optimized 25-point McClellan operator, with frequency dependent coefficients and a 1-D operator of 25 points (13 terms). The non-linear computation time can be reduced by calculating the optimized coefficients for a wavenumber range instead of every wavenumber. In the shown example only four sub domains of the total wavenumber domain of interest are used to keep the time to compute the McClellan factors small. It is also possible to optimize the coefficients independent of the wavenumber frequency or for different shaped McClellan filters, see Blacquière (1991).

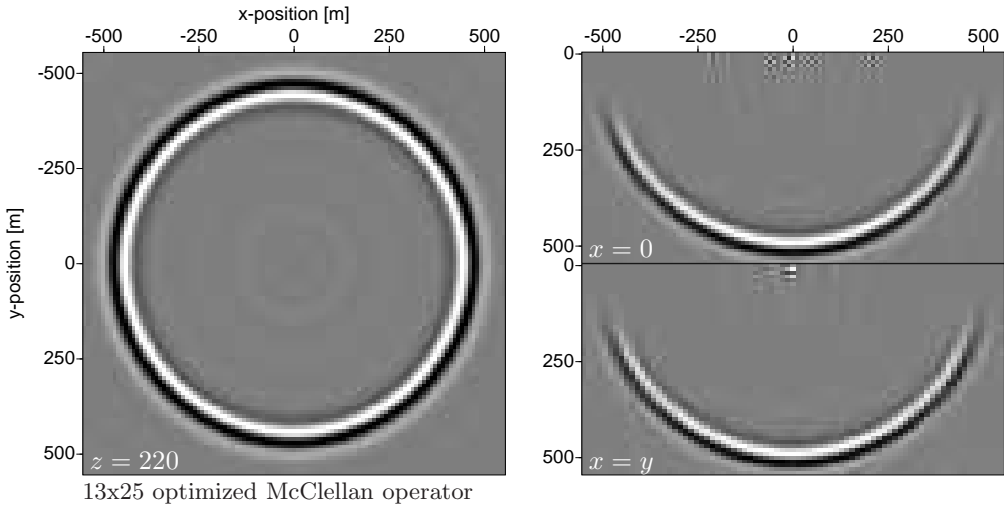


**Figure A.38** Depth slice at  $z = 220$  m, a vertical slice for  $x=0$  (top right) and bottom right a vertical slice for  $x=y$  with optimized McClellan coefficients. Note the circular shape and the small artifacts.

### Rotated Coefficients

Biondi and Palacharla (1994) describe a method which reduces the error of the deviation of the circle at the diagonal in the  $(k_x, k_y)$  plane by using a rotated McClellan operator, the rotation angle being  $\frac{\pi}{4}$ . In the downward extrapolation scheme the rotated McClellan operator and the original McClellan filters are alternately used as convolution operator. The convolution with the rotated McClellan operator can be implemented in an efficient way. For a more detailed discussion the reader is referred to Biondi and Palacharla (1994).

### Series expansion in $\cos(k_r \Delta x)$

All improvements described thus far make use of the Chebychev recursion scheme, but it is also possible to use a direct expansion in  $\cos(k_r \Delta x)$ . To see the difference between the two schemes the Chebychev recursion scheme and the direct scheme are given below

$$\tilde{Y}(k_r) \approx \sum_{m=0}^M Y_m T_m(\cos(k_r \Delta x)) \quad (\text{A.60})$$

$$\approx \sum_{m=0}^M a_m \cos(k_r \Delta x)^m \quad (\text{A.61})$$

$$\approx \sum_{m=0}^M \hat{a}_m \tilde{h}^m(k_x, k_y) \quad (\text{A.62})$$

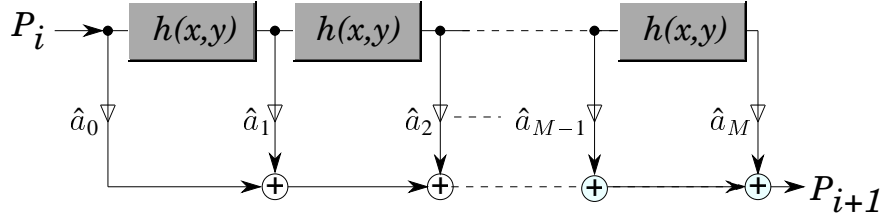


**Figure A.39** Direct scheme for series expansion in  $\cos(k_r \Delta x)$ . Note the simple structure in comparison with the Chebychev recursion scheme.

with

$$\tilde{h}(k_x, k_y) \approx \cos(k_r \Delta x) \quad (\text{A.63})$$

In equation (A.62)  $\tilde{h}$  (defined in equation (A.63)) is optimized first and with this approximation to  $\cos(k_r \Delta x)$   $\hat{a}_m$  is optimized. In equation (A.60), the Chebychev recursion scheme, the optimization of  $\cos(k_r \Delta x)$  is independent of the optimization of  $Y_m$ . The series expansion of equation (A.62) will in principle give a better operator, because the optimization of the series coefficients is dependent on the approximation to  $\cos(k_r \Delta x)$ . To optimize the expansion factors  $\hat{a}_m$  the WLSQ method is used. To approximate  $\cos(k_r \Delta x)$  the McClellan or Hazra and Reddy transformation can be used, but it is also possible to use the WLSQ optimization method as described before.

The recursive convolution scheme of equation (A.62) is given in figure A.39. This scheme is less complicated to implement in the computer and more important it can be optimized better by the compiler and user. In figure A.40a the impulse response is shown with the McClellan coefficients of equation (A.52) for the approximation to  $\cos(k_r \Delta x)$ . The number of expansion terms is chosen equal to 13. In figure A.40b the series expansion in  $\cos(k_r \Delta x)$  is done with an approximation to  $\cos(k_r \Delta x)$  obtained with the WLSQ method introduced in section A.2.1. Note that with a 9 point approximation to  $\cos(k_r \Delta x)$  the result is accurate up to the higher angles. In the next subsection a detailed error analysis is given for all discussed McClellan methods.

#### Error analysis

Using the analysis technique, which was introduced by the direct method, it is possible to analyze the performance of the different McClellan transformations. In table A.8 the errors are given for five types of McClellan transformations; the original McClellan transformation in first (\*x9) and second (\*x17) order, the optimized Hazra & Reddy factors (HR) in first order, the non-linear optimized factors in the expanded second order (\*x25) and the series expansion in  $\cos(k_r \Delta x)$  with the Hazra and Reddy coefficients and the WLSQ operators. From the results in the table and fig-

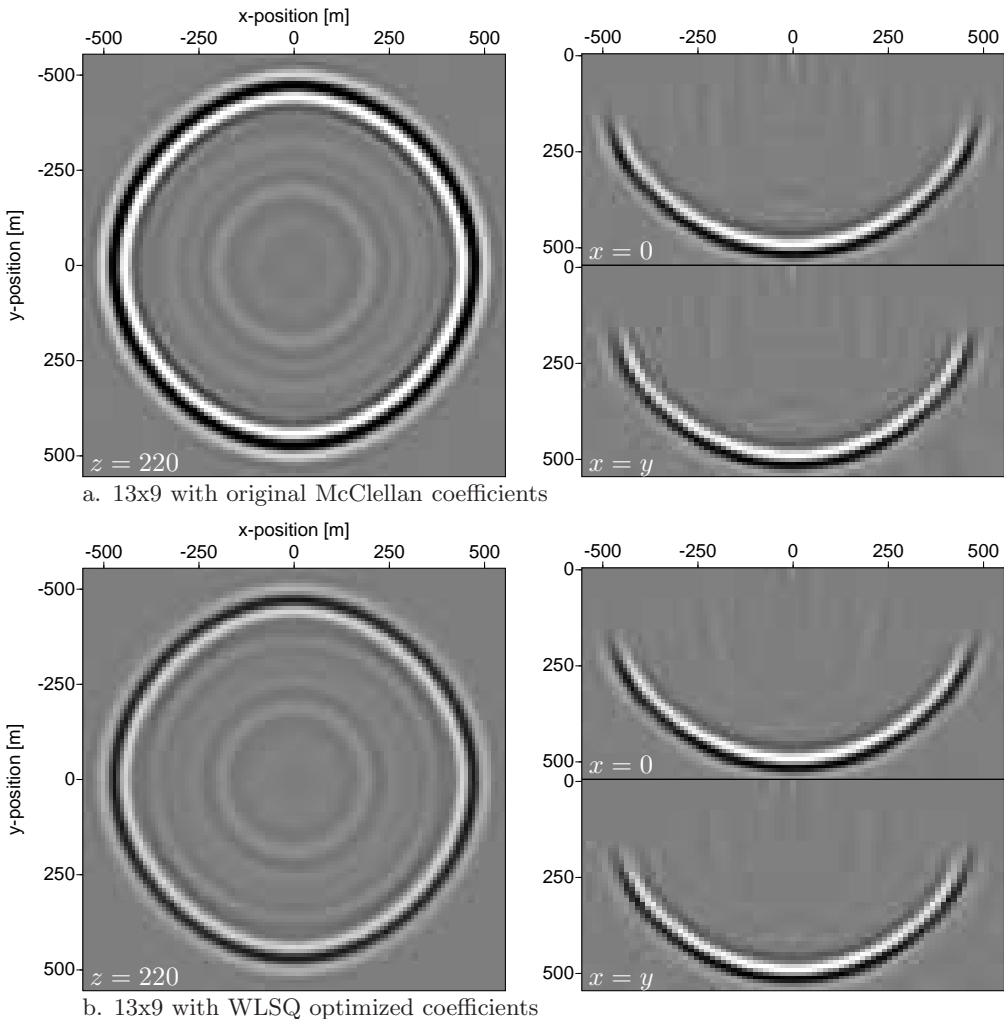


**Figure A.40** Impulse response of the expansion in  $\cos(k_r \Delta x)$  with original McClellan and WLSQ optimized coefficients for  $\cos(k_r \Delta x)$ . The series coefficients in all examples are optimized by using the WLSQ method.

ures A.33, A.36, A.38, A.40 the following remarks can be made;

- (1) For higher frequencies the  $\varepsilon^p$  error in the original McClellan transformation increases significantly for both the first and second order approximation.
- (2) The differences in pulse responses between the methods with, the original McClellan factors, the Hazra & Reddy factors, the non-linear optimized factors or the series expansion can be determined from the  $\varepsilon^p$  error. In figure A.41 the phase error and the  $\frac{\partial}{\partial k_r}$  of the phase error, as used in equation A.42, for the different methods

Operator	5 Hz			20 Hz			40 Hz		
	$\varepsilon_2$	$\varepsilon_{\infty}^a$	$\varepsilon^p$	$\varepsilon_2$	$\varepsilon_{\infty}^a$	$\varepsilon^p$	$\varepsilon_2$	$\varepsilon_{\infty}^a$	$\varepsilon^p$
McClellan									
10x9	1.7e-3	1.0e-3	4.5e-4	6.6e-3	2.2e-3	4.8e-3	5.1e-2	1.5e-3	3.8e-2
13x9	1.4e-3	1.2e-3	3.2e-4	6.3e-3	1.7e-3	3.9e-3	5.2e-2	1.4e-3	3.8e-2
16x9	1.1e-3	1.3e-3	2.3e-4	6.3e-3	1.1e-3	3.7e-3	5.1e-2	1.6e-3	3.9e-2
10x17	1.7e-3	1.0e-3	4.4e-4	1.8e-3	2.4e-3	2.7e-3	2.4e-2	1.5e-3	2.2e-2
13x17	1.3e-3	1.2e-3	3.1e-4	1.1e-3	2.0e-3	1.4e-3	2.4e-2	1.6e-3	2.3e-2
16x17	1.1e-3	1.3e-3	2.3e-4	7.8e-4	1.4e-3	9.7e-4	2.4e-2	1.9e-3	2.3e-2
HR	5 Hz			20 Hz			40 Hz		
10x9	2.6e-3	1.2e-3	8.1e-4	7.2e-3	1.7e-3	2.8e-3	8.2e-2	7.7e-3	1.8e-2
13x9	1.2e-3	6.7e-4	2.9e-4	7.1e-3	2.7e-3	2.3e-3	8.2e-2	1.6e-2	1.8e-2
16x9	1.4e-3	1.4e-3	3.2e-4	7.2e-3	1.7e-3	1.9e-3	8.2e-2	2.7e-2	1.8e-2
Optimized	5 Hz			20 Hz			40 Hz		
10x25	1.7e-3	1.0e-3	4.4e-4	1.8e-3	2.4e-3	2.6e-3	7.2e-3	1.5e-3	9.4e-3
13x25	1.4e-3	1.2e-3	3.2e-4	1.2e-3	2.0e-3	1.4e-3	7.2e-3	1.9e-3	8.6e-3
16x25	1.1e-3	1.3e-3	2.3e-4	9.2e-4	1.4e-3	1.0e-3	7.2e-3	2.3e-3	8.5e-3
Series HR	5 Hz			20 Hz			40 Hz		
10x9	5.2e-3	2.5e-3	1.6e-3	1.7e-3	1.8e-3	2.5e-3	8.4e-3	2.3e-3	6.7e-3
13x9	2.0e-3	1.5e-3	5.3e-4	9.8e-4	1.3e-3	1.4e-3	8.4e-3	2.4e-3	5.6e-3
16x9	1.5e-3	7.7e-4	3.6e-4	6.4e-4	1.2e-3	8.4e-4	8.4e-3	2.2e-3	5.2e-3
Series WLSQ	5 Hz			20 Hz			40 Hz		
10x9	2.8e-3	1.8e-3	8.2e-4	5.1e-3	1.7e-3	3.8e-3	2.2e-3	2.3e-3	4.5e-3
13x9	1.3e-3	6.2e-4	3.4e-4	5.0e-3	1.4e-3	3.4e-3	2.0e-3	1.6e-3	3.6e-3
16x9	5.3e-4	3.4e-4	1.1e-4	5.0e-4	4.1e-4	3.2e-3	1.9e-3	4.2e-4	3.4e-3
10x25	2.2e-3	1.2e-3	6.4e-4	8.3e-4	8.4e-4	1.2e-3	1.4e-3	1.6e-3	2.8e-3
13x25	1.3e-3	4.1e-4	3.2e-4	4.3e-4	6.9e-4	5.9e-4	1.2e-3	1.2e-3	1.5e-3
16x25	5.7e-4	2.7e-4	1.2e-4	1.9e-4	2.9e-4	2.6e-4	1.1e-3	3.4e-3	1.4e-3

**Table A.8** Errors in the extrapolation operators for; the original McClellan transformation in first (\*x9) and second (\*x17) order, the optimized Hazra & Reddy factors (HR) in first order, non-linear optimized factors in the expanded second order and the series expansion in  $\cos(k_r)$  with the Hazra and Reddy coefficients and WLSQ operators. The maximum angle of interest is  $60^\circ$ .

are displayed for a frequency of 40 Hz, a maximum angle of  $60^\circ$  and 13 terms in the expansion. The second order method with the original McClellan factors give a rapidly increasing phase error where the largest errors occurs at the diagonal from  $(0, 0)$  to  $(k_{x,N}, k_{y,N})$ . The phase error of the Hazra & Reddy method is less rapidly increasing and the smallest error is positioned at the diagonal from  $(0, 0)$  to  $(k_{x,N}, k_{y,N})$ . The non-linear optimized method gives error peaks at the edges of the domain of

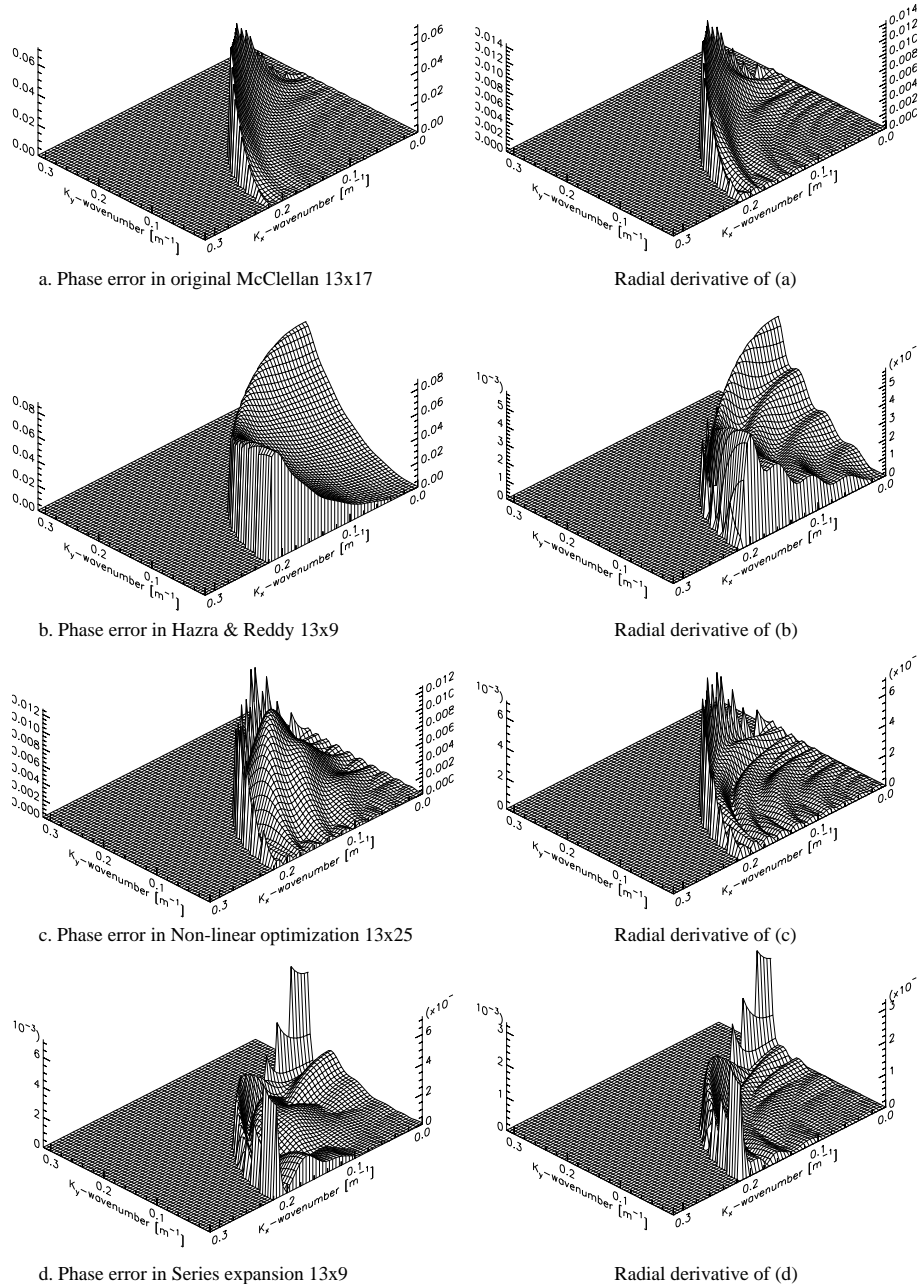


**Figure A.41** Phase errors and the radial derivative of the phase error for the different McClellan methods. Note the different scales on the vertical axes.

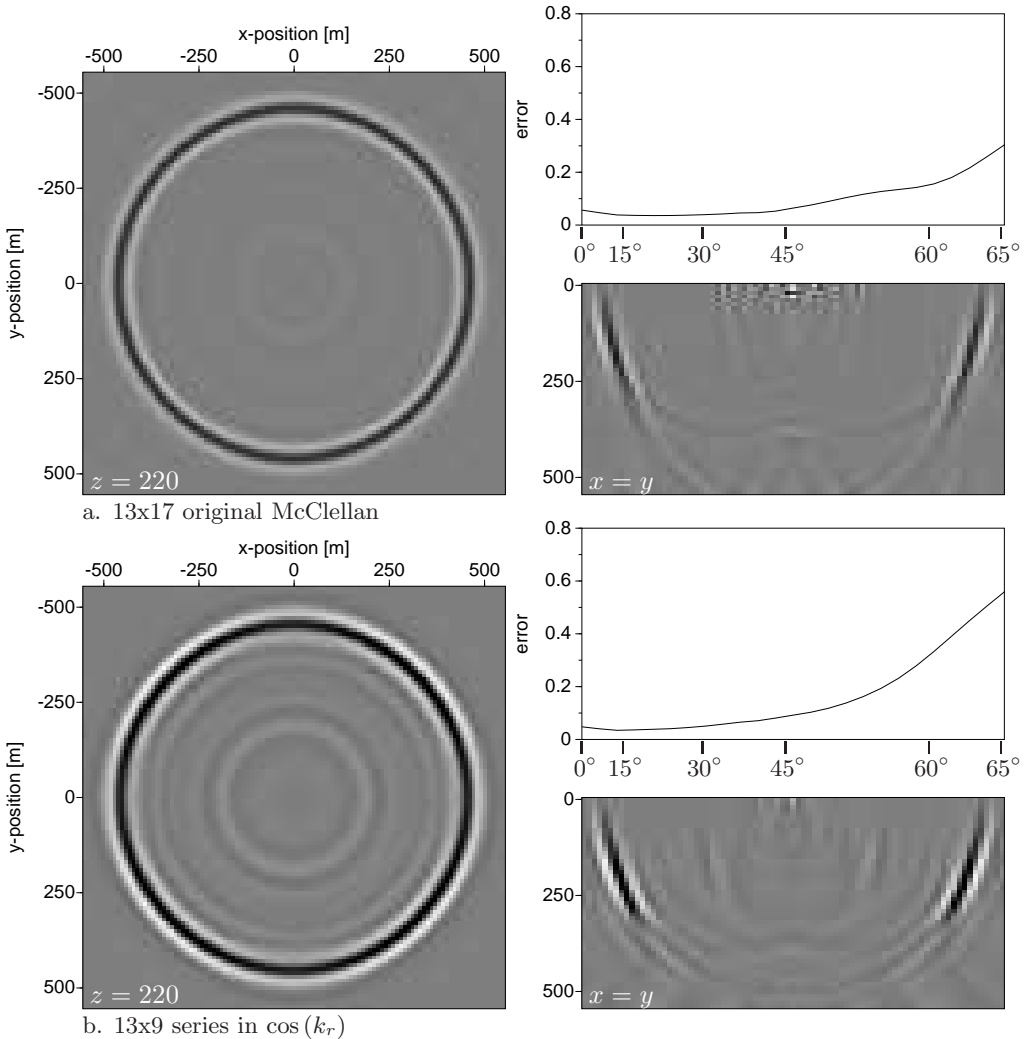


**Figure A.42** Error in the impulse response of the Chebychev expansion in  $\cos(k_r \Delta x)$  with original McClellan (a) and for a series expansion in  $\cos(k_r \Delta x)$  with WLSQ optimized coefficients (b).

interest and has the largest error at the diagonal from  $(0,0)$  to  $(k_{x,N}, k_{y,N})$ . The series expansion method with a WLSQ approximation to  $\cos(k_r \Delta x)$  gives the smallest errors with error peaks at the edges on  $k_x$  and  $k_y$  axes.

(4) The approximation to  $\cos(k_r \Delta x)$  can be done with many different methods. Crucial in the performance of the operator is that the coefficients in the expansion (Chebychev or series) are optimized by using the approximation to  $\cos(k_r \Delta x)$ .

In figure A.42 the spatial error is given for a horizontal cross section at  $65^\circ$  and a

vertical cross section at  $x = y$  for both the original second order McClellan transformation (13x17) and the series expansion in  $\cos(k_r \Delta x)$  (13x9). The original McClellan scheme gives dispersive artifacts for the higher angles. The expansion in  $\cos(k_r \Delta x)$  (with less coefficients in the approximation to  $\cos(k_r \Delta x)$ ) does not have these artifacts but is less accurate in amplitude for the higher angles.

In table A.9 the shortest accurate operator is given as function of the maximum angle of interest. For small angles the original first order McClellan transformation in Chebychev series gives already good results. For intermediate angles the second order McClellan scheme or the first order Hazra & Reddy factors are sufficient, for higher angles the series expansion with WLSQ optimized series coefficients gives the best results. The method of Hazra & Reddy cannot be found back in table A.9 because of the large  $\varepsilon_2$  error at the higher frequencies caused by the stretching of the operator. For the  $75^\circ$  angle a 5x5 approximation to  $\cos(k_r \Delta x)$  is needed.

Operator			40 Hz			Average		
angle	size	method	$\varepsilon_2$	$\bar{\varepsilon}_\infty^a$	$\bar{\varepsilon}^p$	$\bar{\varepsilon}_2$	$\bar{\varepsilon}_\infty^a$	$\bar{\varepsilon}^p$
15	4x9	McC	1.7e-3	2.9e-3	1.5e-4	1.8e-3	2.0e-3	1.0e-4
30	5x9	McC	3.9e-3	2.0e-3	1.0e-3	3.1e-3	2.0e-3	5.4e-4
45	7x17	McC	5.2e-3	2.5e-3	3.3e-3	3.1e-3	2.0e-3	1.5e-3
60	10x9	Series	2.2e-3	2.3e-3	4.5e-3	3.4e-3	1.9e-3	3.0e-3
75	18x25	Series	6.9e-3	2.6e-3	2.6e-2	4.7e-3	1.9e-3	1.2e-2

**Table A.9** Optimum operators which are accurate up to a maximum angle of interest.

### A.2.3 Expansion in $k_z$

In the previous subsections the direct convolution and the McClellan transformation were explained and impulse responses were shown for different operators. The McClellan transformation uses the coefficients of a 1-D convolution operator and approximates the 2-D Fourier components with an optimum filter. However, it is also possible to approximate the phase shift operator with an expansion other than the cosine terms of the Fourier transformation. Writing space-frequency wavefield extrapolation in an operator notation Berkhouit (1982).

$$P^+(z_{m+1}) = W^+(z_{m+1}, z_m) * P^+(z_m) \quad (\text{A.64})$$

where  $W^+(z_{m+1}, z_m)$  is the propagation operator and  $P^+(z_m)$  is the downgoing wavefield at depth level  $z_m$ . In this notation the most simple approximation to finite difference wavefield extrapolation is made by a single Taylor series expansion.

In the spatial domain with  $\Delta z = z_{m+1} - z_m$  this approximation is given by

$$P^+(z_{m+1}) \approx P^+(z_m) + \frac{\Delta z}{1!} \frac{\partial P^+(z_m)}{\partial z_m} + \frac{\Delta z^2}{2!} \frac{\partial^2 P^+(z_m)}{\partial z_m^2} + \frac{\Delta z^3}{3!} \frac{\partial^3 P^+(z_m)}{\partial z_m^3} + \dots \quad (\text{A.65})$$

The extrapolation scheme given in (A.65) can be divided into two parts; one part deals with the **estimation** of the derivatives  $\frac{\partial^i}{\partial z_m^i}$  with respect to  $z_m$  and the other part deals with the **prediction** with the aid of the Taylor series. In the wavenumber domain this approximation, with  $\frac{\partial \tilde{P}^+}{\partial z_m} = -jk_z \tilde{P}^+$ , is defined as

$$\tilde{P}^+(z_{m+1}) \approx \tilde{P}^+(z_m) - \frac{jk_z \Delta z}{1!} \tilde{P}^+(z_m) - \frac{(k_z \Delta z)^2}{2!} \tilde{P}^+(z_m) + j \frac{(k_z \Delta z)^3}{3!} \tilde{P}^+(z_m) + \dots \quad (\text{A.66})$$

This truncation of the series expansion is an approximation of the phase shift operator by a polynomial in  $k_z$ , according to

$$\exp(-jk_z \Delta z) \approx 1 - j \Delta z k_z + \frac{(j \Delta z)^2}{2!} (k_z)^2 + \mathcal{O}(k_z)^3 \quad (\text{A.67})$$

The coefficients in the series expansion can be obtained by using the constants in the Taylor series as given in equation (A.67) or by using an optimization technique. In the next two subsections two different optimization methods are used; the WLSQ method with the  $L_2$  norm and the Remez exchange method with the  $L_\infty$  norm.

#### Series expansion in $k_z$ with $L_2$ -norm

The advantage of an expansion in  $k_z$  is that if the  $k_z$  operator can be approximated by a short spatial convolution operator, and the number of terms in the series expansion of the phase shift operator remains small, the computation time can be reduced in comparison with the direct 2-D convolution. To arrive at the direct spatial convolution scheme, given in figure A.43, the  $k_z$  operator is transformed in an optimum way to the space domain and applied several times to the data. Every time a 2-D convolution (indicated by the box  $H_1$ ) with the spatial  $k_z$  operator is carried out on

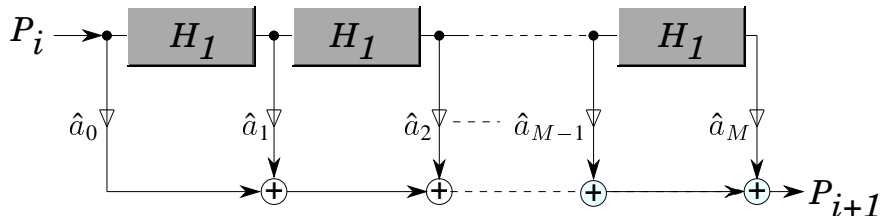


**Figure A.43** Series expansion in terms of  $k_z$ . The  $H_1$  boxes represent the 2-D convolution with the optimized spatial  $k_z \approx \tilde{H}_1$  operator, the  $\hat{a}_m$  represent the optimized coefficients in the series expansion.

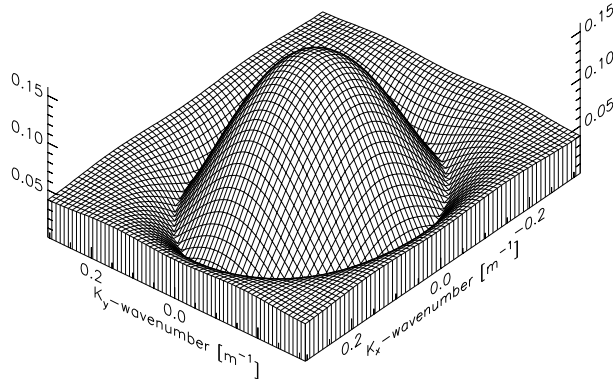


**Figure A.44** Wavenumber spectrum of a circular Fourier reconstructed spatial  $k_z$  convolution operator (5x5).

the data, a new term is added to the series expansion. The scheme given in figure A.43 is more sensitive to numerical errors than the Chebychev recursion scheme but if the number of terms remains small this causes no stability problems. It is interesting to note that an exact analytical expression for  $H_1(x, y)$  ( $H_1 \iff \tilde{H}_1 = k_z$ ) can be derived (see Berkhouit (1982), appendix E). However, a weighted least-squares version yields a shorter operator.

The factors  $\hat{a}_m$  of the series expansion in figure A.43 are obtained by a least-squares

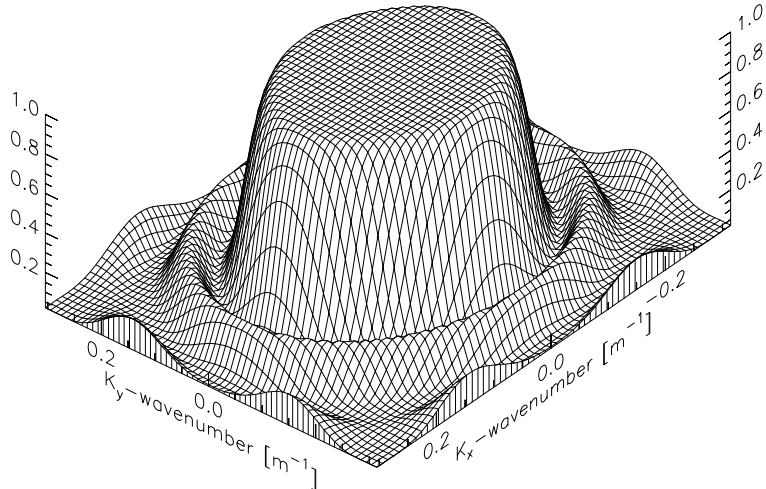


**Figure A.45** Wavenumber spectrum of the approximated phase shift operator with 9 terms in the series expansion,  $128 \times 128 k_x, k_y$  points with  $c = 1000$  m/s,  $f = 25$  Hz,  $\Delta x = \Delta y = \Delta z = 10$  m and a maximum angle of interest of  $65^\circ$ .

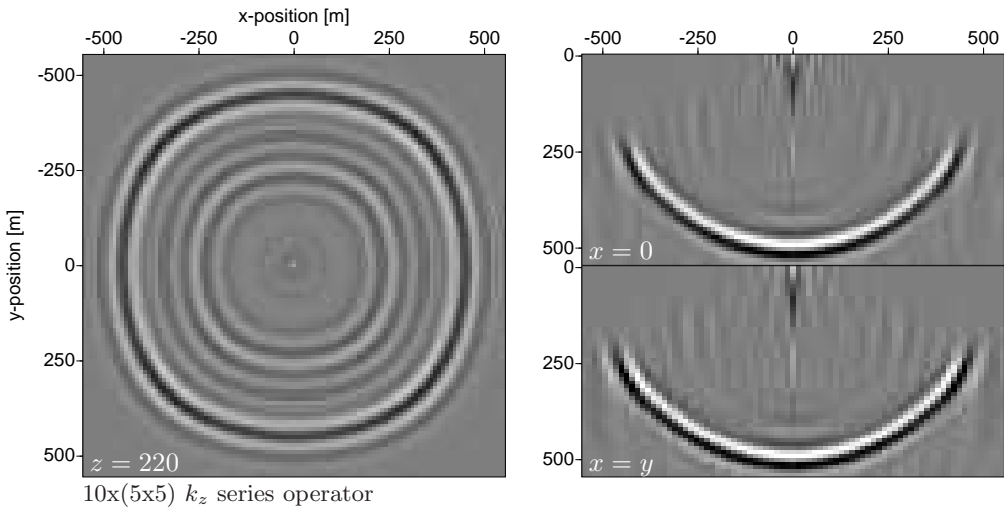


**Figure A.46** Pulse responses obtained with the series expansion in  $k_z$  with a small basis operator ( $5 \times 5$ ) with 10 terms in the series expansion. Note the artifacts at the higher angles.

optimization method with respect to the wavenumber spectrum of the *optimized*  $H_1$  operator. The circular Fourier reconstruction of the  $k_z$  operator results in a circular short spatial convolution operator, the spectrum of an operator is shown in figure A.44 for a  $5 \times 5$  operator. Using this 2-D convolution operator the computational effort can be reduced in comparison with the direct method if the number of terms in the series expansion remains small. Starting with 4 terms in the expansion it was observed that by adding more terms in the series expansion both the amplitude and phase error decrease. However, beyond 9 terms the error remains the same and increasing the number of terms does not improve the result. In that case a better approximation is not possible with the optimized basis function of  $H_1$ . For a better approximation result a better approximation to  $k_z$  must be chosen.

In figure A.45 the wavenumber spectrum of the approximated phase shift operator is shown for a nine order series expansion with optimized coefficients for the *approximated*  $k_z$  operator with a spatial size of  $5 \times 5$  points. Outside the band of interest ( $\alpha_{max} = 65^\circ$ ) the exact  $k_z$  operator (which is used as object function in the optimization) is tapered to zero. Note that with only nine terms there is already a good match with the analytical spectrum. In figure A.46 the pulse response is shown for the single series expansion method. It is observed that convolution with the short basis function of  $5 \times 5$  points gives an image with a non-circular depth slice. Increasing the number of terms in the series expansion from 10 to 15 will reduce the artifacts around the event, but the non-circular behavior remains the same. A longer basis function with  $7 \times 7$  points in the spatial domain gives a better circular slice, but requires much more computation time.

### Chebychev expansion in $k_z$ with $L_\infty$ -norm

Using an optimization method which makes use of the  $L_\infty$  norm and the Chebychev recursion structure for the implementation of the convolution may improve the result of the  $k_z$  expansion. Optimization for the series expansion terms with the  $L_\infty$  norm can be done by reducing the polynomial synthesis to symmetrical spectral synthesis with the aid of a simple transformation (Rabiner and Gold, 1975, page 151). In this optimization only the extreme values of the wavenumber spectrum of the  $H_1$  operator are used and not, as with the  $L_2$  optimization, the whole spectrum of the  $H_1$  operator. The transformation from polynomials to spectral synthesis reduces the 2-D optimization problem to a 1-D optimization problem which can be solved with the Remez exchange algorithm in a fast way.

In figure A.47 the impulse response is shown for a 5 point basis convolution operator with 10 terms in the expansion. As was observed before the basis operator is not accurate enough to define the circular shape properly. A 7 point operator with the same number of terms will give a better result. The difference with  $L_2$  optimization is that due to the equiripple character of the  $L_\infty$  solution the error is smeared over the whole wavenumber domain, while in the  $L_2$  optimization the biggest error occurs at the edges of the domain of interest (defined by  $k = \frac{\omega}{c}$  and  $\alpha$ ) which gives the artifacts as shown in figure A.46. Note that more terms in the series expansion with the same basis operator will reduce the artifacts but it will not improve the circular shape.

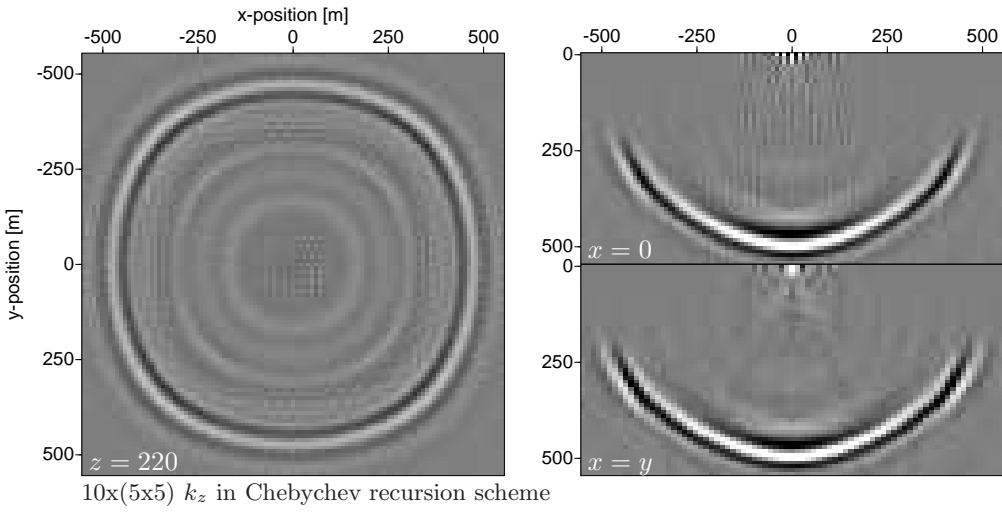


**Figure A.47** Depth image of an impulse response obtained with the Chebychev recursion scheme and a  $L_\infty$  optimization for the coefficients in the expansion in  $k_z$ , a short basis operator (5x5) with 10 terms is used.

### Error analysis

In table A.10 the errors are given for the expansion in  $k_z$  with the direct implementation and the Chebychev recursion scheme. From the results in the table the following remarks can be made;

- (1) The expansion in  $k_z$  gives large  $\varepsilon_2$  errors for most frequencies. So the operator is not very accurate which is observed in the artifacts in the impulse responses.
- (2) Increasing the number of terms with the same size of the basis operator does not improve the result. Increasing the size of the basis operator with the same number of terms gives an improvement. This means that the approximation to the basis operator is the most important factor in the performance of the operator.
- (3) The  $\varepsilon^p$  error indicates that the used basis operator of size  $5 \times 5$  in the single series expansion does not have a good circular shape. The larger operator of size  $7 \times 7$  gives an improvement but is still inaccurate.
- (4) Optimization of the series coefficients with the  $L_\infty$  norm and the use of the Chebychev recursion scheme gives a better result than  $L_2$  optimization and a direct recursion scheme.

The shortest accurate operator as function of the maximum angle of interest is not worked out for the expansion in  $k_z$  because this method cannot be designed accurate enough within a reasonable computation effort.

size	5 Hz			20 Hz			40 Hz					
	Series	$\varepsilon_2$	$\varepsilon_\infty^a$	$\varepsilon^p$	Series	$\varepsilon_2$	$\varepsilon_\infty^a$	$\varepsilon^p$	Series	$\varepsilon_2$	$\varepsilon_\infty^a$	$\varepsilon^p$
10x(5x5)		1.8e-3	1.8e-3	4.3e-4		1.5e-2	3.6e-3	7.5e-3		2.0e-2	5.6e-3	7.5e-3
15x(5x5)		7.4e-4	6.3e-4	1.4e-4		1.5e-2	3.9e-3	7.6e-3		2.0e-2	5.2e-3	7.1e-3
10x(7x7)		5.8e-4	1.2e-3	1.1e-4		7.6e-3	1.8e-3	3.5e-3		1.2e-2	1.9e-3	8.9e-3
15x(7x7)		4.7e-4	1.2e-3	6.5e-5		7.6e-3	3.8e-3	3.5e-3		1.2e-2	4.0e-3	8.6e-3
Chebychev	5 Hz			20 Hz			40 Hz					
10x(5x5)		1.9e-2	2.1e-3	2.8e-3		2.1e-2	2.8e-3	9.1e-3		3.5e-2	2.5e-3	5.2e-2
15x(5x5)		2.0e-2	2.2e-3	2.7e-3		2.1e-2	4.3e-3	8.9e-3		3.5e-2	2.5e-3	5.3e-2
10x(7x7)		9.2e-2	2.5e-3	2.6e-3		3.6e-2	1.1e-2	1.4e-2		1.4e-2	2.7e-3	2.1e-2
15x(7x7)		9.2e-3	2.1e-3	2.7e-3		3.6e-2	1.5e-2	1.4e-2		1.3e-2	2.4e-3	2.1e-2

**Table A.10** Errors in the extrapolation operators for the direct series expansion in  $k_z$  and a Chebychev recursion scheme in  $k_z$ . The maximum angle of interest is  $60^\circ$ .

#### A.2.4 Expansion in $k_x^2 + k_y^2$

By using an additional series expansion, i.e.  $k_z$  is expanded in terms of  $k_x^2 + k_y^2 (= k_r^2)$  (see equation (A.68)) ,

$$k_z = k \sqrt{1 - k_r^2} \approx k \left( 1 - \frac{k_r^2}{2} - \frac{(k_r^2)^2}{8} - \frac{(k_r^2)^3}{16} - \frac{5(k_r^2)^4}{128} - \frac{7(k_r^2)^5}{256} + \mathcal{O}((k_r^2)^6) \right) \quad (\text{A.68})$$

there is an extra advantage (chapter 10 Berkhout, 1982, see). The basic spatial convolution operators are reduced to the simple 1-D convolution operators:  $d_2(x)$  and  $d_2(y)$ . The double series expansion in  $k_x^2 + k_y^2$  is given in equation (A.69)

$$\begin{aligned} \exp(jk_z \Delta z) \approx & 1 - \\ & \frac{j\Delta z}{2k} (k_x^2 + k_y^2) - \\ & \frac{j\Delta z}{8k^3} (1 - jk\Delta z) (k_x^2 + k_y^2)^2 - \\ & \frac{j\Delta z}{16k^5} (1 - jk\Delta z + \frac{(jk\Delta z)^2}{3}) (k_x^2 + k_y^2)^3 + \\ & \mathcal{O}((k_x^2 + k_y^2)^4) \end{aligned} \quad (\text{A.69})$$

where the terms of the series expansion are derived from the Taylor series, but this is not an optimum choice (Hoff, 1995). This same expansion can also be regarded as an approximation to the cosine terms in equation (A.46). So there are two different ways to look at the double series expansion

$$\tilde{Y}_0(k_x, k_y) = \exp(-jk_z \Delta z) \quad (\text{A.70})$$

$$\approx \sum_{m=0}^M a_m T_m(\cos(k_r)) \quad (\text{A.71})$$

$$\approx \sum_{m=0}^M b_m T_m(k_r) \quad (\text{A.72})$$

$$\approx \sum_{m=0}^M c_m k_r^m \quad (\text{A.73})$$

where  $T_m$  is a Chebychev polynomial of the  $m$ 'th order. First the series of equation (A.73) is discussed and next the Chebychev recursion of equation (A.72) is discussed.

#### Series expansion in $k_x^2 + k_y^2$ with $L_2$ -norm

The same techniques as discussed in the section with the series expansion in  $k_z$  can be used again, the spatial versions of  $k_x^2$  and  $k_y^2$ , i.e.  $d_2(x)$  and  $d_2(y)$ , are determined by a weighted least-squares process. In figure A.48 two wavenumber spectra are shown for short spatial convolution operators, with operator lengths of 5 and 7 points, which represent the second order differentiation. Note that for these short operator the approximation to the exact function within the band of interest is within a reasonable

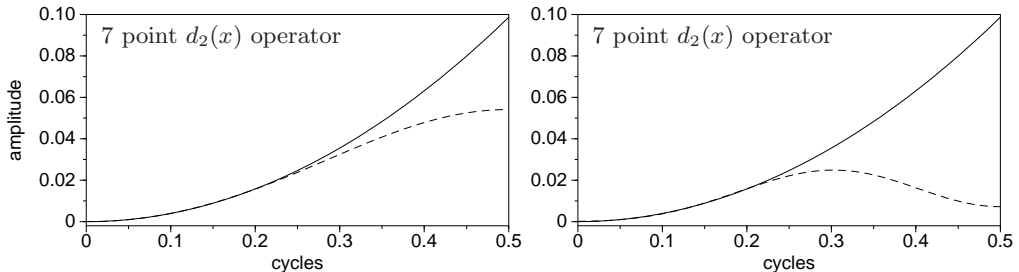


**Figure A.48** Spectrum of two differentiation operator for 5 and 7 points. The maximum wavenumber of interest is given by  $k_x^{max} = \frac{2\pi 25}{1000} = 0.25$ .

error. The convolution scheme is given in figure A.49 where  $d_2(x, y)$  stands for the spatial Laplacian operator  $d_2(x) + d_2(y)$ . The factors  $\hat{b}_m$  of the series expansion in figure A.49 are obtained by a weighted least-squares optimization method with respect to the wavenumber spectrum of the *optimized*  $k_x^2 + k_y^2$  operator. The length of the 1-D convolution operators depends on the maximum wavenumber of interest. Hoff (1995) showed that the value of the coefficients in the series expansion grows rapidly with increasing order. For the higher order terms values in the order of 1e19 are normal. This means that after a certain number of terms the accuracy cannot be improved any further due to the limit of the floating point representation in the computer. This indicates also that adding higher order terms will not improve the result significant.

The WLSQ optimization scheme proposed in this section uses the whole wavenumber spectrum to obtain the series coefficients. In figure A.50 the impulse response is shown where 15 coefficients are used in the series expansion and different operator lengths are used for the short convolution operators. For the small wavenumbers an operator length of 3 points is used for the representation of the differential operator, for larger wavenumber values the length increases with 2 points up to 7 point for the largest wavenumbers. The impulse response in figure A.50 shows artifacts at the

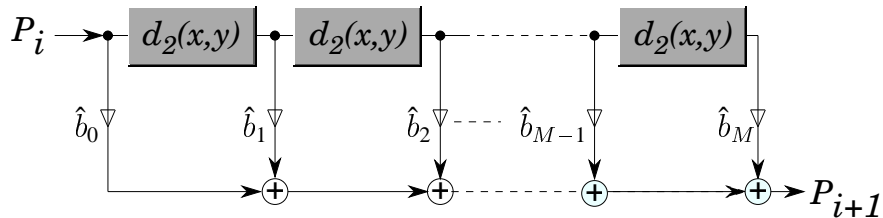


**Figure A.49** Series expansion in terms of  $k_x^2 + k_y^2 = \tilde{L}$ . The  $d_2(x, y)$  boxes represent the two 1-D convolutions with the optimized Laplacian operator; the  $\hat{b}_m$  represent the optimized coefficients in the series expansion.

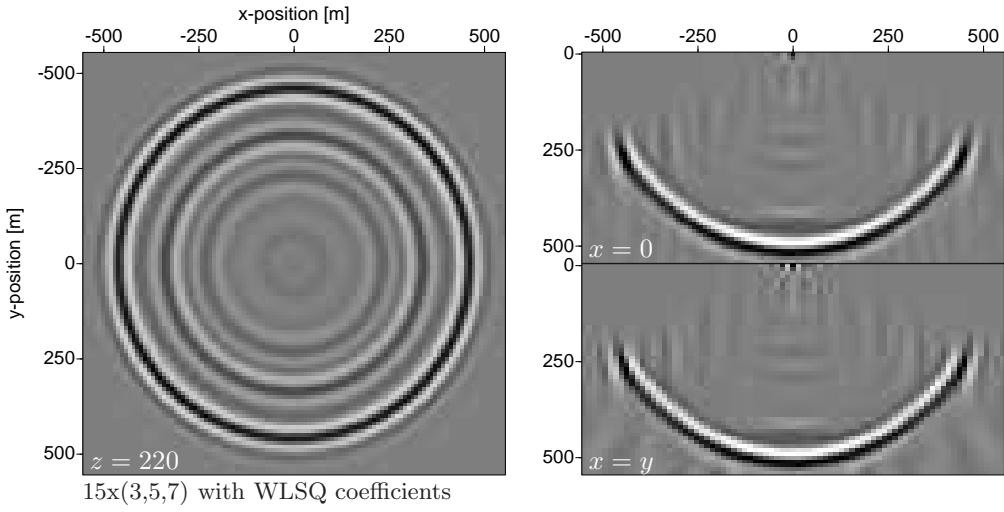


**Figure A.50** Depth images of pulse responses obtained with the series expansion in  $k_x^2 + k_y^2$  with a basis operator with optimized operator lengths with 15 terms in the series expansion (example made by Jochum Hoff).

higher angles which are due to edge effects of the used WLSQ method. In WLSQ design the edges of the domain of interest contain relative large error peaks. It may therefore be better to use an  $L_\infty$  norm in the design of the series coefficients.

#### Chebychev expansion in $k_x^2 + k_y^2$ with $L_\infty$ -norm

Soubaras (1996) used the same type of expansion in  $k_x^2 + k_y^2$ , but in his method the optimization technique for both the terms in the series expansion and the convolution operators is the Remez exchange algorithm with the  $L_\infty$  norm. The advantage of the Chebychev recursion scheme, given in figure A.51 over the series expansion, which was discussed in the previous subsection, is that the coefficients in the Chebychev expansion are less sensitive to numerical errors. Sollid and Arntsen (1994) used also

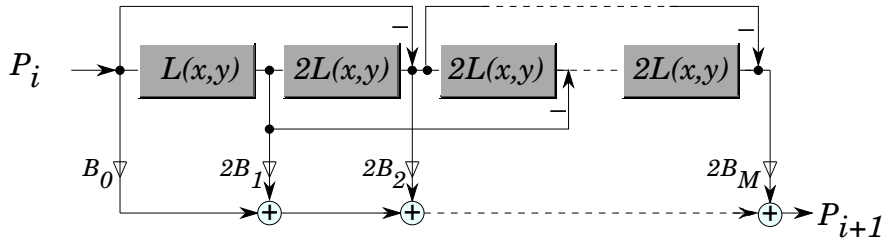


**Figure A.51** Expansion in terms of  $k_x^2 + k_y^2 = \tilde{L}$ . The  $d_2(x, y)$  boxes represent the two 1-D convolutions with the optimized  $L$  operator, the  $B_m$  represent the optimized coefficients in the series expansion.

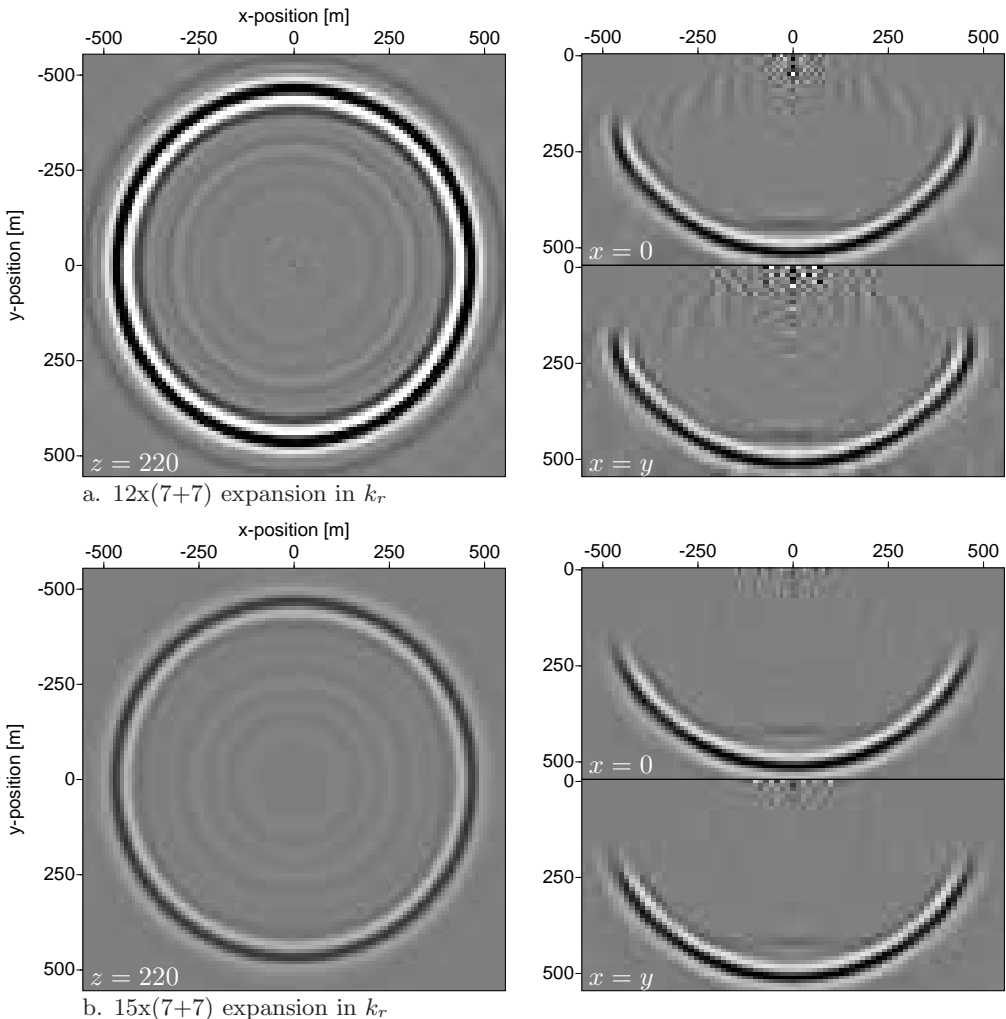


**Figure A.52** Depth images of pulse responses obtained with the series expansion in  $k_x^2 + k_y^2$  with  $L_\infty$  optimization; a) shows a 7 point 1D convolution operator with 12 terms in the series expansion and b) with the same basis operator and 15 terms in the series expansion. Note that more terms in the series expansion gives a better result.

the Chebychev recursion scheme but the optimization is done with respect to the  $L_2$  norm and non-linear methods were used to obtain the coefficients of the expansion.

Optimization of the differentiation operators with the  $L_\infty$  norm gives equiripple operators. Optimization for the series expansion terms with the  $L_\infty$  norm can be done by reducing the polynomial synthesis to symmetrical spectral synthesis with the aid of a simple transformation. In this transformation only the extreme values of the

wavenumber spectrum of the differentiation operator are used in the optimization and not, as with the  $L_2$  optimization the whole spectrum of the differentiation operator. The transformation from polynomials to spectral synthesis reduces the 2-D optimization problem to a 1-D optimization problem which can be solved with the Remez exchange algorithm in a fast way. In the extrapolation scheme the differentiation operator remains the same for all frequencies. However, the terms in the series expansion are calculated for every frequency.

In figure A.52 two pulse responses are shown for a 7+7 point operator with 12 and 15 terms in the expansion. The pulse response obtained with 12 terms in the recursion scheme is shown in figure A.52a and has a circular response with only small artifacts. Using 15 terms in the expansion gives an even better result with less artifacts.

### Error analysis

In table A.11 gives the errors for the series expansion in  $k_x^2 + k_y^2$  implemented in a direct recursion scheme with  $L_2$  optimization and the Chebychev recursion scheme with  $L_\infty$  optimization. From the results in the table the following remarks are made; (1) In both optimization methods the number of terms is less essential to the accuracy than the length of the  $d_2$  operator. Increasing the number of terms improves the result only a little, while increasing the length of the  $d_2$  operator gives a significant improvement on the result.

(2) The artifacts present in the impulse response with the series expansion scheme are due to instabilities at the higher angles. This effect is possibly due to the use of the  $L_2$  norm optimization. In the  $L_\infty$  norm optimization unstable error peaks are not likely to occur. The artifacts can be removed with an additional optimization step in the  $L_2$  optimization (Hoff, 1995).

(3) Although the  $\varepsilon_2$  errors for the lower frequencies in the  $L_\infty$  norm optimization are larger than the errors in the  $L_2$  norm optimization the impulse response contains less artifacts at the higher angles.

size	5 Hz			20 Hz			40 Hz		
	$\varepsilon_2$	$\varepsilon_\infty^a$	$\varepsilon^p$	$\varepsilon_2$	$\varepsilon_\infty^a$	$\varepsilon^p$	$\varepsilon_2$	$\varepsilon_\infty^a$	$\varepsilon^p$
10x(3,5,7)	5.8e-3	1.9e-3	1.8e-3	3.2e-3	3.7e-3	4.6e-3	3.4e-3	3.4e-3	6.4e-3
12x(3,5,7)	6.1e-3	2.8e-3	1.9e-3	3.0e-3	3.2e-3	4.1e-3	3.1e-3	3.4e-3	5.1e-3
15x(3,5,7)	6.1e-3	3.5e-3	1.9e-3	2.4e-3	3.2e-3	3.3e-3	3.0e-3	3.9e-3	4.8e-3
Chebychev	5 Hz			20 Hz			40 Hz		
	4.0e-2	3.7e-3	2.3e-3	7.1e-3	3.0e-3	4.5e-3	4.3e-3	1.9e-3	6.5e-3
10x(7+7)	4.0e-2	7.6e-3	2.1e-3	7.1e-3	5.0e-3	4.4e-3	4.1e-3	4.9e-3	5.8e-3
12x(7+7)	4.0e-2	1.2e-2	2.4e-3	6.8e-3	5.8e-3	3.4e-3	4.1e-3	6.5e-3	5.0e-3

**Table A.11** Errors in the extrapolation operators for the direct series expansion in  $k_x^2 + k_y^2$  and a Chebychev recursion scheme in  $k_x^2 + k_y^2$ . The maximum angle of interest is  $60^\circ$ .

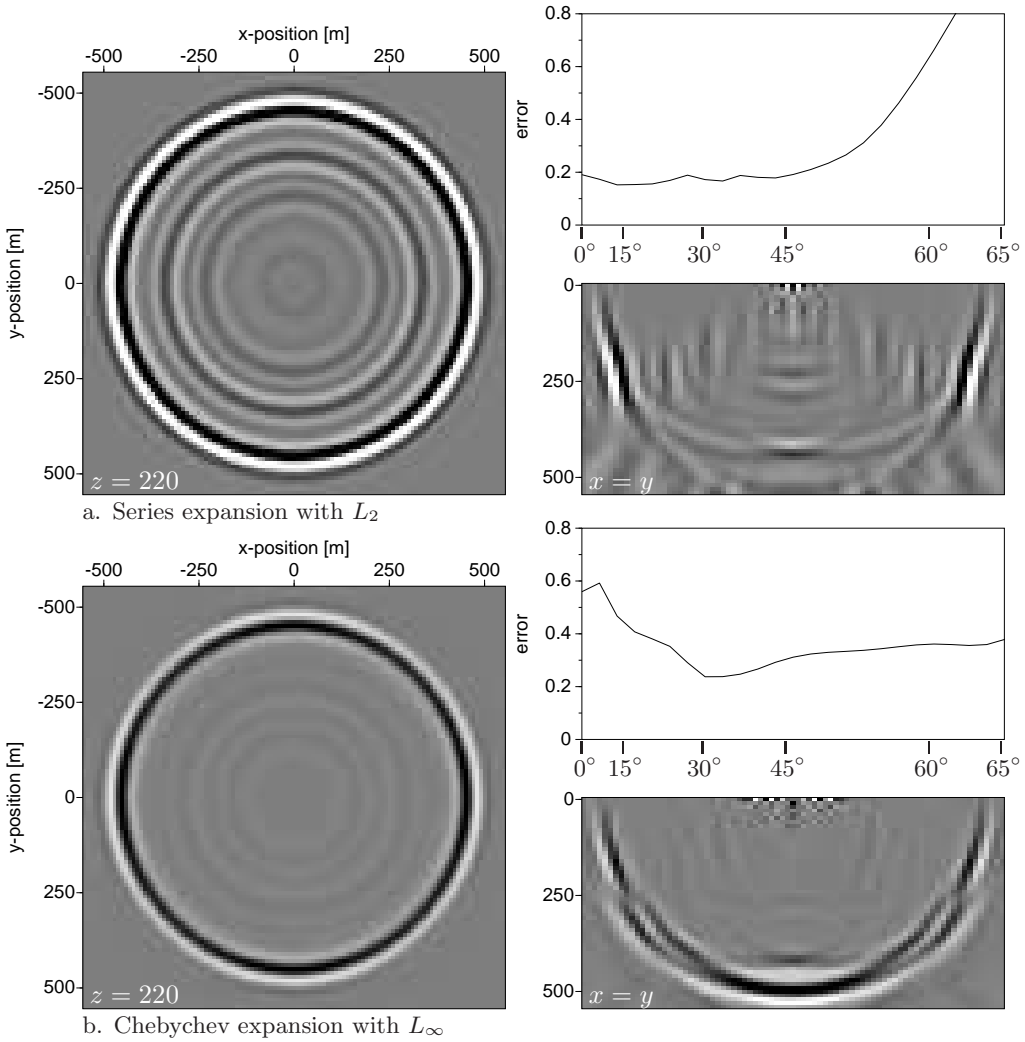


**Figure A.53** Error in the impulse response of the Laplacian expansion in  $k_x^2 + k_y^2$  for a series expansion and a Chebychev recursion scheme.

The difference with the reference error in the spatial domain is given in figure A.53. In this figure the series expansion method with 15x(3,5,7) terms and  $L_2$  optimization can be compared with the Chebychev recursion scheme of 15x(7+7) terms and  $L_\infty$  optimization. From this comparison we see that the errors in the  $L_\infty$  optimization are smeared out over the whole wavenumber range while the  $L_2$  optimization has an error peak. The amplitude and phase accuracy is better for the  $L_2$  optimization, but it suffers from artifacts at the higher angles. Choosing larger basis convolution operators to represent the differentiation will solve this problem.

Operator		20 Hz			Average		
angle	size	$\varepsilon_2$	$\varepsilon_\infty^a$	$\varepsilon^p$	$\bar{\varepsilon}_2$	$\bar{\varepsilon}_\infty^a$	$\bar{\varepsilon}^p$
15	5x(7+7)	8.6e-3	5.1e-3	1.7e-4	9.6e-3	9.7e-3	5.0e-4
30	5x(7+7)	3.0e-3	1.9e-3	3.9e-3	1.2e-2	6.1e-3	3.7e-3
45	7x(7+7)	5.0e-3	4.5e-3	2.0e-3	1.5e-2	5.8e-3	1.0e-2
60	9x(7+7)	8.3e-3	1.8e-3	6.3e-2	1.7e-2	2.3e-3	4.0e-2

**Table A.12** Optimum operators which are accurate up to a maximum angle of interest.

In table A.12 the shortest accurate operator in  $L_\infty$  optimization is given as function of the maximum angle of interest. The  $\varepsilon_2$  error is the most sensitive error in the  $L_\infty$  optimization. For  $15^\circ$  and  $30^\circ$  angle the same number of terms must be used, a lower number of terms leads to unacceptable  $\varepsilon_2$  errors for the low and middle frequencies. The optimum operator size can be found by trying to make the  $\varepsilon_2$  as small as possible by choosing the number of terms high. The optimum number of terms is then found by lowering the number of terms until the  $\varepsilon_2$  is changing significant. The high average errors are due to the high errors at low frequencies. For a maximum angle of  $75^\circ$  it was not possible to obtain stable operators within the current implementation.

#### A.2.5 Computation times

The computation times of the different 3-D extrapolation methods in the space-frequency domain is given in table A.13. The given time represent 55 recursive depth steps for one frequency (20 Hz.) with  $c = 1000$  m/s,  $\Delta x = \Delta y = \Delta z = 10$  m on a x,y grid of  $111 \times 111$  samples wide. All routines which are used are written in C and Fortran and are translated with the same type of compiler options without using options for parallel computation (see Table A.14). However, parallel processing is easily implemented on the main frequency loop in the extrapolation algorithm. On the Convex (C-220) the -O2 option is used for vectorization of the loops. It was not possible to vectorize the C-code with specific compiler directives, therefore the convolution schemes were written in Fortran code which vectorize well. Note that in general the Fortran compilers are better in optimization than the C compilers.

In the direct implementation of the 2-D convolution the even symmetry in the convolution operator is used. This implementation is designed to work fast on a Vector computer. In the implementation of the McClellan transformation and the  $k_z$  expansion the circular symmetry in the basis operators is used by first adding the common terms to each other and then multiplication with the appropriate operator point. This reduces the number of multiplications with a factor 8 in comparison with a full convolution. The computation times given in table A.13 are real-time computation times measured during the calculation. The time needed to calculate the operators is not included in this time.

Due to the use of the even symmetry in the operator the computation time for the direct convolution is a real challenge for the other methods (Note that the direct scheme can be made even faster when  $\Delta x = \Delta y$  and the circular symmetry is used). The first and second order McClellan implementations and the series expansion in  $\cos(k_r \Delta x)$  are the fastest algorithms on all machines. The series expansion in  $k_z$  and in  $k_x^2 + k_y^2$  are comparable with the McClellan transformation. The difference between the  $k_x^2 + k_y^2$  expansion in  $L_2$  and  $L_\infty$  is that in the  $L_2$  scheme the direct series expansion is used and for the  $L_\infty$  the Chebychev recursion scheme is used. From the

Machine	Direct			McClellan 1			McClellan 2		
	19x19	25x25	31x31	10x9	13x9	16x9	10x17	13x17	16x17
SUN C	63.5	104.6	157.3	24.5	31.1	38.7	33.4	44.8	55.3
SUN F	52.6	88.0	144.8	20.3	27.0	31.7	28.8	39.0	47.8
Convex F	34.7	61.9	85.9	12.4	17.4	21.6	21.1	27.6	33.5
DEC C	28.3	46.9	71.6	9.4	13.7	15.7	13.4	17.8	21.5
DEC F	11.5	19.9	28.0	5.6	7.2	8.8	6.7	8.6	10.5
HP C	18.6	30.0	44.7	10.0	13.2	16.5	20.5	23.5	27.7
HP F	6.8	10.6	15.1	6.6	8.6	10.6	19.2	20.8	24.5
Machine	McClellan 2+			$\cos(k_r \Delta x) \times 9$			$\cos(k_r \Delta x) \times 25$		
	10x25	13x25	16x25	10x9	13x9	16x9	10x25	13x25	16x25
SUN C	41.9	55.0	67.2	18.0	23.5	29.2	35.0	45.9	59.9
SUN F	36.8	48.0	58.3	16.8	21.1	25.7	32.6	42.9	54.3
Convex F	33.4	45.5	54.1	11.6	16.2	18.5	34.0	42.3	53.9
DEC C	14.6	18.5	24.3	7.0	9.3	10.8	12.1	15.6	19.2
DEC F	7.5	9.6	11.8	4.4	5.6	6.7	6.2	7.9	9.6
HP C	23.3	26.4	30.4	7.9	10.3	12.3	13.4	17.0	20.8
HP F	15.1	18.2	22.0	4.0	5.1	6.2	12.2	14.6	17.4
Machine	$k_z$			$k_x^2 + k_y^2$ $L_2$			$k_x^2 + k_y^2$ $L_\infty$		
	10x(5x5)	15x(5x5)	10x(7x7)	12x5	12x7	15x7	12x5	12x7	15x7
SUN C	36.3	54.3	61.2	25.7	32.8	41.2	33.4	41.9	51.7
SUN F	33.2	49.0	57.2	21.2	26.2	35.5	27.9	32.0	39.9
Convex F	31.5	49.6	71.1	15.1	19.7	24.3	19.0	24.2	30.0
DEC C	11.8	17.6	26.3	8.6	9.6	11.9	13.6	15.2	19.2
DEC F	6.2	9.1	8.5	5.6	5.6	6.8	7.0	7.7	9.8
HP C	12.8	18.8	18.5	15.9	21.4	27.4	14.6	18.1	22.3
HP F	9.5	14.7	20.1	13.5	20.0	25.3	11.8	15.8	18.3

**Table A.13** 2-D convolution computation time (in seconds) for one frequency on different machines for different operator sizes and extrapolation methods.

table it is clear that the hardware design of the computer system can be optimum for some specific implementation. For example the HP has a good performance on the direct scheme and less on the McClellan schemes. The DEC has a good performance on all expansion schemes.

Which scheme is preferred depends also on the desired accuracy of the result. If one uses the extrapolation only to get a first idea of the subsurface, or to estimate the macro model, a first order McClellan scheme can be used. For a higher accuracy the direct convolution or a series expansion method with a high number of terms can be used.

In table A.14 a detailed specification for the different machines is given. On the SUN the gcc compiler is used because it produces faster code than the standard cc compiler delivered by SUN. Note that for the optimization options only the most common used options are chosen, it may therefore be possible that by choosing another option the scheme will perform better as described in this Appendix (suggestions for better options are welcome).

Machine	type	RAM (Mb)	bits	C	F	C-opt	F-opt
SUN	10/514	256	32	gcc	f77	-O2	-O2
Convex	C-220	256	32	cc	fc	-O2	-O2
DEC	3000-500	96	64	cc	f77	-O2	-O3
HP	9000-735	144	32	cc	fort77	+O4	+O4

**Table A.14** Specification for the used machines. Note that the optimization is done for one CPU and parallel processing is not used.

#### A.2.6 Concluding remarks

The 3-D extrapolation algorithm that is used in recursive depth migration can be implemented in several ways. In this section the direct method, the McClellan transformation and three series expansion methods have been discussed. For the direct method a 2-dimensional convolution operator is needed. The proposed weighted least-squares optimization method is an efficient procedure which gives stable and accurate convolution operators (Thorbecke and Rietveld, 1994). This method can be further improved by a second optimization step; for example, the Lawson algorithm (Rice and Usow, 1968), which will adjust the weight function in such a way that after several steps it will converge to a Chebychev-norm solution see for example Al-gazi et al. (1986). The Fourier reconstruction method is a fast and simple method to obtain 2-D circular convolution operators but must be improved further to give accurate results.

The McClellan scheme which makes use of the 1-D optimized operator coefficients

is attractive with respect to the computation effort and by using optimized McClellan factors the accuracy for the higher angles can be improved significantly without much effort. Using a series expansion of the phase shift operator also reduces the computation time in comparison with a direct 2-dimensional convolution. Two expansions were discussed in this section one in  $k_z$  and one in  $k_x^2 + k_y^2$ . The  $k_z$  expansion is not recommended because it is difficult to optimize the parameters used in the optimization.

All these different approaches to the phase shift operator can be summarized in the following equations

$$\tilde{Y}_0(k_x, k_y) = \exp(-jk_z\Delta z) \quad (\text{A.74})$$

$$\approx \sum_{m=0}^M \sum_{n=0}^N Y_{mn} \cos(k_x m \Delta x) \cos(k_y n \Delta y) \quad (\text{A.75})$$

$$\tilde{Y}_0(k_x, k_y) \approx \sum_{m=0}^M Y_m T_m(\cos(\sqrt{k_x^2 + k_y^2} \Delta x)) \quad (\text{A.76})$$

$$\approx \sum_{m=0}^M a_m \cos^m(\sqrt{k_x^2 + k_y^2} \Delta x) \quad (\text{A.77})$$

$$\tilde{Y}_0(k_x, k_y) \approx \sum_{m=0}^M B_m T_m(k_x^2 + k_y^2) \quad (\text{A.78})$$

$$\approx \sum_{m=0}^M b_m (k_x^2 + k_y^2)^m \quad (\text{A.79})$$

$$\tilde{Y}_0(k_x, k_y) \approx \sum_{m=0}^M C_m T_m(k_z) \quad (\text{A.80})$$

$$\approx \sum_{m=0}^M c_m k_z^m \quad (\text{A.81})$$

with

$$\cos(\sqrt{k_x^2 + k_y^2}) \approx \sum_{p=0}^P \sum_{q=0}^Q c_{pq} \cos(p k_x) \cos(q k_y) \quad (\text{A.82})$$

$$\cos(\sqrt{k_x^2 + k_y^2}) \approx a_0 + b_1 \sqrt{k_x^2 + k_y^2} \quad (\text{A.83})$$

Equation (A.75) represents the direct method, equation (A.76) combined with equation (A.82) is the McClellan approach with the Chebychev recursion scheme. Equation (A.77) represents the series expansion in  $\cos(k_r \Delta x)$  with a dependent optimization between the series coefficients and the approximation to  $\cos(k_r \Delta x)$ . Equation (A.78) combined with equation (A.83) represents the expansion in  $k_x^2 + k_y^2$  with the

Chebychev recursion scheme. Equation (A.79) is the series expansion in  $k_x^2 + k_y^2$ , the use of this series expansion in recursive migration was already proposed by Berkhout (1982). Equation (A.80) represents the expansion in  $k_z$  in a Chebychev recursion scheme and Equation (A.80) represents the series expansion in  $k_z$ .

From an efficiency point of view the expansion in  $k_x^2 + k_y^2$  and the use of the McClellan transformation are the most interesting schemes. The approximation to  $\cos(k_r \Delta x)$  used in the McClellan transformation can be done with many different methods. Crucial in the performance of the extrapolation operator is that the coefficients in the expansion (Chebychev or series) are optimized by using this approximation to  $\cos(k_r \Delta x)$ . The big advantage of the expansion in  $k_x^2 + k_y^2$  is that short 1-dimensional convolution operators can be used instead of the small 2-dimensional convolution operators used in the McClellan schemes. A disadvantage of these schemes is that it is not possible to write the algorithms in computer 'friendly' way due to the recursive structure in the scheme. This fact is displayed in the computation times given in table A.13. The most accurate extrapolation is the direct convolution scheme. Another advantage of the direct scheme is that the algorithm can be designed in an efficient way. A disadvantage of the direct scheme is the intensive computation needed to compute the 2-dimensional convolution operators.

Method	accuracy	stable	circ	operator	simple	vector	scalar
Direct	++	+	++	-	++	+	□
McC1	□	++	□	+	□	+	++
McC2	□	++	□	+	□	+	++
McC2+	+	+	+	+	-	+	+
$\cos(k_r \Delta x)$	+/++	+	++	□	+	+	++
$k_z$	-	□	□	□	+	-	□
$k_x^2 + k_y^2 L_2$	□	□	+	+	□	□	+
$k_x^2 + k_y^2 L_\infty$	□	+	+	++	-	□	+

**Table A.15** Comparison of the different extrapolation methods with respect to computation effort and stability. Note that in the McClellan schemes the optimized McClellan factors are used.

In table A.15 a simplified summary is given for the different extrapolation schemes used in the section. In table A.15 the different columns have the following meaning:

- *accuracy*: the average  $\varepsilon_2$  error over the whole frequency range.
- *stable*: the stability of the method over the whole frequency range for all wavenumbers ( $\varepsilon_\infty^a$  error). A  $\square$  means that some wavenumber components can become unstable.
- *circ*: the circularity of the impulse response ( $\varepsilon^p$  error). The McClellan in Chebychev expansion and the  $k_z$  scheme have problems with the circularity.
- *operator*: the effort to compute all the coefficients which are needed in the convo-

lution scheme. For example in the direct method a 2-D convolution operator must be computed, in the McClellan scheme a 1-D convolution operator and the (optimized) McClellan factors are needed. In the table  $++$  means a minimum computation effort to compute the coefficients. Note that the operator coefficients can be calculated in advance and stored in an operator table.

- *simple*: the simplicity of the implementation of the convolution. The recursive schemes require more complex algorithms, so the compilers have to be good in optimization to make these schemes fast. In the recursive schemes it is difficult to make the program faster by changing the algorithm in a more computer 'friendly' way. A direct convolution requires more multiplications and additions but the algorithm can be made very efficient. This fact explains the fast computation time of the direct scheme in comparison with the other schemes (see Appendix A).
- *vector*: the performance of the scheme on a vector computer. The direct scheme is the only scheme which can be implemented in a vector efficient way.
- *scalar*: the performance of the scheme on a modern scalar computer. Note that some scalar computers may have an architecture which can be more advantageous for some implementations.

**In conclusion;** taking into account the *computation time* of the different methods, the *simplicity* of the algorithms and most important the *accuracy* of the result then the **direct method** (A.75) is the best method for 3-D extrapolation. The 2-D convolution operators should be stored in an efficient way, by using the symmetry of the operator (one octant need be stored only), in an operator table that can be calculated in advance. If a series expansion version is used the expansion in  $\cos(k_r \Delta x)$  is preferred, Chebychev recursion is not an advantage.



## Appendix B

### Matrix notation

In this appendix the matrix notation of seismic data, first introduced by Berkhouit (1982) and used in this thesis, will be explained in more detail. The matrix notation takes the discrete sampling, in both space and time, of seismic data into account. A consequence of this discrete representation of seismic data is that all wave theory based operations are carried out as discrete summations and multiplications in the computer. Nice features of the matrix notation are its simplicity for the description of (one-way) wavefield operators, for example propagation and reflection, and the close relation with the actual implementation in a computer algorithm. The matrix notation will be introduced for 2-dimensional and 3-dimensional seismic data.

#### B.1 2-Dimensional wavefields

As the earth is considered as a time-invariant medium the seismic problem can be described in frequency components which are independent from each other. Consider a 2-dimensional wavefield, measured for only one component (e.g. pressure) at the surface at a constant depth level  $z_r$  and originating from a source at  $x_s$ , described by

$$p(x_r, x_s, z_r, t), \quad (\text{B.1})$$

Then the temporal Fourier transform of this wavefield is defined as

$$p(x_r, x_s, z_r, t) @>>> \mathcal{F}_t > P(x_r, x_s, z_r, \omega), \quad (\text{B.2})$$

where  $\mathcal{F}_t$  stands for the Fourier transformation from time to frequency. From Fourier theory it is known that the negative frequency components of the Fourier transformation of a real signal, are by definition equal to the complex conjugate of the positive frequency components. As the measured wavefield is a causal and real signal, the positive frequency components describe the wavefield completely. Therefore in the discretized version of equation (B.2) only the positive frequency components have

to be taken into account. The discretized version for one (positive) frequency component reads the so called data vector

$$\mathbf{P}(z_r) = [P(\Delta x_r, z_r, x_s), \dots, P(m\Delta x_r, z_r, x_s), \dots, P(M\Delta x_r, z_r, x_s)]^T,$$

where the dependency on frequency is omitted for notational convenience. Combining several monochromatic data vectors for different seismic experiments into one matrix gives (one seismic experiment: fixed  $x_s$ )

$$\mathbf{P}(z_r) = \begin{bmatrix} P(\Delta x_r, z_r, \Delta x_s) & \dots & \dots & P(\Delta x_r, z_r, n\Delta x_s) & \dots & P(\Delta x_r, z_r, N\Delta x_s) \\ P(2\Delta x_r, z_r, \Delta x_s) & \dots & \dots & P(2\Delta x_r, z_r, n\Delta x_s) & \dots & P(2\Delta x_r, z_r, N\Delta x_s) \\ \vdots & \ddots & \dots & \dots & \dots & \vdots \\ P(m\Delta x_r, z_r, \Delta x_s) & \dots & \dots & P(m\Delta x_r, z_r, n\Delta x_s) & \dots & P(m\Delta x_r, z_r, N\Delta x_s) \\ \vdots & \dots & \ddots & \dots & \dots & \vdots \\ P(M\Delta x_r, z_r, \Delta x_s) & \dots & \dots & P(M\Delta x_r, z_r, n\Delta x_s) & \dots & P(M\Delta x_r, z_r, N\Delta x_s) \end{bmatrix},$$

which is known as the data matrix and where the variable  $z_r$  indicates the depth level  $z = z_r$  to which the matrix is related to. Each element  $P_{m,n} = P(m\Delta x_r, z_r, n\Delta x_s)$  in the data matrix corresponds to a fixed receiver coordinate and a fixed lateral source coordinate. One column of the data matrix represents one monochromatic seismic experiment (common source gather) and one row represents one common receiver gather. The diagonal elements of the data matrix contain common offset data with the zero offset data on the main diagonal, the anti-diagonal elements contain common midpoint data. In figure B.1 a pictorial representation of the construction of the data matrix is shown. A shot record measured at the surface is transformed to the frequency-domain. One frequency component of this transformed shot record is placed in the data matrix as a column vector at its source position.

For a fixed spread configuration the data matrix is completely filled. However, for true seismic acquisition patterns the data matrix is generally differently filled due to the used acquisition pattern in the field. For example, missing near offsets can be recognized as a band matrix with the band around the diagonal filled with zeros, on the other hand one sided marine data has an upper or lower matrix structure. With the introduced matrix notation a lateral convolution operator (e.g. wavefield propagation) on a single frequency component of the wavefield is equivalent to a matrix-vector multiplication. As an example of a matrix operator working on the data matrix the one-way propagation matrix is discussed in more detail in the next subsection.

### Propagation operators

The  $\mathbf{W}$  matrices, defined in the forward model discussed in chapter 3, represent the operation of propagation of a wavefield from one depth level to another depth level

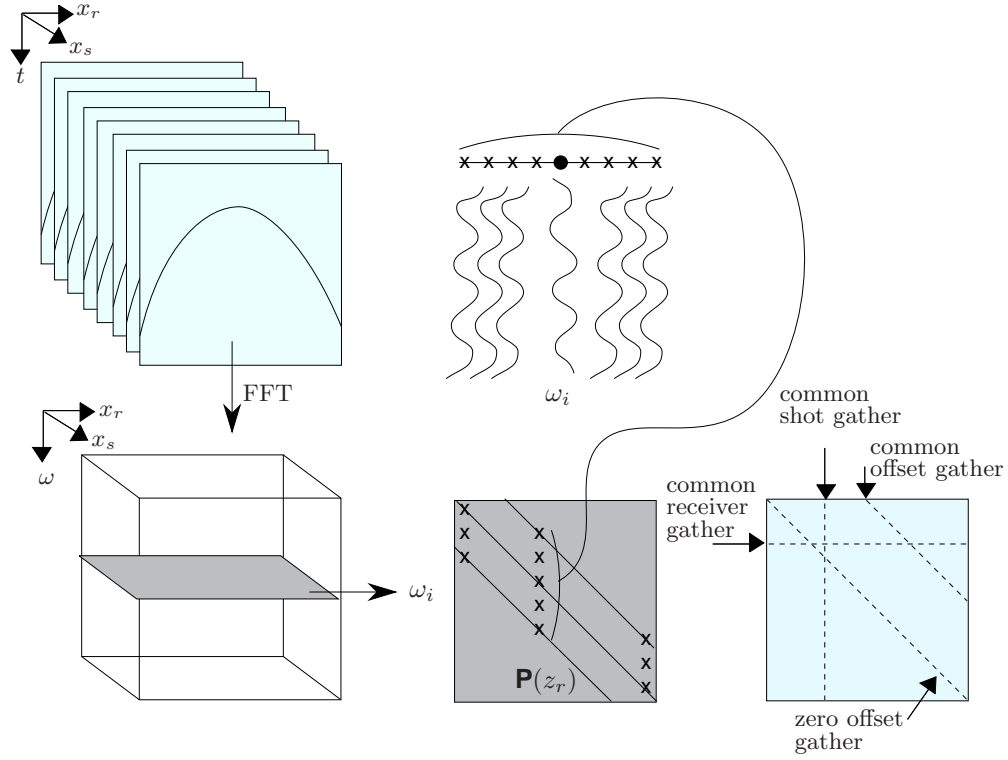


**Figure B.1** The definition of the data matrix  $\mathbf{P}(z_r)$ . The matrix  $\mathbf{P}(z_r)$  consists of one monochromatic seismic experiment combined for different shot positions into one matrix. Within the data matrix several well known seismic data gathers can be recognized.

as shown in figure B.2 and which is mathematically expressed by

$$\mathbf{P}^+(z_m) = \mathbf{W}^+(z_m, z_0) \mathbf{P}^+(z_0). \quad (\text{B.3})$$

One column vector of the data matrix (which represent the receivers from one shot) is extrapolated from depth level  $z_0$  to depth level  $z_m$  by a spatial convolution process. The convolution operators, obtained from one of the procedures described in appendix A, are placed as row vectors in the propagation matrix  $\mathbf{W}^+$ . Every single operator describes the propagation from one depth level to another depth level for the same lateral position. In figure B.2 it can be seen how one operator is stored as a row vector in the propagation matrix  $\mathbf{W}^+$ . For a 1-dimensional medium all the operators are the same for all lateral positions, meaning that the propagation matrix  $\mathbf{W}^+$  has a Toeplitz structure.

Note the similarity of the propagation matrix  $\mathbf{W}^+$  with the data matrix  $\mathbf{P}^+(z_0)$ . Note also an important difference. Opposed to the data matrix, which contains physical wavefields obtained from acoustic experiments, the propagation matrix con-

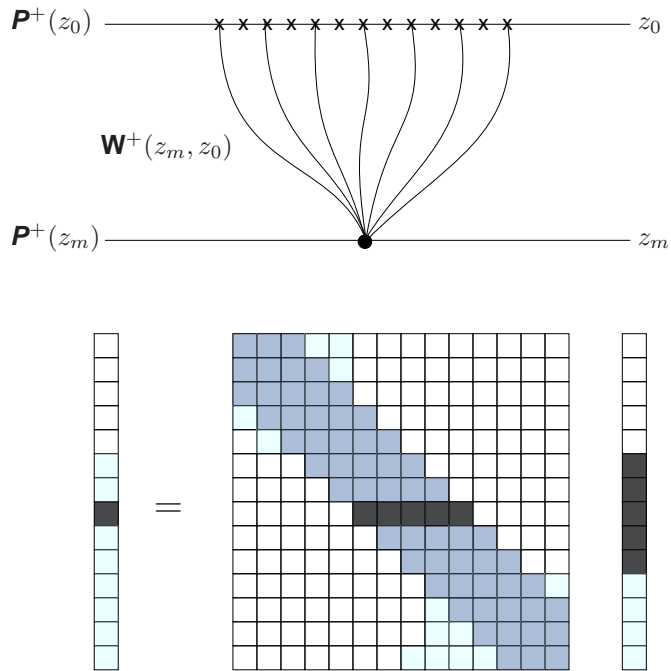


**Figure B.2** Pictorial presentation of the propagation matrix  $\mathbf{W}^+$ ; one extrapolation (convolution) operator for one lateral position is stored as a row vector in the propagation matrix. For a 1-dimensional medium  $\mathbf{W}^+$  is a Toeplitz matrix.

tains mathematical wavefields obtained numerically from the macro model and one of the optimization methods discussed in appendix A.

## B.2 3-Dimensional wavefields

The 3-dimensional measurements are combined in a 2-dimensional matrix, similar to the 2-dimensional case. Again all traces are transformed to the frequency domain and data matrices per Fourier component are constructed. The data, for all receivers in the  $x - y$  plane, of one shot record position are stored into one column of the data matrix as shown in figure B.3. Within this matrix notation one column still corresponds with a common source gather and one row with a common receiver gather. The matrix multiplications describe now 2-dimensional spatial convolution in the  $x - y$  direction. Note that diagonals do not contain common offset information anymore, except for the main diagonal (Verschuur, 1991).

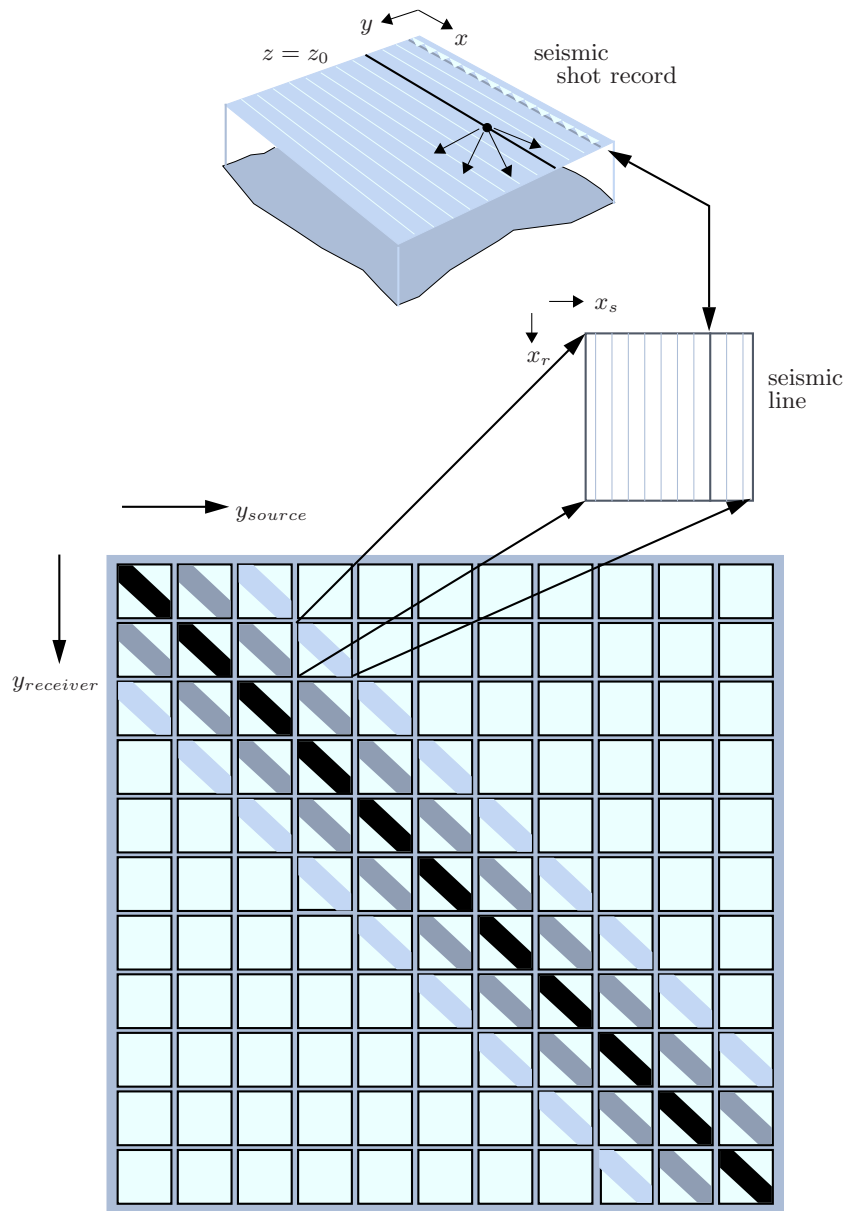


**Figure B.3** A data matrix for a 3D acquisition on a grid in the  $x - y$  plane consists of a 2D submatrix for each  $y$ -source coordinate and for each receiver  $y$ -coordinate. One column still describes a multi streamer shot record (in this example 5 streamers are shown) and one row describes a 3D common receiver gather (figure used with courtesy of Eric Verschuur).



# Appendix C

## Algorithms

CFP technology involves two focusing steps. The first focusing step transforms shot records to CFP gathers and the second focusing step transforms CFP gathers to image traces. In CFP technology preprocessing and velocity analysis occurs *between* the two focusing steps. In this appendix the calculation algorithms of the two focusing steps and the analysis modules are discussed. The difference between time and frequency processing is also explained and the numerical implementation of the time-domain scheme is discussed in more detail.

### C.1 Processing flow

The general block diagram for CFP processing is shown in figure C.1, where the emphasis is put on the data-control during the processing. To construct the CFP-gather from the shot records an initial focusing operator is needed. This initial operator can be based on stacking velocities or an initial macro model. In the latter case the initial focusing operator is calculated by positioning a dipole at the focus point followed by a forward modeling algorithm to calculate the response at the surface. Measuring the response at the detector positions yields an operator for focusing in detection and measuring the response at the source positions yields an operator for focusing in emission.

The first focusing step, where the important Fresnel stack takes place, is calculated by a convolution along the time axis of the traces in the shot record and the focusing operator. The result of the first focusing step can be compared with the focusing operator, indicated in figure C.1 by the move-out analysis block, and the focusing operator and/or macro model can be updated. In the comparison the operator must be time coincident with the focus point response in the CFP gather (principle of equal traveltime). Combining focus point responses for the same lateral position into one gather gives the CFP image gather which is calculated in the second focusing step. Every CFP image trace can be compared with a 'reference trace' to calculate the

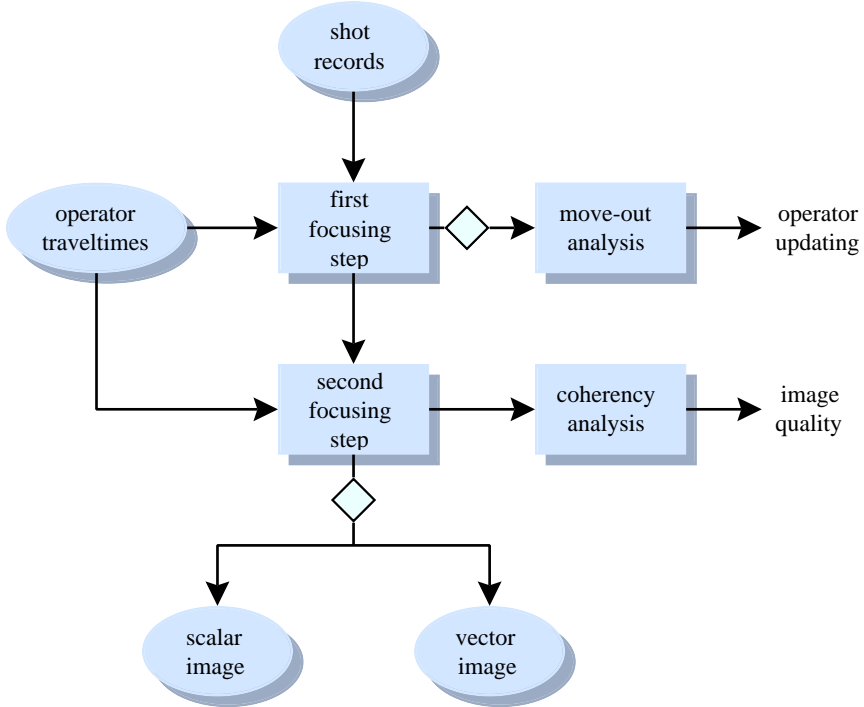


**Figure C.1** Schematic representation of the CFP algorithm. Note that the processing is done in a shot gather stream, which makes the in and output straightforward. The  $\diamond$  in the scheme means that the result for more than one shot record is needed to proceed in the scheme.

coherency in the CFP image gather. This coherency analysis is based on equation (5.3.3). The traces in a CFP image gather are added together to construct the one-way time image (scalar image). The  $\diamond$  in the scheme means that the result for more than one shot record is needed to proceed in the scheme. This means in the algorithm that either these traces must be stored in memory or on disk. For the direct calculation of the scalar image the only traces to be kept in memory are the traces representing the final result; the one-way time image. For the calculation of the vector image all the traces in a CFP gather are used. The vector image is obtained by a 2-dimensional convolution between the focusing operator and the CFP gather.

## C.2 Time- and Frequency-domain processing

The integral to be calculated for the first focusing step in detection is given by (after equation (4.19))

$$P^{-,s}(\mathbf{x}, \mathbf{x}_s) = \int_{\partial D_1} G^{+,*}(\mathbf{x}, \mathbf{x}_r) P^{-,s}(\mathbf{x}_r, \mathbf{x}_s) d^2 \mathbf{x}_r, \quad (\text{C.1})$$

where  $\partial D_1$  is the surface the detectors are positioned on and  $P^{-,s}(\mathbf{x}_r, \mathbf{x}_s)$  the observed upgoing wavefield after pre-processing, to remove the direct wave and the multiple reflections related to the surface. The Green's function occurring in equation (C.1) can be calculated in several ways. For this thesis two calculation methods are implemented; one carried out in the time-domain and another one in the frequency-domain.

The frequency domain method is the most accurate one because it uses equation (C.1) directly. The only assumptions are made in the calculation of  $G^{+,*}(\mathbf{x}, \mathbf{x}_r)$ , which is mainly determined by the accuracy of the macro model. A good method to calculate the Green's function is the recursive extrapolation technique based on the extrapolation operators discussed in appendix A.

For the time-domain method the Green's function in equation (C.1) is replaced with its ray-asymptotic form given by

$$G^{+,*}(\mathbf{x}, \mathbf{x}_r) \simeq A(\mathbf{x}, \mathbf{x}_r) \exp(j\omega\tau(\mathbf{x}, \mathbf{x}_r)), \quad (\text{C.2})$$

where  $\tau$  satisfies the Eikonal equation and  $A$  the transport equation. The traveltimes  $\tau$  can be calculated by making use of a ray-tracing program, or an Eikonal solver. The amplitudes of the Green's function,  $A$  can be approximated by  $\cos(\phi) \frac{\sqrt{j\omega}}{\sqrt{r}}$ , resulting in the expression

$$P^{-,s}(\mathbf{x}, \mathbf{x}_s) \approx \Delta x \sum_{\partial D_1} \cos(\phi) \frac{\sqrt{j\omega}}{\sqrt{r}} P^{-,s}(\mathbf{x}_r, \mathbf{x}_s) \exp(j\omega\tau(\mathbf{x}, \mathbf{x}_r)), \quad (\text{C.3})$$

where  $\sqrt{j\omega}$  represents the 2-dimensional propagation factor,  $\cos(\phi)$  the directivity of the dipole,  $\sqrt{r} = \sqrt{(z_0 - z_r)^2 + (x_0 - x_r)^2}$  the distance from the focus point  $(x_0, z_0)$  to the receiver position at  $(x_r, z_r)$  and  $\Delta x$  the distance between the receivers. Note that this linear distance does not describe the length of the ray-path correctly in inhomogeneous media.

For the time-domain calculation of one CFP trace for focusing in detection the traces in the shot record are shifted upward with the times given by the focusing operator. Which is equivalent to a convolution in the time domain with a time shifted delta function. The amplitude of this delta function is defined by the amplitudes belonging to the operator times. If the time given by the focusing operator does not fit on the discrete time-grid of the shot record a linear interpolation to the operator time is

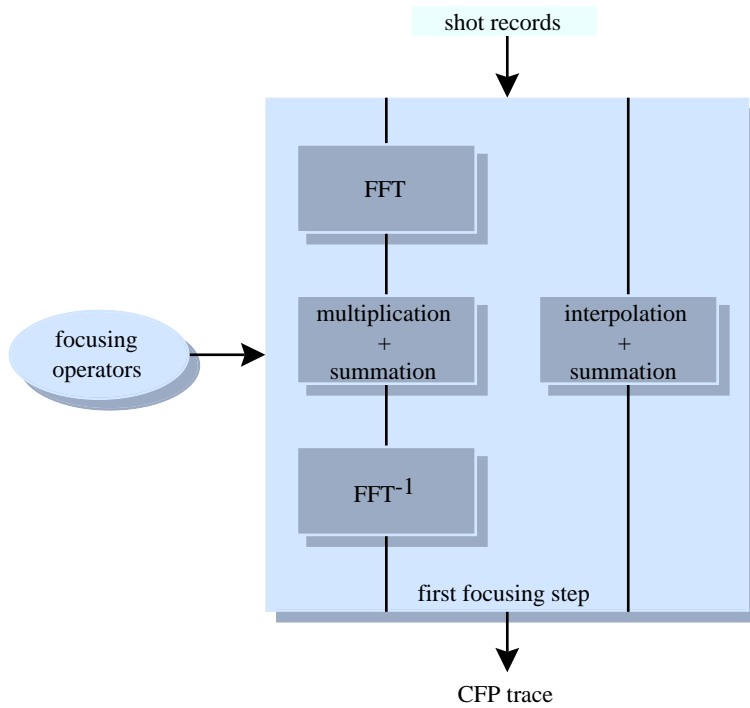


**Figure C.2** Difference between time and frequency processing for the first focusing step. Note that the great computation difference is the FFT.

carried out. Optional in the first focusing step is an additional time correction with the time defined by the traveltime between the focus point to the source position. This additional correction performs the move-out correction on the CFP trace and is useful in the move-out analysis.

The frequency-domain method is easier to implement, but takes much more computation time as shown in figure C.2. The shot record and the synthesis operator are both transformed to the frequency domain and multiplied with each other. Which is equivalent to a time convolution of the traces in the shot record and the traces in the focusing operator. After the multiplication the summation over all traces in the shot record is carried out and the resulting CFP trace is transformed back to the time-domain. In a homogeneous medium the main difference between the time and frequency method is that the time-domain method uses linear interpolation and the frequency-domain method uses sinc functions for the interpolation to calculate the CFP corrected traces of the shot record. For non-homogeneous media the time-domain method can only take one arrival time into account, the frequency domain method can take in principle all arrival times into account. For the extraction of AVO information the frequency-domain method is recommended, because it allows the best treatment of the amplitude information present in the data.

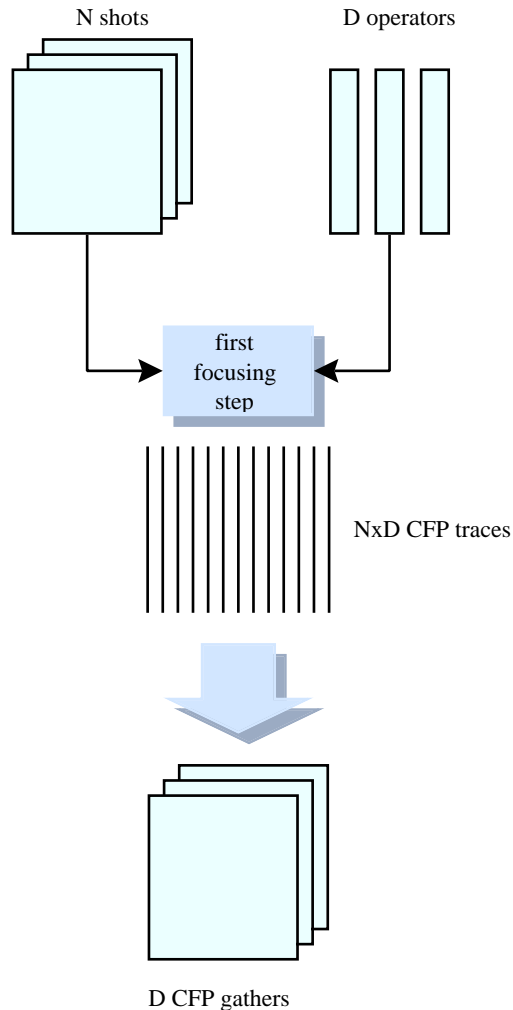


**Figure C.3** Scheme of the data flow used to calculate CFP gathers. For an efficient implementation the focusing operators are kept in memory. Every shot record gives one trace of a shot gather.

### C.3 Numerical implementation (time-domain)

The time-domain implementation of the CFP processing scheme works with any initial focusing operator defined by traveltimes and amplitudes as given in equation (C.2). The initial focusing operator used in the examples of this thesis are obtained with a finite difference calculation method based on the method and software of Vidale (1988). Vidale's method calculates traveltimes through any velocity structure

on a 2- or 3-dimensional numerical grid, amplitudes are not calculated in Vidale's scheme. The amplitudes belonging to the traveltimes are calculated by determining the shortest distance between the focus point and the receiver position, where ray bending is not included. The traveltimes and amplitudes of the focusing operators are stored as single traces in an operator file on disk. In the CFP calculation program the focusing operators are read into memory and stored in an operator table.

An alternative for using Vidale's operators in the first and second focusing step, are focusing operators based on a root mean-square velocity, as obtained after conventional NMO analysis. The advantage is that only a root mean-square velocity model has to be read in and the focusing operators can be calculated easily within the program. The big disadvantage is that a homogeneous medium assumption is used implicitly in this approach.

For every input shot record one CFP trace is calculated for all the defined focusing operators, which results in a collection of CFP traces as shown in figure C.3. A shot record contributes to a CFP gather if the lateral distance between the focus point and the source position does not exceed a certain distance set by the user. After all shot records have been treated the traces which belong to one focus point are collected and the CFP gather is available. In the scheme it is possible to write the already calculated CFP traces to disk and do the sorting into CFP gathers afterwards. If not that many CFP traces are calculated it is more convenient to keep them in memory. Optional in the processing scheme are a move-out correction to calculate the CFP move-out panel and a mute factor to remove the 'non-causal' events in the CFP gather, which occur before the times of the focusing operator. For focusing in emission the traces in every common receiver gather are used to construct the CFP trace. This means that to complete the summation along the source coordinate of the common receiver gather all the shot records which contain the receiver of interest have to be read in.

The second focusing step is carried out by combining time selections of the CFP traces generated in the first focusing step for focus points defined at the same lateral position as shown in figure C.4. The first focusing step is adjusted to this selection by calculation only those time samples in the CFP trace which are needed in the second focusing step. To carry out the second focusing step a synthesis operator is needed at every time sample. The focusing operators for times (or depths) in between two focusing operators of the first focusing step are obtained by linear interpolation of the operator times. The interpolated operators are used to correct the events in the CFP gather. If the correct operators are used all events in the CFP image gather should after the time correction align at the one-way image time. Due to the convergence of the focusing operators at higher offset a stretching is introduced in the second focusing step. The user can set a stretch mute factor to control the amount of stretching. The user can also control which shot record contributes to the image gather by restricting the maximum lateral distance between the shot record

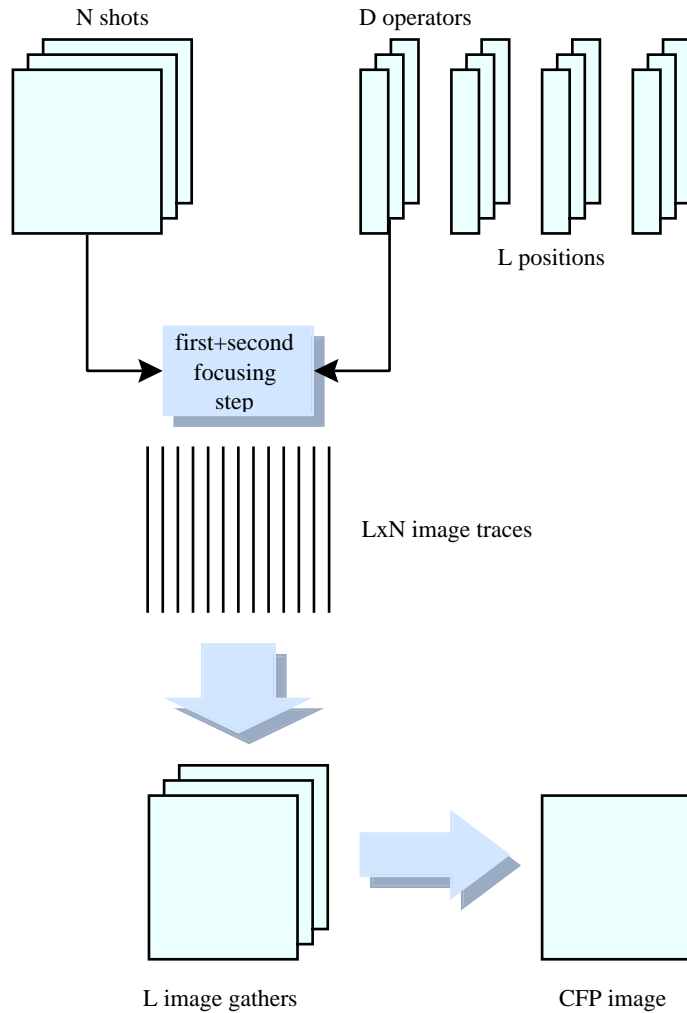


**Figure C.4** Scheme of the data flow used to calculate CFP image gathers. Note that it is possible to implement the first and second focusing step in an efficient way.

and the focus point.

The CFP image is calculated by a summation along the traces in CFP image gather. The result is positioned at the lateral position of the focusing operator at the one-way image time, or depth, of the synthesis operator. Looking at the shape of the focusing beams as presented chapter 5, the first focusing process may allow a coarse focus point sampling ( $\Delta T$ ) and still be accurate for the second focusing step. Typically  $\Delta T$  ranges from 40 to 100 [ms].



## Bibliography

---

Abramowitz, M. and Stegun, I. A. (1968). *Handbook of Mathematical Functions*. Dover publications Inc., New York.

Alá'i, R. (1997). *Improving predrilling views by pseudo seismic borehole data*. Ph.D. thesis, Delft University of Technology. in progress.

Alford, R. M., Kelly, K. R., and Boore, D. M. (1974). Accuracy of finite-difference modeling of the acoustic wave equation. *Geophysics*, **39**, 834–842.

Algazi, V. R., Suk, M., and Rim, C. S. (1986). Design of almost minimax FIR filters in one and two dimensions by WLS techniques. *IEEE Trans. Circuits and Systems*, **CAS-33**, 590–596.

Aminzadeh, F., Burkhard, N., Kunz, T., Nicoletis, L., and Rocca, F. (1995). 3-D modeling project; 3rd report. *The Leading Edge*, **15**, 125–128.

Berkhout, A. J. (1982). *Imaging of acoustic energy by wave field extrapolation (2nd edition)*. Elsevier, Amsterdam.

Berkhout, A. J. (1984). *Seismic resolution: resolving power of acoustic echo techniques*. Geophysical Press Ltd.

Berkhout, A. J. (1987). *Applied seismic wave theory*. Elsevier, Amsterdam.

Berkhout, A. J. (1992). Areal shot record technology. *Journal of Seismic Exploration*, **1**(2), 251–264.

Berkhout, A. J. (1996a). Pushing the limits of seismic imaging: part I. *Geophysics*, **61**, in print.

Berkhout, A. J. (1996b). Pushing the limits of seismic imaging: part II. *Geophysics*, **61**, in print.

Berkhout, A. J. and Rietveld, W. E. A. (1995). Prestack migration in terms of double dynamic focusing. In *65th Annual Internat. Mtg., Soc. Expl. Geophys., Expanded Abstracts*, pages 1228–1231. Soc. Expl. Geophys.

Berkhout, A. J. and Thorbecke, J. W. (1996). Regularization of prestack data. In *DOLPHIN: Optimum Data Acquisition Technology for Maximum Image Quality*, volume 1, chapter 4. Delft University of Technology.

Berkhout, A. J. and van Wulfften Palthe, D. W. (1979). Migration in terms of spatial deconvolution. *Geophysical Prospecting*, **27**, 261–291.

Berkhout, A. J. and Verschuur, D. J. (1996a). CFP migration and multiple scattering. In *DELPHI: From seismic measurements to rock and pore parameters*, volume 7, chapter 11. Delft University of Technology.

Berkhout, A. J. and Verschuur, D. J. (1996b). Pushing the limits of seismic imaging part III: CFP migration and multiple removal. In *DELPHI: From seismic measurements to rock and pore parameters*, volume 7, chapter 10. Delft University of Technology.

Berkhout, A. J. and Wapenaar, C. P. A. (1989). One-way versions of the Kirchhoff integral. *Geophysics*, **54**, 460–467.

Berkhout, A. J., Wapenaar, C. P. A., and Verschuur, D. J. (1996). CFP migration and mode-converted data. In *DELPHI: From seismic measurements to rock and pore parameters*, volume 7, chapter 12. Delft University of Technology.

Biondi, B. and Palacharla, G. (1994). 3D depth migration using rotated McClellan filters. In *Expanded Abstracts of Papers*, page B45. EAEG.

Black, J. L. and Brzostowski, M. A. (1994). Systematics of time-migration errors. *Geophysics*, **59**(9), 1419–1434.

Blacqui  re, G. (1989). *3D wave field extrapolation in seismic depth migration*. Ph.D. thesis, Delft University of Technology.

Blacqui  re, G. (1991). Optimized McClellan transformation filters applied in one-pass 3-D depth migration. In *Expanded Abstracts*, pages 1126–1129. SEG.

Blacqui  re, G., Debeye, H. W. J., Wapenaar, C. P. A., and Berkhout, A. J. (1989). 3D table-driven migration. *Geophysical Prospecting*, **37**(8), 925–958.

Bleistein, N. (1984). *Mathematical methods for wave phenomena*. Academic Press, Inc., Orlando.

Bojarski, N. N. (1983). Generalized reaction principles and reciprocity theorems for the wave equations, and the relationship between the time-advanced and time-retarded fields. *Journal of the Acoustical Society of America*, **74**, 281–285.

Born, M. and Wolf, E. (1970). *Principle of optics*. Pergamon press, New York, fourth edition.

Bracewell, R. N. (1986). *The Fourier transform and its applications, second edition*. McGraw-Hill, Singapore.

Claerbout, J. F. (1971). Towards a unified theory of reflector mapping. *Geophysics*, **36**, 467–481.

Claerbout, J. F. (1976). *Fundamentals of geophysical data processing*. McGraw-Hill.

Clayton, R. W. and Stolt, R. H. (1981). A Born-WKBJ inversion method for acoustic reflection data. *Geophysics*, **46**, 1559–1567.

Corones, J. (1975). Bremmer series that correct parabolic approximations. *Journal of Mathematical Analysis and Applications*, **50**, 361–372.

Cox, H. L. H. (1991). *Estimation of macro velocity models by wave field extrapolation*. Ph.D. thesis, Delft University of Technology.

de Bruin, C. (1992). *Linear AVO inversion by pre-stack depth migration*. Ph.D. thesis, Delft University of Technology.

de Hoop, A. T. (1988). Time-domain reciprocity theorems for acoustic wave fields in fluids with relaxation. *Journal of the Acoustical Society of America*, **84**, 1877–1882.

de Hoop, M. V. (1992). *Directional decomposition of transient acoustic wave fields*. Ph.D. thesis, Delft University of Technology.

Devaney, A. J. (1982). A filtered backpropagation algorithm for diffraction tomography. *Ultrasonic Imaging*, **4**, 336–350.

Esmersoy, C. and Oristaglio, M. L. (1988). Reverse-time wave-field extrapolation, imaging and inversion. *Geophysics*, **1**, 97–106.

Fishman, L., McCoy, J. J., and Wales, S. C. (1987). Factorization and path integration of the Helmholtz equation: Numerical algorithms. *Journal of the Acoustical Society of America*, **81**, 1355–1376.

Fokkema, J. T. and van den Berg, P. M. (1993). *Seismic applications of acoustic reciprocity*. Elsevier, Amsterdam.

French, W. S. (1974). Two-dimensional and three-dimensional migration of model-experiment reflection profiles. *Geophysics*, **39**, 265–277.

French, W. S. (1975). Computer migration of oblique seismic reflection profiles. *Geophysics*, **40**, 961–980.

Gaiser, J. E. (1994). Optimum transformation and filter structure for explicit finite-difference 3D migration. In *Expanded Abstracts of Papers*, page B42. EAEG.

Gardner, G. H. F. (1985). Migration of seismic data. In *Geophysics reprint series*, volume 4. Society of exploration geophysicists.

Gazdag, J. (1978). Wave equation migration with the phase-shift method. *Geophysics*, **43**, 1342–1351.

Geoltrain, S. and Brac, J. (1993). Can we image complex structures with first-arrival traveltimes? *Geophysics*, **58**, 564–575.

Gray, S. H. and May, W. P. (1994). Kirchhoff migration using eikonal equation traveltimes. *Geophysics*, **59**, 810–817.

Grimbergen, J. L. T., Wapenaar, C. P. A., and Dessing, F. J. (1996). Modal expansion of one-way operators in laterally varying media. *Geophysics*, page (submitted).

Hagedoorn, J. G. (1954). A process of seismic reflection interpretation. *Geophysical Prospecting*, **2**, 85–127.

Hale, D. (1991a). 3-D depth migration via McClellan transformations. *Geophysics*, **56**, 1778–1785.

Hale, D. (1991b). Stable explicit extrapolation of seismic wavefields. *Geophysics*, **56**, 1770–1777.

Hatton, L., Larner, K., and Gibson, B. S. (1990). Migration of seismic data from inhomogeneous media. *Geophysics*, **46**, 751–767.

Hazra, S. N. and Reddy, M. S. (1986). Design of circularly symmetric low-pass two-dimensional FIR digital filters using transformation. *IEEE Trans. Circuits and Systems*, **CAS-33**, 1022–1026.

Hegge, R. F. and Fokkema, J. T. (1996). Macro model updating by global inversion of CFP operators. In *66th Annual Internat. Mtg., Soc. Expl. Geophys., Expanded Abstracts*, page accepted. Soc. Expl. Geophys.

Herrmann, P. (1992). *Decomposition of multi-component measurements into P and S waves*. Ph.D. thesis, Delft University of Technology.

Hoff, J. D. (1995). *3D one-way wave field extrapolation by using 1D convolution operators*. Master's thesis, Delft University of Technology.

Holberg, O. (1988). Towards optimum one-way wave propagation. *Geophysical Prospecting*, **36**, 99–114.

Hondius, C. J. (1993). *Design of stress source arrays for predefined P- or S-wavefields*. Master's thesis, Delft University of Technology.

Hubral, P. (1977). Time migration-some ray theoretical aspects. *Geophysical Prospecting*, **25**, 738–745.

Hubral, P., Schleicher, J., and Tygel, M. (1996). A unified approach to 3-D seismic reflection imaging, Part I: Basic concepts. *Geophysics*, **61**, 742–758.

Hulshoff, A. (1993). *Design of source arrays for pure P- or S-wave radiation*. Master's thesis, Delft University of Technology.

Johnson, L. W. and Riess, R. D. (1977). *Numerical Analysis*. Addison-Wesley.

Kabir, M. M. N. and Verschuur, D. J. (1993). Parallel computing of the parabolic Radon transform - Application for CMP-based preprocessing. In *63rd Annual Internat. Mtg., Soc. Expl. Geophys., Expanded Abstracts*, volume 93, pages 193–196.

Kabir, M. N. N. (1997). *Macro model estimation of the complex subsurface using the common focus point technology*. Ph.D. thesis, Delft University of Technology. in progress.

Kabir, M. N. N. and Verschuur, D. J. (1996). Macro model estimation using primary and multiple reflections. In *DELPHI: From seismic measurements to rock and pore parameters*, volume 7, chapter 7. Delft University of Technology.

Kao, J., G.Li, and C.Yang (1994). Optimized 2D filters for 3D wavefield extrapolation on the massively parallel processors. In *Expanded Abstracts of Papers*, page B48. EAEG.

Kato, H. and Matsumoto, G. (1982). Design of circularly symmetric 2-D FIR digital filters using Fourier reconstruction technique. *IEEE Trans. Acoustics, Speech and Signal Processing*, **ASSP-30**, 505–508.

Koek, E. A. (1997). *Physical modeling of irregularly sampled data*. Ph.D. thesis, Delft University of Technology. in progress.

Koek, E. A., Faber, G., and Ongkiehong, L. (1996). Physical modelling of irregularly sampled data. In *58th Mtg. Eur. Assoc. Expl. Geophys., Extended Abstracts*, page Session:B048. Eur. Assoc. Expl. Geophys.

Kogbetliantz, E. G. (1960). *Generation of Elementary Functions*, volume 1 of *Mathematical Methods for Digital Computers*, pages 7–35. New York: John Wiley & Sons.

Krebs, J. R., Fara, D. R., and Berlin, A. E. (1996). Accurate migration using offset-checkshot surveys. In *58th Mtg. Eur. Assoc. Expl. Geophys., Extended Abstracts*, page Session:X020. Eur. Assoc. Expl. Geophys.

Larner, K. and Hatton, L. (1990). Wave equation migration: two approaches. *First Break*, **8**(12), 433–448.

Lindsey, J. P. (1989). The Fresnel zone and its interpretive significance. *The Leading Edge*, **8**, 33–39.

Loewenthal, D., Roberson, R., and Sherwood, J. (1976). The wave equation applied to migration. *Geophysical Prospecting*, **24**, 380–399.

McClellan, J. H. (1973). The design of two-dimensional digital filters by transformations. In *Princeton Conf. on Inform. Sci. and Sys.*, pages 247–251. Princeton.

McClellan, J. H. and Chan, D. S. K. (1977). A 2-D FIR filter structure derived from the Chebychev recursion. *IEEE Trans. Circuits and Systems*, **CAS-24**, 372–378.

McClellan, J. H. and Parks, T. W. (1972). Equiripple approximation of fan filters. *Geophysics*, **37**, 573–583.

McClellan, J. H., Parks, T. W., and Rabiner, L. R. (1973). A computer program for designing optimum FIR linear phase digital filters. *IEEE Trans. Audio Electroacoust.*, **AU-21**, 506–526.

McMechan, G. A. (1983). Migration by extrapolation of time dependent boundary values. *Geophysical Prospecting*, **31**, 413–420.

Mersereau, R. M., Mecklenbräuker, W. F. G., and Quatieri, T. F. (1976). McClellan transformations for two-dimensional digital filtering: I-design. *IEEE Trans. Circuits and Systems*, **CAS-23**, 405–413.

Morton, S. A. and Thorbecke, J. W. (1996). Automating prestack migration analysis using common focus point gathers. In *66th Annual Internat. Mtg., Soc. Expl. Geophys., Expanded Abstracts*, pages 1262–1265. Soc. Expl. Geophys.

Mufti, I. R., Pita, J. A., and Huntley, R. W. (1996). Finite-difference depth migration of exploration-scale 3-D seismic data. *Geophysics*, **61**, 776–794.

Nautiyal, A., Gray, S. H., Whitmore, N. D., and Garing, J. D. (1993). Stability versus accuracy for an explicit wavefield extrapolation operator. *Geophysics*, **58**, 277–283.

Neidell, N. S. and Taner, T. M. (1971). Semblance and other coherency measures for multichannel data. *Geophysics*, **36**, 482–497.

O'Brien, M. J. and Gray, S. H. (1996). Can we image beneath salt? *The Leading Edge*, **15**, 17–22.

Oristaglio, M. L. (1989). An inverse scattering formula that uses all the data. *Inverse Problems*, **5**, 1097–1105.

Parkes, G. and Hatton, L. (1987). Towards a systematic understanding of the effects of velocity model errors on depth and time migration of seismic data. *First Break*, **5**(4), 121–133.

Parks, T. W. and Burrus, C. S. (1987). *Digital Filter Design*. New York: John Wiley & Sons.

Pessoa, F. (1990). *Het boek der rusteloosheid door Bernardo Soares*. Arbeiderspers, Amsterdam.

Powell, M. J. D. (1981). *Approximations theory and methods*. Cambridge University Press.

Press, W. H., Teukolsky, S. A., Vetterling, W. T., and Flannery, B. P. (1992). *Numerical recipes in C, The art of scientific computing*. Cambridge University Press, second edition.

Rabiner, L. R. and Gold, B. (1975). *Theory and application of Digital Signal Processing*. Prentice Hall.

Ralston, A. (1967). *Rational Chebyshev approximation*, volume 2 of *Mathematical Methods for Digital Computers*, pages 264–285. New York: John Wiley & Sons.

Rayleigh, J. W. (1894). *Theory of sound*, volume II. Macmillan, London, 1945; second, edition.

Rice, J. R. and Usow, K. H. (1968). The Lawson algorithm and extensions. *Math. Comp.*, **22**, 118–127.

Rieber, F. (1936). A new reflection system with controlled directional sensitivity. *Geophysics*, **1**, 97–106.

Rietveld, W. E. A. (1995). *Controlled illumination in prestack seismic migration*. Ph.D. thesis, Delft University of Technology.

Rietveld, W. E. A. and Thorbecke, J. W. (1994). Areal shot record technology: macro model estimation. In *DELPHI: From seismic measurements to rock and pore parameters*, volume 5, chapter 10. Delft University of Technology.

Schneider, W. A. (1978). Integral formulation for migration in two-dimensions and three-dimensions. *Geophysics*, **43**(1), 49–76.

Schultz, P. S. and Sherwood, J. W. C. (1980). Depth migration before stack. *Geophysics*, **45**, 376–393.

Sollid, A. and Arntsen, B. (1994). Cost-effective 3D one-pass depth migration. *Geophysical Prospecting*, **42**, 755–776.

Soubaras, R. (1996). Explicit 3-D migration using equiripple polynomial expansion and Laplacian synthesis. *Geophysics*, **61**, 1386–1393.

Stolt, R. H. (1978). Migration by Fourier transform. *Geophysics*, **43**(1), 23–48.

Tarantola, A. (1984a). Inversion of seismic reflection data in the acoustic approximation. *Geophysics*, **49**, 1259–1266.

Tarantola, A. (1984b). Linearized inversion of seismic reflection data. *Geophysical Prospecting*, **32**, 998–1015.

Thorbecke, J. W. (1992). Weathered layer corrections. In *DELPHI: From seismic measurements to rock and pore parameters*, volume 3, chapter 4. Delft University of Technology.

Thorbecke, J. W. (1994). Estimation of near surface effects; an alternative approach to statics. In *DELPHI: From seismic measurements to rock and pore parameters*, volume 5, chapter 3. Delft University of Technology.

Thorbecke, J. W. (1995). 3D Wave field extrapolation; a comparison between different methods. <http://wwwak.tn.tudelft.nl/jan/articles/3Doperators.ps.Z>.

Thorbecke, J. W. and Berkhouw, A. J. (1993). Estimation of near surface effects. In *DELPHI: From seismic measurements to rock and pore parameters*, volume 4, chapter 3. Delft University of Technology.

Thorbecke, J. W. and Berkhouw, A. J. (1994). 3-D recursive extrapolation operators: An overview. In *64th Annual Internat. Mtg., Soc. Expl. Geophys., Expanded Abstracts*, pages 1262–1265. Soc. Expl. Geophys.

Thorbecke, J. W. and Berkhouw, A. J. (1995). 3-D recursive extrapolation operators - A comparison. In *57th Mtg. Eur. Assoc. Expl. Geophys., Extended Abstracts*, page Session:P094. Eur. Assoc. Expl. Geophys.

Thorbecke, J. W. and Rietveld, W. E. A. (1994). Optimum extrapolation operators - a comparison. In *56th Mtg. Eur. Assoc. Expl. Geophys., Extended Abstracts*, page Session:P105. Eur. Assoc. Expl. Geophys.

Thorbecke, J. W., Berkhouw, A. J., and Wapenaar, C. P. A. (1992). Weathered layer corrections in combination with wavefield decomposition. In *54th Mtg. Eur. Assoc. Expl. Geophys., Abstracts*, pages 558–559. Eur. Assoc. Expl. Geophys.

Timmerman, J. I. H. (1993). *Removal of finite aperture artefacts*. Master's thesis, Delft University of Technology.

Tits, A. L. and Zhou, L. H. (1996). User's guide for CFSQP version 2.4: A C-code for solving (large scale) constrained nonlinear (minimax) optimization problems, generating iterates satisfying all inequality constraints. personal notes from the author.

Ursin, B. (1983). Review of elastic and electromagnetic wave propagation in horizontally layered media. *Geophysics*, **48**, 1063–1081.

Verschuur, D. J. (1991). *Surface related multiple elimination, an inversion approach*. Ph.D. thesis, Delft University of Technology.

Verschuur, D. J., Berkhouit, A. J., and Wapenaar, C. P. A. (1992). Adaptive surface-related multiple elimination. *Geophysics*, **57**(9), 1166–1177.

Versteeg, R. and Grau, G. (1991). The Marmousi experience . In *EAEG workshop on practical aspects of seismic data inversion*. Eur. Assoc. Expl. Geophys.

Vidale, J. (1988). Finite-difference calculation of travel times. *Bulletin of the Seismological Society of America*, **78**(6), 2062–2076.

Wapenaar, C. P. A. (1991). On finite aperture artefacts. Technical report, Delft University of Technology.

Wapenaar, C. P. A. (1996a). One-way representations of seismic data. *Geophysical Journal International*, **127**, 178–188.

Wapenaar, C. P. A. (1996b). Reciprocity theorems for two-way and one-way wave vectors: a comparison. *Journal of the Acoustical Society of America*, **100**, (December issue).

Wapenaar, C. P. A. (1996c). Short note: Reciprocity of one-way propagators. *Geophysics*, ?, submitted for publication.

Wapenaar, C. P. A. (1997). Three-dimensional migration of cross-spread data: resolution and amplitude aspects. *Geophysics*, **62**, (accepted).

Wapenaar, C. P. A. and Berkhouit, A. J. (1989). *Elastic wave field extrapolation*. Elsevier, Amsterdam.

Wapenaar, C. P. A. and Grimbergen, J. L. T. (1996). Reciprocity theorems for one-way wave fields. *Geophysical Journal International*, **127**, 169–177.

Wapenaar, C. P. A., Peels, G. L., Budejicky, V., and Berkhouit, A. J. (1989). Inverse extrapolation of primary seismic waves. *Geophysics*, **54**(7), 853–863.



# Summary

---

## Common Focus Point Technology

The subject of this thesis is a new method for imaging of seismic data and is based on the systems oriented **WRW** model. This new imaging procedure can be considered as a conventional Kirchhoff migration broken up into two separate focusing steps. By dividing the imaging step into two separate focusing steps the understanding of the seismic migration process has been made easier. The result after one focusing step, called the Common Focus Point gather, is a very convenient domain for analysis on seismic data. For example, traveltime and amplitude analysis can be carried out in the CFP domain in a straightforward manner. One of the most important contributions of the CFP technology is the possibility to estimate the correct focusing operators without estimating a macro model. In this way a high quality seismic image can be generated without knowing the underlying macro model.

To construct the CFP-gather from the shot records an initial focusing operator is needed. This initial operator can be based on stacking velocities or an initial macro model. In the latter case the initial focusing operator is calculated by positioning a source at the focus point followed by a forward modeling algorithm to calculate the response at the surface. Measuring the response at the detector positions yields the time-reversed operator for focusing in detection and measuring the response at the source positions yields the time-reversed operator for focusing in emission. Using this initial focusing operator, a trace of the Common Focus Point gather is constructed by a frequency-domain multiplication between the traces of the focusing operators and the traces in the shot record followed by an integration over all the receivers present in the shot record. The most important contribution in the integration result is determined by the Fresnel zone which contribution is defined by the ray-path from the source position via the focus point to the surface.

Once the complete CFP gather is built the focus point response can be compared with the focusing operator. If the correct focusing operator is used then the principle of equal traveltime holds, which means that the traveltime of the time-reversed focusing operator is equal to the traveltime of the focus point response. If the wrong operator is used the principle of equal traveltime does not hold anymore and

the focusing operator must be updated for a correct focusing result. The updated focusing operator can be found in between the traveltimes of the focus point response and the erroneous focusing operator. A convenient choice is the travelttime in the middle of the focus point response and the focusing operator. With this updated operator a new CFP gather can be constructed and the principle of equal travelttime can be used again to check the result. In most cases one or two iterations are sufficient to arrive at a correct focusing operator. Once the correct operator has been found the second focusing step can be carried out.

In the second focusing step the information in the focus point response is added together to construct the image. For this step the same focusing operator as used in the first focusing step can be used again. The imaging result is positioned on the same lateral position as the defined focus point at one-way image time or depth. The one-way image time is defined as the time a wave needs to travel from the focus point to the surface, where the lateral position at the surface is the same as the focus point. Due to the tube-like shape of the focusing beam only a limited number of focusing operators is needed in the first focusing step to illuminate the complete subsurface.

The examples in this thesis demonstrate the new opportunities of the CFP technology in operator updating and structural imaging. By dividing the imaging process into two focusing steps the problems in structural imaging are investigated again, but now with the tools made available by the double focusing procedure. Based of the CFP technology new ideas are developed for AVO analysis, reflector dip estimation, regularization of irregular data, resolution analysis and 3-dimensional imaging. By computing the so-called focusing beams, the influence of the data acquisition geometry on the migration result can be clearly demonstrated. Based on the operator updating process an automatic operator updating scheme is currently developed, which makes it possible to compute an image without user interaction. The collection of estimated focusing operators that are generated during the structural imaging process will be used in the future to estimate the macro model by a one-way tomographic inversion process (global inversion).

## Samenvatting

---

### Een techniek gebaseerd op metingen met een gemeenschappelijk brandpunt

In de seismiek worden technieken gebruikt om seismische metingen aan het aardoppervlak om te zetten in een afbeelding van de ondergrond. In dit proefschrift wordt een nieuwe seismische afbeeldingstechniek geïntroduceerd die gebaseerd is op het systeem-georienteerde **WRW** model. De nieuwe techniek bestaat uit twee aparte focusseringsstappen die na elkaar worden uitgevoerd. Dit in tegenstelling tot het conventionele Kirchhoff migratie proces, dat de twee focusserings stappen tegelijkertijd uitvoert. Het opsplitsen in twee focusseringsstappen verhoogt het inzicht in het afbeeldingsproces. Het resultaat na de eerste focusserings stap is een dataset met een gemeenschappelijk brandpunt (afgekort CFP) en kan gebruikt worden voor het analyseren van reflectie-tijden en reflectie-amplituden. Het is mogelijk om de correcte focusseringsoperator te schatten zonder gebruik te maken van een voortplantingssnelheidmodel. Hiermee is het mogelijk om een afbeelding van de ondergrond te maken zonder dat er enige kennis is vereist over de voortplantingssnelheid van die ondergrond.

Een CFP meting wordt berekend door een focusseringsoperator toe te passen op de seismische metingen. De focusseringsoperator is gebaseerd op een gemiddelde voortplantingssnelheid als functie van de verticale looptijd of op een snelheidsmodel gegeven als functie van de diepte. In dit laatste geval wordt de operator berekend door een bron op het brandpunt te plaatsen gevolgd door toepassing van een algoritme om het golfveld, afkomstig van het brandpunt, aan het aardoppervlak te berekenen. Een operator voor focusering in detectie wordt verkregen door het golfveld te meten op de posities van de ontvangers, een meting op de bronposities defineert een operator voor focusering in zenden. Een CFP dataset wordt geconstrueerd door een frequentie-domein vermenigvuldiging (in tijd een convolutie) tussen de traces van de seismische meting en de focusserings operator, gevolgd door een optelling over de ontvangers in één meting. De belangrijkste bijdrage in het resultaat na optelling wordt bepaald door de Fresnel-zone. De Fresnel-zone is gedefineerd rond het golppad dat loopt vanaf de bronpositie via het brandpunt naar het aardoppervlak.

Als de complete CFP dataset is opgebouwd dan kan de responsie van het brandpunt vergeleken worden met de focuserings operator. Als de juiste operator is gebruikt dan is de looptijd van de, in tijd gespiegelde, operator gelijk aan de looptijd van de responsie van het brandpunt. Als er een verkeerde operator is gebruikt dan is dit niet het geval en moet de focussing operator worden aangepast om een correct focuseringsresultaat te verkrijgen. De correcte focuseringsoperator kan gevonden worden tussen de looptijden van de (verkeerde) focuseringsoperator en de responsie van het brandpunt. Een handige keuze voor de gecorrigeerde operator is een looptijd precies in het midden van de respons en de operator. Met deze gecorrigeerde operator kan een nieuwe CFP dataset worden berekend en het resultaat kan weer worden geanalyseerd. In de meeste gevallen zijn een of twee iteraties genoeg om tot de correcte operator te komen. Als de correcte operator is gevonden dan kan de tweede focuseringsstap worden uitgevoerd.

In de tweede focuseringsstap wordt alle informatie van het brandpunt bij elkaar opgeteld om zo een afbeelding van het focus punt te verkrijgen. Voor deze tweede focuseringsstap moet dezelfde operator als in de eerste focuseringsstap gebruikt worden. Het resultaat wordt op dezelfde laterale positie neergezet als het brandpunt, in een-weg afbeeldingstijd, of direct in diepte. De een-weg afbeeldingstijd is gedefineerd als de looptijd die een golf nodig heeft om van het brandpunt naar dezelfde laterale positie aan het oppervlak te komen. Rond het brandpunt is de belichting niet beperkt tot het brandpunt alleen. Dit maakt het mogelijk om in de eerste focuseringsstap een beperkt aantal brandpunten te gebruiken om toch de gehele ondergrond voldoende te belichten. In de tweede focuserings stap worden geinterpoleerde operatoren gebruikt om op alle diepten de afbeelding te kunnen berekenen.

De voorbeelden in dit proefschrift laten de mogelijkheden zien van de CFP technologie voor het schatten van de operatoren en, vervolgens, het afbeelden van structuren in de ondergrond. Door het afbeeldingsproces te verdelen in twee aparte focuseringsstappen is er een fundamenteel nieuwe manier onstaan om het afbeeldingsproces te verbeteren. Zo zijn er nieuwe ideeën ontwikkeld voor amplitude analyse, schatting van de helling van een reflector, het regulariseren van onregelmatig gesampelde data, het uitvoeren van een resolutieanalyse en het afbeelden in een 3-dimensionale ruimte. De focuserende bundel geeft informatie over de invloed van de acquisitie op het afbeeldingsresultaat. Op het ogenblik wordt er in de industrie een automatische operatorcorrectie algoritme ontworpen dat gebaseerd is op het operator correctieschema. Dit project maakt het mogelijk om een afbeelding van de ondergrond te maken zonder interactie van de gebruiker. De verzameling van operatoren, die tijdens het afbeeldingsproces worden verkregen, kan in de toekomst gebruikt worden om een snelheidssmodel te schatten door gebruik te maken van een een-weg tomographisch inversie proces.

# Curriculum vitae

---

## PERSONAL

Name: Jan Willem Thorbecke  
Born: November 9 1965, Oostzaan  
Nationality: Dutch

## EDUCATION

1978 - 1979: 'Zaanlands Lyceum', Zaandam  
1979 - 1985: 'R.S.G. Brokede', Breukelen  
1985 - 1991: Applied Earth Sciences, Delft University of Technology  
MSc thesis, Technical Geophysics,  
"Scattering by a strip in a homogeneous medium"  
1991 - 1991: Philosophy, Leiden University  
1991 - 1996: Applied Physics, Delft University of Technology  
PhD thesis, Laboratory of Seismics and Acoustics,  
"Common Focus Point Technology"

## WORK

1996 - present: research geophysicist at Cray Research /  
Silicon Graphics, De Meern, The Netherlands

